Influenza virus assembly: targeting and transport of viral ribonucleoprotein complexes

DISSERTATION

zur Erlangung des akademischen Grades
d o c t o r r e r u m n a t u r a l i u m
(Dr. rer. nat.)
im Fach Biophysik

eingereicht an der
Lebenswissenschaftlichen Fakultät
der Humboldt-Universität zu Berlin

von
Diplom-Biophysikerin Chris Tina Höfer

Präsident der Humboldt-Universität zu Berlin
Prof. Dr. Jan-Hendrik Olbertz

Dekan der Lebenswissenschaftlichen Fakultät
Prof. Dr. Richard Lucius

Gutachter: 1. Prof. Dr. Andreas Herrmann

2. PD Dr. Michael Veit

3. PD Dr. Thorsten Wolff

Tag der mündlichen Prüfung: 08. Mai 2015

Zusammenfassung

Influenzaviren sind membranumhüllte Viren mit segmentiertem, negativsträngigem RNA-Genom. Sie replizieren im Zellkern und knospen von der apikalen Plasmamembran der Wirtszelle. Die Virusassemblierung erfordert den Transport der neu gebildeten viralen Komponenten zur Plasmamembran. Die Virionen bestehen aus einer Hüllmembran, einer vom viralen Matrixprotein M1 gebildeten Schicht unterhalb der Hüllmembran sowie den viralen RNA-Genomsegmenten, die in Form von viralen Ribonukleoprotein (vRNP)-Komplexen vorliegen. Die Hüllmembran wird von der Plasmamembran der Wirtszelle abgeleitet und enthält die drei viralen Transmembranproteine.Während der apikale Transport der viralen Transmembran-Glykoproteine seit vielen Jahren untersucht wird und die intrinsischen Signale hierfür identifiziert werden konnten, ist bisher wenig darüber bekannt, wie das virale Genom transportiert, an die Knospungszone rekrutiert und in die neu entstehenden Virionen eingebaut wird. Ein Ziel dieser Arbeit war es, experimentelle Grundlagen zu etablieren, um neu gebildete vRNPs und deren Transport in lebenden, infizierten Zellen zu untersuchen. Außerdem wurden mögliche molekulare Mechanismen für den zielgerichteten Transport der vRNPs analysiert, insbesondere die Membranassoziation und die intrinsischen Lokalisationssignale des Nukleoproteins (NP), eines Hauptbestandteils der vRNPs.

Im ersten Teil dieser Arbeit wurden die Membranbindungseigenschaften von vRNPs *in vitro* mittels Flotationsversuchen mit großen unilamellaren Vesikeln verschiedener Lipidzusammensetzung untersucht. Es wurde festgestellt, dass vRNPs allein nicht in der Lage sind, mit Modell-Lipidmembranen zu assoziieren. Vor dem Hintergrund der Hypothese, dass vRNPs durch Interaktion mit M1 an zelluläre Membranen binden, wurde zusätzlich M1 in diese Versuche eingebracht. Die Ergebnisse zeigen, dass M1 in der Tat eine Bindung der vRNPs an negativ geladene Membranen vermittelt und somit in der Lage sein könnte, die Assoziation von vRNPs an Transportvesikel oder an die virale Knospungszone zu befördern. Des Weiteren wurden Phosphatidylinositole in die Lipidbindungsstudien miteinbezogen. Es handelt sich hierbei um eine kleine Gruppe zellulärer Phospholipide, die unter anderem an Signaltransduktionsprozessen, Membrantransport und der Festlegung spezifischer Charakteristika von Organellen beteiligt sind. Es konnte eine Interaktion zwischen M1 und Phosphatidylinositol-4-phosphat (PtdIns(4)P) detektiert werden, welche überraschenderweise eine gleichzeitige Interaktion von M1 mit vRNPs auszuschließen scheint. Die physiologische Bedeutung dieser Beobachtung für die Virusreplikation wird diskutiert.

Im Weiteren wurden Transport und Lokalisation von vRNPs im zellulären Kontext betrachtet. Hierbei wurden die Lokalisation, die subzelluläre Dynamik sowie ortsspezifische Affinitäten von NP charakterisiert, was durch die Expression von fluoreszierenden NP-Fusionsproteinen

und Fluoreszenz-Photoaktivierungsmessungen unter Verwendung von obligatorisch monomeren NP-Mutanten möglich war. Es wird gezeigt, dass NP keine bevorzugte Assoziation mit bestimmten cytoplasmatischen Strukturen oder zellulären Membranen durch intrinsische Affinität aufweist. Allerdings konnte eine ausgeprägte Interaktion des NP mit dem Zellkern festgestellt werden, sowie unterschiedliche Affinitäten zu verschiedenen Kernstrukturen. Ein NP-Konstrukt mit Kernexportsequenz wurde exprimiert, um die NP-Konzentration im Kern zu senken, wodurch es möglich war, Nucleoli und kleine punktförmige NP-reiche Domänen als Kerndomänen mit der höchsten Affinität für NP zu identifizieren. Die kleinen punktförmigen Domänen ähneln den Kernkörperchen (engl. „nuclear bodies“) und werden daher hier als NP-Körperchen bezeichnet. Die auffallend hohen Affinitäten der beiden Kernstrukturen für NP wurden mittels Fluoreszenz-Photoaktivierung bestätigt. Die Verringerung der NP-Konzentration im Zellkern erleichterte zudem Kolokalisationsstudien und ermöglichte die Beobachtung, dass NP-Körperchen häufig in unmittelbarer Nähe zu Cajal-Körperchen und PML-Körperchen zu finden sind. Dies konnte auch für das NP-Wildtyp-Protein bestätigt werden.

Die Rolle der spezifischen Lokalisation des NP in bestimmten Kernstrukturen wird hier im Hinblick auf die Virusreplikation und die funktionelle Organisation des Kerns diskutiert. Es wird vermutet, dass die starke Bindung des NP an Nucleoli möglicherweise die bereits beschriebene Auflösung der Nucleoli während der viralen Replikation erfordert, um Komponenten der Nucleoli rekrutieren zu können. Des Weiteren wird in Betracht gezogen, dass die gezielte Lokalisation des NP angrenzend an PML-Körperchen für die Lokalisation ganzer vRNP-Komplexe in räumlicher Nähe zu Orten der zellulären SUMOylierung und der Bildung von Kernexportkomplexen von Bedeutung sein könnte.

Schlussendlich hatte diese Arbeit zum Ziel, Methoden zu etablieren, um die Dynamik neu gebildeter vRNPs während der Virusassemblierung in lebenden Zellen zu studieren. In einem ersten Ansatz gelang es, rekombinante Viren mit einem Tetracystein (TC)-Tag in der NP Sequenz herzustellen. Diese konnten in infizierten Zellen spezifisch fluoreszenzmarkiert werden, erwiesen sich jedoch als ungeeignet für die Beobachtung dynamischer Prozesse, was vermutlich auf eine Vernetzung der TC-Tags durch bifunktionale Farbstoffmoleküle zurückzuführen ist. In einem zweiten Ansatz wurde die Coexpression von fluoreszierenden NP-Fusionsproteinen in infizierten Zellen optimiert, um neu entstehende vRNPs durch Inkorporation dieser NP-Konstrukte zu markieren. Die fluoreszenzmarkierten Partikel konnten während des cytoplasmatischen und nucleocytoplasmatischen Transports beobachtet werden und auch der Co-Transport mit Rab11-positiven Recycling-Endosomen konnte verfolgt werden. Die Analysen der Bewegungen einzelner Partikel (engl. *Single particle tracking*) zeigen bisher unbekannte Details des vRNP-Transportes auf. Die Partikel erfahren einen relativ schnellen, gerichteten Transport im unmittelbaren Anschluss an den Kernexport,

was auf eine direkte Verbindung zwischen dem Kernexport und einem Cytoskelett-vermittelten cytoplasmatischen Transport schließen lässt. Weiterhin wurde beobachtet, dass die markierten Teilchen auch nach Ankunft an der Plasmamembran eine hohe Mobilität zeigen und offenbar entlang der Plasmamembran weiter transportiert werden. Auf Grundlage dieser Beobachtungen werden hier drei Phasen des cytoplasmatischen vRNP-Transports vorgeschlagen: im ersten Schritt ein unmittelbar auf den Kernexport folgender Cytoskelett-vermittelter gerichteter Transport, im zweiten Schritt ein vesikulärer, Rab11-vermittelter Transport zwischen dem Mikrotubuli-organisierenden Zentrum und der Plasmamembran und schließlich eine Bewegung entlang der Plasmamembran, was den letzten Schritt im Transport zur viralen Knospungszone darstellen könnte.

Summary

Influenza viruses are negative-stranded enveloped RNA viruses which replicate in the cell nucleus and bud from the apical plasma membrane of the host cell. Virus assembly requires the delivery of the different viral components to the budding site. The viruses consist of a viral membrane, harboring the three viral transmembrane proteins, a matrix layer underneath the membrane, formed by the matrix protein M1, and the viral genomic RNA segments which are packed in form of viral ribonucleoprotein (vRNP) complexes. While apical targeting of the viral transmembrane proteins has been studied for many years and intrinsic targeting signals were identified, it is still poorly understood how the viral genome is transported, targeted and incorporated into progeny virus particles. It was one major goal of this study to establish an experimental system that enables analysis of progeny vRNPs in living infected cells. Further, potential targeting mechanisms including membrane association and intrinsic targeting of the nucleoprotein (NP), as a major component of vRNP complexes, were examined.

In the first part of this study, membrane binding properties of vRNPs were investigated *in vitro*, performing flotation with large unilamellar vesicles of various lipid compositions. It was found that vRNPs alone are not able to associate with model lipid membranes. Since it is a long-standing hypothesis that vRNPs might be targeted to cellular membranes through interaction with M1, M1 was included in these experiments. The results indicate that M1 is in fact able to mediate binding of vRNPs to negatively charged lipid bilayers and may thus support association of vRNPs with vesicular transport or with the budding site. Phosphoinositides were further included in lipid binding studies. They represent a small fraction of cellular phospholipids involved in signaling processes, membrane trafficking and

organelle identity. Interaction of M1 with phosphatidylinositol-4-phosphate (PtdIns(4)P) was detected, and surprisingly, this interaction seems to exclude simultaneous binding of M1 to vRNPs. The physiological relevance of this observation for viral replication is discussed.

Targeting and transport of vRNPs were then addressed in a cellular context. Expression of fluorescent NP fusion proteins and fluorescence photoactivation studies in combination with the use of obligate monomeric NP mutants allowed characterizing the localization, the subcellular dynamics and site-specific affinities of NP. The results show that NP does not target to specific cytoplasmic structures or cellular membranes by intrinsic affinity. However, NP extensively interacted with the nuclear compartment and targeted different subnuclear domains with different affinities. Expression of an NP construct with a nuclear export sequence to lower the nuclear NP concentration revealed nucleoli and small punctate NP-rich domains as nuclear domains with the highest affinities for NP. These latter domains resemble nuclear bodies and are therefore here termed NP bodies. Their prominent affinities for NP were confirmed by fluorescence photoactivation. Nuclear depletion of NP further facilitated colocalization analysis and revealed that NP bodies frequently localized in close proximity to Cajal bodies and PML bodies. This could be confirmed also for wild-type NP.

The role of NP subnuclear targeting is discussed in the light of virus replication and in the context of functional nuclear organization. It is proposed that high-affinity binding of NP to nucleoli might require the previously reported nucleolar fragmentation process in ongoing viral replication for recruitment of nucleolar factors. It is further considered that targeting of NP to the vicinity of PML NBs might be of importance for the targeting of entire vRNP complexes close to sites of cellular SUMOylation and vRNP nuclear export complex formation.

Finally, this study aimed at developing an experimental approach for monitoring the dynamics of progeny vRNPs during virus assembly in living cells. In a first approach, recombinant viruses encoding a tetracysteine (TC)-tag in the NP coding sequence were successfully generated and could be specifically labeled during virus infection. Yet, they proved unsuitable for the detection of dynamic processes during virus infection, possibly due to crosslinking of TC-tags through the bifunctional dye molecules. In a second approach, coexpression of fluorescent NP fusion proteins in infected cells was optimized in order to label progeny vRNPs by incorporation of fluorescently tagged NP molecules. Fluorescently tagged complexes were successfully monitored during cytoplasmic and nuclear-cytoplasmic transport. Further, cotransport with Rab11-positive recycling endosomes was demonstrated. An experimental approach is thus provided for investigations of progeny vRNPs in living infected cells. Notably, the results from single particle tracking reveal yet unrecognized aspects of vRNP transport. Particles were found to undergo relatively rapid directional transport immediately subsequent to nuclear export, indicating a link between nuclear export

and cytoskeleton-assisted cytoplasmic transport. It was further observed that particles continue to move underneath the plasma membrane after arrival. According to these observations, three stages of cytoplasmic vRNP transport are suggested: in the first stage, cytoskeleton-assisted long-range directional transport subsequent to nuclear exit, in the second stage, Rab11-vesicular cytoplasmic transport between the microtubule organizing center and the plasma membrane and, finally, transport underneath the plasma membrane, which might represent the final step of targeting to the viral budding site.

Abbreviations

Standard abbreviations for units of measurement, metric prefixes, chemical elements, nucleic and amino acid sequences are used according to the International system of units (SI) and the IUPAC (International Union of Pure and Applied Chemistry) nomenclature and are not included in the following list of abbreviations.

aa	amino acid
AO	acridine orange
APS	ammonium persulfate
ATCC	American Type Culture Collection (resource center)
A.U.	arbitrary units
b	bases
BAL	British Anti-Lewisite (2,3-dimercapto-1-propanol)
BSA	bovine serum albumin
BCA	bicinchoninic acid
C-	carboxy-
CB	Cajal body
cDNA	copy DNA (synthesized from RNA template)
CFP	cyan fluorescent protein
CHO	chinese hamster ovary (cell line)
Chol	cholesterol
CMV	cytomegalovirus
CPE	cytopathic effect
cRNA/RNP	complementary RNA/RNP (the viral replication intermediate)
DAB	diaminobenzidine
DAPI	4′,6-Diamidin-2-phenylindol
ddH_2O	double-distilled water
DI	defective-interfering
DMEM	Dulbecco's Modified Eagle Medium
DMSO	dimethyl sulfoxide
DNA	deoxyribonucleic acid
dNTP	desoxyribonucleosidtriphosphate (dATP, dCTP, dGTP, dTTP)
DO	di-oleoyl

DP	di-palmitoyl
DPBS	Dulbecco`s phosphate buffered saline
ds	double-stranded
EDT	1,2-ethanedithiol
EDTA	ethylenediaminetetraacetic acid
EM	electron microscopy
ER	endoplasmic reticulum
FBS	fetal bovine serum
FISH	fluorescence *in situ* hybridization
FlAsH	fluorescein arsenical hairpin binder
FPV	fowl plague virus
FRET	fluorescence resonance energy transfer
fw	forward (primer sense)
x **g**	standard gravitational acceleration (9.81 m s^{-2})
HA	hemagglutinin
HEPES	4-(2-hydroxyethyl) piperazine-1-ethanesulfonic acid
HRP	horseradish peroxidase
IF	immunofluorescence
IFN	interferon
IgG	immunoglobulin G
IUPAC	International Union of Pure and Applied Chemistry
K_D	dissociation constant
LUV	large unilamellar vesicle
M	mol L^{-1}
MAPK	mitogen-activated protein kinase
MDCK	Madin-Darby canine kidney (cell line)
mEYFP	monomeric enhanced yellow fluorescent protein
MOI	multiplicity of infection
mRNA	messenger RNA
MTOC	microtubule organizing center
MW	molecular weight
N-	amino-
NA	neuraminidase
N.A.	numerical aperture

NBD	nitrobenzoxadiazole (7-nitrobenz-2-oxa-1,3-diazol-4-yl)
NB	nuclear body
NEP	nuclear export protein
NES	nuclear export signal
NLS	nuclear localization sequence
NP	nucleoprotein
NS1	non-structural protein 1
nt	nucleotide
ORF	open reading frame
p.i.	post infection
p.t.	post transfection
PA	polymerase acidic protein
PAGE	polyacrylamide gel electrophoresis
PARP1	poly(ADP-ribose)-polymerase 1
PB1, PB2	polymerase basic protein 1, polymerase basic protein 2
PBS	phosphate buffered saline
PC	phosphatidylcholine
PCR	polymerase chain reaction
PE	phosphatidylethanoamine
PI	propidium iodide
PML	promyelocytic leukemia (protein)
PMT	photomultiplier tube
Pol I	RNA polymerase I
Pol II	RNA polymerase II
PARP1	poly(ADP-ribose)-polymerase 1
PS	phosphatidylserine
PdtIns	phosphatidylinositol
PtdIns(x)P	phosphatidylinositol(x)phosphate (x = 3, 4 or 5)
PtdIns(x,y)P_2	phosphatidylinositol(x,y)bisphosphate (x, y = 3, 4 or 5)
PtdIns(3,4,5)P_3	phosphatidylinositol(3,4,5)trisphosphate
PKR	protein kinase R
ReAsH	resofurin arsenical hairpin binder
RE	recycling endosome
rev	reverse (primer sense)

RFP	red fluorescent protein
RNA	ribonucleic acid
RNP	ribonucleoprotein
RT	room temperature
RT-PCR	reverse-transcription polymerase chain reaction
sca	small Cajal body-specific
SD	standard deviation
SDS	sodium dodecyl sulfate
SEM	standard error of the mean
SI	*Système international d'unités* (engl. International system of units)
SIM	SUMO interaction motif
SM	sphingomyelin
S/N	signal-to-noise
sn	small nuclear
sno	small nucleolar
SPT	single particle tracking
ss	single-stranded
SUMO	small ubiquitin-like modifier
TBS	Tris buffered saline
TEM	transmission electron microscopy
TEMED	N,N,N',N'-tetramethyl-ethane-1,2-diamine
TPCK	N-*p*-Tosyl-L-phenylalanine chloromethyl ketone
TREX	transcription/export (multiprotein complex)
Tris	2-Amino-2-hydroxymethyl-propane-1,3-diol
UTR	untranslated region
UV	ultraviolet
v/v	volume per volume
vRNA	viral RNA
vRNP	viral ribonucleoprotein
w/v	weight per volume
w/w	weight per weight
WB	Western blotting
WSN	Wilson Smith Neurotropic (Influenza virus strain)
wt	wild-type

Index

1 Introduction

1.1 Influenza A viruses

Influenza viruses are enveloped viruses with a segmented single-stranded negative-sense RNA genome. They belong to the family of *Orthomyxoviridae* and are divided into three genera, designated as Influenza A, B and C viruses. While all three genera are human pathogens, Influenza A viruses are responsible for the most severe cases of disease, causing recurring seasonal epidemics and occasional pandemics. The World Health Organization states that three to five million cases of severe illness are caused by Influenza viruses every year and up to 500 000 deaths.

This study focuses on Influenza A viruses. The natural hosts of Influenza A viruses are wild aquatic birds, but the host range extends also to domestic birds, pigs, horses and marine mammals as well as humans [1]. Influenza A viruses are divided into different subtypes according to antigenic variations that occur among the viral surface proteins hemagglutinin (HA) and neuraminidase (NA). There are currently 18 known HA-subtypes (H) and 11 known NA-subtypes (N). All known Influenza virus subtypes (except for newly discovered H17, H18, N10 and N11 which have been isolated from bats [2]) circulate in birds [3]. The prevalent circulating strains in the human population are H3N2 and H1N1 subtypes, but also H2N2, H5N1, H7N2, H7N3, H7N7, H7N9, H9N2 and H10N8 subtypes have been isolated from humans.

The large reservoir of Influenza viruses in animal populations and the possibility of genetic reassortment and crossing of species barriers constitute the major pandemic potential of Influenza viruses [4,5]. New Influenza virus strains with unprecedented properties can suddenly emerge by reassortment of genetic material from different Influenza A subtypes (termed “genetic shift”), but also minor changes in form of mutations can gradually accumulate in the viral genome and enable the virus to evade the host immune recognition (termed “genetic drift”), causing recurring outbreaks of circulating Influenza virus strains. The genetic drift is an important parameter of Influenza virus epidemiology since Influenza viruses like many other RNA viruses experience a high mutation frequency due to a high error rate of the viral RNA-dependent RNA polymerase. It replicates the viral genome with approximately one mutation per replicated genome [6].

1.2 Structure and morphology of Influenza A virions

The Influenza A virus genome consists of eight single-stranded (ss) RNA segments which are packed in form of viral ribonucleoprotein (vRNP) complexes and which are surrounded by the viral lipid envelope. Influenza A virions are pleomorphic. They display spherical and filamentous shapes with diameters of about 100 nm [7,8]. The length of filamentous particles varies widely and can reach more than 20 µm. Viral morphology was shown to be influenced by several viral proteins and by the host cell [9,10,11,12,13,14,15]. Cryo-electron microscopy images of spherical and filamentous virions are shown in Fig. 1 A–C.

The viral envelope is derived from the host cell plasma membrane, and – compared to the donor membrane – it is specifically enriched in sphingolipids and cholesterol [16]. It also harbors the three viral transmembrane proteins: the two glycoproteins, HA and NA, and the proton channel M2 (Fig. 1D). While the homotrimeric HA plays a major role during cell entry, being responsible for receptor binding and membrane fusion [17], the homotetrameric NA supports release and spread of progeny virions by enzymatic cleavage of sialic acids, which are the major HA-binding motif on cell surfaces. [18,19]. HA is the most abundant among the viral envelope proteins (about 80 %) [20]. Sphingolipid- and cholesterol-rich lipid domains in the plasma membrane of infected cells, which are also termed lipid rafts, are thought to serve as platforms for virus assembly and envelope fomation since both HA and NA are targeted to raft domains by intrinsic affinity, leading to local concentration and clustering [21]. In case of M2, only a few copies of the protein are embedded in the viral membrane, even though it is abundantly expressed in infected cells [22,23]. Unlike HA and NA, M2 does not partition into raft domains [24,25], even though it is a cholesterol-binding protein [26]. It forms a homotetrameric proton channel [27,28] and is critically involved in pH-dependent uncoating of the viral genome [29]. Furthermore, M2 is required for membrane scission and release of budding virus particles [30].

Underneath the viral membrane, the matrix protein M1 forms a layer in close contact to the viral membrane [31,32]. M1 is most highly conserved among Influenza A virus proteins [33] and it is also the most abundant protein within virus particles (see Tab. 1). It is considered to play a central role during virus assembly since it interacts with all other viral components, including the viral membrane and M1 itself [21,34]. It polymerizes underneath the membrane, forming a two-dimensional lattice, which is relatively flexible and enables a wide range of curvature as shown by cryo-electron microscopy [31]. This seems to be an important basis for the reported pleomorphism of Influenza viruses. In filamentous virions, M1 was shown to form a highly ordered helical arrangement, yielding a cylindrical shape, while M1 in spherical

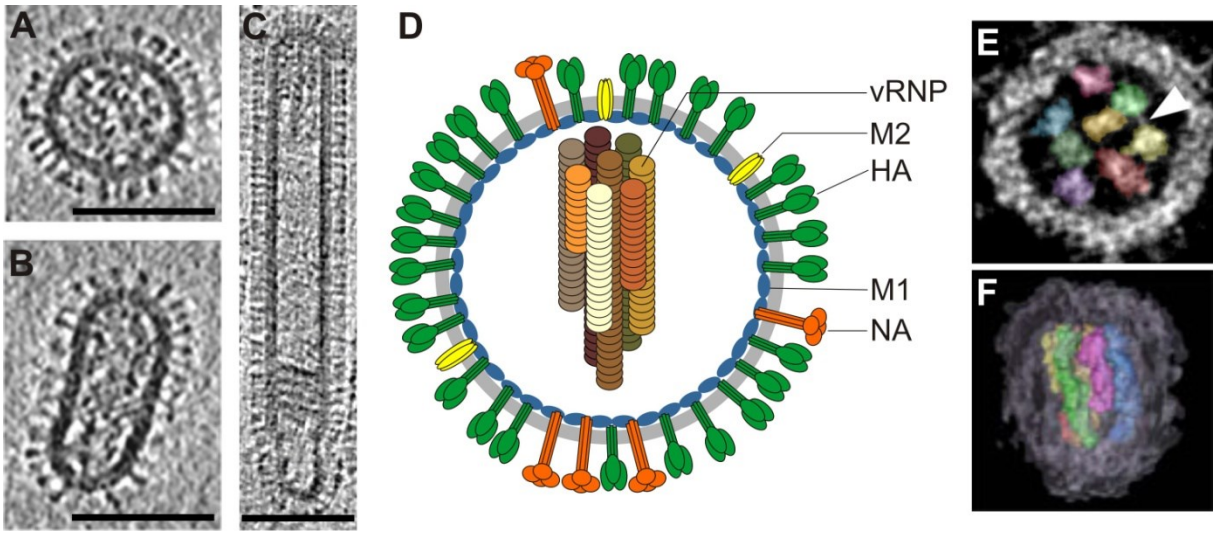

Fig. 1: Structure and morphology of Influenza A viruses. (A-C) Influenza A viruses are pleomorphic. Cryo-electronmicrographs show a (A) spherical, (B) elongated and (C) filamentous virus particle (images taken from [8] and [31]). (D) Schematic representation of an Influenza A virus particle. (E, F) Scanning transmission electron tomography images (from [35]). A transverse section of a virus particle shows the characteristic 7+1 arrangement of eight vRNPs, which are represented in pseudo color (E). A three-dimensional model, reconstructed from tomography data, shows a virus particle along the longitudinal axis of the vRNPs (F). Scale bar, 100 nm.

particles seems to adopt a less ordered conformation and spiral structure. These findings are consistent with reports that M1 is an important determinant of viral morphology [12,13,36,37]. M1 is thought to be specifically recruited to the site of virus assembly and budding through interaction with the cytoplasmic tails of the viral transmembrane proteins [24,38,39,40], and upon oligomerization and in intact viral particles, it might crosslink the components of the viral envelope [41]. M1 is further a well-established membrane-binding protein. In addition to studies demonstrating membrane association via electrostatic interaction [42,43,44,45], several studies suggested partial insertion of M1 into lipid membranes [46,47,48,49] and M1-membrane interaction of non-electrostatic nature [50,51]. Whether M1 might affect viral morphology and virus budding by inducing or stabilizing membrane curvature through direct membrane interaction, or whether this requires additionally (or primarily) interactions with the viral transmembrane proteins is still unclear (reviewed in [34]).

The viral core underneath the matrix layer comprises the genomic vRNPs. vRNPs are flexible double-helical rod-like structures with a diameter of about 12 nm and between 30 and 120 nm in length [52,53]. Each vRNP consists of a viral RNA (vRNA) segment, multiple copies of the nucleoprotein (NP) and the heterotrimeric viral RNA-dependent RNA polymerase comprising subunits PB1, PB2 and PA [54]. vRNPs represent transcription- and replication-competent

units [54]. A list of the 8 vRNA segments and their encoded proteins is given in Tab. 1. More detailed information on vRNP structure and genome organization is given in section 1.3.

In a large fraction of virus particles and independent from viral morphology, vRNPs are incorporated as a highly organized set of eight vRNPs. The rod-like structures of differing lengths are arranged in a distinct pattern: they form a parallel bundle of seven segments surrounding a central segment (Fig. 1 E, F). At one end, the multisegmental arrangement is attached to the viral envelope, which inside budding virions was found to be the budding tip [8,31,35,53,55]. Most virions comprise eight unique vRNAs and thus a complete set of the viral genome [56]. Also filamentous particles do not contain more than eight vRNPs, the majority of the viral inner volume being empty [31,53].

A small number of the viral nuclear export protein (NEP), previously known as non-structural

Tab. 1: RNA segments and proteins of Influenza A viruses (adapted from [59], further including data from [60,61,62,63,64,65]). Viral proteins are multifunctional proteins. The main currently known protein functions are indicated.

RNA segment	number of nucleotides	**gene product(s)**	number of amino acids	molecules per virion	function
1	2341	**PB2**	759	30–60	viral polymerase subunit; mRNA cap binding
2	2341	**PB1**	757	30–60	viral polymerase subunit; RNA polymerase activity
		PB1-F2	87	–	mitochondrial targeting, induction of apoptosis
		PB1-N40	718	–	unknown
3	2233	**PA**	716	30–60	viral polymerase subunit; endonuclease activity
		PA-X	270	–	virulence factor
		PA-N155	562	–	unknown
		PA-N182	535	–	unknown
4	1778	**HA**	566	500	envelope glycoprotein; receptor binding, membrane fusion
5	1565	**NP**	498	1000	encapsidation of vRNA and cRNA, nuclear targeting of vRNPs
6	1413	**NA**	454	100	envelope glycoprotein; neuraminidase activity, virus release
7	1027	**M1**	252	3000	matrix protein; virus assembly, vRNP nucleocytoplasmic transport
		M2	97	20–60	proton channel; viral uncoating, membrane scission
		M42	99	–	proton channel
8	890	**NS1**	230	–	non-structural protein; interferon antagonist, posttranscriptional regulation
		NS2/NEP	121	130–200	structural protein; vRNP nuclear export
		NS3	187	–	unknown

protein 2 (NS2), can further be found within virus particles [57,58]. NEP mediates the nuclear export of vRNPs during infection [66,67]. Its localization within virus particles is yet unknown.

Through interaction with vRNPs, it is assumed that M1 can link the viral genome to the viral envelope and promote incorporation of vRNPs into budding virions [68]. This is consistent with findings that deletion of HA and NA cytoplasmic tails causes reduction of both M1 and vRNP incorporation into virions [9,24]. However, except for the site of vRNP attachment, regular contacts between vRNPs and the matrix layer inside virions along the length of vRNPs are not observed [31]. On the other hand, it was shown that the interaction strength between M1 and vRNPs correlates with viral morphology [69], and furthermore, specific NP residues and their interplay with M1 were found to determine viral morphology [14]. This suggests that interactions between M1 and vRNPs might indeed play an important role during virus formation.

1.3 Genome organization and structure of vRNP complexes

The Influenza A virus genome has a total size of about 13,600 nucleotides (nt). It is subdivided into eight vRNA segments, which range between 890 and 2341 nt in length (Tab. 1). Each vRNA segment comprises a central coding region and 3′ and 5′ terminal untranslated regions (UTRs) (Fig. 2). Each segment encodes one to four viral proteins. The UTRs can be further subdivided into two regions: a segment-specific sequence (8–45 nt) and furthermore 12 and 13 highly conserved nucleotides at the 3′ and 5′ end, respectively. These 12 and 13 nt are conserved in all vRNA segments and among all Influenza A virus strains [70]. They are partially complementary and represent the bipartite viral promoter, which is recognized by the viral polymerase in both vRNA and positive-sense complementary RNA (cRNA) [71,72]. 3′ and 5′ termini were reported to form a corkscrew structure in both cRNA and vRNA. This structure features two short intrastrand hairpin loops, a single bulged unpaired nucleotide and a short interstrand base-paired region (Fig. 3A) [73,74,75,76]. Despite similarities, structural differences were reported between cRNA and vRNA promoter structures that might explain differential recognition by the viral polymerase [77]. Indeed, different regions on PB1 were reported to be involved in promoter binding on cRNA and vRNA, respectively [78,79], and also subunit PA was reported to be differentially involved in binding of cRNA and vRNA promoter regions [80]. (For further information on the promoter structure and its function, see also section 1.4.3.2.)

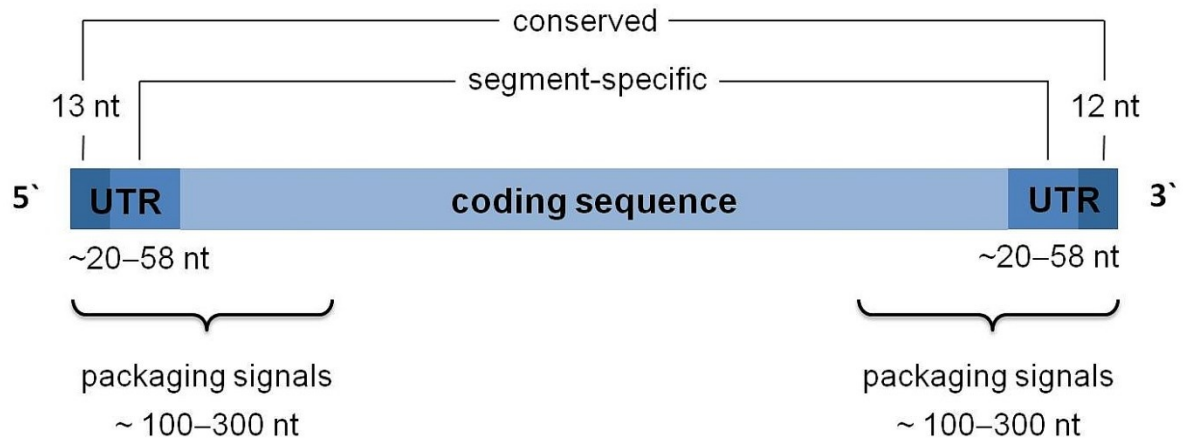

Fig. 2: Model of genomic vRNA structure. The eight genomic vRNA segments comprise 890–2341 nt and share common characteristic features. They all harbour a central coding sequence, which is flanked by terminal untranslated regions (UTRs). The first 13 nt at the 5' end and 12 nt at the 3' end are highly conserved among vRNA segments of all Influenza A virus strains. The UTRs comprise furthermore segment-specific sequences of variable lengths (8–45 nt). Packaging signals for genome incorporation into progeny virions were mapped to regions of 100–300 nt at both ends, spanning the UTRs and part of the coding sequence.

Genomic vRNA segments and cRNA replication intermediates are packed in form of RNP complexes (Fig. 3) [81,82]. Viral RNPs consist of viral single-stranded RNA, a heterotrimeric viral RNA-dependent RNA polymerase complex and multiple copies of NP. They are flexible rod-like structures with a diameter of about 12 nm and between 30 and 120 nm in length [52,53]. vRNPs reportedly maintain their structural integrity throughout the replication cycle and further represent the minimal replicative unit of Influenza viruses [83]. They are capable of transcription and replication, and a complete set of eight vRNPs is sufficient to initiate infection and virus production in cells [84,85,86].

Within RNP complexes, each RNA segment is coated by NP along its phosphate-sugar backbone [87], and the RNA-protein strand is folded back on itself and twisted into a supercoiled double-helical structure (Fig. 3A) [52,82]. Cryo-electron microscopy studies revealed a loop at one end of native vRNPs and binding of the viral polymerase complex to the other end. The two antiparallel NP-RNA strands were furthermore shown to associate with each other, apparently by interaction between NP molecules, forming a double helical structure with a major and a minor groove (Fig. 3 B–D) [88,89].

NP cooperatively polymerizes onto the RNA strand and forms the protein scaffold, while RNA is thought to be wrapped around the NP core on the outside [90,91,92,93]. While the RNA backbone electrostatically interacts with NP with high affinity, the RNA nucleotide bases are exposed to the solvent, which makes them accessible for viral transcription and replication [87,91]. Viral RNPs are consistently sensitive to RNAse digestion [94,95]. NP

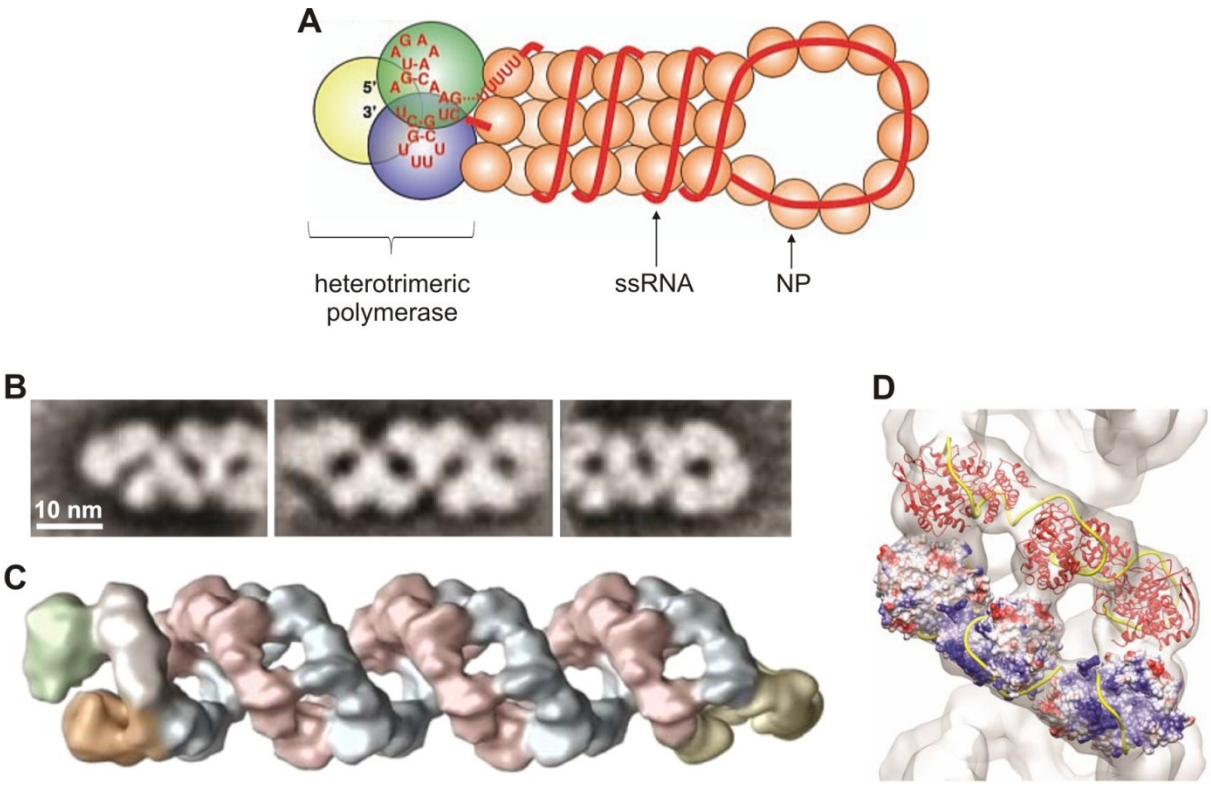

Fig. 3: Structure of Influenza A virus ribonucleoprotein complexes. (A) Model of a vRNP complex (adapted from [54]). Single-stranded vRNA is shown to be wrapped around a double-helical NP core and to associate with the heterotrimeric polymerase complex via its 3′ and 5′ terminal sequences. The highly conserved 3′ and 5′ terminal sequences are depicted according to the corkscrew model of the viral promoter structure. The position of the polyadenylation signal is indicated as oligo-U stretch. (B) Two-dimensional averages of cryo-EM images show the polymerase-containing terminus (left), the central region (middle) and the terminal loop region (right) of native vRNPs. (C) Model for vRNP structure based on separate three-dimensional cryo-EM reconstruction from central and terminal parts of native vRNPs. (D) Docking of the NP crystal structure ([93]) into antiparallel strands of the double helical vRNP reconstruction shown in (C). NP subunits of the lower strand are shown with electrostatic surface potentials and subunits of the opposite strand are shown as ribbon structure. The position of the RNA, inferred from the surface potential, is indicated as yellow line. Note that differing results for docking of NP were implicated in [89,92]. Images B, C and D were taken and adapted from [88].

binds to RNA without sequence-specificity. It binds with a stoichiometry of about 24 nt per NP subunit [52,93,96]. While it was postulated that NP melts RNA secondary structure by scaffolding the RNA backbone, susceptibility of model RNPs to double strand-specific RNAse nevertheless seems to indicate the existence of some base-paired regions [87,91]. (For further information on the role of NP in vRNP formation, see also section 1.5.)

One copy of the heterotrimeric viral polymerase is attached to the loose ends of each RNP complex, thus conferring a closed conformation to viral RNP complexes [88,89,94,97]. The presence of the viral polymerase on vRNP complexes enables vRNPs to initiate the first round of transcription in newly infected cells. Differential recognition of cRNA and vRNA promoter structures was further suggested to enable selective nuclear export of vRNPs, while cRNPs are retained in the nucleus [98]. Packaging signals of vRNPs for incorporation into progeny

virus particles were further reported to reside within the first 100–300 nt at the 3′ and 5′ termini of vRNAs, and thus in a region of vRNPs adjacent to the polymerase binding site, spanning the UTRs and also part of the coding sequences (Fig. 2) [99,100].
Later during infection, vRNPs reportedly interact with several newly synthesized viral proteins like NS1, NEP and M1 [101,102] and with numerous host factors [103], which most likely contribute to regulation and progression of viral infection.

1.4 Replication of Influenza A viruses

In humans, Influenza A viruses infect and replicate in epithelial cells of the respiratory tract. Progeny virions are released from the apical cell surfaces into the airway lumen of infected persons, spreading the infection to new hosts by airborne transmission [104].

1.4.1 Attachment, internalization and uncoating

For replication, Influenza viruses depend on the host cell machinery. They must enter the cell and deliver the viral genome to the host cell nucleus where viral transcription and replication take place (Fig. 4). Initial attachment to the host cell is mediated by the viral envelope protein HA, which recognizes terminal sialic acid residues of cell surface glycoproteins and glycolipids [17]. The virus is then internalized by endocytosis. Two different endocytic pathways were shown to be involved in the uptake of Influenza viruses. The first internalization route identified is the receptor-mediated clathrin-dependent endocytosis [105], which is triggered by virus binding and involves epsin-1 as cargo-specific adaptor for clathrin recruitment [106]. More recently, macropinocytosis was identified as the second internalization route used by Influenzs virions [107]. Macropinocytosis was shown to be the primary entry mechansim of filamentous virus particles [108]. Specific receptors and the molecular mechanisms triggering viral uptake are still unknown.
Via both pathways, virions are delivered to the late endosomal compartment in the perinuclear region [108,109]. They undergo a three-stage active transport process within endosomal vesicles, beginning with an actin-dependent movement in the cell periphery followed by two stages of microtubule-dependent transport through the cytoplasm towards the nucleus [109,110].
Acidification of the endosomal compartment during endosome maturation [111] triggers a conformational change in the viral surface protein HA, leading to exposure of a hydrophobic fusion peptide, which then inserts into the endosomal membrane and mediates fusion of the

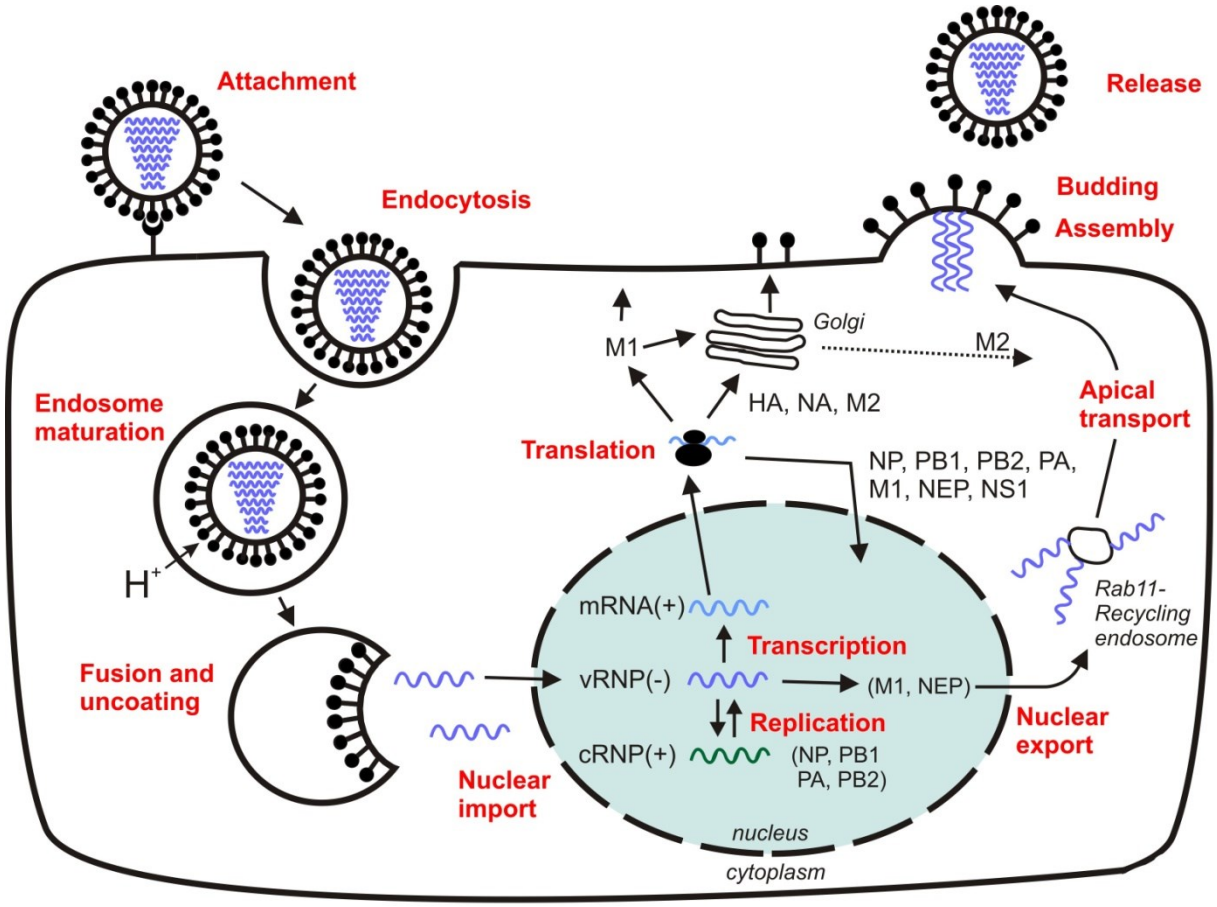

Fig. 4: Replication cycle of Influenza A virus. Influenza A virions bind via hemagglutinin (HA) to sialic acid residues on the cell surface and are internalized into the cell by clathrin-dependent endocytosis or macropinocytosis. Acidification of the endosomal lumen during endosome maturation triggers HA-mediated membrane fusion between viral and endosomal membranes and disassembly of the matrix protein M1. This leads to uncoating and release of the viral genome in the perinuclear region. Via nuclear pore complexes, genomic vRNPs are then imported into the nucleus where viral transcription and replication take place. Viral proteins are synthesized in the cytoplasm, using the cellular translation machinery, and while the envelope proteins undergo apical transport along the secretory pathway, the core proteins NP, PB1, PB2 and PA are required within the nucleus for formation of progeny vRNPs and cRNPs. Also M1 and the nuclear export protein (NEP) are imported into the nucleus to associate with vRNPs and form vRNP nuclear export complexes. Following nuclear export, vRNPs are transported to the apical plasma membrane along with Rab11-positive recycling endosomes. Even though it was shown that Rab11 also plays a role in transport of the proton channel M2, it is unknown whether M2 might be in part cotransported with vRNPs and Rab11-positive vesicles. M1 further independently targets to the Golgi complex and to the plasma membrane. It might preassemble with the viral envelope proteins, polymerize and crosslink the different viral components. The viral components assemble at specific sites of the plasma membrane rich in cholesterol and sphingomyelin, which form the budding site. Complete sets of eight distinct vRNPs are packaged into newly forming virions. It is unknown though at which stage of the replication cycle vRNP segments specifically assemble into multisegment genomic complexes. Bud formation is thought to be mediated by the viral glycoproteins and M1, followed by M2-mediated membrane scission and virus release. For further information, please refer to the text. NA: neuraminidase; NS1: non-structural protein 1; NP: nucleoprotein; PB1, PB2, PA: polymerase subunits.

viral envelope with the endosomal membrane [17]. Simultaneously, the viral proton channel M2 enables a proton flux across the viral membrane and mediates acidification of the viral lumen, leading to pH-triggered disassembly of the viral matrix layer [32,112] and dissociation of M1 from vRNPs [113,114]. vRNPs are released into the cytoplasm and are then transported into the nucleus independent from M1 [115]. M2 proton channel activity was shown to be essential to prime the viral genome for nuclear import. Since M1 is critically involved also in nuclear export of progeny vRNPs at late stages of infection, M1 is considered as a factor that modulates the bidirectionality of vRNP nuclear-cytoplasmic transport [116]. Exposure to acidic pH herein serves as a switch for M1 function [29].

1.4.2 Nuclear import of the viral genome

After release into the cytoplasm, vRNPs are rapidly imported into the nucleus via the nuclear pore complex (NPC) [85,115,117]. This process is mediated by NP and depends on interaction of NP nuclear localization sequences (NLSs) with cellular importins [118,119,120]. NP has at least two highly conserved NLSs, the N-terminal unconventional NLS1 (residues 3–13) [121] and the classical bipartite NLS2 (residues 198–216) [122]. Both sequences were shown to contribute to nuclear localization of vRNPs, but while NLS1 could be shown to be the principal mediator of nuclear import of vRNPs (and of NP), contributions from NLS2 were limited [118,120,123]. NLS2, on the other hand, was found to be indispensable for targeting of newly synthesized NP to nucleoli [123]. A single particle tracking study in living cells revealed that, late in infection when M1 is abundantly present, interaction between cytoplasmic vRNPs and NPCs is efficiently inhibited, suggesting that M1 by association with vRNPs might mask NP-binding sites for nuclear import receptors [117], thereby preventing vRNPs from entering the nucleus (as demonstrated in [29,124]).

Genome-wide RNA interference screenings during the last few years have identified a multitude of cellular factors which are critically involved in Influenza virus replication. Their specific functions are mostly unknown though [125]. It is possible that yet unidentified cellular machinery might further be involved in vRNP transport from the endosome into the cell nucleus, as indicated by the work of Su *et al.* [126].

1.4.3 Transcription and replication

In the nucleus, transcription and replication of the viral genome take place, involving numerous host cell factors [127,128]. Influenza viruses extensively interact with the nuclear

compartment, not only to hijack cellular machinery (e.g. transcription, splicing and nuclear export machinery), but also in order to optimize the cellular environment and cellular resources for viral replication, antagonizing the host cell innate immune response and downregulating cellular syntheses, which is also known as virus-induced host cell shut-off [127,129,130]. Influenza virus infection induces a number of rearrangements of the nuclear architecture. The functional significance of these changes is still unknown though [131,132].
vRNPs are the minimal functional unit for transcription and replication and serve as template for both processes [54,86,133]. They act as independent units. The different vRNP species do not significantly colocalize with each other inside the nucleus, but spread throughout the nucleoplasm [134]. The viral polymerase accomplishes both transcription and replication, using different mechanisms of initiation and termination, generating 5′-capped and 3′-polyadenylated viral mRNAs as well as full-length copies of viral genomic RNA [135].

1.4.3.1 Viral transcription and protein expression

For transcription initiation, the viral polymerase requires 5′-capped primers, which are derived from host pre-mRNAs by a mechanism termed “cap-snatching”. Therefore, the polymerase subunit PB2 binds to the 5′ 7-methyl guanosine cap of cellular mRNA, which is then cleaved by endonucleolytic activity of PA 10–13 nucleotides downstream of the cap structure. This short nucleotide fragment is then used as primer for mRNA synthesis by the viral polymerase subunit PB1. Cap-snatching activity, and thus transcription initiation, requires association of the trimeric polymerase with the vRNA template [136]. Viral transcription further depends on active cellular transcription, which is mediated by cellular RNA polymerase II (Pol II). Not only viral mRNA synthesis [137], but also mRNA nuclear export [138] were shown to depend on Pol II activity. Pol II assembles with a plethora of cellular proteins during transcription, which cotranscriptionally mediate pre-mRNA processing like capping, splicing, polyadenylation and mRNP assembly. Sites of active Pol II transcription are also termed “transcription factories”. Direct interaction between the viral polymerase and active Pol II is assumed to facilitate access to mRNA cap-structures and to ensure close proximity of viral transcription to cellular transcription factories and thus also to cellular machinery for pre-mRNA splicing and nuclear export [127,139]. In line with this, it was shown by electron microscopy that Influenza virus RNAs are synthesized at specific nuclear sites, so-called “nuclear cages”, where also cellular RNAs are synthesized [140]. Fluorescence microcopy studies further confirmed accumulation of the viral polymerase at sites of Pol II transcription during infection [139].

Elongation of viral transcription by PB1 proceeds until it reaches a sequence of uridine residues close to the 5′ end of the vRNA template. This stretch of 5–7 uridine residues is then reiteratively copied, serving as template for 3′ polyadenylation [141,142,143]. This process is independent from host cell machinery [144], but critically depends on a hairpin loop structure within the highly conserved 5′ terminal vRNA promoter sequence [145]. Even though viral strategies for polyadenylation and 5′-capping are distinct from cellular mechanisms, Influenza viruses generate mRNAs which are structurally indistinguishable from cellular mRNAs and thus can access cellular pathways, finally leading to protein expression through the cellular translation machinery [146]. The cellular cap-binding complex (CBC) and polyadenylate-binding protein 1 (PABP1) reportedly associate with both cellular and viral mRNA [147]. The CBC protects mRNA from degradation and is essential for cellular mRNA maturation and assembly of mRNPs [148].

Nuclear export of cellular mRNA is tightly coupled to cotranscriptional mRNA maturation, which includes the recruitment of numerous RNA-binding proteins to nascent mRNA, namely the CBC, the exon-junction complex (EJC) and the transcription/export (TREX) complex. These proteins function as adapter proteins for the recruitment of the major cellular mRNA nuclear export receptor NXF-1. NXF-1 is the primary export pathway known to be implicated also in Influenza A virus mRNA export [146]. Yet, a differential dependence of distinct viral mRNA species on NXF-1 was reported [149]. The molecular details of viral mRNP assembly and nuclear export are still poorly understood. It is believed that – also in case of viral mRNA – transcription, mRNA maturation, assembly and nuclear export are closely linked processes [135].

The eight genomic vRNA segments encode up to 17 viral proteins (Tab. 1). Ten of these proteins have been known for several decades and are well characterized. They are known as key players of the viral replications cycle. They comprise the nine structural proteins HA, NA, M2, M1, NP, PB1, PB2, PA and NEP, as described in section 1.2, and the non-structural protein 1 (NS1). The cellular splicing machinery is required for generation of M2 and NEP by splicing of segment 7 and segment 8 mRNA, respectively. Another 7 virally encoded proteins were discovered only in recent years: PB1-F2, PB1-N40, PA-N155 and PA-N182 are generated from segment 2 and segment 3 mRNAs by use of alternative translation initiation sites [60,62,63]; PA-X is synthesized from segment 3 mRNA by ribosomal frameshifting [61], and proteins M42 and NS3 are generated from segment 7 and segment 8 mRNAs by alternative splicing, respectively [64,65]. The functions of these proteins are currently poorly understood, and their general significance for Influenza A virus infections yet remains to be

demonstrated. They may act as strain-specific virulence factors like PB1-F2 [150,151] and PA-X [61] or play a role in adaption to mammalian hosts as suggested for NS3.

The ten major viral proteins are subdivided into early and late proteins according to their temporal expression patterns during infection [149,152,153,154]. The core proteins NP, PA, PB1, PB2 as well as NS1 are synthesized first, followed by expression of M1, NEP and the envelope proteins. The viral transmembrane proteins are synthesized at the rough endoplasmic reticulum (ER) where they enter the secretory pathway to the plasma membrane. The other proteins, except for NEP, contain nuclear localization signals and are transported into the nucleus after synthesis at cytoplasmic ribosomes [155]. NEP, with only 14 kDa, can enter the nucleus through passive diffusion [156]. While nuclear import of NP and polymerase subunits is required for the formation of progeny vRNPs, M1 and NEP have to enter the nucleus to mediate nuclear export of the newly formed vRNPs.
NS1, on the other hand, is an important virulence factor and a multifunctional protein (reviewed in [129,157]). It is the major viral interferon antagonist and further modulates both cellular and viral protein expression. NS1 was shown to associate with viral mRNAs [147,158] and has been implicated in the regulation of viral mRNA splicing [159], viral mRNA nuclear export [157] and selective enhancement of translation initiation [160,161,162]. It is not required though for primary viral transcription and protein expression since it is not present in incoming virus particles. Further, NS1 contributes to the virus-induced downregulation of cellular syntheses. It reportedly interferes with several steps of host mRNA maturation, including mRNA elongation, splicing and nuclear export. By association with transcription elongation complex hPAF1C, NS1 was shown to specifically impair transcription elongation of inducible antiviral genes [163]. NS1 was further shown to interact extensively with the host cell splicing machinery [164,165,166] and to inhibit host pre-mRNA splicing [167,168,169]. By interaction with the cellular cleavage and polyadenylation specificity factor (CPSF) and the poly(A)-binding protein 2 (PABP2), NS1 furthermore inhibits polyadenylation and 3′ end formation of host pre-mRNA and thus selectively impairs the formation of mature export-competent cellular mRNPs [170,171].

Synthesis of viral mRNA peaks between 2 and 6 h p.i. Thereafter, mRNA synthesis declines rapidly, but nevertheless viral protein synthesis continues at maximum rates from previously synthesized mRNA [152,172]. It has been suggested that the drop in viral mRNA production might be due to exhaustion of mRNA-cap structures and to virus-induced inhibition and degradation of cellular Pol II [130]. Unlike mRNA generation, the synthesis of genomic

vRNA continues also late in infection. Production of the different viral RNA species is apparently differentially regulated. The molecular basis that controls the activity of the viral RNP complexes and the switch from viral transcription to replication is currently still unknown and subject of ongoing research (see also 1.4.3.2).

1.4.3.2 Viral replication

Viral replication involves the generation of full-length complementary RNA (cRNA) as positive-strand replication intermediates. cRNAs – just like vRNAs – are encapsidated by NP and the viral polymerase, forming cRNP complexes, which then in turn serve as templates for the generation of new vRNA molecules. Full-length replication products are neither 5′ capped nor 3′ polyadenylated. Their synthesis requires mechanisms of initiation and termination that are distinct from those of viral transcription [54,135]. Triphosphate groups at the 5′ ends of cRNA and vRNA segments suggest a primer-independent initiation mechanism [173].
Since encapsidation with NP is selective for viral replication products, but not for viral mRNA, it was proposed that encapsidation and initiation mechanisms might be coupled [174]. While the 5′ cap structure of mRNA leads to cotranscriptional recruitment of mRNA processing machinery, it was suggested that the highly conserved 5′ terminal promoter sequence of nascent full-length RNA instead might associate with the viral polymerase due to specific recognition and trigger (by interaction between NP and the polymerase) the recruitment of NP, thereby initiating co-replicational RNA encapsidation in 5′ to 3′ direction [89,175]. Subsequent incorporation of other NP molecules into RNP complexes was found to be driven by NP-NP homooligomerization, but not by NP binding to RNA [90]. A functional relationship between NP oligomerization and RNA-binding was reported though, and also a role of NP (de)phosphorylation for oligomerization and RNA-binding has been indicated [92,176]. Replication elongation and encapsidation with NP were further reported to be facilitated by cellular factors like UAP56, Tat-SF1 and MCM, which may act as chaperones [177,178,179]. Consistent with co-replicational RNA encapsidation, Moeller *et al.* reported detection of branched RNP structures by electron microscopy, featuring a polymerase at the junction between the smaller (nascent) RNP and the full-length RNP [89].

Various models have been proposed for the regulation of viral replication versus transcription, but numerous aspects are still unclear (reviewed in [54]). It was initially hypothesized that accumulation of free NP might be a regulatory viral factor that can switch polymerase activity from transcription to replication. This was based on the finding that viral protein expression is

critically required for the onset of cRNA synthesis in infection. Replication in the presence of a protein synthesis inhibitor was further shown to be be rescued by preexpression of NP and the viral polymerase [180,181]. Evidence was moreover provided for a direct functional interaction between NP and polymerase subunits PB1 and PB2, supporting the assumption that newly synthesized NP might be able to modulate polymerase activity by direct interaction [182,183,184]. It was also proposed that interaction of soluble NP with vRNP templates or with nascent RNPs might bias the specific activity of vRNPs [71,185].

Today, however, the perception of the role of NP has changed. Accumulating evidence suggests that NP does not determine the mode of initiation and termination performed by the viral polymerase. It was demonstrated that purified vRNPs can synthesize both mRNA and cRNA in the absence of added protein *in vitro* [186], and that the viral polymerase produces full-length positive- and negative-strand copies from short vRNA-like templates in the absence of NP *in vivo* [90]. Nevertheless, NP might be an important contributor to efficient replication since it was shown to facilitate promoter escape of the viral polymerase when exogenously added, promoting elongation of full-length transcripts [177]. It was further shown to protect newly formed replication products from degradation in cells [187].

Importantly though, interaction of NP with the viral polymerase was found to be essential for polymerase activity in general. Highly conserved residues in the NP head domain, which were shown to interact with the polymerase, were found to be critically required for both mRNA and full-length RNA synthesis in cells [188]. Other temperature-sensitive NP mutants, on the other hand, were reported to selectively support mRNA and vRNA synthesis, but not cRNA synthesis [183], and vice versa [189].

More recently, a *trans*-complementation study shifted the focus from NP towards the role of the viral polymerase itself and suggested that two distinct populations of the viral polymerase might be responsible for transcription and replication [175]. A model was proposed according to which the vRNP-bound polymerase complex mediates transcription in *cis*, while newly synthesized soluble *trans*-acting polymerase complexes are responsible for replication (from cRNPs into vRNPs). This model has increasingly gained support by then following studies, but it is also consistent with data from earlier studies [180,181,187]. The model provides a possible explanation how initiation, encapsidation and termination might be mechanistically coupled [54,89], and it is consistent with the observation of different conformational states reported for free, vRNA-bound and RNP-bound polymerase complexes, indicating distinct functional states [54].

Apart from NP and the viral polymerase, also other viral factors were reported to be implicated in replication regulation (reviewed in [54]). NS1 associates with vRNPs by interaction with NP, and a temperature-sensitive mutant of NS1 was shown to affect vRNA synthesis, but not the production of positive-strand viral RNA species [102,190]. Accumulating evidence furthermore supports a role of NEP as co-factor of the viral polymerase. NEP interacts with polymerase subunits PB1 and PB2 and enhances the formation of unprimed full-length replications products, while reducing accumulation of mRNA, which is independent from its function as nuclear export factor [191,192,193]. Differential regulation of all three viral RNA species during infection is thus apparently accomplished by complex interplay of a variety of factors.

Not only transcription versus replication, but also full-length cRNA and vRNA synthesis were shown to be differentially regulated. While cRNAs are synthesized early in infection during a short period of time, vRNA synthesis continues also late in infection and yields considerably higher copy numbers [152,172]. vRNPs are then selectively exported to the cytoplasm and become incorporated into progeny virions, while cRNPs are retained in the nucleus, where they serve as templates for continued vRNA synthesis [98,152]. Even though cRNAs and vRNAs seem to form identical structural complexes with NP and the viral polymerase, they must contain structural features that enable their discrimination as functionally different classes of molecules. Differences in the conserved terminal RNA sequences and their recognition by the viral polymerase were suggested to enable differential regulation and functioning.

cRNAs and vRNAs contain short terminal sequences which are highly conserved among all segments [70]. These sequences comprise 13 nucleotides at the 5′ end and 12 nucleotides at the 3′ end of vRNA. Together both ends constitute the viral promoter which is bound by the viral polymerase [71,72]. The polymerase associates with both positive- and negative-strand promoter sequences, yet, different regions on PB1 were reported to be involved in recognition of the specific cRNA and vRNA sequences [78,79]. The promoter structure of both cRNA and vRNA has been described by a corkscrew model, containing two short intrastrand hairpin loops, a single bulged unpaired nucleotide and a short interstrand base-paired region [73,74,75,76]. Despite similarities, structural differences were reported that might explain differential recognition by the viral polymerase [77]. The polymerase, and specifically subunit PB1, was shown to display a higher affinity for the 5′ end of vRNA than for the 3′ end [72,79], while it interacts with both 5′ and 3′ ends of cRNA with similar affinities [78]. Furthermore, also a requirement of the PA subunit for cRNA and vRNA promoter binding has

been indicated. PA seems to contribute more importantly to cRNA promoter binding than to vRNA promoter binding [80].

Transcription initiation was shown to critically require interaction of the viral polymerase with both termini of vRNA [71,136]. vRNA terminal sequences apparently serve as essential polymerase cofactors during cap-snatching. Polymerase cap binding activity was shown to require association with the vRNA 5′ end, while its endonuclease activity requires the vRNA 3′ end [194,195]. Notably, when associated with the cRNA promoter instead, the polymerase was shown to be unable to perform cap-snatching [194,196]. Specific recognition of the vRNA promoter thus seems to determine that transcription is initiated only on negative-strand genomic templates and that only vRNAs serve as template for viral mRNA synthesis.

Differences between cRNA and vRNA promoter regions were furthermore suggested to be responsible also for distinct initiation mechanisms of cRNA and vRNA synthesis. It was shown that vRNA synthesis is initiated internally at positions 4 and 5 of the 3′ end of cRNA and that a synthesized dinucleotide is then realigned to position 1 and 2 for full-length replication. In contrast, cRNA synthesis was reported to be initiated at position 2 of the vRNA 3′ end without the need of realignment [197,198,199]. The dinstinct mechanisms were suggested to be involved in differential regulation of cRNA and vRNA levels. The molecular details are still unknown though.

Taken together, allosteric modulation of polymerase activity through different RNA promoter structures is thus currently considered to be a determinant of vRNP-specific transcription and to be an important aspect of vRNA and cRNA synthesis, but also recognition of vRNPs for nuclear export and packaging might be closely related to these processes. Extensive further investigations are still required to understand functioning and regulation of the viral replication machinery.

1.4.4 Viral protein trafficking and virus assembly

To participate in virus formation, the different newly synthesized viral components, including M1, vRNP complexes and the viral transmembrane proteins, need to be transported to the apical plasma membrane of infected cells. For this purpose, viral envelope proteins and the viral genome use different transport pathways.

1.4.4.1 Viral envelope proteins and the role of lipid rafts

The transmembrane proteins are synthesized at membrane-bound ribosomes of the rough endoplasmic reticulum (ER) and travel through the Golgi apparatus to the plasma membrane. Soon after synthesis, HA assembles into homotrimers [200], while NA and M2 form homotetramers [201,202,203]. During their passage through ER and Golgi, HA, NA and M2 acquire a number of posttranslational modifications: HA and NA become glycosylated [204,205], HA and M2 are S-acylated [206,207].

It was initially thought that the viral envelope proteins, and in particular HA as major viral envelope protein, might be determinants of polarized virus budding since they are intrinsically sorted to the apical plasma membrane of polarized epithelial cells [208,209,210]. Recombinant viruses, however, expressing HA mutants that are sorted to the basolateral plasma membrane or distribute in a non-polarized fashion, were still found to bud almost exclusively from the apical cell surface, suggesting a minor role for HA alone for selection of the budding site [211,212]. The determinant of the budding site is currently unknown, but might result from interaction of distinct apically targeted viral proteins and their ability to establish the viral budzone. The signals for apical transport of HA and NA reside in the protein transmembrane domains. They were identified not as discrete motifs, but as dispersed residues within the transmembrane regions [39,213,214,215]. The apical targeting signal of M2 has not been identified yet.

HA and NA were further shown to associate with lipid rafts domains, specific membrane domains enriched in cholesterol and sphingolipids. (For further information on membrane organization and lipid rafts see 1.6). Targeting of HA and NA to lipid rafts plays a central role during viral replication, contributing to several steps of the replication cycle, e.g. protein trafficking and processing, virus assembly, virus budding and fusion of viral and endosomal membranes during virus entry into the host cell (reviewed in [21]).

HA is one of the best characterized examples of raft-associated proteins. Its association with lipid raft domains was demonstrated by a variety of methods: In early studies, HA lipid raft targeting was based on biochemical analyses, demonstrating cofractionation of HA with detergent-resistant membrane fractions, which were considered as the biochemical equivalent of lipid raft domains in cells [24,216,217,218]. Later on, more advanced techniques with high spatial and temporal resolution were applied, which confirmed cholesterol-sensitive clustering of HA in fixed and living cells [219,220,221,222,223].

The concept of lipid rafts in biological membranes for lateral organization and functional compartmentalization has been known for almost three decades [224,225]. It was originally introduced to explain selective sorting of lipids and proteins to the apical or basolateral plasma membrane in polarized epithelial cells [226,227]. The propensity of sphingolipids, cholesterol and specific proteins to self-assemble was suggested to promote lateral segregation of apical membrane constituents with increasing cholesterol and sphingolipid concentrations within the Golgi and facilitate sorting of apical and basolateral components into separate transport vesicles. Accordingly, raft association was suggested to play a role also in intracellular trafficking of HA and NA. HA was consistently found to fractionate with lipid raft components during late stages of transport to the cell surface [218].

The raft targeting signals of HA and NA were mapped to the protein transmembrane domains, in particular to amino acids located at the exoplasmic leaflet of the lipid bilayer, and to the cytoplasmic tails [24,39,215,217,223,228,229]. Notably, though, raft targeting signals overlap, but are not identical with the apical targeting signals of the proteins. Several mutations of HA or NA were described which disrupt association with lipid rafts, but do not affect apical targeting, indicating interactions with the apical sorting machinery independent from lipid raft localization [39,215,223,229]. Conversely, also HA mutants could be generated which associate with lipid rafts, but which are not properly sorted to the apical surface [214]. Evidence thus suggests that lipid raft targeting and apical localization are independent features of the viral glycoproteins.

Nonetheless, lipid raft association was shown to accelerate apical transport of HA and NA, presumably by its ability to promote clustering of HA and NA during transport [230]. Partitioning into lipid rafts was further reported to play a role for Golgi-localized processing of HA: Acquisition of Endo-H resistant carbohydrates, proteolytic cleavage and transport across the Golgi were shown to be severely retarded by mutation of the raft targeting signal in the HA transmembrane domain, while HA-trimerization in the ER and apical targeting were not affected by the same mutation [231].

Lipid raft domains further appear to be used by many enveloped viruses, such as HIV-1, Ebola and Influenza virus, as a platform for virus assembly. They are thought to facilitate concentration of viral proteins and the formation of functionalized domains for virus budding [232,233]. The envelope of Influenza viruses was shown to be selectively enriched in cholesterol and sphingolipids as compared to the host cell plasma membrane [16,234]. This and the fact that HA and NA form large clusters at the cell surface, which are sensitive to cholesterol extraction, sensitive to disruption of lipid raft targeting and furthermore colocalize

with a lipid raft marker, strongly support the notion that Influenza viruses assemble in and bud from lipid raft domains [25,220,221,223]. HA clusters range from 20 to 900 nm in size as observed by immunoelectron microscopy and between 40 nm and several micrometers according to super-resolution fluorescence microscopy in living cells [220,221]. Very small and highly dynamic raft domains (~10 nm–100 nm) are thought to be activated by the presence of viral proteins, leading to stabilization and coalescence of lipid rafts into larger functional domains which are the precursor of the viral membrane. Targeting of HA and NA to lipid rafts is thought to play a central role in this process. Disruption of lipid raft targeting signals in HA and/or NA was shown to cause severe replication defects, to decrease incorporation of the respective glycoprotein(s) into progeny virus particles and to alter the viral lipid composition [24,223,228].

Also viral M1 and the actin cytoskeleton were suggested to be involved in stabilization of lipid raft-based viral protein clusters and organization of the viral budzone. Accumulating evidence supports that actin plays a key role in organizing lipid raft domains and modulating their stability [235,236,237]. A link between the cytoskeleton and lipid rafts is well documented [238,239]. Upon expression of HA in the absence of infection, HA was shown to be organized in elongated and irregular membrane domains, which colocalize with cellular actin on the nanoscale. Dynamics measurements further revealed confinement and reduced mobility of HA in areas of high actin density, indicating a role for actin in stabilization of HA clusters. Exclusion of the actin-remodelling protein cofilin from these HA clusters further implied that HA itself influences actin organization [240]. It was speculated that actin organization might be affected by HA through its ability to activate Raf/MEK/ERK signaling, which depends on accumulation of HA at the cell membrane and tight association with lipid raft domains [241,242]. In infected cells, also M1 and NP were shown to accumulate at elongated plasma membrane domains and to redistribute together with HA in response to actin disruption, correlating with the underlying cortical actin filaments [243]. A role for cortical actin in virus assembly and budding was further indicated by proteomic analysis, demonstrating the presence of actin inside virus particles [244], and by perturbations of cellular actin, leading to inhibition of filamentous, but not spherical virus particle formation [15,243]. Strong evidence for functional involvement of actin in lipid-raft based formation of the viral budzone was further given by a fluorescence resonance energy transfer (FRET) study, demonstrating close association of HA and M2 upon coexpression, even though M2 is a non-raft protein. This association was shown to depend on the lipid raft targeting signal of HA

and on an intact actin cytoskeleton, suggesting actin-dependent association of M2 with preformed lipid raft-based membrane clusters of HA [245].

Apart from actin, also the matrix protein M1 is believed to promote stabilization and coalescence of lipid raft-based viral protein clusters by its ability to oligomerize [44] and to interact with the transmembrane protein cytoplasmic tails [38,39]. M1 does not intrinsically target to lipid raft domains, but is recruited to lipid rafts in the presence of HA and NA [24,38,39]. During infection, M1 becomes increasingly associated with lipid raft domains [38], and it was proposed to link the viral ion channel M2 to the viral budzone, which likewise was shown to acquire raft association during infection [30]. Nevertheless, it seems that M2 in reverse is required for incorporation of M1 and the viral genome. It directly interacts with M1 via its cytoplasmic tail [40,246]. M2 might hence be recruited to the viral budzone by the presence of HA (and possibly M1) and play an important role itself to incorporate the internal viral components.

M2 further contains two motifs in its cytoplasmic tail that typically support lipid raft targeting: a cholesterol-binding site and a palmitoylation site [11,26,207]. Nevertheless, M2 was shown to be excluded from lipid raft domains and from lipid raft-based clusters of HA and NA at the plasma membrane of infected cells [24,25]. The relatively short transmembrane domain of M2 (with 19 amino acids (aa) as compared to HA and NA with about 27 and 30 aa) might impair partitioning of M2 into lipid raft domains since cholesterol-rich membrane domains are comparably thick and favor incorporation of proteins with long transmembrane domains [247,248]. It was therefore proposed that M2 might localize at the raft/non-raft interface of the viral budzone where the transmembrane region would reside in the non-raft bilayer while the cytoplasmic tail would immerge into the lipid raft domain [26]. Consistently, it was observed that M2 is excluded from protruding viral filaments at the cell surface and specifically localizes only to the budding neck of these filaments [11,30]. This could further explain why M2 is largely excluded from virus particles [22,23].

The function of cholesterol binding by M2 has been the subject of several studies, but still remains elusive. Loss of cholesterol-binding by mutation of the M2 cytoplasmic tail did not affect recruitment of M2 to the budding site and only slightly reduced cofractionation with lipid raft domains in infected cells, suggesting that cholesterol-binding is not required for association of M2 with the viral budzone [11]. FRET measurements confirmed that neither the acylation nor cholesterol binding motif is required for apical targeting of M2 or for clustering of M2 with HA microdomains upon coexpression [249].

A crucial role for M2 cholesterol-binding was then revealed by the finding that M2 can modulate membrane curvature in a cholesterol-dependent manner: It was shown that M2 by itself is capable of mediating membrane budding in cells and in model membranes with low cholesterol content. The amphipathic helix of the M2 cytoplasmic tail was furthermore shown to be both necessary and sufficient to mediate membrane scission [30]. It was proposed that the amphipathic helix might be able to induce membrane curvature by wedge-like insertion into membranes or by modulating the line tension that occurs at the boundary between membrane domains.

Since M2 was found to localize specifically to the budding neck of virus particles, it was hypothesized that the M2-cholesterol interplay might regulate membrane curvature during the budding process, either stabilizing the viral budzone and enabling filamentous virion formation or inducing positive curvature and promoting membrane scission [11]. The hypothesis is supported by numerous experimental findings: The cholesterol-binding motif in the M2 amphipathic helix as well as plasma membrane cholesterol were shown to be essential for the formation of filamentous virus particles, suggesting stabilization of budding filaments by M2 and cholesterol [11]. Similarly, depletion of cholesterol from the plasma membrane was found to cause rapid release of virus particles [250]. Numerous virus strains, including spherical and filamentous viruses, further seem to require M2 for membrane scission since deletion of M2 or mutation of the M2 cytoplasmic tail were shown to reduce virus particle release and to cause morphological changes that display the characteristics of incomplete virus budding (e.g. incompletely budded virions appear as “beads on a chain”) [10,30,246]. These observations clearly demonstrate that M2 is not necessary for initiation of virus budding, but for its completion. According to the current view, M2 is thus considered as a viral factor that is essential for efficient membrane scission and virus release.

How the different functions of the M2 cytoplasmic tail (i.e. sensing of cholesterol, regulation of membrane curvature, ability to support filament formation, interaction with M1 and incorporation of internal viral components) might be interrelated is unclear.

Transport of M2 to the viral budding site is currently not well understood. Systematic analysis of the transport pathway is missing, and the intrinsic apical targeting signal of M2 has not yet been identified. Evidence suggests though that M2 is not transported along the classical secretory pathway together with HA and NA, but that it takes an alternative route from the *trans*-Golgi network to the plasma membrane along with Rab11-dependent recycling endosomes: M2 localizes to the *trans*-Golgi network, to apical recycling endosomes and to the apical plasma membrane by intrinsic targeting [251], and accumulation of M2 at the cell

surface was shown to depend on expression of the small GTPase Rab11 [30]. Upon depletion of Rab11, a failure of budding virions to pinch-off was observed, consistent with a failure in membrane scission due to lack of M2 [252]. M2 has further been assigned a role in raising the intralumenal pH of the Golgi apparatus to prevent untimely, low pH-induced conformational change of HA [253,254,255], and also an effect of M2 on recycling endosomal trafficking was reported [251]. Ion channel activity of M2 was shown to delay transport of HA and other glycoproteins specifically in compartments involved in apical delivery, including the *trans*-Golgi network, secretory vesicles and recycling endosomes, while other acidified compartments were not affected, correlating with the localization of M2 [203,251,256].
Whether apical transport of the viral genome – which likewise depends on Rab11 – might be functionally linked to or coordinated with transport of M2 is unknown.

1.4.4.2 Matrix protein M1 – functions in nuclear export and virus assembly

The matrix protein M1, which is the most abundant protein in virus particles, does not contain intrinsic signals for apical targeting and accumulation at the viral budding site. Upon expression in the absence of infection, M1 localizes to the cell nucleus, to the cytosol and to intracellular membranes [257]. Since M1 is a central structural element of virus particles and able to interact with each of the other viral constituents, it is assumed that M1 preassembles with individual viral components in infected cells already during transport. M1 might be transported to the viral budding site piggy-back through interaction with the viral transmembrane protein cytoplasmic tails, through direct membrane interaction or by association with vRNPs [20,41].

1.4.4.2.1 Role of M1 in vRNP nuclear export

Part of the newly synthesized M1 accumulates in the nucleus of infected cells due to its NLS (aa 101–105) [258] where it is required to mediate nuclear export of the viral genome [116,259]. Phospohorylation was further reported to play a role in nuclear localization of M1 and to affect nuclear export of vRNPs [260,261,262,263].
Also viral NEP [66,264] and the cellular nuclear export receptor CRM1 [265,266,267,268] were shown to be required for vRNP nuclear export. M1 interacts with NEP via its N-terminus (aa 1–164) [57,269,270,271] and with vRNPs presumably via its C-terminal domain (aa 165–252) [42] why it was suggested that vRNPs, M1 and NEP form a “daisy chain” type complex, which is recognized by the export receptor CRM1 [83,272]. While M1 does not functionally interact with CRM1 [269], NEP contains two nuclear export sequences (NESs)

which are both recognized by CRM1 [67]. NEP thus seems to bridge the interaction between vRNP/M1 complexes and export factor CRM1, binding to M1 via its C-terminus [269,270] and interacting with CRM1 via the NESs in its N-terminus [67].
In addition to NEP, also M1 and NP contain NESs [273,274]. The relative contributions of these NESs to vRNP nuclear export are not clear though. The identified NES of M1 is highly conserved and recognized by a CRM1-independent nuclear export mechanism.

It should further be noted that attempts to identify the M1 domain for vRNP-binding yielded conflicting results, which were not all in accordance with the daisy chain model. Instead of the M1 C-terminus – as mentioned above –, it was also reported that the M1 N-terminus might be required for interaction with vRNPs [68,275]. Data further seem to suggest that the M1 NLS could be involved in interaction with both NEP [269] and vRNPs [275]. The molecular basis of vRNP-M1 interaction is thus currently not well understood.

A refined and more complex model for nuclear export complex formation was proposed very recently, suggesting that NEP does not only recruit CRM1 to vRNP/M1 complexes, but that it is also required for association of M1 with vRNPs. It was shown that M1 alone is unable to establish interaction with vRNPs within the nucleus [101]. NEP by itself, on the other hand, can associate with vRNPs via the viral polymerase and enhances vRNA replication [191,192]. Notably, the same residues of NEP involved in regulation of polymerase activity were shown to be required also for assembly of vRNP/M1/NEP nuclear export complexes, indicating a close coordination of these two functions; consistently, the presence of M1 interferes with the polymerase-enhancing function of NEP [101]. A model was thus suggested according to which M1 attaches to vRNP-bound NEP, which becomes involved in ternary interaction with M1, vRNPs and CRM1, neutralizing the polymerase-enhancing function of NEP, stabilizing interaction between vRNPs and M1 and recruiting CRM1 to vRNPs. Intriguingly, the C-terminus of NEP was demonstrated to be sufficient to stabilize vRNP/M1 complexes or to constitutively enhance polymerase activity. The NEP N-terminus, on the other hand, impairs the C-terminal functions by autoregulatory intramolecular interaction, suggesting an additional layer of complexity for regulation of vRNP export complex formation and vRNA replication. It was thus speculated that binding of CRM1 to the N-terminal domain of NEP might prevent those intramolecular interactions and stabilize M1 binding during export. Release of CRM1, on the other hand, subsequent to nuclear export was proposed to enable the NEP N-terminus to disrupt M1 binding [101,193].

On the molecular level, numerous details on the interaction between M1 and vRNPs are still unknown: neither stoichiometry, nor stability within cells, nor the binding sites have been characterized.

SUMOylation (the attachment of a small ubiquitin-like modifier (SUMO)) at residue K242 was found to be an essential posttranslational modification of M1 that is required for vRNP-M1 interaction and vRNP nuclear export [276]. Consistently, M1 and also NEP (another SUMOylation target) were found to localize to nuclear promyelocytic leukemia (PML) bodies during infection, which are known as hot spots of cellular SUMOylation [277]. A SUMOylated form of M1 was however not detected in mature virions, which might be due to rapid turnover of SUMO-conjugations [276]. Previous work suggests involvement of SUMOylation in CRM1-mediated nuclear export processes [278].

Physical association between M1 and vRNPs was previously demonstrated by purification of complexes from intact virions [275,279]. Yet, no such complexes have so far been isolated from cells [101]. It is unclear whether vRNP/M1/NEP complexes rapidly disassemble after nuclear export and release of CRM1, or whether they undergo cotransport to the budding site. In this context, it should be noted that M1 was not only shown to promote nuclear export but also to prevent reimport of vRNPs into the nucleus [116,124]. And since further NEP was detected as component of mature virus particles that is attached to the viral core together with M1, it was inferred that vRNPs, M1 and NEP remain associated during cytoplasmic transport and become incorporated into virions as complexes [57,58]. However, it was also reported that vRNPs do not contain detectable amounts of M1 during Rab11-dependent apical transport [280].

1.4.4.2.2 Role of M1 oligomerization and membrane binding in virus budding

Apart from its role in nulear export of vRNPs, M1 plays a central role also in viral budzone formation and the budding process.

M1 is a membrane-binding protein that associates with both cellular [51,281] and model membranes [42,43,45,47]. It is an unusual peripheral membrane protein, which tightly associates with membranes, most likely involving extended surface regions or multiple binding sites [47,50,51,257,282]. In some studies, a predominantly electrostatic nature of M1-membrane interaction was reported [42,45]. In other studies also non-electrostatic contributions [43,44,282] and association by partial insertion of M1 into the membrane were demonstrated [46,47,282]. It was further reported that M1 could not be detached from cellular membranes under high-salt conditions, which usually leads to release of peripheral membrane

proteins [50,51,281]. In agreement with partial insertion of M1 into the membrane, it was further reported that recruitment of M1 to detergent-resistant membranes by HA is not only mediated by the HA cytoplasmic tail, but also by its transmembrane region [38]. A more recently developed computational model based on tritium planigraphy data from intact virus particles suggests interaction of M1 with the viral membrane via a large part of the protein, involving also considerable electrostatic interactions [282].

Within cells, M1 can be found to accumulate at the Golgi membrane by intrinsic affinity [257]. The molecular basis of this interaction is unknown. During infection and upon coexpression of HA, M1 and HA colocalize at the Golgi membrane, and both proteins apparently undergo cotransport, indicating the possibility that M1 might preassemble with viral envelope proteins at the Golgi membrane [38].
It was suggested that M1 within cells is either soluble and monomeric or has a higher affinity for membranes and tends to oligomerize [283]. More recent work reports that M1 forms a stable dimer in solution by interaction of the C-terminal domains. The N-terminus, on the other hand, seems to be responsible for pH-dependent oligomerization [112]. The ability of M1 to homooligomerize is essential for the formation of the viral matrix layer underneath the viral membrane [45,284]; the matrix layer is thought to crosslink and concentrate viral proteins at the viral budzone and to promote membrane bending during the budding process [34]. It is not clear, however, which factors drive and coordinate M1 polymerization.
Polymerization of M1 should be a regulated process that is locally restricted and functionally linked to virus assembly. Only recently, evidence was provided that membrane binding in fact strongly enhances oligomerization of M1. Data obtained by fluorescence correlation spectroscopy, raster image correlation spectroscopy, atomic force microscopy and use of negatively charged model membranes suggest a model according to which M1 associates with lipid membranes first and then multimerizes by recruitment of M1 molecules from solution [285]. Most notably, number and brightness microcopy performed on M1-expressing cells demonstrated further that M1 multimerizes specifically underneath the plasma membrane rather than on intracellular membranes or in the cytosol. This observation indicates that M1 – even though it is apparently not enriched at the plasma membrane – nevertheless associates with the plasma membrane. M1 acts possibly similar to a cationic biosensor, detecting the strongly negative surface charge of the plasma membrane [286].

During virus infection, M1 might be increasingly recruited to the viral budzone by interaction with the viral envelope proteins HA, NA and M2, which by promoting M1 membrane

association might enhance also M1 polymerization. Clusters of HA and NA thus could function as nucleation points of M1 polymerization. Diverging results were reported though on the quantitative effect of HA and NA on M1 membrane association. While some studies show significant stimulation of M1 membrane binding in the presence of viral glycoproteins [281,287], others found no such enhancement [50,51]. By recruitment of M1 to lipid raft domains, HA and NA might nonetheless locally concentrate M1 on the plasma membrane even if the overall amount of membrane-bound M1 might not change [24,38,39].

The hypothesis of enhanced M1 membrane-binding and M1 polymerization due to the presence of viral transmembrane proteins is further supported by results from transfection-based virus-like particle (VLP) production. This assay is commonly applied to test the ability of single viral proteins to induce membrane budding, comprising the ability for bud initiation and bud completion. Using this approach, it could be shown that M1 alone is unable cause budding of VLPs from cells [288,289]. More detailed analyses suggested though that most likely the lack of intrinsic plasma membrane targeting is responsible for the failure of M1 to induce budding: In fact, targeting of M1 to the plasma membrane by addition of a membrane anchor in form of acylation was shown to be sufficient to enable M1-driven VLP budding [289]. Viral transmembrane proteins are thought to act analogously as membrane anchors for M1 in infected cells, and consistently, it was reported that the presence of M2 leads to relocalization of M1 to the plasma membrane and allows formation of VLPs, critically requiring the M2 cytoplasmic tail for M1 binding [289]. Similarly, cytoplasmic tails of HA and NA were shown to be required for efficient incorporation of M1 into HA- and NA-driven VLPs. Notably, HA and NA are able to mediate VLP budding in the absence of other viral proteins [288]. It was demonstrated though that M1 significantly enhances the ability of HA to produce VLPs upon coexpression, underlining the capacity of M1 to support budding and to function synergistically with HA [287,288].

A current model of virus budding was described by Rossman *et al.*, summarizing the findings from VLP budding assays [34]. Considering that several viral proteins (including HA, NA, M2 and membrane-targeted M1) were found to be capable of mediating VLP budding, they suggest that each protein might "provide its additive effect on budding in a sequential manner driving budding in a defined, organized fashion".

They conclude that HA and NA seem to be the only driving forces that are able to initiate virus budding, possibly by concentrating in lipid rafts domains and inducing local membrane curvature, and that further recruitment of M1 to these membrane domains stimulates M1 polymerization, which promotes membrane bending and drives progression of the budding

process. The helical structure of polymerized M1 might further determine membrane curvature [31]. Finally, M2 seems to be most efficient to mediate membrane scission and to complete the budding process [34].

The ability of M2 to associate with M1 [40] and HA [245] seems to suggest that M2 might be recruited to the viral budding site by interaction with either M1 and/or HA. The implied hierarchy in protein assembly during virus budding is less clear though, seeing that mutations of the M2 cytoplasmic tails (which impair M1-M2 interaction) significantly reduce incorporation of M1 into virus particles and severely affect further incorporation of the viral genome [40,246,290]. Also mutation of HA and NA cytoplasmic tails were shown to cause greatly reduced M1 and vRNP packing into newly forming virions [9,291]. According to these findings, it is a possible scenario that M2 is recruited to the viral budzone defined by HA and NA and drives membrane scission independent from the presence of M1. Interaction between M1 and M2, however, might strongly increase the probability of proper packing of the viral core components. Furthermore, not only M1, but also interaction between M1 and M2 were reported to be determinants of virus morphology, stressing the central function of this interaction during the budding process [10,11,37,246].

Since defective incorporation of M1 into virus particles is typically accompanied by reduced genome packing, it is commonly hypothesized that M1 mediates incorporation of vRNPs into virions by bridging the interaction between viral envelope and viral genome. Specific interactions between vRNPs and the M1 layer have not yet been identified though, i.e. no evidence has been provided whether vRNPs interact directly with the M1 layer or whether they might interact (also) with the transmembrane protein cytoplasmic tails.

Notably, the role of the viral genome during virus budding has not been characterized until today and is mostly neglected in current models. vRNPs might have a yet unrecognized mechanistic or regulatory function during the budding process in order to ensure production of infectious virus particles. It was suggested earlier that the interaction strength between vRNPs and M1 might be related to virus morphology [69]. More recent work strongly supports the idea of functional involvement of vRNPs in virus budding, showing that NP affects virus morphology by interplay with M1 involving specific NP residues [14]. No mechanistic function of NP has however been determined in this process. How virus budding is coordinated with the arrival and incorporation of the viral genome remains thus issue of investigations.

1.4.4.3 The viral genome – from the nucleus to the budding site – vRNP transport and genome packaging

Only in the last few years, it has become apparent that efficient delivery of vRNPs from the site of vRNP formation to the site of virus assembly requires a well-organized sequence of events and the concerted action of different mechanisms. This includes the complex process of nuclear export, the apical targeting mechanism, which is closely related to the underlying mechanisms of cytoplasmic transport, and finally, assembly of vRNPs during or prior to genome incorporation and assembly of virus particles.

Upon formation in the cell nucleus, vRNPs assemble with M1 and NEP and undergo CRM1-dependent nuclear export, as described in section 1.4.4.2.1. Additional cellular factors and signaling cascades were further reported to be involved in vRNP nuclear export, suggesting a complex interplay between host cell and vRNPs. According to biochemical fractionation experiments, it appears that vRNPs become tightly associated with host cell chromatin prior to nuclear export, which was proposed to facilitate access to the cellular nuclear export machinery [292]. The mitogen-activated protein kinase (MAPK) signaling cascade and also apoptosis-regulating caspase 3 were further shown to promote vRNP nuclear export in infected cells [293,294]. Intriguingly, it was reported that accumulation of HA in lipid raft domains of the plasma membrane results in activation of MAPK signaling and thus triggers enhanced nuclear export of vRNPs, suggesting a mechanism to coordinate nuclear export of the viral genome with viral envelope formation [241].

The cellular vRNP-binding protein YB-1 was reported to relocate from the cytoplasm to nuclear PML bodies during virus infection where it assumedly associates with vRNP nuclear export complexes. Evidence was presented that YB-1 is required subsequent to nuclear export to target vRNPs to microtubules and to the microtubule organizing center (MTOC), ensuring efficient cytoplasmic transport and progeny virus production [295].
vRNPs reportedly use Rab11- and microtubule-dependent recycling endosomal transport machinery across the cytoplasm to reach the apical plasma membrane [280,296,297,298]. They transiently accumulate at the MTOC early during infection and, later on, redistribute to the cell periphery, colocalizing with Rab11 and adopting a punctate appearance. Pull-down experiments suggest that association between vRNPs and recycling endosomes is mediated by direct interaction between the active GTP-bound form of Rab11 and the viral polymerase subunit PB2 [280,296].

In earlier work, also lipid raft-dependent apical targeting of vRNPs was proposed, based on the observation that NP was found to be intrinsically targeted to the apical cell periphery in a cholesterol-dependent manner [299]. The molecular basis of this observation was not identified though, and the significance of lipid rafts for transport of internal viral components has been paid little attention since. Possible contributions of NP to vesicular transport of vRNPs or virus assembly cannot be excluded. Lipid-raft based targeting of intact vRNPs remains to be demonstrated though.
Speculations that M1 might mediate apical transport of vRNPs by forming a piggy-back complex with the viral transmembrane proteins were not confirmed [300].

Another important aspect of virus assembly is the process of genome packaging. Due to the segmented nature of the viral genome, genome packaging has been a matter of debate over many years. Genome segmentation into eight distinct vRNP species provides evolutionary advantages like the reassortment of genetic material, but it also challenges viral infectivity since efficient viral replication requires the complete viral genome.
At the beginning of this debate, two opposing models of Influenza virus genome packaging were suggested, both of which seemed to be supported by experimental data: the random versus the selective packaging model [100,301]. In both cases, a mechanism is required to discriminate genomic vRNA from positive-sense viral cRNA and other RNA species. The random packaging model implies that sufficient numbers of vRNPs need to be incorporated into virions for the production of infectious virus particles, which would further be accompanied by the formation of a high proportion of noninfectious virus particles. Specific packaging, however, requires specific packaging signals to distinguish between the different vRNA segments and to ensure that one copy of each vRNA species is incorporated into budding virus particles. First strong evidence supporting a selective packaging mechanism was provided by studies on naturally occurring defective-interfering (DI) vRNAs and by characterization of *cis*-acting packaging signals within vRNA sequences [302,303,304]. DI RNAs are internally deleted vRNAs, which lack part of the coding sequence but retain the terminal regions and compete with the corresponding full-length segments for incorporation into virus particles.
A more detailed model on packaging signals and genome organization was obtained only during the last ten years by contributions from a variety of approaches, including cryo-electron tomography, fluorescence *in situ* hybridization (FISH) and reverse genetics. Striking evidence for selective and highly organized packaging of vRNPs was provided by high-resolution structural data from intact and budding virus particles, demonstrating that most

virus particles contain a highly organized set of eight (presumably different) vRNPs (Fig. 1) [8,31,35,53,305,306]. Segment-specific detection of vRNAs by multicolor single-molecule FISH further confirmed that the majority of virus particles contain one copy of each vRNA segment and thus incorporate a complete set of the viral genome [56]. The regular arrangement of vRNPs indicates a well-defined mechanism of assembly and a well-ordered process of genome incorporation. However, also marked morphological and ultrastructural differences between particles were reported, and existence of distinct morphogenetic pathways was suggested [307].

Reverse genetics studies allowed characterizing the packaging signals within RNA sequences of all eight vRNA segments (reviewed in [100,305,308]). Even though specific nucleotides contributing to the packaging motifs are poorly defined in most cases, the packaging signals share common features. They can be described as discontinuous *cis*-acting RNA sequences spanning the 3′ and 5′ terminal regions of vRNAs, comprising both coding and non-coding sequences. Minimal sequences for efficient packaging were reported to include between nine and 80 nucleotides of the coding sequence at either end [308]. Theoretical considerations on nucleotide variability in the viral genome (due to redundancy in the genetic code) confirmed evolutionary pressure on codon conservation in the terminal regions of vRNAs independent from amino acid conservation [309].

A hierarchical network of interactions among vRNPs was further suggested based on observations that defective packaging of one segment can affect also packaging of other segments in *trans* [310,311,312,313,314]. Not all segments appear to be equally important though. In particular, segments 1, 3, 5 and 7 seem to play an important role for genome assembly, while segments 2, 4, 6 and 8 appear to be less critical for incorporation of other segments, which might facilitate exchange of antigenic determinants among strains [315]. The characteristic “7+1” arrangement of vRNPs within virus particles (Fig. 1) similarly seems to suggest that the central vRNP segment in genomic complexes might be more important for assembly than the surrounding segments. Fournier *et al.* however reported that segment 4, encoding HA, is a likely candidate to occupy the position of the central segment in the genome of H3N2 virus A/Moscow/10/99 [306].

Even though the existence of packaging signals is well established by now, the molecular mechanism of selective packaging is still not fully understood. First evidence was obtained though. A single interaction network was demonstrated to be formed between vRNAs *in vitro*, involving all eight vRNAs by at least one interaction, supporting that supramolecular complexes can be formed by nucleotide base pairing and thus by direct interaction of vRNAs.

The relevance of the observed interactions was verified by deletions of known packaging signals which strongly affected vRNA-vRNA interactions *in vitro* [305]. Furthermore, nucleotides mediating interaction *in vitro* could be identified and were tested for their function in genome packaging in infected cells, using reverse genetics [316]. The results strongly suggested that these nucleotides mediate interaction between vRNPs during virus assembly and that multisegmental genomic complexes are formd by base pairing between vRNA segments. This hypothesis is furthermore in agreement with the architecture of vRNP complexes as described by Baudin *et al.*, indicating that nucleotide bases of NP-bound vRNA are exposed to the solvent and that NP increases the accessibility of vRNA bases, presumably by unfolding RNA secondary structure [87]. Nevertheless, it was pointed out by Fournier *et al.* that it is still not fully clear whether vRNA is (or is not) able to form secondary structure within vRNP complexes [305,306]. It addition to the vRNA nucleotide sequence, it was reported that also specific highly conserved amino acids in NP, clustering around the RNA-binding groove, seem to play an important role in incorporation of multisegmental vRNP complexes [317].
Strain-specific differences between vRNA interaction networks *in vitro* were demonstrated by comparison of vRNA segments from H3N2 and H5N2 virus strains [318]. Also analysis of codon conservation indicated strain-specific differences in certain packaging signals, which might have implications for genetic reassortment [309]. In case of H5N2 virus (A/Finch/England/205/91), several sequences involved in vRNA-vRNA interactions *in vitro* were unexpectedly found to locate in the central region of vRNA segments. These were previously not identified as part of the packaging signals [318]. Similarly, analysis of codon conservation revealed low variability of some codons in the central part of vRNA segments, suggesting unrecognized functions of these genomic sequences [309].

Together, data obtained on Influenza virus genome packaging strongly support a selective packaging mechanism; they indicate however also a certain flexibility in genome packaging, allowing incorporation of seven or nine vRNP segments instead of eight and tolerating mutations to varying degrees [309,311,312,313,319,320,321,322]. Also incorporation of reporter genes without specific packaging signals [98,314,323] and selection of efficient packaging signals from randomized sequences without a clear consensus motif for packaging support this flexibility and variability of packaging signals [324,325]. Hutchinson *et al.* stated that “although the evidence for a specific packaging method is overwhelming, the mechanism is clearly not perfect” [100]. They further speculate that an imperfect packaging strategy might be beneficial to virus fitness. Evolution of Influenza viruses either by reassortment or

by accumulation of mutations in the protein coding sequences or promoter regions might benfit from a certain flexibility or imprecision of packaging signals.

The structural organization of multisegmental vRNP complexes within virus particles – as revealed by electron tomography – seems to be in accordance with studies on vRNP packaging signals and the reported vRNA-vRNA interactions. A “transition zone” underneath the viral membrane was described where the bundle of parallel oriented vRNPs forms a tightly interconnected platform and establishes close contact with the viral matrix layer and the viral envelope. This zone was reported to be long enough (13.3 to 17.5 nm) to comprise an average of 206–271 nucleotides from both ends of vRNA, which is consistent with terminal packaging signals that closely interact by nucleotide base pairing [306]. Observations are inconsistent though regarding the question whether vRNPs are connected along their entire length. While, on the one hand, it was stated that no close contacts between vRNPs outside the transition zone could be observed [306], another study reported frequent direct contacts between vRNPs throughout the virus by short string-like structures resembling RNA [35]. It cannot be excluded that different observations might result from analysis of distinct viral strains.

At which stage of the replication cycle higher-order assembly of vRNPs into genomic complexes takes place is unknown. Colocalization analysis of vRNA segments in infected cells, using FISH with single molecule sensitivity, strongly suggested that vRNPs are exported individually from the nucleus, localizing separately first, and assemble during cytoplasmic transport with Rab11-positive vesicles, colocalizing at high frequency on recycling endosomes before their arrival at the plasma membrane. Rab11 was further shown to be required for efficient colocalization of vRNA segments in the cytoplasm, indicating that recycling endosomes might serve as platform to gather vRNPs before they reach the plasma membrane [134]. Momose *et al.* proposed that interaction between Rab11 and the viral polymerase might help to orient and align vRNPs on the vesicular membrane and thus facilitate interaction of the terminal packaging signals adjacent to the polymerase-binding site [298]. The work further suggests that before reaching the MTOC vRNPs do not colocalize in the cytoplasm early during infection, but can be found separately adjacent to microtubules. As opposed to this, another study came to the conclusion that subcomplexes of vRNP segments might preassemble already within the nucleus [326]. However, colocalization of vRNPs prior to nuclear export is difficult to assess due to the high local density of vRNPs in the nucleus.

vRNP complexes are finally transferred from recycling endosomes to the budding site, most likely as complete sets of 8 vRNPs. The targeting mechanism and the physical interaction responsible for local association with the viral envelope have not been identified yet. As aforementioned, the presence of M1 and interaction of M1 with viral envelope proteins were shown to be important for efficient incorporation of the viral genome, even though tight interaction between vRNPs and the M1 layer within virions is generally not observed by electron tomography (1.4.4.2). vRNPs might be delivered to the plasma membrane together with viral protein M2 on Rab11-positive endosomes, even though cotransport and targeting mechanism of M2 remain to be demonstrated (1.4.4.1). Evidence suggests that M2 promotes membrane scission, eventually leading to release of virus particles, which is further supported by enzymatic activity of NA [10,18,30,246].

1.5 The Influenza A virus nucleoprotein (NP)

NP is a 498-aa protein, encoded by segment 5 vRNA [327], which is highly conserved among Influenza A virus strains [309,328,329,330]. Analysis of 617 NP sequences from Influenza A viruses demonstrated 85 % amino acid identity in more than 95 % of the sequences [309]. Comparison of 2500 NP sequences further revealed that only 30 % of residues in NP are polymorphic [331]. Significant similarities were also reported among Influenza A, B and C virus NP [332]. Structural similarities can be observed also with nucleoproteins from other negative-sense RNA viruses [333].

NP consists of two domains, a head and a body domain, and further a tail loop (aa 402–428) which is connected to head and body domain by two flexible linkers (Fig. 5). X-ray crystal structures were obtained from NP homotrimers, revealing that the tail loop enters the neighbouring NP subunit and drives homooligomerization by electrostatic, hydrophobic and beta-sheet interaction [93,333]. The flexibility of the linkers is assumed to allow formation of various oligomeric structures of NP. Purified NP (free from RNA) was shown to form trimers, tetramers, pentamers, hexamers, rings of 7 to 11 NP subunits and even helical and double-helical RNP-like structures [334]. Oligomerization *in vitro* was found to be strongly dependent on the ionic strength [335].

The secondary structure of NP is mostly α-helical. Head and body domain of NP are tightly interconnected by three polypeptide regions. They are formed by discontiguous sequences of the polypeptide chain which repeatedly goes back and forth between both domains. This specific organization of NP tertiary structure might explain why it was formerly difficult to

assign functions like RNA-binding, homooligomerization or interaction with M1 to specific regions of the NP primary sequence like the protein N- or C-terminal domains.

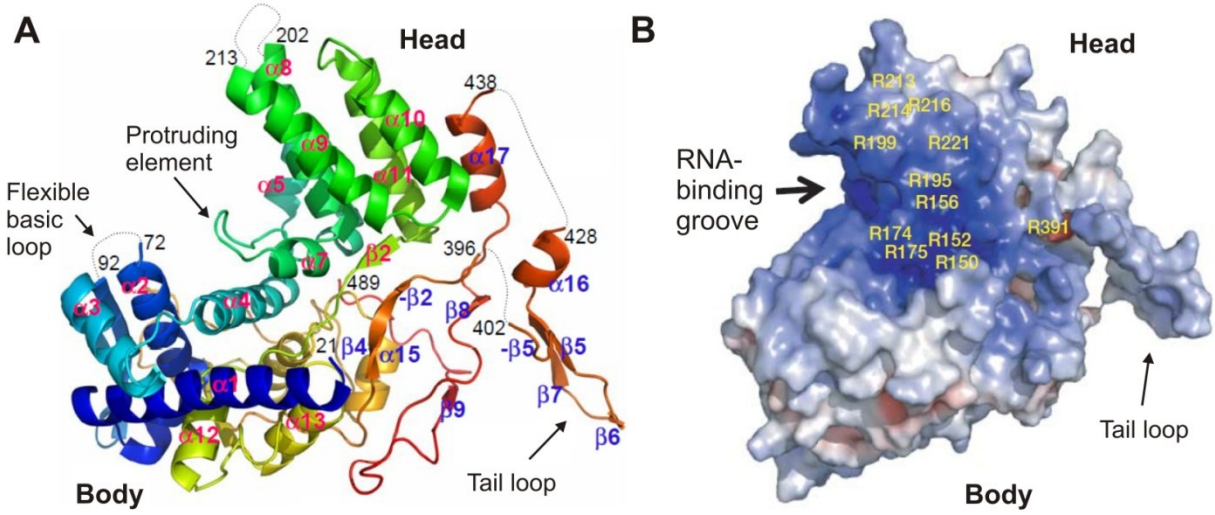

Fig. 5: Crystal structure of NP from Influenza A/WSN/1933, depicting one NP subunit of an NP homotrimer (PDB 2IQH). Illustrations are adapted from [93]. (A) Representation of secondary structure elements, including denotations of the 19 α-helices and 8 β-strands. Assignment of flexible basic loop and protruding element are based on [333]. (B) Electrostatic surface potential representation of NP, indicating a potential RNA-binding site rich in conserved arginine residues. Positive electrostatic potentials are shown in blue, negative potentials in red. Both representations A and B show a side view of NP.

NP is a ssRNA-binding protein, which encapsidates both cRNA and vRNA in infection. It has a net positive charge at neutral pH and is rich in arginine residues. A net charge of +14 was reported for Influenza A/PR/8/34 NP at pH 6.5 [327]. A positively charged groove between head and body domain was shown to be implicated in RNA-binding and is thus termed "RNA-binding groove" (Fig. 5B) [93,333]. It contains numerous highly conserved arginine residues, which are spread throughout the primary sequence, consistent with the finding that NP-RNA contact is mediated throughout the entire polypeptide [336]. Two structural features were further identified in close proximity to the RNA-binding groove: a flexible basic loop (aa 73–91) and a protruding element (aa 167–186), both containing numerous positively charged residues. Mutational analysis confirmed that residues R74, R75, R174 and R175 in flexible loop and protruding element as well as the close-by residue R221 together are essential for RNA-binding; also residues along the binding groove (R150, R152, R156 and R162) were shown to be implicaed in RNA-binding. Since deletion of the flexible loop significantly reduced the affinity for RNA, a model was postulated according to which the

flexible loop might capture RNA and deliver it into the binding groove where the protruding element might clamp the RNA into the groove [333]. Molecular dynamics studies support that the flexibility of the basic loop (aa 73–91) and further flexibility of the loop spanning residues 200–214 are required for RNA-binding and most likely for conformational changes, which are induced by RNA-binding [337].

Structural data and mutational analysis are in accordance with results that were obtained in earlier studies. Already in 1970, it was postulated that NP binds vRNA electrostatically via its phosphate backbone [338]. In 1994, chemical modification experiments confirmed NP-binding to the RNA phosphate backbone, while showing that the nucleotide bases of NP-bound RNA are exposed to the solvent. Consistently, NP associates with ssRNA with high affinity, but without sequence specificity [87,91]. Accessibility of RNA on the outside of the NP protein scaffold is furthermore in accordance with the reported sensitivity of vRNPs to RNAse digestion. In 1999, Elton *et al.* suggested – based on chemical modification experiments and intrinsic protein fluorescence measurements – that arginines and tryptophanes are involved in RNA-binding, but not lysines [336]. Independent studies reported dissociation constants of NP and ssRNA of about 20 nM [87,187,333,339]. A binding stoichiometry of 20–24 nucleotides per NP subunit was estimated [52,93,96]. RNA fragments of 18 nt were furthermore shown to be protected within RNP complexes from RNAse digestion [95].

Evidence suggests that RNA-binding and NP oligomerization are coordinated and cooperative processes. NP was reported to self-associate with lower affinity in the absence of RNA than in its presence [92], and binding of NP to ssRNA was shown to be highly cooperative *in vitro* [91]. Mutations of RNA-binding sites were moreover found to affect NP oligomerization and vice versa, suggesting that both functions are linked via protein conformation: While, on the one hand, tail loop mutant R416A, yielding obligate monomeric NP, was found to display strongly reduced RNA-binding affinity [335,336,340], RNA-binding mutants R361A and R204A-R208A were shown to display an oligomerization defect [337].

Structure determination revealed that the overall structure of monomeric NP-R416A is mostly identical to the structure of wild-type (wt) NP, except for C-terminal residues 386–498. The C-terminus of the mutant was shown to be rearranged on the NP surface and reaches into the RNA binding groove, thus lowering the positive charge of this groove [176]. NP-R416A was further found to be unable to support transcription in a minireplicon assay, suggesting also a failure of NP-R416A to interact with the viral polymerase [317]. Notably, mutations R361A and R204A-R208A were postulated to affect RNA-binding and NP oligomerization by a

completely different molecular mechanism, namely by decreasing the flexibility of two flexible loops involved in RNA-binding and oligomerization [337].

Even though NP reportedly forms oligomers *in vitro* [334,335] and in cells [44], it was indicated that only monomeric NP can efficiently polymerize onto RNA, forming larger structures [176]. Longtime, it has been unclear how NP oligomerization and RNA-binding might be controlled in infected cells until more recently phosphorylation of residue S165 was found to stabilize the monomeric state of NP and to reduce its RNA-binding affinity [176,261]. This residue is highly conserved among Influenza A and B viruses, and it was found to be phosphorylated during infection. It locates in a region reported to be involved in intermolecular NP-NP interaction (aa 160–167) and adjacent to the protruding element involved in RNA-binding (aa 167–186) [331]. Phosphorylation thus might be a tool to control polymerization and RNA-binding of NP in infected cells, even though its regulation in the context of viral infection and replication might be more complex.

Apart from viral RNA, NP interacts also with another constituent of viral RNPs, namely the viral polymerase. Direct interaction between NP and polymerase subunits PB1 and PB2 was demonstrated [182,341,342]. NP residues R204, W207 and R208 were further identified to interact with the polymerase complex and to be essential for both viral replication and transcription [188]. Independent from its RNA-binding activity, NP was shown to interact with the viral polymerase and stimulate replication of short model RNA templates *in vitro* why NP was suggested to function as polymerase cofactor [343]. *In vitro* analysis further revealed that NP facilitates promoter escape of the viral polymerase, thus acting as elongation factor of the viral polymerase [177].

The recruitment of NP onto nascent full-length RNPs was found to be driven by NP oligomerization rather than RNA-binding, suggesting that RNA-binding might occur subsequent to NP oligomerization during RNP assembly. New NP subunits were shown to be added in a “tail loop-first” orientation [90]. Nevertheless, RNA-binding activity of NP is critically required for stabilization of full-length viral replication intermediates in cells and for successful viral replication [90,177,187]. The cellular RNA helicase and NP-binding protein UAP56 was further shown to promote encapsidation of viral RNA species by NP, presumably acting as chaperone during this process [177].

A broadly accepted model on viral RNA encapsidation suggests that specific encapsidation of viral RNA species is initiated by the viral polymerase, which selectively binds to the 5′

terminal promoter sequences of nascent viral RNAs. It thus forms a nucleation point for recruitment of NP, followed by NP homooligomerization [54,175]. Consistently, data seem to indicate that NP by itself is not sufficient to stabilize viral replication intermediates in cells, but requires the presence of the viral polymerase complex [181].
A molecular mechanism was postulated by which the viral polymerase might facilitate NP oligomerization and RNA-binding: The flexibility of loop 200–214 was proposed to be important for RNA-binding [337], and it harbours further conserved residues R204, W207 and R208 for polymerase-binding, leading to the suggestion that interaction between NP and the viral polymerase might induce conformational changes in NP, thereby increasing its RNA-binding affinity and promoting cooperative binding of other NP molecules to the "primed NP-RNA site" [176]. As indicated above, also regulatory factors like dephosphorylation of monomeric NP or involvement of RNA helicase UAP56 might play a role in this process.

It should be furthermore considered that interaction between NP and viral polymerase could possibly involve different interfaces on NP depending on whether NP is part of the RNP template structure or part of nascent RNP complexes. Potential interaction sites for polymerase-binding apart from R204, W207 and R208 have not been identified though, albeit residues selectively affecting different polymerase functions were reported [183,317]. Host-specific adaption of residue 627 in PB2 was furthermore postulated to affect NP-PB2 interaction in a host factor-dependent way [344]. This was, however, later on questioned by the work of Cauldwell *et al.* [345].

Apart from tail loop-mediated linear polymerization of NP, NP establishes also intrastrand contacts within the double-helical structure of viral RNPs. An NP-NP dimer interface was consistently identified, which allows NP subunits to bind to each other in an antiparallel constellation [92]. In those NP dimers, the RNA-binding groove was shown to be fully accessible and the RNA-binding affinity is indistinguishable from that of wt NP. The dimerization interface involves two polypeptide regions, comprising residues 149–167 and 482–498. Disruption of the dimer interface by mutation D491A was shown to prevent dimerization but did not affect tail loop-mediated oligomerization. However, failure to dimerize severely affected the ability of NP to support replication and transcription. The dimerization interface is considered to be essential to organize RNP strands into functional double-helical structures [92].
Close physical contact between the two antiparallel NP strands of double-helical vRNP structures was consistently observed also within three-dimensional cryo-electron microscopy

(EM) reconstructions of purified native vRNPs [88,89]. However, docking of the NP crystal structure into cryo-EM reconstructions led to deviating results in independent studies. While one study suggested NP protomers of antiparallel strands to interact via their N-terminal domains, the body domains facing each other (Fig. 3) [88], another study concluded that interaction between RNP strands involves a region nearby the NP head domain [89]. The identified dimer interface might help to define the position of NP (and thus of viral RNA) within RNP strands more precisely and contribute to understand the functioning of the viral replication machinery on the molecular level.

Apart from the structural role of NP and its function in viral replication and transcription, NP plays an important role also as adaptor to the host cell. It is involved in multiple interactions with host cell proteins and has been implicated in Influenza virus-induced signaling.

NP was shown to induce apoptosis in airway epithelial cells, presumably by direct interaction with the anti-apoptotic cellular factor clusterin [346], and it counteracts the protein kinase R (PKR)-mediated cellular innate immune response by association with heat shock protein 40 (Hsp40) and subsequent release of PKR inhibitor p58IPK [347]. These mechanisms enable NP to interfere with the host interferon response and to contribute to virus-induced apoptosis, which reportedly promotes efficient viral replication late in infection [348].

NP further interacts with the antiviral cellular protein RUVBL2, which disrupts NP oligomerization and inhibits viral polymerase activity [349]. On the other hand, NP interacts with cellular factors which promote viral replication like the RNA helicase UAP56, which acts as a chaperone of NP for RNA encapsidation [177,350], and further with HMGB1, which was shown to increase viral polymerase activity, requiring therefore DNA-binding activity [351]. Furthermore, NP and also vRNP complexes bind to histone tails [352]. The function of this interaction is still unclear though. More detailed analysis revealed that NP specifically interacts with histone modifications characteristic for transcriptionally inactive chromatin, suggesting potential functions in chromatin remodeling, host cell shut-off or subnuclear targeting of vRNPs [353].

Cell fractionation experiments furthermore suggest association of NP with cytoskeleton elements in infected and transfected cells [339,354]. F-actin was identified as interaction partner of purified NP *in vitro* [339], and β-actin, vimentin and several tubulin isoforms were co-immunoprecipitated with reconstituted vRNPs from cells [103]. An NP interaction site for actin was proposed (aa 327–345), which – according to structure determination – is however buried within the NP molecule [93]. NP was found to colocalize with actin stress fibres in transfected cells, and disruption of F-actin-binding was shown to be accompanied by nuclear

accumulation of NP [339]. More recent studies, however, support a presumably indirect interplay between NP and actin filaments during infection. Upon disruption of cortical actin in infected cells, NP (most likely in form of vRNPs) was shown to reorganize underneath the plasma membrane together with actin, HA and M1 [243]. Interaction and colocalization was further demonstrated between NP and the actin-binding protein α-actinin-4, which crosslinks and bundles F-actin, forms stress fibers and anchors actin to membranes. Knock-down of α-actinin-4 was shown to greatly impair viral replication, reducing transcription, replication and nuclear localization of NP [355].

Another important host-dependent function of NP is further the nuclear-cytoplasmic transport of NP and genomic vRNPs. Functional interaction between NP and a number of nuclear import receptors, namely importin-α1, -α3, -α5 and -α7, was demonstrated [119,121,340,356,357,358]. Since efficient nuclear import of both NP and the viral genome is absolutely essential for viral replication, it is not surprising that specificity of NP for different importin isoforms is a critical determinant of host range. Adaption of avian Influenza viruses to mammalian hosts was shown to be accompanied by emergence of importin-α7 specificity of NP, while NP from avian strains displays specificity for importin-α3 [356]. Adaptive mutations in NP were further shown to enhance affinity between NP and importin-α1, thereby promoting viral transcription and replication in mammalian hosts [359].

NP accumulates in the cell nucleus due to nuclear localization sequences (NLSs), which are recognized by nuclear import receptors. NP contains at least two highly conserved NLSs: an unconventional N-terminal NLS (NLS1, aa 3–13) [121] and a classical bipartite NLS (NLS2, aa 198–216) [122]. A third functional NLS was identified, which is strain-specific though (aa 90–121) [360]. Evidence from several independent studies strongly suggests that NLS1 acts as major nuclear import signal of NP, driving nuclear import of NP and vRNP complexes, while only minor contributions by NLS2 were reported (see also 1.4.2) [118,120,123,361]. Consistently, structural information proved that NLS2 is unlikely to function as bipartite NLS in NP since the distance between the bipartite binding sites is too short within the NP molecule [93]. Instead, a nucleolar targeting signal was identified within NLS2, spanning residues 213–216 [123]. This sequence is not only responsible for accumulation of NP in nucleoli, but was furthermore shown to be essential for transcriptional activity of vRNPs. Various other (above-mentioned) functions have been assigned to the putative bipartite NLS2 as well: residues 200–214 represent a loop in the NP structure whose flexibility has been implicated in RNA-binding [337]; residues R204, W207 and R208 were reported to interact

with the viral polymerase and to be essential for polymerase activity in viral transcription and replication [188], and finally, residues 214 and 217 were reported to play a role in filamentous virion formation, presumably through interplay with M1 [14].

In addition to nuclear import signals, NP possesses also signals for nuclear export. In early studies on NP expression, it was already demonstrated that NP is a shuttling protein between nucleus and cytoplasm [124]. Even though NP with 56 kDa is not freely diffusible across the nuclear membrane, several studies reported relocalization of NP to the cytoplasm after initial accumulation in the nucleus. This shift to cytoplasmic localization was reported to be promoted by high cell densities [339], high NP expression levels and phosphorylation [362,363]. Leptomycin B, an inhibitor of the nuclear export receptor CRM1, was further shown to prevent relocalization of NP to the cytoplasm, indicating the presence of a CRM1-dependent nuclear export signal (NES) in NP [265]. Only recently, three functional NESs were identified in NP: NES1 (aa 24–49), NES2 (aa 183–197) and NES3 (aa 248–274) [274]. While NES1 and NES2 mediate CRM1-independent nuclear export, the function of NES3 was shown to be CRM1-dependent. Notably, NP oligomerization was found to be essential for nuclear export of NP [274]. (By contrast, upon interaction with import receptor importin-α5, NP was shown to be maintained in a monomeric state instead [340].)
Since oligomerized NP is the major protein component of vRNPs, a role of NP in nuclear export of vRNP complexes was consequently suggested. Experimental results, however, lack conclusive evidence that NP NESs might be involved in vRNP nuclear export, but indicate instead nuclear export complex formation with viral proteins M1 and NEP and CRM1-dependent nuclear export involving NEP NESs [66,67,101,116,264,267,280]. Whether the different NESs can be integrated in one coherent model for vRNP nuclear export remains to be determined.

NP is furthermore a phosphoprotein [364,365,366]. Only recently, seven sites in NP were identified which are phosphorylated during infection and/or within purified virions [261]. They are exposed on the NP surface, and five of them are highly conserved (S9/Y10, S165, Y296/S297, S402/S403, S457). Another phosphorylation site at conserved residue S3/T3 was previously demonstrated [367,368]. The overall phosphorylation pattern of NP was shown to be strain-specific and dependent on the host cell [369]. It further changes during the infection cycle [368]. In case of S165 and S402/S403, phosphomimetic mutations S165D and S402D suggested that constitutive phosphorylation is more detrimental to virus growth than lack of phosphorylation by alanine mutation S165A or S402A [261].

Phosphorylation sites were found to be located within well-characterized functional regions of NP: S402/S403 locates within the NP tail loop, driving NP oligomerization, S3 and S9/Y10 reside within the unconventional N-terminal NLS, and S165 is part of the RNA-binding groove, affecting RNA-binding and oligomerization. Regulatory functions of NP phosphorylation were hence proposed in nuclear-cytoplasmic transport and vRNP assembly [176,261,370]. General stimulation or inhibition of cellular phosphorylation was consistently found to affect nuclear accumulation of NP [363]. Alternative functions of NP phosphorylation were suggested also in virus entry, vRNP trafficking, virus assembly or immune response. [261].

1.6 Biological membranes and lipid rafts

Biological membranes are an essential prerequisite of life. They enclose all types of cells from bacteria to mammalian cells, forming a selective permeable barrier against the environment. They allow enrichment of nutrients and storage of energy and information in form of chemical gradients. Membranes further compartmentalize eukaryotic cells and enable formation of functionally specialized reaction spaces.

Membranes are formed by amphiphilic lipids, which self-assemble into lipid bilayers (Fig. 6A). The hydrophobic effect causes the hydrophobic (”water-fearing”) moieties of lipids to assemble as hydrophobic core of the membrane, while the polar lipid headgroups face the aequeous environment and provide solubility to the lipid bilayer within aequeous surroundings [371,372]. The hydrophobic core excludes polar substances and thus constitutes a barrier for hydrophilic (“water-loving”) molecules. The so-formed lipid bilayers can embed varying amounts of diverse peripheral and transmembrane proteins. This general design is conserved and common to all biological membranes; yet, the specific lipid and protein composition can vary widely and defines specific functions and properties of biological membranes [373,374].

The three most abundant lipid classes in eukaryotic membranes are the glycerophospholipids, the sphingolipids and the sterols (Fig. 7).

In glycerophospholipids, a glycerol backbone is ester-linked to two acyl chains in positions 1 and 2 and contains a phosphate ester at position 3 (Fig. 7A). The simplest glycerophospholipid is phosphatidic acid (PA) with only one phosphate group. This phosphate can establish a diester-bond to various headgroups like choline, ethanolamine, serine and inositol, yielding phosphatidylcholine (PC), phosphatidylethanolamine (PE),

phosphatidylserine (PS) and phosphatidylinositol (PtdIns), respectively. Inositol can be phosphorylated to varying degrees, yielding seven different types of phosphoinositides. They represent a minor group of membrane lipids, but play an important role in signal transduction processes and membrane trafficking [375]. Apart from their headgroups, glycerophospholipids differ also by the lengths and the saturation of their fatty acid chains. These can be saturated or mono- or polyunsaturated.

The backbone of sphingolipids is formed by sphingosine. Sphingosine can be amide-linked to a fatty acid chain, forming ceramide, which by further addition of a phosphocholine or carbohydrate headgroup becomes sphingomyelin (SM) or a glycosphingolipid, respectively

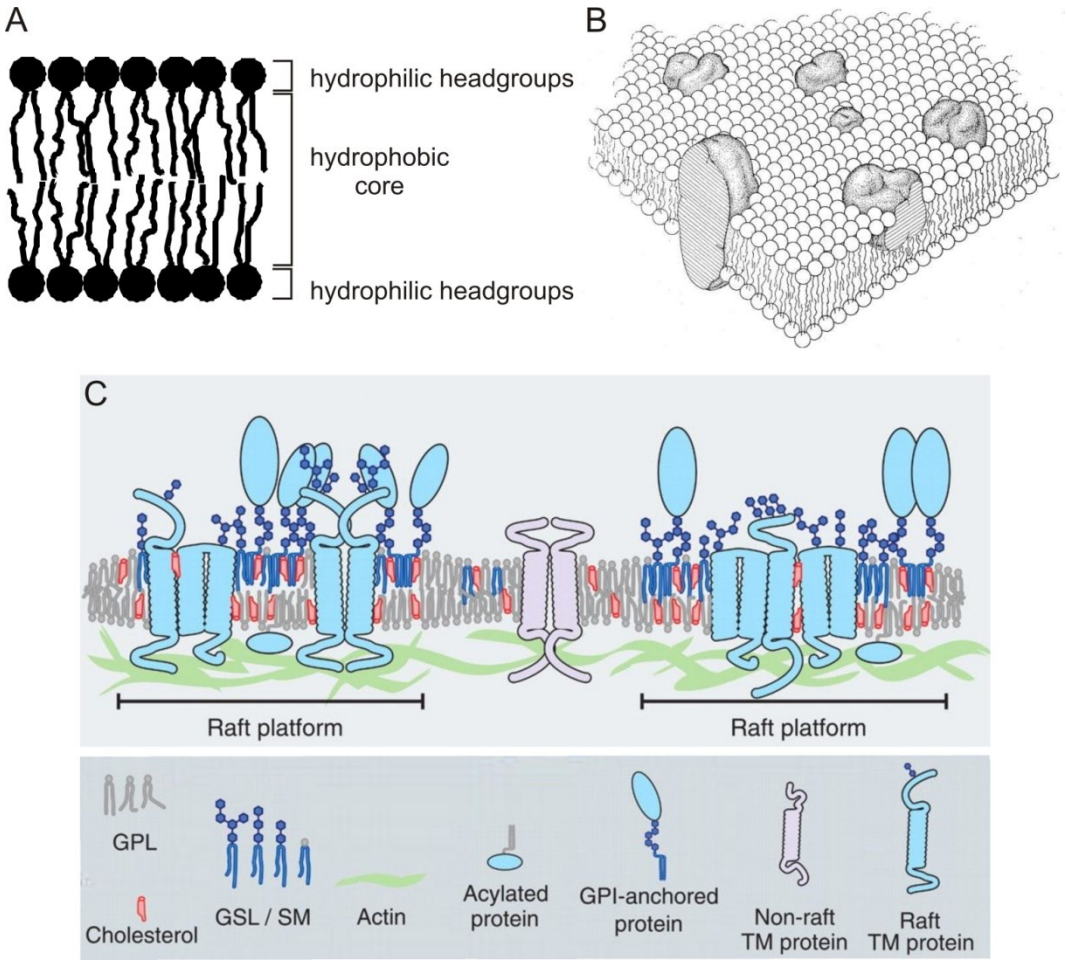

Fig. 6: Biological membrane organization. (A) Structure of a phospholipid bilayer. The acyl chains of phospholipids form the hydrophobic core, while the hydrophilic lipid headgroups constitute the bilayer surface that is in contact with the aqueous environment. (B) Fluid mosaic model of biological membranes according to Singer and Nicolson [376]. (C) Model of a biological membrane with lateral raft-based heterogeneity. Rafts are enriched in cholesterol and SM and display higher membrane thickness. GSLs and SM are enriched in the external membrane leaflet, while GPLs constitute the majority of the cytoplasmic leaflet. Proteins display preferential association with raft or non-raft domains, biased by intrinsic properties or protein modifications. Membrane domains can be stabilized by cortical actin. Illustration adapted from [373]. GL: glycerophospholipid, GSL: glycosphingolipid, SM: sphingomyelin, TM: transmembrane.

(Fig. 7B). Sphingolipids are enriched in the plasma membrane of mammalian cells; SM represents a major component of nerve cell membranes. The acyl chains of sphingolipids are commonly saturated.

Sterols are an important component of biological membranes despite their inability to form lipid bilayers by themselves. They have a less amphiphilic character than glycerophospho- and sphingolipids. The sterol found in mammalian cells is cholesterol (Fig. 7C). It has a planar four-ring structure with a small hydroxyl headgroup. It incorporates into the hydrophobic core of lipid bilayers where it intercalates between the fatty acid chains and is shielded by the large headgroups of sphingo- and glycerolipids. The ability of lipid bilayers to solubilize cholesterol by shielding it from contact with water has been described as "umbrella model" [377,378].

In 1972, Singer and Nicolson proposed the "fluid mosaic model" of biological membranes (Fig. 6B) [376]. In this model, lipid bilayers were regarded as two-dimensional liquids, in which lipids and proteins can freely diffuse. The role of lipids was considered to be rather passive, serving as solvent of the embedded proteins and constituting a barrier for cell compartmentalization.

This model of biological membranes has dramatically evolved since 1972. A huge variety of several hundred lipid species has been discovered in eukaryotic cells, indicating considerable complexity in membrane organization [379,380,381,382]. Furthermore, biological membranes were found to be packed with substantial amounts of proteins [383,384] and to be tightly interconnected with the cellular cytoskeleton [238,385]. About 20–30 % of genes in most organisms, including humans, were predicted to encode membrane proteins, which corresponds to several thousand genes of the human genome [386,387].

Both lipids and proteins were shown to be heterogeneously distributed within and across cellular membranes and to display a high degree of spatial organization, which has to be actively maintained (Fig. 6C). Asymmetric distribution of lipids and proteins between membrane leaflets was reported [388,389]. While glycerophospholipids PS, PE and PI were shown to localize predominantly on the inner plasma membrane leaflet, PC, SM and glycosylated lipids localize preferentially on the outer leaflet. The loss of membrane asymmetry and exposure of PS on the extracellular leaflet of plasma membranes is recognized as signal of apoptosis by a variety of organisms [390].

Cholesterol, an uncharged lipid, can move rapidly between the two membrane leaflets. It was assumed to be more abundant in the exoplasmic membrane leaflet due to its affinity for sphingolipids, yet, experimental findings suggest enrichment of cholesterol in the

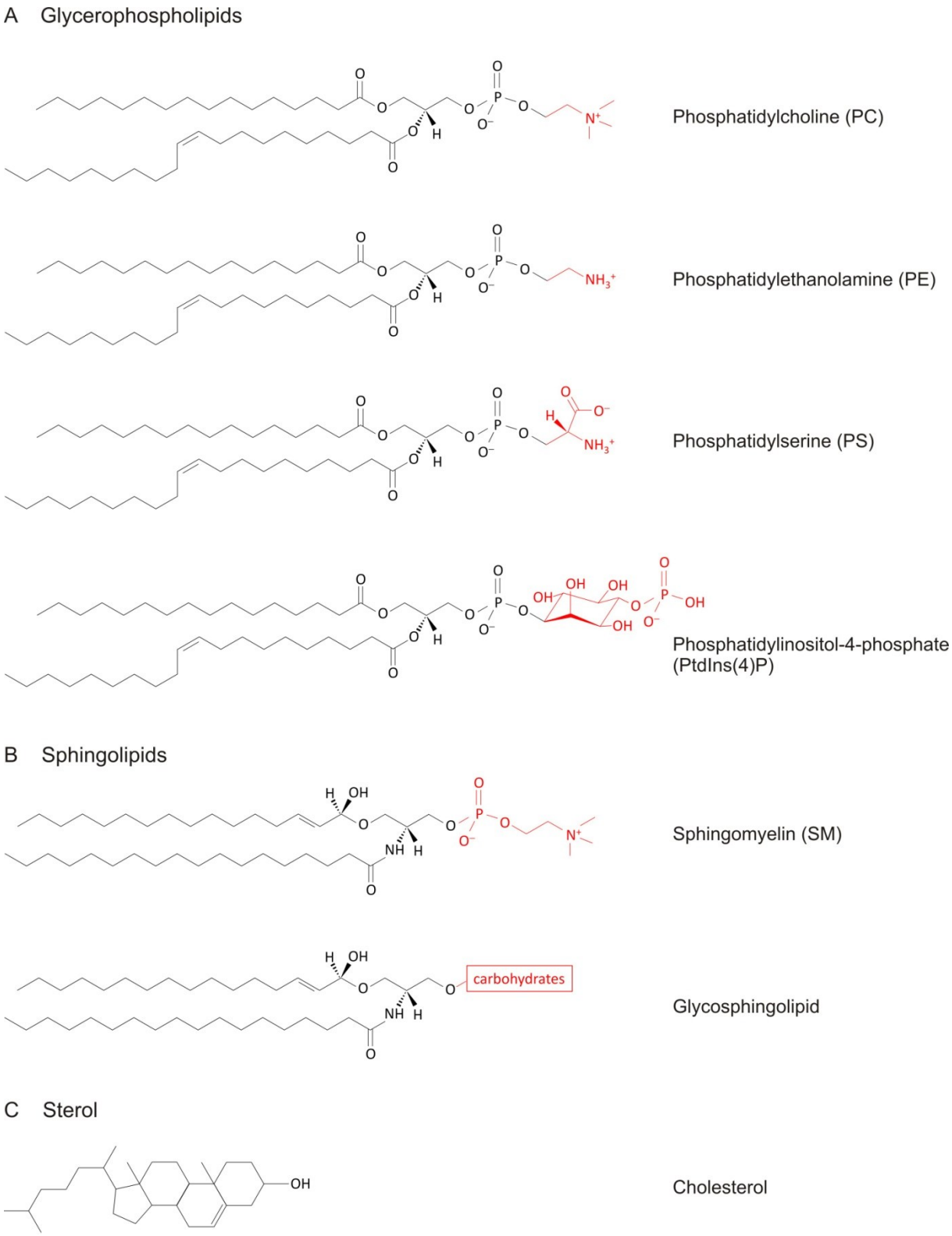

Fig. 7: Molecular lipid structures. Lipid species from the three most abundant lipid classes in eukaryotic membranes are presented. (A) Glycerophospholipids. (B) Sphingolipids. (C) Sterols. The lipid headgroups attached to either (A) the glycerophosphate backbone or (B) the sphingosine backbone are highlighted in red. The acyl chain in position 2 of the glycerol backbone is commonly unsaturated (A).

cytoplasmic leaflet [391]. How 40 mol% of cholesterol are distributed within the plasma membrane is still not finally clarified.
It has furthermore been established that dynamic behavior and organization of the two membrane leaflets in model and cellular membranes is interconnected by a phenomenon known as “transbilayer coupling” [391,392,393,394]. Whether transbilayer coupling is mediated by transmembrane proteins, spanning both leaflets, or rather by lipid-lipid interaction and interdigitation of acyl chains is still subject to ongoing research [395,396].

Apart from transverse membrane asymmetry, also lateral heterogeneity and formation of membrane domains were reported in both artificial lipid bilayers and biological membranes.
The formation of large-scale membrane domains due to lipid-lipid interaction has been extensively studied in model membrane systems, demonstrating that specific lipids like sphingolipids, cholesterol and saturated phospholipids preferentially associate and form liquid-ordered membrane domains within liquid-disordered membranes. These domains, formed by phase separation, can be visualized microscopically, using fluorescent probes which preferentially partition into one or the other phase [397]. In biological membranes, the existence of lateral sorting mechanisms was first implied by observation of different lipid and protein compositions in the apical and basolateral plasma membrane of polarized epithelial cells [224]. Distinct compositions are maintained despite extensive membrane trafficking among the different intracellular compartments and the plasma membrane, which led to postulation of the so-called “raft hypothesis”, suggesting lipid and protein sorting based on the formation of sphingolipid- and cholesterol-rich platforms, termed rafts, which are formed in the Golgi apparatus (where sphingolipids are synthesized) and which preferentially incorporate specific proteins and lipids in transit to the apical plasma membrane [226]. Initially, rafts were thus considered as sorting platforms for lipids and proteins which concentrate specific proteins and thus allow compartmentalization of membrane-bound processes. Due to their small size, however, lipid rafts in biological membranes cannot be visualized by standard optical microscopy. While raft domains were initially defined biochemically as membrane fraction which is resistant to cold detergent extraction [398,399,400,401], more advanced techniques with high spatial and temporal resolution later confirmed the existence of cholesterol-dependent nanoscale domains within membranes of living cells [402,403,404]. While the existence of nanoscale assemblies in biological membranes is generally accepted, their exact nature remains still elusive. Properties like stability, size, dynamics, composition and the players involved in modulation and formation of membrane domains are still controversially discussed [405,406].

Sphingolipid- and cholesterol-rich membrane domains were shown to display characteristic features like tight packing and high order of their acyl chains [407], low diffusional mobility of their components [408] and increased membrane thickness [409]. As compared to liquid-disordered domains, the high degree of order and increased membrane thickness are caused by the presence of saturated fatty acid chains in all-*trans* configuration and intercalation of cholesterol, which stabilizes the stretched conformation of the acyl chains [410]. Atomic force measurements in living cells demonstrated greater stiffness of membrane domains harboring typical raft marker proteins than of the surrounding non-raft membrane [411]. The large fraction of raft lipids in polarized epithelial cells is thought to contribute considerably to the robustness of the cell membrane [412] and also to environmental stability of enveloped viruses such as Influenza viruses [413].

Physical properties of raft domains are considered to be important for formation and functionality of rafts in biological membranes. Membrane thickness is a critical determinant for partitioning of transmembrane proteins into raft domains, driven by the energetic cost of hydrophobic mismatch. Proteins residing in ER and Golgi apparatus reportedly feature shorter transmembrane domains than proteins of the plasma membrane [247,414], which is consistent with increasing cholesterol and sphingolipid concentrations along the exocytic pathway [415]. The length of transmembrane domains is thought to facilitate protein sorting and to be one determinant of subcellular targeting and protein localization [416]. It is not fully clear though whether proteins associate with preformed lipid raft domains, or whether it is rather the proteins determining membrane thickness [417] and inducing assembly of raft domains by protein-lipid interaction [418,419].

Line tension that arises at the phase boundary between liquid-ordered and liquid-disordered phases due to hydrophobic mismatch was shown to drive coalescence and formation of large-scale domains in model membranes [420,421]. The small size of rafts in biological membranes was proposed to be stabilized by the actin cytoskeleton, which causes confinement of molecules and prevents merger of raft domains into large-scale domains [406]. Micrometer-sized domains are reversibly formed upon cooling in plasma membrane-derived vesicles (“blebs”) where the membrane is detached from the underlying cytoskeleton [422]. Lipid diversity in cell membranes and lipid species acting as interfacially active agents (linactants) were further suggested to contribute to lowering line tension in biological membranes and enable regulation of lateral heterogeneity [423,424,425]. Nevertheless, there is a large body of evidence that actin plays an important role in the organization of membrane domains [235,238,426]. Actin was shown to be critically involved in raft-based cell signaling

and in the formation and stabilization of large-scale raft-based membrane domains (signaling platforms) in response to external stimuli [239,427,428]. Functionalized large-scale domains can be observed for instance upon T-cell activation during formation of antigen receptor signaling foci (known as “immunological synapses”) [429,430].
The physical properties of membrane domains like bilayer thickness, curvature and lateral pressure can furthermore also directly affect protein function [431]. Bilayer thickness was reported to regulate ion channel activity, presumably by altering protein conformation [432], and also the functions of curvature-sensing proteins are usually tightly regulated by direct interplay with the membrane [433].

Lipid raft domains are thought to concentrate specific proteins due to protein motifs that promote their association with lipid raft phases. Apart from the length of protein transmembrane domains, also acylation with saturated fatty acids or modification with a glycosylphosphatidylinositol (GPI) anchor are strong indications for preferential partitioning of proteins into lipid rafts. Yet, also the presence of specific lipid binding sites, specific protein-protein interactions or “multi key recognition” of several distinct interaction partners determine protein targeting.
Raft association of Influenza virus membrane proteins has been well characterized. It is a prerequisite for lipid raft-based virus budding. Also other enveloped viruses were shown to use lipid rafts as platform for virus assembly and budding, e.g. HIV-1, Ebola and Measles virus [21,232,233]. They exploit the fact that rafts can merge into larger platforms and be functionalized by viral proteins to establish the viral budding site.
In case of Influenza viruses, lipid raft- and actin-dependent clustering of Influenza virus membrane proteins HA and M2 was demonstrated [245,249]. HA by itself was further shown to form nanometer- to micrometer-sized elongated domains in the plasma membrane [220] which correlate with actin-rich plasma membrane regions [240]. In infected cells, not only clustering of HA but also actin-dependent organization of Influenza virus core proteins NP and M1 was observed within large-scale plasma membrane domains together with HA [243]. Lipid raft association of HA was reported to be essential for efficient viral replication [434].
Assembly of virus particles in raft domains was furthermore suggested to facilitate virus budding, based on the inherent property of lipid raft domains in model membranes to promote membrane curvature and domain-induced budding. These effects are driven by the tendency to minimize energy costs of interfacial line tension [435,436]. Moreover, also a role for lipid rafts in virus-mediated membrane fusion during cell entry was postulated [437].

The initial concept of membrane rafts was shaped by the description of relatively stable, large-scale liquid-ordered domains in model membranes, which are observed at thermodynamic equilibrium. A more current definition of biological rafts, dating from 2006 and taking into account data from a variety of different approaches with high spatial and temporal resolution, emphasizes the small size, the heterogeneity and the dynamic nature of rafts. It describes rafts as "small (10–200 nm), heterogeneous, highly dynamic, sterol- and sphingolipid-enriched domains that compartmentalize cellular processes. Small rafts can sometimes be stabilized to form larger platforms through protein-protein or protein-lipid interactions" [438]. More recent experimental evidence suggests also the existence of long-lived, yet mobile, nanoscale rafts [405]. The functionality of raft domains (e.g. in cell signaling) relies on dynamic regulation of raft platforms though.

Most recent advances in understanding the complex phase behavior of lipid membranes and in unifying the diverse raft-associated phenomena have been made by including fluctuations into the description of phase behavior [439,440]. This can explain how macroscopic phase separation can be related to nanoscale rafts behaving as microemulsions, and how direct transitions between coexisting phases and microemulsions can be effectuated by thermal fluctuations [441]. In biological membranes, the membrane composition is thought to be tuned close to a critical point where the different phases coexist as interconverting fluctuations, which allows rapid and marked changes of membrane organization at low energy costs in response to small compositional or environmental changes [442,443]. It is thus conceivable that membrane organization can be easily manipulated by activity of lipid modifying enzymes, protein binding or the presence of viral proteins.

2 Aim of this study

The formation of infectious progeny Influenza A virions requires targeting and transport of the eight genomic vRNPs from the site of viral replication in the nucleus to the site of virus budding at the plasma membrane. These late events of the viral replication cycle, and specifically the mechanisms governing vRNP targeting and transport, are still very poorly understood.

A widely accepted hypothesis that M1 might contribute to target vRNPs to vesicular transport and/or to the viral budding site has evolved from *in vitro* membrane binding studies in conjunction with in-cell studies, showing that M1 is a membrane binding protein and that M1 also interacts with vRNPs and mediates vRNP nuclear export during infection. Yet, no evidence has so far been provided for the ability of M1 to simultaneously interact with vRNPs and membranes. Findings from microscopy studies on this issue are controversial. Previous studies further indicate the possibility that NP as major vRNP constituent might be equipped with an intrinsic targeting signal to the apical plasma membrane.

In this study, therefore, the capacity of vRNPs to associate with lipid membranes in the presence and absence of M1 should be explored using model membranes. Intrinsic subcellular targeting of NP should further be examined in the context of living cells. Fluorescent NP constructs and photoactivatable fluorophores were considered as ideal tools in this context to reveal information not only on NP localization, but also on site-specific NP dynamics and affinities in living cells.

In addition to analysis of the molecular mechanisms involved in vRNP transport, this study furthermore aimed at a more general approach to study the complex process of virus assembly. Numerous aspects still remain to be elucidated to fully understand how the virus hijacks the cellular machinery for efficient delivery of viral genomes to the site of virus formation. It remains to be determined how and where vRNP nuclear export complexes are assembled and if they are disassembled in the cytoplasm, how vRNPs are targeted to recycling endosomes and how they are transferred from recycling endosomes to the budding site, whether and at which stage individual vRNPs form stable multisegment complexes, and which factors finally initiate virus budding. The poor availability of data on these aspects of viral replication might be due to the difficulties to detect progeny vRNPs during infection and to study vRNPs further in the absence of infection. A major part of this work was therefore motivated by the objective to develop an experimental approach that allows studying targeting and transport of vRNPs in living infected cells in order to enable a comprehensive picture of Influenza genome transport during virus assembly and to approach the above-listed questions.

3 Material and Methods

3.1 Material

3.1.1 Biological material

3.1.1.1 Eukaryotic cells lines

CHO-K1	*Chinese hamster ovary cells (epithelial-like)*	ATCC CCL-61
HeLa	*Human cervical cells (epithelial)*	ATCC CCL-2
MDCK II	*Madin-Darby canine kidney cells (epithelial)*	ATCC CCL-34
293T	*Human embryonic kidney cells (epithelial)*	ATCC CCL-1573

3.1.1.2 Bacteria

E.coli DH5α chemically competent, provided by Christine Klaus (Humboldt-Universität)

genotype: F^- *endA1 recA1 hsdR17*($rk^- mk^+$) *supE44* λ^- *thi-1 gyrA*(Na1) *relA1* Φ80 *lacZ*ΔM15Δ *(lacZY* A-*argF)*

3.1.1.3 Viruses

Influenza A/X-31 (H3N2) virus and Influenza A/FPV/Rostock/1934 (H7N1) virus (abbreviated as FPV) were grown in 10-day-old embryonated chicken eggs and purified as described previously [444]. Allantoic fluid or concentrated virus were stored at –80°C.

Influenza A/WSN/1933 (H1N1) (abbreviated as WSN) was generated as recombinant virus in 293T cells and propagated on MDCK II cells.

3.1.1.4 Recombinant proteins

Recombinant proteins M1 (recM1) and NP were provided by Nadine Jungnick (Humboldt-Universität, Berlin). The protein sequences from Influenza A/FPV virus were expressed in *E.coli* and purified by His-tag affinity chromatography. His-tags with the amino acid sequence MGSSHHHHHHSSGLVPRGSH were fused N-terminally to the protein sequences. For further information see [445].

3.1.1.5 Cell culture media and reagents

The following media and reagents were purchased from PAA Laboratories GmbH, Pasching, Austria, if not stated otherwise.

- Agarose (SeaPlaque) for plaque assay [Lonza, Verviers, Belgium]
- Bovine serum albumin (BSA, 35 % in DPBS) [Sigma-Aldrich, Taufkirchen, Germany]
- DMSO for cell culture [Sigma-Aldrich, Taufkirchen, Germany]
- Dulbecco's Modified Eagle's Medium (DMEM) with phenol red, high glucose (for virus propagation only)
- DMEM without phenol red, high glucose (standard)
- DPBS with Ca^{2+} and Mg^{2+}
- DPBS without Ca^{2+} and Mg^{2+}
- EMEM (2×) [Lonza, Verviers, Belgium]
- Fetal bovine serum (FBS)
- L-glutamine (200 mM)
- Lipofectamine™ 2000 Transfection Reagent [Invitrogen, Karlsruhe, Germany]
- Neomycin solution (10 mg/ml), sterile filtered [Sigma-Aldrich, Taufkirchen, Germany]
- Neutral red (3.3 g/l) [Sigma-Aldrich, Taufkirchen, Germany]
- Penicillin/streptomycin (100×: 10,000 U/ml / 10 mg/ml)
- Trypsin, TPCK-treated [Sigma-Aldrich, Taufkirchen, Germany]
- Trypsin/EDTA
- TurboFect™ Transfection Reagent [Fermentas, St. Leon-Rot, Germany]

3.1.1.6 Antibodies

Dilutions for immunofluorescence (IF) and Western blotting (WB) are indicated.

Primary antibodies

- anti-β-actin antibody, clone AC-74, monoclonal (mouse IgG2a), WB 1:5000 [Sigma-Aldrich, Taufkirchen, Germany, #A2228]

- anti-coilin antibody, clone IH10, monoclonal (mouse IgG2b) , IF 1:1000
  [Abcam, Cambridge, UK, #ab87913]
- anti-GFP antibody, polyclonal (rabbit IgG), 1:3000
  [Invitrogen, Karlsruhe, Germany, # A11122]
- anti-Influenza A Hemagglutinin H7 (anti-HA), clone 9A9, monoclonal (mouse IgG2a)
  [HyTest, Turku, Finland], IF 1:6000
- anti-Influenza A nucleoprotein antibody (anti-NP), clone A1, monoclonal (mouse IgG2a)
  [Chemicon, Schwalbach, Germany, #MAB8257], IF 1:1000, WB 1:5000
- anti-Influenza A nucleoprotein antibody FITC-conjugated (anti-NP-FITC), clone A1, monoclonal (mouse IgG2a) [Chemicon, Schwalbach, Germany, #MAB8257F], IF 1:1000
- anti-Influenza A virus H3N2 antibody, polyclonal (goat IgG), WB 1:5000
  [Virostat, Portland, ME, USA, #1311]
- anti-Influenza A virus M1 antibody, polyclonal (goat IgG), IF 1:1000, WB 1:3000
  [Abcam, Cambridge, UK, #ab34848], for IF applications and WB if not otherwise indicated
- anti-Influenza A virus M1 antibody, polyclonal (goat IgG), WB 1:3000
  [Virostat, Portland, ME, USA, #1321], used for WB where indicated (section 4.1)
- anti-membrin antibody, clone 4HAD6, monoclonal (mouse IgG1), IF 1:1000
  [Abcam, Cambridge, UK, #ab13511]
- anti-PML protein antibody, clone H238, monoclonal (rabbit IgG), IF 1:1000
  [Santa-Cruz Biotechnology, Heidelberg, Germany, #SC-5621]
- anti-SC35 antibody, monoclonal (mouse IgG1), 1:1000
  [BD Bioscience, Heidelberg, Germany, #556363]

Secondary antibodies

- AlexaFluor® 568 goat-anti-mouse IgG, IF 1:1000
  [Invitrogen, Karlsruhe, Germany, #11004]
- AlexaFluor® 594 goat-anti-rabbit IgG, IF 1:1000
  [Invitrogen, Karlsruhe, Germany, #11012]
- Atto 647N goat-anti-mouse IgG, IF 1:1000
  [Sigma-Aldrich, Taufkirchen, Germany, #50185]
- Cy3 rabbit-anti-goat IgG, IF 1:1000
  [Sigma-Aldrich, Taufkirchen, Germany, #C2821]

- donkey-anti-goat IgG horseradish peroxidase conjugate (DAGPO), WB 1:5000
  [Santa-Cruz Biotechnology, Heidelberg, Germany, #L1605]
- goat-anti-mouse IgG horseradish peroxidase conjugate (GAMPO), WB 1:5000
  [Bio-Rad, München, Germany, #170-6516]
- goat-anti-rabbit IgG horseradish peroxidase conjugate (GARPO), WB 1:5000
  [Bio-Rad, München, Germany, #170-6615]
- IRDye-680 donkey-anti-goat IgG, WB 1:10.000
  [LI-COR Bioscience, Bad Homburg, Germany, #926-32224]
- IRDye-680 goat-anti-mouse IgG, WB 1:10.000
  [LI-COR Bioscience, Bad Homburg, Germany, #926-32220]

3.1.1.7 Enzymes, molecular biology reagents and kits

- Agarose [Biozym Scientific, Hessisch Oldendorf, Germany]
- DNA Loading Dye (6×) [Fermentas, St. Leon-Rot, Germany]
- dNTP-Mix, 10 mM each [Fermentas, St. Leon-Rot, Germany]
- GeneRuler™ 1kb DNA Ladder [Fermentas, St. Leon-Rot, Germany]
- Ligase: T4-DNA-Ligase [New England Biolabs, Frankfurt/Main, Germany]
- Phosphatase: Calf Intestinal Alkaline Phosphatase (CIP) [New England Biolabs, Frankfurt/Main, Germany]
- Polymerases:
  peqGOLD Taq-DNA-Polymerase for colony PCR with 10× buffer Y [PEQLAB, Erlangen, Germany]
  Phusion™ High-Fidelity DNA Polymerase [Finnzymes, Espoo, Finland]
- Restriction enzymes:
  *Afl*II, *Age*I, *Bam*HI, *Bsa*I HF, *BsrG*I, *Sac*II, *Xho*I [New England Biolabs, Frankfurt/Main, Germany]; Esp3I [Fermentas, St. Leon-Rot, Germany]
- Rotiphorese® 10× TBE buffer, running buffer for agarose gel electrophoresis [Carl Roth, Karlsruhe Germany]
- SYBR® Safe DNA Gel Stain (1000×) [Invitrogen, Karlsruhe, Germany]

Kits for DNA and RNA preparation

- QIAquick Gel Extraction Kit [Qiagen, Hilden, Germany]

- QIAprep Spin Miniprep Kit [Qiagen, Hilden, Germany]
- QIAGEN Plasmid Maxi Kit [Qiagen, Hilden, Germany]
- RNeasy Mini Kit [Qiagen, Hilden, Germany]

3.1.1.8 Oligonucleotides and plasmids

Three basic cloning vectors (**pEYFP-C1**, **pEYFP-N1** and **pDendra2-N** (Clontech, Saint-Germain-en-Laye, France)) were used to generate vectors for expression of fluorescent and non-fluorescent Influenza NP constructs as listed in Tab. 2. They all encode a fluorescent protein under control of a constitutive cytomegalovirus (CMV) immediate early promoter for expression in mammalian cells and feature a multiple cloning site either upstream or downstream of the fluorescent protein open reading frame for insertion of the sequence of interest. To prevent dimerization of EYFP as described in [446], pEYFP-C1 and pEYFP-N1 plasmids carrying a single codon change in the EYFP sequence (A206K) were used. These plasmids termed **pmEYFP-C1** and **pmEYFP-N1** encode the monomeric form of EYFP (mEYFP) and were kindly provided by Silvia Scolari [447].

Cloning and expression vectors encoding other fluorescent proteins were constructed based on the plasmids described above. For the generation of **pDendra2-C**, the open reading frame (ORF) of Dendra2 was amplified by polymerase chain reaction (PCR) from the template plasmid **pDendra2-N** and was then digested with *Age*I and *Xho*I. The mEYFP encoding sequence was removed from pmEYFP-C1 by digestion with *Age*I and *Xho*I and was replaced by the Dendra2 ORF. The primers designed for PCR and including the appropriate restriction sites are listed in Tab. 3 ({6}, {7}). **pmCherry-C1** was obtained by cutting the mCherry ORF from plasmid pmCherry-gp41 (provided by Roland Schwarzer, HU Berlin, Germany) using *Age*I and *BsrG*I and subsequent ligation into pmEYFP-C1 which had been digested with the same enzymes thereby replacing the mEYFP ORF by an mCherry ORF.

The plasmid **pHH21-NP** ([448], kindly provided by Michael Veit, Freie Universität Berlin, Germany) contains the cDNA of Influenza A/FPV/Rostock/1934 segment 5 vRNA, and served as template for amplification of the NP ORF from Influenza A/FPV/Rostock/1934, which was subsequently inserted at the multiple cloning sites of the fluorescent protein expression vectors that were described above. The sequence was thereafter further mutated if required. NP expressing plasmids generated in this work are specified in Tab. 2, the corresponding primer pairs are listed in Tab. 3. Plasmids for the expression of M1 from

Influenza A/FPV/Rostock/1934 were kindly provided by Bastian Thaa (Freie Universität Berlin, Germany): **pCFP-M1-NES** [257,449].

pRab11-RFP was obtained from Maik Lehmann (Humboldt-Universität, Berlin) [450].

Tab. 2: Plasmids generated for the expression of Influenza A/FPV/Rostock/1934 NP. The vector, the insert with restriction sites (in brackets) and the primer pairs that were used for construction of each designated plasmid are listed. All NP inserts were amplified from pHH21-NP. Mutations were introduced by PCR-based QuikChange mutagenesis using the indicated primer pairs. (Tags that were introduced code for the following amino acid sequences: nuclear export signal (NES): LQLPPLERLTL; tetracysteine (TC)-tag: CCPGCC)

name	vector	insert/mutation	primers
pmCherry-C1	pmEYFP-C1	mCherry (*Age*I, *Bsr*GI) cut from plasmid pmCherry-gp41	
pDendra2-C1	pmEYFP-C1	Dendra2 (*Age*I, *Xho*I)	{6}, {7}
pNP	pmEYFP-NP-N1	NP (*Afl*II, *Xho*I) cut from pmEYFP-NP-C1	
pmCherry-NP	pmCherry-C1	NP (*Xho*I, *Bam*HI)	{3}, {2}
pDendra2-NP	pDendra2-C1	NP (*Xho*I, *Bam*HI)	{1}, {2}
pNP-Dendra2	pDendra2-N	NP (*Xho*I, *Sac*II)	{3}, {4}
pmEYFP-NP	pmEYFP-C1	NP (*Xho*I, *Bam*HI)	{1}, {2}
pNP-mEYFP	pmEYFP-N1	NP (*Xho*I, *Sac*II)	{3}, {4}
pNP-E339A-Dendra2	pNP-Dendra2	NP mutation E339A	{8}, {9}
pNP-R416A-Dendra2	pNP-Dendra2	NP mutation R416A	{10}, {11}
pNP-NES	pDendra2-N	NP-NES(-Stop) (*Xho*I, *Bam*HI)	{1}, {5}
pDendra2-NP-NES	pDendra2-C1	NP-NES (*Xho*I, *Bam*HI)	{1}, {5}
pmEYFP-NP-NES	pmEYFP-C1	NP-NES (*Xho*I, *Bam*HI)	{1}, {5}
pNP-TC100	pNP	TC-tag insertion QuikChange mutagenesis	{12}, {13}
pNP-TC125	pNP	TC-tag insertion QuikChange mutagenesis	{14}, {15}
pNP-TC247	pNP	TC-tag insertion QuikChange mutagenesis	{16}, {17}
pNP-TC288	pNP	TC-tag insertion QuikChange mutagenesis	{18}, {19}
pNP-TC372	pNP	TC-tag insertion QuikChange mutagenesis	{20}, {21}

Tab. 3: DNA oligonucleotides used for PCR amplification and mutagenesis of Influenza A/FPV/Rostock/1934 NP. Restriction sites are underlined. Bold letters indicate mutation sites or sequence insertions. Oligonucleotides were synthesized by Invitrogen, Karlsruhe, Germany.

No.	name	sequence (5′ → 3′)	purpose
{1}	fw_NP_pEYFP-C1 (*Xho*I)	ACG TTA CTC GAG AAA TGG CGT CTC AAG GC	cloning/PCR
{2}	rev_NP_pEYFP-C1 (*Bam*HI)	AGC TGC GGA TCC TTA ATT GTC ATA CTC CTC TGC	cloning/PCR
{3}	fw_NP_pEYFP-N1 (*Xho*I)	ACG TTA CTC GAG ATG GCG TCT CAA GGC	cloning/PCR
{4}	rev_NP_pEYFP-N1 (*Sac*II)	ACA GTA CCG CGG ATT GTC ATA CTC CTC TGC	cloning/PCR
{5}	rev_NP_NES (*Bam*HI)	TCG GAT CCT TA**A AGA GTA AGT CTC TCA AGC GGT GGT AGC TGA AG**A TTG TCA TAC TCC TCT GC	cloning/PCR
{6}	fw_Dendra-C (*Age*I)	ACT TAC CGG TCG CCA CCA TGA ACA CCC C	cloning/PCR
{7}	rev_Dendra-C (*Xho*I)	ACT TCT CGA GAT CTG AGT CCG GAC CAC ACC TGG CTG GGC	cloning/PCR
{8}	NP_E339A_1	CCA TTC TGC AGC ATT TG**C** AGA CCT GAG AGT GTC AAG C	mutagenesis
{9}	NP_E339A_2	GCT TGA CAC TCT CAG GTC T**G**C AAA TGC TGC AGA ATG G	mutagenesis
{10}	NP_R416A_1	CCC ACT TTC TCT GTA CAG **GC**A AAT CTC CCT TTC GAG AGA GCG	mutagenesis
{11}	NP_R416A_2	CGC TCT CTC GAA AGG GAG ATT T**GC** CTG TAC AGA GAA AGT GGG	mutagenesis
{12}	fw_TC-insert_100-101_FPV	CCA ATC TAT AGA CGG AGA **TGC TGC CCA GGA TGC TGC** GAT GGA AAA TGG G	mutagenesis
{13}	rev_TC-insert_100-101_FPV	CCC ATT TTC CAT C**GC AGC ATC CTG GGC AGC A**TC TCC GTC TAT AGA TTG G	mutagenesis
{14}	fw_TC-insert_125-126_FPV	GCC AAG CGA ACA AT**T GCT GCC CAG GAT GCT GC**G GAG AGG ACG CAA C	mutagenesis
{15}	rev_TC-insert_125-126_FPV	GTT GCG TCC TCT CC**GC AGC ATC CTG GGC AGC A**A TTG TTC GCT TGG C	mutagenesis
{16}	fw_TC-insert_247-248_FPV	GGG AAA GCC GGA AT**T GCT GCC CAG GAT GCT GC**C CTG GGA ATG CTG	mutagenesis
{17}	rev_TC-insert_247-248_FPV	CAG CAT TCC CAG G**GC AGC ATC CTG GGC AGC A**AT TCC GGC TTT CCC	mutagenesis
{18}	fw_TC-insert_288-289_FPV	GCT GTG GCC AGT GGG **TGC TGC CCA GGA TGC TGC** TAC GAC TTT GAG AG	mutagenesis
{19}	rev_TC-insert_288-289_FPV	CTC TCA AAG TCG TA**GC AGC ATC CTG GGC AGC A**C CCA CTG GCC ACA GC	mutagenesis
{20}	fw_TC-insert_372-373_FPV	CAA ATG AGA ACA TGG AG**T GCT GCC CAG GAT GCT GC**A CAA TGG ATT CCA GC	mutagenesis
{21}	rev_TC-insert_372-373_FPV	GCT GGA ATC CAT TGT **GC AGC ATC CTG GGC AGC A**CTC CAT GTT CTC ATT TG	mutagenesis

Generation of recombinant Influenza A/WSN/1933 virus by reverse genetics was performed using plasmids **pHW181-PB2, pHW182-PB1, pHW183-PA, pHW184-HA, pHW185-NP, pHW186-NA, pHW187-M, pHW188-NS** [451]. For insertion of the sequence encoding the tetracysteine (TC)-tag into segment 5 vRNA at various positions, two-stage PCR-based mutagenesis of plasmid pHW185-NP was carried out (3.2.1.5). An overview of all generated mutant pHW185-NP plasmids is given in Tab. 5 with the corresponding mutagenesis primer pairs in Tab. 6.

In the particular case of TC-tag insertion at the 3′ end of the NP ORF of segment 5 vRNA, duplication of 60 3′ nucleotides of the NP ORF was required to preserve the segment 5 packaging signal for genome incorporation into progeny virus particles. Therefore, sequences encoding modified segment 5 vRNA were inserted into the cloning vector **pHW2000** at the *Bsm*BI/*Esp*3I restriction site yielding **pHW185-NP60mut-nTC-NP** and **pHW185-NP60mut-FLN-TC-NP**. This will be described in more detail in section 4.2.3. Details on primer pairs and inserts are given in Tab. 5 and Tab. 6. pHW2000 was a generous gift by Robert Webster (St. Jude Children's Research Hospital, Memphis, TN, USA).

The sequences of all constructs generated in this work were verified by sequencing of the ORFs. Sequencing and sequencing primer synthesis were performed by Invitek GmbH, (Berlin, Germany). Tab. 4 displays the oligonucleotides that were used for sequence analysis or for the amplification of control fragments by colony PCR to verify successful sequence insertion.

Tab. 4: DNA oligonucleotides used for sequencing and colony PCR. Oligonucleotides were synthesized by Invitrogen, Karlsruhe, Germany, or Invitek, Berlin, Germany.

No.	name	sequence	purpose
{39}	control_fw_NP	GGC TGA TCC AGA ACA GCA TAA C	colony PCR
{40}	control_rev_NP	GCC ACA GCA AGT CCA TAT ACA C	colony PCR
{41}	control_fw_EYFP	CGA CGT AAA CGG CCA CAA G	colony PCR
{42}	control_rev_EYFP	CAG CAG GAC CAT GTG ATC G	colony PCR
{43}	fw_TC-tag_control	TGC TGC CCA GGA TGC TGC	colony PCR
{44}	CMV for	CGC AAA TGG GCG GTA GGC GTG	sequencing
{45}	XFP_fw	GGC AAC ATC CTG GGG CAC AAG CTG GAG TAC	sequencing
{46}	fw_NP_1	CCC ATT TGA TGA TCT GGC ATT CC	sequencing (FPV)
{47}	fw_NP_2	GAC AAC TAT CCA CCA GAG GAG TC	sequencing (FPV)
{48}	fw_WSN-NP_A	TGC TGC AGT CAA AGG AGT TGG	sequencing (WSN)
{49}	fw_WSN-NP_B	AAG CAG ATA CTG GGC CAT AAG G	sequencing (WSN)

Tab. 5: pHW185-NP derived plasmids generated for reverse genetics with Influenza A/WSN/1933. Mutations were introduced by PCR-based QuikChange mutagenesis using the primer pairs listed. For cloning, the inserts were amplified from the vectors using the specified primers and were digested with the indicated restriction enzymes. Ligation of the two insert fragments with plasmid pHW2000 was performed simultaneously to insert both fragments consecutively at the *Bsm*BI/*Esp*3I site of pHW2000. (Amino acid sequences of the tags that were fused to the NP open reading frame, TC: CCPGCC; nTC: MAGG-CCPGCC; FLN-TC: M-FLN-CCPGCC-MEP)

name	vector	mutation/insert	primer
pHW185-NP-TC125	pHW185-NP	TC-tag insertion QuikChange mutagenesis	{22}, {23}
pHW185-NP-TC288	pHW185-NP	TC-tag insertion QuikChange mutagenesis	{24}, {25}
pHW185-NP-TC292	pHW185-NP	TC-tag insertion QuikChange mutagenesis	{26}, {27}
pHW185-NP-TC372	pHW185-NP	TC-tag insertion QuikChange mutagenesis	{28}, {29}
pHW185-NP-2ATG	pHW185-NP	ATG → ATC codon mutations: 38 G → C and 49 G → C (NP ORF)	{30}, {31}
pHW185-NP-3ATG	pHW185-NP-ATCmut	ATG → GCG codon mutation: (1,2) AT → GC (NP ORF)	{32}, {33}
pHW185-NP60mut-nTC-NP	pHW2000	insert 1: vRNA-NP60mut-Kozak (*Esp*3I, *Bsa*I) amplified from pHW185-NP-3ATG	{34}, {35}
		insert 2:Kozak-nTC-NP-vRNA (*Bsa*I, *Esp*3I) amplified from pHW185-NP	{36}, {37}
pHW185-NP60mut-FLN-TC-NP	pHW2000	insert 1: vRNA-NP60mut-Kozak (*Esp*3I, *Bsa*I) amplified from pHW185-NP-3ATG	{34}, {35}
		insert 2: Kozak-FLN-TC-MEP-NP-vRNA (*Bsa*I, *Esp*3I) amplified from pHW185-NP	{38}, {37}

Tab. 6: DNA oligonucleotides used for PCR amplification and mutagenesis of Influenza A/WSN/1933. Restriction sites are underlined. Bold letters indicate mutation sites or sequence insertion. Oligonucleotides were synthesized by Invitrogen, Karlsruhe, Germany, or BioTez, Berlin, Germany.

No.	name	sequence (5' → 3')	purpose
{22}	fw_TC-insert_125-126_WSN	GCC AAG CTA ATA AT**T GCT GCC CAG GAT GCT GC**G GTG ACG ATG CAA C	mutagenesis
{23}	rev_TC-insert_125-126_WSN	GTT GCA TCG TCA CC**G CAG CAT CCT GGG CAG CA**A TTA TTA GCT TGG C	mutagenesis
{24}	fw_TC-insert_288-289_WSN	GCC GTA GCC AGT GGA **TGC TGC CCA GGA TGC TGC** TAC GAC TTT GAA AG	mutagenesis
{25}	rev_TC-insert_288-289_WSN	CTT TCA AAG TCG TA**G CAG CAT CCT GGG CAG CA**T CCA CTG GCT ACG GC	mutagenesis
{26}	fw_TC-insert_292-293_WSN	GGA TAC GAC TTT GAA **TGC TGC CCA GGA TGC TGC** AGA GAG GGA TAC TC	mutagenesis
{27}	rev_TC-insert_292-293_WSN	GAG TAT CCC TCT CT**G CAG CAT CCT GGG CAG CA**T TCA AAG TCG TAT CC	mutagenesis
{28}	fw_TC-insert_372-373_WSN	CCA ATG AAA ACA TGG AG**T GCT GCC CAG GAT GCT GC**A CTA TGG AAT CAA GTA CC	mutagenesis
{29}	rev_TC-insert_372-373_WSN	GGT ACT TGA TTC CAT AGT **GCA GCA TCC TGG GCA GCA** CTC CAT GTT TTC ATT GG	mutagenesis
{30}	ATC_fw	CGA TCT TAC GAA CAG AT**C** GAG ACT GAT **C**GA GAA CGC CAG AAT GC	mutagenesis ATG→ATC
{31}	ATC_rev	GCA TTC TGG CGT TCT C**G**A TCA GTC TC**G** ATC TGT TCG TAA GAT CG	mutagenesis ATG→ATC
{32}	ATG-GCG_fw	GAC ATC GAA ATC **GC**G GCG ACC AAA GGC	mutagenesis ATG→GCG
{33}	ATG-GCG_rev	GCC TTT GGT CGC C**GC** GAT TTC GAT GTC	mutagenesis ATG→GCG
{34}	NP60mut_fw (*Esp*3I)	ATC AT**C GTC T**CG GGG AGC AAA AGC AGG	cloning/PCR; vRNA-NP60$_{ATGmut}$
{35}	NP60mut_rev (*Bsa*I)	ATT TGG TCT CGG CGG CCT GGC GTT CTC GAT C	cloning/PCR; vRNA-NP60$_{ATGmut}$
{36}	nTC-NP(*Bsa*I)_fw	ATC TGG TCT CTC CGC C**AT GGC TGG TGG CTG CTG CCC AGG ATG CTG C**AT GGC GAC CAA AGG C	cloning/PCR; TC-NP-vRNA
{37}	nTC-NP(*Esp*3I)_rev	CTA T**CG TCT C**TT ATT AGT AGA AAC AAG G	cloning/PCR; TC-NP-vRNA
{38}	nFLNTCMEP-NP(*Bsa*I)_fw	ATC TGG TCT CTC CGC CAT G**TT CCT GAA CTG CTG CCC AGG ATG CTG CAT GG AGC CC**A TGG CGA CCA AAG GC	cloning/PCR; FLN-TC-MEP-NP-vRNA

3.1.2 Chemicals

Chemicals that are not included in the following list were purchased either from Sigma-Aldrich (Taufkirchen, Germany) or Carl Roth (Karlsruhe, Germany) in analytical standard quality. Phospholipids and fluorescent phospholipid analogues were obtained from Avanti Polar Lipids (Alabaster, AL, USA).

- Acetic acid, 100% [Carl Roth, Karlsruhe, Germany]
- Acrylamide/bisacrylamide (37.5:1) 30 %, "Rotiphorese® Gel 30" [Carl Roth, Karlsruhe, Germany]
- Aminotriazole (3-amino-1,2,4-triazole) [Sigma-Aldrich, Taufkirchen, Germany]
- Ammonium persulfate (APS) [Sigma-Aldrich, Taufkirchen, Germany]
- Bacto™ agar, Bacto™ tryptone, Bacto™ yeast extract [BD Biosciences, Heidelberg, Germany]
- BAL, British Anti-Lewisite (2,3-dimercapto-1-propanol) [Sigma-Aldrich, Taufkirchen, Germany]
- BAL wash buffer (In-Cell Tetracysteine Tag Detection Kit) [Invitrogen, Karlsruhe, Germany]
- BCA Protein Assay Kit Pierce, #23225 [Thermo Fisher Scientific, Bonn, Germany]
- Chloroform Uvasol® for spectroscopy [Merck, Darmstadt, Germany]
- Cholesterol [Sigma-Aldrich, Taufkirchen, Germany]
- Coomassie Brilliant Blue R-250 [Carl Roth, Karlsruhe, Germany]
- Cytochalasin D [Sigma-Aldrich, Taufkirchen, Germany]
- DAB (3,3′-diaminobenzidine tetrahydrochloride) [Sigma-Aldrich, Taufkirchen, Germany]
- DAPI nucleic acid stain [Invitrogen, Karlsruhe, Germany]
- DiD lipophilic carbocyanine dye [Invitrogen, Karlsruhe, Germany]
- ER-Tracker™ Red (BODIPY® TR Glibenclamide) [Invitrogen, Karlsruhe, Germany]
- Ethanol for spectroscopy, >99.5 % Ph. Eur. [Carl Roth, Karlsruhe, Germany]
- Ethylenediaminetetraacetic acid (EDTA) [SERVA, Heidelberg, Germany]
- FlAsH-EDT_2 labeling reagent (TC-FlAsH™ II In-Cell Tetracysteine Tag Detection Kit) [Invitrogen, Karlsruhe, Germany]
- Formaldehyde 37 % (w/v) [Fluka/Sigma-Aldrich, Taufkirchen, Germany], for silver staining
- Formalin solution, 10 %, neutral buffered [Sigma-Aldrich, Taufkirchen, Germany], for cell fixation

- Glutaraldehyde solution, Grade I, 50% in H_2O, for use as fixative for electron microscopy [Sigma-Aldrich, Taufkirchen, Germany]
- Glycine [Sigma-Aldrich, Taufkirchen, Germany]
- Lysophosphatidylcholine (Lyso-PC) from egg yolk [Sigma-Aldrich, Taufkirchen, Germany]
- Methanol Uvasol® for spectroscopy [Merck, Darmstadt, Germany]
- Mowiol® 4-88 reagent [Calbiochem/Merck, Darmstadt, Germany]
- Octyl β-D-glucopyranoside [Sigma-Aldrich, Taufkirchen, Germany]
- Potassium cyanide (KCN) [Sigma-Aldrich, Taufkirchen, Germany]
- ReAsH-EDT_2 labeling reagent (TC-ReAsH™ II In-Cell Tetracysteine Tag Detection Kit) [Invitrogen, Karlsruhe, Germany]
- Rhodamine phalloidin [Tebu-bio, Offenbach, Germany]
- Sodium dodecyl sulfate (SDS) [Carl Roth, Karlsruhe, Germany]
- Sucrose [AppliChem, Darmstadt, Germany]
- TEMED (N,N,N',N'-Tetramethyl-ethane-1,2-diamine)) [Sigma-Aldrich, Taufkirchen, Germany]

3.1.3 Buffers and solutions

- **Cell culture media**

  Complete medium: DMEM with 10 % (v/v) FBS, 2 mM L-glutamine and penicillin/streptomycin (100 U/ml, 100 µg/ml)

  Freezing medium: 70 % (v/v) DMEM, 20 % (v/v) FBS, 10 % (v/v) DMSO

  Infection medium: DMEM with 0.2 % (w/v) BSA (for cell culture), 0.1 % (v/v) FBS, 2 mM L-glutamine, 1 µg/ml trypsin TPCK-treated, penicillin/streptomycin (100 U/ml, 100 µg/ml)

  Overlay medium (plaque assay): EMEM (2×) with 0.4 % (w/v) BSA, 0.2 % FBS, 4 mM L-glutamine, 2 µg/ml trypsin (TPCK-treated) and penicillin/streptomycin (200 U/ml, 200 µg/ml) mixed with equal volume of 1.8 % (w/v) SeaPlaque agarose (autoclaved)

  Live-cell imaging medium: DMEM with 20 mM HEPES, pH 7.4

- **Coomassie staining solutions**

  Coomassie staining solution: 45 % (v/v) ethanol, 10 % (v/v) acetic acid, 2.5 g/l Coomassie Brilliant Blue R-250

  Coomassie destaining solution: 40 % (v/v) ethanol, 7.5 % (v/v) acetic acid

- **Flotation assay and LUV preparation**

  Flotation buffer: 10 mM $NaPO_4$, 120 mM KCl, pH 7.0

  Sucrose step gradient: 25 % and 75 % (w/v) sucrose in flotation buffer

- **Immunofluorescence solutions**

  Fixative: 4 % formalin in DPBS with Ca^{2+} and Mg^{2+} (made from a 10 % formalin stock solution, Sigma-Aldrich, Taufkirchen, Germany)

  Blocking buffer: 3 % (w/v) BSA in DPBS for cell culture

  Permeabilization buffer: 0.5 % (v/v) Triton X-100 in DPBS

- **Isolation of vRNPs**

  All buffers were prepared with ultrapure RNAse-free water from a Millipore Milli-Q® system and using RNAse-free pipet tips.

  Lysis buffer: 100 mM KPO_4, 100 mM KCl, 5 mM $MgCl_2$, 5 % (w/v) glycerol, 1.5 mM dithiothreitol, 50 mM Octyl β-D-glucopyranoside, 10 mg/ml lysophophatidylcholine from egg yolk, pH 8.1

  Gradient buffer: 100 mM KPO_4, 150 mM NaCl, pH 7.8 with 33 %, 40 %, 50 % or 70 % (w/v) glycerol

  Resuspension buffer: 10 mM KPO_4, 120 mM KCl, pH 8.0

- **Media for propagation of *E.coli***

  LB medium: 10 g/l Bacto™ tryptone, 5 g/l Bacto™ yeast extract, 5 g/l NaCl with 50 µg/ml kanamycin or 100 µg/ml ampicillin

  LB agar: LB medium with 15 g/l agar, 50 µg/ml kanamycin or 100 µg/ml ampicillin

  Antibiotic stocks: 50 mg/ml ampicillin; 100 mg/ml kanamycin (in ddH_2O, sterile filtered)

- PBS: 137 mM NaCl, 2.7 mM KCl, 8.1 mM Na_2HPO_4, 1.5 mM KH_2PO_4, pH 7.2

- **PIP strip buffers**

  TBS: 10 mM Tris-HCl, 150 mM KCl, pH 8.0

  TBS-T: TBS with 0.1 % (v/v) Tween®-20

  Blocking buffer: TBS with 3 % BSA (w/v)

- **ReAsH photoconversion for electron microscopy**

  Cacodylate buffer: 0.2 M cacodylate, pH 7.4

  Fixation buffer: cacodylate buffer with 2 % (w/w) glutaraldehyde

  Photoconversion blocking buffer: 20 mM glycine, 10 mM KCN, 10 mM aminotriazole in cacodylate buffer

  DAB solution: 0.5 mg/ml DAB in cacodylate buffer (freshly oxygenated)

- **SDS-PAGE buffers**

  Stacking gel (5 %): 5 % (w/v) acrylamide/bisacrylamide (37.5:1; 30 % stock solution "Rotiphorese® Gel 30", Carl Roth, Karlsruhe, Germany), 125 mM Tris-HCl pH 6.8, 0.1 % (w/v) SDS, 0.1 % (w/v) APS, 0.1 % (v/v) TEMED

  Resolving gel (10 %): 10 % (w/v) acrylamide/bisacrylamide, 375 mM Tris-HCl pH 8.8, 0.1 % (w/v) SDS, 0.1 % (w/v) APS, 0.04 % (v/v) TEMED

  Resolving gel (12 %): 12 % (w/v) acrylamide/bisacrylamide, 375 mM Tris-HCl pH 8.8, 0.1 % (w/v) SDS, 0.1 % (w/v) APS, 0.04 % (v/v) TEMED

  SDS sample buffer, non reducing (4×): 5 % (w/v) SDS, 0.5 g/l bromophenol blue, 25 % (v/v) glycerol, 500 mM Tris-HCl pH 6.8

  SDS sample buffer, reducing (4×): 5 % (w/v) SDS, 0.5 g/l bromophenol blue, 25 % (v/v) β-mercaptoethanol, 25 % (v/v) glycerol, 500 mM Tris-HCl pH 6.8

  Protein standards: Precision Plus Protein All Blue Standards [Bio-Rad, München, Germany]; PageRuler™ Prestained Protein Ladder [Fermentas, St. Leon-Rot, Germany]

  Running buffer: 3 g/l Tris-HCl, 1 g/l SDS, 14.4 g/l glycine; pH 8.3

- **Silver staining solutions**

  Fixative: 30 % (v/v) ethanol, 10 % (v/v) acetic acid

  Sensitizer: 30 % (v/v) ethanol, 0.5 % (w/v) glutaraldehyde, 0.5 M sodium acetate, 0.2 % (w/v) sodium thiosulfate

  Staining solution: 0.1 % (w/v) silver nitrate, 0.74 % (w/v) formaldehyde

  Developer: 2.5 % (w/v) sodium carbonate, 0.37 % (w/v) formaldehyde

  Stop solution: 0.05 M EDTA

- **Virus purification**

  TNE buffer **:** 10 mM Tris-HCl; 100 mM NaCl, 1 mM EDTA, pH 7.4

  TNE sucrose gradient: linear gradient formed from 20 % and 60 % (w/v) sucrose in TNE buffer

- **Western blotting solutions**

  Transfer buffer: 40 % (v/v) running buffer, 20 % (v/v) methanol, 0.06 % (w/v) SDS

  Blocking and washing buffer (for horseradish peroxidase chemiluminescence detection): PBS with 0.5 % (v/v) Tween®-20 and 5 % (w/v) skimmed milk powder

  Blocking buffer (for IR-dye coupled secondary antibodies and fluorescence detection): Odyssey® Blocking Buffer 1:2 in PBS

  Washing buffer (for IR-dye coupled secondary antibodies and fluorescence detection): PBS with 0.1 % (v/v) Tween®-20 (PBS-T)

  Amersham ECL™ Advance Western Blotting Detection Kit [GE Healthcare, München,

Germany]

Fixer and Developer solutions T-Matic for film development [ADEFO-CHEMIE, Dietzenbach, Germany]

3.1.4 Consumables

Basic laboratory consumables are not included in this list.

- Amicon Ultra-15 Centrifugal Filter Units with molecular weight cut-off 10 kDa or 50 kDa [Millipore, Schwalbach, Germany]
- Beckman Microfuge Tube, 1.5 ml, polyallomer [Beckman Coulter, Krefeld, Germany]
- Cell culture flasks T25, T75, T175 [Nunc, Langenselbold, Germany]
- Cell culture plates 6-well and 12-well [Nunc, Langenselbold, Germany]
- Cuvettes, acrylic, and semi-micro cuvettes, polystyrene [Sarstedt, Nümbrecht, Germany]
- Extruder filter support 610014 [Avanti Polar Lipids, Alabaster, AL, USA]
- Extruder Nuclepore track-etched membrane 100 nm pore size, 13 mm diameter [Whatman, Dassel, Germany]
- Microscopy glass bottom culture dishes, 35 mm, uncoated [MatTek, Ashland, U.S.A, # P35G-1,5-14C]
- Microscopy glass bottom culture dishes, gridded [MatTek, Ashland, U.S.A, #P35G-2-14-CGRD]
- Microscopy glass cover slips, glass thickness no.1 (24×60 mm; Ø12 mm) [Carl Roth, Karlsruhe, Germany]
- PIP Strips™, P-6001 [Echelon Biosciences, Salt Lake City, UT, U.S.A]
- RNAse-free filtered pipette tips [STARLAB, Hamburg, Germany]
- Transwell plates, Corning Transwell® polycarbonate membrane permeable support, pore size 0.4 µm, Ø 24 mm [VWR, Darmstadt, Germany]
- Western blotting: Amersham Hyperfilm ECL [GE Healthcare, Freiburg, Germany]
- Western blotting: Amersham nitrocellulose membrane Hybond ECL [GE Healthcare, Freiburg, Germany]
- Western blotting: Extra thick blot paper [Bio-Rad, München, Germany]

3.1.5 Equipment and instruments

Basic laboratory equipment is not included in this list.

- Biophotometer plus [Eppendorf, Hamburg, Germany]
- Centrifuge Avanti J-20XP (Rotor JLA10.500) [Beckman Coulter, Krefeld, Germany]
- Centrifuge Heraeus Biofuge Stratos [Thermo Scientific, Langenselbold, Germany]
- DEASAGA Digital documentation system CabUVIS [Sarstedt, Nümbrecht, Germany] with CCD camera HV-C20A (Hitachi)
- Density gradient fractionators "Auto Densi-Flow" [Labcono, Kansas City, MO, USA]
- Electrophoresis equipment (agarose gel electrophoresis): Mini-Sub Cell GT Systems [Bio-Rad, München, Germany]
- Electrophoresis equipment (SDS-PAGE): Mini-PROTEAN 3 electrophoresis system with accessories [Bio-Rad, München, Germany]
- Extruder, Mini [Avanti Polar Lipids, Alabaster, AL, USA]
- Gradient Master ip [Biocomp Instruments, Fredericton, Canada]
- Incubators Heraeus [Thermo Scientific, Langenselbold, Germany]
- Laminar hood Heraeus [Thermo Scientific, Langenselbold, Germany]
- Microscope: Confocal laser scanning microscope FluoView™ FV1000; 60× (N.A. 1.2) water immersion objective UplanSApo; 60× (N.A. 1.35) oil immersion objective UplanSApo [Olympus, Hamburg, Germany]
- Microscope: IX-81 inverted epifluorescence microscope [Olympus, Hamburg, Germany]
- Microscope (single particle tracking): Nikon TE2000 inverted epifluorescence microscope [Nikon, Düsseldorf, Deutschland] with back-illuminated Andor iXon3 897 single photon detection EMCCD camera, 512×512 pixels, 16×16 µm pixel size [Andor Technologies, Belfast, UK]; equipped with Sapphire Laser 488 nm, 30 mW and Compass Laser 561 nm, 25 mW [Coherent, Göttingen, Germany]; objective Plan Apo VC 60× Oil (N.A. 1.4) [Nikon, Düsseldorf, Germany]
- Microscope (cell culture): Telaval 31, phase contrast inverted microscope, [Zeiss, Göttingen, Germany]
- Milli-Q ultra pure water purification system [Millipore, Schwalbach, Germany]
- Odyssey® Infrared imaging system [LI-COR Bioscience, Bad Homburg, Germany]
- Phosphorimager: Fluorescent image analyzer FLA-3000 [Fujifilm, Düsseldorf, Germany]

- Power supply for electrophoresis and Western blotting: PowerPac 1000 [Bio-Rad, München, Germany] and Amersham EPS 601 [GE Healthcare, Freiburg, Germany]
- Rotary evaporator Rotavapor R-200 [Büchi Labortechnik, Essen, Germany]
- Shaker: Mini-rocker MR-1 [Bioscan, Paris, France]; rocking shaker [GFL, Burgwedel, Germany]
- Spectrofluorometer AMINCO-Bowman™ Series 2 [Thermo Electron Corporation, Germany]
- Thermal Cycler MyCycler™ [Bio-Rad, München, Germany]
- Thermomixer comfort [Eppendorf, Hamburg, Germany]
- Ultracentrifuge TL-100, tabletop, rotor TLA 100.3 [Beckman Coulter, Krefeld, Germany]
- Ultracentrifuge XL-70 and Optima L-100K [Beckman Coulter, Krefeld, Germany]
- UV transilluminator [Vilber Lourmat, Eberhardzell, Germany]
- UV-Vis spectrophotometer UV1 [Thermo Electron Corporation, Germany]
- Western blot: Trans-Blot® SD semi-dry electrophoretic transfer cell [Bio-Rad, München, Germany]

3.1.6 Software

- **Andor iQ** [Andor Technologies, Belfast, UK]: device control and image viewing software for EMCCD camera Andor iXon3 897
- **Clone Manager** [Sci-Ed, Cary, NC, USA]: cloning simulation; DNA sequence viewing, alignment, editing and ORF analysis
- **FV 10-ASW FluoView1000** [Olympus, Hamburg, Germany]: device control, image viewing and data analysis software for confocal microscope FV1000
- **ImageJ** Version 1.46e (http://imagej.nih.gov/ij/) [Wayne Rasband, National Institute of Health, Bethesda, MD, USA] [452]: signal quantification, particle tracking, image processing
- ImageJ plugin **MtrackJ** (http://www.imagescience.org/meijering/software/mtrackj/) [Erik Meijering, Biomedical Imaging Group, Erasmus MC, Rotterdam, Netherlands] [453]
- ImageJ plugin **Spot Tracker** (http://bigwww.epfl.ch/sage/soft/spottracker/) [Daniel Sage, Biomedical Imaging Group, Ecole Polytechnique Fédérale de Lausanne, Switzerland] [454]
- **EMBOSS** (http://www.ebi.ac.uk/Tools/emboss/) [European Bioinformatics Institute, Cambridge, UK]: DNA translation, sequence alignment
- **The PyMOL Molecular Graphics System**, Version 1.1eval Schrödinger, LLC. [DeLano Scientific, SanFrancisco, CA, USA]: molecular visualization of protein structures

3.2 Methods

3.2.1 Molecular biology

Plasmid constructs were generated by application of standard molecular biology techniques. The specific DNA sequences to be encoded in a plasmid for protein expression were generated by polymerase chain reaction (PCR) (3.2.1.1) and inserted into the plasmid by restriction digest and ligation (3.2.1.3). Point mutations were introduced by site-directed mutagenesis (3.2.1.4). The plasmids for generation of recombinant viruses were processed in the same way. Plasmids were amplified in *E.coli* (3.2.1.6 and 3.2.1.7), and the open reading frame (ORF) of each newly generated plasmid was checked for correctness by sequencing (Invitek GmbH, Berlin, Germany). Sequencing primers are listed in Tab. 4.

3.2.1.1 Polymerase chain reaction (PCR)

DNA fragments to be inserted into a plasmid were specifically amplified from a template DNA by PCR. For each PCR, two oligonucleotide primers defining the beginning and the end of the fragment were designed (Tab. 3 and Tab. 6). They were complementary to the first 10–15 nucleobases of the fragment (forward primer, fw) and reverse complementary to 10–15 of the terminal nucleobases (reverse primer, rev), respectively. Adjacent to these sequences, restriction sites were added matching the restriction sites of the plasmid into which the PCR product was to be inserted. Furthermore, terminal tags like the nuclear export signal (NES) and the TC-tag were encoded by the PCR primers and thereby fused to the gene of interest. For PCR, template DNA (2 ng), forward and reverse primers (0.5 µM), a nucleotide mix (dNTPs, 200 µM each), HF buffer (as supplied with the polymerase) and the heat-stable Phusion high-fidelity DNA polymerase (0.02 U/µl) were mixed in a final volume of 50 µl and subjected to repeated temperature changes in a thermal cycler. The double-stranded template DNA was initially denatured at 98 °C for 30 s followed by the reaction cycle of DNA denaturation at 98 °C for 10 s, annealing of the primers with template DNA at 54 °C for 30 s and elongation of the primers by synthesis of template-complementary DNA at 72 °C. The duration of the elongation step was 20 s per 1000 nucleotides of DNA fragment to be synthesized. The reaction cycle was repeated 35 times and the PCR was completed by 10 min at 72 °C. The PCR product was detected and purified by agarose gel electrophoresis (3.2.1.2).

Another application of PCR, the colony PCR, was performed to verify successful insertion of DNA into a plasmid or the uptake of a certain plasmid by *E.coli*. The same PCR protocol was followed as described before, but the initial denaturation time was extended to 10 min. Instead

of the template DNA, part of an *E.coli* colony was picked and resuspended in the reaction mixture. The colony PCR primers (Tab. 4) did not contain restriction sites and were chosen for amplification of an arbitrary fragment of the target gene.

3.2.1.2 Agarose gel electrophoresis

Agarose gels were produced with 1 % (w/v) agarose in TBE buffer supplemented with the DNA stain SYBR Safe. Electrophoresis was run at 70 mA to separate negatively charged DNA fragments according to their size. For further applications, DNA bands were cut from the gel and the DNA was extracted using the QIAquick Gel Extraction Kit.

3.2.1.3 Restriction digestion and ligation

A DNA insert, generated by PCR and flanked by two restriction sites, and about 1 µg of the target plasmid were separately digested with the same two restriction endonucleases for 2 h at 37 °C. The buffer composition was chosen according to the requirements of the enzymes as given by the manufacturer's instructions. The reactions produced overhanging ends of unpaired nucleotides ("sticky ends") at both ends of the DNA molecules. To prevent self-ligation of the plasmid in the following ligation reaction, the reaction mixture for digestion of the plasmid was supplemented with calf intestinal alkaline phosphatase to remove the reactive 5′ phosphate. The reaction products were analyzed and purified by agarose gel electrophoresis (3.2.1.2), and DNA fragments were extracted with the QIAquick Gel Extraction kit for subsequent ligation. As insert and plasmid possessed complementary sticky ends, they could be linked by formation of a phosphodiester bond between the 3′ hydroxy and 5' phosphate groups catalyzed by the T4-DNA-ligase. For this reaction, the linearized plasmid was incubated with an excess of DNA insert and the T4-DNA-ligase in T4-DNA-ligase buffer at 16 °C for at least 1 h. The solution was stored at 4 °C until transformation of *E.coli* (3.2.1.6). Prior to transformation the ligase was heat-inactivated at 65 °C for 10 min.

3.2.1.4 Site-directed mutagenesis

Point mutations were introduced into plasmid DNA by PCR-based site-directed mutagenesis based on the QuikChange protocol by Stratagene. A complementary primer pair was designed that anneals to the target sequence on the plasmid where the mutations were supposed to be introduced. These primers carry the desired point mutation(s) flanked by 10–15 nucleotides of the matching sequences on both sides, terminated by two or more G and/or C bases (Tab. 3; Tab. 6) (Primer Design Guidelines, QuikChange® site-directed mutagenesis kit, #200518,

Stratagene). PCR was carried out by mixing 25 µM of each primer, 200 mM dNTPs, 50 ng of template DNA, 1× HF buffer and 0.02 U/µl Phusion HF DNA polymerase in a final volume of 50 µl and the DNA was amplified by thermal cycling. An initial denaturation step (3 min, 98 °C) was followed by 20 cycles of 98°C for 10 s, 70 °C for 30 s and 72 °C for 3 min. The duration of the DNA elongation step at 72 °C was chosen long enough that the full length of the plasmid could be synthesized. The reaction was completed by final extension at 72 °C for 10 min. The reaction yielded unmethylated linear copies of the plasmid. The methylated template DNA was thereafter digested with the restriction endonuclease *Dpn*I (0.2 U/µl) for 1 h at 37 °C leaving the unmethylated PCR products. *E.coli* DH5α were transformed for amplification (see 3.2.1.6), subsequent purification (3.2.1.7) and sequencing (Invitek, Berlin, Germany) of the mutated plasmids.

3.2.1.5 Two-stage PCR mutagenesis for insertion of large segments

For insertion of long nucleotide sequences like the tetracysteine (TC)-tag encoded by 18 bases, a modified QuikChange protocol was applied. The procedure was essentially the same as described in section 3.2.1.4 adapted according to the two-stage PCR protocol for site-directed mutagenesis described by Wang and Malcolm [455]. Mutagenesis primers were designed as described above carrying the new insert sequence flanked by complementary sequences of the plasmid (Tab. 3; Tab. 6). Unlike the standard QuikChange protocol for point mutations, the thermal cycling reaction for plasmid amplification was preceded by a primer extension step. Therefore, two separate PCR reaction mixtures were prepared with the same composition as in 3.2.1.4, but only containing either the forward or the reverse primer. The two reaction mixtures were subjected to initial denaturation at 98 °C for 30 s and three cycles of 98 °C for 10 s and 72 °C for 3 min. Subsequently, 25 µl of both reaction mixtures were combined, now containing elongated mutagenesis primers with higher affinity for the plasmid than for each other, and the standard PCR protocol for site-directed mutagenesis comprising amplification and *Dpn*I digestion was resumed (see 3.2.1.4).

3.2.1.6 Transformation of *E.coli*

To amplify plasmids obtained by insert ligation or mutagenesis, they were introduced into chemically competent *E.coli* DH5α by transformation. 100 µl aliquots of bacteria were carefully thawed on ice and mixed with a few nanograms of plasmid. The suspension was incubated on ice for 10 min, treated by heat-shock at 42 °C for 45 s and placed back on ice for 5 min. Bacteria were pelleted by centrifugation at 6,000 × **g** for 5 min and resuspended in

50 µl LB medium before plating them on agar plates containing the appropriate antibiotic for selection of bacteria carrying the plasmid. Plates were incubated overnight at 37 °C and single colonies were picked for colony PCR (3.2.1.1) or plasmid purification (3.2.1.7). Clones were stored in 30 % glycerol-LB medium at –80 °C.

3.2.1.7 Plasmid purification

For plasmid purification, single colonies were picked from agar plates for inoculation of LB-medium with selection antibiotic and propagation at 37 °C for 16 h in a shaking incubator. Bacteria were then pelleted, and plasmids were isolated using the QIAprep Spin Miniprep Kit (for 5 ml culture) or QIAGEN Plasmid Maxi Kit (for 100 ml culture) according to manual. DNA concentrations were determined photometrically by measuring the absorbance at 260 nm (Biophotometer plus), and the plasmids were used for sequencing, transfection of eukaryotic cells or molecular biology.

3.2.2 Cell biology

3.2.2.1 Cell culture

Adherent CHO-K1, HeLa, MDCK II and 293T cells were maintained in complete medium (DMEM supplemented with 10 % FBS, 2 mM L-glutamine and penicillin/streptomycin) under cell culture conditions (humidified atmosphere with 5 % CO_2, 37 °C). They were routinely passaged in 75-cm^2 cell culture flasks (T75) every 3–4 days when reaching confluency. For passaging, cells were washed twice with DPBS and incubated with 2 ml trypsin/EDTA at 37 °C until detachment. Then, the cells were mixed with 10 ml complete medium. They were seeded into appropriate dishes or used for continued culture (typically 1/12). Treatment of cells was under sterile conditions (laminar flow bench). Cell culture was routinely maintained in DMEM without phenol red to avoid interference of the dye with fluorescence methods.

For long term storage, cells were detached from the T75 flask, diluted in DMEM, pelleted for 3 min at 300× **g** and transferred into 1.5 ml freezing medium. After cooling down to -80 °C overnight, cell stocks were stored in liquid nitrogen at –196 °C. For unfreezing, the cells were rapidly thawed in a 37 °C water bath, diluted with 10 volumes of complete medium and pelleted for 3 min at 300× **g.** The cell pellet was gently resuspended in pre-warmed culture

medium and transferred into a cell culture flask. Cells were then grown under cell culture conditions as described before.

3.2.2.2 Transfection

Transfection of plasmid DNA into eukaryotic cells (CHO-K1, HeLa, MDCK II) was performed using the cationic lipid-based Lipofectamine 2000 transfection reagent according to the manufacturer's instructions. A total of 4 µg DNA was used for transfection of cells grown to 90 % confluency in 35-mm dishes. The DNA was mixed with DMEM to a final volume of 250 µl, while 10 µl of Lipofectamine 2000 were added to 240 µl of DMEM. Solutions were incubated for 5 min at room temperature (RT), combined and thoroughly mixed. After another 20 min at RT, the transfection mixture was added dropwise to the cells that had been washed with DPBS (containing Ca^{2+} and Mg^{2+}) and been covered with 1.5 ml of DMEM. The dishes were then gently swirled and incubated at 37 °C. The transfection medium was replaced by DMEM after 4 h. Subsequent processing for live-cell imaging, immunofluorescence or analysis of cell lysates was done as described in the respective sections.

For production of recombinant Influenza viruses in 293T cells (3.2.4.3), the transfection reagent TurboFect, a cationic polymer solution, was used. 1 µg DNA of each of the eight required plasmids was thoroughly mixed with 800 µl DMEM plus 12 µl of TurboFect. The mixture was incubated 15 min at RT and then added dropwise to 293T cells grown to about 60 % confluency on 60-mm dishes. Before addition, the cells had been washed and covered with 4 ml of fresh DMEM. The medium was removed after 4–6 hours and 5 ml of infection medium were added.

3.2.2.3 Cell polarization

Epithelial cells can form polarized layers of tightly associated cells with structurally and functionally distinct apical and basolateral domains. For polarization, MDCK II cells were grown in Transwells (permeable polycarbonate supports with pores of 0.4 µm that allow uptake of nutrients and exchange of substances across the basal cell membrane). The cells were seeded into the Transwells and supplied with complete growth medium from both sides. Transfection with Lipofectamine 2000 was performed one day after seeding when the cells were about 80 % confluent. At 4 h post-transfection (p.t.), the transfection medium was replaced by complete medium and was thereafter changed every day, now supplemented with

250 µg/ml Neomycin. Neomycin exerts a positive selection pressure on cells that have been transfected with a plasmid carrying a neomycin resistance gene. 13 days after transfection, cells were washed with DPBS (with Ca^{2+} and Mg^{2+}) and either imaged as living cells or fixed for 45 min in 4 % formalin solution and further subjected to immunofluorescence staining. For imaging, the membrane was cut into large pieces and placed upside down on a microscope slide for observation with an inverted microscope. Apical localization of the control protein HAmYFP was used to verify the polarization state of the cells.

3.2.2.4 Fluorescence labeling of fixed and living cells

For fluorescence imaging, cells were grown in 35-mm glass-bottom dishes or on glass cover slips in 12-well cell culture plates. To avoid photobleaching of fluorophores, samples were protected from light during processing.

3.2.2.4.1 Immunofluorescence (IF)

For the detection of specific (transfected, viral or endogenous) proteins by IF, the cells were transfected or infected as required and fixed with 4 % formalin at RT for 30 min. Cells were then washed twice with DPBS, permeabilized for 8 to 10 min with 0.5 % (v/v) Triton-X100 and washed twice. Unspecific binding sites were then blocked with 3 % (w/v) BSA in DPBS for 1 h. Use of BSA-containing solutions was omitted in case of FlAsH-labeled cells (3.2.2.4.3) due to unspecific binding of FlAsH to BSA. DPBS was used instead. Primary and secondary antibodies were generally diluted 1:1000 in blocking buffer (anti-HA, 1:6000). Cells were incubated with the primary antibody for 1–1.5 h, washed three times with blocking buffer and subsequently incubated for another hour with the secondary fluorescently labeled antibody. When anti-NP-FITC was used, a secondary antibody was not required. For co-staining of different target proteins, a mixture of antibodies was applied. Finally, the cells were washed three times in blocking buffer and twice in DPBS. Cells in glass-bottom dishes were covered with DPBS and stored at 4 °C. Glass cover slips were mounted on microscope slides with 20 µl of Mowiol 4-88 Reagent. The samples were analyzed by fluorescence microscopy within two days.

3.2.2.4.2 Labeling of subcellular structures

For visualization of DNA, nucleoli or actin filaments, fixed and permeabilized cells were stained with DAPI, propidium iodide (PI) or rhodamine phalloidin, respectively. This was generally done following immunostaining.

Counterstaining of the cell nuclei was performed by incubation of the cells with 100 nM DAPI in DPBS at RT for 3 min. Nucleic acids and in particular nucleoli as prominent structures were labeled with 500 nM PI in PBS for 5 min [456]. For staining of F-actin, permeabilized cells were incubated with rhodamine phalloidin (100 nM) for 30 min. Staining procedures were followed by three washing steps with DPBS before mounting the cover slips on microscope slides with Mowiol 4-88 Reagent or covering the cells with DPBS.

The endoplasmic reticulum (ER) was labeled with the cell-permeant, live-cell stain ER-Tracker RED, a BODIPY TR labeled glibenclamide that binds to a receptor which is prominent on the ER. The dye was diluted to 1 µM in pre-warmed DPBS with Ca^{2+} and Mg^{2+}, and the cells were rinsed with DPBS before incubation with the staining solution for 25 min at 37 °C. Subsequently, the cells were washed and fixed in 4 % formalin solution for 30 min or directly analyzed by live-cell fluorescence microscopy.

3.2.2.4.3 Labeling of tetracysteine-tags with biarsenical dyes

Labeling of the tetracysteine (TC) tag of proteins expressed in transfected or infected cells was performed with the green-fluorescent Fluorescein Arsenical Hairpin Binder (FlAsH) or the red-fluorescent Resofurin Arsenical Hairpin Binder (ReAsH) in living cells [457]. The labeling reagents FlAsH-EDT_2 and ReAsH-EDT_2 precomplexed with 1,2-ethanedithiol (EDT) were freshly diluted to 1 µM in DMEM at RT. The dyes are membrane permeable and upon formation of four covalent bonds between the two arsenic atoms of the dye and the four thiol groups of the peptide tag, the fluorescence intensity of the fluorophores increases considerably. Cells in 35-mm dishes were rinsed with DMEM and incubated with 500 µl of the dye solution for 1 h at RT. Washing buffer was prepared diluting 100× BAL washing buffer (2,3-dimercapto-1-propanol) in DMEM to a final concentration of 250 µM. The staining solution was removed from the cells which were then rinsed with DMEM and washed twice with 1 ml BAL washing buffer for 10 min at RT to reduce the background signal. Finally, the cells were rinsed with DMEM and either analyzed by live-cell fluorescence microscopy or fixed in 4 % formalin solution for subsequent immunostaining. The labeling was stable for some days consistent with the dissociation rate constant determined for FlAsH with various model peptides in vitro to be in the range of 10^{-6}/s.

3.2.3 Microscopy

For live-cell imaging, cells were grown in 35-mm glass-bottom dishes and were maintained in imaging medium (DMEM supplemented with 20 mM HEPES, pH 7.4). Fixed cells were kept in DPBS or mounted on microscope slides with Mowiol 4-88 Reagent.

3.2.3.1 Confocal fluorescence microscopy (CLSM)

Images of living or fixed fluorescently labeled cells were acquired by confocal laser scanning microscopy (CLSM) using an Olympus FV1000 inverted microscope. In CLSM, the samples are scanned by point illumination with a laser beam and the fluorescence signal of each point is detected by a photomultiplier tube (PMT) after spatial filtering through a pinhole that eliminates out-of-focus light thereby improving the image quality. The primary photon signal generates an electronic output from the PMT that is converted into digital pixel values from which the images are reconstructed. The microscope was equipped with a 405-nm diode laser, a 559-nm diode laser, a 635-nm diode laser and a multi-line Argon laser (458-nm, 488-nm, 515-nm). Images were acquired with a 60× (N.A.1.35) oil immersion objective or a 60× (N.A. 1.2) water immersion objective (UplanSApo, Olympus). Image acquisition with different fluorophores was performed in a sequential mode of excitation to avoid spectral crosstalk of the detecting PMT channels. Fluorophores were excited at 405 nm (DAPI), 458 nm (CFP), 488 nm (FITC), 488 or 515 nm (mEYFP), 559 nm (AlexaFluor568, AlexaFluor594, mCherry, RFP, PI, rhodamine) or 633 nm (Atto 647N).

Fluorescence emission was recorded for DAPI between 425 and 475 nm, for CFP between 475 to 500 nm, for FITC from 500 to 545 nm, for mEYFP between 500 and 545 nm or 525 and 550 nm, for Atto 647N between 655 and 755 nm and for AlexaFluor568, AlexaFluor594, mCherry, RFP, PI and rhodamine from 570 to 670 nm. When specific combinations of dyes were used, the emission ranges had to be narrowed to avoid spectral overlap, e.g. AlexaFluor594 was detected between 570 and 603 nm when in combination with Atto 647N. The settings were adjusted by appropriate negative control samples.

3.2.3.2 Fluorescence photoactivation

The dynamic behaviour of NP in living cells was measured by fluorescence photoactivation of Dendra2 fusion proteins. Dendra2 is a photoactivatable fluorophore that can be switched irreversibly from a green- to a red-fluorescent state by irradiation at around 400 nm. This causes a break of the polypeptide backbone adjacent to the chromophore. The formation of an

additional double bond leads to an extended π-electron system and causes a shift of excitation and emission spectra to longer wavelengths [458] .

Photoactivation measurements of Dendra2 constructs in living cells were performed at RT. The green state of the fluorophore was excited at 488 nm and recorded from 500 to 545 nm. An image of the initial distribution of total Dendra2-tagged protein (green state) was taken, and the region of interest (ROI) for photoactivation was chosen with a diameter of 10–25 pixels (between 3 and 21 μm^2). Irradiation of the ROI at 405 nm was performed in the fast Tornado scanning mode (50 mW diode laser, output 5 %, 20 µs/pixel, three repeats). Irradiation time and intensity were kept constant for all measurements. Images of the activated red state were scanned at 2 µs/pixel by excitation at 559 nm and detection from 570 to 670 nm. A time series of images consisting of 20 pre-activation and 230 post-activation frames was acquired at intervals of 428 ms. Illumination conditions for imaging of the red state were chosen so that fluorescence bleaching was negligible. The intensity of the red-fluorescent state in the photoactivated area was analyzed using the microscopy software FluoView FV10-ASW (Olympus).

As bleaching controls, cells expressing free Dendra2 were photoactivated within a large area of the cell in order to photoconvert a significant fraction of the fluorophore. After 4 min when the fluorophore had evenly spread throughout the cell to a steady-state distribution, a time series of the activated red state was acquired and the conditions of illumination (laser intensity, illumination time per pixel and scanning frequency) were checked for bleaching effects.

3.2.3.3 Single particle tracking (SPT)

For single particle tracking of NP constructs in living cells, time-lapse imaging was performed at 37 °C using either the inverted epifluorescence microscope Nikon TE2000 equipped with a highly sensitive back-illuminated EMCCD camera or the confocal laser scanning microscope Olympus FV1000. Using the epifluorescence microscope with EMCCD camera, images (512×512 pixels) were acquired at intervals of 0.5 s, while confocal laser scanning microscopy allowed a frame rate of one image per 1.1 s or 1.6 s, depending on the scanning speed of 2 µs/pixel or 4 µs/pixel, respectively. Confocal imaging was preferentially performed to study single particle movements at the nuclear surface or underneath the plasma membrane, while fast epifluorescence imaging was used to analyze trajectories and velocities of cytoplasmic particle movements in general.

Imaging was performed in two dimensions monitoring single cross-sections of cells over time. Pixel size corresponded to 0.178 µm in case of epifluorescence imaging and to 0.103 µm in case of confocal imaging. For fast dual color imaging of cotransport of mEYFP-NP and Rab11-RFP, images were recorded alternately by excitation at 488 nm or 561 nm, respectively, with exposure times of 30 ms/image.

Image processing and particle tracking analysis were performed using the software ImageJ. The procedure was as follows: The median projection of an image sequence was formed and subsequently subtracted from each image of the stack. This helped to reduce signals of static fluorescent structures like the cell nucleus which is highly enriched with fluorescent NP constructs, while signals from mobile particles were retained. Subsequently, the Spot Enhancing Filter of the Spot Tracker plugin was applied [454], which is based on a Mexican hat filter (Laplacian of a Gaussian operator) to detect edges (intensity changes) and enhance the contours of Gaussian-like spots for improved detection of single particle fluorescent signals. Tracking of punctate fluorescent signals was then performed using the Spot Tracker tracking algorithm. Movements of particles to be traced were selected manually by specification of the starting point, followed by a semi-automated tracking procedure implementing a cost function, which could be adjusted by introducing user-defined constraints like an intensity factor or a movement constraint. A fully automated tracking approach was not feasible due to high particle densities. When numerous bright and (often static) signals in close proximity to the moving particle complicated automated tracking and led to confusion of particles identities and false results, additional node points could be added to further constrain the path of the particle and correct the trajectory. Instant velocities were calculated from the signal coordinates between consecutive frames. Using an in-house generated python script (Dr. Martin Seeger), the data was transferred to the MTrackJ plugin [453] for graphic representation of trajectories in the original fluorescence image stacks.

3.2.3.4 Correlated fluorescence and electron microscopy of tetracysteine-tagged proteins

Correlated electron microscopy with tetracysteine (TC)-tagged proteins is based on the fact that the TC-binding dye ReAsH is not only a fluorophore, but can also mediate efficient photoconversion of 3,3'-diaminobenzidine (DAB) into an osmiophilic precipitate that can be visualized by electron microscopy [459,460]. Upon intense illumination, excited ReAsH catalyzes the formation of singlet oxygen that causes the localized oxidative polymerization of DAB. This method allows combining the specific detection of a genetically encoded tag with high resolution imaging by electron microscopy.

The protocol was performed according to [460]. MDCK II cells were grown on glass-bottom dishes with a photo-etched grid structure (600 × 600 µm squares; MatTek) to facilitate preparation and identification of photoconverted cells in electron microscopy. The cells were infected with Influenza A/WSN/33 virus mutants carrying TC-tagged NP. 20 h p.i. cells were washed and labeled for 1 h at RT with 1 µM ReAsH in DMEM (see 3.2.2.4.3). Subsequently, the cells were incubated for 5 min in pre-warmed cacodylate buffer with 2 % (w/w) glutaraldehyde for rapid fixation. The samples were cooled down to 4 °C and fixation was continued for another 30 min. The solution was removed and cells were washed four times with ice-cold cacodylate buffer. They were briefly imaged by confocal microscopy to choose an area of infected cells for photoconversion and were then covered with photoconversion blocking buffer (20 mM glycine, 10 mM KCN, 10 mM aminotriazole, 0.2 M cacodylate, pH 7.4) for 30 min at 4 °C. In the meantime, 0.5 mg/ml DAB was freshly prepared in ice-cold cacodylate buffer diluted from a 10 mg/ml stock solution stored at –80 °C. The DAB solution was oxygenated for 5 min by constant bubbling with pure oxygen. Following the photoconversion blocking step, cells were rinsed once with cacodylate buffer and incubated with the oxygenated DAB solution. Illumination for photoconversion and imaging were performed using the inverted epifluorescence IX-81 microscope with a U-MWG2 filter unit (Olympus) and maximum intensity illumination from a mercury lamp. Differential interference contrast (DIC) and fluorescence images were taken with the 40× (N.A. 0.75) objective UplanFL prior to constant illumination for photoconversion. Irradiation was performed for about 15 min on a 4°C temperature controlled stage insert. The DAB solution was refreshed every 3 min until brown precipitates were observed by transmitted light. This procedure was repeated for two or three areas on the same dish followed by five final washing steps with cacodylate buffer on ice, each for the duration of 3 min. The following processing of the samples for transmission electron microscopy (TEM) and image acquisition were performed by Maik Lehmann and Gabriele Drescher (Humboldt-Universität, Molekulare Parasitologie). This included post-fixation with 1 % (v/v) osmium tetroxide for 1 h, *en bloc* staining with 0.5 % (v/v) uranyl acetate for 1 h, stepwise dehydration with ethanol, embedding with EMBed 812 (Electron Microscopy Science) and sectioning. After infiltration of the sample with embedding medium, a small cylindrical block of polymerized resin (used like a stamp) was placed on the region of the gridded cover slip where photoconversion had been performed. After polymerization at 70 °C for 48 h and cooling down, the glass cover slip was briefly placed on a hot plate and removed from the base of the cylinder. The cells and the imprint of the grid were thereby transferred to the block surface and the block was trimmed

leaving only the brown area of photoconversion. Cells were cut *en face* into 70–90 nm sections and sections were counterstained with 4% (w/v) uranyl acetate followed by lead citrate. Images were acquired using a transmission electron microscope equipped with a wide-angle CCD camera (Zeiss EM 900, TRS Systems).

3.2.4 Virological methods

3.2.4.1 Infection and virus propagation

For infection of eukaryotic cells with Influenza A virus, cells were washed with DPBS (with Mg^{2+} and Ca^{2+}) and covered with the virus suspension, diluted appropriately in DMEM, for 1 h under cell culture conditions while gently agitating every 15 min. Thereafter, the virus supernatant was removed, cells were washed twice in DPBS and the medium for cell maintenance was chosen according to the experimental objective. For microscopy of infected cells, cells were supplied with DMEM without further additions. For virus propagation, cells were maintained in infection medium that was freshly supplemented with TPCK-trypsin for cleavage of HA on newly formed virus particles to allow multiple infection cycles.

For preparation of virus stock solutions, MDCK II cells of 80 % confluency were infected with a multiplicity of infection (MOI) of 0.01 (MOI 0.1 for virus mutants). The supernatant containing newly released virus particles was harvested 1–3 days after infection upon observation of a cytopathic effect (CPE) and was cleared from cell debris by centrifugation for 5 min at 2000× **g**. Aliquots were stored at –80 °C.

3.2.4.2 Virus purification and labeling

For purification and labeling of Influenza A virus, MDCK II cells were infected (MOI 0.1) and harvested from three T175 flasks as described in 3.2.4.1. The virus-containing supernatant that had been cleared from cell debris was subsequently centrifuged for 2 h at 100,000× **g**. The virus pellet was resuspended in 200–500 µl TNE buffer and mixed with 2 µM FlAsH-EDT_2 or ReAsH-EDT_2. The labeling solution was incubated at RT for 1.5 h or at 4 °C overnight and was then layered on top of a linear sucrose gradient (20–60 % (w/v) in TNE buffer) that was centrifuged for 4 h at 100,000× **g**. The virus appearing as a turbid layer was collected, diluted with 10 ml DPBS and pelleted at 100,000× **g** for 2 h. The virus pellet was finally resuspended in 200 µl DPBS or TNE buffer and was analyzed by SDS-PAGE or confocal microscopy, or it was stored at –80 °C.

3.2.4.3 Reverse genetics

Recombinant Influenza A/WSN/1933 virus was generated by reverse genetics using the eight plasmid system described by Hoffmann *et al.* [451]. Each plasmid contains the cDNA of one of the viral RNA segments flanked by the promoter sequences of human RNA polymerase I and II (Pol I and Pol II) and by termination and polyadenylation signals for the production of full-length RNA or capped and polyadenylated mRNA, respectively. For the generation of genetically modified viruses, the desired modification (e.g. TC-tag insertion) was introduced into the respective plasmid cDNA by molecular biology techniques (see 3.2.1.4). The eight plasmids were transfected into 293T cells as described in section 3.2.2.2. Subsequently, the cells were maintained in infection medium and those that were successfully co-transfected with all eight plasmids formed virus particles which could infect other cells and replicate. 2 d p.t. the supernatant was collected and cell debris was removed by centrifugation (5 min, 2000× **g**). For virus propagation, subconfluent MDCK II cells in a T25 flask were infected with 1 ml of the supernatant for 1 h. 4 ml of infection medium were added and finally the supernatant was harvested upon observation of a CPE, but not later than three days after infection. The recovered supernatant was purified from debris as before and stored at –80 °C. Successful generation of recombinant virus was verified by plaque assay (3.2.4.4) and by immunofluorescence (3.2.2.4.1) of NP in infected cells. The modifications introduced in to the viral genome by mutagenesis of segment 5 cDNA were verified by sequencing of purified viral RNA. Therefore, virus was propagated and harvested from three 175-cm² flasks as described in 3.2.4.1. It was pelleted by centrifugation for 2 h at 100,000× **g**. Total viral RNA was extracted using the Rneasy Mini Kit (Qiagen) according to the manufacturer's instructions. cDNA synthesis of segment 5 vRNA and sequencing was performed by Meixner GmbH (Berlin, Germany).

3.2.4.4 Plaque assay

Plaque assays were performed to determine the viral titer (the concentration of infectious viral particles in a suspension). To this end, MDCK II cells were grown to confluency in 6-well plates. A ten-fold serial dilution of the virus stock solution was prepared in DMEM. The cells were washed with DPBS (with Mg^{2+} and Ca^{2+}) and infected with 500 µl of virus dilutions for 1 h. Then, the virus suspension was removed by aspiration followed by two washing steps with DPBS (with Mg^{2+} and Ca^{2+}) and addition of 2 ml of overlay medium per well which was freshly prepared from pre-warmed solutions at 37 °C. The overlay was allowed to solidify at RT before incubating the plates for three days under cell culture conditions. As

viruses that are released from infected cells cannot diffuse freely in the gel matrix of the overlay medium and infect only the neighbouring cells, locally restricted plaques are formed. After three days, cells were stained with Neutral Red for 3 h to visualize the plaques as cell-free areas within the cell layer. Plaques were counted for every dilution that displayed an appropriate, low density of discernible plaques, each of which under these conditions most likely represents a single infection event with one infectious unit (virus particle). The titer of the stock solution in plaque-forming units (PFU) per millilitre was determined from the number of plaques and the corresponding dilution factor normalized to the applied volume.

3.2.4.5 Determination of viral titer by immunofluorescence

If recombinant Influenza A WSN virus mutants were unable to form clear plaques, the titer was determined by immunofluorescence detection of NP expression. Three dilutions of the virus stock solution were prepared and MDCK II cells were infected as described in 3.2.4.4. After infection, cells were maintained in DMEM and fixed at 20 h p.i. Immunofluorescence staining with anti-NP-FITC antibody and nuclear DAPI staining were carried out as in 3.2.2.4, and the fraction of infected cells (nuclei positive for NP) was determined by fluorescence microscopy of at least 400 cells. The multiplicity of infection (MOI) was calculated, which is defined as the number of infectious particles per number of target cells. The calculation is based on the Poisson distribution $P(n) = (MOI)^n \times e^{-MOI} / (n!)$, which describes the probability that one cell is infected by n virus particles at a given MOI. The fraction of uninfected cells (p_0) (as a measure for the probability of infection with n = 0) allowed the calculation of the MOI: $MOI = -\ln(p_0)$. Hence, the titer of the virus could be derived from the number of infected cells, the dilution factor of the virus and the applied volume of the virus stock.

3.2.4.6 Growth curve

Growth curves were recorded to describe the replication rate of Influenza virus strains. MDCK II cells in 12 dishes, about 80 % confluent, were simultaneously infected at an MOI of 0.01 (0.1 in case of WSN nTC virus) as described in section 3.2.4.1 and were subsequently maintained in 1 ml of infection medium. The MOI of the WSN nTC virus was based on the titer value determined by immunofluorescence analysis (3.2.4.5). Samples were prepared in duplicate for each time point. Supernatant was collected at 0, 8, 16, 24 and 48 h p.i. and briefly centrifuged at 2000× **g** for 5 min. Samples were stored at –80 °C and the virus titer of each sample was determined by plaque assay (see 3.2.4.4).

3.2.5 Biochemical methods

3.2.5.1 Protein determination

The protein content of virus preparations and purified vRNPs was quantified using the BCA Protein Assay Kit (Pierce) according to the manufacturer's instructions. The assay is based on the reduction of Cu^{2+} by proteins in alkaline solution combined with the colorimetric detection of resulting Cu^{+} ions by chelation with bicinchoninic acid (BCA). The enhanced protocol with a reaction temperature of 60 °C was used allowing the detection of protein in the range of 5–250 µg/ml. The absorbance of Cu^{+}/BCA was measured at 562 nm using the UV-Vis spectrophotometer UV1, and the sample concentration was determined within the range of the standard curve obtained from BSA standards. As the addition of 2 % SDS to the virus preparations did not affect the results, an interfering effect of lipids was excluded [461]. This allowed the comparison of protein contents of different virus mutants even though they can potentially differ in protein-lipid ratio.

3.2.5.2 Purification of vRNPs

vRNPs were purified for *in vitro* studies from Influenza A/X-31 virus according to the protocol described by Babcock *et al.* [117]. Concentrated virus (2 mg protein, about 1 ml) was diluted with 5 ml PBS and pelleted for 40 min at 41,100 rpm and 4 °C (rotor 70.1 Ti, Beckman Coulter). The pellet was thoroughly resuspended in 2 ml pre-warmed lysis buffer and incubated for 35 min at 31 °C. Glycerol gradients were formed with 7 ml 70 %, 0.75 ml 50 %, 0.375 ml 40 % and 1.8 ml 33 % (w/v) glycerol in gradient buffer. Detergent-disrupted virus was loaded onto the gradient and centrifuged for 4 h (190,000× **g**, 4 °C). Thereafter, 300-µl fractions were collected and aliquots (4 µl) were analyzed by SDS-PAGE with subsequent silver staining or Western blotting. The vRNP containing fractions were identified by the presence of NP and pooled. They were diluted with 5 ml resuspension buffer and centrifuged at 190,000× **g** and 4 °C for 2 h. Then, the supernatant was carefully removed and the pellet was resuspended in 100 µl resuspension buffer and stored at –20 °C.

For removal of contaminating M1 protein prior to flotation assay (3.2.5.5), the vRNP preparation was filtrated with a molecular weight cut-off of 50 kDa using Amicon Ultra-15 centrifugational filters. To retain M1, the filtration molecular weight cut-off was 10 kDa. Filtration was performed by diluting the sample four times in 10 ml resuspension buffer and centrifugation at 4000× **g** to a final volume of 200 µl. Finally, the sample was analyzed by SDS-PAGE (3.2.5.6) and stored at –20 °C.

3.2.5.3 Spectrofluorometric analysis of vRNPs by nucleic acids stains

The presence of RNA in purified vRNPs was probed with two different nucleic acid stains, the intercalating propidium iodide (PI) and the electrostatically interacting acridine orange (AO). Measurements were performed in 200 µl flotation buffer using a quartz microcuvette and an AMINCO-Bowman Series 2 spectrofluorometer. PI emission and excitation spectra were recorded by excitation at 535 nm and fluorescence detection at 607 nm, respectively. Pure buffer spectra were measured before addition of 1.5 µM PI and recording of the PI spectrum in buffer. Finally, 5 µl of purified vRNPs (1/20 of a preparation from 2 mg virus protein) (3.2.5.2) were added and the spectra were again recorded with the same settings. Difference spectra were computed. AO was used at 20 nM and excited at 460 nm. The excitation maximum of RNA-bound AO is at 460 nm, but it is also an appropriate wavelength for excitation of free or intercalated AO. The fluorescence emission spectrum was recorded between 500 and 700 nm and was checked for an emission peak at 650 nm which is characteristic RNA-bound AO. AO was measured in solution and after successive addition of 6 and 3 µl of vRNP preparation.

3.2.5.4 Preparation of large unilamellar vesicles (LUVs)

LUVs were prepared with different lipid compositions. Lipid stock solutions in chloroform, stored at –20 °C, were mixed at the desired molar ratios to a total amount of 2 µmol. Further, 0.5 or 1 mol% of the fluorescent lipid analogue N-NBD-DPPE (1,2-dipalmitoyl-*sn*-glycero-3-phosphoethanol-amine-N-(7-nitro-2-1,3-benzoxadiazol-4-yl)) was added and the solvent was evaporated under a stream of nitrogen while rotating the round-bottom glass tube to obtain a thin lipid film. Lipids were then pre-dissolved in 5 µl of ethanol and subsequently hydrated with 1 ml of flotation buffer yielding a 2 mM lipid suspension. Vigorous vortexing was applied for 3 min to accomplish the formation of multilamellar vesicles, followed by five freeze-thaw cycles. Finally, to obtain unilamellar vesicles of the desired mean size [462], the suspension was extruded 10 times through a polycarbonate membrane filter with a pore size of 100 nm using a mini extruder with compressed nitrogen to apply the required pressure. The temperature was kept above the phase separation temperature of the lipid mixture which was commonly at RT, but raised to 55 °C when cholesterol (Chol) and sphingomyelin (SM) were contained. LUVs were stored at 4 °C and used within one week.

Assuming that the different lipids were equally solubilized, the fluorescence intensity of N-NBD-DPPE in each liposome preparation was determined by fluorescence spectroscopy and

used as a measure of lipid concentration to apply comparable amounts of lipids in the flotation assay. NBD was excited at 468 nm and emission was detected at 536 nm (FluoroMax-4, Horiba Yobin Yvon).

3.2.5.5 Flotation assay

The flotation assay allows characterizing the membrane-binding ability of proteins *in vitro* [463]. The assay is based on the separation of liposomes and soluble proteins according to their densities. Liposome-bound proteins partition into lower density fractions of a density gradient than proteins alone. The proteins or protein complexes of interest (e.g. vRNPs, M1, NP or the control protein PDC-109) were mixed with 100 µl of liposomes in a total volume of 150 µl. Liposomes were prepared with an initial concentration of 2 mM lipid (see 3.2.5.4). For each experiment comparing different liposome preparations, the lipid concentrations of the samples were adjusted as described in 3.2.5.4. Protein concentrations were applied as follows: 12 µM PDC-109, 1.5 µM recombinant NP, 1.5 µM recombinant M1 or 0.5 µM recombinant M1, if mixed with vRNPs. For vRNPs, 1/8 of a vRNP preparation made from 2 mg/ml virus was used for each flotation (about 2.5 µg protein). Incubation times of proteins and LUVs prior to flotation were as follows: recombinant M1 and NP for 5 min on ice, vRNP and vRNP/M1 for 30 min on ice and in case of a two-step incubation, recombinant M1 or vRNPs with LUVs for 15 min on ice prior to addition of vRNPs or M1, respectively. For PDC-109, an incubation period with liposomes was not necessary. The protein-liposome mixture was then adjusted to 30 % (w/v) sucrose by addition of 100 µl of a 75 % (w/v) sucrose solution in flotation buffer. The gradient was formed by layering 200 µl of 25 % (w/v) sucrose solution and 50 µl of flotation buffer on top of the high-density fraction. Centrifugation was performed for 1 h at 4 °C in a TL-100 tabletop ultracentrifuge at 240,000× **g**. Subsequently, fractions of 80 µl, 200 µl and 200 µl were collected manually from the top to the bottom. Collection of fractions was done under UV light to visualize the fluorescently labeled liposomes. To test for protein adsorption to the centrifugation tube, the tube was rinsed with 50 µl of prewarmed SDS sample buffer which was collected for further analysis. 20 µl of each fraction (named ‘0 %’, ’25 %’, ’30 %’ and ‘T’ for tube) were analyzed by SDS-PAGE.

3.2.5.6 SDS polyacrylamide gel electrophoresis (SDS-PAGE)

By SDS-PAGE, proteins were separated according to their electrophoretic mobility which is, due to the stoichiometric binding of anionic sodium dodecyl sulfate (SDS), principally based

on the molecular weight (MW) of the proteins [464]. Discontinuous polyacrylamide gels [465] were prepared using the equipment of the Mini-PROTEAN 3 system (Bio-Rad). Composition of buffers and gels are specified in section 3.1.3. Resolving gels of 10 or 12 % acrylamide/bisacrylamide at pH 8.8 were casted and overlaid with a 5 % stacking gel of pH 6.8. Samples were incubated with SDS sample buffer at 98 °C for 5 min and loaded onto the gel. To analyze tetracysteine-tagged proteins labeled with FlAsH or ReAsH, non-reducing sample buffer was used and incubation temperature was reduced to 70 °C. Electrophoresis was run at constant voltage of 120 V (stacking gel) and then raised to 180 V in the resolving gel. For detection of the proteins after electrophoresis, the gel was processed by silver staining, Coomassie staining or Western blotting (see 3.2.5.8, 3.2.5.7 and 3.2.5.9). Fluorescently labeled proteins were directly detected with the Fluorescent Image Analyzer FLA-3000 (FujiFilm) by scanning the gel at 473 nm and 532 nm for excitation of FlAsH and ReAsH, respectively. This was usually followed by Western blotting or Coomassie staining.

3.2.5.7 Coomassie staining

For the detection of total protein in an SDS polyacrylamide gel, the gel was incubated for at least 2 h in Coomassie staining solution followed by incubation with destaining solution until the background was sufficiently removed. The detection limit is about 0.1 µg of protein per spot. The result was recorded at 700 nm with the Odyssey Infrared Imaging System (LI-COR).

3.2.5.8 Silver staining

Silver staining is one of the most sensitive techniques for the visualization of total protein in a polyacrylamide gel with a detection limit of a few nanogrammes per band. All solutions were freshly prepared and incubation steps were carried out under constant agitation at RT. After electrophoresis the gel was fixed for at least 30 min in 30 % (v/v) ethanol and 10 % (v/v) acetic acid followed by incubation with sensitizer solution for 30 min and three extensive 10 min washing steps with ultrapure water. Subsequently, the staining solution with 0.1 % (w/v) silver nitrate was added for 30 min allowing the Ag^+ ions to form non-stoichiometric complexes with the proteins. Excess Ag^+ ions were removed by washing with water for 30 s, and the Ag^+ ions that were complexed by proteins were then reduced to elemental silver by the developer solution, which was incubated with the gel until the protein bands became clearly visible. The reaction was terminated by addition of the stop solution (0.05 M EDTA).

3.2.5.9 Western blotting

Western blotting was performed after electrophoretic separation of proteins (0) to identify specific protein bands by antibody recognition. To this end, the proteins were transferred (‘blotted’) from the gel onto a nitrocellulose membrane. Subsequent to SDS-PAGE, the gel was placed onto the membrane which was soaked in transfer buffer and together they were squeezed between two thick blotting papers also soaked in transfer buffer. An electric field was applied perpendicular to the stack with 20 V for 30 min using a Trans-Blot Semi-Dry Transfer Cell (Bio-Rad). The efficiency of the transfer was verified by use of a prestained molecular weight marker that had previously been loaded onto the gel for SDS-PAGE. Since the membrane unspecifically binds all proteins, it was blocked after the transfer to prevent unspecific binding of antibodies. Blocking was done by incubating the membrane for 1 h with milk solution or Odyssey Blocking Buffer (LI-COR) depending on the detection method. For chemiluminescence detection with horseradish peroxidase (HRP)-linked antibodies, milk was used as blocking reagent, whereas the Odyssey Blocking Buffer was used with near infrared dye (IRDye)-labeled antibodies. The membrane was gently agitated during all incubation steps. Antibodies were diluted in the respective blocking buffer with up to 0.5 % (v/v) Tween-20. Primary antibodies were typically used 1:3,000 and secondary antibodies 1:10,000. The primary antibody which is specific for the protein of interested was incubated with the blot for 1 h at RT or at 4°C overnight, followed by three times washing for 10 min with PBS-T and incubation with the secondary antibody for 1 h. Finally, the membrane was washed as before and rinsed twice with PBS. If the secondary antibody was linked to a HRP for chemiluminescence detection, the blot was treated with the ECL Detection Kit (Amersham) and the light signal produced by a HRP-mediated reaction was captured on a photographic film. Secondary antibodies labeled with an IRDye were detected with the LI-COR Odyssey scanner by excitation at 700 nm.

3.2.5.10 PIP strip lipid-binding specificity assay

Lipid-binding capacity and specificity of purified Influenza virus RNPs and M1 *in vitro* was tested on PIP Strips (Echelon). PIP Strips are hydrophobic membranes spotted with eight different phosphoinositides and seven other biologically relevant lipids. The membrane was blocked with 3 % (w/v) fatty acid free BSA in TBS for 1 h at RT and was subsequently incubated with vRNP-M1 preparations purified from virus particles (0) and diluted in 4 ml blocking buffer. After 1 h at RT the membrane was washed three times with TBS-T for 10 min and incubated with primary anti-M1 (Virostat) or anti-NP antibodies (1:1000 in blocking

buffer) for 1 h at RT. The membrane was washed as before followed by incubation with secondary HRP-linked antibodies (1:5000 in blocking buffer) for another hour. Finally, the membrane was washed three times for 10 min in TBS-T and treated with the ECL detection reagent (Amersham) for 5 min. The chemiluminescence signal of the HRP-mediated reaction was detected on a photographic film.

To reduce unspecific background of NP immunodetection with anti-NP and GAMPO antibodies, the same protocol was also carried out replacing BSA blocking buffer by 1 % milk in TBS. Results were not affected by the change of blocking reagent.

4 Results

4.1 *In vitro* studies of Influenza A virus ribonucleoprotein interactions with lipid membranes

Association of Influenza A viral ribonucleoproteins (vRNPs) with the viral envelope is crucial for the formation of progeny virus particles. In the first part of this study, the intrinsic ability of vRNPs to interact with lipid membranes was analyzed, and the capacity of the matrix protein M1 to mediate membrane association of vRNPs was investigated using an *in vitro* approach with model membranes, purified M1 and vRNPs.

4.1.1 Purification of Influenza A/X-31 vRNPs

For *in vitro* analysis, intact vRNP complexes had to be purified from virus particles. Detergent-disrupted Influenza A/X-31 virus was fractionated by density gradient centrifugation according to Babcock *et al.* [117], and the protein content of each fraction was analyzed by SDS-PAGE and silver staining (Fig. 8). The major protein bands visualized by silver staining were also detectable by anti-Influenza A virus H3N2 polyclonal antibody in Western blot analysis (data not shown). In addition to the viral proteins, small amounts of the cellular protein β-actin were identified by Western blotting and shown to be present exclusively in the low-density membrane fractions of the gradient (Fig. 8A). β-actin was further found in virus that had been purified by sucrose gradient Fig. 8G) indicating that the presence of membrane-bound β-actin is not an external contamination of the virus preparation.

The vRNP complexes were expected to partition into high-density fractions and to be detectable by the presence of NP as the major protein component of vRNPs. Two protein bands were observed in fractions of higher density, typically in fractions 12 to 19 (Fig. 8A); these could be identified as NP (56 kDa) and as matrix protein M1 (27 kDa) by Western blot analysis (Fig. 8B, D, E). Additionally, a faint protein band of about 80 kDa indicates the presence of the viral polymerase subunits as part of intact vRNP complexes in these fractions (PA 82.6 kDa; PB1 86.6 kDa; PB2 86.1 kDa). The presence of the matrix protein M1 in the same fractions was however unexpected based on the protocol described by Babcock *et al.* [117]. Western blot analysis showed that M1 could be found in all fractions (Fig. 8B). To obtain purified vRNPs in the presence of M1, fractions which were clearly devoid of other proteins (typically fractions 14 to 17) were pooled and concentrated. The protein content was

then again verified by SDS-PAGE (Fig. 8C) and immunodetection of NP and M1 (Fig. 8D, E). If the resolution of protein bands in the gel was high, NP was resolved as a double band (Fig. 8C, F) which is known to be due to the differential phosphorylation states of NP [364].

For the following experiments, vRNPs were prepared in the presence or in the absence of M1. Therefore, isolated vRNPs were filtrated with a molecular weight cut-off of 10 kDa to maintain M1 (in the following referred to as "vRNP/M1") and with a cut-off of 50 kDa to remove M1 (Fig. 8F). A small fraction of residual M1 was usually retained in the sample after filtration with 50 kDa cut-off, even when the number of washing steps was increased indicating an association of M1 with larger vRNP complexes or oligomerisation of M1. Acidification of the complexes for dissociation of M1 was avoided to prevent conformational changes. Such changes usually prime vRNPs during cell entry by endocytosis [29,279,466], but might also mark them as incoming vRNPs and affect properties required for transport and assembly. A difference between newly formed progeny vRNPs and acidified incoming vRNPs has not been reported yet, but cannot be excluded.

To verify that the purified proteins were indeed part of intact RNA-containing RNP complexes, the samples were further analyzed by electron microscopy (performed by Kai Ludwig, Freie Universität Berlin) and by fluorescence spectroscopy with RNA-binding dyes. Electron micrographs of isolated vRNP/M1 preparations (Fig. 9) showed elongated and flexibly curved structures in the range of 100 nm in length strongly resembling vRNP structures that had been previously reported [52,82]. The textured, heterogeneous background of the images might have been caused by the presence of the M1 protein, but this remains unproved. Clustering of vRNP segments was not observed. As it had been reported that NP can form large polymeric structures resembling vRNPs even in the absence of RNA [334], and as RNP-bound vRNA is sensitive to RNAse [94,95], the presence of RNA in purified complexes was additionally verified by propidium iodide (PI) and acridine orange (AO) fluorescence spectroscopy (Fig. 10). PI is an intercalating nucleic acid dye that undergoes substantial spectral changes upon binding to single-stranded (ss) or double-stranded (ds) nucleic acids [467,468,469]. This allows specific detection of RNA and DNA. Compared to free PI in buffer, nucleic acid-bound PI exhibits a bathochromic shift of the excitation spectrum to longer wavelengths and a hypsochromic shift of the fluorescence emission to shorter wavelengths. To analyze the RNA content of vRNP preparations, excitation and emission spectra were measured for 1.5 µM PI in the presence and absence of 5 µl of a vRNP/M1 preparation (1/20 of one preparation, corresponding to about 1 µg protein). Difference spectra were calculated (Fig. 10A). The pure buffer spectra were subtracted from

the PI spectra in buffer to obtain those spectral components that are caused by free PI in an aqueous buffered environment (PI-buffer spectra). Further, the spectra of PI in buffer were subtracted from PI spectra in the presence of vRNP/M1 giving those spectral components that result from the interaction of PI with the vRNP/M1 sample (PI-vRNP spectra). The vRNP/M1 sample itself was non-fluorescent in the analyzed range. A clear shift of PI excitation and

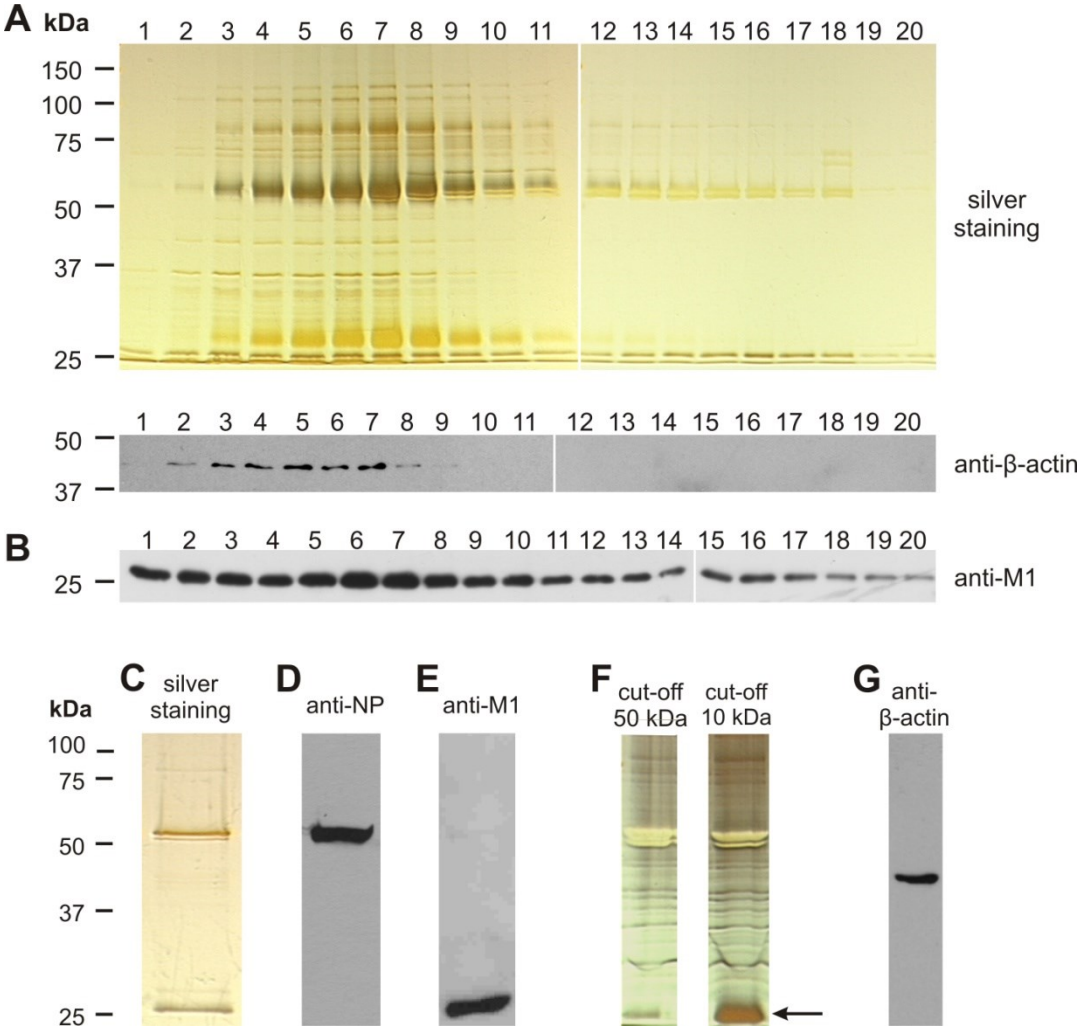

Fig. 8: Purification of Influenza vRNPs. Detergent-disrupted Influenza A/X-31 virus was fractionated by density gradient centrifugation in a glycerol gradient. (A) Fractions were analyzed by SDS-PAGE and subsequent silver staining. Membrane proteins can predominantly be found in low density fractions 3 to 11. A protein around 40 kDa of non-viral origin could be identified as β-actin by Western blotting and was exclusively present in low density membrane fractions. Fractions 12 to 19 typically contained NP (56 kDa) and the matrix protein M1 (27 kDa). (B) M1 was identified by Western blotting in all fractions throughout the gradient. (C–E) Higher density fractions supposed to contain vRNPs and showing exclusively NP and M1 signals were pooled, washed and analyzed by SDS-PAGE. The two proteins were detected by silver staining (C) and specifically probed by Western blotting with anti-NP (D) and anti-M1 (Virostat) (E) antibodies and HRP-coupled detection. (F) Pooled vRNP fractions were filtrated with a molecular weight cut-off of 10 or 50 kDa and proteins were detected by SDS-PAGE and silver staining showing removal of most of M1 (arrow) by cut-off 50. (G) Intact virions purified by sucrose gradient were analyzed for the presence of β-actin by Western blotting.

emission spectra upon addition of the vRNP/M1 preparation was observed which is characteristic for the binding of PI to nucleic acids and which demonstrates the presence of nucleic acids within the vRNP/M1 isolates from Influenza A virus. The excitation maximum of PI in buffer was about 480 nm compared to 530 nm in the presence of the vRNP/M1 preparation. The maximum of fluorescence emission shifted from about 632 nm to 615 nm upon interaction with the vRNP/M1 sample and the fluorescence intensity increased. To further confirm that the nucleic acid that had been detected by PI fluorescence was single-stranded and complexed by proteins, a second nucleic acid dye was used. AO in contrast to PI intercalates only into ds DNA or RNA and binds to ss nucleic acids by electrostatic interaction with the phosphate backbone [470,471]. These binding modes can be differentiated by their characteristic orthochromatic and metachromatic fluorescence spectra. When intercalated into DNA, AO emits green fluorescence at 525 nm. In a complex with RNA, red fluorescence is detectable with an emission maximum at 650 nm. The fluorescence spectra of AO were measured before and after addition of purified vRNP/M1 (Fig. 10B). An increase of fluorescence emission at 650 nm, which is characteristic for electrostatic complex formation of AO with ss RNA, was not detectable, although the amount of added vRNP/M1 preparation was comparable to the amount used to monitor PI spectral changes. An increase of fluorescence intensity at 525 nm indicating intercalation of AO into ds DNA was not observed either. Instead, fluorescence intensity at 525 nm decreased due to dilution. Obviously, the nucleic acids that could be detected by PI were undetectable by AO. These results allow the interpretation that the shifts of PI spectra were caused by PI intercalation into ss nucleic acids, a binding mode that is not suitable for detection by AO, and that the phosphate backbone of the ss nucleic acids is inaccessible for electrostatic interactions with AO. This is consistent with our knowledge about the vRNP structure where ss vRNA is bound to the NP scaffold by electrostatic interactions via the RNA phosphate backbone [87,93].

In summary, the results of SDS-PAGE analysis, electron microscopy and fluorescence spectroscopy confirm that intact vRNPs of appropriate size consisting of NP, vRNA and polymerases were successfully purified from Influenza A/X-31 virus particles.

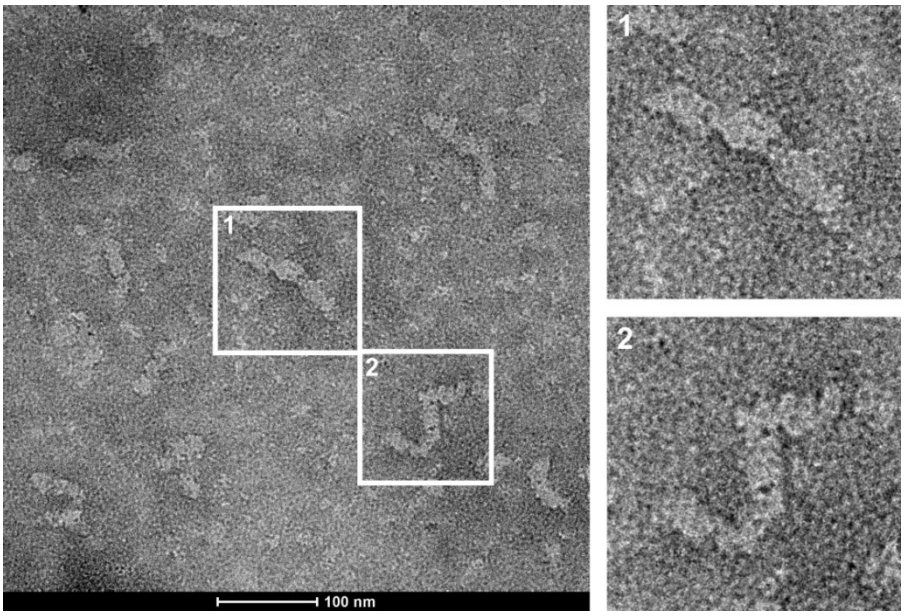

Fig. 9: Negative stain electron micrographs of Influenza vRNPs purified from detergent-disrupted Influenza A/X-31 virus. Uranyl acetate was used as contrast agent. Sample processing for transmission electron microscopy (TEM) and image acquisition were performed by Kai Ludwig (Freie Universität, Berlin).

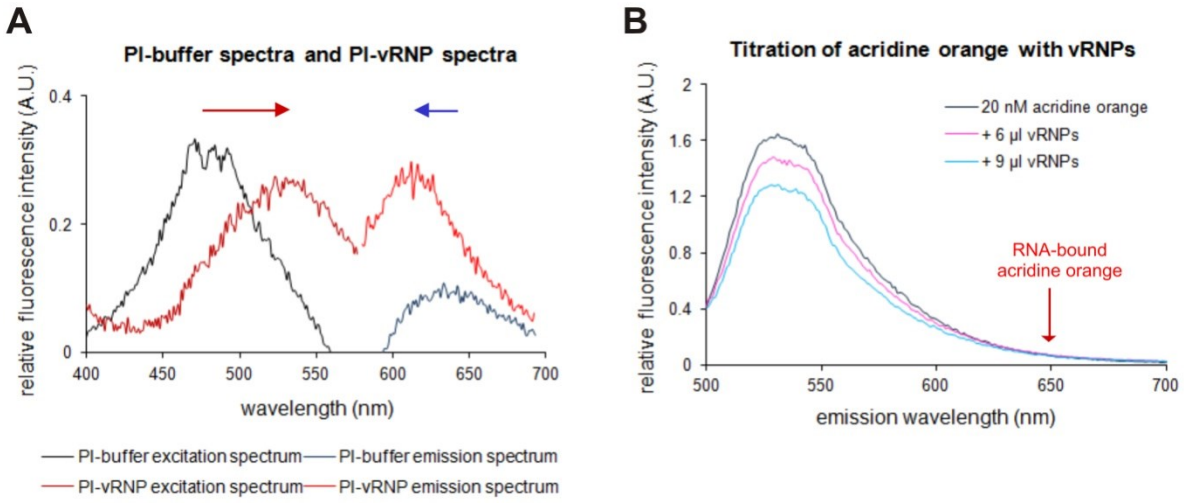

Fig. 10: Spectrofluorometric analysis of purified vRNP/M1 with nucleic acid dyes propidium iodide (PI) and acridine orange (AO). (A) Difference spectra of PI. Fluorescence emission and excitation spectra of 1.5 µM PI in buffer were recorded. Difference spectra were formed by subtracting pure buffer spectra from PI spectra in buffer (blue, black). The same measurement was repeated after addition of 5 µl purified vRNPs/M1 and difference spectra were calculated by subtraction of PI spectra in buffer (light red, dark red). Additional spectral components of PI in the presence of vRNP/M1 result from interactions of PI with the vRNP sample. The vRNP/M1 sample itself is non-fluorescent (not shown). Arrows indicate the red shift and the blue shift of excitation and emission spectra, respectively, upon interaction of PI with the vRNP/M1 sample. (B) Fluorescence spectra of 20 nM AO were recorded in buffer and after addition of purified vRNPs. The fluorescence signal decreased (due to dilution). An additional emission peak at 650 nm, which is characteristic for electrostatic interaction of AO with RNA, was not observed.

4.1.2 Analysis of vRNP binding to membranes by flotation assay with liposomes

To study the ability of the vRNP segments to associate with pure lipid bilayers, the purified viral complexes from Influenza A/X-31 virus were analyzed by flotation assay with large unilamellar vesicles (LUVs) of various lipid compositions. Instead of pelletizing the liposomes, flotation was chosen as experimental approach to obtain a clear separation of membrane-bound floating protein complexes from protein aggregates and proteins that adsorbed to the test tube. Protein adsorption to the tube was found to be a major problem in preliminary tests, particularly in the presence of M1 (see also Fig. 12C, D). LUVs were prepared according to a well-established method by extrusion through polycarbonate filters of 100 nm pore size [462]. To mimic typical features of cellular membranes and analyze potential requirements for vRNP interaction with membranes, LUVs of various lipid compositions were produced and tested for the association of purified proteins. Due to variable loss of lipid during LUV generation caused by incomplete dissolution or adsorption to the filter membrane, the lipid concentration of different LUV preparations had to be adjusted for comparability after extrusion. Therefore, the fluorescence signal (being proportional to the concentration) of the lipid analogue N-NBD-DPPE in each preparation was determined and served as a measure to apply equal amounts of each liposome species for flotation. Differences among the preparations were typically less than 10 % and never larger than 20 %. For the binding assay, lipids were applied in molar excess of protein to exclude that protein binding is limited by the amount of available lipid. The protein to lipid ratio was typically chosen in the order of 1 to 1000. A schematic overview of the experimental procedure is given in Fig. 11A. Proteins and LUVs were mixed and separated by density gradient centrifugation. Liposomes (and associated proteins) partitioned to the top of the gradient, which could be visualized by UV-light detection of N-NBD-DPPE fluorescence. Collected fractions were analyzed by SDS-PAGE which conveniently allowed detection of the NBD-labeled lipid in the gel by fluorescence detection in parallel to the standard protein detection by silver staining.

For evaluation of the method, a positive control experiment (Fig. 11B) was performed using PDC-109, a seminal plasma protein that is known to specifically bind to choline lipid headgroups [472,473]. LUVs made from pure 1,2-dioleoyl-*sn*-glycero-3-phosphocholine (DOPC) were mixed with PDC-109 at molar protein/lipid ratios from 1/10 to 1/80. PDC-109 purified from the seminal plasma of Holstein bulls as described in [474] was kindly provided by Peter Müller (Humboldt-Universität, Berlin). In the absence of liposomes, flotation of

PDC-109 was not observed. An increasing amount of floating, membrane-bound PDC-109 could be detected with increasing lipid concentration (Fig. 11B). At a protein/lipid ratio of 1/40, the entire protein was found in the two liposome-containing top fractions (0 % and 25 % sucrose), whereas at a ratio of 1/20, part of the protein remained in the pellet fraction (30 % sucrose). Considering that only half of the lipid is exposed on the outer leaflet of the liposomal bilayer, the results are consistent with a binding stoichiometry of 10–20 lipids per protein that had been described before [475].

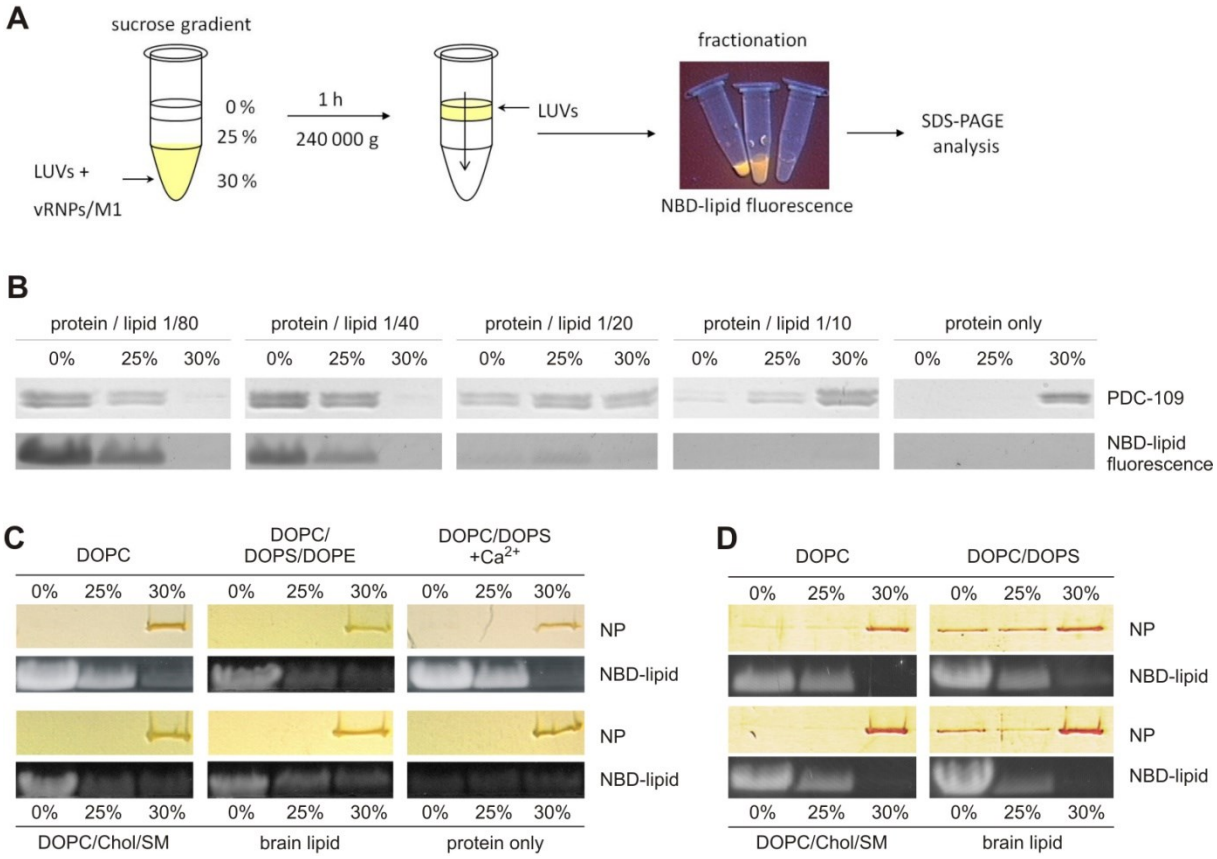

Fig. 11: Membrane-binding analysis by liposome flotation assay. (A) Schematic representation of the flotation assay procedure. The presence of large unilamellar vesicles (LUVs) containing a fluorescent NBD-lipid is represented by yellow color. (B–D) Sucrose gradient fractions from flotation assay were analyzed - after ultracentrifugation - by SDS-PAGE and subsequent silver staining. The fluorescent NBD-lipid was detected in the SDS-gel by Fluorescence Image Analyzer. Lipids were predominantly present in the low-density fractions (0 % (w/v) sucrose). Collected fractions are designated according to their sucrose concentration, 0 %, 25 %, 30 % (w/v) sucrose (B) Positive control for flotation with the seminal plasma protein PDC-109. PDC-109 binds specifically to the choline lipid headgroup and was analyzed with DOPC LUVs at various molar protein to lipid ratios. (C) Flotation of vRNPs purified from Influenza A/X-31 virus and separated from M1 by filtration (cut-off 50 kDa). vRNPs were incubated with LUVs of different compositions for 30 min on ice prior to flotation. LUVs were prepared from DOPC, DOPC/DOPS/DOPE (8/1/1), DOPC/DOPS (8/2), DOPC/Chol/SM (5/2.5/2.5) or total brain lipid extract. Flotation of DOPC/DOPS was performed in the presence of 1 mM $CaCl_2$. (D) Flotation of recombinant NP with LUVs made from DOPC, DOPC/DOPS (8/2), DOPC/Chol/SM (5/2.5/2.5) and brain lipid. NP was incubated with LUVs for 5 min prior to flotation. His-tag purified recombinant NP from Influenza A/FPV was kindly provided by Nadine Jungnick (Humboldt-Universität, Berlin).

The same experiment was performed with purified vRNPs (devoid of M1 protein) from Influenza A/X-31 virus (Fig. 11C). LUVs were incubated with vRNP complexes for 30 min before flotation. A variety of different lipid compositions was analyzed. First, liposomes made of pure DOPC were chosen because unsaturated phosphatidylcholines represent a major constitutent of cellular membranes [412]. Further, DOPC was mixed with dioleoyl-phosphatidylserine (DOPS) and dioleoyl-phosphatidylethanolamine (DOPE) (8/1/1), which both represent phospholipids that characteristically locate on the inner leaflet of cellular plasma membranes [389], the site of Influenza virus assembly. As Influenza vRNPs are negatively charged complexes, a beneficial role of divalent Ca^{2+} ions for association with negatively charged DOPC/DOPS (8/2) LUVs was also tested. Taking into consideration that the Influenza viral envelope is specifically enriched in raft lipids like sphingomyelin (SM) and cholesterol (Chol) [16,234] and that membrane rafts have for a long time been assumed to be locations of virus assembly, a lipid raft mixture consisting of DOPC/SM/Chol (5/2.5/2.5) was prepared for analysis. Finally, vRNP binding was investigated with LUVs prepared from total brain lipid extract. This endogenous lipid mixture allowed to cover a broad range of natural lipid diversity and to include also specialized, minor lipid species like phosphoinositides. Representative results of vRNP flotation with the different types of LUVs are shown in Fig. 11C. Association of vRNPs with liposomes could not be detected for any of the lipid compositions. NP as representative component of vRNPs was entirely found in the pellet fractions (30 %). Recovery of the liposomes in the two floating fractions (0 % and 25 %) was verified by the NBD-lipid fluorescence signal in the SDS-gel.
In addition to the results from flotation analysis, it was not possible to observe purified vRNPs bound to lipid membranes of giant unilamellar vesicles (GUVs) using fluorescence microscopy (data not shown).

As reports have indicated accumulation of NP at the apical membrane of polarized cells in the absence of other viral components [299], membrane-binding was also investigated for NP alone. His-tag purified recombinant Influenza A/FPV virus NP was kindly provided by Carina Glöckner and Nadine Jungnick (Humboldt-Universität, Berlin). Results are shown in Fig. 11D. NP did not associate with pure DOPC LUVs. Although apical accumulation of NP in transfected cells had previously been suggested to be lipid raft-dependent [299], direct binding of NP to a classical lipid raft mixture could not be observed either. However, a fraction of NP was found to associate with DOPC/DOPS LUVs and with liposomes made from total brain lipid extract. Both types of LUVs shared the presence of negatively charged lipids. DOPC/DOPS LUVs contained 20 % DOPS. The total brain lipid extract comprised

11 % DOPS, but also other negatively charged lipids like phosphatidic acid and phosphtidylinositol. As NP is known to be a basic protein with a net positive charge of +14 at pH 6.5 [327], binding to negatively charged liposomes was expected. Such association was not observed for NP being part of the vRNP complexes (Fig. 11C), when NP is electrostatically bound to vRNA and its basic residues are thus neutralized. This indicates that NP binding to DOPC/DOPS and brain lipid LUVs competes with RNA binding and is presumably of electrostatic nature. As the observed membrane association of NP is apparently not functionally relevant for vRNP complexes, the NP interaction with negatively charged liposomes was not further investigated. Nevertheless, this finding might reflect a property of NP that can potentially contribute to the subcellular targeting of NP when expressed alone. Negative surface charges of cellular membranes have been reported to contribute to the subcellular localization of proteins with polybasic clusters directing strongly cationic proteins like NP to the plasma membrane [286]. Even though this does not fully explain a lipid-raft dependent targeting of NP to the apical plasma membrane as suggested by Carrasco *et al*. [299], co-segregation of negatively charged PS with sphingolipid and cholesterol-enriched liquid-ordered membrane domains as described by Fairn *et al.* [476] might offer an explanation for lipid raft-dependent behavior of NP.

After intrinsic membrane binding of vRNPs and NP could not be demonstrated *in vitro*, the capacity of M1 to mediate membrane association of vRNPs was examined. A key role of M1 for assembly and simultaneous cross-linking of the different viral components has been suggested for a long time [20,34,41,50], but a direct role in mediating association between vRNPs and membranes has not been demonstrated yet. Preparations of purified vRNP/M1 were analyzed by flotation with liposomes made of DOPC, DOPC/DOPS/DOPE, raft lipids (DOPC/SM/Chol) or total brain lipid extract (Fig. 12). In the absence of LUVs, vRNPs (detected by NP) and M1 remained entirely in the pellet fraction, whereas upon flotation with negatively charged LUVs, a small but distinct fraction of M1 together with vRNPs partitioned into the liposome-containing low-density fraction (Fig. 12A; DOPC/DOPS/DOPE and brain lipid). In case of uncharged liposomes made of DOPC or raft lipids, trace amounts of NP close to background levels were sometimes detected in the floating fractions, which was presumably caused by contamination during fractionation. The requirement for highly sensitive protein detection due to low protein recovery is a drawback of this experimental approach and will be discussed below together with an alternative approach for improved detection of membrane binding. M1 had previously been reported to bind to negatively charged membranes [42,43,45]. For vRNPs, it has been demonstrated above (Fig. 11C) that

they do not possess intrinsic membrane binding properties under the selected conditions. The results of the combined flotation of vRNPs and M1 therefore indicate that the presence of M1 can promote association of vRNPs with negatively charged liposomes, even though the extent of membrane association was rather poor (Fig. 12A). The majority of M1 and NP remained unbound in the pellet fractions thereby questioning the significance of the observed interaction of M1 and vRNPs with membranes. Inefficient binding of M1 to an excess of negatively charged liposomes was unexpected in comparison to efficient flotation of M1 alone (Fig. 12B, bottom). This indicates that M1 might cluster with the negatively charged vRNPs and might thereby be partially prevented from membrane binding. Indeed, *in vitro* clustering of vRNP-M1 complexes was previously visualized by electron microscopy [42] and was further reported for purified vRNP/M1 by Kemler *et al.* [85].

To provide more free M1 protein and to obtain a larger fraction of membrane-associated proteins, purified vRNP/M1 complexes were combined with additional, recombinantly generated M1 protein for flotation analysis. In a parallel control experiment, flotation was performed with recombinant M1 alone (Fig. 12B). The His-tag purified recombinant M1 was kindly provided by Nadine Jungnick (Humboldt-Universität, Berlin) [445]. M1 alone (1.5 µM) bound very efficiently to negatively charged liposomes consisting of DOPC/DOPS/DOPE or total brain lipid extract (Fig. 12B, bottom), i.e. the protein was exclusively detected in the liposome-containing floating fractions. Surprisingly, in the absence of liposomes and in case of M1 flotation with DOPC or raft lipid LUVs, only very faint signals of M1 could be detected at all. This observation suggested that, in the absence of negatively charged M1-binding surfaces, M1 precipitated and adsorbed to the test tube. This was confirmed by experiments in which protein adsorption to the test tube was analyzed by recovering the adsorbed protein in SDS sample buffer. The protein recovered from the test tube is referred to as fraction “T” in Fig. 12. It was found that M1 adsorbed almost completely to the test tube in the absence of liposomes and that a considerable fraction of M1 could be prevented from precipitation by addition of negatively charged liposomes (Fig. 12C). The negatively charged liposomes apparently competed with the test tube surface for M1 binding explaining reduced recovery of soluble protein in the absence of membrane binding. Incubation of M1 with vRNPs (15 min on ice) prior to flotation led to precipitation and adsorption of the entire protein even in the presence of negatively charged liposomes and inhibited M1 binding to the liposomes (Fig. 12C). This observation suggests strong interactions, possibly aggregation, among M1 and vRNPs and is consistent with the above-

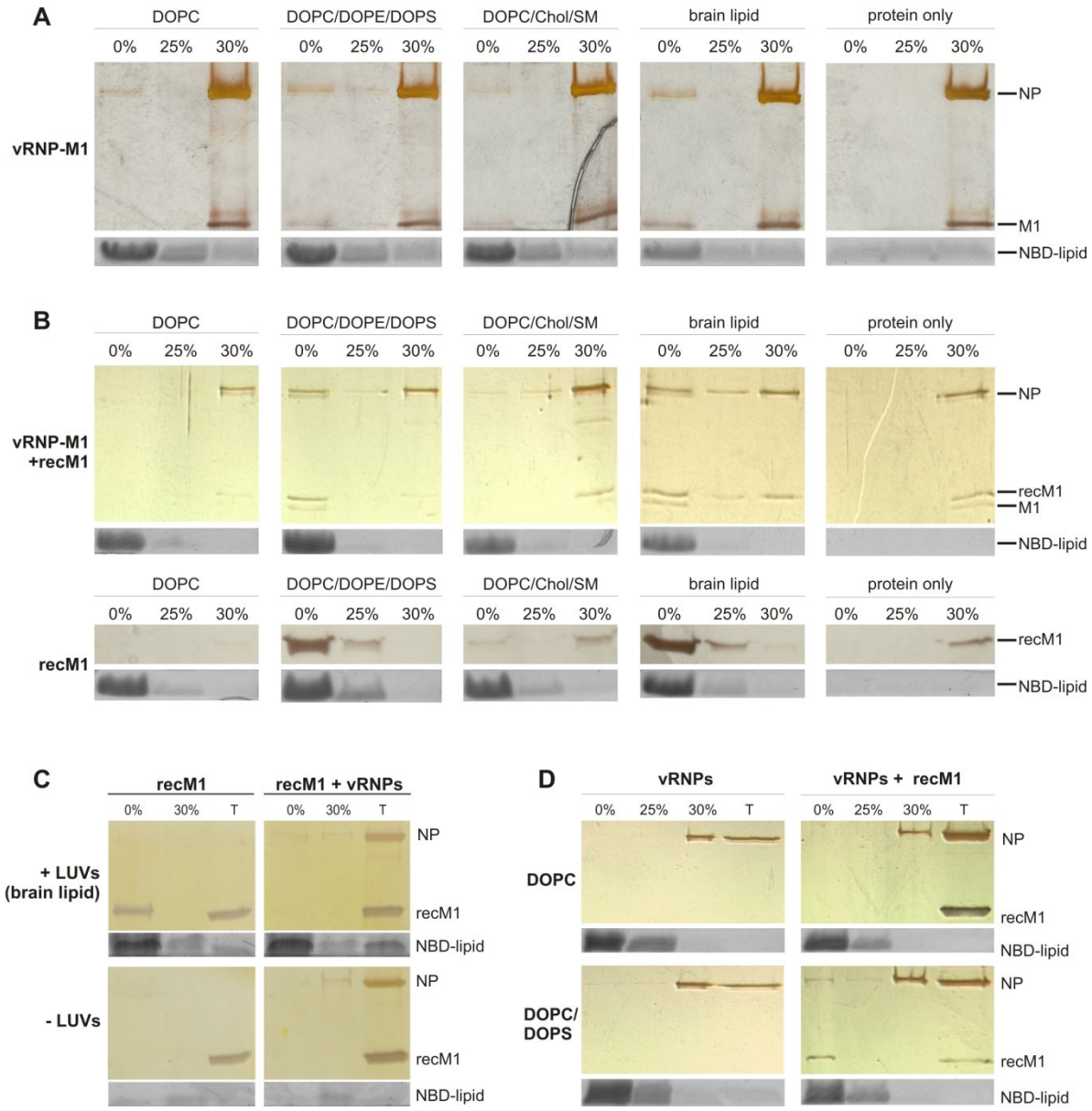

Fig. 12: Membrane-binding studies of purified vRNPs in the presence of M1 (Flotation assay). Liposomes were prepared with the following lipid compositions: pure DOPC, DOPC/DOPS/DOPE (7/2/1), DOPC/DOPS (8/2), DOPC/Chol/SM (5/2.5/2.5) or total brain lipid extract. Each mixture was labeled with 0.5 mol% N-NBD-DPPE. Flotation was performed by sucrose density gradient centrifugation. The gradient (0 %, 25 % and 30 % (w/v) sucrose) was fractionated and the protein content was analyzed by SDS-PAGE and silver staining. The fluorescent marker lipid NBD-DPPE was detected in the SDS-gel by fluorescence imaging showing that LUVs were predominantly present in the low density fractions (0 % sucrose). (A) Flotation of vRNP/M1 purified from Influenza A/X-31 virus particles (filtration cut-off 10 kDa). (B) *top*: Flotation of vRNP/M1 with LUVs that were incubated with recombinant M1 (recM1) for 15 min prior to flotation. *bottom*: Flotation of recombinant M1 alone. (C) Flotation of recombinant M1 with brain lipid LUVs in the presence and absence of vRNPs. Protein adsorption to the centrifugation tube was analyzed by recovering the adsorbed protein in SDS sample buffer (fraction "T"). M1 adsorbed almost completely to the tube in the absence of liposomes, which could be reduced by addition of LUVs causing partial flotation of recM1. The incubation of M1 with vRNPs for 15 min prior to flotation led to precipitation of all protein and prevented M1 from binding to the liposomes. (D) vRNPs separated from M1 by filtration (cut-off 50 kDa) were subjected to flotation with DOPC and DOPC/DOPS LUVs in the presence and the absence of recombinant M1. Recombinant M1 increased vRNP adsorption to the reaction tube, but also mediated liposome binding of a minor fraction of vRNPs to DOPC/DOPS LUVs. Experiments (B) and (C) were performed in collaboration with N. Jungnick (Humboldt-Universität, Berlin), who kindly provided the recombinant His-tagged Influenza A/FPV M1.

described inefficient binding of purified vRNP/M1 complexes to negatively charged membranes.

Therefore, another experimental procedure was tested for combined flotation of vRNP/M1 with recombinant M1: liposomes were provided first, mixed with recombinant M1 and incubated for 15 min on ice (coating). Subsequently, vRNPs were added and incubation was continued for another 15 min on ice. It was found that incubation of M1 with liposomes prior to addition of vRNPs was favorable for membrane binding of M1 and vRNPs (Fig. 12D). This procedure was therefore chosen for flotation analysis of vRNP/M1 in combination with recombinant M1. Representative results are shown in Fig. 12B (upper panel). This experiment clearly reproduced the results obtained by flotation of purified vRNP/M1 (Fig. 12A) indicating M1-mediated association of vRNPs to negatively charged liposomes. However, a substantial improvement of protein detection and membrane association was not achieved. On the contrary, the total amount of detectable protein appeared to be reduced. Notably, the more recombinant M1 was added, the less protein was detectable suggesting protein precipitation. Best results were obtained with 0.5 μM recombinant M1 as presented in Fig. 12B. For negatively charged liposomes made of DOPC/DOPS/DOPE or brain lipid extract, the viral M1 as well as the slightly larger His-tagged recombinant M1 associated with the liposome-containing fractions, whereas in the absence of liposomes or in the presence of uncharged liposomes, M1 remained in the bottom fraction. In the latter case, the detection of M1 was weak. For NP, the signals showed a clear correlation with the behaviour of M1. A prominent fraction of vRNPs associated with the liposome fractions of the negatively charged LUV species together with M1, and like for M1, membrane association was not observed upon flotation with DOPC or raft lipid LUVs. Unbound vRNPs were instead detected in the pellet fraction of these samples.

Taken together, the above-described results are reproducible and consistent with previous reports on M1-binding to negatively charged lipid membranes [45], but they provide beyond that evidence for the capacity of M1 to mediate association of vRNPs with pure lipid membranes. The effect of M1 on vRNP membrane-binding independently from other viral or cellular factors could be demonstrated in this *in vitro* assay. However, the presence of vRNPs, on the other hand, seemed to interfere with M1 membrane-binding and enhance precipitation. Extensive precipitation appears to be the major limitation of this *in vitro* method for studying vRNP and M1 membrane binding. Due to this experimental artifact, low signal detection should therefore not be interpreted as insignificance or inefficiency of the observed interaction, but as a methodological restriction. However, high affinity binding of vRNP-M1

complexes to negatively charged membranes cannot be concluded either. A quantitative evaluation is not possible. Nevertheless, the data suggests that M1 can simultaneously bind to lipid membranes and vRNP complexes and that vRNPs can acquire membrane association due to the presence of M1.

4.1.3 Probing lipid binding specificity of purified Influenza virus vRNPs and M1 protein with phosphoinositides

Major lipid constituents of cellular membranes were included in the membrane binding studies of vRNPs and M1 by flotation assay (section 4.1.2) for probing characteristic features of membranes that can serve for protein recognition, e.g. electrostatic properties, fluidity, lipid packing and lipid headgroups. Cellular membranes consist, however, of hundreds of different lipid species, some of which are only marginally present and serve as regulatory factors in cell physiology and in signaling pathways. An important group herein are the phosphoinositides, reversibly phosphorylated forms of phosphatidylinositol (PtdIns) carrying phosphate groups at position 3, 4 and/or 5 of the inositol ring. Besides functions in signaling processes, they act as constitutive signals for regulation of membrane trafficking, cytoskeleton remodeling, membrane permeability and definition of organelle identity [477], which makes them an attractive target for viral proteins to exploit or interfere with cellular machinery.
Commercially available PIP-strips, lipid-spotted membranes, offer the possibility to test specific recognition of phosphoinositides by purified vRNP/M1 preparations from Influenza A/X-31 virus. Besides the seven phosphoinositide species also other lipid species are presented for comparison (Fig. 13B).

vRNP/M1 were purified as described in (4.1.1), and the protein content of the sample was verified by SDS-PAGE (Fig. 13A). The preparation was then incubated with the PIP-strip membrane and analyzed by immunodetection with anti-M1 and anti-NP antibodies (Fig. 13B and D). The results were reproduced in two independent experiments.
For M1, the strongest binding and most prominent signal was detected with PtdIns(4)P. This interaction seems to represent a highly specific recognition as M1 displayed a clear preference for PtdIns(4)P compared to the very closely related PtdIns(3)P and PtdIns(5)P. In this context, electrostatic interactions seem to play a minor role considering that the more negatively charged bis- and trisphosphates could not recruit M1 more efficiently than PtdIns(4)P. M1 was found to associate to a minor degree with the other six phosphoinositides and phosphatidic acid. A very faint signal was further detected for PS. In a control experiment, it was ruled out that the signals were caused by unspecific antibody binding (Fig. 13C).

This result obtained for purified M1 from Influenza A/X-31 virus in the presence of vRNPs is very similar although not identical with PIP-strip analysis of M1 that was recombinantly generated and contained an N-terminal His-tag as described in [445]. However, both results agree in the central finding that M1 specifically and most strongly bound to PtdIns(4)P.

When turning to the other lipid species presented on the PIP-strip which displayed lower or no M1 signal, it was remarkable that a pronounced association of M1 with PS could not be observed (Fig. 13B), even though the presence of PS clearly induced binding of M1 to liposomes in flotation analyses (Fig. 12B). This might be due to differential organization and exposure of the lipids in both systems. In liposomes, the lipid molecules form bilayers with a certain fluidity, whereas the organization of lipids on the PIP-strip is unknown except for the fact that the molecules have to be stably anchored to the support membrane. It is possible that either the PS headgroups are not properly exposed on the PIP-strip for M1 association or that the hydrophobic part of the lipid bilayer with flexible fatty acid chains plays an essential role for M1 association with PS-containing liposomes. The latter assumption is supported by early work on M1 membrane association suggesting that M1 partially inserts into liposomal bilayers [43,46,47,48] or into cellular membranes [50], and by later studies showing a major electrostatic component of M1 membrane interactions, but not excluding a possible initial binding by electrostatic interactions that proceeds to a tighter association which is no longer purely electrostatic [45]. A contributory role of the hydrophobic lipid moiety for M1 binding is further supported by another observation. On the PIP-strip membrane, M1 was clearly detected to associate with phosphatidic acid but not with lysophosphatidic acid, although the two lipids differ only by the presence of one fatty acid. The headgroup and the charge of the molecules are the same. Differential behavior of M1 might be caused either by distinct exposure of the headgroups or by differences in overall structural organization including the fatty acid moiety. However, it has to be pointed out that the role of the hydrophobic part of a biological membrane for protein binding can hardly be characterized in the context of lipids that were spotted onto a nitrocellulose membrane. Nevertheless, differential M1 binding to phosphatidic acid and lysophosphatidic acid or to PS on PIP strips and to PS in liposomes indicates that - besides specific molecular recognition of the headgroup and simple electrostatic attraction - specific aspects of the lipid bilayer structure (orientation, packing, accessibility of fatty acids) might be crucial for M1 binding.

In the present study, not only M1 but in particular vRNP binding to lipids was addressed. Therefore, simultaneous binding of vRNPs and M1 to PIP-strips was studied by NP

immunodetection (Fig. 13D). vRNPs were however not detected to associate with any of the lipid species presented on the PIP-strip. This result suggests that vRNPs do not specifically recognize phosphoinositide headgroups, neither can they be recruited to these lipid species by M1 mediated binding. The latter is in clear contrast to M1-mediated association of vRNPs to negatively charged liposomes that was observed by flotation analysis (Fig. 11 & Fig. 12). Differences might be due to the different experimental systems that are compared, but also to the different lipid species that are compared. Based on investigations by circular dichroism measurements that were performed in the group of Prof. A. Herrmann [445], M1 undergoes differential conformational changes upon binding to DOPS- or PtdIns(4)P-containing LUVs. These conformational states of M1 might differ by their ability to interact with vRNPs. Differential modes of membrane binding by M1 might correlate with different functions of M1 in the viral replication cycle. For vRNPs, it can be concluded that even though they can be recruited to membranes by the presence of M1, they do not inevitably associate with M1 when the latter is bound to lipids.

To characterize the often discussed multifunctionality of M1 and its consequences, vRNP/M1 should be analyzed with PtdIns(4)P liposomes by flotation assay for comparison with DOPS liposome flotation. However, within this study, assembly is studied with focus on vRNPs and their fate during assembly and budding, leaving this aspect open future work.

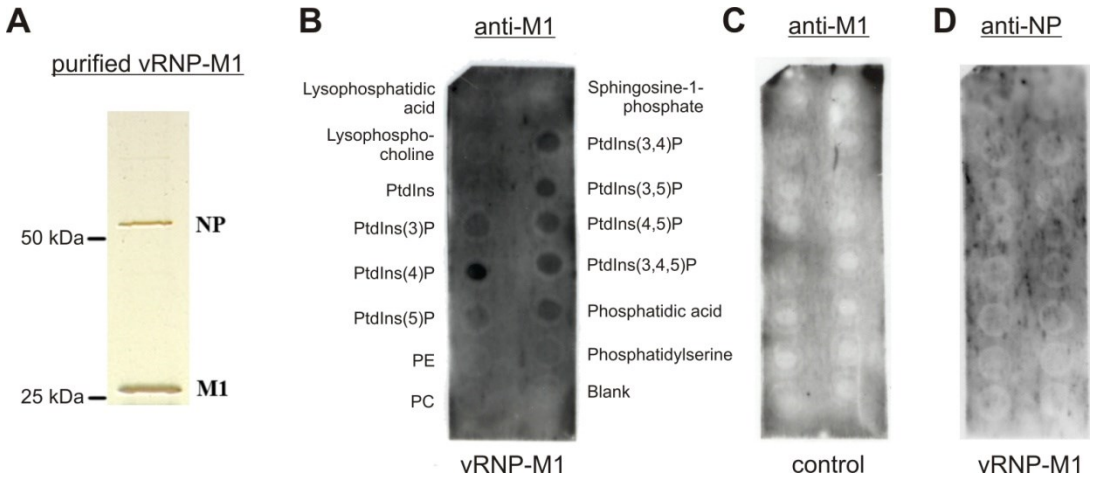

Fig. 13: Analysis of lipid specificity of vRNPs and M1 by PIP-strip immunodetection. (A) vRNP/M1 preparation from detergent-disrupted virus was filtrated with a molecular weight cut-off of 10 kDa and analyzed by SDS-PAGE and silver staining. The same sample was applied in (B) and (D) for lipid binding analysis on a PIP-strip membrane, onto which the indicated lipids are spotted. Incubation of vRNP/M1 with the lipid-spotted membrane was followed by immunodetection with (B) anti-M1 (Virostat) or (D) anti-NP antibodies. (C) In a negative control experiment, vRNP/M1 incubation was omitted, while immunodetection was performed as in (B). PtdIns(3)P: phosphatidylinositol(3)phosphate; PtdIns(4)P: phosphatidylinositol(4)phosphate; PtdIns(5)P: phos-phatidylinositol(5)phosphate; PtdIns(3,4)P_2: phosphatidylinositol-(3,4)bisphosphate; PtdIns(3,5)P_2: phos-phatidylinositol(3,5)bisphosphate; PtdIns(4,5)P_2: phosphatidylinositol(4,5)bisphosphate; PtdIns(3,4,5)P_3: phos-phatidylinositol(3,4,5)tris-phosphate; PC: phosphatidylcholine; PE: phosphatidylethanolamine.

4.2 Generation of tetracysteine-tagged recombinant Influenza viruses for (live-cell) studies of genomic vRNP segments during viral replication

For studying Influenza virus RNPs during viral infection, an experimental system is required that allows live-cell imaging combined with high resolution analysis of newly formed vRNPs during viral assembly. As the processes of viral entry are experimentally more easily accessible (*in vitro* and in cells), they have been studied for many years and in more detail than the mechanisms of virus assembly. Only very recently, the transport pathway of vRNPs from the nucleus to the budding site was identified [280,297,298]. But still, essential aspects remain to be addressed for a comprehensive picture of the processes involving vRNPs during assembly, e.g. the location where the eight segments are assembled into a multisegmental complex, the question if the incorporation of vRNPs into virus particles is a rate-limiting step and if and how vRNPs specifically target the budzone of the preforming viral envelope.
The following part of this work therefore deals with the development of a tool that can permit experimental access to these processes. Recombinant viruses were generated containing a genetically encoded tetracysteine (TC)-tag in the NP sequence to allow fluorescent labeling of vRNPs for live-cell imaging combined with high resolution analysis by correlated electron microscopy. Working with recombinant viruses ensures that the vRNPs assembled during infection are functional and replication competent complexes. Furthermore, there are no interfering effects due to transfection and exogenous viral protein expression. Additionally, specific labeling of the viral genome also in intact virus particles opens up new options for studying vRNPs during viral entry, e.g. fusion-dependent genome release from the endosomes, uptake into the nucleus and targeting of specific subnuclear sites. NP as the major protein component of vRNP complexes was chosen for attachment of the tag, promising efficient labeling and a good signal-to-noise ratio. Furthermore, NP staining of cytosolic progeny vRNPs in infection can be readily distinguished by their granular appearance from free homogenously distributed cytosolic NP.

4.2.1 Construction of Influenza A virus NP with tetracysteine (TC)-tag insertion

The TC-tag is a small, genetically encoded six amino acid sequence (CCPGCC) which can be fused to a protein of interest for site-specific labeling with biarsenical fluorescent ligands in living cells [459]. Biarsenical dyes such as FlAsH or ReAsH are specifically designed to match the spacing between the two pairs of cysteines of the peptide motif to enable the formation of a metal chelate complex with high affinity [457,478]. The *in vitro* dissociation

constants of TC peptides with biarsenical dyes were shown to be in the picomolar range [457]. The formation of four covalent bonds between the two arsenic atoms of the dye and the thiol groups of the peptide leads to a substantial increase of fluorescence intensity of the dye allowing site-specific labeling and reduced background detection [478].

Due to its small size (0.6 kDa), the TC-tag can not only be fused to the protein termini like the considerably larger, intrinsically fluorescent proteins (~27 kDa), but it can more flexibly be inserted within the protein sequence, for instance in loop regions [479]. This makes it a suitable tool to overcome limitations of Influenza reverse genetics that are imposed by the specific architecture of the viral genome. The TC-tag was previously successfully inserted into the NS1 sequence of recombinant Influenza virus [480]. The Influenza virus genome is characterized by terminal packaging sequences in each of the genomic segments that have to be maintained for efficient replication and genome incorporation [100,306]. These packaging signals comprise the non-coding regions as well as parts of the open reading frames at the 3′ and 5′ terminal ends of the vRNA (Fig. 14A). Modifications within these regions, like the insertion of terminal protein tags, can interfere with viral replication at the genomic level and affect genome incorporation even though the protein functions might not be impaired.
Segment 5 vRNA (encoding NP) has recently been reported to play an important role for the genome packaging process [315] and it was further shown that 105 nucleotides (nt) of the 3′ end and 143 nt of the 5′ end of segment 5 vRNA are sufficient for incorporation of a reporter gene into virions [123]. Therefore, for insertion of the TC-tag into the NP sequence, these terminal vRNA regions were left unaltered and only the middle part of the NP open reading frame (corresponding to amino acids 61 to 458) was considered for the introduction of the tag (Fig. 14A).

Various criteria further guided the choice of the positions for TC-tag insertion: Based on the crystal structure of NP (Fig. 14B) [93], surface loops were selected to avoid disruption of secondary structure elements by the helix-breaking residues proline and glycine in the tag sequence and to facilitate the accessibility of the tag for the dye. In the next step, surface loops were excluded to which specific functions had been assigned, like the flexible linker mediating NP oligomerization (aa 429–436), polymerase interacting residues (aa 204, 207 and 208) or the nuclear localization signal (aa 198–216). The selection was further based on the mutational analysis of highly conserved residues performed by Li and coworkers [317]. Conserved amino acid changes in recombinant viruses classified as ‘nonviable’, ‘attenuated’ and ‘little attenuated’ were plotted into the NP structure (Fig. 14B; red, yellow and white

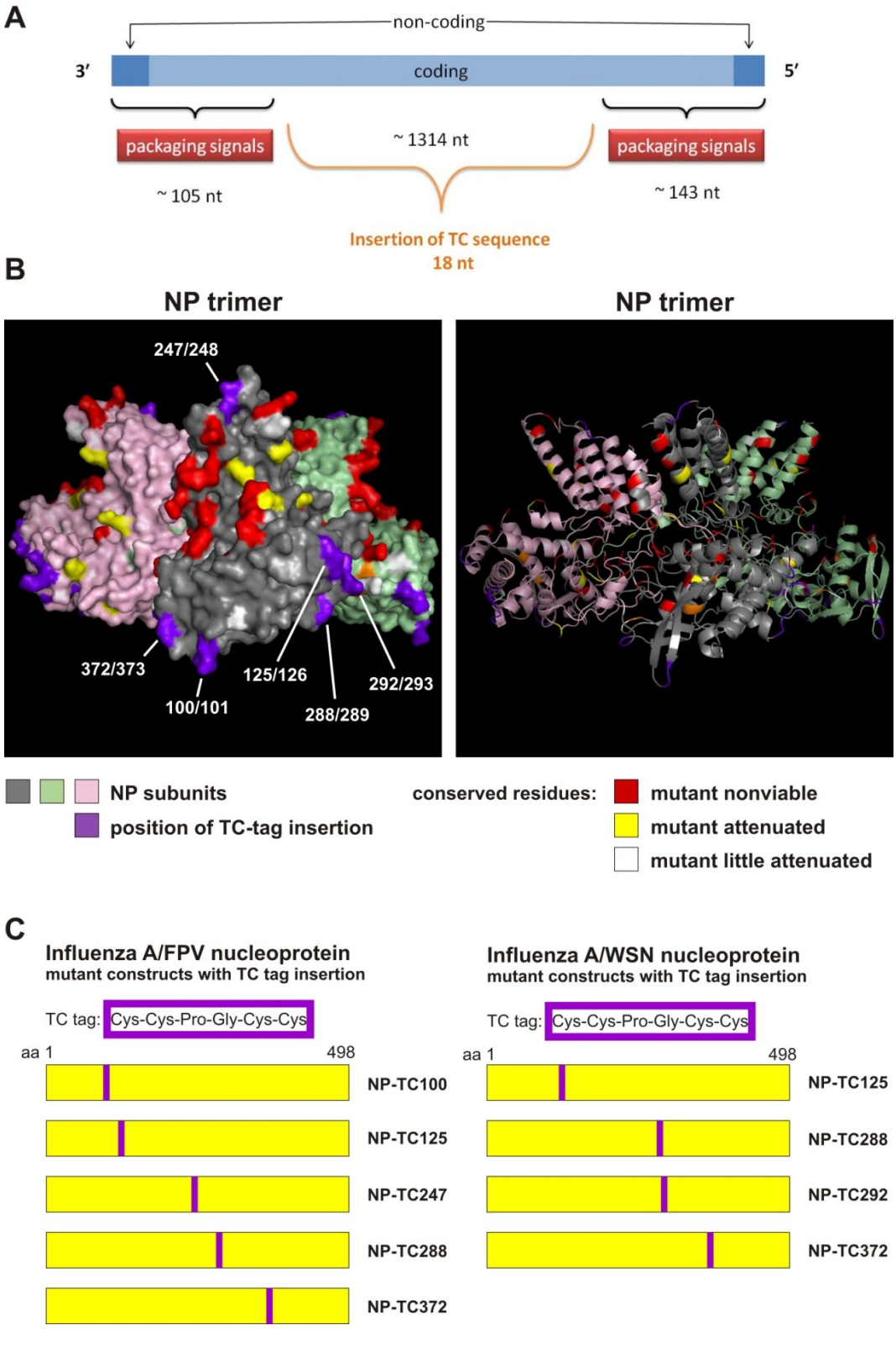

Fig. 14: Design of NP mutants with TC-tag insertion based on structure and sequence information. (A) Schematic representation of Influenza A virus segment 5 vRNA. The non-coding (dark blue) and parts of the coding regions (light blue) at the 3′ and 5′ ends of Influenza vRNA constitute signals that are critical for genome packaging into progeny virions. The size of the packaging signals is mapped according to Ozawa *et al.* [123]. TC-tag insertions were introduced into the middle region of the open reading frame as indicated. (B) Crystal structure of an NP trimer from Influenza A/WSN virus (PDB 2IQH, [93]). The structure was edited with PyMOL. Conserved residues that were characterized by mutational analysis and reverse genetics [317] are highlighted

labels); such loops containing residues that critically affect replication were hence excluded for TC-tag insertion. Furthermore alignment of more than 2500 NP sequences [331] has revealed the presence of a few hypervariable residues in NP. Some of these hypervariable residues (residues 100, 101, 371, 373 and 375) are located in two NP surface loops which are in close proximity in the tertiary structure. Five surface loops were finally chosen for modification by TC-tag insertion, one of them located in the head domain of the NP structure, the other four in the body domain (Fig. 14B; as indicated by TC-tag positions in purple).

To assess the effect of TC-tag insertion on NP expression and subcellular localization, preliminary expression experiments were performed, and efficient biarsenical labeling of each TC-tagged construct was tested before proceeding to recombinant virus generation.

The TC-tag was therefore first introduced into Influenza A/FPV NP at amino acid positions 100/101, 125/126, 247/248, 288/289 or 372/373. Insertion of the six amino acid sequence was performed by two-stage PCR-based mutagenesis of the NP expressing plasmid pNP (Tab. 2) as described in section 3.2.1.5. Resulting NP mutant constructs were designated NP-TC100, NP-TC125, NP-TC247, NP-TC288 and NP-TC372. An overview of all NP constructs with TC-tag insertion is given in Fig. 14C.

Each construct was expressed in MDCK II cells, followed by labeling with the biarsenical dye FlAsH (Fig. 15A). All constructs showed distinct fluorescence signals indicating efficient expression and labeling of the inserted TC-tags. In contrast, control cells expressing wt NP showed only a background FlAsH signals confirming the specificity of FlAsH for the TC-tag. Control cells were further immunostained for NP to verify successful transfection and wt NP expression. Three of the TC-tagged constructs, namely NP-TC125, NP-TC288 and NP-TC372, showed a predominantly nuclear localization of the FlAsH signal and a coarsely structured nuclear distribution similar to typical NP wt expression (compare with immunofluorescence of NP wt). NP-TC100, in contrast, showed a clearly distinct, granular and exclusively cytoplasmic staining indicating misfolding or incorrect targeting of the

(red, yellow, white). Surface loops with hypervariable residues (R100, D101, V371, A373, D375; [71]) were chosen for TC-tag insertion. The sites finally selected for introduction of the TC-tag (purple) are indicated by the positions of the two flanking amino acids. (**C**) Overview of the NP mutant constructs with TC-tag insertion generated within this study. (Left) TC-tag insertion into Influenza A /FPV virus NP was performed by two-stage PCR-based site-directed mutagenesis of pNP expression vector. (Right) TC-tag insertion into Influenza A /WSN virus NP was performed by two-stage PCR-based site-directed mutagenesis of plasmid pHW185-NP for reverse genetics. The designation of each construct indicates the amino acid position after which the TC-tag was inserted.

construct. For NP-TC247, the subcellular localization was less clear. Therefore, NP-TC247-expressing cells were further subjected to immunofluorescence (IF) staining (Fig. 15B), which revealed diverse phenotypes of NP-TC247 expression that clearly differed from NP wt expression. Due to the (partial) failure to localize to the nucleus, both mutants NP-TC100 and NP-TC247 were considered as unsuitable for the generation of recombinant viruses and were hence discarded.

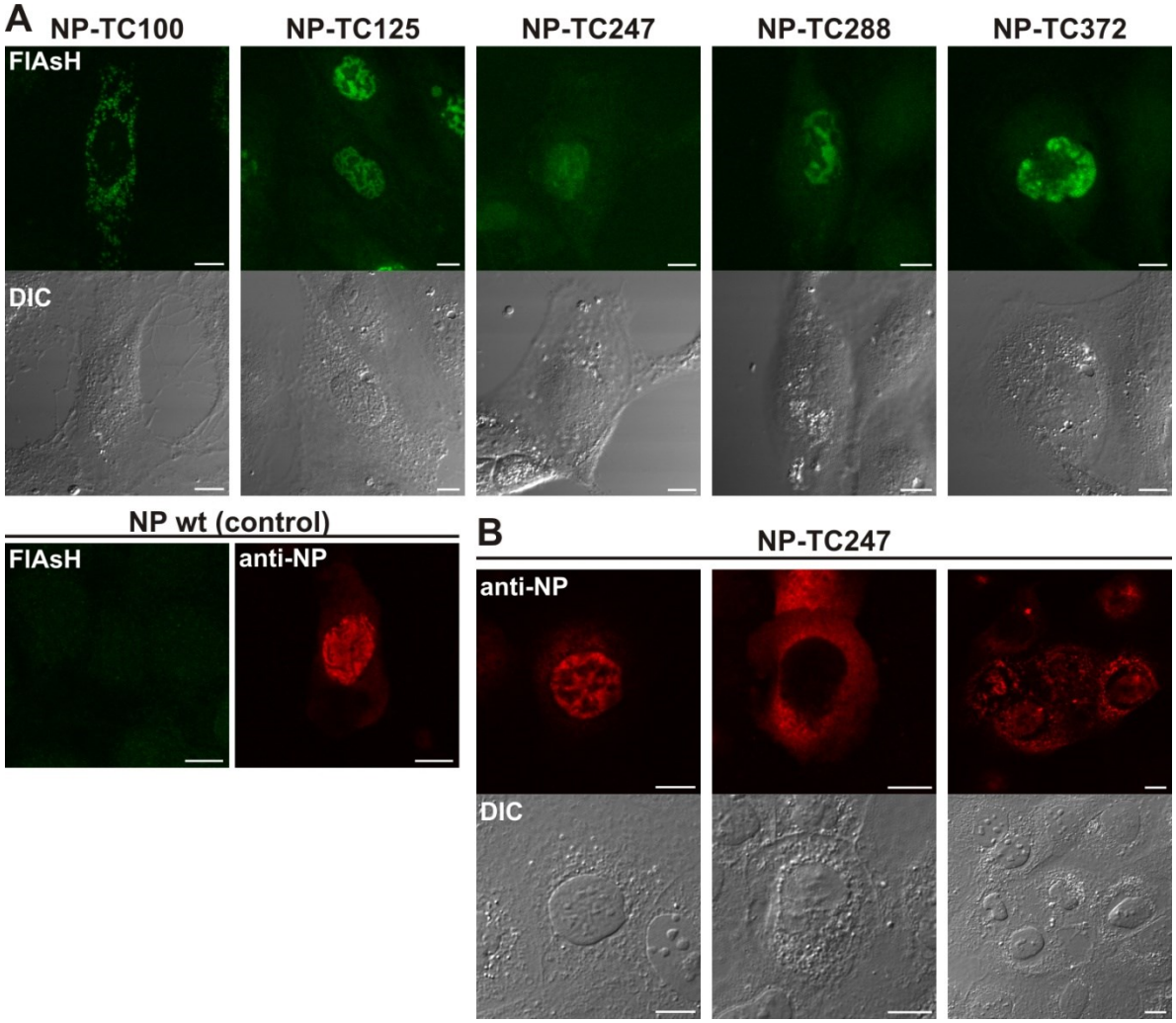

Fig. 15: Expression and FlAsH labeling of TC-tagged NP mutants from Influenza A/FPV virus in MDCK II cells. (A) Cells were transfected with NP mutant constructs NP-TC100, NP-TC125, NP-TC247, NP-TC288 or NP-TC372. For comparison, cells were also transfected with NP wt. FlAsH labeling (green) was performed at 24 h p.t. The cells were then fixed and studied by confocal fluorescence microscopy. NP wt transfected cells were further immunostained with anti-NP and Alexa568-anti-mouse antibodies (red). FlAsH did not unspecifically label NP wt. Representative pictures are displayed. Constructs NP-TC125, NP-TC288 and NP-TC372 displayed the expected characteristic nuclear accumulation like NP wt. Due to diffuse and non-uniform FlAsH signal of NP-TC247, this construct was additionally analyzed by IF (B). (B) NP-TC247 was expressed and the cells were fixed at 24 h p.t. Immunostaining was performed using anti-NP and Alexa568-anti-mouse antibodies. NP-TC247 displayed various types of subcellular distribution. Scale bar, 10 µm.

For the generation of recombinant Influenza virus (strain A/WSN/1933), TC-tag insertions were then introduced into plasmid pHW185-NP (Tab. 5), which comprises segment 5 cDNA and is part of the eight plasmid system for reverse genetics of Influenza A/WSN virus (3.2.4.3). The tag was introduced between residues 125/126, 288/289 or 372/373 of the NP sequence analogously to the above-described constructs, and additionally at position 292/293, yielding plasmids pHW185-NP-TC125, pHW185-NP-TC288, pHW185-NP-TC292 and pHW185-NP-TC372. Insertion was again performed by two-stage PCR-based mutagenesis (3.2.1.5).

Protein expression of the TC-tagged constructs was then analyzed in MDCK II cells by transfection followed by immunofluorescence for NP (Fig. 16). As before for FPV NP, the three constructs NP-TC125, NP-TC288 and NP-TC372 of the WSN virus strain localized predominantly to the cell nucleus similarly to NP wt. The strongest tendency for cytoplasmic accumulation was detected for NP-TC292, which sometimes displayed equal distribution between nucleus and cytoplasm. The NP signals indicated protein stability and expression close to NP wt levels.

All four TC-tagged NP variants were chosen for reverse genetics experiments for the generation of recombinant virus mutants.

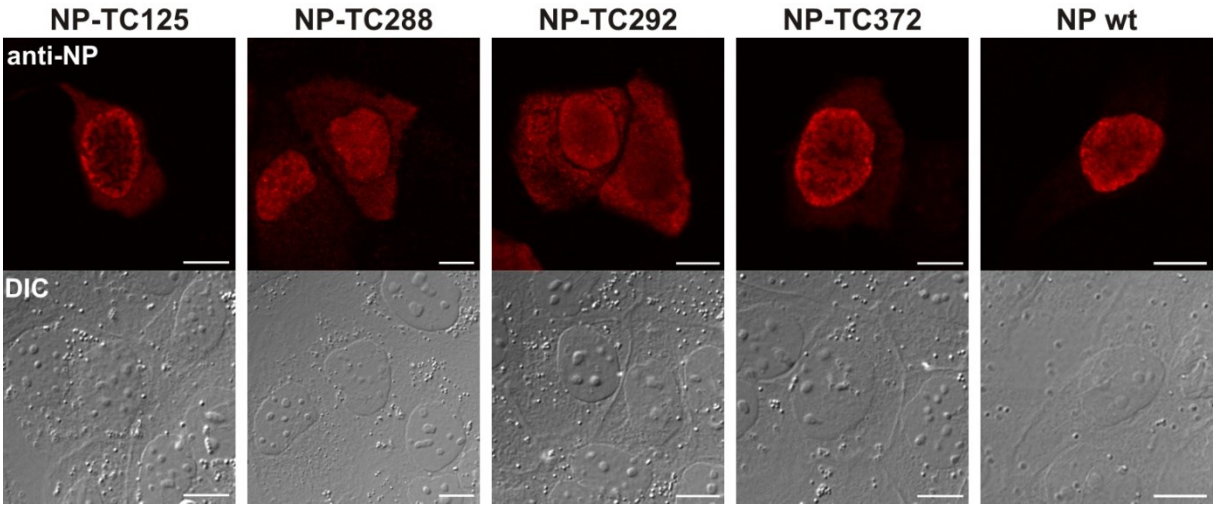

Fig. 16: Expression of TC-tagged NP mutants (Influenza A/WSN virus) in MDCK II cells. Cells were transfected with pHW185-NP-based plasmids expressing WSN NP-TC125, NP-TC288, NP-TC292, NP-TC372 or NP wt. At 23 h p.t. cells were immunostained with anti-NP and Alexa568-anti-mouse antibodies and analyzed by confocal fluorescence microscopy. All constructs displayed nuclear localization. NP-TC288 and NP-TC292 had a stronger tendency to localize in the cytoplasm than the other constructs. Scale bar, 10 µm.

4.2.2 Generation of recombinant Influenza A/WSN virus mutants carrying segment 5 vRNA with TC-tag insertion

Generation of recombinant Influenza A/WSN virus was performed as described in 3.2.4.3. First, 293T cells were transfected with the eight-plasmid system for reverse genetics [451]. Upon successful transfection of a cell with all eight plasmids, viral proteins and the eight vRNA segments are synthesized, and infectious virus particles can be assembled and released (Fig. 17). For the generation of recombinant mutant virus with TC-tag insertion in segment 5 vRNA, plasmid pHW185-NP (wild-type) was replaced by the modified plasmids pHW185-NP-TC125, pHW185-NP-TC288, pHW185-NP-TC292 or pHW185-NP-TC372 (Tab. 5). These plasmids are described in 4.2.1 and were tested for efficient NP expression (Fig. 16).

Recombinant virus mutants encoding NP-TC125, NP-TC292 or NP-TC372 failed formation

When pHW185-NP (encoding the wild-type sequence of segment 5) was used, production of recombinant WSN wt virus was succesfull in five different control experiments. These virus preparations showed a considerable cytopathic effect (CPE) on MDCK II cells and were clearly quantifiable in plaque assays. They further showed typical NP expression in immunofluorescence analysis of infected MDCK II cells at 8, 17, 21 and 41 h p.i. (data not shown).

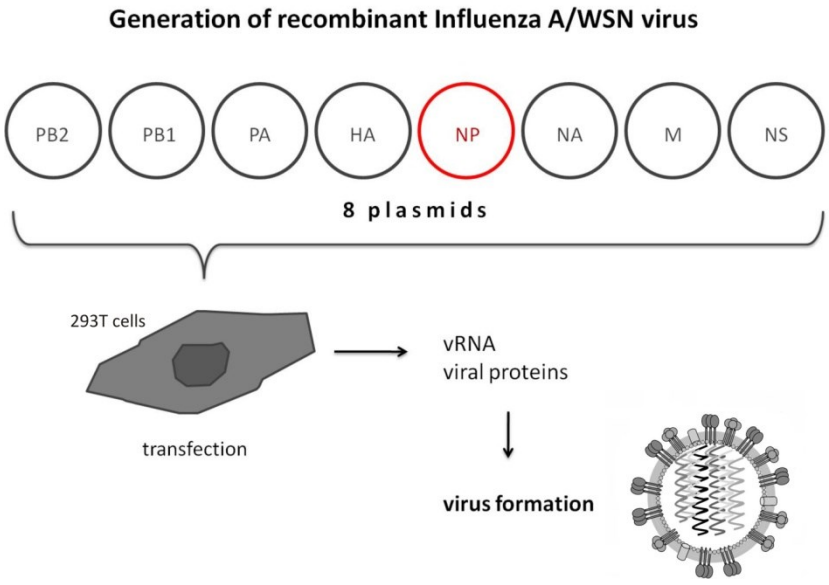

Fig. 17: Reverese genetics. Schematic presentation of the generation of recombinant Influenza A/WSN virus. 293T cells were transfected with eight plasmids encoding viral mRNA and full-length viral RNA under control of human Pol II and Pol I promoters. For generation of mutant viruses with TC-tagged NP, the wt plasmid pHW185-NP was replaced by a plasmid carrying the modified NP gene segment. Production of all eight viral proteins and vRNAs in transfected cells led to formation of virus particles.

In contrast, recombinant virus could not be recovered when using pHW185-NP-TC125, pHW185-NP-TC292 or pHW185-NP-TC372 in four independent experiments that were conducted in parallel to WSN wt virus generation. When infecting MDCK II cells with the initial supernatant from transfected 293T cells for virus propagation, a CPE was not observed, not even after 4 days. The failure to produce mutant virus with NP-TC125, NP-TC292 or NP-TC372 was confirmed by plaque assay and immunofluorescence analysis. Neither plaques nor NP expression (at 17 or 41 h p.i.) were detectable upon infection of MDCK II cells with the supernatant from the first passage. Notably, the result for generation of recombinant virus using plasmid pHW185-NP-TC288 was different (see Fig. 18).

Abortive replication of WSN TC288 virus

A schematic overview of the characterization of WSN TC288 virus is shown in Fig. 18. A considerable CPE of recombinant WSN TC288 virus was observed during the first passage on MDCK II cells. However, infectious virus particles could not be detected in the supernatant of the first passage, neither by plaque assay nor by immunofluorescence analysis of infected MDCK II cells at 24 or 41 h p.i. This finding was consistent with the fact that a CPE was not observable anymore during the second passage on MDCK II cells. As the supernatant initially generated from transfected 293T cells had caused a CPE on MDCK II cells, the same suspension was analyzed by infection of MDCK II cells and subsequent immunostaining for NP. Indeed, NP-TC288 expression clearly demonstrated successful infection of the cells and viral protein synthesis by newly generated recombinant virus particles (Fig. 18, top right image). However, the same virus preparation was not able to form plaques (Fig. 18, top left) indicating failed multicycle replication as plaques require several rounds of replication to form.

These findings indicate that virus particles were efficiently produced from plasmid DNA in transfected cells, but that the virus was not able to undergo a complete round of replication upon infection of cells. Therefore, the TC-tag apparently affected processes of viral replication that were bypassed in transfected cells, i.e. the RNA synthesis. The failure to replicate the viral genome might explain the complete abrogation of infectious particle production in the first round of replication.

Comparison of MDCK II cells infected with WSN wt and WSN TC288 virus by immunofluorescence analysis at 24, 48 and 72 h p.i. (Fig. 19) showed that NP wt accumulated as punctate signals in the cytoplasm around 24 h p.i., whereas NP-TC288 did not appear as granular cytoplasmic signal at any of the observed time points, but remained in the nucleus

instead (Fig. 19e, f). Appearance of punctate cytoplasmic NP late in infection reflects the nuclear export of newly formed progeny vRNPs [297]; therefore, the results suggest that WSN TC288 virus is defective in vRNP formation or in vRNP nuclear export. As vRNP nuclear export must have occured during initial formation of WSN TC288 virus, this result supports that the replication defect has to be on the level vRNP formation.

As judged by the immunofluorescence signal of NP (Fig. 19), infection kinetics of the WSN TC288 virus appeared to be slower than the kinetics of the wt virus. WSN wt virus showed highest NP expression levels at 24 h p.i. and a considerable CPE with a decreasing number of infected cells 48 h p.i., whereas WSN TC288 virus showed strongest NP expression only at 48 h p.i. and a decreasing number of infected cells and expression levels at 72 h p.i. In conclusion, this experiment shows that the time points chosen for harvesting and for characterization of WSN TC288 virus during this study were appropriate to obtain significant data.

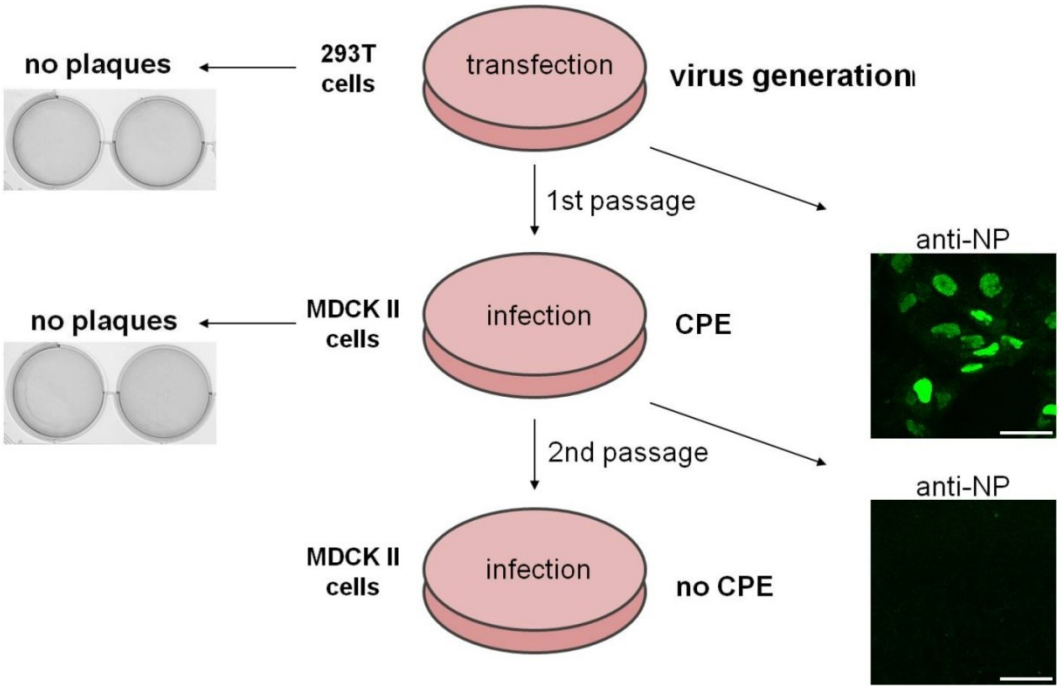

Fig. 18: Analysis of recombinantly generated Influenza A/WSN mutant virus TC288. The virus was generated by reverese genetics, i.e. transfection of 293T cells with eight plasmids encoding the viral proteins and vRNAs. The virus released into the supernatant was used for infection of MDCK II cells (1st passage) causing a clear cytopathic effect (CPE). This is consistent with IF analysis of infected MDCK II cells at 24 h p.i. with anti-NP-FITC antibody showing a positive NP expression signal in the nuclei of infected cells. The 2nd passage on MDCK II cells, however, did produce neither CPE nor a positive signal for NP expression by IF indicating that infectious virus was not produced during the 1st passage. Consistently, WSN TC288 mutant virus was not able to form plaques (within 4 days). Scale bar (IF images), 50 µm.

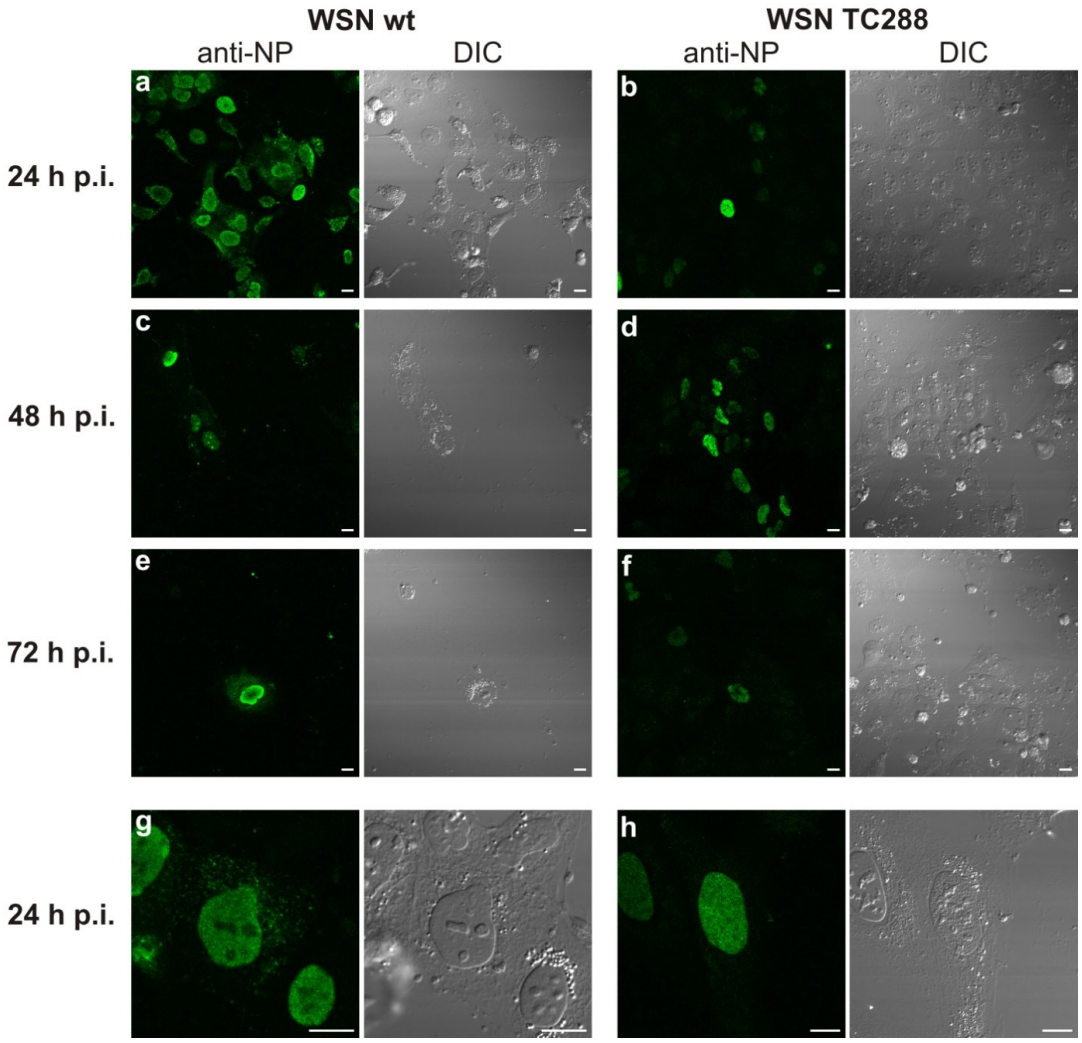

Fig. 19: Comparison of Influenza A/WSN wt and TC288 mutant virus infection in MDCK II cells. Infection was performed with newly generated recombinant WSN TC288 mutant virus (293T cell supernatant, 330 µl) and WSN wt virus (MOI 1). Cells were fixed at (a, b) 24 h, (c, d) 48 h and (e, f) 72 h p.i., immunostained with anti-NP-FITC and analyzed by confocal fluorescence microscopy. The NP expression level and the CPE increased more rapidly in WSN wt virus infection than in mutant virus infection. The highest number of infected cells and the highest NP expression levels were detected at 24 h p.i. for WSN wt virus infection and at 48 h p.i. for WSN TC288 virus infection. (g, h) At 24 h p.i., granular cytoplasmic NP signals were observed in WSN wt virus infection (indicating newly formed vRNPs which underwent nuclear export) (g). Punctate cytoplasmic NP signals were not observed at any time in WSN TC288 mutant virus-infected cells. Scale bar, 10 µm.

Rescue of virus mutants with TC-tag insertion by supplementation with wt NP

In a second approach to rescue a recombinant mutant virus encoding NP-TC125, NP-TC288, NP-TC292 or NP-TC372, a mixture of WSN wt and WSN mutant virus was produced to support viral replication of the TC-tagged virus by the presence of wt NP. Therefore, when generating recombinant virus by transfection of 293T cells, the mutated plasmids pHW185-NP-TC125, pHW185-NP-TC288, pHW185-NP-TC292 or pHW185-NP-TC372 were mixed with plasmid pHW185-NP encoding the wt segment 5 sequence (ratio 2:1). These recombinant, mixed virus productions were propagated on MDCK II cells and produced a

considerable CPE during the first passage. The CPE of WSN TC288/wt virus was consistently lower than the CPE of the other virus preparations suggesting an inhibitory effect of NP-TC288 on viral replication. Virus preparations were then analyzed by infection of MDCK II cells (Fig. 20). Infection of 100 % of the cells ensured multiple infections of most cells and coexpression of wt and TC-tagged NP. At 21 h p.i., the cells were stained with FlAsH followed by immunostaining of NP for comparative analysis of both signals.

All four different virus preparations supposed to contain mutant virus and wt virus genomes successfully infected MDCK II cells and apparently induced expression of both wt and TC-tagged NP: NP expression could be detected by immunofluorescence as well as TC-tag-specific FlAsH signal (Fig. 20 b–e). WSN wt virus-infected control cells displayed only NP immunofluorescence, but lacked the FlAsH signal confirming the specificity of the TC-tag for FlAsH labeling (Fig. 20a). Hence, recombinant WSN virus was successfully generated carrying modified segment 5 vRNA with TC-tag insertion that allowed TC-tagged NP expression in infected cells.

However, a remarkable disparity of NP localization was observed when comparing NP immunodetection and TC-tag-specific FlAsH labeling, suggesting differential behavior of wt and TC-tagged NP in infected cells of each sample. In WSN TC372/wt infected cells (Fig. 20e), a considerable fraction of NP accumulated as punctate structures in the cytoplasm as shown by immunofluorescence, whereas FlAsH-labeled NP remained almost exclusively in the cell nucleus. This observation suggests that NP-TC372 failed to be exported from the nucleus as part of intact vRNP complexes and that cytoplasmic vRNPs were constituted primarily of wt NP. In WSN TC288/wt virus-infected cells (Fig. 20c) FlAsH and immunofluorescence signals were mostly overlapping, but in this case cytoplasmic NP was hardly detected. This indicates an impairment of vRNP formation or vRNP nuclear export by the presence of NP-TC288 similarly as in cells infected with WSN TC288 (Fig. 19). In both WSN TC292/wt and WSN TC125/wt virus-infected cells, unusual broad patches of FlAsH signal were detected in the cytoplasm that were typically not observed for wt NP in infection (Fig. 20b, d). In addition, characteristic punctate NP signals resembling cytoplasmic vRNPs in infection were observed; they were however largely devoid of FlAsH staining.

Even though all four modified segment 5 vRNAs with TC-tag insertion could be efficiently replicated in the presence of wt NP and TC-tagged NP was expressed in infected cells, FlAsH labeling of cytoplasmic NP structures to study transport and assembly of newly formed vRNPs was not achieved. NP-TC125, NP-TC292 and NP-TC372 might be unable to compete with wt NP for incorporation into vRNP complexes and/or may interfere with vRNP

formation or transport when once incorporated. NP-TC288 instead might generally interfere with vRNP formation, as indicated above.

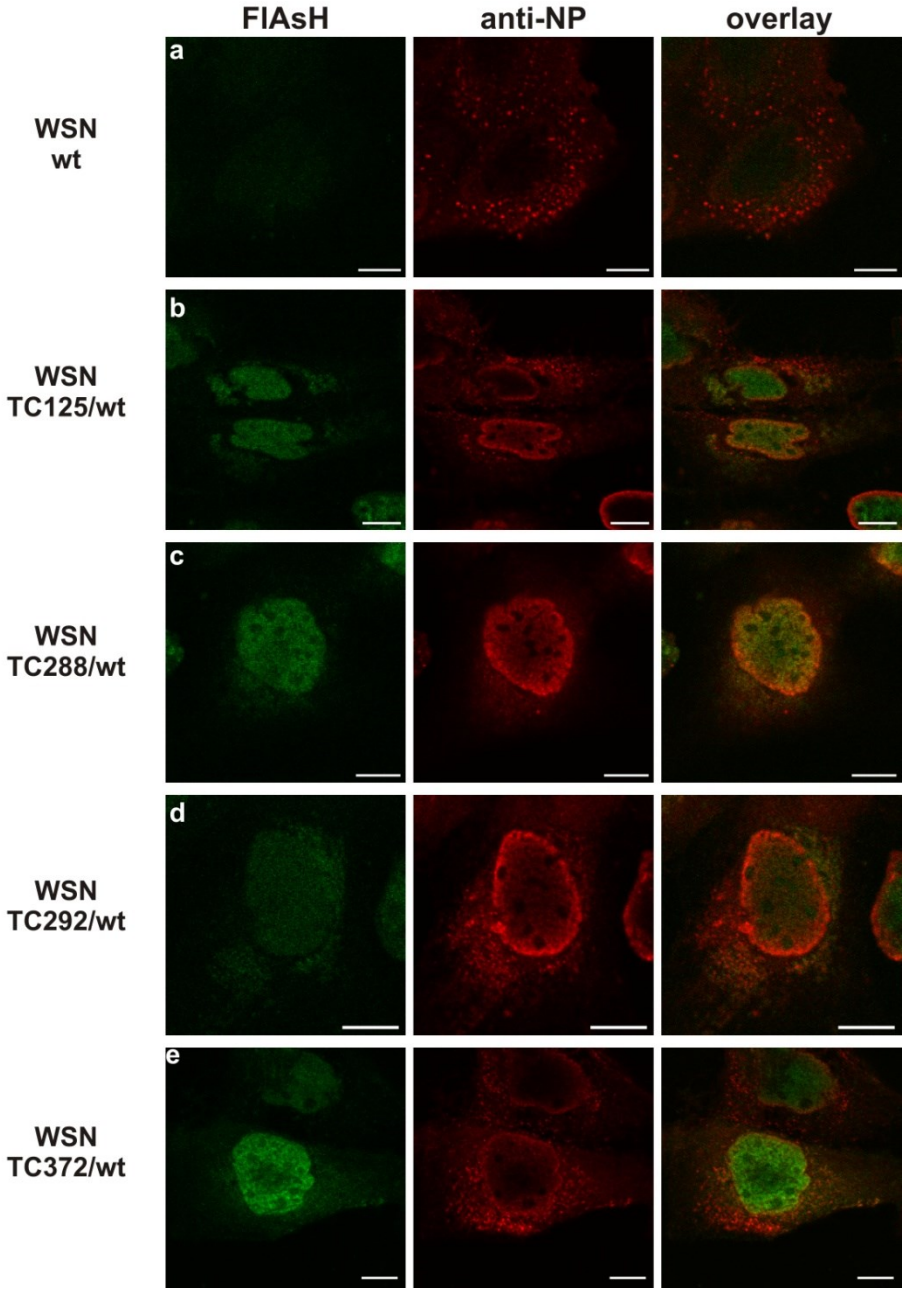

Fig. 20: Rescue of recombinant Influenza A/WSN mutant viruses carrying NP gene segments with TC-tag insertion by mixed formation with WSN wt virus. Comparison of FlAsH signals with NP immunofluorescence. Recombinant viruses with mutated segment 5 vRNA with TC-tag insertion (NP-TC125, NP-TC288, NP-TC292, NP-TC372) were generated by reverse genetics by cotransfection of pHW185-NP wt and pHW185-NP-TC mutant plasmids (ratio 1:2). After the 1st passage, the virus mixture was analyzed by infection of MDCK II cells with subsequent FlAsH labeling and IF staining (anti-NP/Alexa568-anti-mouse) at 21 h p.i. Representative confocal fluorescence microscopy images of the cells are presented. (a) WSN wt virus-infected cells did not show unspecific FlAsH staining, and NP was detected predominantly cytoplasmic. (b–e) All samples with mixed infections of the indicated TC-tagged mutant virus with wt virus were positive for TC-tagged NP expression as shown by FlAsH signals. Granular, cytosolic IF signals of NP did not correlate with the FlAsH signal. WSN TC288/wt virus infections displayed very little cytosolic NP signal compared to other mixed or wt virus infections (c). Particularly low FlAsH signals were observed for WSN TC292/wt infected cells (d). Scale bar, 10 µm.

4.2.3 Generation of recombinant Influenza A/WSN virus mutants encoding N-terminally TC-tagged NP

As TC-tag insertion *into* the highly conserved NP sequence failed to produce infectious recombinant viruses (4.2.2), a segment 5 vRNA was constructed encoding NP with an *N-terminal* TC-tag.

To circumvent the disruption of the segment 5 packaging signal by an N-terminal insertion, the 3′ terminal packaging sequence was restored by duplicating part of the packaging signal according to Ozawa *et al.* [123] (Fig. 21). As the first 60 nucleotides of the NP ORF have been shown to be sufficient for incorporation of the segment into progeny virus particles, the corresponding vRNA nucleotides 46–105 were duplicated and the three ATG codons within the first duplicate were removed by point mutations. The TC-tag sequence, preceded by an ATG start codon, was introduced right before the unmodified complete NP ORF. Thereby, the terminal packaging sequence was left largely unaltered, except for four point mutations, and the functional ORF now including the N-terminal TC-tag insertion was shifted behind the vRNA packaging signal.

Technically, the vRNA encoding plasmid pHW185-NP for reverse genetics was sequentially mutated by site-directed PCR-based mutagenesis (3.2.1.4) using primer pairs {30, 31} and {32, 33} (Tab. 6) for elimination of the first three ATG codons of the vRNA 3′ end yielding pHW185-NP-3ATG (Tab. 5). Subsequently, two PCR products were generated (3.2.1.1) for insertion into pHW2000, which is the basic cloning vector of the eight-plasmid system for reverse genetics [451]. One PCR insert was amplified from the modified plasmid pHW185-NP-3ATG encompassing the non-coding 3′ end of the vRNA, the first 60 nt of the NP ORF lacking all ATG codons and part of an additional Kozak consensus sequence (using primers {34}, {35}; Tab. 6). The other PCR fragment was amplified from the unmodified plasmid pHW185-NP and comprised the other half of the Kozak consensus sequence and the TC-tag sequence followed by the complete NP ORF and the non-coding 5′ end of the vRNA. Depending on the TC-tag sequence that was introduced, this PCR product was termed “Kozak-nTC-NP-vRNA” or “Kozak-FLN-TC-MEP-NP-vRNA” (generated with primer pairs {36, 37} or {38, 37}, respectively; Tab. 6). The two PCR fragments were then ligated with each other and with plasmid pHW2000 using restriction sites *Esp*3I and *Bsa*I (3.2.1.3) finally yielding the plasmids pHW185-NP60mut-nTC-NP or pHW185-NP60mut-FLN-TC-NP for reverse genetics (Tab. 5). The two plasmid differ only by the specific sequence of the TC-tag depending on the use of “Kozak-nTC-NP-vRNA” or “Kozak-FLN-TC-MEP-NP-vRNA” for ligation.

Two different N-terminal TC-tag sequences were used: The first TC-tag termed “nTC”-tag (amino acid sequence MAGGCCPGCC) consisted of the essential TC sequence (CCPGCC) and another four amino acids that were added for stabilization of the N-terminus. The other TC-tag termed “FLN” (amino acid sequence MFLNCCPGCCMEP) comprised the essential six amino acid TC-tag (underlined) flanked by three amino acids on both sides for improved fluorescence signals. Higher affinity and increased fluorescence quantum yield has been reported for the FLN sequence [481].

Generation of recombinant Influenza A /WSN mutant virus encoding N-terminally TC-tagged NP was performed as described in 3.2.4.3. pHW185-NP encoding wt vRNA was therefore replaced by pHW185-NP60mut-nTC-NP or pHW185-NP60mut-FLN-TC-NP for the production of WSN nTC and WSN FLN mutant virus, respectively. During the first passage on MDCK II cells, a clear CPE was observed for both mutants. Viruses were further propagated for sequencing of segment 5 vRNA (3.2.4.3). The sequencing results confirmed successful generation of WSN nTC and WSN FLN mutant viruses encoding the correct vRNA

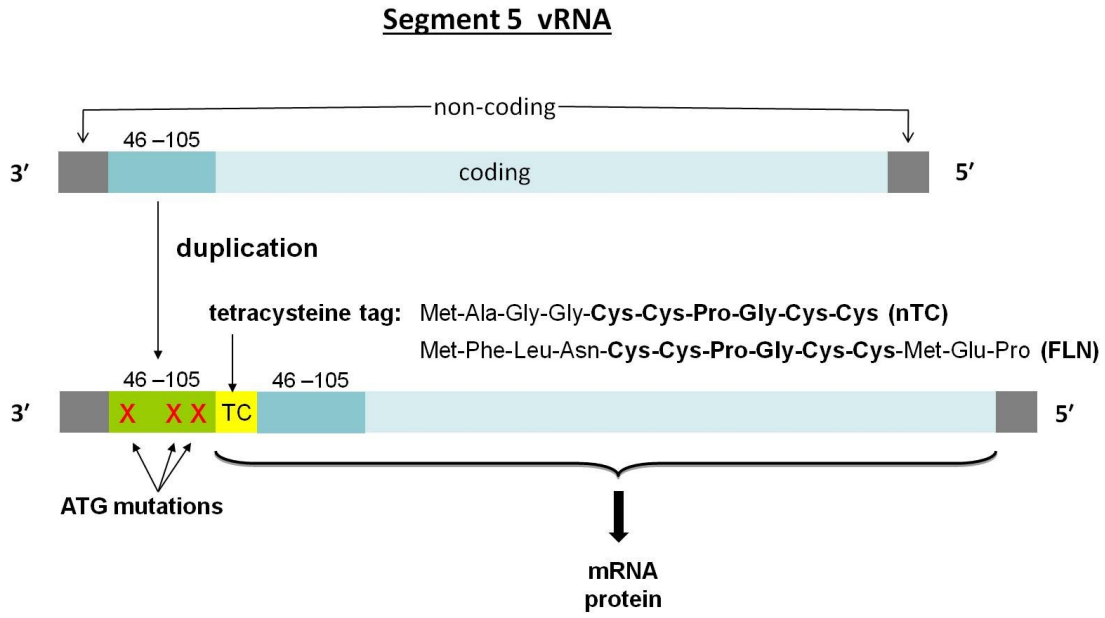

Fig. 21: Generation of segment 5 vRNA encoding N-terminally TC-tagged NP for reverse genetics. Illustration adapted from Ozawa *et al.* [123]. The 3′ terminal packaging signal of segments 5 vRNA (46–105) consists of the non-coding sequence (grey) and part of the coding sequence (mid blue). The first 60 bases of the coding sequence were duplicated (green) and three ATG start codons were replaced by point mutations [123]. The TC-tag was introduced in front of the NP coding sequence, starting with an ATG codon and indicating the beginning of the functional ORF. Two types of TC-tag were designed: the “nTC” terminal tag consisting of four N-terminal stabilizing amino acids (MAGG) followed by the six amino acids of the TC-tag (CCPGCC), and the “FLN” terminal tag containing the TC sequence (CCPGCC) flanked by the amino acid sequences (MFLN) and (MEP) for improved fluorescence signals.

sequences as designed. Modifications of segment 5 were apparently maintained during several replication cycles and neither NP function nor vRNA packaging was fundamentally affected.
For following experiments, WSN nTC and WSN FLN virus were preferentially utilized from the first passage, as viral titers tended to decrease over several passages, in particular for WSN FLN virus (see also 4.2.5). When WSN FLN virus was subjected to successive passaging by infecting cells always with the same fraction of the supernatant from the preceding passage, the titer rapidly decreased, and after the fourth passage virus could not be detected anymore by NP immunofluorescence analysis (data not shown).

4.2.4 Qualitative and quantitative analysis of biarsenical labeling of N-terminally TC-tagged NP in virus infection

The recombinantly generated viruses WSN nTC and WSN FLN (4.2.3) were first analyzed for the labeling efficiency and specificity of the TC-tagged NP variants during infection.

4.2.4.1 Specificity of biarsenical labeling for nTC-NP and FLN-NP in infection

MDCK II cells were infected with either WSN nTC, WSN FLN or WSN wt virus and stained with the green or red fluorescent biarsenical dyes FlAsH or ReAsH at 20 h p.i. For comparison with NP-specific signals, the cells were subsequently fixed and immunostained for NP with anti-NP-FITC or anti-NP and Alexa568-anti-mouse antibodies, respectively. WSN nTC and WSN FLN virus-infected cells clearly showed efficient expression of TC-tagged NP and efficient labeling with both FlAsH and ReAsH (Fig. 22A, B). In contrast, WSN wt virus-infected cells lacked any NP-specific FlAsH or ReAsH signal, demonstrating that wt NP was not unspecifically labeled by the biarsenical dyes (Fig. 22C); instead FlAsH and ReAsH specifically stained NP with nTC-tag or FLN-tag. Immunofluorescence signals of NP showed that there were no pools of NP in cells infected with WSN nTC or WSN FLN virus that were not stained with the biarsenical dyes (Fig. 22A, B). However, in some of the cells occasional NP-independent nucleolar staining was observed, which was further analyzed and will be set out below in more detail (Fig. 23; not obvious in selection of Fig. 22).
An unspecific, diffuse background signal of the biarsenical dyes was generally detected in infected and uninfected MDCK II cells. The signal-to-noise ratio was better in ReAsH- than in FlAsH-labeled cells. It was noted though that the background staining was higher in samples of wt virus infection (Fig. 22C) than in viral infections with TC-tag expression (Fig. 22A, B). This is likely due to a higher free concentration of the dye in wt virus-infected cells, where the dye does not become partially bound by the TC-tag. The reduction of the free dye

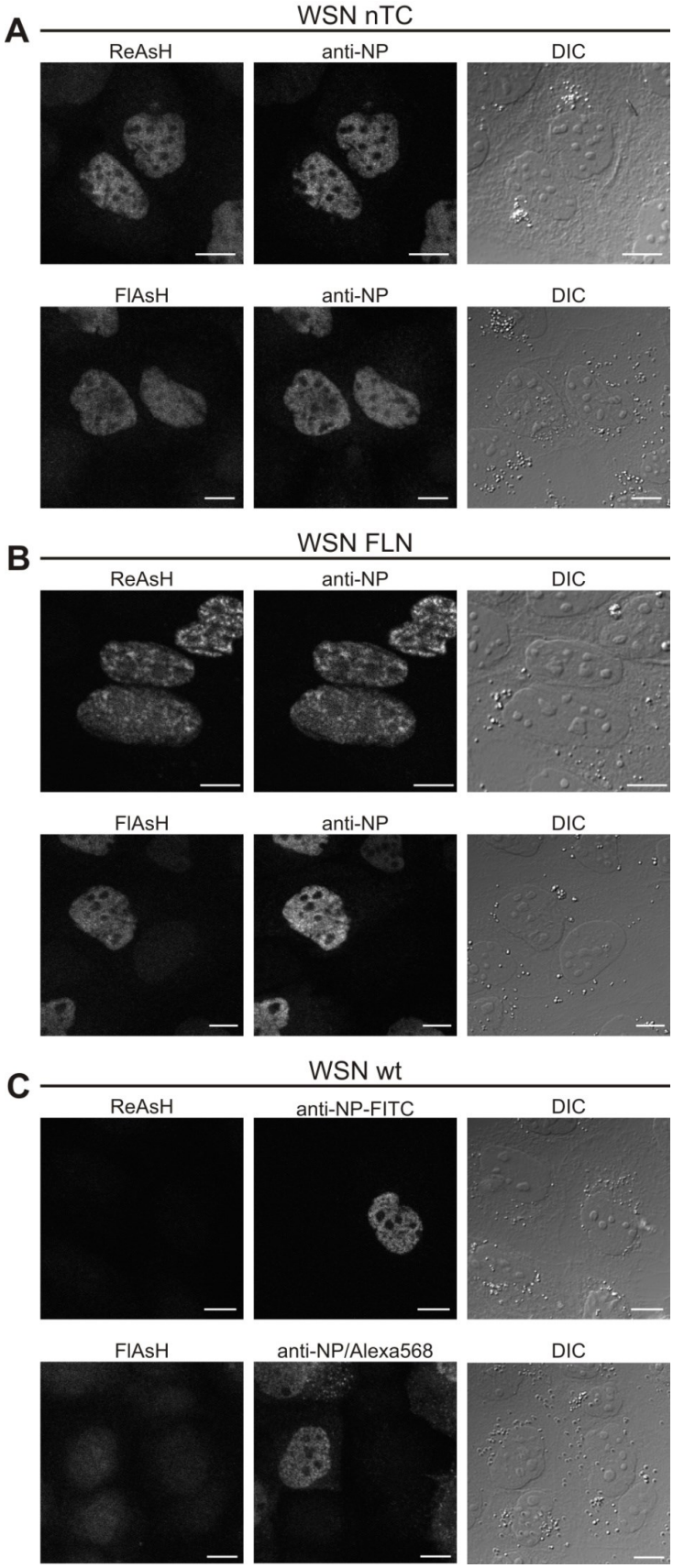

Fig. 22: Specificity of FlAsH and ReAsH labeling for TC-tagged NP in Influenza A/WSN mutant virus-infected cells. MDCK II cells were infected with (A) WSN nTC, (B) WSN FLN or (C) WSN wt virus (MOI 0.5), labeled with ReAsH or FlAsH at 20 h p.i. as indicated and subsequently immunostained with anti-NP-FITC or anti-NP/Alexa568-anti-mouse antibodies, respectively. Cells were visualized by confocal fluorescence microscopy. Representative images are shown. Scale bar, 10 µm.

concentration within TC-tag-expressing cells due to complexation by the tag cannot be determined though since the concentration of the TC-tag and the exchange rates of the dye with the cell culture supernatant (the main reservoir of the dye) are unknown. In general, the cellular background of biarsenical labeling was found to be strongly dependent on the dye concentration. Under the conditions of labeling applied here (see 3.2.2.4.3), the diffuse background was however low compared to the specific TC-tag signals, and a prominent unspecific labeling of cellular structures was not systematically observed. Intriguingly, however, some cells occasionally displayed as already mentioned a distinct nucleolar FlAsH or ReAsH fluorescence signal.

It was therefore examined if infection with WSN virus might induce unspecific biarsenical labeling of cellular structures. MDCK II cells were thus infected with WSN wt virus at different multiplicities of infection (MOI 0.05 and MOI 5). The results of the ReAsH labeling at 20 h p.i. in comparison with NP immunostaining as a marker for infection demonstrated that WSN wt virus infection did in fact cause unspecific, TC-tag-independent labeling of subnuclear structures (Fig. 23A). By comparison with the DIC images, it was inferred that these structures are nucleoli. The number of cells with nucleolar staining was considerably increased with the number of infected cells, which becomes obvious when comparing infections at MOI 0.05 and MOI 5 (bottom and top in Fig. 23A, respectively). All infected and uninfected cells displayed a diffuse ReAsH background, but only a fraction of the infected cells showed additional bright nucleolar signals. This was also seen for FlAsH labeling of WSN wt virus-infected cells (Fig. 23B).

Unspecific nucleolar labeling with FlAsH and ReAsH was also examined upon infection with the two mutant virus strains WSN nTC and WSN FLN. Infected cells were labeled with FlAsH or ReAsH and subsequently immunostained for NP to distinguish between unspecific and NP-specific FlAsH or ReAsH signals. In WSN nTC infection, several infected cells displayed a nucleolar FlAsH or ReAsH staining, which did not colocalize with the immunofluorescence signal of NP, suggesting an unspecific nucleolar labeling with the biarsenical dyes just like in wt virus infection (Fig. 23B). Occasionally, morphological changes of the nucleolar structure were seen in WSN wt and nTC virus-infected cells by DIC imaging (Fig. 23B, enlarged sections). They were typically accompanied by prominent unspecific biarsenical. In contrast, unspecific nucleolar staining with FlAsH or ReAsH was not observed in cells infected with WSN FLN virus, nor were there any prominent morphological changes of nucleoli.

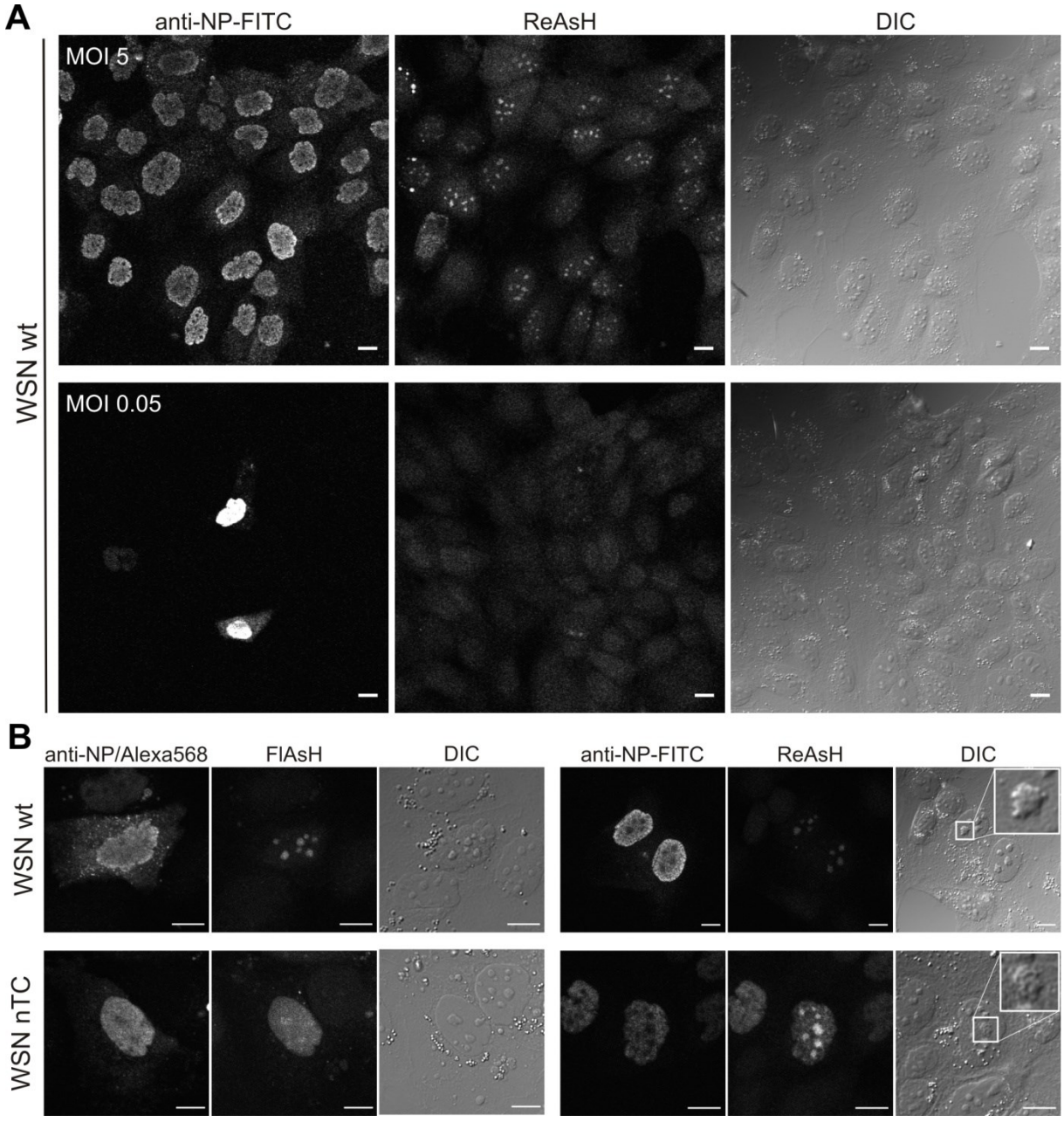

Fig. 23: Analysis of unspecific FlAsH and ReAsH labeling induced by Influenza A/WSN virus infection. (A) MDCK II cells were infected with WSN wt virus at two different MOI (top: MOI 5; bottom: MOI 0.05). At 20 h p.i., cells were labeled with ReAsH followed by immunostaining with anti-NP-FITC. Confocal fluorescence images were acquired with constant settings. In a fraction of the infected cells, unspecific labeling of nucleoli by ReAsH was observed. (B) Examples of WSN wt and WSN nTC infected cells showing nucleolar FlAsH and ReAsH labeling. Infection was identified by positive anti-NP immunostaining. The nucleolar FlAsH and ReAsH signals of WSN nTC infected cells did not correlate with immunodetection of TC-tagged NP demonstrating unspecific staining. Morphological changes of nucleoli frequently observed in infected cells are shown in enlarged sections of the DIC images on the right. Scale bar, 10 µm.

In conclusion, N-terminal TC-tagging of NP with duplication of the vRNA packaging signal in the recombinant viruses WSN nTC and FLN allows for efficient and specific labeling of TC-tagged NP with FlAsH and ReAsH, while care must be taken with respect to staining of nucleoli, which can be induced unspecifically by Influenza A/WSN virus infection. Thus, in

following experiments, nucleoli were excluded from analysis of biarsenical labeling in infected cells.

4.2.4.2 Comparative analysis of labeling efficiencies of nTC-NP and FLN-NP with FlAsH and ReAsH

For the determination of optimal conditions for fluorescence imaging of TC-tagged NP, the two different tag sequences nTC and FLN and the two biarsenical dyes FlAsH and ReAsH were tested in all possible combinations (Fig. 24). The signals were quantified relative to each other and relative to a common reference, and they were set into context with the fluorescence background signals.

For this purpose, MDCK II cells were infected with WSN nTC or WSN FLN virus and then labeled competitively with FlAsH and ReAsH at 20 h p.i. as described in 3.2.2.4.3. The cells were fixed and imaged by confocal fluorescence microscopy with constant settings (Fig. 24A). The images show that the two tags were efficiently labeled with both FlAsH and ReAsH. For quantification, the nuclei (which present the major signal in the cells) were manually selected and the mean intensity was measured with ImageJ. The FlAsH-to-ReAsH signal ratio was calculated and compared (Fig. 24A). The result clearly shows that the two tags have a differential preference for the two dyes, the nTC-tag displaying a higher FlAsH-to-ReAsH signal ratio than the FLN-tag. This difference might be due to either distinct affinities or to a distinct fluorescence brightness of these tag-dye combinations. To determine more precisely which tag-dye combination is preferable, FlAsH and ReAsH signals were compared to a reference signal, in this case the immunofluorescence (IF) signal of NP, in order to normalize the signals to the NP concentration. To this end, MDCK II cells were infected with WSN nTC, FLN or wt virus. They were then labeled with either FlAsH or ReAsH at 20 h p.i. and subsequently immunostained with anti-NP/Alexa568-anti-mouse or anti-NP-FITC antibodies, respectively. It is assumed here that the affinity of the monoclonal anti-NP antibody is unaffected by the presence of the tags. Image acquisition and quantification were performed as before, and the FlAsH-to-IF and ReAsH-to-IF signal ratios were calculated (Fig. 24B, C). Consistent with results from the competitive labeling assay (Fig. 24A), nTC-NP was more efficiently labeled with FlAsH than FLN-NP, whereas FLN-NP showed a considerably higher ReAsH signal than nTC-NP. Consequently, FlAsH appears to be better suitable to label nTC-NP, whereas ReAsH was apparently better for FLN-NP staining. A general improvement of the TC-tag by the flanking sequences in the FLN-tag

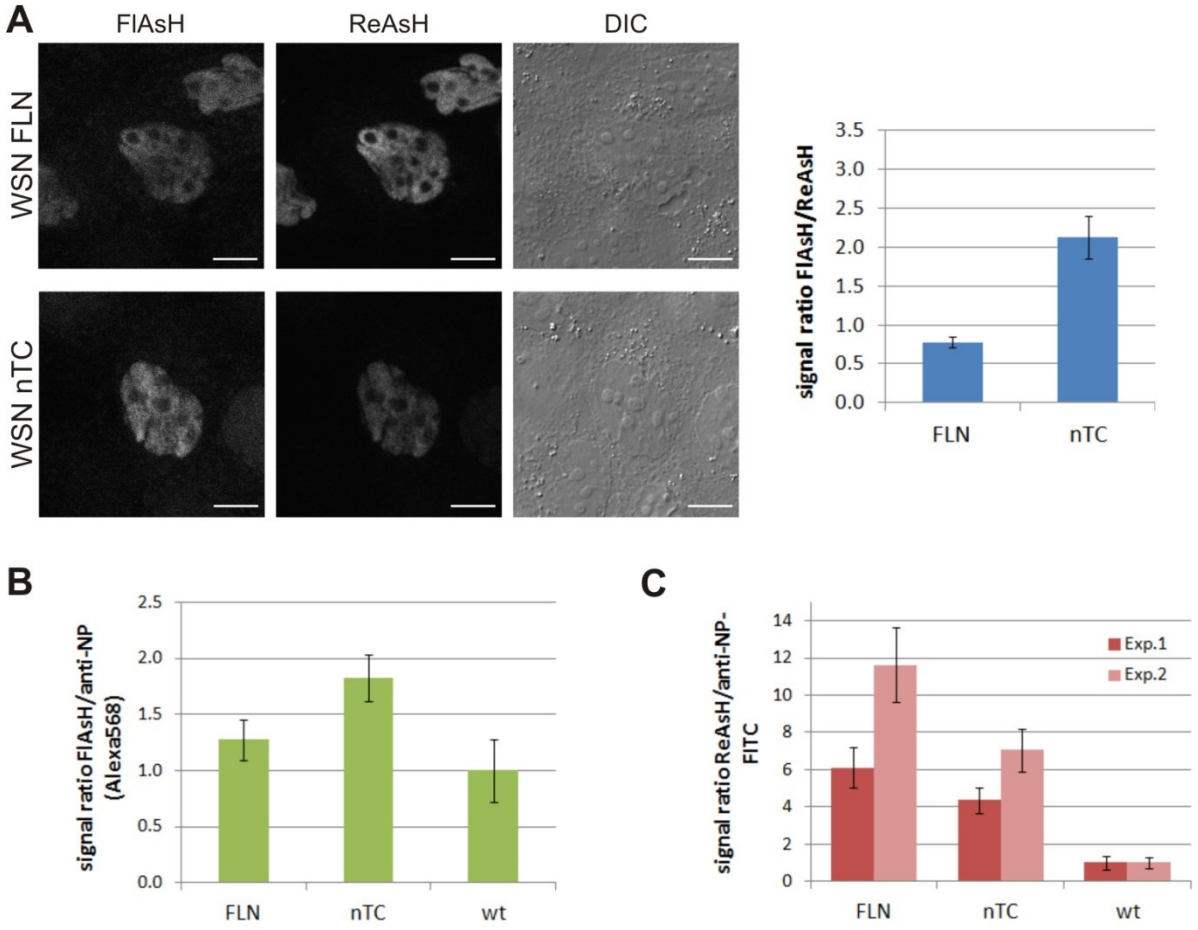

Fig. 24: Quantitative analysis of FlAsH and ReAsH labeling of WSN nTC and WSN FLN virus-infected cells. MDCK II cells were infected and labeled at 20 h p.i. The fluorescence signals were detected by confocal fluorescence microscopy and the mean signal intensities of the cell nuclei were determined using ImageJ. FlAsH and ReAsH nuclear signals were quantified (A) relative to each other, or (B, C) relative to immunofluorescence signals of NP. The signal ratios strictly depend on the acquisition parameters, which were kept constant during the experiments, using standard settings if not stated otherwise. (A) Competitive labeling of WSN FLN virus (top) and WSN nTC virus (bottom) with FlAsH and ReAsH. Fluorescence images show efficient labeling of the TC-tagged NP constructs with both dyes (Scale bar, 10 µm). The FlAsH-to-ReAsH signal ratio was determined for 27 nuclei of WSN nTC and 41 nuclei of WSN FLN virus-infected cells, mean vaues ± SD are displayed on the right-hand side. (B) FlAsH signals and (C) ReAsH signals of WSN FLN, WSN nTC and WSN wt virus-infected cell nuclei were quantified relative to the NP immunofluoresence signal for normalization to the amount of NP (B: anti-NP/Alexa568-anti-mouse; C: anti-NP-FITC). The dye-to-IF ratio for WSN wt was set to 1. The ratios of unspecific FlAsH and ReAsH labeling in wt virus infection relative to IF signals of NP depend on the NP expression level and present an average value of background signal relative to NP expression in the detected range, for comparison with the normalized FlAsH and ReAsH signals of nTC-NP and FLN-NP. Two independent experiments (Exp.1, Exp.2) are shown in (C) differing by the duration of ReAsH labeling (Exp.1: 1 h; Exp.2: 1.5 h) and the FITC detection range (exceptionally, Exp.1: 500–540 nm; Exp.2: 500–530 nm). At least 13 cells of each sample were analyzed. The results are given as mean signal ratio ± SD.

[481] could not be confirmed by comparison to labeling results of the nTC-tag. To assess unspecific background signals, signals of both dyes in the nuclei of wt virus-infected cells were quantified relative to the IF signal of NP. This ratio, unlike the ratios of nTC- and FLN-NP labeling, is dependent on the NP expression level, but it presents an average value of background signal relative to NP expression in the detected range and can therefore be used

for comparison with the relative nTC- and FLN-tag-specific signals. Comparison indicates that the signal-to-noise ratio was considerably better for ReAsH labeling than for FlAsH labeling under the applied conditions. The relative ReAsH signals of nTC-NP and FLN-NP were several-fold above the average unspecific relative background signal of ReAsH in wt virus infection, whereas the relative FlAsH signals of nTC-NP and FLN-NP were only less than two fold higher than the average FlAsH background ratio. This difference becomes important especially for detection of low-expressing cells. In particular, the combination of FlAsH with the FLN-tag was shown to be unfavorable producing signals close the average background staining.

4.2.4.3 Analysis of cytoplasmic nTC-NP and FLN-NP in infection with biarsenical labeling

Late in Influenza virus infection, NP characteristically appears as granular cytoplasmic structures representing progeny vRNPs which are in transit to the plasma membrane using the recycling endosomal transport pathway as reported in [297]. For studying transport and assembly of newly generated vRNPs in infection using the tetracysteine labeling technique, the labeling efficiency and specificity were tested in particular for the cytoplasmic NP structures in WSN nTC and WSN FLN virus-infected cells.

To qualitatively examine the presence and the local distribution of cytoplasmic NP signals, WSN nTC, FLN and wt virus-infected cells were labeled with ReAsH at 20 h p.i. and were subsequently immunostained with anti-NP-FITC antibody. Unexpectedly, cells infected with WSN FLN virus did not show the characteristic prominent accumulation of punctate NP in the cytoplasm. WSN FLN virus was therefore excluded from this analysis. In WSN nTC virus infection, however, the characteristic patterns of NP distribution were observed like in WSN wt virus infection (Fig. 25). Unlike wt virus-infected cells, only few WSN nTC virus-infected cells displayed cytoplasmic NP though (see also Fig. 28D and 4.2.5). Both nTC-NP and wt NP were frequently found to accumulate as punctate signals in a single focus of the juxtanuclear region, and from this site, NP spots were spread throughout the cytoplasm (Fig. 25a, b). This juxtanuclear site of prominent NP accumulation is probably the microtubule organizing center (MTOC) as identified before [280]. In other cases, the punctate NP signals were dispersed throughout the cytoplasm and near the plasma membrane being laterally restricted to one side of the cell nucleus, resulting in a laterally polarized distribution (Fig. 25c, d). These phenotypic distributions of NP have been described previously [297]. Immunofluorescence and ReAsH signals in the cytoplasm of WSN nTC virus-infected cells

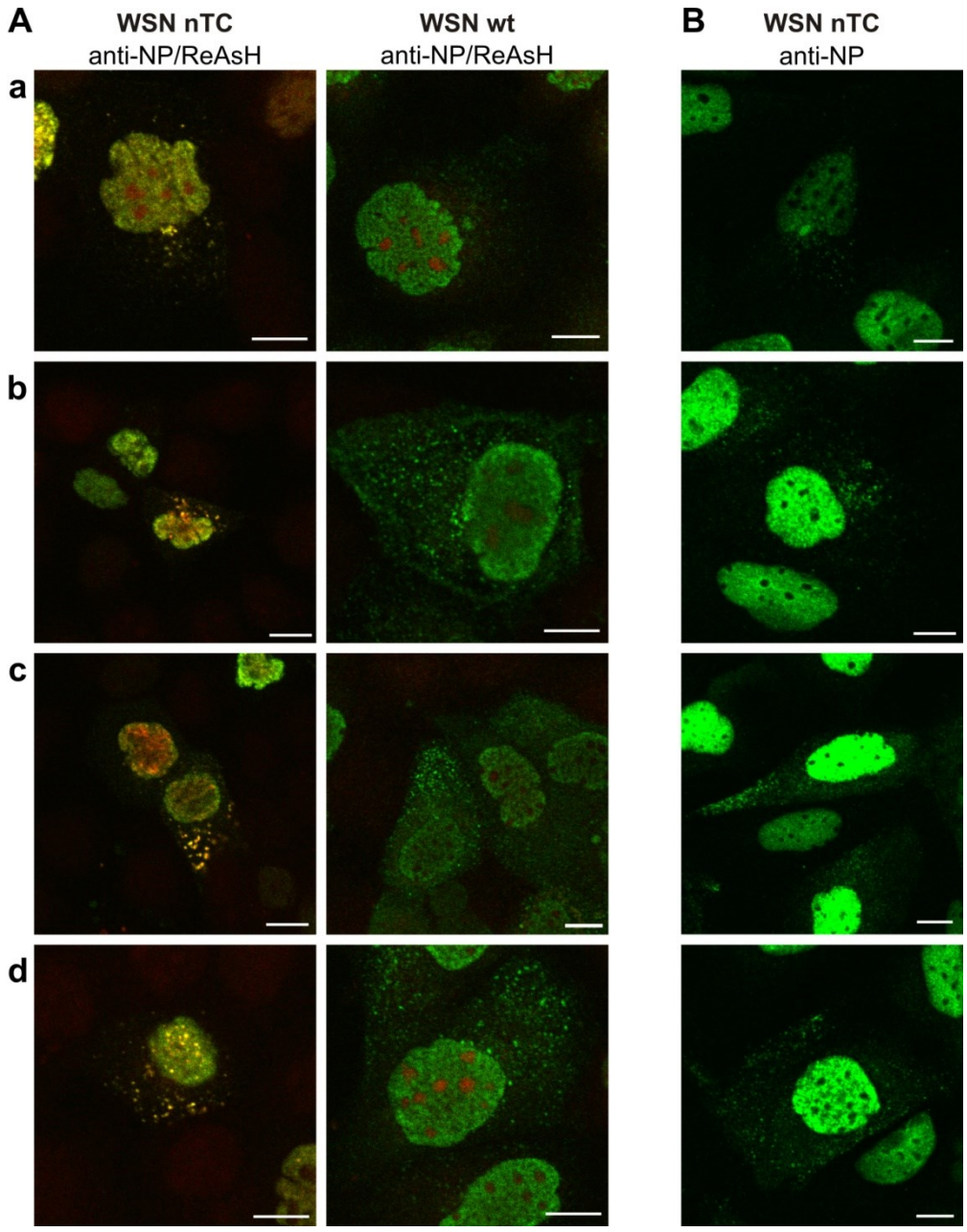

Fig. 25: Comparison of cytoplasmic NP distribution in WSN nTC and WSN wt infected cells. (A) MDCK II cells infected with WSN nTC or WSN wt virus were labeled with ReAsH at 20 h p.i., subsequently fixed and immunostained with anti-NP-FITC antibody. ReAsH fluorescence (red) and NP immunofluorescence (green) are presented as overlay. (B) WSN nTC virus-infected cells were fixed at 20 h p.i. and immunostained with anti-NP-FITC antibody. Confocal fluorescence images of infected cells with representative cytoplasmic NP distribution patterns are shown. Scale bar, 10 µm.

perfectly colocalized, confirming the specificity of ReAsH for nTC-NP (Fig. 25A, left-hand panel). Furthermore, it was noticed that punctate NP signals in ReAsH-labeled wt virus-infected cells were finer and smaller than in cells infected with nTC mutant virus (Fig. 25A, compare left-hand and right-hand panel). When the cells were fixed and immunostained without preceding ReAsH labeling, cytoplasmic nTC-NP was finely dispersed similar to wt NP in infection (Fig. 25B). This might indicate TC-tag-dependent aggregation of NP due to

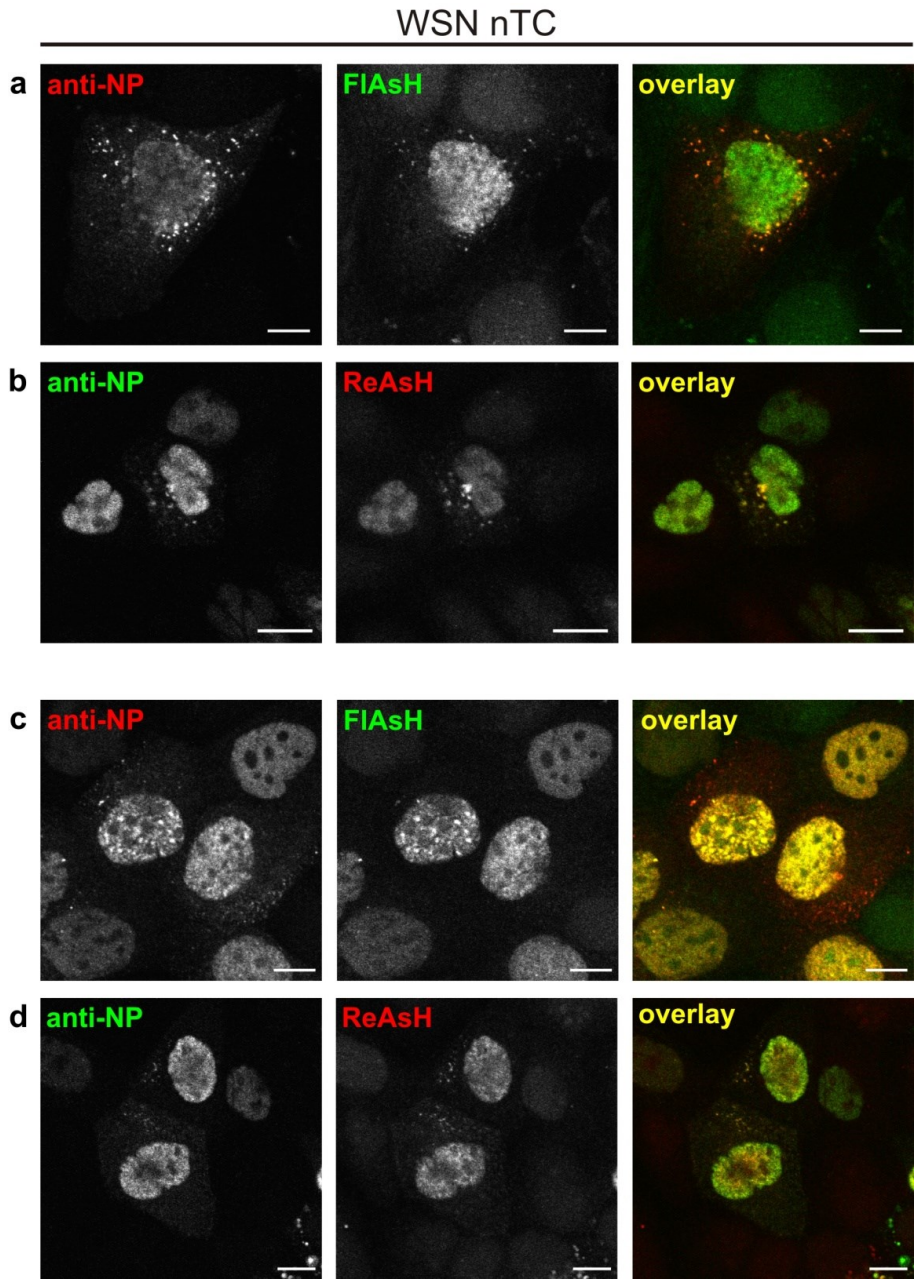

Fig. 26: Differential staining of cytoplasmic nTC-NP in infection using FlAsH and ReAsH. MDCK II cells were infected with WSN nTC virus and labeled with (a, c) FlAsH or (b, d) ReAsH at 20 h p.i. Subsequently, immunofluorescence was performed (a, c: anti-NP/Alexa568-anti-mouse; b, d: anti-NP-FITC). Cells with very bright and with low cytoplasmic IF signals are presented. (a) Labeling of cytoplasmic NP with FlAsH was less efficient than the immunostaining (relative to the nuclear signals). (c) Cytoplasmic NP with faint IF signals was not detectable by FlAsH labeling. (b, d) ReAsH and IF staining identified the same cytoplasmic NP structures. Relative to the nuclear signals, the ReAsH staining of cytoplasmic NP was stronger than the immunostaining. Scale bar, 10 µm.

biarsenical labeling.

When comparing ReAsH and FlAsH labeling of cytoplasmic nTC-NP in infection, a preference of the nTC-NP for ReAsH was observed (Fig. 26). For this analysis, FlAsH and ReAsH labeling were performed in cells infected with WSN nTC virus at 20 h p.i. as before,

and the signals were compared to the IF signal of NP as internal reference. Notably, the signal intensities of the biarsenical labeling and the immunostaining did not correlate uniformly within one cell. The intensity of the cytoplasmic signal relative to that of the nuclear signal was clearly higher for ReAsH than for IF detection (Fig. 26b). On the contrary, for FlAsH, this ratio was reversed. The signal in the cytoplasm relative to the nuclear signal was significantly weaker for FlAsH compared to the IF signal (Fig. 26a). As the same monoclonal primary antibody was used for IF staining of FlAsH and ReAsH-labeled cells, the compartment-specific differences between FlAsH and ReAsH labeling relative to the immunostaining were most likely due to different properties of the biarsenical dyes. FlAsH and ReAsH might differ by their affinity or by their fluorescence brightness when bound to nTC-NP, and these differences seem to occur in a compartment-specific way. The FlAsH labeling of cytosolic nTC-NP was very low compared to the IF signal, but it was also remarkably low compared to the nuclear FlAsH labeling and to the unspecific cellular FlAsH background (Fig. 26a). Moreover, when considering specifically very fine cytoplasmic nTC-NP structures, which were detected by a relatively low IF signal, these structures were distinctly detectable with ReAsH labeling (Fig. 26d), but remained undetectable with FlAsH labeling (Fig. 26c). The disparity of the two NP populations in the nucleus and in the cytoplasm might possibly result from the specific state of NP as preferentially uncomplexed or vRNP-bound protein. In addition, cytoplasmic vRNPs are very likely associated with M1, and NP might be N-terminally phosphorylated. The constraints of NP in cytoplasmic vRNP complexes may impose conformational restrictions or obstruct the accessibility of the nTC-tag. The slightly larger molecular size of FlAsH (664.5 Da) compared to ReAsH (545.4 Da) might hence explain the impairment of FlAsH labeling of cytoplasmic vRNPs, whereas ReAsH can efficiently stain the TC-tag in cytoplasmic nTC-NP. Differences of the environment-dependent fluorescence brightness of FlAsH and ReAsH can however not be excluded.

In conclusion, FlAsH was found to be unfavorable for labeling cytoplasmic nTC-NP in infection, whereas ReAsH performed comparably well and yielded excellent cytoplasmic nTC-NP-specific signals. The nTC-tag with the ReAsH ligand is hence the favorable tag-dye combination for detection of cytoplasmic vRNPs in infection with recombinant virus.

ReAsH has been reported to have a phenotypic effect on labeled cells causing a transient rounding and disruption of the cell shape [482]. ReAsH thus appears to transiently disrupt the cytoskeleton. A similar effect was observed with MDCK II cells in the present study; rounding of the cells briefly after labeling ceased after about 30 minutes. Therefore, the effect

of ReAsH and FlAsH labeling on nuclear export and the presence of cytoplasmic vRNPs in infection was analyzed (Tab. 7). MDCK II cells were infected with equal amounts of WSN nTC virus (MOI~0.8). At 19 h p.i., they were then labeled with FlAsH or ReAsH. Control cells were treated without dye. The signals of the subsequent immunostaining of NP were analyzed for the fraction of infected cells with characteristic cytoplasmic vRNP signals (Tab. 7). The results demonstrate that neither FlAsH- nor ReAsH-labeled cells displayed significantly altered fractions of cells with cytoplasmic vRNP signals compared to non-labeled cells. Being aware of the variations of the fractions of infected cells among the samples (due to a very heterogeneous distribution of infected cells), the fractions of cells with cytoplasmic signal were determined relative to the number of infected cells of each of the sections which was randomly chosen for analysis. It was shown before that the cytoplasmic distribution of nTC-NP after ReAsH labeling was qualitatively comparable to the characteristic wt NP distribution in infection (Fig. 25). Solely the formation of enlarged NP spots was observed specifically for nTC-NP, but not for wt NP after ReAsH labeling, suggesting that this was an effect due to the nTC-tag itself and not to the interference of ReAsH with the cytoskeleton. Accordingly, an effect of ReAsH on the presence and the distribution of cytoplasmic vRNPs could not be observed.

	total number of cells	fraction of infected cells +/- SD [%]	**fraction of infected cells with NP cytosolic signal [%]**	**SD [%]**
with ReAsH	294	60.1 +/- 15.5	**10.0**	**7.5**
w/o ReAsH	342	38.9 +/- 9.7	**10.1**	**5.1**
with FlAsH	423	42.2 +/- 12.5	**12.4**	**4.6**
w/o FlAsH	303	54.5 +/- 7.3	**10.7**	**4.7**

Tab. 7: Effect of FlAsH and ReAsH labeling on the presence of cytoplasmic NP in WSN nTC virus infection. The fraction of infected MDCK II cells displaying cytosolic NP signals were determined for ReAsH- and FlAsH-labeled cells at 19 h p.i. in comparison to non-labeled cells. The fractions of infected cells and of infected cells with a cytosolic NP signal were determined by immunofluorescence detection of NP. IF detection in ReAsH-labeled cells was performed with anti-NP-FITC; IF detection in FlAsH-labeled cells was performed with anti-NP/Alexa568-anti-mouse. At least seven frames per sample were evaluated. The results are given as mean value with SD.

Additionally, the effect of biarsenical labeling on virus formation was analyzed independently of the TC-tag (Fig. 27). To this end, MDCK II cells were infected with WSN wt virus and the supernatant was collected at 19 h p.i. Infected cells were then labeled with FlAsH or ReAsH according to 3.2.2.4.3. Control cells were treated without dye. The labeling solution was then replaced by normal medium and the supernatant was again collected after 3 h or 5 h. The viral titers of the samples collected before and after labeling were analyzed by immunofluorescence analysis (as described in 3.2.4.5). The results show that labeling of the cells with either FlAsH or ReAsH had no particular effect on the virus titer compared to the titer of virus released from unlabeled control cells (Fig. 27). This implies that the formation of infectious virus particles is not affected by the biarsenical dyes and that the cytoskeleton remains functional for transport and budding processes.

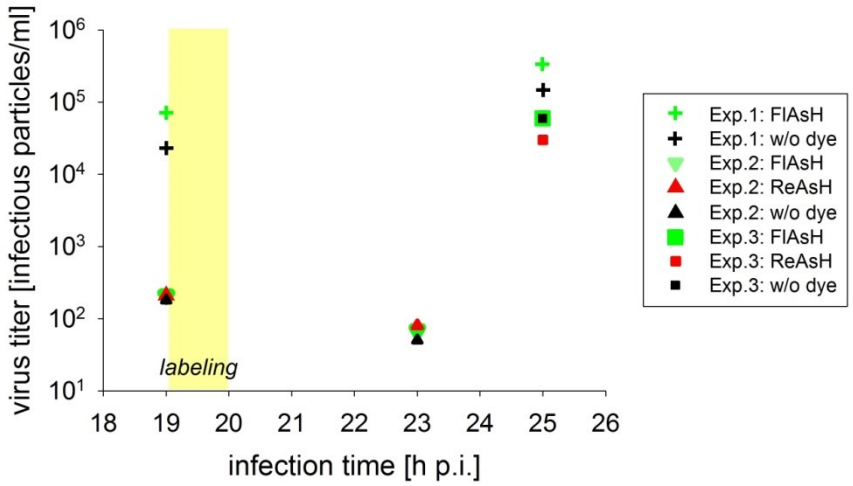

Fig. 27: Comparison of Influenza A/WSN wt virus production in the presence and absence of biarsenical dyes. In three independent experiments, MDCK II cells were infected with WSN wt virus (Exp.1: MOI 0.4; Exp.2: MOI 0.3; Exp.3: MOI 0.3). The supernatant was collected at 19 h p.i. and the cells were subsequently labeled with 1 µM FlAsH or ReAsH for 1 h at RT according to the standard labeling procedure (3.2.2.4.3). Control cells (w/o dye) were incubated with pure DMEM instead. The supernatant was again collected at 23 or 25 h p.i. The virus titer of labeled and non-labeled samples was determined by IF analysis (3.2.4.5).

4.2.5 Characterization of viral replication of recombinant Influenza A/WSN nTC and A/WSN FLN virus

The recombinant Influenza mutant viruses with TC-tagged NP were analyzed regarding viral replication kinetics and the effect of biarsenical labeling on replication.

At first, plaque assay (3.2.4.4) was employed to determine the titer of the recombinant WSN viruses. WSN wt virus formed distinct, round plaques after three days as shown in Fig. 28B, and the number of plaque forming units (PFU) could be determined. In contrast, no distinct plaques were formed by WSN FLN virus indicating that this virus mutant was not able to undergo multiple replication cycles. For WSN nTC virus, plaques could sometimes be observed, but they appeared vague and blurry (Fig. 28B). Not all of the small, faint and semi-translucent patches could unambiguously be identified as plaques. When looking closely at the cell layer using an inverted microscope, the rounded, translucent areas with a more or less strong CPE still enclosed living cells, suggesting a low pathogenic effect on the cells. Unusually, when cells were infected with a ten times higher virus concentration than the concentration at which plaques were observed, the formation of ten times more plaques did not occur. Instead, a homogenously distributed CPE was observed and the confluent cell layer completely disintegrated (macroscopically observed by a semi-translucent cell layer in Fig. 28B). This effect is shown for WSN nTC virus which was harvested from the first passage on MDCK II cells and was analyzed at dilutions 10^{-1} and 10^{-2}. The nonlinear effect suggests an underestimation of the correct number of infected cells by plaque detection, and it indicates a large fraction of infected cells which are unable to form plaques. Incomplete packaging of the viral genome might be able to explain these data. Hence, the determination of mutant virus titers by plaque assay was not feasible.

Therefore, the titer of WSN mutant viruses was determined by immunofluorescence analysis of infected cells (see 3.2.4.5) where infected cells are detected based on viral protein expression. In this case, titer determination does not depend on the ability of the virus to perform multiple cycles of replication, which is of particular importance for viruses with replication or packaging defects. Based on the Poisson-distribution $P(n) = (MOI)^n \times e^{-MOI} / (n!)$, which describes the probability that a cell at a given MOI is infected with n virus particles, the MOI and thereby the titer of a virus suspension was calculated from the fraction of uninfected cells (p_0): $MOI = -\ln(p_0)$, with p_0 determined by immunofluorescence detection of NP expression. The titer values thus obtained differed clearly from those obtained by plaque assay: The first passage of newly generated WSN nTC virus typically yielded an apparent titer of about 10^3 PFU/ml when analyzed by plaque assay,

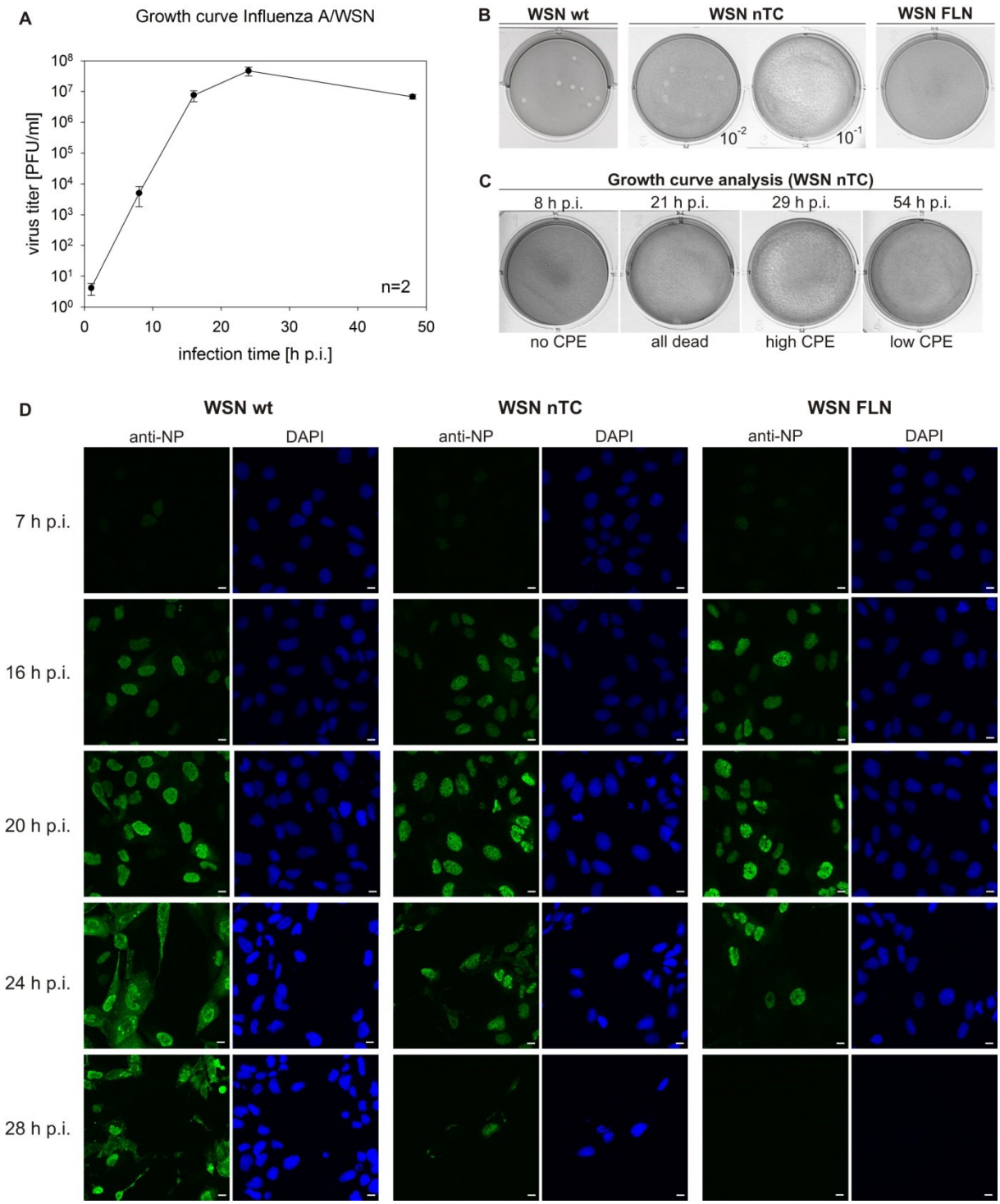

Fig. 28: Characterization of viral infection and growth kinetics of recombinant Influenza A/WSN viruses. (A) Growth curve of WSN wt virus. The titer of virus collected from infected cells (MOI 0.01) at different time points post infection was determined by plaque assay (duplicate, mean ± SEM). (B) Plaque formation of WSN wt, WSN nTC and WSN FLN virus. (C) WSN nTC virus collected from infected cells (MOI 0.1) at different time points post-infection was analyzed by plaque assay. Plaques could not be observed, but a varying degree of CPE was seen (and confirmed by microscopy). The most pronounced CPE was caused by virus collected at 21 h p.i. (D) Time course of infection with WSN wt, WSN nTC and WSN FLN virus analyzed by IF and confocal microscopy. MDCK II cells were infected (MOI 1), fixed at different time points post-infection and immunostained with anti-NP-FITC antibody and DAPI. Scale bar, 10 µm.

whereas the titer of the same preparations determined by immunofluorescence analysis of NP expression revealed titers of about 10^6 infectious particles/ml. WSN wt virus in comparison usually yielded titers of about 10^8 PFU/ml, but about 10^9 infectious particles/ml determined by immunofluorescence analysis. For WSN FLN virus, the titer of newly generated virus after the first passage determined by immunofluorescence analysis was in the range of 10^6 infectious particles/ml.

To characterize the replication kinetics of WSN wt and mutant virus, MDCK II cells were infected and the supernatants were harvested and analyzed for the amount of newly generated virus at various time points post-infection (see 3.2.4.6). The growth curve for WSN wt virus as determined by plaque assay is presented in Fig. 28A. In case of WSN nTC virus, the analyzed samples did not produce distinct plaques as outlined above. Therefore, quantitative titer determination was precluded, but it was possible to evaluate the extent of CPE that was induced by the pure supernatant harvested at different time points post-infection. No CPE was observed for the virus produced until 8 h p.i.; the highest degree of CPE showing all cells dead was found for the viral supernatant harvested at 21 h p.i. and a successively decreasing CPE was observed for the supernatants at 29 and 54 h p.i (Fig. 28C). Qualitatively, the degree of cell damage reflecting the number of infectious virus particles increased and decreased in a time-dependent manner comparably to the growth curve of WSN wt virus (Fig. 28A). Alternative immunofluorescence-based titer determination (3.2.4.5) providing quantitative data for the WSN nTC virus growth curve was however not pursued, because a strong dependence of the replication kinetics on the initial MOI was expected after realizing the non-linear relation between number of infections and the production of replication-competent progeny virus particles. A conclusive and sufficient characterization of the virus by this data could therefore not be expected.

As the inability of TC-tagged mutant viruses to form plaques might reflect a vRNP packaging defect, the role of genome packaging was explored (Tab. 8). Cells were infected with two dilutions of WSN wt, nTC and FLN virus, respectively, and the apparent titer (MOI) of each sample was determined by immunofluorescence analysis (see 3.2.4.5). Using standard setting for detection of NP expression in infected cells, very low levels of NP were not detected. The MOI ratio of the two dilutions was then compared with the actual dilution factor (see Tab. 8, bold figures). For all viral strains, the decrease of the MOI by dilution of the virus as detected by immunofluorescence was higher than the actual dilution of the virus concentration. However, it was only 2.6 times higher for wt virus infections, while it was 22 times higher in

case of WSN nTC virus infections. For FLN virus, infected cells were not observed anymore upon infection with a fivefold diluted virus suspension. The MOI and MOI ratio could therefore not be determined. Nevertheless, the MOI ratio for FLN virus infections appeared to be considerably higher than fivefold. According to calculations, 5.1 % of the 644 counted cells would have been expected to be infected.

strain	relative dilution factor	number of frames	number of cells	number of infected cells	fraction of infected cells [%]	SEM [%]	MOI [infectious units/cell]	ratio of MOI
wt	**10**	6	481	8	1.4	0.6	0.014	**26**
	1	5	484	145	30.1	2.1	0.358	
nTC	**5**	7	547	1	0.4	0.5	0.004	**110**
	1	9	561	203	37.0	4.1	0.462	
FLN	**5**	8	644	0	0.0	0.0	0.000	
	1	8	612	129	23.0	3.8	0.262	

Tab. 8: Comparison of the relative amount of virus applied for infection with the actually observed amount of infectious virus as determined by MOI calculation. MDCK II cells were infected with two dilutions of Influenza A/WSN wt, nTC and FLN virus, respectively. The fraction of infected cells was determined by immunofluorescence with anti-NP-FITC antibody and DAPI staining at 20 h p.i. by analyzing at least five different frames and 480 cells of each sample (2nd column). The results are given as mean value with SEM (3rd column). The multiplicity of infection (MOI) (4th column) was calculated by MOI = $-\ln(P_0)$. P_0, the fraction of non-infected cells. The ratio of the MOI of the two virus dilutions (4th column) was calculated for comparison with the actual dilution factor (1st column).

Thus, the effective titer of infectious virus particles in the virus preparations decreased more than expected upon dilution of the virus suspensions. The data suggests that by reduction of the number of virus particles the probability of infection per virus particle was decreased. This was in particular true for the mutant virus strains WSN nTC and WSN FLN. Conversely, the probability of infection per virus particle obviously increased with a higher virus concentration, when also the probability increases that one cell is infected by more than one virus particle. Individual defects can then be compensated. This correlation suggests that a fraction of the virus particles might be deficient of critical components for infection and might form infectious units only in combination with other defective virions. As the probability of infection with a specific number of virus particles at a given MOI is Poisson-distributed, the probability of infection with a combination of different virus particles generally increases with a higher MOI. In case of infectious units that consist of more than one virus particle, a higher MOI would therefore result in detection of a higher effective number of infectious units, which non-linearly increases with the virus concentration. The experimental data (Tab. 8) is hence consistent with the existence of infectious units that comprise more than one virus particle. This analysis supports the assumption of a packaging defect in WSN nTC and WSN

FLN virus particles, albeit it does not stringently prove such a defect. Other explanations for this non-linear relation between virus dilution and the detectable virus titer (based on the number of infected cells) might be possible, e.g. infection of cells with some of the newly released virus particles (despite the lack of HA cleavage for activation) or the influence of cellular responses to differing multiplicities of infection. However, these effects would be expected to be similar for WSN wt virus. Considering the structural role of NP in the genomic complexes and modification of the packaging signal in the NP segment, it is reasonable to assume a packaging defect in the first place. For sufficient evidence, though, further experiments are required, e.g. cryo-electron tomography, quantitative RT-PCR or a reporter gene assay.

As the replication kinetics of the WSN nTC and WSN FLN virus as a multi-cycle process could not be compared to those of WSN wt virus by standard growth curve, the course of infection of WSN wt, nTC and FLN virus (at MOI 1) was comparatively analyzed by NP-specific immunofluorescence at various time points post-infection (Fig. 28D). As judged by the intensity of the NP signal, expression of NP progressed equally for all three strains. This finding indicates that expression rates were apparently not affected by the TC-tag. One significant difference between WSN wt and WSN mutant viruses was the larger fraction of cells displaying cytoplasmic NP found in wt virus infection at 20 h and in particular at 24 h p.i. Besides, also the amount of cytoplasmic NP was higher in wt virus infections. These data indicate an attenuated formation and/or transport of vRNPs in nTC and FLN mutant virus infections. The above-postulated packaging defect of vRNPs in mutant virus particles might also have contributed to this result. When assuming infections with an incomplete set of genomic segments, the lack of segments encoding proteins like M1 and NEP would result in impaired nuclear export of vRNPs, which might partially explain the reduced number of cells with cytoplasmic NP signal.

Incomplete genome packaging might furthermore be the reason for another observation presented in Fig. 28D. At 28 h p.i., the CPE of mutant virus-infected cells was more pronounced than in the wt case. Most cells in WSN nTC and FLN virus infections had died and detached at that time point, even the apparently uninfected (NP-negative) cells, whereas in wt virus infection, many infected and uninfected cells were still intact, suggesting that in mutant virus infections the number of infected cells was actually higher than the number detected by NP-specific immunofluorescence. A lack of NP expression in some of the infected cells might explain this observation, supporting the hypothesized packaging defect of the viral genome in the mutant viruses. Sequence analysis of segment 5 vRNA did not reveal any

sequence variations in WSN nTC or FLN virus which might explain a partial expression defect. Due to underestimation of the virus titer by immunofluorescence detection, the actual MOI applied for WSN nTC and WSN FLN virus infection might have been higher than the MOI of wt virus infection. Nevertheless, in the following, the virus titer was determined by immunofluoresence analysis of infected cells, as it provides a defined measure that has been shown to be reasonably comparable to wt virus infection in the applied range (Fig. 28D).

4.2.6 Studying fluorescently labeled vRNPs during virus entry

4.2.6.1 Analysis of FlAsH and ReAsH labeling of vRNPs in intact virus particles

For application of the recombinantly generated WSN nTC and WSN FLN virus particles in cell entry studies, the labeling of vRNPs with FlAsH or ReAsH in intact virus particles was examined first. SDS-PAGE followed by fluorescence analysis of the size-separated viral proteins was performed to verify covalent binding of the biarsenical dye molecules to the TC-tagged NP. Therefore, WSN wt, nTC and FLN virus particles were propagated, labeled and purified as described in 3.2.4.2. After labeling with 2 µM FlAsH or ReAsH, the virus was purified by sucrose gradient centrifugation and the protein concentration of each sample was determined. Equal amounts of each sample were applied to SDS-PAGE, and the fluorescence of FlAsH or ReAsH within the gel was detected with the Fluorescent Image Analyzer followed by Coomassie staining or Western blotting (Fig. 29). As the instrument settings did not allow optimal detection of FlAsH and ReAsH fluorescence, the absolute signal intensities should not be interpreted in comparison to Coomassie staining and Western blotting signals. The Coomassie-stained gels displayed the characteristic bands of the Influenza virus proteins (Fig. 29A, B). The relative amounts of NP (56 kDa) and M1 protein (27 kDa) varied among different preparations. A constantly lower incorporation of NP and M1 into mutant virus particles compared to wt virus preparations cannot be reported, but it was frequently observed (compare Fig. 29A & Fig. 29B). The results show that ReAsH and FlAsH bound specifically to TC-tagged NP of nTC and FLN virus, but not to wt NP. This was confirmed by comparison of FlAsH fluorescence with NP-specific immunodetection in Western blot analysis (Fig. 29C). Unexpectedly, though, the protein M1 was unspecifically (i.e. TC-tag independently) labeled with FlAsH and ReAsH (Fig. 29A, B). Western blotting and M1 immunodetection in comparison to the FlAsH-signal identified M1 as fluorescently labeled protein (Fig. 29C). Unspecific fluorescent protein bands after biarsenical labeling and SDS-PAGE have been reported previously [483,484]. It is possible that the signal is an artifact of the denaturated

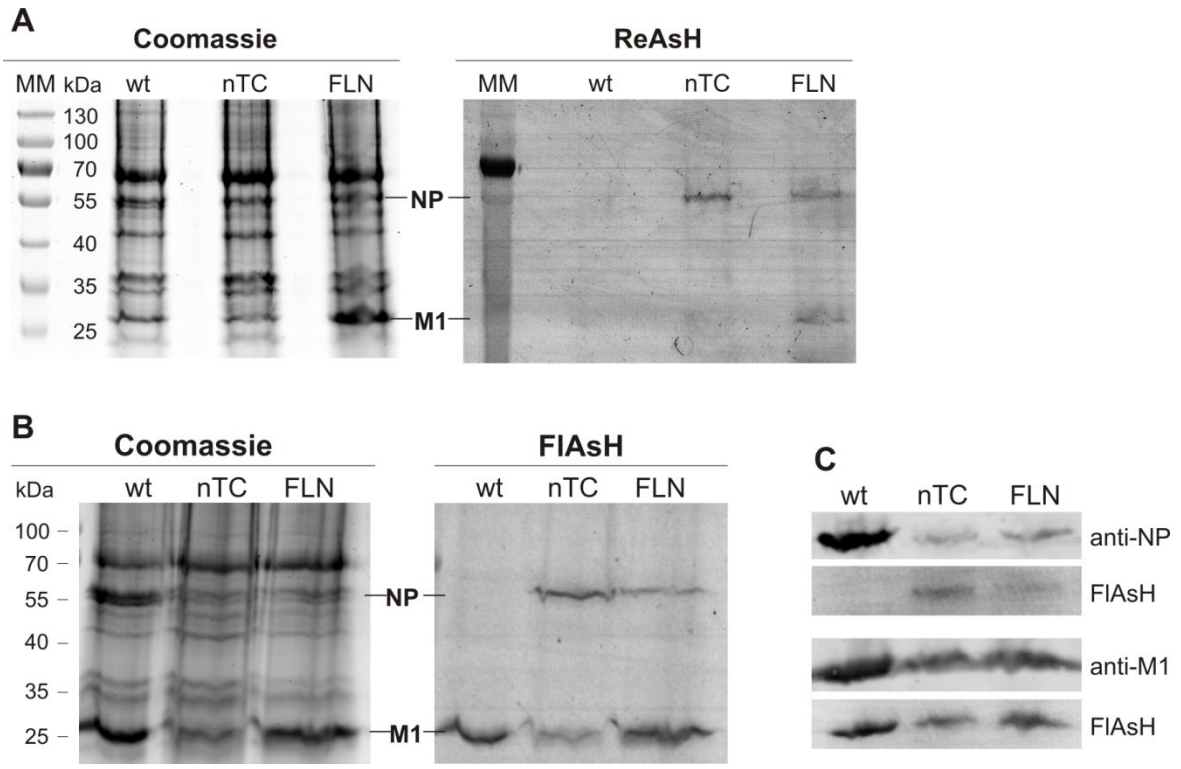

Fig. 29: Analysis of purified FlAsH- and ReAsH-labeled virus by SDS-PAGE and fluorescence detection. Influenza A/WSN wt virus and WSN nTC and FLN mutant viruses were labeled with FlAsH or ReAsH, purified by sucrose gradient centrifugation and analyzed by SDS-PAGE (non-reducing conditions). The same amount of protein of each virus preparation was applied. The gels were scanned for (A) FlAsH or (B) ReAsH fluorescence and the total protein was visualized by Coomassie staining. (A) SDS-PAGE with ReAsH-labeled virus (200 µg protein of each preparation). (B) SDS-PAGE with FlAsH-labeled virus (104 µg of each sample). (C) Western blotting analysis of FlAsH-labeled virus (50 µg). FlAsH fluorescence in the gel was detected, followed by blotting and immunodetection of NP or M1. MM: molecular weight marker.

state of M1 in SDS-PAGE and of the flexible accessibility of its cysteine residues. However, to exclude any contribution of M1 to the FlAsH or ReAsH signals in infected cells, the fluorescence of FlAsH and ReAsH in infected and non-infected cells was quantified in WSN wt virus-infected samples that were labeled with FlAsH and ReAsH simultaneously (Fig. 30). Typically, M1 is abundantly expressed at 20 h p.i. and is distributed throughout the infected cells. M1-specific staining should therefore result in an overall increase in fluorescence signal in infection. Infected cells were identified by immunostaining with anti-NP and Atto647N-anti-mouse antibodies, and the signals of infected and non-infected cells (Fig. 30A, top) were quantified and compared (Fig. 30B). Obviously, native M1 in infection did not affect the cellular fluorescence background signals of FlAsH and ReAsH (nor did any viral protein) suggesting that M1 in its native state and under physiological conditions is not labeled with biarsenical dyes.

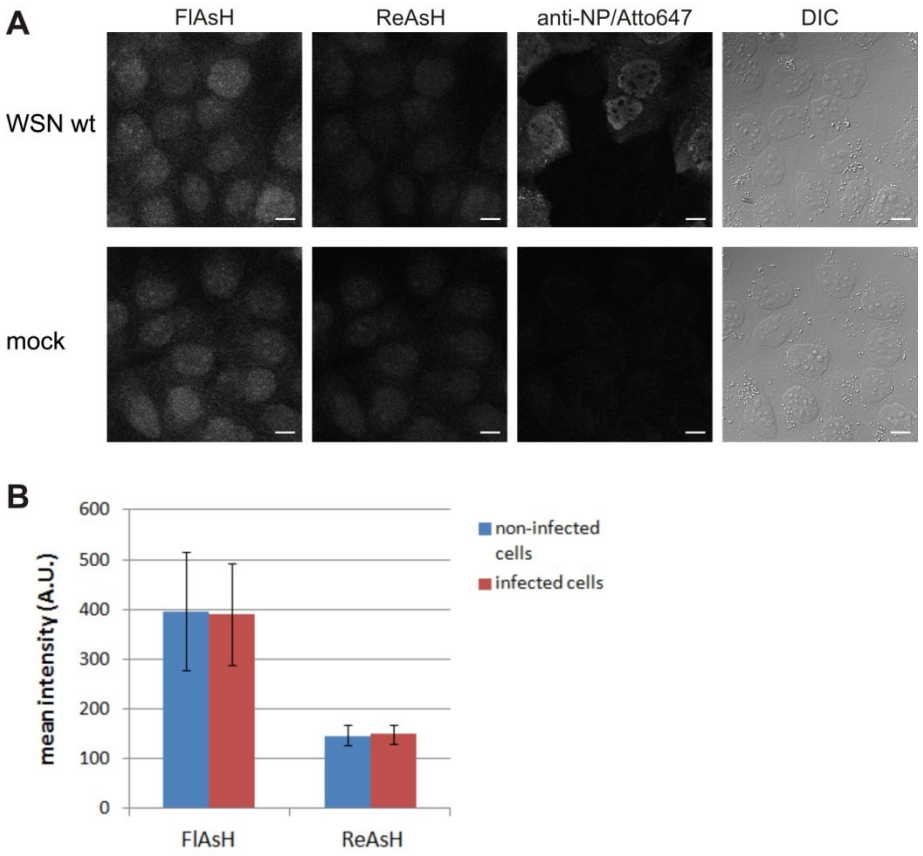

Fig. 30: Quantitative analysis of unspecific cellular FlAsH or ReAsH labeling induced by Influenza A/WSN virus infection. WSN wt virus-infected and mock-infected MDCK II cells were labeled with both FlAsH and ReAsH at 20 h p.i. followed by immunostaining with anti-NP and Atto 647N-anti-mouse antibodies. (A) Confocal fluorescence images were acquired with constant settings. Scale bar, 10 µm. (B) FlAsH and ReAsH signals from 24 infected and 48 non-infected cells of the WSN wt virus-infected sample were quantified using ImageJ. Infected cells were identified by positive anti-NP immunofluorescence signal. An increase of unspecific FlAsH or ReAsH background labeling was not induced by Influenza A/WSN virus infection. Results are given as mean intensity of the cell nuclei ± SD.

4.2.6.2 Virus entry and infection with labeled WSN nTC and WSN FLN virus

Purified and labeled virus was then applied to study virus entry in MDCK II cells. This experiment was performed in collaboration with Christian Sieben (Humboldt-Universität, Berlin) (Fig. 31). The TC-tagged viruses were labeled with 0.4 µM FlAsH overnight followed by staining of the viral envelope with the lipophilic marker DiD for another 2 h. The virus was filtrated with 200 µm pore size and was added to the cells for 10 min on ice. The uptake was then traced by confocal microscopy for more than 60 min, and z-stacks of images were acquired about every 10 min. The time points 5 min and 40 min p.i. are presented in Fig. 31 for WSN FLN virus. Signals of FlAsH and DiD clearly colocalized in small dots within infected cells and were often found in the periphery of the cell nuclei as expected for virus particles after uptake. However, FlAsH and DiD signals did not separate within the observation period indicating that a separation of the viral envelope and the viral genome did

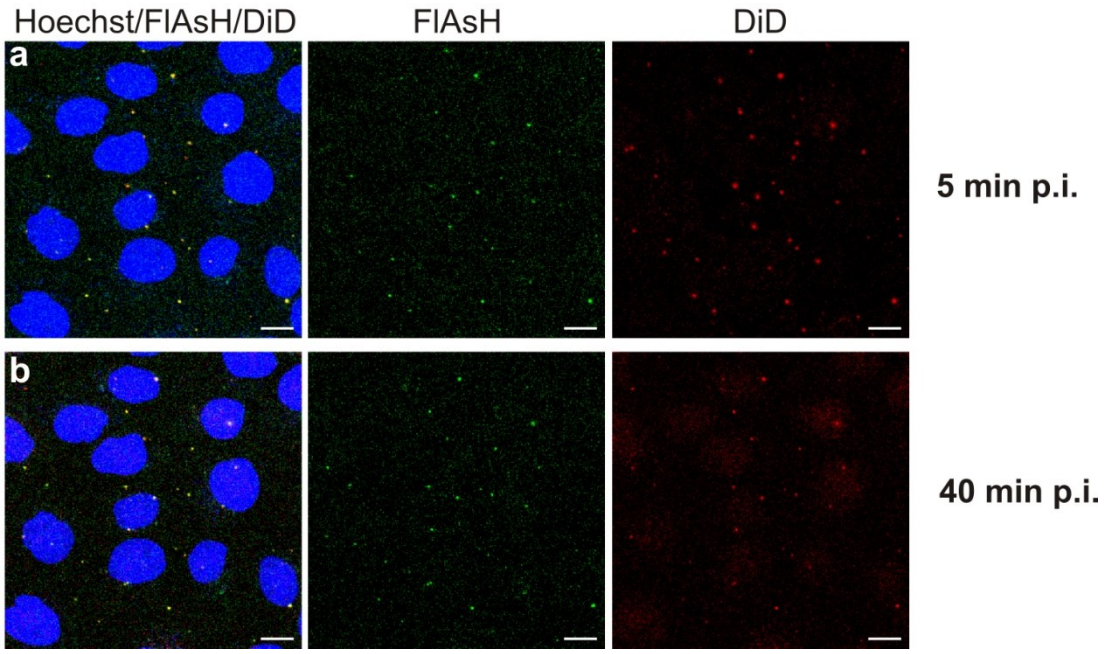

Fig. 31: Visualization of virus entry into MDCK II cells using FlAsH-labeled WSN FLN virus. This experimental data was kindly provided by Christian Sieben (Humboldt-Universität, Berlin). MDCK II cells were infected with Influenza A/WSN FLN virus labeled with FlAsH and the lipophilic dye DiD. The cells were incubated with virus on ice for 10 min and unbound virus was subsequently removed by washing. The cells were then stained with Hoechst dye (blue, DNA) and the uptake was observed for over 60 min. Infected cells (z-stack) at (a) 5 min and (b) 40 min after virus incubation show colocalization of FlAsH and DiD signals. The signals did not separate within the observation period and FlAsH was not found to accumulate in the cell nuclei. Scale bar, 10 µm.

not occur. Consistently, an accumulation of the FlAsH signal in the cell nuclei was not observed, even though the viral genome would have been expected to reach the cell nuclei within the first hour [115]. The decrease of the DiD signal relative to the FlAsH signal observed over time might have been due to fusion of the viral membrane with the endosomal membrane; evidence for successful fusion was however not obtained in this assay. The same results were obtained when performing the experiment with WSN nTC virus (not shown).

As the data indicate a failure of the TC-tagged and FlAsH-labeled viral genome to enter the nucleus, the assumed impairment of infection was tested by detection of viral NP expression several hours after infection with labeled virus particles (Fig. 32). As before, WSN nTC and WSN FLN virus, but also WSN wt virus were labeled with FlAsH or ReAsH for 1.5 h at RT and were then purified by sucrose gradient centrifugation. The protein content was determined and the same amount of virus protein of each strain (typically, 10 to 18 µg) was used to infect about 10^6 cells. Similar amounts had also been used for imaging of virus entry (Fig. 31), although for imaging, the virus had been additionally filtrated to eliminate virus aggregates. Cells were incubated with the virus for 10 min on ice and the unbound virus was then removed. Infection was allowed to proceed for 17 h, followed by immunostaining of NP and

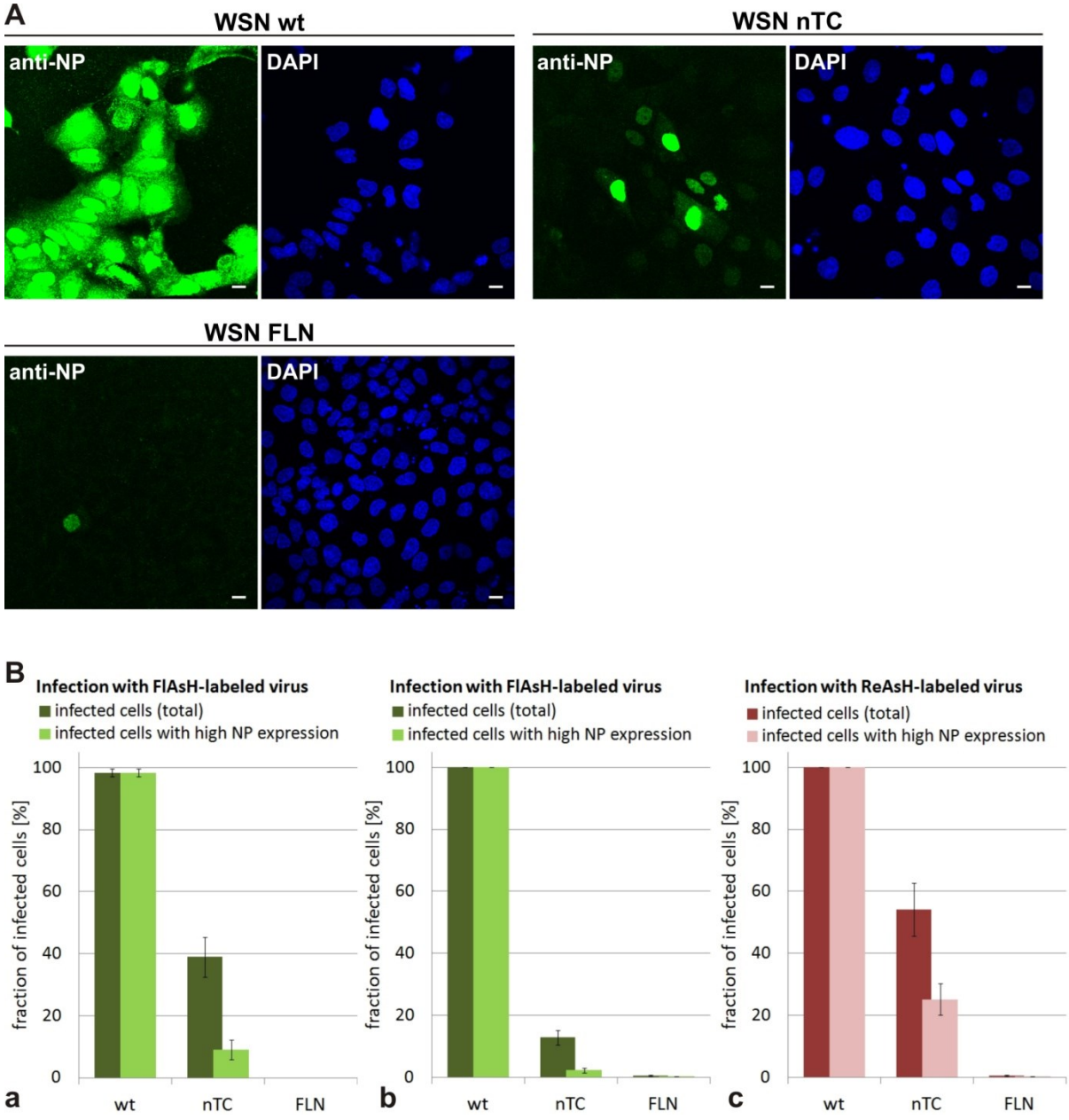

Fig. 32: Infection of MDCK II cells with FlAsH- or ReAsH-labeled virus. WSN wt, nTC and FLN virus preparations were labeled with 2 µM FlAsH or ReAsH for 1.5 h and purified by sucrose gradient (3.2.4.2). MDCK II cells (~1x10^6 per dish) were then infected with equal amounts of the labeled virus according to protein determination (A: 10 µg; B: (a) 18 µg, (b) 15 µg, (c) 10 µg). At 17 h p.i., cells were fixed and immunostained with anti-NP-FITC antibody. DNA counterstaining was performed with DAPI. Images were acquired with constant settings and quantitatively analyzed for the fraction of infected (NP-positive) cells. (A) Infection with ReAsH-labeled virus at 17 h p.i. Confocal fluorescence images show varying NP expression levels between wt, nTC and FLN virus-infected cells and a varying degree of the cytopathic effect. Scale bar, 10 µm. (B) Results of three independent experiments are represented in graphs a, b and c. Data in (a) are exceptionally referring to infection at 20 h p.i. At least seven frames were analyzed per sample and not less than 150 cells. Results are given as mean value ± SEM. The total fraction of infected cells (dark green/red) was determined as the number of NP expressing cells per number of cell nuclei (DAPI signals). The fraction of cells with high NP expression (light green/red) was evaluated by the number of NP nuclear signals reaching the maximally detectable pixel intensity (an arbitrary threshold that is met by all wt virus-infected cells) per total number of cell nuclei.

analysis by confocal fluorescence microscopy (Fig. 32A). According to NP expression and the CPE, the infectivity of FlAsH- and ReAsH-labeled WSN nTC virus was significantly reduced compared to WSN wt virus. One hundred percent of wt virus-treated cells were infected and expressed NP, whereas only a fraction of nTC virus-treated cells were infected according to NP detection. Consistently, the CPE was considerably reduced in WSN nTC virus infection compared to WSN wt virus infection, and the NP expression levels in nTC mutant virus-infected cells were found to be far below those of wt virus-infected cells. Albeit, it was the WSN FLN virus-infected sample which was most attenuated compared to wt virus infection. The labeled WSN FLN virus was, with few exceptions, not able to infect the cells. A CPE was not detectable, and NP expression levels were very low compared to nTC and wt virus infections.

For a quantitative comparison, the total fraction of infected (i.e. NP-expressing) cells was determined in three independent experiments (Fig. 32B). For both mutant virus strains, which were labeled with either FlAsH or ReAsH, the fraction of infected cells was found to be significantly lower than the fraction of infected cells in wt virus infection. These data suggest that even though numerous mutant virus particles were added and were probably endocytosed by the cells (compare Fig. 31) (possibly similar numbers as in wt virus infection where the same amount of protein was applied), only a small number of cells actually became infected. This is consistent with the finding that numerous FlAsH- and DiD-labeled virus particles were observed in virus-treated cells, but release of the genome and transport into the nucleus as a prerequisite for infection were not observed (Fig. 31). The small fraction of viral genomes of WSN nTC virus that entered the nucleus for successful infection (Fig. 32A, B), might have been missed when studying virus entry at the single particle level due to the large majority of non-infecting virus particles. It is also possible that a delayed release of the labeled genomes from the endosomes might have occurred only after the observation period (which was within the first hour after infection).

Overall, the results of reduced infectivity are consistent with the finding that the viral genomes of the mutant viruses were largely unable to enter the cell nucleus. In conclusion, the use of fluorescently labeled WSN FLN virus to study virus entry is apparently not feasible. The use of labeled WSN nTC virus, though, might allow the acquisition of data regarding genome release and nuclear import. However, it remains doubtable if such data is representative for wt virus infection, e.g. for measuring the pH dependence of vRNP release or the kinetics of vRNP nuclear import.

As the signal intensities of NP expression (Fig. 32A) differed markedly among the three strains, not only the total fraction of infected cells, but also the fraction of infected cells with high NP expression was determined for each sample (Fig. 32B, pale green/red). To this end, an arbitrary fluorescence intensity threshold was chosen that included all wt virus-infected cells and that was supposed to exclude all cells with low NP signals which may result from incoming NP rather than newly expressed NP or from infection with strongly attenuated virus. It was found that cells with strongly attenuated NP expression represented a large fraction of the cells infected with labeled mutant viruses (Fig. 32B).

4.2.7 Live-cell imaging of the fluorescently labeled viral genome in WSN nTC virus-infected cells

Recombinant WSN nTC mutant virus was finally used to study fluorescently labeled viral genomes during transport and assembly in the cytoplasm of living infected cells.

To this end, MDCK II cells were infected with WSN nTC virus (MOI 1). WSN wt virus-infected cells served as control cells to assess unspecific background labeling. Since preliminary experiments had shown that ReAsH was better suitable to label cytoplasmic NP than FlAsH (4.2.4.3) and since the signal-to-noise ratio was generally better for ReAsH than for FlAsH labeling, biarsenical labeling of the infected cells was performed with ReAsH. At first, standard labeling was performed at 7 h p.i. with 1 µM ReAsH for 1 h at RT (3.2.2.4.3). Images were then acquired with an inverted epifluorescence microscope equipped with a highly sensitive CCD camera. For tracking the infected cells over time, images were recorded at an interval of 500 ms over a period of 10 min. Measurements were performed at 37 °C. ReAsH efficiently labeled nTC-NP, yielding characteristic nuclear and cytoplasmic NP signals as described above (4.2.4), and even though the cytoplasmic punctate signals were prominent, they were completely immobile. Any fast or slow movement could not be recorded within the acquisition period. Consequently, labeling conditions were altered attempting to preserve the cellular dynamics. The incubation temperature during labeling was shifted to 37 °C. Longer and shorter incubation times were tested as well as higher and lower dye concentrations. Time series were acquired between 7 h and 9 h p.i. or between 16 and 19 h p.i. Specific labeling conditions were as follows: 2 µM ReAsH for 15 min; 0.1 µM ReAsH for either 15 min, 3 h or 4 h; 0.01 µM ReAsH for either 15 min, 1.5 h or 17 h, and finally 0.001 µM ReAsH for 17 h. The labeling results differed markedly regarding absolute signal intensity and bleaching sensitivity, but also with respect to the emergence of unspecific background (including punctate cytoplasmic signals). Labeling with 0.01 µM ReAsH for

1.5 h was found to yield the best results. However, all differently treated samples shared the fact that ReAsH-labeled fluorescent structures did not show any dynamic behavior with a very few exceptions. Small dot-like particles with very low signal intensities were observed occasionally to perform fast directional movements. There were however not more than four mobile particles in 30 samples and a multitude of measurements.

Even though preliminary experiments had shown that ReAsH does not impair replication of WSN wt virus and did not affect the presence of cytoplasmic nTC-NP in infection (4.2.4.3), thereby implying that the cellular cytoskeleton was not critically affected by ReAsH labeling, these results suggest the interference of ReAsH labeling with cytoplasmic transport. For comparison, labeling was additionally performed with FlAsH, for which phenotypic effects on cells have not been reported. However, FlAsH labeling (1 µM, 1 h, 37 °C) yielded the same results as ReAsH labeling: Characteristic nuclear and cytoplasmic nTC-NP staining was detectable, but mobility of the fluorescently labeled structures was repeatedly not observed. Accordingly, it has to be concluded that WSN nTC virus cannot serve to analyze the dynamic behavior of fluorescently labeled vRNP complexes by single particle tracking.

4.2.8 Correlated fluorescence and electron microscopy of infected MDCK II cells

Even though TC-tagged mutant virus was not suitable to study the dynamic behavior of fluorescently labeled vRNPs during infection (4.2.7), ReAsH-labeled nTC-NP was furthermore tested for its usability in correlative fluorescence and electron microscopy for high resolution analysis of vRNP complexes in infection. Correlated electron microscopy is based on the formation of singlet oxygen by excited fluorophores like ReAsH, leading to oxidative polymerization of diaminobenzidine (DAB) which can then be visualized by electron microscopy [460]. Intrinsically fluorescent proteins, which form a β-barrel structure encompassing the fluorophore, are typically unable to mediate photoconversion of DAB. Therefore, the genetically encoded TC-tag binding to ReAsH provides the requirements to couple genetically encoded labeling with high resolution electron microscopy imaging.

To test the applicability of ReAsH-labeled nTC-NP for correlated electron microscopy, samples were prepared as follows: MDCK II cells were infected with WSN wt virus or with a mixture of WSN nTC and WSN wt virus. The mixture of WSN nTC with WSN wt virus was used to dilute nTC-NP with wt NP in order to reduce possible intermolecular cross-linking of the TC-tag by ReAsH labeling. At 20 h p.i., the cells were labeled with ReAsH according to the standard protocol (3.2.2.4.3). Subsequent processing of the samples was based on the

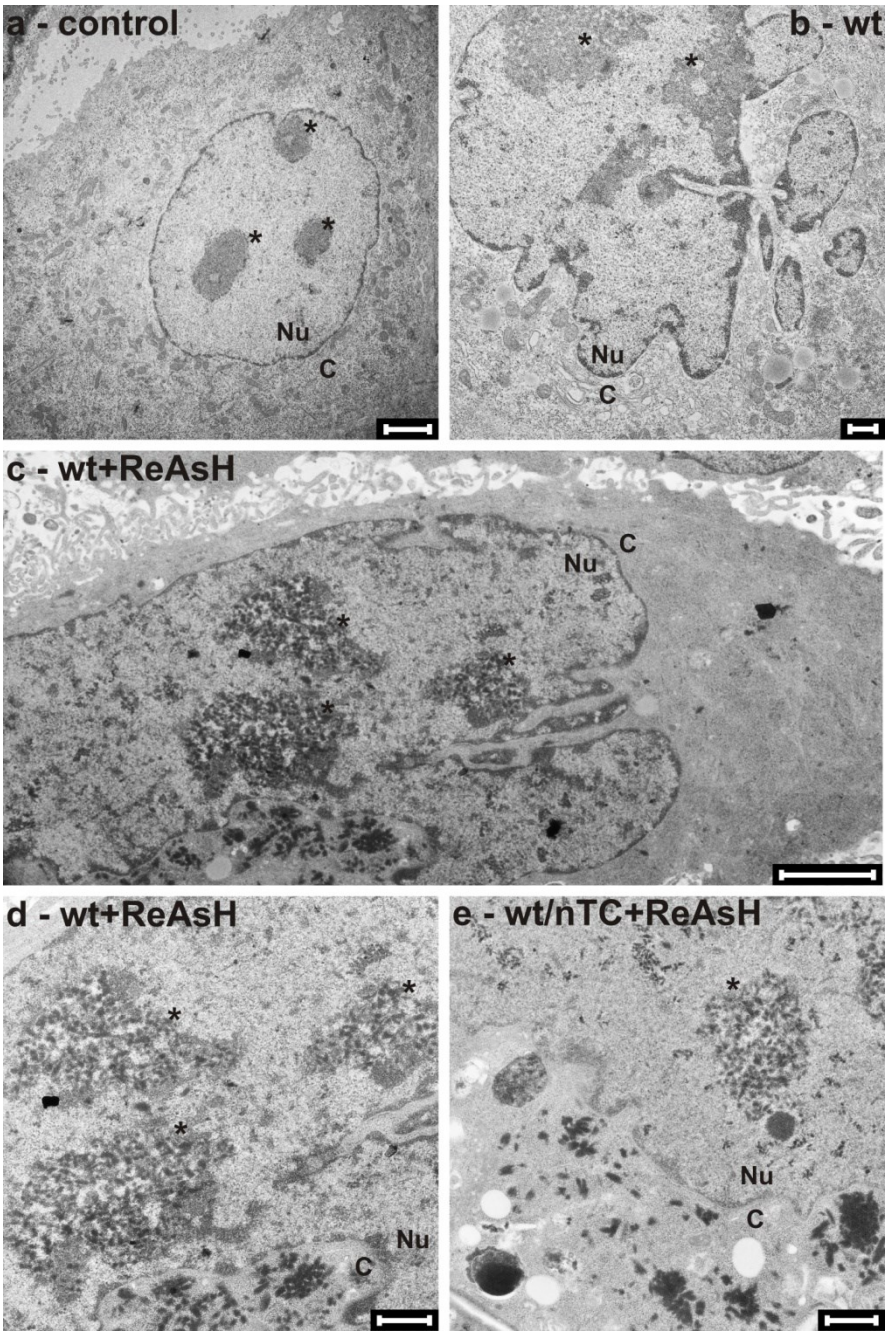

Fig. 33: Transmission electron micrographs of infected MDCK II cells (20 h p.i.). (a) MDCK II cell, untreated. (b, c, d) Cells were infected with Influenza A/WSN wt virus. Representative images were selected with a focus on the cell nuclei. In (c, d), the cells were additionally stained with ReAsH and subjected to photoconversion treatment. (d) Enlargement from (c). (e) Mixed infection with Influenza A/WSN wt and nTC mutant virus followed by ReAsH staining and photoconversion. Nucleoli are marked by asterisk. Nu: nucleus, C: cytoplasm. Scale bar, (a, c) 2500 nm and (b, d, e) 1000 nm.

protocol published by Gaietta *et al.* [460] and is described in detail in section 3.2.3.4. ReAsH-labeled were recorded by fluorescence microscopy. To be able to retrieve the same cells for photoconversion treatment and for electron microscopy, the cells were grown on a gridded cover-slip. Photoconversion was then performed by intense illumination of the cells in the presence an oxygenated solution of DAB until the illuminated area displayed the brown color

of the DAB precipitate. Control samples with uninfected and wt virus-infected cells were neither labeled with ReAsH nor subjected to photoconversion treatment. Processing of the samples for transmission electron microscopy (TEM) was then performed by Maik Lehmann and Gabriele Drescher (Humboldt-Universität, Berlin). The cells which had previously been recorded by fluorescence microscopy and subjected to photoconversion could be precisely retrieved by the distinct, dark DAB precipitates. Cells were post-fixed with osmium tetroxide, stained with uranyl acetate and dehydrated, then embedded, trimmed and finally sectioned (3.2.3.4). TEM images of 70–90 nm sections were acquired and eventually compared to fluorescence images. Representative cells and patterns are shown in Fig. 33 and Fig. 34.

An example of an uninfected and non-labeled control cell is given in Fig. 33a. It displays the typical morphology of MDCK II cells with a round-shaped nucleus and distinct, rounded nucleoli. For comparison, a nucleus from the WSN wt virus-infected cells is displayed in Fig. 33b. Infected cells typically display a fragmented nuclear structure and irregular, coarse-grained nucleoli. When WSN wt virus-infected cells were additionally labeled with ReAsH and treated with DAB for photoconversion (Fig. 33c, d), the contrast of the coarse-grained nucleolar structures was enhanced and they appeared as dark, electron-dense structures. Additionally, elongated and fine structures were observed throughout the nucleus. Furthermore, small, often spindle-shaped structures appeared as electron-dense accumulations in certain regions of the cytoplasm close to the nucleus. This can be seen in the bottom part of Fig. 33c and in the enlarged section in Fig. 33d. Upon magnification, cytoplasmic inclusions were found to be surrounded by dot-like structures resembling ribosomes (not shown). It should be emphasized that these cells did not express TC-tagged NP suggesting that the electron-dense structures were induced by infection with wt virus and photoconversion independently of the TC-tag.

Equivalent electron-dense structures were found in cells infected with a mixture of WSN wt and WSN nTC virus: the coarse-grained, irregular nucleoli, the fine, elongated nuclear structures and the spindle-shaped cytoplasmic accumulations. It seems very tempting to speculate that the fine elongated structures in the nucleus might represent ReAsH-labeled TC-tagged vRNPs. However, the correlation of ReAsH fluorescence signals with the occurrence of elongated nuclear structures in TEM images demonstrated that the fine, elongated structures occurred independently from the ReAsH signal in the nucleus (Fig. 34). Thus, these structures do not represent specifically ReAsH-labeled vRNPs. Phase contrast and ReAsH fluorescence images of infected and ReAsH-labeled cells acquired with an inverted epifluorescence microscope are shown in Fig. 34 a–c, respectively. This section of the sample

was selected and further analyzed by TEM (Fig. 34e). The corresponding cells in electron micrographs were identified by comparison of the cell shape, the cell cluster and distinctive features like the electron-dense spot in one of the cell denoted as cell no. 2. Cell shapes did not perfectly match when comparing phase contrast with TEM images, as the TEM image shows only a 70–90 nm section of the cells, whereas the phase contrast image shows a projection of the whole cells by transmitted light, including also overlapping growth of the cells. Three cells designated “1”, “2” and “3” are shown at higher magnification in Fig. 34g. Cell 1 displayed a relatively smooth appearance of the cytoplasm and the nucleus without any particular electron-dense structures. The nucleus comprised three oval-shaped, intact nucleoli with the characteristic bright fibrillar centers surrounded by the dense fibrillar component (compare [485]). Enlarged sections of the nucleus are shown in Fig. 34h and i. According to characteristic changes which were observed upon infection of the cells with WSN wt virus (Fig. 33), cell 1 was presumably neither infected with WSN wt virus nor with WSN nTC virus which can be inferred from the absence of nuclear ReAsH staining (compare Fig. 34b). In contrast, cell 2 displayed ReAsH labeling of the nucleus indicating infection with WSN nTC virus. Whether a double infection with WSN wt virus had occurred cannot be assessed. The appearance of characteristic electron-dense structures as described before was less pronounced than in other cells, but clearly detectable. The presence of nucleoli could however not be observed. Some electron-dense structures were found in the cytoplasm and fine, elongated electron-dense structures were detected in the nucleus. Enlargements of these elongated nuclear structures are shown in Fig. 34j and k. They often appeared to be either branched or be an accumulation of tangled elements. However, these structures were not specific to nuclei with ReAsH-labeled nTC-NP. The same structures were found in cell 3 (Fig. 34 l–o), which was devoid of any ReAsH signal. This cell featured numerous cytoplasmic spindle-shaped structures, irregular nucleoli and elongated and branched nuclear structures (Fig. 34n, o) suggesting that this cell had been infected with WSN wt virus. nTC-NP expression could be excluded by the absence of ReAsH labeling.

In summary, the treatment of infected cells by ReAsH labeling and the photoconversion procedure apparently enhanced detection of subcellular electron-dense structures that were induced by WSN wt virus infection. Detection of structures specific to WSN nTC virus infection, i.e. detection of TC-tagged vRNPs, was however not achieved. Whether this was a technical problem or a systematic failure remains to be determined. Correlated electron microscopy using ReAsH photoconversion in Influenza virus-infected cells does not seem to provide a satisfactory specificity due to the large number of various electron-dense structures

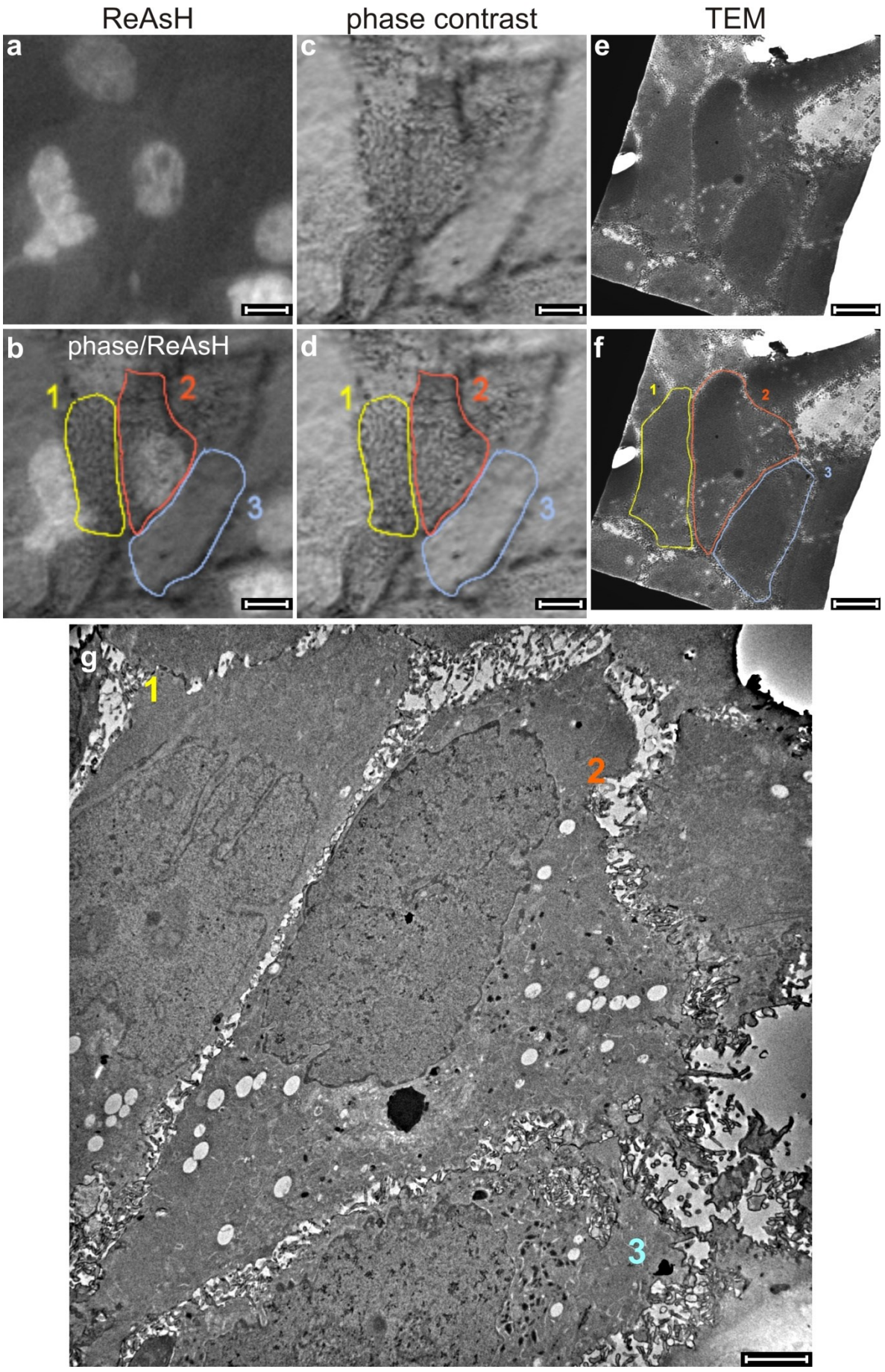
ReAsH
phase contrast
TEM
a
c
e
b
phase/ReAsH
d
f
1
2
3
g
1
2
3

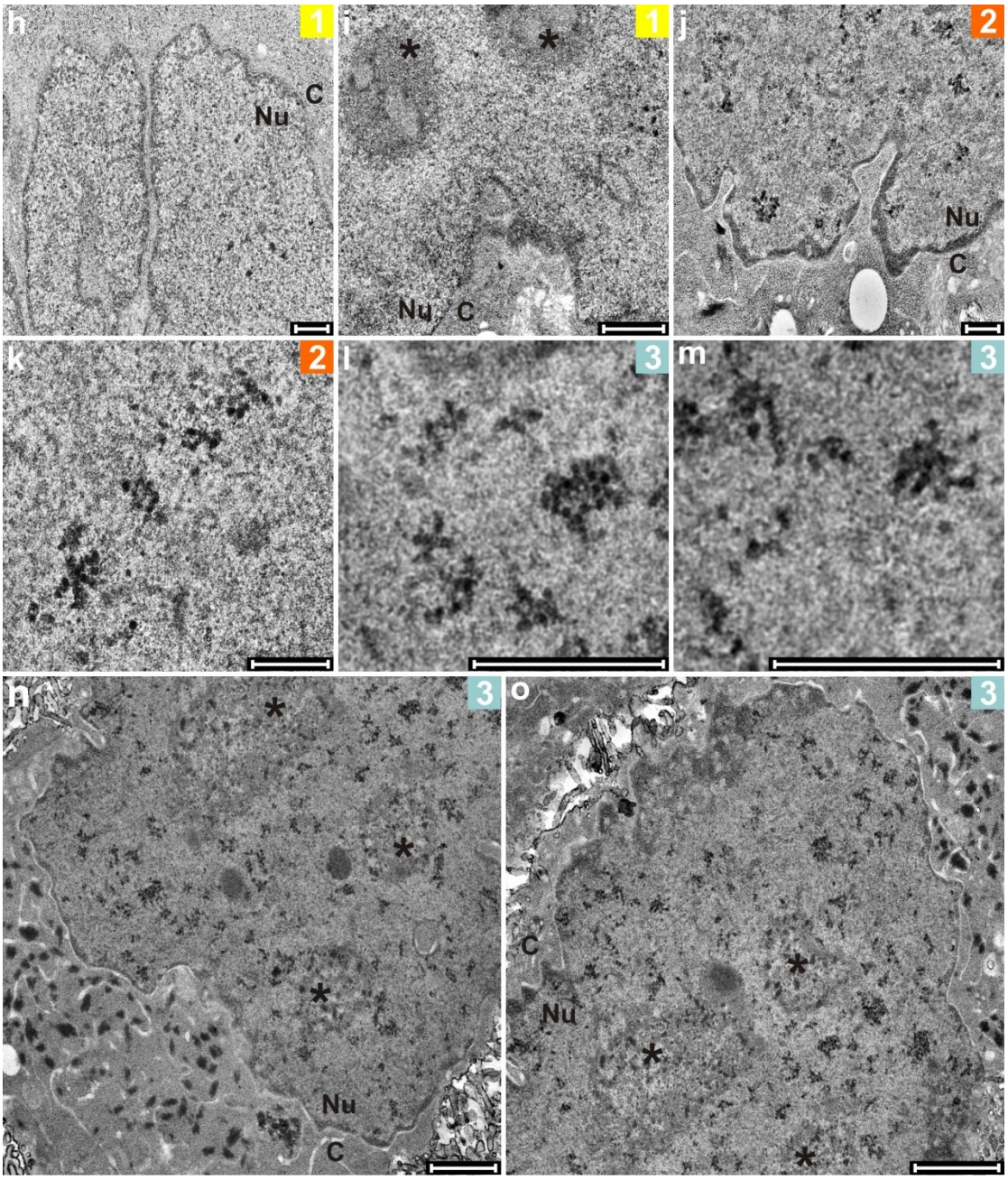

Fig. 34: Correlated fluorescence and transmission electron microscopy. MDCK II cells were infected with a mixture of Influenza A/WSN wt and nTC mutant virus and stained with ReAsH at 20 h p.i. (a, b) ReAsH fluorescence was recorded before photoconversion. (b, c, d) Phase contrast images showing dark, precipitated DAB were acquired after 15 min of photoconversion. (e–o) Transmission electron microscopy (TEM) of the photoconverted cells was performed. (e, f) The cluster of cells that had been detected by light microscopy was identified by cell shape and the electron-dense spot as landmark. (b, d, f) Three cells that were analyzed in more detail are numbered ("1", "2", "3") and marked by outline. Only cell no. 2 displayed a bright nuclear ReAsH signal. (g) Overview of the cells from (f) with higher resolution. Cells no. 2 and 3 contained small, electron-dense, elongated or tangled nuclear structures and dark cytoplasmic spots, whereas cell no. 1 was lacking these structures and displayed round, intact nucleoli. Enlarged sections of the three cells are shown in (h–o): (h, i) Nuclear sections of cell no. 1. The nucleoplasm was relatively smooth with a few small spots. (j, k) Regions of the cell nucleus no. 2 with electron-dense, irregular structures. (l, m) The same type of electron-dense nuclear structures were enlarged from cell nucleus no. 3. (n, o) Sections of cell no. 3, rich in nuclear and cytoplasmic dark structures and with irregular nucleoli. Nu: nucleus, C: cytoplasm, asterisk: nucleolus. Scale bar, (a–f) 5000 nm, (g) 2500 nm, (h, j, k) 500 nm and (i, l–o) 1000 nm.

in infected cells. Therefore, ReAsH photoconversion for detection and high-resolution imaging of TC-tagged viral proteins during infection was not further pursued and is not recommended.

4.3 Analysis of intrinsic subcellular targeting of NP using fluorescent NP fusion proteins

In the third part of this work, the intrinsic properties of NP were studied in a cellular context in the absence of virus infection, using fluorescent NP fusion proteins. The subcellular distribution, sites of preferential targeting and site-specific mobility of NP in living cells were analyzed. Initially, expression of NP constructs was studied in preparation for the use of these fluorescent NP fusion proteins in the context of viral infection (section 4.4). Repeated observation of a non-homogeneous nuclear distribution, however, prompted a detailed analysis of the subnuclear targeting of NP. While NP is known to localize to the cell nucleus, its prominent subnuclear distribution has not been characterized yet. Expression of NP and fluorescent NP constructs has been investigated in previous studies [121,123,124,260,299,360,363], but their focus was the nuclear-cytoplasmic transport of NP and the role of NP in transport processes during infection. Since proteomic and yeast-two-hybrid screens have identified numerous cellular interaction partners of NP in recent years [103,358], these findings indicate a role of NP in host cell interactions apart from transport processes, such as the inhibition of the host's antiviral response [347,350]. In the present study, the site-specific aspect of NP interactions with the host cell, in particular with the cell nucleus, was addressed based on the concept of functional compartmentalization of the nucleus, which was introduced by Schul and coworkers in 1998 [486] and was consolidated during the past years [487,488,489,490]. This concept suggests that the spatial correlation of subnuclear structures is not random and has functional implications. Genomes of other nuclear replicating viruses have previously been reported to be targeted to specific subnuclear sites by viral proteins involved in viral transcription and replication [491,492].

Does NP also target specific subnuclear domains either to recruit cellular machinery for viral replication or to interfere with host cell processes? The subnuclear localization of exogenously expressed NP was hence investigated in more detail than in previous studies. To this end, fluorescent and photoactivatable protein tags were used to study the dynamic behavior of NP and sites of preferential association. Furthermore, special NP constructs with a nuclear export signal (NES) were generated to lower the local nuclear NP concentration and to reveal sites of high affinity for NP.

In the first part of this chapter, expression and detection of various NP constructs will be characterized. In the second part, the application of these constructs to analyze subnuclear

targeting of NP will be described, while in the third part cytoplasmic localization of NP will be addressed.

4.3.1 Expression and analysis of fluorescent NP fusion proteins

4.3.1.1 Expression of NP constructs

A variety of fusion constructs of Influenza A/FPV/Rostock/34 NP with fluorescent proteins was generated using standard molecular biology techniques (3.2.1). An overview of all constructs and technical specifications are given in Tab. 2 (3.1.1.8).
First, fusion proteins of NP with monomeric enhanced yellow fluorescent protein (mEYFP) were expressed in MDCK II (Fig. 35) and CHO-K1 (Fig. 36) cells. C-terminal (a–c) and N-terminal (d–f) mEYFP-tags yielded comparable results in both cell types. As expected from previous studies [121,123], NP constructs accumulated predominantly in the cell nucleus. Characteristic patterns of heterogeneous subnuclear distribution were observed. A selection of frequently detected expression patterns is shown in Fig. 35 and Fig. 36: NP fusion proteins showed varying degrees of local enrichment in the nucleoplasm. They distributed either uniformly with a granular appearance (a, d), or they were found to be locally enriched in speckles or bright irregular structures (b, e). Larger accumulations appearing more compact and highly enriched with fluorescent NP fusion proteins and filling major parts of the nuclear volume were also frequently observed (c, f). Additionally, a small fraction of mEYFP-tagged NP always localized to nucleoli (indicated by arrowheads). But only in a subset of cells, nucleoli appeared as prominent bright structures in which the fluorescent construct was enriched relative to the surrounding nucleoplasm (a, d). Nucleoli were identified by high contrast in DIC images. A nucleolar targeting signal of NP was reported previously [123].
Upon expression of mEYFP alone, the free fluorescent protein distributed rather homogeneously throughout the cells with a slight bias to accumulate in the cell nucleus (Fig. 35g), demonstrating that the intrinsic properties of mEYFP were not responsible for the above-described subcellular distribution of the mEYFP-tagged NP constructs.

The same patterns of subcellular distribution that were detected for NP constructs at 24 h p.t. were also found at earlier and later times post-transfection (Fig. 37): Granular and uniformly distributed nuclear NP-mEYFP as well as irregular subnuclear structures highly enriched with NP-mEYFP were detected at 4 h, 7 h and 48 h p.t. The tendency to form large, localized accumulations was however strongest around 24 h p.t. when expression levels were high, whereas a more uniform distribution with a granular appearance and small speckles was more

frequently found at 4 and 48 h p.t., indicating a correlation with expression levels of NP fusion proteins. A slight increase of the cytoplasmic mEYFP signal over time was possibly caused by free fluorophore molecules which formed as a byproduct in NP-mEYFP expressing cells as demonstrated by immunoblotting (Fig. 40A (c)). A shift of NP localization over time due to intrinsic properties of NP cannot be excluded though.

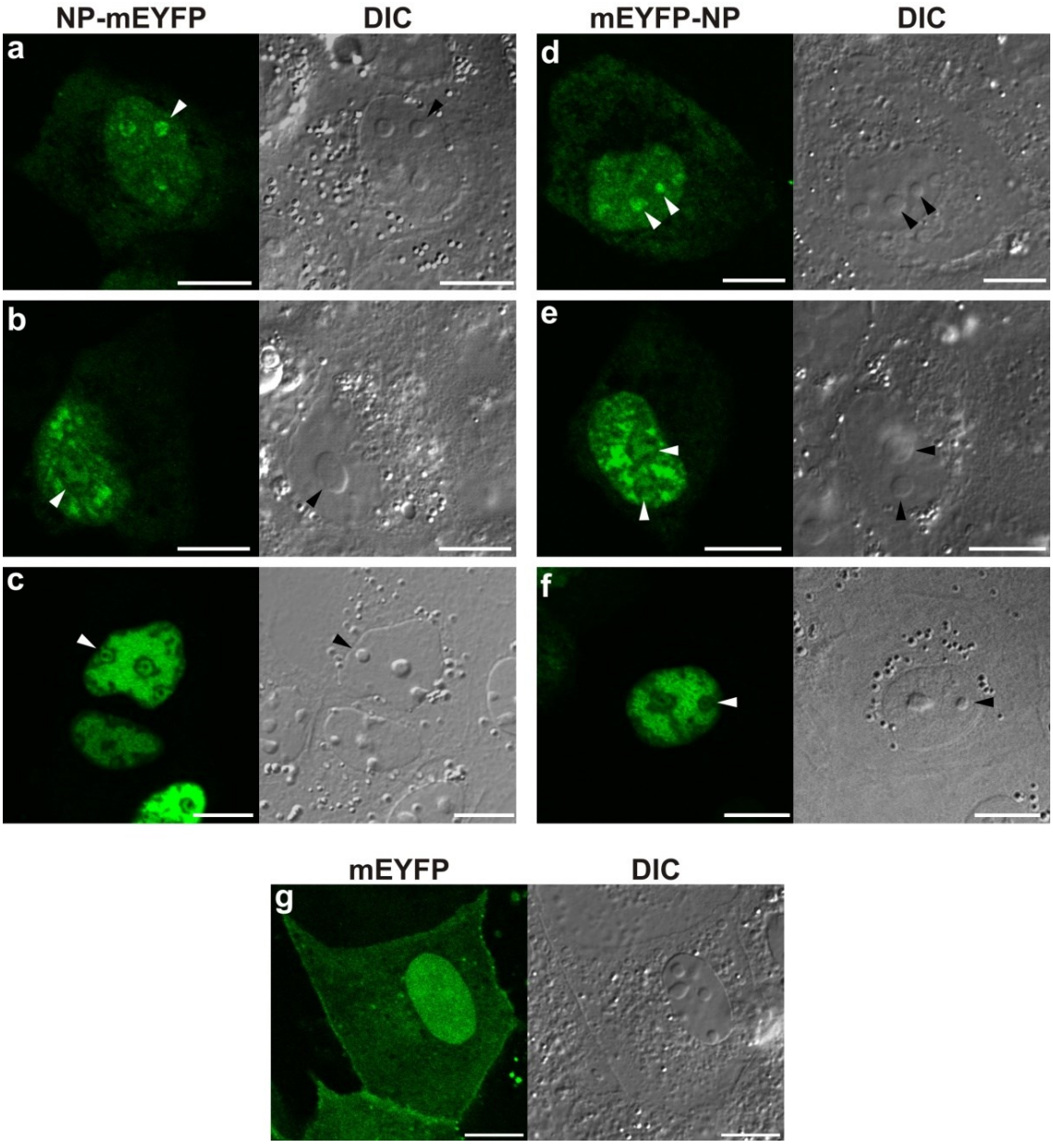

Fig. 35: Expression of mEYFP fusion proteins of NP in MDCK II cells (24 h p.t.). The cells were transfected with (a–c) NP-mEYFP, (d–f) mEYFP-NP or (g) mEYFP and fixed at 24 h p.t. The mEYFP fluorescence signal and corresponding transmitted light DIC images were recorded by confocal fluorescence microscopy. Both NP constructs showed predominantly nuclear accumulation and similar patterns of local enrichment in the cell nucleus. A selection of representative images is shown. Arrowheads point to nucleoli. Scale bar, 10 µm.

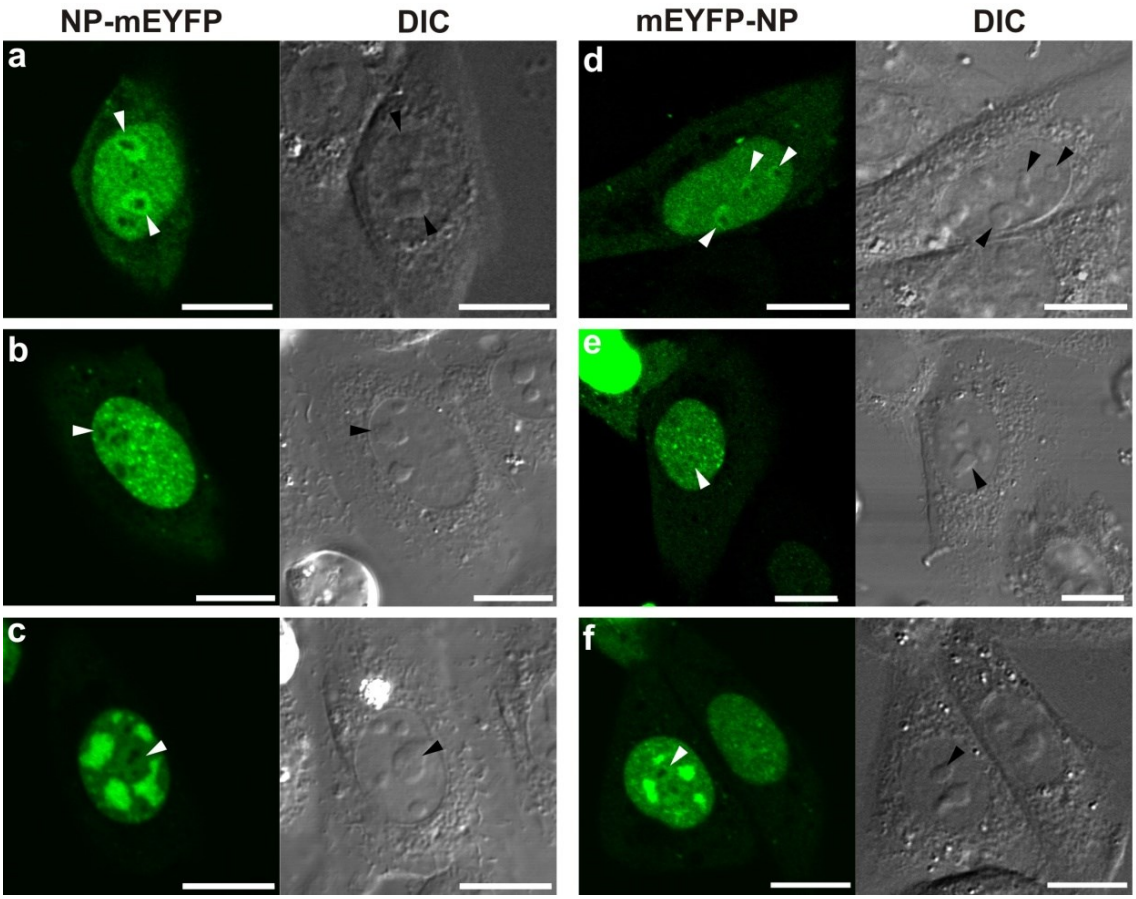

Fig. 36: Expression of mEYFP fusion proteins of NP in CHO-K1 cells (24 h p.t.). (a–c) NP-mEYFP and (d–f) mEYFP-NP were expressed in CHO-K1 cells, and EYFP fluorescence was analyzed in living cells by confocal fluorescence microscopy. Both constructs displayed nuclear accumulation and similar patterns of local enrichment in the cell nucleus with a varying degree of heterogeneity. Representative images are shown. Arrowheads point to nucleoli. Scale bar, 10 µm.

It was speculated that the observed non-homogeneous distribution of NP constructs in the nucleus might result from preferential association of NP with specific subnuclear domains. To test this assumption and to further exclude the possibility that self-polymerization as an intrinsic feature of NP caused the formation of unspecific precipitates, a fusion protein of NP with the photoactivatable fluorophore Dendra2 was generated to monitor protein dynamics, and mutations known to prevent NP oligomerization were subsequently introduced into these NP probes.

Upon expression in MDCK II cells, the fusion protein NP-Dendra2 displayed a predominantly nuclear localization and formed local subnuclear accumulations comparable to those formed by mEYFP-tagged NP (Fig. 38 a–c). The free fluorophore Dendra2, on the contrary, distributed evenly throughout control cells, but was largely absent from nucleoli (Fig. 38d). By introducing the amino acid substitutions E339A or R416A into the NP sequence of NP-Dendra2, yielding NP-E339A-Dendra2 and NP-R416A-Dendra2 (Tab. 2), two different

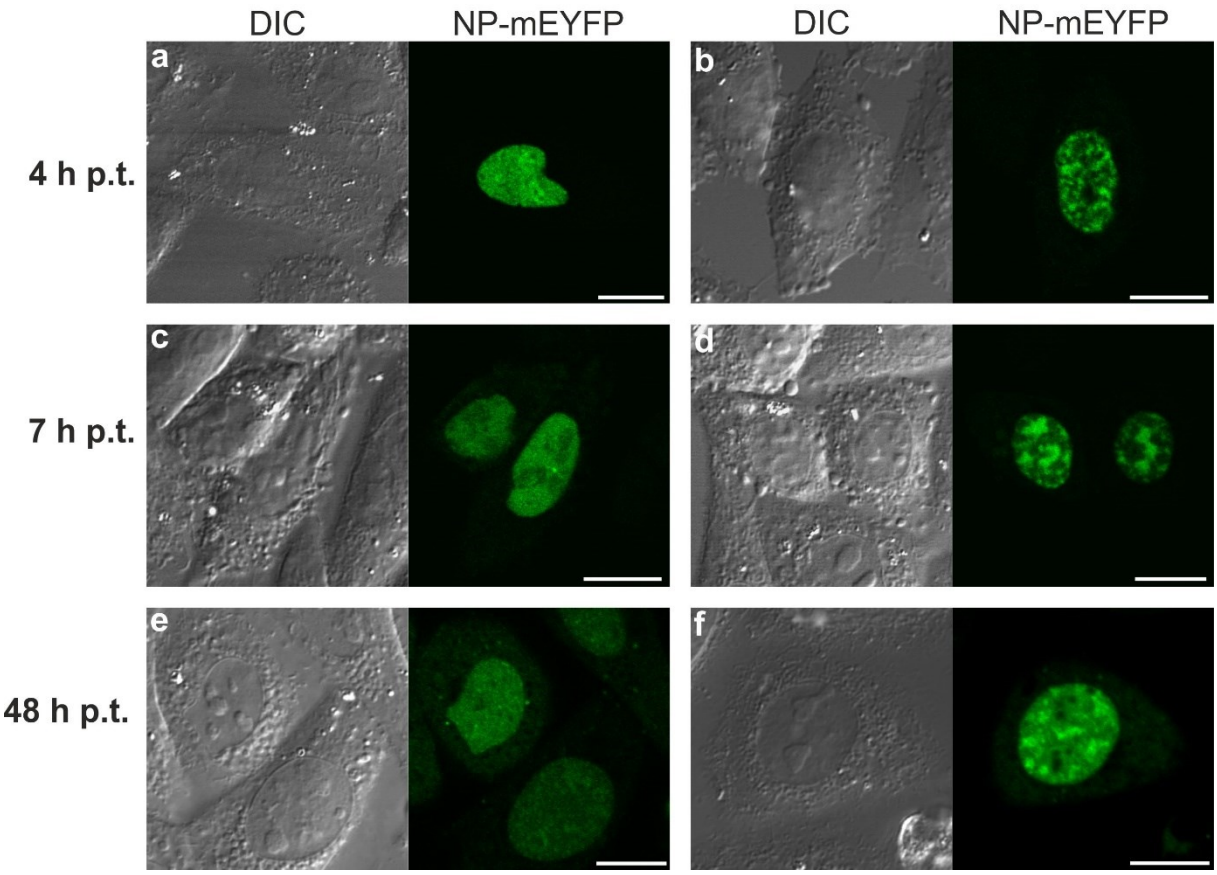

Fig. 37: Expression of NP-mEYFP in CHO-K1 cells at different time points. The EYFP fluorescence signal of NP-mEYFP expression was analyzed by confocal fluorescence microscopy in living CHO-K1 cells at 4 h p.t. (a, b), 7 h p.t. (c, d) and 48 h p.t. (e, f). At each time point, the signal was detected predominantly in the cell nuclei. Representative examples of transfected cells with a uniform, granular distribution of the construct (a, c, e) or with irregularly structured, heterogeneous local accumulations (b, d, f) in the cell nucleus are presented. Scale bar, 10 µm.

monomeric mutants of NP were generated. It was previously shown by electron microscopy [93] and static light scattering [493] that both mutations prevent oligomerization of NP. Remarkably, the two monomeric constructs displayed the same patterns of non-homogeneous subnuclear distribution upon expression in MDCK II cells as the wild-type construct, ranging from a uniformly granular appearance to a speckled appearance or even the formation of large irregular structures highly enriched with the respective protein (Fig. 39). Small, speckled structures were however more frequently observed for the monomeric constructs than in case of wild-type NP-Dendra2, while larger accumulations were less frequently found. These results thus clearly demonstrate that the local accumulations of NP constructs within the nucleus are not the result of NP polymerization, although the formation of larger accumulations was apparently promoted by the ability of NP to self-assemble.

The application of Dendra2 constructs to monitor local protein dynamics as a measure for site-specific affinities will be described in section 4.3.2.

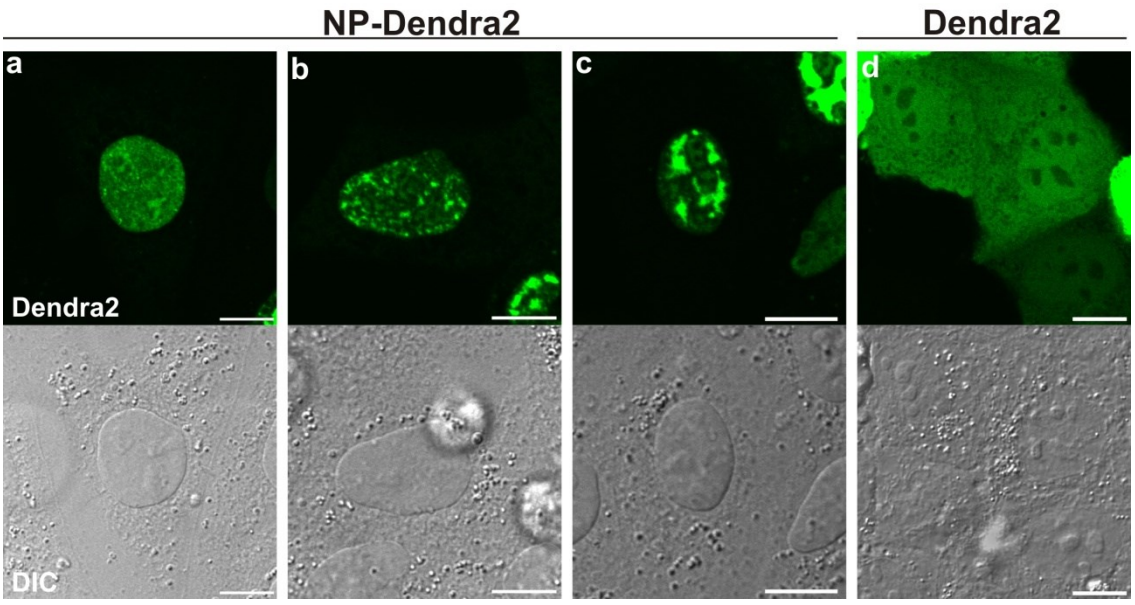

Fig. 38: Expression of NP-Dendra2 fusion protein in MDCK II cells. (a–c) MDCK II cells were transfected with NP-Dendra2 and fixed at 16 h p.t. Dendra2 fluorescence was analyzed by confocal fluorescence microscopy. The construct accumulated in the cell nucleus with a variable degree of heterogeneous local enrichment. Representative images are shown. (d) Control cells expressing free Dendra2 at 16 h p.t. Scale bar, 10 µm.

Expression of the full-length proteins mEYFP-NP, NP-mEYFP, NP-Dendra2, NP-E339A-Dendra2 and NP-R416A-Dendra2 was verified by Western blot analysis of transfected cells by immunodetection of either the mEYFP-tag (Fig. 40A) or the NP moiety (Fig. 40B). An antibody for detection of Dendra2 was not available. In case of NP-specific detection, only protein bands of the size of the full-length proteins (~83 kDa) were detected. Upon detection of the mEYFP-tag however, additional bands demonstrated the presence of truncated mEYFP-tagged proteins in case of NP-mEYFP expression (Fig. 40A, c); the major band aside from the full-length protein corresponded in size to the free fluorescent protein (27 kDa). The failure to detect the truncated forms of NP-mEYFP by monoclonal anti-NP antibody (Fig. 40B) was presumably due to the absence of the antibody-specific epitope from the remaining protein fragments. Neither truncated proteins nor free fluorescent protein were observed by immunodetection of mEYFP in samples expressing the N-terminally tagged mEYFP-NP (Fig. 40A, b). This leads to the conclusion that mEYFP fluorescence signals obtained by fluorescence imaging can unambiguously be assigned to the full-length fusion protein in case of NP expression with an N-terminal mEYFP-tag (mEYFP-NP), whereas expression of the C-terminally tagged NP (NP-mEYFP) was apparently tainted with the formation of free mEYFP and truncated mEYFP-tagged proteins. When NP-mEYFP and mEYFP-NP expression were compared by fluorescence microscopy, contributions of free mEYFP to the NP-mEYFP signal were not obvious though (Fig. 35, Fig. 36). Both constructs apparently displayed qualitatively

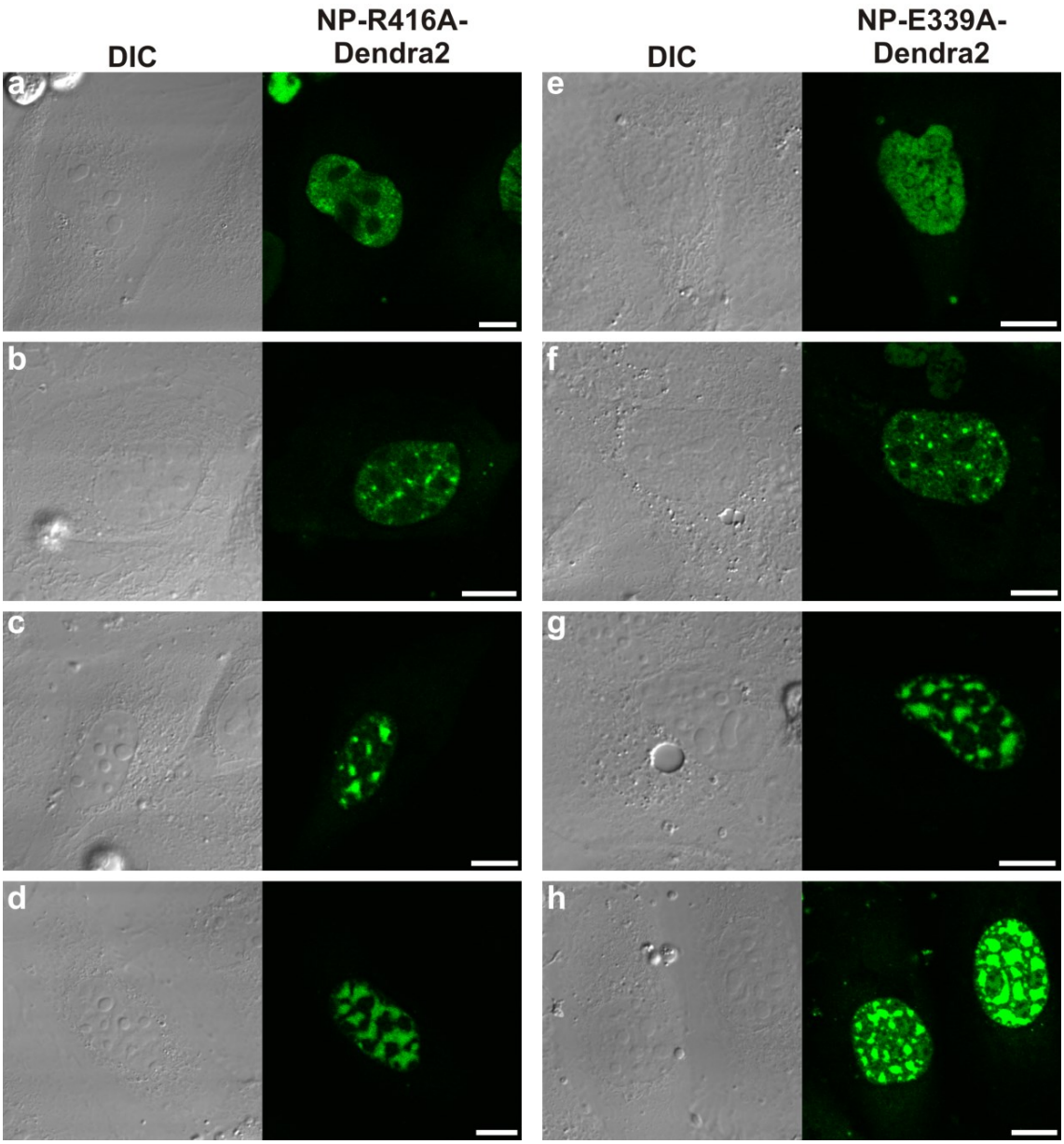

Fig. 39: Expression of NP monomeric mutant constructs NP-R416A-Dendra2 and NP-E339A-Dendra2 in MDCK II cells (16 h p.t). Cells were transfected with (a–d) NP-R416A-Dendra2 and (e–f) NP-E339A-Dendra2. Dendra2 fluorescence was analyzed in living cells by confocal fluorescence microscopy. Representative images are shown. Similar to wt NP constructs, the monomeric NP mutants localized predominantly to the cell nucleus and formed patterns of local accumulations with varying extents of local enrichment. In (h), the Dendra2 signal was detected with considerable detector overload to visualize also fluorescence of lower intensity in nucleoli. Scale bar, 10 µm.

the same subcellular behavior. This was presumably due to the relatively small fraction of free mEYFP in NP-mEYFP expressing cells and its homogenous distribution within the cells. Truncated forms of NP-mEYFP larger than free mEYFP represented a minor fraction of the expressed protein and did apparently not show a noticeable effect on the overall distribution either. This was confirmed by coexpression of C-terminally tagged NP-mEYFP with an N-terminally tagged red-fluorescent NP construct (mCherry-NP, Tab. 2) (data not shown).

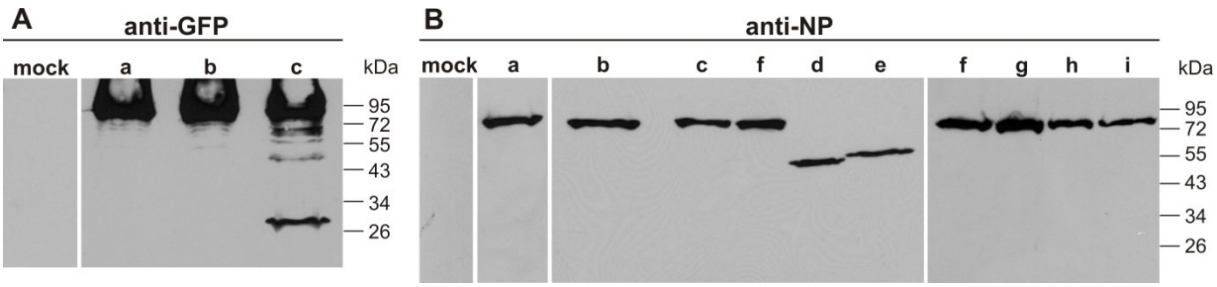

Fig. 40: Western blot analysis of NP fusion protein expression in MDCK II cells. (A) Cell lysates of transfected cells expressing (a) mEYFP-NP-NES, (b) mEYFP-NP and (c) NP-mEYFP were prepared at 24 h p.t. by addition of reducing sample buffer. They were analyzed by SDS-PAGE and Western blotting. Immunodetection of mEYFP was performed with polyclonal anti-GFP antibody and demonstrates efficient expression of the three mEYFP-tagged constructs. The major detected bands correspond to the full-length proteins (~83 kDa). In case of NP-mEYFP (c), additional bands demonstrate the presence of truncated forms of the construct, the main band corresponds in size to the free fluorescent protein (27 kDa). (B) Transfected cells were processed as in (A). Immunodetection of NP constructs was performed with monoclonal anti-NP antibody. Full-length constructs were detected as single bands: (a) mEYFP-NP-NES, (b) mEYFP-NP, (c) NP-mEYFP, (d) NP, (e) NP-NES, (f) NP-Dendra2, (g) NP-R416A-Dendra2, (h) NP-E339A-Dendra2, and (i) Dendra2-NP-NES.

The presence of truncated fluorescent proteins had to be considered more carefully, however, in case of dynamics measurements with Dendra2 constructs (section 4.3.2). It is postulated here that the results for mEYFP-tagged NP constructs can be extrapolated to other fluorescent protein tags which are fused to NP in the same way, e.g. Dendra2. Since the presence of free Dendra2 could not be detected by Western blotting due to the lack of Dendra2-specific antibody, it was therefore assumed that expression of C-terminally tagged NP-Dendra2 (Fig. 38) was – just like in case of NP-mEYFP – accompanied by the formation of free fluorescent protein and truncated forms of the construct. Consequently, an NP fusion protein with N-terminal Dendra2-tag was furthermore generated, which was – by analogy with mEYFP-NP – expected to be untainted by the formation of free Dendra2 or truncated fluorescent proteins, thus suitable to monitor Dendra2-NP mobility as performed in 4.3.2.

Finally, the subcellular distribution of the fluorescent NP constructs was verified to be representative for the expression of untagged wild-type NP. MDCK II cells expressing NP were therefore fixed at 24 h p.t., and the subcellular distribution of NP was visualized by immunofluorescence staining of NP (Fig. 41). NP accumulated in the cell nuclei and showed different types of subnuclear distribution with patterns of local enrichment analogous to fluorescent NP fusion proteins: In some of the cells, NP was enriched in nucleoli (Fig. 41a), while in other cases NP accumulated predominantly in the nucleoplasm and adopted a granular appearance (Fig. 41b). Larger structures, compact and highly enriched with NP as in case of fluorescent NP fusion proteins (Fig. 35b, e), were however not observed for wild-type

NP. Nevertheless, a different type of large, irregular local accumulations was observed by immunodetection of NP. These appeared elongated and curved, surrounding areas depleted of NP (Fig. 41c). It was suspected that these structures were equivalent to the compact, larger structures observed for fluorescent NP fusion proteins, but that only the periphery of these structures was efficiently labeled by immunostaining (implying a very dense packing).

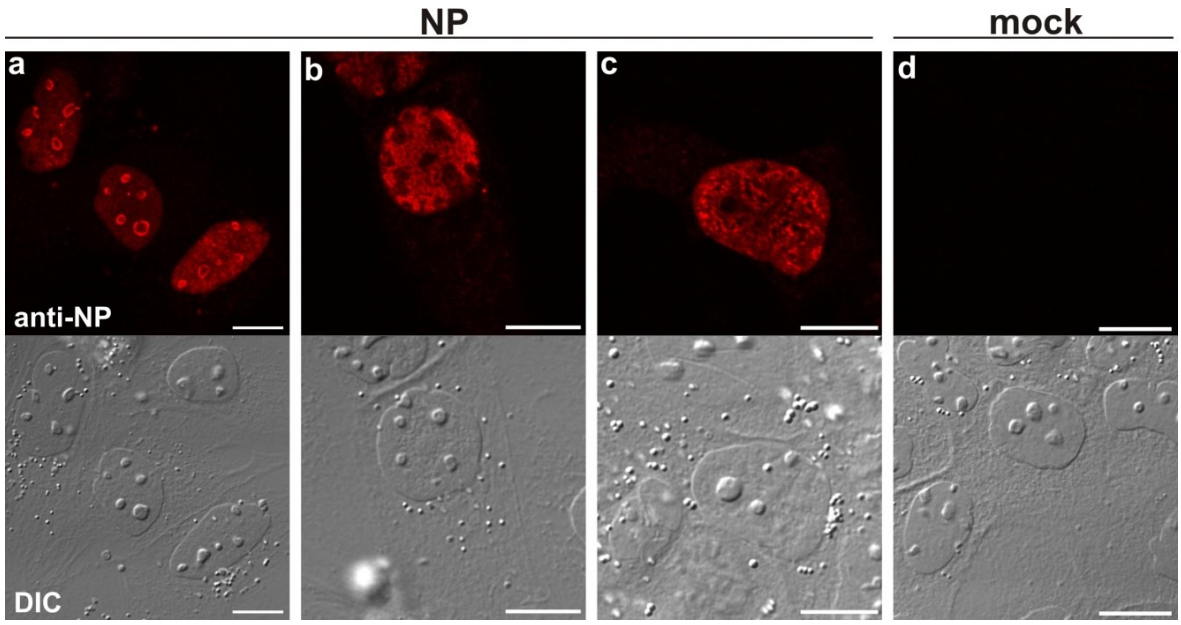

Fig. 41: Immunofluorescence detection of NP expression in MDCK II cells (24 h p.t.). (a–c) MDCK II cells were transfected with NP (from Influenza A/FPV). (d) Control cells were mock-transfected. The cells were fixed at 24 h p.t., immunostained with anti-NP and Alexa568-anti-mouse antibodies and analyzed by confocal fluorescence microscopy. NP localized to the cell nuclei and displayed different patterns of subnuclear distribution. Representative images are shown. Scale bar, 10 µm.

4.3.1.2 Comparative analysis of immunofluorescence and intrinsic protein fluorescence signals

Even though wild-type NP displayed a non-homogeneous subnuclear distribution just like fluorescent NP fusion constructs, slight differences in the appearance of immunofluorescence signals and signals of fluorescent protein tags (compare Fig. 35 and Fig. 38 with Fig. 41) prompted a comparative analysis of the two detection methods. For this analysis, mEYFP-NP-NES was used, an mEYFP-tagged NP construct with a C-terminal nuclear export signal (NES). This construct provided reduced amounts of NP fusion protein in the nucleus and was thereby used later on in this study to unravel sites of preferential association (see 4.3.2). mEYFP-NP-NES was expressed in MDCK II cells which were additionally immunostained for NP. The signal of intrinsically fluorescent mEYFP was then compared to the signal introduced by labeling with NP-specific antibodies (Fig. 42). Expression of the full-length

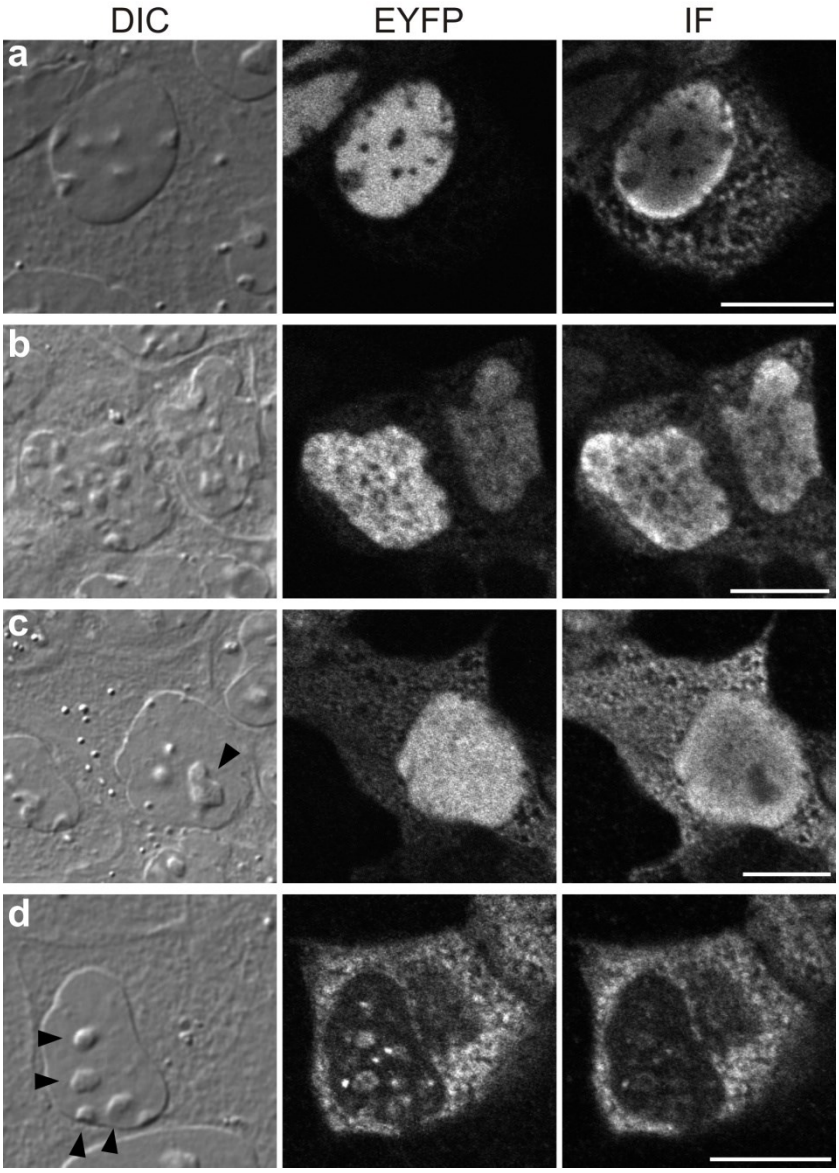

Fig. 42: Comparison of NP immunofluorescence (IF) and EYFP signals in mEYFP-NP-NES-expressing cells. MDCK II cells were transfected with mEYFP-NP-NES and immunostained with anti-NP and Alexa568-anti-mouse antibodies at 24 h p.t. mEYFP and IF (Alexa568) fluorescence signals were sequentially recorded by confocal fluorescence microscopy. Images (a–d) illustrate the discrepancies between IF and instrinsic mEYFP fluorescence. The nuclear export signal (NES) of mYFP-NP-NES caused cytoplasmic accumulation of the construct in a subset of cells, an example of which is shown in (d). Arrowheads point to nucleoli. Scale bar, 10 µm.

protein mEYFP-NP-NES and the absence of truncated fluorescent proteins was verified by Western blotting (Fig. 40, a). Intrinsic mEYFP fluorescence is therefore assumed to accurately report both localization and relative amounts of the full-length NP construct. Nevertheless, striking differences between the NP-specific immunofluorescence signal and the mEYFP signal were observed within cells. In comparison to mEYFP fluorescence, antibodies preferentially labeled cytoplasmic NP rather than nuclear NP (Fig. 42 a–d), leading to the detection of different nuclear-cytoplasmic ratios by immunofluorescence and mEYFP

fluorescence imaging. Presumably, this was the result of a better accessibility of the cytoplasmic compartment for immunostaining. Due to uneven permeation of the antibody through the cells or variable exposure of the NP epitope, immunofluorescence labeling with NP-specific antibodies might be generally more prone to the detection of artifacts than the detection of NP by mEYFP-tag. Prominent differences between immunofluorescence and mEYFP signals were also observed within the nucleus: While mEYFP-NP-NES was spread evenly throughout the entire nuclear volume according to mEYFP fluorescence, immunostaining indicated a preferential accumulation in the periphery of the cell nucleus (Fig. 42 a–c). Preferential peripheral staining might have been caused by a limited perfusion of the inner nuclear compartment with anti-NP antibodies and thus by formation of an antibody concentration gradient. However, other explanations are possible, e.g. a site-specific selective exposure of the NP epitope recognized by the monoclonal anti-NP antibody. Immunofluorescence signals in some cases even implied a polarized distribution of mEYFP-NP-NES in the nucleus (Fig. 42b). Here, the most pronounced immunofluorescence signals typically pointed away from neighboring transfected cells, whereas mEYFP fluorescence signals displayed a non-polarized distribution in the same cells, suggesting again irregularities of the immunostaining, for instance variations of the antibody concentration within the sample due to local depletion or the above-mentioned differential accessibility of the NP epitope.

Another major difference observed refers to the detection of mEYFP-NP-NES in nucleoli. Direct comparison of mEYFP and immunofluorescence signals revealed that the relative amount of mEYFP-NP-NES in nucleoli was typically underestimated by immunofluorescence detection (Fig. 42 c–d). Unlike the mEYFP signal, which frequently indicated similar levels of mEYFP-NP-NES in the nucleoplasm and in nucleoli, the immunofluorescence signal implied that nucleoli were depleted of mEYFP-NP-NES relative to the surrounding nucleoplasm (Fig. 42c). The same failure to detect nucleolar mEYFP-NP-NES by immunostaining was also observed in those cell nuclei that were largely devoid of the NP construct due to the function of the nuclear export signal (Fig. 42d). A predominantly cytoplasmic localization of mEYFP-NP-NES was observed in 42 ± 9 % of the transfected cells (mean ± SD, determined from four independent experiments including a total of 322 cells). In these cells, the remaining nuclear mEYFP-NP-NES associated with nucleoli and speckled structures and was clearly detectable by the mEYFP fluorescence signal, whereas it was only poorly detectable by the immunofluorescence signal. About the reasons for this lack of nucleolar and subnuclear labeling can be speculated as before. Nucleoli were previously shown to be freely accessible

for proteins up to 150 kDa, but the available free volume for penetrating proteins was shown to be reduced compared to the surrounding nucleoplasm, causing a local decrease of freely diffusing proteins like EGFP in nucleoli [494,495]. This might explain the here encountered reduced labeling efficiency of nucleolar proteins by immunostaining with antibodies of 150 kDa. Poor antibody penetration into nucleoli was reported before [496].

The quality of nuclear signals obtained by mEYFP fluorescence was generally better compared to signals obtained by immunofluorescence detection (due to higher and more distinct signals). Intrinsic protein fluorescence was therefore considered promising to gain information on NP subnuclear organization which might have remained unnoticed in previous immunofluorescence studies (see 4.3.2). Moreover, the use of intrinsically fluorescent fusion proteins allows studies in living cells.

The influence of self-quenching of the fluorophores or fluorescence energy transfer between mEYFP and the antibody-coupled fluorophore Alexa568 were considered negligible in this analysis since both Alexa568 and mEYFP have a low tendency of self-quenching [497], and energy transfer from mEYFP to Alexa568 (which requires a close spatial proximity, i.e. high local concentrations or direct interaction) was not consistent with obtained results: Even though site-specific energy transfer can potentially account for higher Alexa568 signals in the cytoplasm or the nuclear periphery, the concentrations of mEYFP-NP-NES were generally lowest in the cytoplasm and thus cannot explain elevated local energy transfer from mEYFP to Alexa568. Furthermore, mEYFP-NP-NES was found to be evenly distributed throughout the nucleus also in the absence of immunostaining, not displaying any enrichment in the nuclear periphery (data not shown). Detection of peripheral enrichment of mEYFP-NP-NES was thus unique to immunofluorescence detection.

Finally, it should be mentioned that the cell-to-cell variability was rather high and not every transfected cell displayed the differences between immunofluorescence and mEYFP signals that were described here. The peripheral nuclear accumulation detected by immunofluorescence seemed to be more pronounced in cells with high expression levels, and differences in detection of nucleolar NP seemed to be affected by a yet unknown factor. However, this comparative analysis clearly showed the general susceptibility of immunofluorescence detection to depict artifacts which do not reflect the actual local protein concentrations.

According to these results, the use of intrinsically fluorescent protein tags is favorable for qualitative and quantitative analysis of NP subcellular distribution in comparison to immunofluorescence detection. Especially the limited accessibility of nuclear NP for

immunostaining strongly suggested the preferential use of intrinsically fluorescent constructs for analysis of the subnuclear localization of NP in following experiments.

4.3.1.3 Comparison of NP expression in infection and transfection

The results obtained for expression of NP constructs in the absence of other viral components were further compared to NP expression in infection (Fig. 43). In infected cells, nuclear accumulation of NP was observed already at 3 h p.i., but in contrast to transfected cells, the distribution of NP shifted to a predominantly cytoplasmic localization later during infection. Cytoplasmic NP appeared here as punctate signals with a laterally polarized distribution, and it frequently accumulated prominently at the plasma membrane (Fig. 43 c–h). Comparable punctate cytoplasmic signals were identified as vRNP complexes by colocalization with

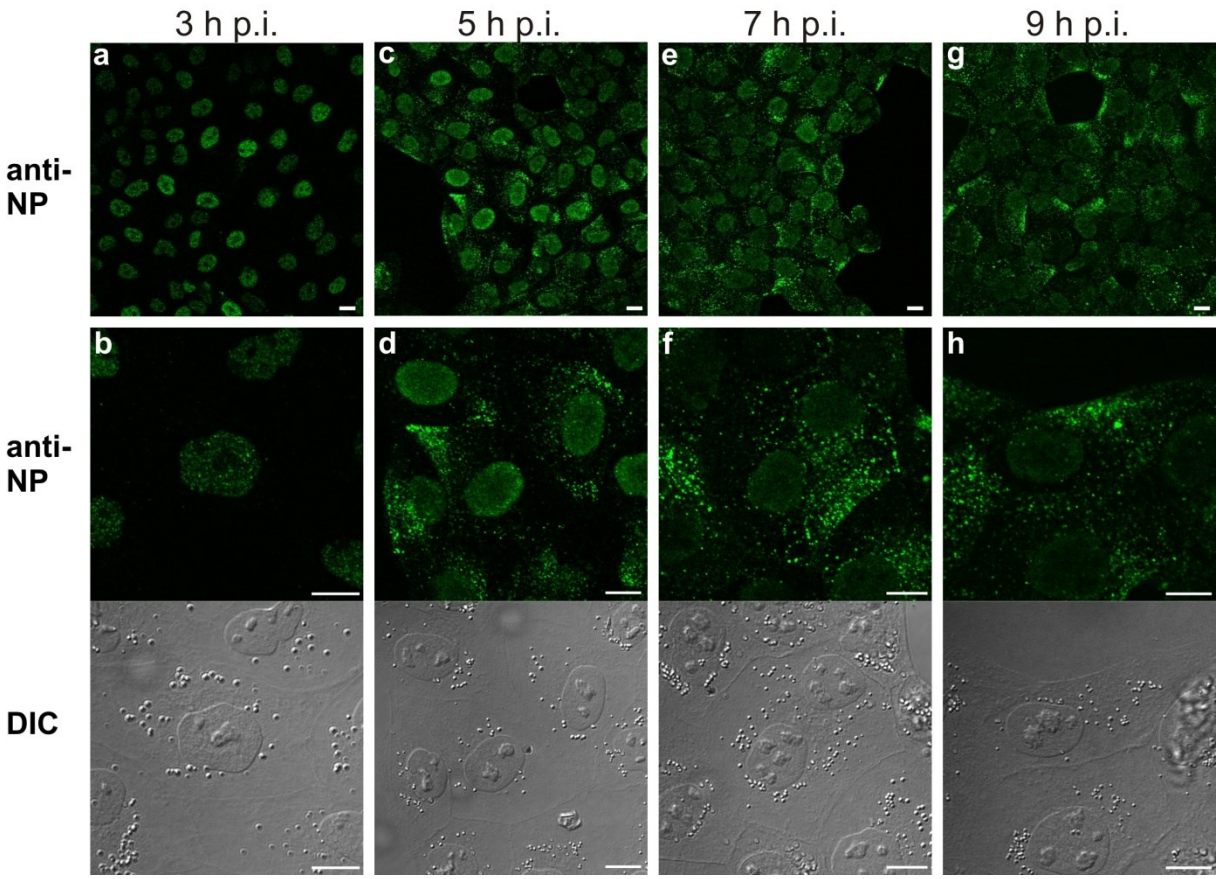

Fig. 43: Immunofluorescence detection of NP in a time series of Influenza A/FPV virus infection. MDCK II cells were infected (MOI 30) and subsequently fixed at (a, b) 3 h p.i., (c, d) 5 h p.i., (e, f) 7 h p.i. or (g, h) 9 h p.i. Immunostaining was performed with anti-NP and Cy2-anti-mouse antibodies. Confocal fluorescence images of the infected cell layer are shown in the top row (a, c, e, g). Individual cells at higher magnification are presented as fluorescence and transmitted light images in (b), (d), (f) and (h). NP localization changed from predominantly nuclear at 3 h p.i. to a more cytosolic localization over time. Scale bar, 10 µm.

vRNA in previous studies [297]. Consistently, such punctate cytoplasmic signals were completely absent from transfected cells expressing only NP or fluorescent NP fusion proteins (Fig. 41, Fig. 35).

In the nucleus of infected cells, viral NP appeared either granular (Fig. 43b) or largely homogenous (Fig. 43f), but prominent local accumulations highly enriched with NP as seen in expression of NP alone were never observed in infected cells (compare Fig. 35, Fig. 36 and Fig. 38 with Fig. 41). According to these results, a heterogeneous organization of nuclear NP with a granular or speckled appearance is a common feature that is found for NP in infection as well as for NP when expressed alone. However, larger nuclear accumulations highly enriched with NP do not seem to represent structures relevant to infection. They might rather be artifacts of NP expression in the absence of infection.

4.3.1.4 NP localizes to the interchromatin space in infection and in transfection

Counterstaining of infected and transfected cells with DAPI revealed that viral NP in infection, and also mEYFP-tagged NP when expressed alone, accumulated preferentially in the interchromatin space (Fig. 44): In infection, viral NP adopted a granular organization and distributed throughout the nucleus preferably into those spaces which were largely devoid of DNA, except for nucleoli (Fig. 44e). The chromatin in infected cells appeared unaltered compared to the chromatin of untreated cells (Fig. 44a), forming a dense network throughout the nucleus and accumulating in tight contact around the nucleoli. In transfected cells, NP-mEYFP also localized preferentially to interchromatin spaces, and this apparently resulted in the characteristic heterogeneous distribution of NP-mEYFP in the nucleus (Fig. 44b). This finding implies that the interchromatin space might represent the underlying template of NP nuclear organization, defining the sites of local NP-mEYFP accumulation. It should be noted at this point that the chromatin in general does not exclude proteins smaller than 100 kDa [495,498]. Instead, a high degree of penetration of such proteins into the chromatin network was reported, the intranuclear space being freely accessible, which is consistent with the homogeneous distribution observed for mEYFP and Dendra2 in the nucleus (Fig. 35g, Fig. 38d). It was further reported that the mobility of such small proteins does not correlate with chromatin density and that the chromatin does not obstruct their diffusion, suggesting that preferential association of NP-mEYFP with the interchromatin space as observed here must be caused by other factors, e.g. specific interactions with components of the nucleoplasm.

In cases of small, punctate and speckled accumulations of NP-mEYFP, the chromatin structure was not evidently changed (Fig. 44b). It was remarkable, however, that the

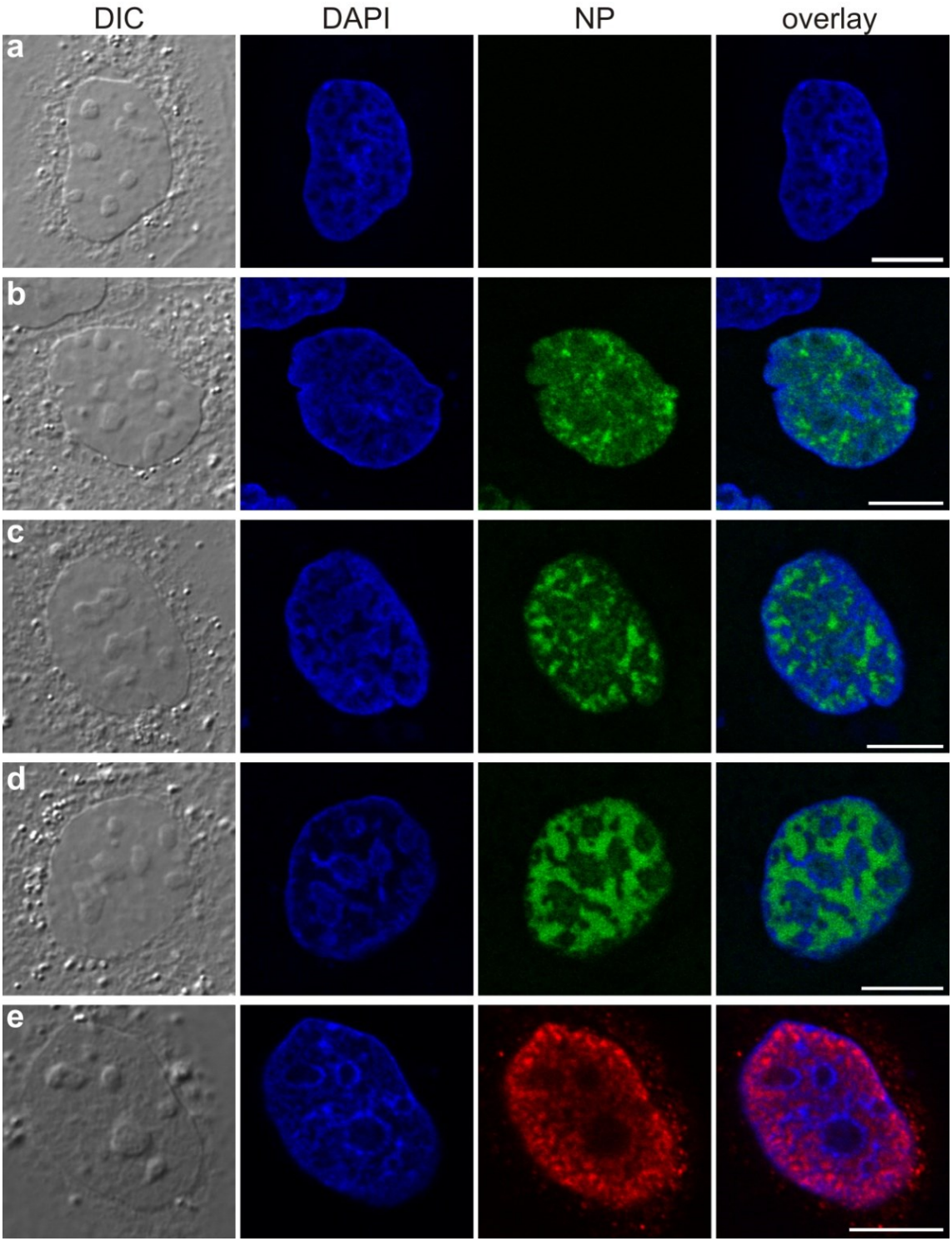

Fig. 44: NP preferentially accumulates in the interchromatin space and can induce rearrangement of chromatin. MDCK II cells (a) untreated, (b, c, d) transfected with NP-mEYFP (11 h p.t.) and (e) infected with Influenza A/FPV virus (MOI 100, 10.5 h p.i.) were fixed, permeablilized and counterstained with DAPI. Infected cells were additionally immunostained with anti-NP and Alexa568-anti-mouse antibodies. mEYFP fluorescence and immunofluorescence signals were detected by confocal fluorescence microscopy. Representative images of nuclei in NP-mEYFP expressing cells (b–d) illustrate the displacement of chromatin by different degrees of NP-mEYFP accumulation in the nucleus. Scale bar, 10 µm.

chromatin seemed to be displaced by NP-mEYFP with increasing accumulation of NP-mEYFP into larger structures, (Fig. 44c, d). In cases of extensive nuclear accumulation of the construct, even major rearrangements of the chromatin were observed (Fig. 44d). The chromatin was then found confined within tubular structures across the nucleoplasm or along the rim of the nucleus, while densely packed NP-mEYFP filled the largely DNA-free nuclear volume. As neither the formation of compact structures highly enriched with NP nor rearrangement of chromatin was observed in infected cells, these effects seemed to be artifacts of NP (over)expression in the absence of infection. However, general aspects of the interplay between NP and chromatin are implied, and despite of the considerable impact of NP-mEYFP on cellular chromatin, a cytopathic effect of the expression of NP constructs was not observed within the first 48 h p.t. (compare Fig. 37).

4.3.2 Analysis of subnuclear targeting of NP

Upon expression in mammalian cells, NP constructs accumulate predominantly in the cell nucleus and distribute non-homogeneously in the interchromatin space as described in the previous section (4.3.1). Exclusion from the chromatin network and local enrichment of NP constructs specifically in the nucleoplasm indicate sites of preferential association for NP. This is supported by the formation of local nuclear accumulations even by monomeric NP constructs. In the here following part, the hypothesis of specific subnuclear targeting of NP was therefore further investigated.

4.3.2.1 Analysis of subnuclear targeting of NP using nuclear export constructs of NP

First, to exclude that local accumulations of NP constructs were caused by precipitation of overexpressed protein, the NP concentration in the nucleus was decreased by fusion of NP constructs to a C-terminal nuclear export signal (NES) (amino acid sequence: LQLPPLERLTL) [499]. It was shown previously that the NES does not prevent transport of proteins into the nucleus, but causes rapid nuclear export via a CRM1-dependent pathway [257]. One of these constructs, mEYFP-NP-NES, comprising NP C-terminally fused to the NES and N-terminally linked to mEYFP, was introduced already in section 4.3.1 and was shown to be expressed as full-length protein by Western blot analysis (Fig. 40). Upon transfection of MDCK II cells (Fig. 45), HeLa cells (Fig. 48) or CHO-K1 cells (not shown), some of the cells displayed an almost exclusive cytoplasmic localization of mEYFP-NP-NES, leaving the cell nuclei largely devoid of the protein. However, a fraction of mEYFP-NP-NES

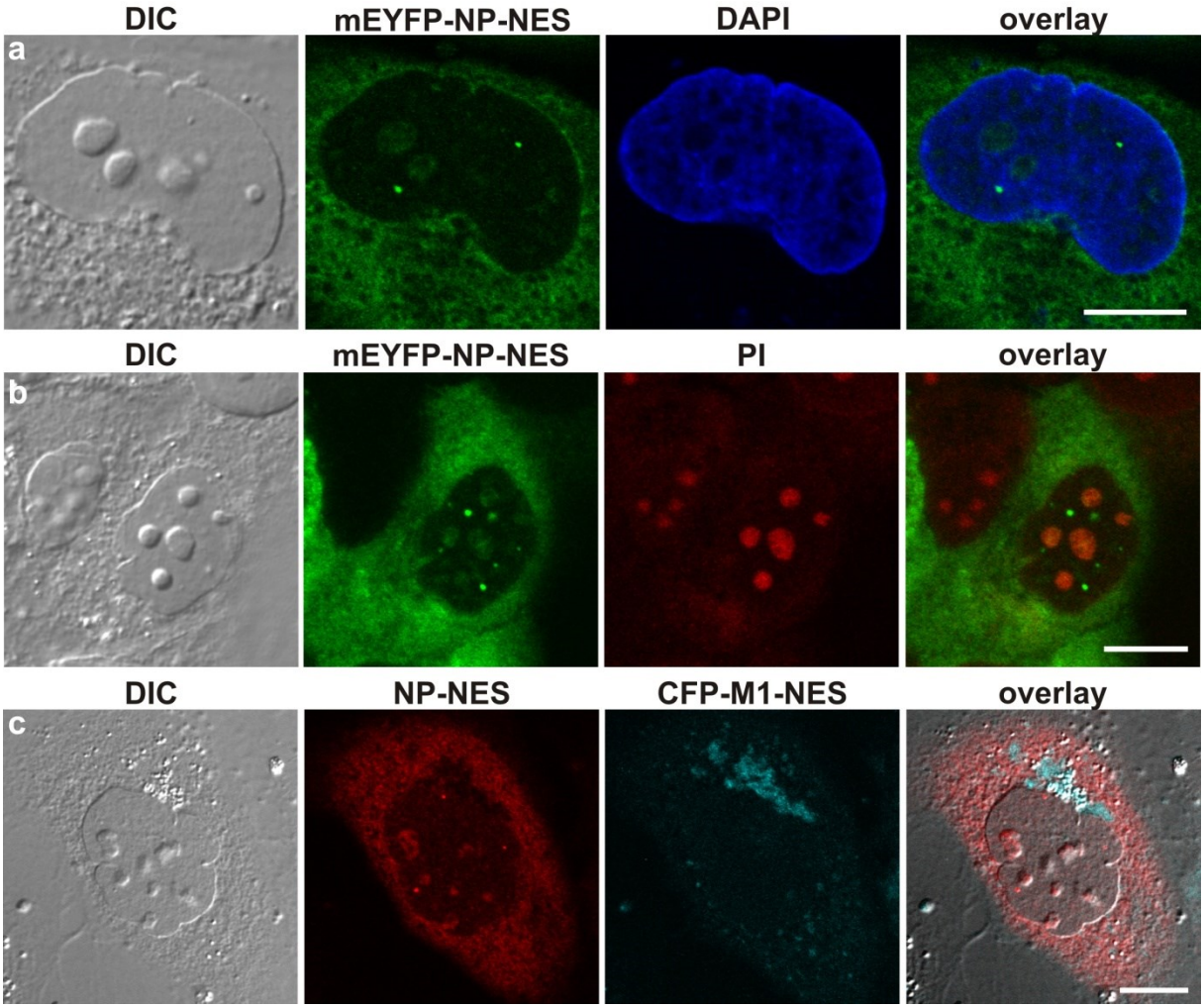

Fig. 45: Expression of NP and M1 constructs comprising a C-terminal nuclear export signal (NES). MDCK II cells were transfected with (a, b) mEYFP-NP-NES or (c) NP-NES together with CFP-M1-NES, and they were fixed at 20 h p.t. DNA counterstaining was performed with DAPI (a). Nucleoli were highlighted with propidium iodide (PI) staining (b), and immunostaining for NP was performed with anti-NP and Alexa568-anti-mouse antibodies (c). Images were acquired by confocal fluorescence microscopy. Representative images of cells are shown that display nuclei largely depleted of NP and M1 constructs. Scale bar, 10 µm.

was found to remain associated with two distinct types of subnuclear structures, indicating subnuclear domains of high affinity for the construct. The first structure could easily be identified as nucleoli by colocalization with propidium iodide staining [500] (Fig. 45b). This was consistent with the previously reported association of NP with nucleoli in infected and in transfected cells [123,361]. The second structure resistant to nuclear export appeared as small, bright dots that located in the interchromatin space (Fig. 45a). Cells displaying these structures typically contained 1–8 of these dots. In most cases, only two or three of them were observed. Their sizes varied from 1.2 µm down to the resolution limit of standard optical microscopy. The formation of larger patches was observed in a few cases (Fig. 48b). It is possible that in infection and during (over)expression of wild-type NP such punctate nuclear

accumulations are usually obscured by excess amounts of NP in the nucleus and have therefore not been described before, making this nuclear export construct of NP an interesting tool to study subnuclear structures with high affinity for NP.

In order to account for the possibility that the fluorescent protein moiety or the NES-tag might be responsible for unspecific accumulation or aggregation of the construct, a control experiment was performed expressing NP-NES (lacking the mEYFP-tag) and CFP-M1-NES, another nuclear protein from Influenza A/FPV/Rostock/34 that was N-terminally fused to the cyan fluorescent protein (CFP) and contained an identical C-terminal NES. CFP-M1-NES was kindly provided by Bastian Thaa (Freie Universität, Berlin). Immunofluorescence detection of NP-NES (Fig. 45c) clearly revealed the same subnuclear patterns as mEYFP-NP-NES in nuclei that were otherwise depleted of the protein; NP-NES was found to associate with nucleoli and small dot-like structures even at very low total nuclear concentrations and in the absence of the mEYFP moiety. In contrast, CFP-M1-NES did not show any residual nuclear signals (Fig. 45c), demonstrating that the NES did not *per se* cause accumulation of proteins in dot-like structures or in nucleoli as a part of its transport mechanism. Since the NES of mEYFP-NP-NES was the same as in CFP-M1-NES, both constructs can be assumed to access the same nuclear export machinery. Together, the results for NP-NES and CFP-M1-NES implied that the NP moiety itself had an affinity for the described subnuclear structures and was responsible for the association of mEYFP-NP-NES with subnuclear domains.

4.3.2.2 Analysis of subnuclear targeting of NP by fluorescence photoactivation studies

As a direct measure for site-specific affinities of NP, fluorescence photoactivation measurements were performed in living cells, and the dynamic behavior of NP constructs in different subcellular structures was analyzed. Therefore, fusion constructs of NP with the photoactivatable protein Dendra2 (introduced in 4.3.1) were applied. Dendra2 can be irreversibly photoconverted from a green- to a red-fluorescent state by illumination with UV light. By selection of a region of interest within transfected cells and localized irradiation, a specific subpopulation of Dendra2 can be activated and subsequently traced (Fig. 46): Dendra2 constructs were therefore expressed in MDCK II cells and photoactivation measurements were performed at 24 h p.t. (as described in 3.2.3.2). Cells were imaged in their pre-activation state, and after the photoactivation pulse in the region of interest, using 405-nm light, time-lapse imaging of the activated red-fluorescent state was performed for about 98 s. 230 frames were taken at intervals of 428 ms.

Examples of time-lapse imaging are presented in Fig. 46, where diffusion of free Dendra2 is compared to diffusion of Dendra2 fusion proteins with different NP variants. The activated free nuclear Dendra2 was found to spread rapidly throughout the entire nucleus within 5 s after photoactivation (Fig. 46, top row). This was followed by slower diffusion across the nuclear membrane into the cytoplasm. After 98 s of time-lapse imaging, the activated protein was still more enriched in the nucleus than in the cytoplasm, but when the same cell was checked again at 7 min post-activation, the equilibrium between nucleus and cytosol was finally established. For a quantitative description, the fluorescence signal of activated Dendra2 within the photoactivated region was plotted over time and compared to the simultaneous signal increase at other subcellular locations (Fig. 47A, left). A rapid and complete equalization of photoactivated molecules within the nucleus was confirmed (compare blue curve and red curve). The increase of the cytoplasmic signal (cyan curve), which corresponded to the slow decay of the nuclear fluorescence, further demonstrated slow diffusion of activated molecules across the nuclear membrane.

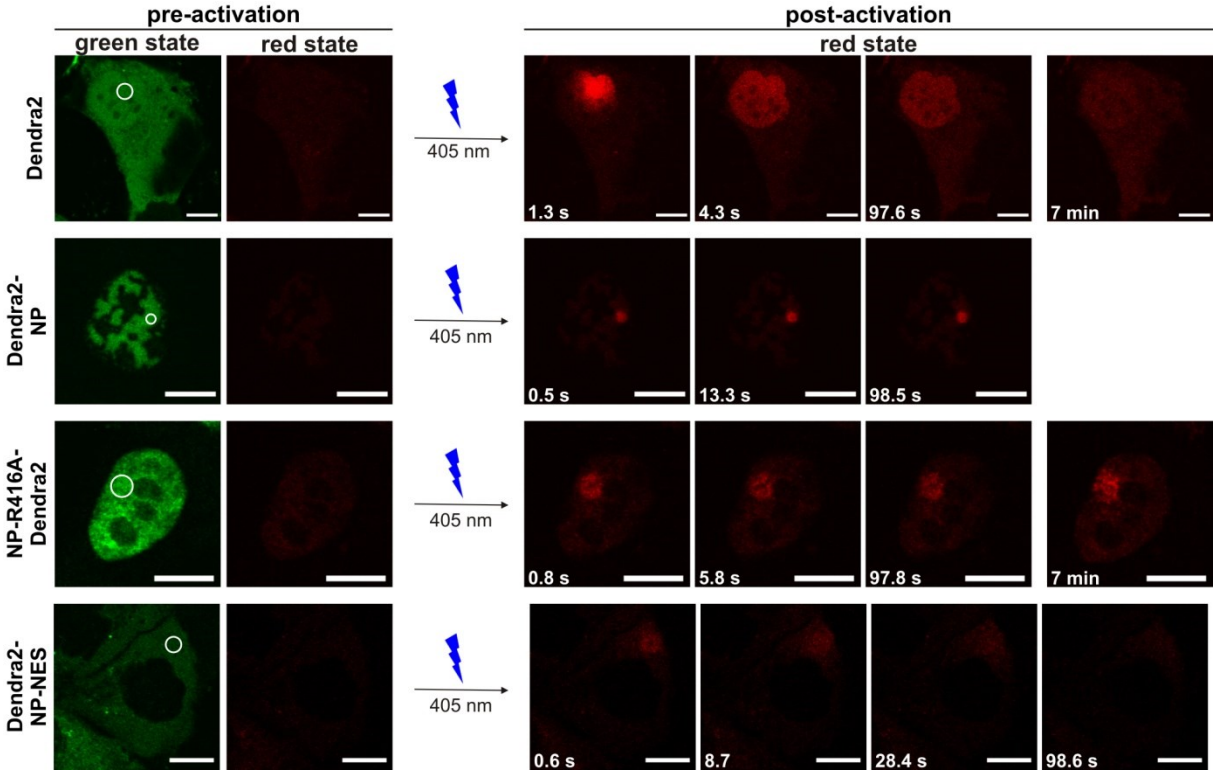

Fig. 46: Photoactivation of Dendra2 constructs and time-lapse imaging of the activated red-fluorescent state. Dendra2 constructs (as indicated) were expressed in MDCK II cells and photoactivation measurements were performed at 24 h p.t. in living cells. Confocal fluorescence images of the green- and the red-fluorescent states of Dendra2 were acquired before activation (left) followed by photoactivation of the region of interest (white circles) by irradiation at 405 nm. Subsequently, time-lapse imaging of the activated red-fluorescent state was performed for about 98 s (right). 230 images were acquired at intervals of 428 ms, a selection of which is presented. Single images were then again recorded at 7 min post-activation to detect long-term changes in the distribution of some of the constructs. Photoactivation was performed the either in nucleus (1st, 2nd, 3rd row) or in the cytoplasm (4th row).

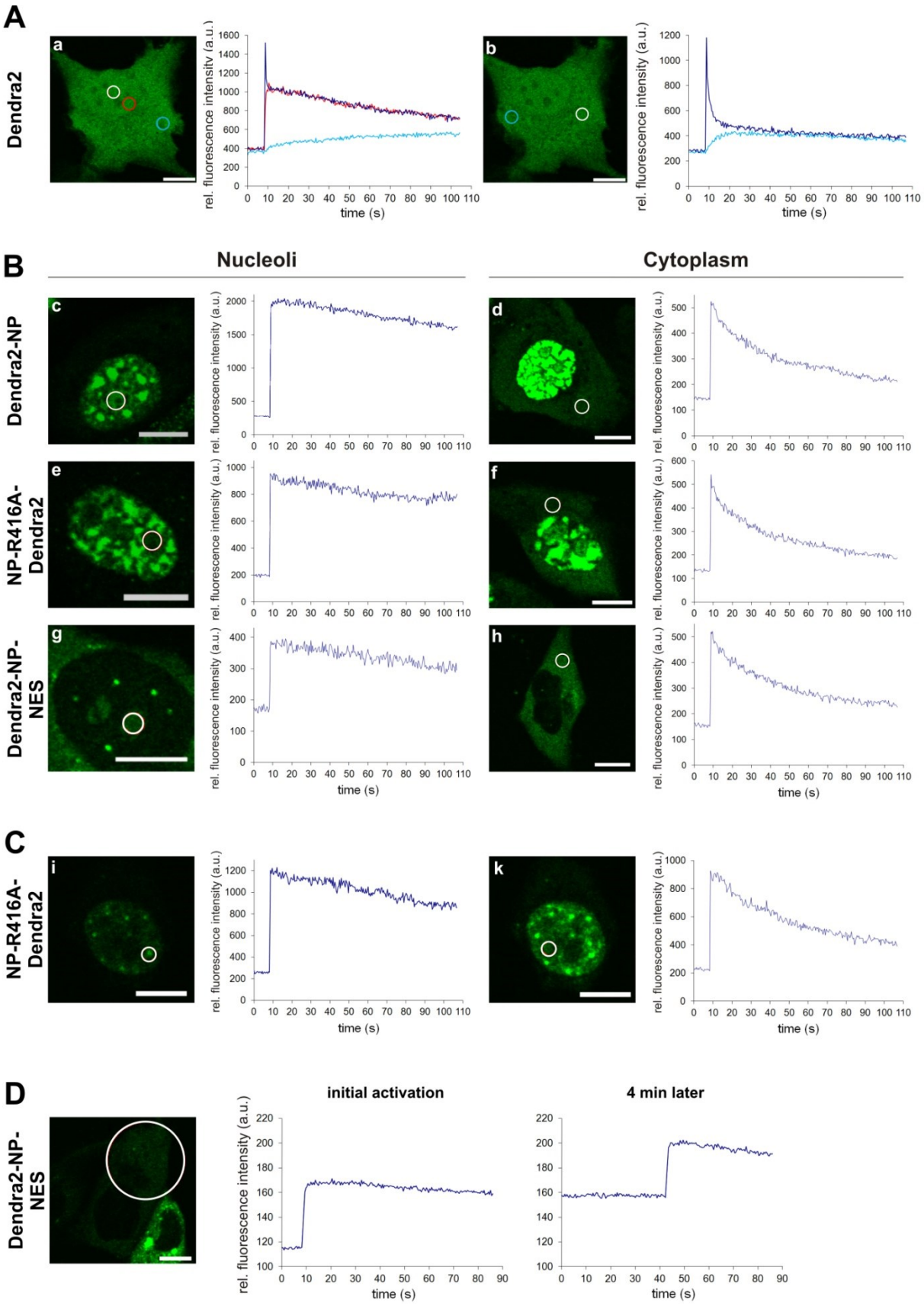
A
Dendra2
a
b
rel. fluorescence intensity (a.u.)
time (s)
B
Nucleoli
Cytoplasm
Dendra2-NP
NP-R416A-Dendra2
Dendra2-NP-NES
c
d
e
f
g
h
C
NP-R416A-Dendra2
i
k
D
Dendra2-NP-NES
initial activation
4 min later

Fig. 47: Comparison of intracellular dynamics of NP constructs by fluorescence photoactivation. MDCK II cells were transfected with (a, b) Dendra2, (c, d) Dendra2-NP, (e, f, i, k) NP-R416A-Dendra2 and (g, h) Dendra2-NP-NES, and photoactivation measurements were performed in living cells at 24 h p.t. For the detection of total Dendra2 in transfected cells, confocal fluorescence images of the Dendra2 green-fluorescent state were acquired prior to photoactivation. A region of interest (ROI) was then selected within transfected cells for site-specific photoactivation by irradiation at 405 nm (white circles). The activated red-fluorescent state was monitored in 20 pre-activation frames and 230 post-activation frames at intervals of 428 ms, and the relative fluorescence intensity within the ROI was plotted over time as presented in the diagrams (blue curves). (A) Photoactivation of free Dendra2 was performed in the nucleus (left) and in the cytoplasm (right), in ROIs as indicated by the white outline. The fluorescence signal of the activated state was further measured and plotted for other regions (red and cyan) to monitor the spreading of the activated molecules within the cell. The increase of signal in these regions reflects the signal decrease that was measured in the activated ROI. (B) Photoactivation measurements in nucleoli and in the cytoplasm were compared for three different NP constructs. (C) Photoactivation measurements with monomeric NP-R416A-Dendra2 in the nucleus were performed for a punctate subnuclear accumulation of the construct (left) and for diffusely distributed nucleoplasmic protein (right). (D) A control measurement to evaluate fluorescence photobleaching with the here applied settings was performed by photoactivation of a major fraction of cellular Dendra2-NP-NES and detection of fluorescence after a time lapse of 4 min when the activated fluorophore had reached a steady-state distribution within the cell and diffusion of the protein did not affect the signal intensity anymore. Photobleaching was not observed within a detection period of 42 s. Repeated photoactivation after 42 s of time-lapse imaging demonstrated that the signal decay was due to initial dispersal of the newly activated fluorophore. Scale bar, 10 µm.

Very different kinetics were however observed when Dendra2 was fused either to wild-type NP, to monomeric NP-R416A or to NP-NES. These NP constructs (Dendra2-NP, NP-R416A-Dendra2 and Dendra2-NP-NES) showed an exceptionally low mobility in the nucleus, but also in the cytoplasm their mobility was reduced as compared to Dendra2 alone (Fig. 46 & Fig. 47). Photoactivation of the wild-type construct Dendra2-NP within compact nuclear structures that were highly enriched with Dendra2-NP caused the localized conversion of Dendra2 which then remained stably associated with the photoactivated area during time-lapse imaging (Fig. 46, second row), indicating immobility and precipitation of Dendra2-NP within these structures. Yet, also the monomeric mutant NP-R416A-Dendra2, which was studied by photoactivation measurement in a more heterogeneous and apparently less densely packed region of the nucleus, showed a considerably reduced mobility as compared to free Dendra2 (Fig. 46, third row). The photoactivated NP-R416A-Dendra2 remained largely confined to the photoactivated area during time-lapse imaging, and only a small fraction of the protein appeared to invade the space closely adjacent to the activated region of interest. Even at 7 min post-activation, the major part of activated NP-R416A-Dendra2 was still found to reside in the initially irradiated area, but spreading of the red-fluorescent state into the adjoining nucleoplasm became more evident at this time point, indicating a continued but very slow diffusion of nuclear NP-R416A-Dendra2. This experiment involving monomeric

NP-R416A-Dendra2 demonstrated that the extraordinarily slow nuclear dynamics of NP constructs were not due to the intrinsic ability of NP to polymerize. Instead, extensive interactions of NP with nuclear components are implied.

It should be noted here that when considering free diffusion along a concentration gradient as described by the *Stokes-Einstein equation* and *Fick's first law of diffusion,* the difference in molecular weight between monomeric Dendra2 (26 kDa) and Dendra2-NP (82 kDa) is merely able to explain a 1.47 times lower diffusion coefficient of Dendra2-NP compared to Dendra2 and thus a 1.47 times lower flux of photoactivated molecules. For application of the *Stokes-Einstein equation* a spherical protein shape and a molecular volume proportional to the molecular weight have to be assumed. Previously, however, it was shown for EGFP oligomers (monomers to tetramers) that their diffusion coefficients do not match the expected values for globular proteins [498]. The measured kinetics were found to be better fitted by a model for rod-like proteins consistently with their actual 3D structure, nevertheless the nuclear diffusion coefficients between a monomeric 27-kDa protein and a trimeric 81-kDa protein differed only by a factor of 2.1. Differences of this scale cannot account for the reduced nuclear mobility observed for NP-R416A-Dendra2 in comparison to free Dendra2 though (see Fig. 47a, e, i, k). In previous studies, it was furthermore shown that the mobility of proteins in the range from 27 to 108 kDa is not affected by the local chromatin density in the nucleus [495,498], and the diffusion coefficients of such average-sized proteins were reported to be only 3.5 times larger in nuclei than in aqueous solution [494], confirming a low nucleoplasmic viscosity for proteins and small molecules in contrast to a higher mesoscale nuclear viscosity reported for particles larger than 100 nm [501]. A considerable steric obstruction of free diffusion of monomeric NP constructs in the nucleus (e.g. due to the chromatin network or other subnuclear structures) can therefore be excluded. And even though the apparent viscosities of the cytoplasm and the nucleoplasm were reported to be identical for proteins between 30 and 150 kDa [494], the mobility of NP constructs was found to be distinctly higher in the cytoplasm than in the nuclear compartment (Fig. 46 & Fig. 47), thus strongly supporting the assumption that NP constructs are involved in numerous high-affinity interactions specifically in the nucleus.

For the NES-tagged construct Dendra2-NP-NES, which was generated to visualize sites of high affinity in the nucleus, it was shown that the NES-tag did not significantly affect the diffusion kinetics of the construct as compared to wild-type Dendra2-NP, neither in the cytoplasm nor in nucleoli (Fig. 47B, c–d, g–h). Expression of the full-length protein was verified by Western blotting (Fig. 40). Comparable local protein dynamics of the NES-tagged

construct and the wild-type protein support the validity of the results obtained with Dendra2-NP-NES to describe subnuclear targeting of NP. Both proteins displayed the same slow signal decay after photoactivation in nucleoli, which indicates a very low exchange rate of photoactivated molecules for the nucleolar compartment. The same kinetics were furthermore observed for the monomeric NP-R416A-Dendra2 (Fig. 47B, left), demonstrating that interactions of NP constructs with nucleoli were not affected by the polymerization state of NP. Control experiments confirmed that effects of photobleaching were negligible under the applied conditions (Fig. 47D). Accordingly, the signal decay observed in photoactivation measurements was solely due to protein diffusion, and NP constructs in association with nucleoli were hence not immobilized, but displayed an extraordinarily slow mobility compared to NP constructs in the cytoplasm (Fig. 47B) or in the nucleoplasm (Fig. 47k). Photoactivation measurements thus confirmed that low exchange rates are responsible for persistent association of Dendra2-NP-NES with nucleoli, even under conditions of ongoing nuclear export.

Localized punctate accumulations in the nucleoplasm were the second type of Dendra2-NP-NES accumulation in the nucleus that was found to resist nuclear export. These punctate structures were studied by the use of monomeric NP-R416A-Dendra2 to exclude effects of polymerization on protein dynamics and to be able to compare protein mobility at different locations primarily based on site-specific interactions. Measurements with NP-R416A-Dendra2 revealed that exchange rates of such punctate nuclear accumulations with the surrounding nucleoplasm were similarly low as for nucleoli, both structures featuring a linear signal decay after photoactivation (Fig. 47e, i). In contrast, the mobility of photoactivated NP-R416A-Dendra2 in the surrounding nucleoplasm was clearly higher, causing an exponential decay of the photoactivated signal (Fig. 47k). These results support that punctate accumulations in the nucleus were not static precipitates of NP constructs, but rather dynamic structures that exchanged molecules with the nucleoplasm, implying a certain functionality. The results further confirmed that nucleoli as well as punctate accumulations were the two cellular structures that displayed the highest affinity for NP constructs as it had been hypothesized based on results for NES-tagged NP constructs (Fig. 45).

It should be noted that free Dendra2 was expected to be expressed as a byproduct and minor fraction in NP-R416A-Dendra2 expression as inferred from Western blot analysis (4.3.1, Fig. 40). However, upon photoactivation of NP-R416A-Dendra2 (Fig. 47B, C), a fast component of the signal decay comparable to the signal decay of free Dendra2 was not observed (Fig. 47A), even though it would be expected to be well-distinct from the particularly slow nuclear

and cytoplasmic dynamics observed for NP-R416A-Dendra2. A possible contribution of free Dendra2 to fluorescence detection of NP-R416A-Dendra2 was thus apparently negligible.

To summarize the results of the photoactivation studies, a remarkably slow subcellular mobility of NP constructs was observed in comparison to the mobility of the free fluorescent protein, indicating that NP is engaged in numerous interactions with cellular components. This was reinforced by considerations on the molecule size and by the finding that slow diffusion was independent of the ability of NP to polymerize. Retardation of diffusion and thus interaction with the host cell were distinctly more pronounced in nuclei than in the cytoplasm, suggesting that nuclear accumulation of NP constructs in transfection and infection might not only be due to the nuclear localization sequences of NP, but also to nuclear retention due to extensive interaction.

Within nuclei, sites of different affinities for NP constructs could be distinguished. The highest mobility was observed in the nucleoplasm for homogenously distributed monomeric NP-R416A-Dendra2, whereas the least mobile fractions of NP were detected in nucleoli and small punctate nuclear accumulations, which also associated with NP constructs even at low concentrations. The kinetic data confirmed that these sites did not accumulate immobilized (non-functional) precipitates, but represented sites of high affinity that displayed the lowest exchange rates measured in cells.

Complete absence of mobility was only seen in the case of larger, irregular nuclear accumulations which appeared as compact structures and were densely packed with NP constructs (Fig. 46, second row). The dynamic behavior thus indicated non-functional precipitation within these structures, consistent with the absence of such structures from infected cells and their tendency to displace chromatin (Fig. 44). It cannot be excluded though that these compact structures initially formed by specific association of NP with structures of high affinity, which then continued to grow and possibly aggregated due to high local concentration and/or extensive self-polymerization. It is further possible that exchange of molecules between these structures and the nucleoplasm occurs only along their boundaries.

4.3.2.3 Analysis of subnuclear targeting of NP by colocalization studies with subnuclear domains

The next step was the identification of the subnuclear structures with high affinity for NP. Targeting of NP to nucleoli by a specific nucleolar localization signal has been described before [123] and is consistent with our observations (Fig. 45b). The description of dot-like accumulations of NP is however unprecedented, and the assignment of these structures to

specific, functional nuclear domains is less obvious. However, the recurring observation of interchromatin dots of similar size and number in cells expressing mEYFP-NP-NES (Fig. 45a) strongly implied a non-random nuclear organization similar to that of nuclear bodies (NBs) [490,502].

The cell nucleus is a highly organized compartment and, even though membraneless, the interchromatin space is known to be compartmentalized into functionally specialized domains [488,489]. To test the assumption that punctate mEYFP-NP-NES accumulations are non-random foci, they were correlated with known subnuclear structures by immunostaining of marker proteins of NBs. It was found that SC35, a component of splicing speckles [503], did not colocalize with mEYFP-NP-NES nuclear dots, neither in HeLa cells (Fig. 48c) nor in MDCK II cells (data not shown). Spatial correlation could not be inferred from the data due to

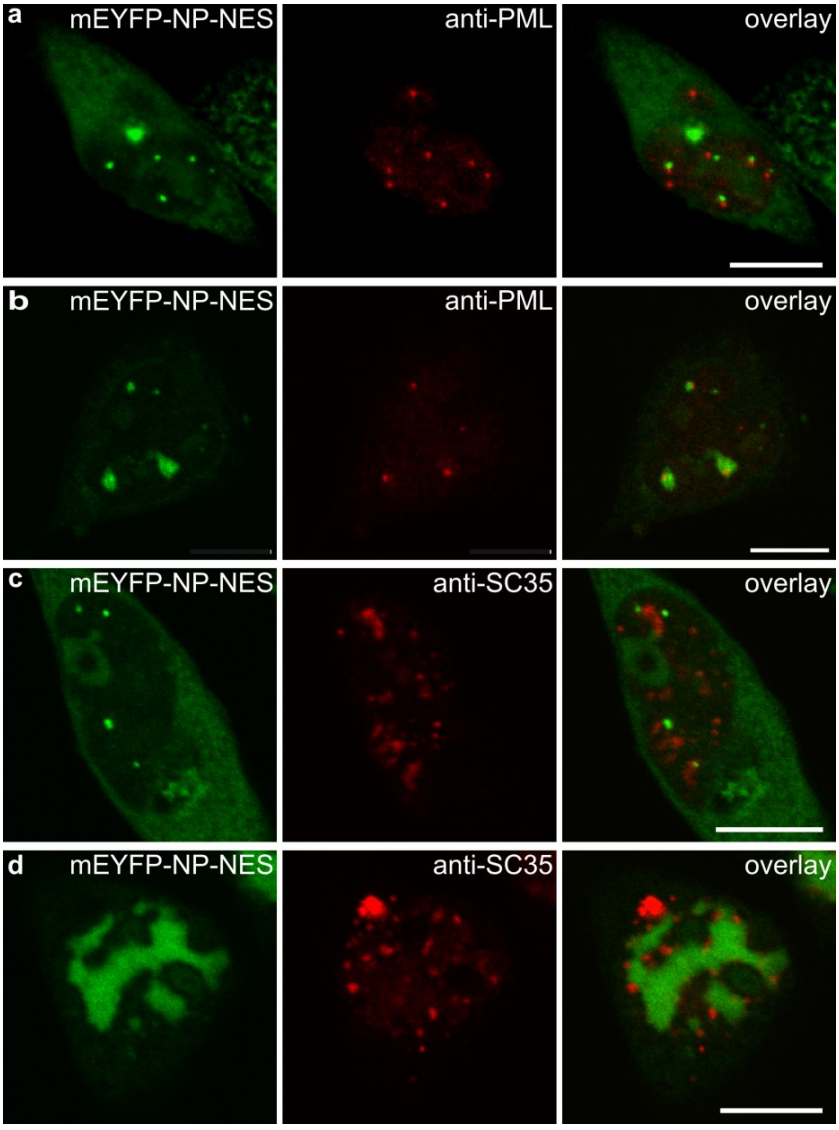

Fig. 48: Expression of mEYFP-NP-NES in HeLa cells and colocalization analysis with nuclear body proteins. Cells were fixed at 20 h p.t. and immunostained for nuclear body proteins, the PML protein (a, b) and the speckle protein SC35 (c, d). A z-projection made from the sum of confocal images of the cell nucleus is presented in (a). Single confocal fluorescence images are shown in (b–d). Scale bar, 10 µm.

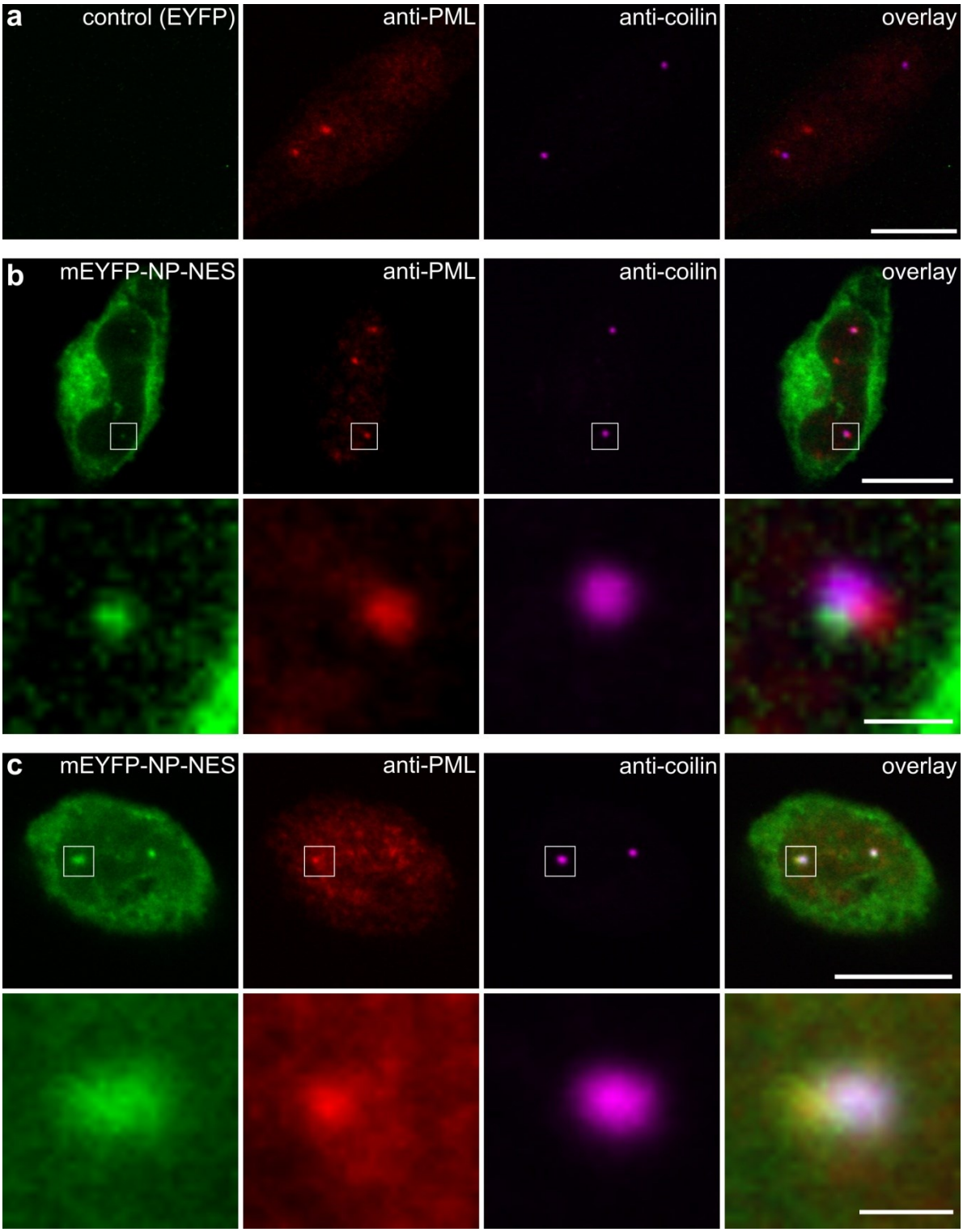

Fig. 49: Colocalization of mEYFP-NP-NES with PML and Cajal bodies in HeLa cells. (a) Untreated cells or (b, c) cells transfected with mEYFP-NP-NES were fixed at 23 h p.t. and immunostained for subnuclear domains with anti-PML and anti-coilin antibodies (with secondary Alexa594-anti-rabbit and Atto647-anti-mouse, respectively). PML is a marker protein of PML bodies and coilin is a protein of Cajal bodies. Z-projections of the cells are presented which were obtained by forming the sum of confocal fluorescence images throughout the nucleus. White squares indicate enlargement of the outlined sections in subadjacent images. In (b), the contrast of mEYFP-signals in the enlarged images was enhanced using Image J. Scale bar, 10 µm (for enlarged sections 1 µm).

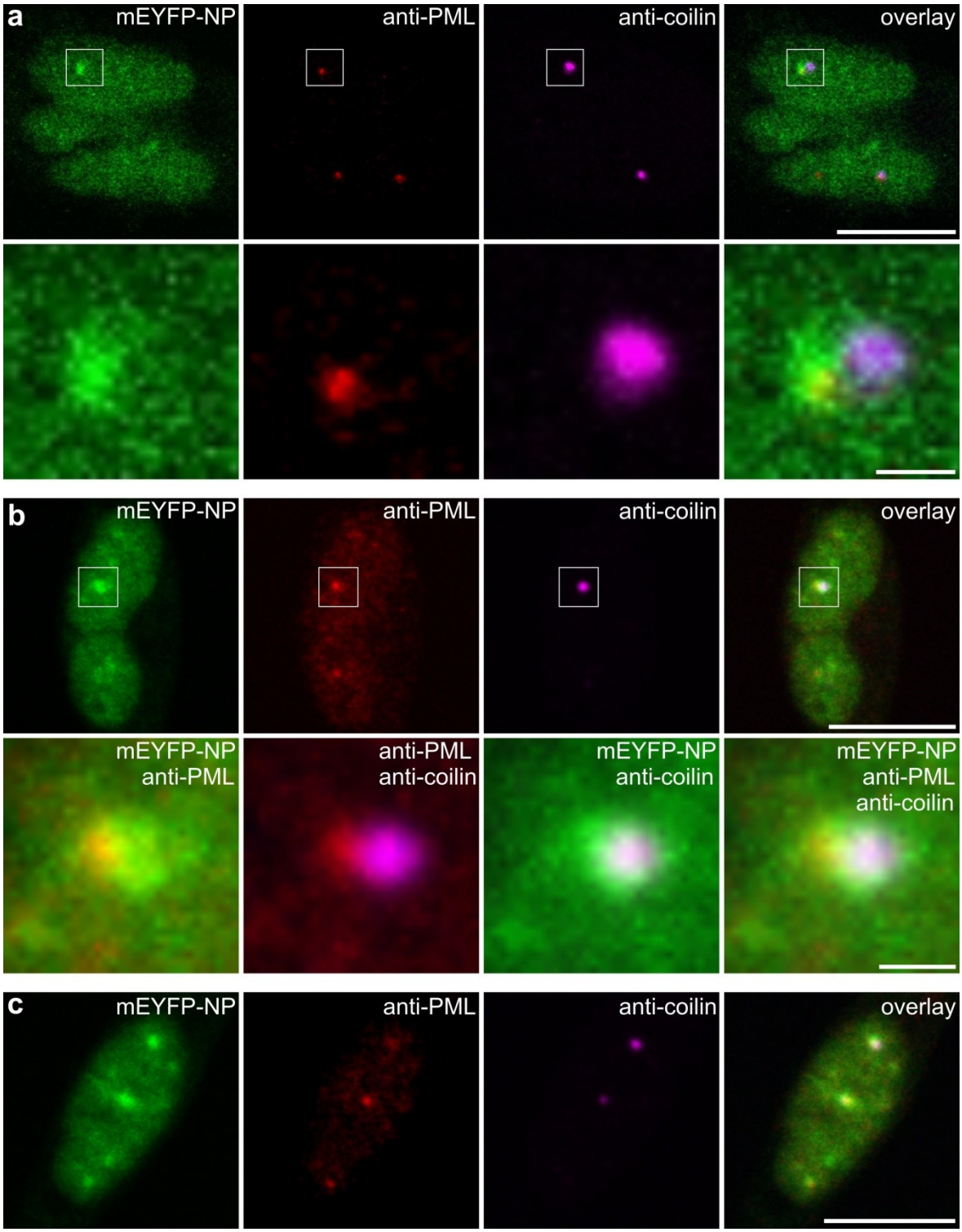

Fig. 50: Colocalization of mEYFP-NP with PML and Cajal bodies in HeLa cells. Transfected cells were fixed at 23 h p.t. and immunostained with anti-PML and anti-coilin antibodies (with secondary Alexa594-anti-rabbit and Atto647-anti-mouse, respectively). In (a), fluorescence images represent single confocal planes. In (b) and (c), cells are presented as z-projections made from the sum of confocal fluorescence images throughout the nucleus. White squares indicate an enlargement of the outlined section in subadjacent images. Scale bar, 10 µm (1 µm for enlarged sections).

the high number of SC35 speckles and the corresponding high probability to detect mEYFP-NP-NES dots in close proximity to SC35 signals. The promyleocytic leukemia (PML) protein, the defining component of PML bodies, did not show strict colocalization with mEYFP-NP-NES dots either, but was frequently found adjacent to or partially overlapping with them (Fig. 48a). The dots were judged as adjacent structures when they were directly associated or in close proximity to each other (i.e. at a distance shorter than the average radius of the spots). Interestingly, when mEYFP-NP-NES formed larger accumulations, PML bodies typically localized within these domains (Fig. 48b), whereas SC35 speckles were generally excluded from these domains (Fig. 48d). This indicates a very different interplay of PML bodies and splicing speckles with mEYFP-NP-NES-rich domains.

In the following, punctate nuclear accumulations of NP constructs will also be referred to as "NP bodies". It should be noted that PML and NP bodies frequently occurred as adjacent structures, but each type was also found separately, indicating a correlated arrangement of a subset of these domains, but not a mutual dependence. 31 cells from three independent transfection experiments were analyzed. They displayed residual mEYFP-NP-NES subnuclear structures in otherwise depleted nuclei, and 87 % of the cells contained at least one pair of closely associated PML and NP bodies. 52 % of the cells even contained the highest possible number of adjacent pairs, limited by the number of the less abundant structure. In average, 69 % of the PML bodies and 54 % of the mEYFP-NP-NES dots per cell were detected in a paired arrangement. These results strongly support the assumption that punctate accumulations of mEYFP-NP-NES are not randomly distributed in the nucleus, but can be found in specific surroundings.

A similar observation as for mEYFP-NP-NES dots was previously reported for the relation of PML with Cajal bodies (CBs), a subnuclear structure which frequently associates with PML bodies, but which is not strictly correlated [504,505]. CBs are a subtype of nuclear bodies involved in posttranscriptional modification of small nuclear (sn) RNA and biogenesis of snRNPs. Coilin is the marker protein of CBs. Costaining of mEYFP-NP-NES-transfected cells for PML NBs and CBs was performed using anti-PML and anti-coilin antibodies, and indeed, punctate nuclear accumulations of mEYFP-NP-NES were found to associate with PML bodies as well as with CBs (Fig. 49b, c). The three domains were frequently found in triplet arrangements, but also pairs of two were observed in every possible combination. They typically displayed a partial overlap, but complete colocalization of NP bodies with one of these nuclear domains was not detected. This result hence supports the hypothesis of specific

subnuclear targeting of NP constructs, but the primary target of mEYFP-NP-NES was apparently neither PML bodies nor CBs.

The same immunofluorescence analysis was then performed with mEYFP-NP lacking the "artificial" NES. As considerable nuclear accumulation of this construct was suspected to obscure targeting of NP to specific subnuclear sites, cells with low expression levels were selected for this analysis. At 23 h p.t., most of the transfected cells displayed a strongly heterogeneous accumulation of mEYFP-NP in the nucleus, and only very few cells showed low expression levels and a more homogeneous distribution with few distinct patches that were enriched with mEYFP-NP and appeared bright against the generally high nuclear signal. These prominent accumulations were dot-like just as residual nuclear signals of mEYFP-NP-NES, and, just like these, most of them colocalized with PML and/or CBs (Fig. 50). They either formed adjacent structures or partly overlapped with each other. Typically, these were the sites with the highest mEYFP-NP concentrations in the entire nucleus. These results are consistent with the findings for mEYFP-NP-NES, thus strongly indicating that nuclear sites of particularly high mEYFP-NP concentration (Fig. 50) represent the same structures as the domains that remain associated with mEYFP-NP-NES in almost depleted nuclei (Fig. 49).

Even though a considerable fraction of local mEYFP-NP accumulations colocalized with PML and CBs, not all of the NP bodies were found adjacent to PML or Cajal bodies, and not all of the PML and Cajal bodies were flanked by NP bodies. For a quantitative description, 10 cells with distinct punctate nuclear accumulations of mEYFP-NP were evaluated. They comprised a total of 30 NP bodies, 20 PML bodies and 19 Cajal bodies. It should be noted that for mEYFP-NP only the brightest spots were counted, although the cells occasionally also showed diffuse accumulations of mEYFP-NP. Similarly, only distinct bright spots were considered in case of PML. It is possible that due to the overall presence of PML in the nucleus, some PML bodies might have been missed, but even if they were not identified as PML bodies, elevated PML levels were often found in regions highly enriched with mEYFP-NP. Neglecting these cases of weak or diffuse colocalization, still 37 % of NP bodies were found to colocalize with both PML and CBs, additional 13 % localized to PML bodies and 17 % were found adjacent to CBs. Altogether, a large fraction of NP bodies (67 %) was hence localized in close proximity to PML and/or Cajal bodies. Accordingly, 33 % of NP bodies were found as solitary domains. In cases of PML bodies and CBs, only 15 % and 5 % represented solitary structures, respectively, and another 10 % were paired in the absence of NP bodies. The largest fractions of PML and CBs (75 % and 84 %, respectively) were

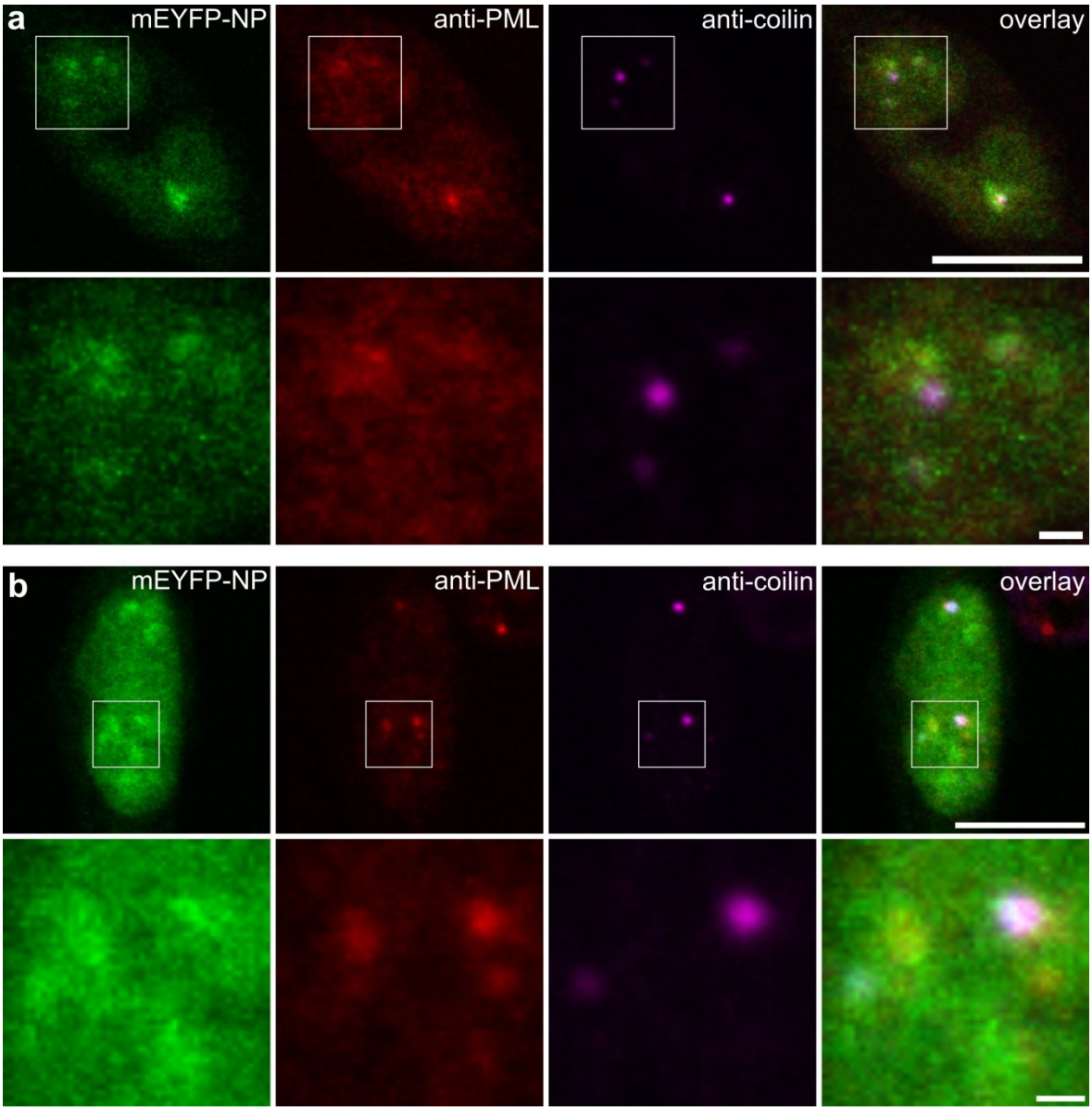

Fig. 51: Colocalization analysis of heterogeneously distributed nuclear mEYFP-NP with PML and Cajal bodies in HeLa cells. Transfected cells were fixed at 23 h p.t., and immunostaining was performed with anti-PML and anti-coilin antibodies (with secondary Alexa594-anti-rabbit and Atto647-anti-mouse). Confocal fluorescence images are presented which specifically display nuclei with subnuclear enrichment of mEYFP-NP in form of broad, irregular and diffuse patches. A single confocal plane of the nucleus is presented in (a), while a projection of confocal fluorescence images of the nucleus is shown in (b). White squares indicate enlargement of the outlined sections in the images beneath. Scale bar, (a, b) 10 µm (1 µm for enlarged sections).

however involved in a close spatial relation with NP bodies. 55 % of PML bodies and 58 % of CBs were even part of closely associated CBs, PML and NP bodies forming triplet structures.

In those cases of mEYFP-NP expression when nuclear mEYFP-NP accumulations were larger, more irregular and diffuse, but less punctate than described above (Fig. 50), a spatial correlation of mEYFP-NP with PML and CBs was still clearly observed (Fig. 51). Diffuse mEYFP-NP accumulations did not resemble nuclear bodies in size or shape, but nevertheless

they broadly overlapped with PML and coilin. It is not clear from these data if a varying appearance of mEYFP-NP subnuclear distribution possibly correlates with the distribution of subnuclear factors or domains other than PML and CBs.

It should be noted in the context of this analysis that a general problem in spatial correlation and neighborhood analysis is the non-assessable effect of nuclear crowding and of limited interchromatin space on the actual likelihood of random association [506]. This makes it impossible so far to classify the observed distances as non-random or random localization according to a theoretical model. Therefore, only those nuclear bodies were considered as correlated structures in the present analysis which were either directly associated or at a distance shorter than the average radius of the dots, assuming that this is a non-random association.
This appeared to be a reasonable criterion since in case of random association of NP bodies with subnuclear domains a close proximity of NP bodies to their own kind should have been observed with similar frequencies. Pairs of equal kind were however not detected at all. Furthermore, in case of random organization, the probability for NP bodies to localize in a short distance to PML and CBs is generally larger than the probability to overlap with one of these structures, which is due to the same probability of presence at each location. However, NP bodies were rarely observed at a short distance to PML or CBs; instead, the vast majority of NP bodies (67 % in case of mEYFP-NP) was closely associated with these subnuclear domains. This strongly supports the non-random character of this close association. The specific influence of the nuclear architecture is not included into these theoretical considerations, but a non-random correlation under actual experimental conditions was furthermore supported by the fact that PML and CBs are known interacting domains which associate non-randomly [505]. They were observed to associate with NP bodies at a similar frequency as to each other, thus supporting the non-randomness of this association.

Summarizing, the results suggest that punctate nuclear accumulations of NP constructs represent subnuclear sites of high affinity for NP which localize preferentially in close proximity to PML and CBs. The data furthermore indicate that NP has the intrinsic property to specifically target these subnuclear domains, thereby implying an interplay of NP with host cell processes, e.g. to support efficient viral replication or as a target for the cellular antiviral response.

4.3.3 Analysis of cytoplasmic targeting of NP

Based on previous studies indicating the intrinsic ability of NP to target the apical plasma membrane [299], the subcellular distribution of fluorescently tagged and non-tagged NP constructs was analyzed in polarized MDCK II cells. For polarization, MDCK II cells expressing NP constructs were grown on porous filter membranes for 13 days. Transfection with NP constructs was performed one day after seeding and the cells were maintained in selective medium during growth as described in 3.2.2.3. The polarization state of the cells was

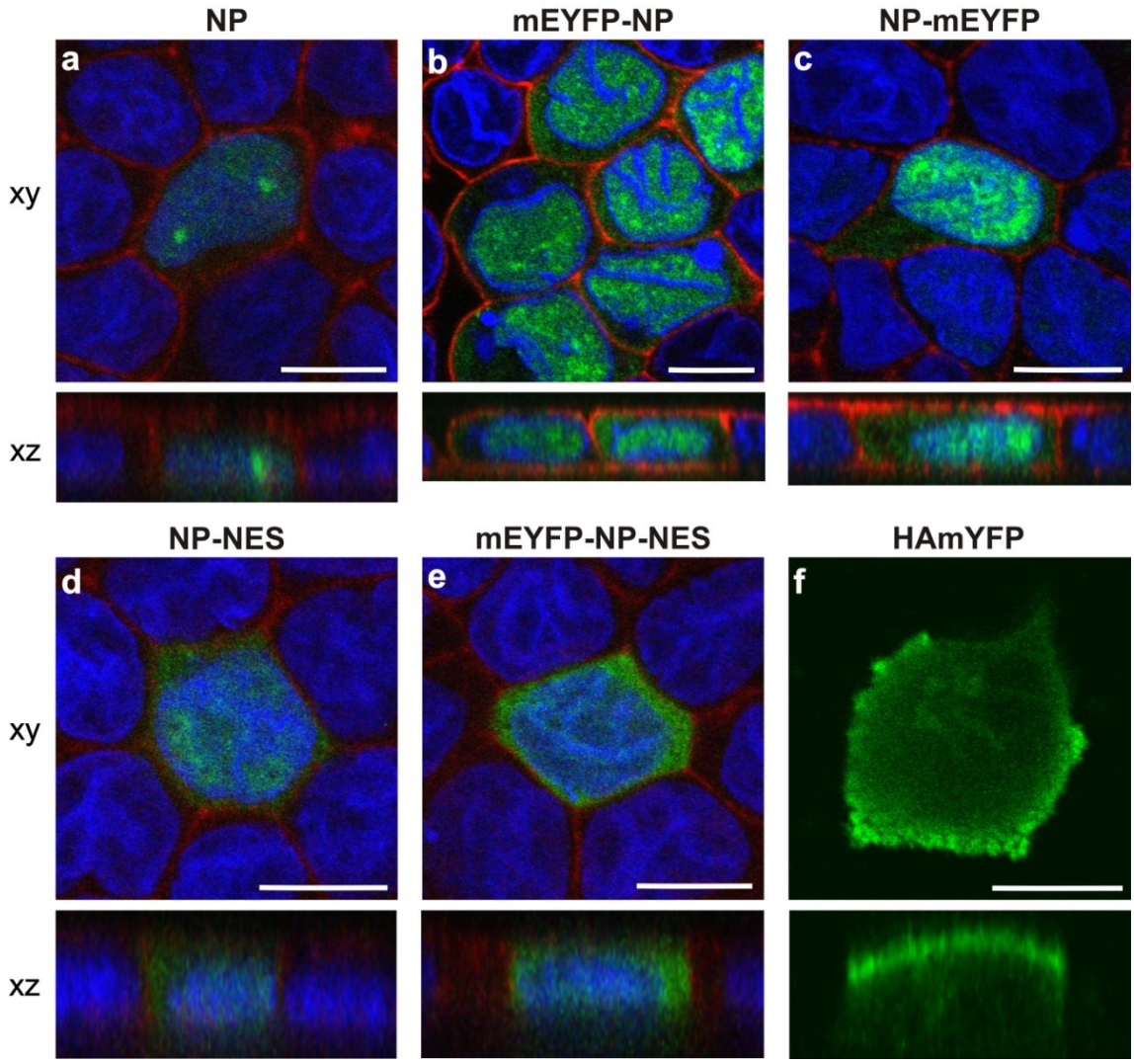

Fig. 52: Expression of NP and NP fusion proteins in polarized MDCK II cells. MDCK II cells were grown on porous filter membranes for polarization. One day after seeding, they were transfected with (a) NP, (b) mEYFP-NP, (c) NP-mEYFP, (d) NP-NES, (e) mEYFP-NP-NES or (f) HAmYFP. After 13 days, the cells were fixed, permeabilized and stained with DAPI (blue) and rhodamine phalloidin (red) to label the cell nuclei and F-actin, respectively (a–e). Non-fluorescent proteins NP and NP-NES were additionally immunostained with anti-NP-FITC (green). Intrinsic fluorescence of mEYFP is also displayed in green. Cells expressing HAmYFP were not further processed after fixation (f). Representative confocal fluorescence images of transfected cells are displayed. Images of xy-confocal planes are shown accompanied by a lateral view of the cells in xz-dimension beneath, which was generated by z-axis reconstructions of confocal image stacks. Scale bar, 10 µm.

checked after 13 days in control cells expressing the apically targeted protein HAmYFP as positive control. This construct was kindly provided by Silvia Scolari [447] and comprised the Influenza A virus HA transmembrane domain, the cytoplasmic tail and an N-terminal mEYFP-tag.

HAmYFP was found exclusively on the apical plasma membrane after 13 days of polarized growth and confirmed efficient differentiation of apical and basolateral membranes (Fig. 52f). In contrast, none of the NP constructs displayed a bias to localize to the apical side of the cell. NP and fluorescent fusion proteins of NP that were N-terminally or C-terminally tagged with mEYFP were still found predominantly in the cell nucleus. The small fraction of cytoplasmic NP distributed evenly throughout the cytoplasm (Fig. 52a–c). The same non-polarized distribution was observed for the NES-tagged constructs NP-NES and mEYFP-NP-NES, which were used to increase the total amount of cytoplasmic NP (Fig. 52d, e). Evidence for intrinsic apical targeting of NP was not obtained.

4.4 Monitoring newly formed vRNPs in living infected cells by coexpression of fluorescent NP fusion proteins

The first approach to establish an experimental system that allows studying newly formed vRNPs in living Influenza virus-infected cells was described in section 4.2. Yet, the biarsenical labeling technology was shown to be unfeasible for live-cell studies on vRNPs. The second approach to monitor vRNPs in living infected cells is reported here, using intrinsically fluorescent proteins.

Fluorescent NP fusion proteins were therefore coexpressed in infection to be incorporated into newly forming vRNPs. It is known from the work of Loucaides and coworkers [507] that transcription-competent vRNP complexes can be successfully reconstituted using GFP-tagged NP in plasmid-based reconstitution, indicating the possibility to label vRNPs by incorporation of fluorescent NP fusion proteins also during infection.

In the absence of infection, expression of NP fusion proteins was extensively characterized (see 4.3). NP constructs show a predominantly nuclear localization, and only a small fraction is homogeneously spread in the cytoplasm (Fig. 35). This NP expression pattern can be clearly distinguished from the punctate cytoplasmic signal that is characteristic for NP late in infection, resulting from nuclear export of progeny vRNPs (Fig. 43, immunostaining of NP in infected cells). It was therefore assumed that efficient incorporation of fluorescent NP fusion proteins into vRNPs and subsequent nuclear export of the complexes would lead to the appearance of characteristic punctate cytoplasmic signals of progeny vRNPs, which then can be analyzed as intrinsically fluorescent complexes by single particle tracking (SPT) and provide information on the dynamics of vRNP transport and virus assembly.

4.4.1 Optimization of experimental conditions for coexpression of mEYFP-NP in infected cells

The major challenge of this approach was to simultaneously establish infection and exogenous NP expression in the same cell. Since Influenza virus infection is known to induce host cell shut-off, it is most likely that also exogenous protein expression from plasmid DNA is downregulated. On the other hand, NP as a viral protein is likely to have an impact on viral replication, causing disturbances if expressed exogenously. A variety of experimental conditions thus had to be tested.

In all experiments, infections were performed with the Influenza A/FPV strain. The NP sequence of exogenously expressed NP constructs was derived from the same virus strain.

In a first attempt, MDCK II cells were transfected with fluorescent NP constructs several hours ahead of infection. Infection at MOI 50 was performed at either 4 h p.t. or 17 h p.t. when expression of mEYFP-tagged NP was already detectable. Infection was then allowed to proceed for another 6 h. Both N- and C-terminally mEYFP-tagged NP constructs were tested, but in none of these experiments superinfection had an impact on the localization of mEYFP-tagged NP in comparison to non-infected cells. A redistribution of mEYFP-tagged NP to the cytoplasm was not observed. The result is shown exemplarily for mEYFP-NP expression in superinfected and in mock-infected cells fixed at 10 h p.t. and 6 h p.i. (Fig. 53). In order to

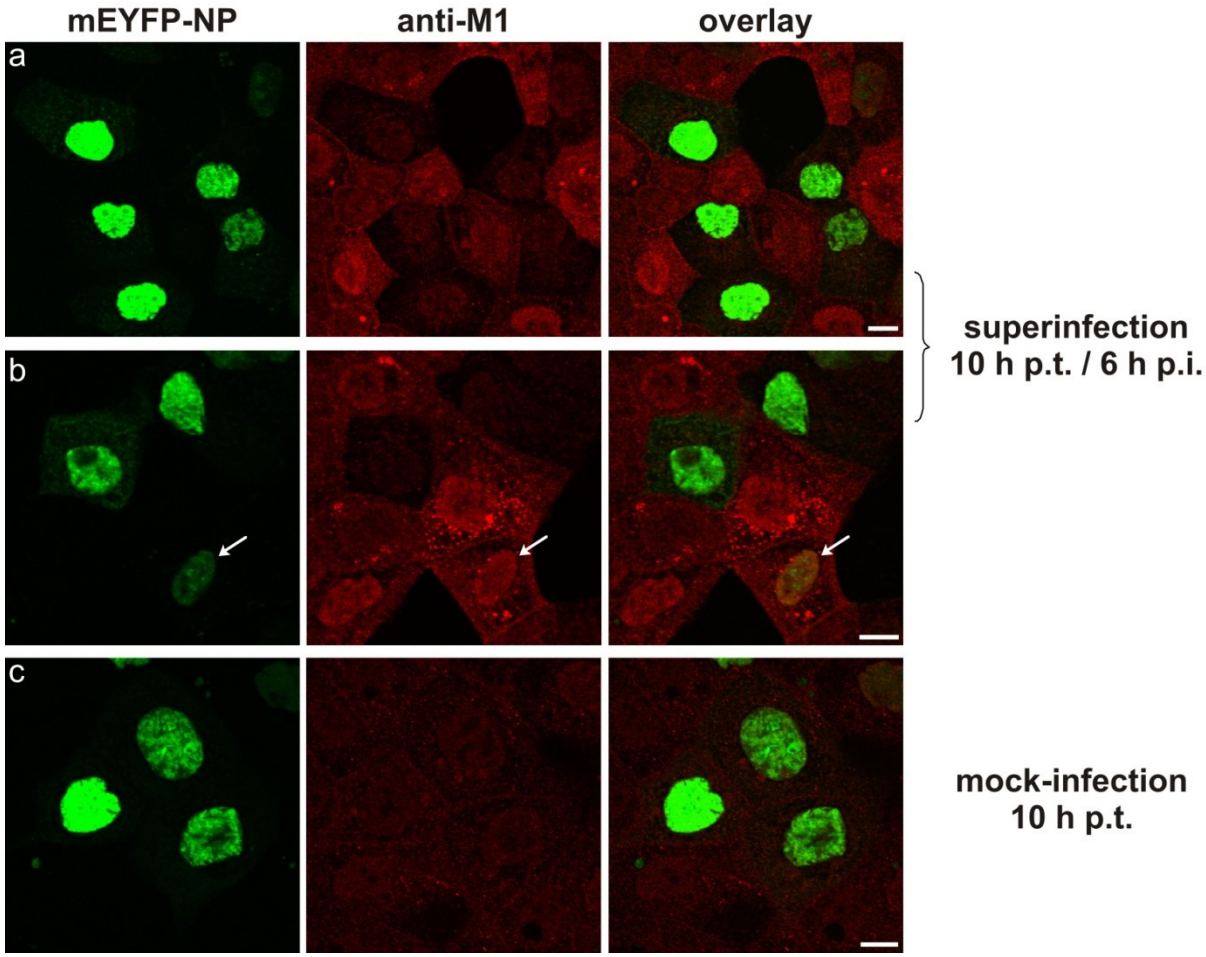

Fig. 53: Superinfection of mEYFP-NP expressing cells. MDCK II cells were first transfected with mEYFP-NP. At 4 h p.t., the cells were then superinfected with Influenza A/FPV virus (MOI 50) and incubated for another 6 h. At 10 h p.t. and 6 h p.i., the cells were fixed and subjected to immunostaining with polyclonal anti-M1 and secondary Cy3-anti-rabbit antibody. Confocal fluorescence images were recorded, and the cells were analyzed for mEYFP-NP expression and viral M1 expression as an indicator for virus infection. (a) In superinfected samples, the mEYFP-NP signal showed a predominantly nuclear localization like in the absence of infection. As judged by the viral M1 signal, infection was inhibited or considerably retarded in most transfected cells as compared to neighbouring non-transfected cells. (b) In a few cases, the M1 signal in mEYFP-NP expressing cells indicated successful superinfection (arrow). mEYFP-NP expression levels were comparably low in these cells. Cytoplasmic accumulation of NP constructs was not observed. (c) The M1 immunostaining was found to be slightly unspecific in mock-infected control cells. It is therefore not clear if infection is completely inhibited or strongly delayed in transfected cells (a). Scale bar, 10 µm.

verify successful viral infection, additional immunofluorescence detection of viral M1 was performed and revealed that M1 expression was strongly reduced in most mEYFP-NP expressing cells, indicating specific impairment of infection in transfected cells with exogenous NP expression (Fig. 53a). It is not clear though if infection was completely prevented or just considerably retarded since low levels of unspecific immunofluorescence staining were also observed in mock-infected cells (Fig. 53c).
A successful infection of transfected cells was detected in very rare cases and only in cells expressing particularly low levels of NP fusion proteins (Fig. 53b, arrow). Relocalization of exogenously expressed NP to the cytoplasm was however not observed in these cells.

The findings from this first of set experiments, performing superinfection of transfected cells, indicate that the premature presence of exogenous NP constructs at early stages of infection inhibits progression of viral replication very efficiently. Even though transfection in general was found to have a negative effect on virus infection, as verified by expression of free mEYFP (not shown), the effect was considerably more pronounced when NP constructs were expressed. Since viral NP most likely contributes to coordinated progression of viral replication (affecting e.g. the switch between viral transcription and replication), prematurely expressed NP constructs might critically disturb the sequence of events during infection and lead to abortion of viral replication in an early phase.
In conclusion, transfection and plasmid-based NP expression prior to infection was found to be largely detrimental to viral replication and was therefore not further pursued.

In the next approach, the order of events was reversed, performing first infection followed by subsequent transfection. MDCK II cell were therefore infected with Influenza A/FPV (MOI 50). Transfection was performed either at 1 h p.i., 2 h p.i. or 3 h p.i. The different samples were then analyzed for the efficiency to establish exogenous NP expression in infected cells.
When transfection was performed at 3 h p.i. and the cells were fixed at 7 h p.i. and 4 p.t., the number of infected cells was about 100 % (Fig. 54a, c). Infection was obviously efficiently established within the first three hours of infection. The transfection efficiency on the other hand was very low in these cells. The number of mEYFP-NP expressing cells and mEYFP-NP expression levels were highly attenuated in comparison to mock-infected cells (Fig. 54b, d).
High NP expression levels similar to those in mock-infected cells were exclusively observed in cells lacking infection, which occasionally occurred also in infected samples (Fig. 54c,

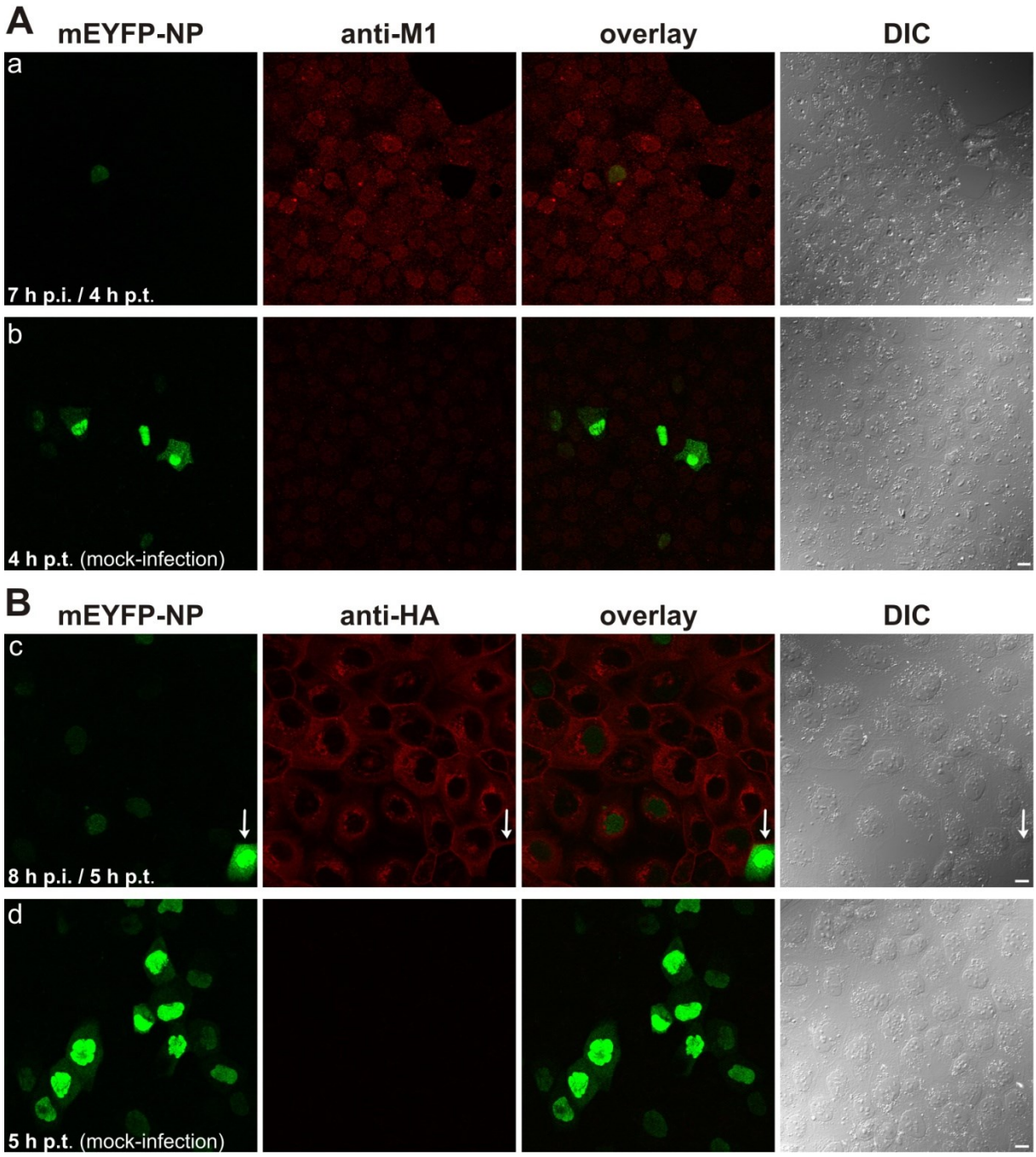

Fig. 54: Supertransfection of virus-infected cells with mEYFP-NP at 3 h p.i. MDCK II cells were first infected with Influenza A/FPV (MOI 50). At 3 h p.i., the cells were then transfected with mEYFP-NP. At (A) 7 h p.i and 4 h p.t. and (B) 8 h p.i and 5 h p.t., the cells were fixed and immunostained with (A) anti-M1 and Cy3-anti-rabbit antibodies and (B) anti-HA and Alexa568-anti-mouse antibodies. (a, c) According to M1 and HA immunostainings, the cells were about 100 % infected. In comparison to mock-infected cells (b, d), expression levels of mEYFP-NP were found to be reduced in infected cells. The highest mEYFP-NP expression levels in infected samples were found in occasionally observed uninfected cells (identified by the lack of HA staining) (c, arrow), indicating that infection efficiently downregulated mEYFP-NP expression. Scale bar, 10 µm.

arrow). These findings indicate downregulation of mEYFP-NP expression specifically in infected cells, which could be a consequence of the virus-induced host cell shut-off.

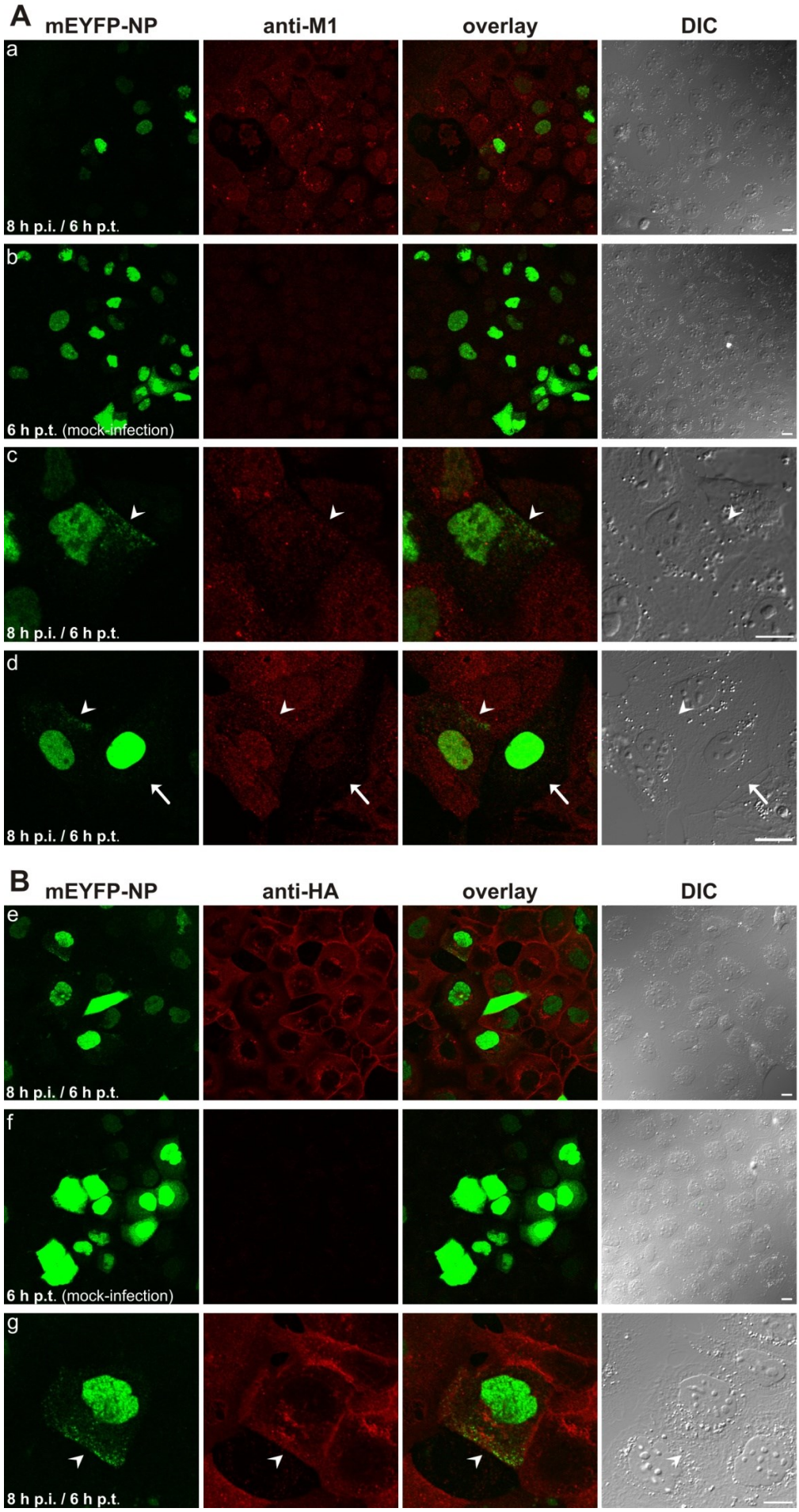
A
mEYFP-NP
anti-M1
overlay
DIC
a
8 h p.i. / 6 h p.t.
b
6 h p.t. (mock-infection)
c
8 h p.i. / 6 h p.t.
d
8 h p.i. / 6 h p.t.
B
mEYFP-NP
anti-HA
overlay
DIC
e
8 h p.i. / 6 h p.t.
f
6 h p.t. (mock-infection)
g
8 h p.i. / 6 h p.t.

Fig. 55: Coexpression of mEYFP-NP in virus-infected cells by transfection at 2 h p.i. MDCK II cells were infected (MOI 50) with Influenza A/FPV 2 h prior to transfection with mEYFP-NP. At 8 h p.i and 6 h p.t., the cells were fixed and analyzed for (A) viral M1 expression or (B) viral HA expression by immunostaining with anti-M1 and Cy3-anti-rabbit antibodies or anti-HA and Alexa568-anti-mouse antibodies, respectively. Images were recorded by confocal fluorescence microscopy. Overview images of the cell lawn are given in a, b, e and f. Selected individual cells are shown at higher magnification in c, d and g. (a, e) Infected (M1 or HA expressing) cells were successfully transfected with mEYFP-NP. Expression levels of mEYFP-NP and the number of transfected cells were however lower than in mock-infected samples at 6 h p.t. (compare with b and f). (c, g) A fraction of infected cells coexpressing mEYFP-NP displayed a clear cytoplasmic mEYFP-NP signal with a punctate appearance and laterally polarized distribution (arrowhead), indicating nuclear export in form of vRNP complexes. (d) In the absence of infection or in case of delayed infection, expression levels of mEYFP-NP were relatively high, but a punctate cytoplasmic NP signal was missing (arrow, right cell). A direct comparison between a simultaneously transfected and infected cell and a transfected non-infected cell is shown. Scale bar, 10 µm.

Notably, in infected cells weakly coexpressing mEYFP-NP, mEYFP-NP often relocalized to the cytoplasm and formed punctate cytoplasmic signals with a laterally polarized distribution (not shown), indicating the formation of mEYFP-tagged vRNP complexes. The fluorescence signal bleached very rapidly though due to overall low signal intensities.
In conclusion, the low yield of infected cells coexpressing mEYFP-NP and barely detectable cytoplasmic signals suggested that the conditions for mEYFP-NP expression in infection had to be further improved.

In the then following approach, transfection was performed already at 2 h p.i. (Fig. 55). Considerably more transfected cells and higher mEYFP-NP expression levels were attained in comparison to samples transfected at 3 h p.i., but also a delay of infection could be more frequently observed in form of reduced M1 expression levels (Fig. 55d). Apparently, an improvement of exogenous NP expression was achieved at the expense of viral replication.
While transfection at 3 h p.i. yielded mainly two populations of infected cells (untransfected cells and cells weakly coexpressing mEYFP-NP), the transfection performed at 2 h p.i. yielded a larger variety of cellular conditions. Different levels of mEYFP-NP expression were observed in infected cells (Fig. 55a, e), and infections were delayed to a varying extent (Fig. 55d). A strict correlation between exogenous NP expression level and delay in infection was however not observed.
As expected, a redistribution of mEYFP-NP to the cytoplasm was exclusively observed in infected cells, indicating functional incorporation of mEYFP-NP into vRNPs. Cytoplasmic accumulating mEYFP-NP had a punctate appearance and displayed a laterally polarized distribution (Fig. 55c, d, g), resembling the cytoplasmic distribution of viral NP in infection. On the contrary, when infection was considerably retarded or suppressed, the distribution of mEYFP-NP seemed to be unaffected by Influenza virus infection, and mEYFP-NP remained

primarily in the cell nucleus. A direct comparison between mEYFP-NP expressing cells in the presence and absence of ongoing virus replication is exemplarily shown in Fig. 55d.

In order to examine if coexpression of mEYFP-NP in infected cells could be even further improved, the gap between infection and subsequent transfection was further reduced to 1 h. Yet, an improvement of the results was not obtained under these conditions. On the contrary, in an increasing number of mEYFP-NP expressing cells, viral replication was efficiently suppressed as shown by the lack of viral HA expression (Fig. 56a, asterisks). Infected cells coexpressing mEYFP-NP on the other hand displayed relatively low mEYFP-NP expression levels. Cytoplasmic signals were close to the fluorescence background (Fig. 56b).

Among the tested experimental approaches, the best results to establish coexpression of fluorescent NP constructs in the context of infection were hence obtained when transfection was performed at 2 h p.i. Under these conditions, the highest mEYFP-NP expression levels in infected cells and the most prominent cytoplasmic mEYFP-NP signals were attained. No significant differences were further observed when C-terminally tagged NP-mEYFP was expressed instead of N-terminally tagged mEYFP-NP. The use of C-terminally tagged NP-mEYFP was abandoned though due to the co-occuring formation of free mEYFP (Fig. 40). Satisfying results were further obtained when the MOI was increased from 50 to 100 (see 4.4.2).

It has to be pointed out that despite optimization of the experimental conditions, the total yield of infected cells coexpressing mEYFP-NP and showing redistribution of mEYFP-NP to the cytoplasm was below 1 %. An even smaller fraction, comprising less than 1 ‰ of the cells, displayed sufficiently bright cytoplasmic mEYFP-NP signals for application in time-lapse imaging for over 10 min and 1200 frames without a critical degree of bleaching.
The low yield of cells showing prominent cytoplasmic mEYFP-NP signals did not impede analyses on the single cell level like subcellular localization studies and single particle tracking (SPT). Bulk experiments or biochemical analysis on the other hand were unsuitable to characterize the specific subset of cells or the progeny viruses produced from these cells. Evidence for successful incorporation of mEYFP-NP into vRNPs during infection and formation of mEYFP-tagged viruses were therefore difficult to obtain.
The high variability among the cells is believed to be due to a fragile equilibrium between transfection and infection and to a very tight time window that determines which of these processes finally dominates over the other or whether they will coexist. According to the findings obtained by modulating the delay between infection and transfection, the critical time

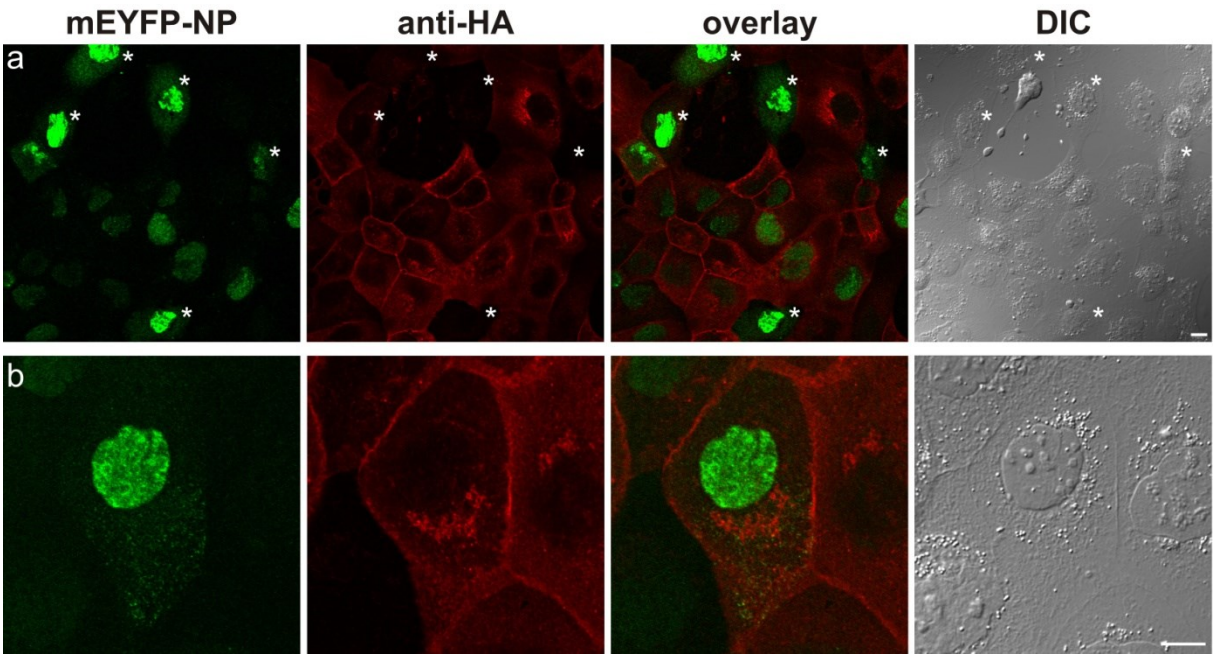

Fig. 56: Supertransfection of virus-infected cells at 1 h p.i. MDCK II cells were infected with Influenza A/FPV at MOI 50, subsequently transfected with mEYFP-NP at 1 h p.i. and finally fixed at 8 h p.i. and 7 h p.t. The cells were immunostained for viral HA to visualize infection, and they were monitored by confocal fluorescence microscopy. Representative images are shown. (a) High transfection efficiencies were attained in infected samples. In particular in mEYFP-NP expressing cells, infection was frequently found to be delayed or inhibited (asterisk). Despite MOI 50, effective infection was thus observed in less than 100 % of the cells. (b) Fine, punctate mEYFP-NP signals could be detected in the cytoplasm of some infected cells coexpressing mEYFP-NP. Cytoplasmic mEYFP-NP signals were however low compared to the nuclear signal and close to fluorescence background levels. Scale bar, 10 µm.

to establish exogenous mEYFP-NP expression in infected cells seems to be between 1 h p.i. and 3 h p.i. During this time, mEYFP-NP expression coincides with increasing viral transcription and protein synthesis [116,187], whereas host cell shut-off and inhibition of exogenous protein expression do not seem to be fully established yet. The critical time for the shut-down of exogenous protein expression is apparently between 2 h p.i. and 3 h p.i., since after 2 h of infection, the transfection was found to be still very effective (Fig. 55), whereas after 3 h p.i. mEYFP-NP expression was almost completely aborted (Fig. 54). A different susceptibility of the cells to be either transfected or infected might further contribute to the diversity of cellular states. As a consequence, the critical phase to establish coexpression of NP in infected cells might vary among the cells, but according to the experimental data it apparently ranges between 1 h p.i. and 3 h p.i.

Based on these considerations, further optimization of the experimental approach is considered to be limited by the heterogeneity of the cells. Following experiments were therefore focused on single cell analyses.

4.4.2 Cytoplasmic mEYFP-NP is cotransported with Rab11-positive recycling endosomes in infected cells

It was an important finding from experiments combining infection and exogenous mEYFP-NP expression (4.4.1) that infection is in fact able to induce relocalization of mEYFP-NP to the cytoplasm in form of small discrete particles, which adopt a laterally polarized distribution and tend to accumulate at the plasma membrane (Fig. 55g).

These observations suggest that a fraction of the fluorescent NP construct is incorporated into vRNPs and undergoes export from the nucleus towards the viral budding site at the plasma membrane. The granular appearance of mEYFP-NP in the cytoplasm of infected cells gives a first hint that mEYFP-NP indeed forms part of larger complexes. The observed distribution is further consistent with the characteristic cytoplasmic appearance of vRNPs during infection as previously shown by fluorescence *in situ* hybridization of vRNA and NP immunostainings [280,298].

However, it cannot be entirely excluded that mEYFP-NP by itself is affected by infection and redistributes to the cytoplasm. As aforementioned, biochemical analysis of cell lysates to provide evidence for incorporation of mEYFP-NP into vRNPs travelling the cytosol are not an appropriate tool due to the particularly small fraction of infected cells coexpressing mEYFP-NP and displaying further cytoplasmic localization of the construct.

While the current work was in progress, three other studies were published dealing with the mechanism of apical transport of vRNPs during infection. It was shown that vRNPs colocalize with Rab11-positive recycling endosomes (RE) [297,298] and associate with Rab11 via the PB2 subunit of the viral polymerase [280].

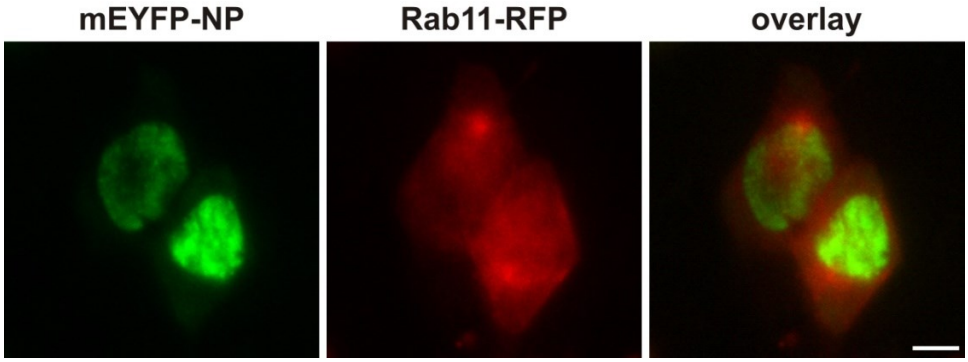

Fig. 57: Coexpression of mEYFP-NP and Rab11-RFP in MDCK II cells (8 h p.t.). MDCK II cells were cotransfected with mEYFP-NP and Rab11-RFP. The living cells were imaged with an epifluorescence microscope at 8 h p.t. Representative images are shown. mEYFP-NP localized predominantly in the nucleus, while the majority of Rab11-RFP could be found in the cytoplasm. Cytoplasmic fractions of both proteins had a relatively homogenous appearance, Rab11-RFP displaying the highest local concentration in a distinct juxtanuclear region. Scale bar, 10 µm.

In order to verify that the here established experimental system to analyze vRNP transport in living infected cells is consistent with the Rab11-dependent transport mechanism that was described in the above-mentioned studies, mEYFP-NP was cotransfected with the red-fluorescent Rab11-RFP in the presence or absence of infection.

Cotransfection experiments with mEYFP-NP and Rab11-RFP in the absence of infection demonstrated that mEYFP-NP and Rab11-RFP adopt largely distinct subcellular distributions (Fig. 57). Just like when expressed by itself, the vast majority of mEYFP-NP targeted to the nucleus, and only a small fraction could be found diffusely spread throughout the cytoplasm. Rab11, on the other hand, which is a pericentriolar recycling endosomal marker [508], displayed the most prominent local accumulation in a juxtanuclear region likely to be the MTOC and was further diffusely distributed throughout the cytoplasm. Coexpression of Rab11-RFP did not seem to affect the subcellular localization of mEYFP-NP.

Upon coexpression of mEYFP-NP and Rab11-RFP in virus-infected cells, the distribution of Rab11-RFP changed into a more punctate appearance, and a more prominent perinuclear accumulation was observed (Fig. 58). Similar infection-induced changes have been reported also for endogenous Rab11 [280,297].
In some cells, infection-induced relocalization of mEYFP-NP to the cytoplasm was observed as described in 4.4.1; whenever such accumulation of mEYFP-NP in form of punctate cytoplasmic structures was detected, an excellent degree of colocalization between mEYFP-NP and Rab11-RFP was observed (Fig. 58). The two proteins colocalized most prominently in the juxtanuclear region likely to be associated with the MTOC and in more dispersed speckled

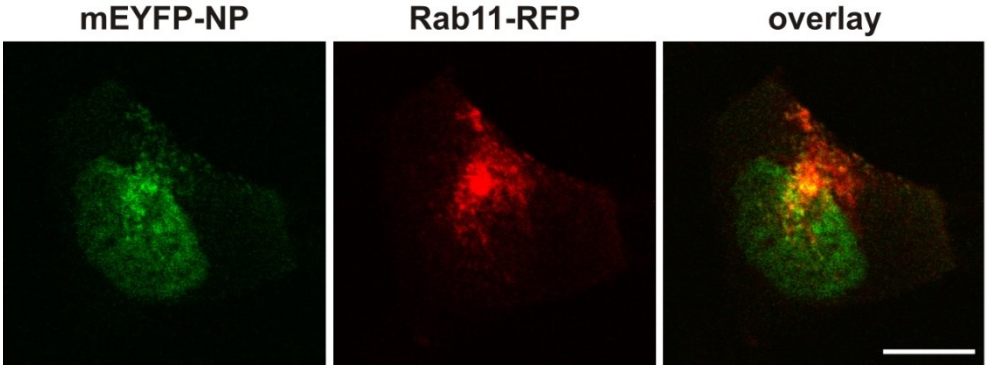

Fig. 58: Coexpression of mEYFP-NP and Rab11-RFP in Influenza virus-infected cells (9 h p.i., 7 h p.t). MDCK II cells were infected with Influenza A/FPV at MOI 100, and transfection with mEYFP-NP and Rab11-RFP was performed at 2 h p.i. Confocal fluorescence images were acquired at 9 h p.i. and 7 h p.t. Punctate cytoplasmic mEYFP-NP signals colocalized with Rab11-RFP in the perinuclear region and in the cell periphery. (The prominent juxtanuclear local accumulations of mEYFP-NP and Rab11-RFP shown here were imaged within the focal plane, which was positioned slightly above the nuclear compartment, highly enriched with mEYFP-NP, which can be observed as stray light). Scale bar, 10 µm.

structures in the peripheral cytoplasm. The majority of cytoplasmic mEYFP-NP apparently became associated with the recycling endosomal compartment.

The findings are consistent with the reported colocalization between vRNPs and Rab11 during Influenza virus infection, and they suggest that also mEYFP-NP associates with the recycling endosomal compartment in form of vRNP complexes.
Considering that the interaction between vRNPs and Rab11 was previously shown to be mediated by the viral polymerase [280,298], it is most likely that also mEYFP-NP targets to Rab11-positive structures in form of vRNPs through interaction with the polymerase subunit. This is supported by the finding that mEYFP-NP associates with recycling endosomes in infected cells, but not in the absence of infection (Fig. 57 & Fig. 58).
In conclusion, control experiments support the initial assumption that the fraction of mEYFP-NP which accumulates as punctate structures in the cytoplasm of infected cells represents intact vRNP complexes. Such mEYFP-tagged vRNPs, formed by incorporation of mEYFP-NP, apparently target the Rab11-dependent vesicular transport system just like vRNPs in normal infection.

Using the established experimental approach, it could not only be demonstrated that mEYFP-NP colocalized with Rab11 in infected cells, but it was also possible to monitor cotransport of mEYFP-NP with Rab11 in living infected cells.
Living infected cells coexpressing mEYFP-NP and Rab11-RFP were therefore imaged over 10 min in two dimensions with a frame rate of 2 frames per second. Image processing and analysis was performed as described in Material and Methods (3.2.3.3). Cytoplasmic mEYFP-NP typically localized in double-labeled structures together with Rab11-RFP, sharing the same dynamic behavior. Many of these particles remained static for long periods of time or even during the entire observation period, while other particles displayed fast saltatory movements, which are characteristic for microtubule-based transport.
For one representative cell, a random selection of 33 particles displaying movements between 2 and 20 µm was analyzed (Fig. 59). For each particle, mEYFP and RFP signals were independently traced. The results are shown in Fig. 59b and Fig. 59c. The overlay of the trajectories confirms cotrafficking of mEYFP-NP and Rab11-RFP (Fig. 59d, yellow and blue lines, respectively). The congruence of the tracks further demonstrates that the movement of particles could be relatively precisely and reliably be described, using the here applied semi-automated tracking method.
16 particles were initially selected from RFP fluorescence images, and 17 particles were

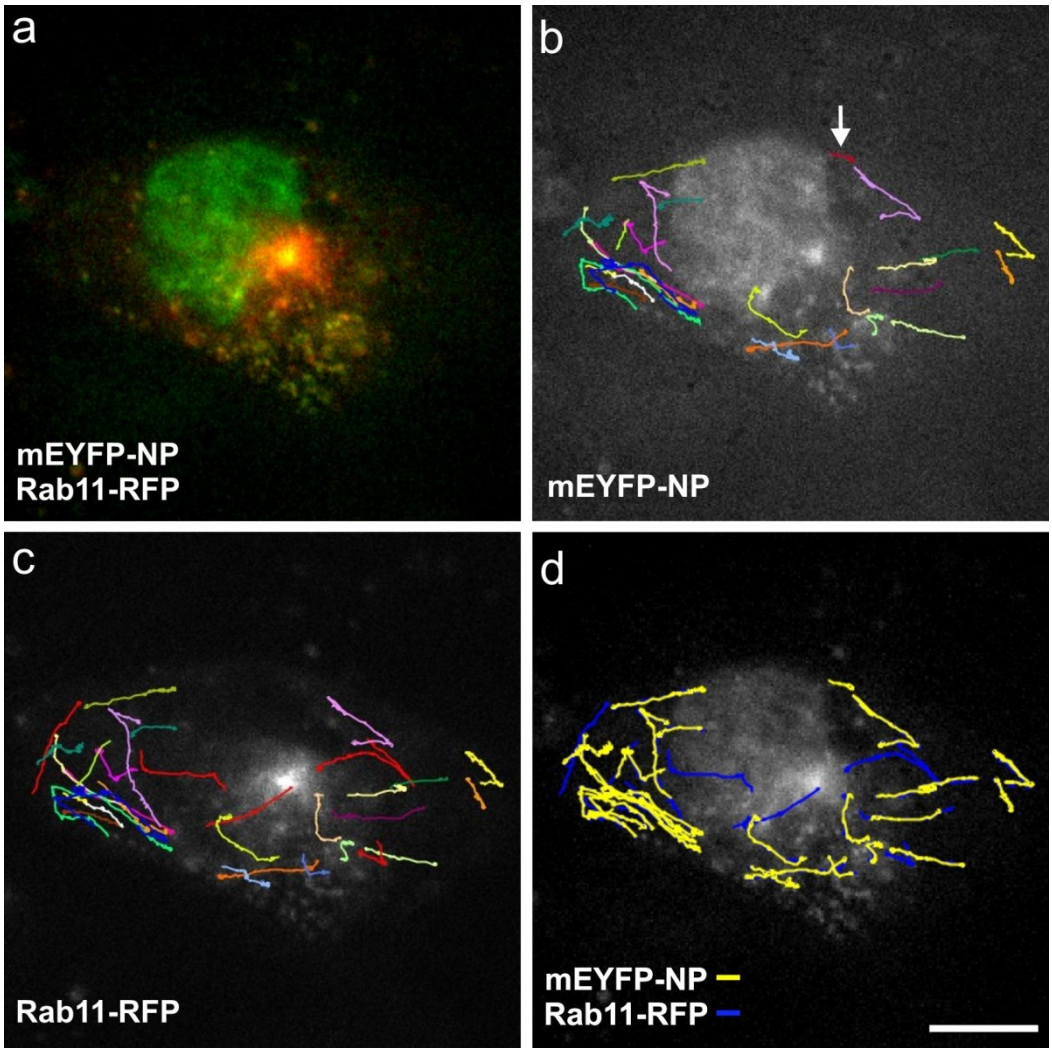

Fig. 59: Single particle tracking of mEYFP-NP and Rab11-RFP in living infected cells (10 h p.i. and 8 h p.t.). MDCK II cells were infected with Influenza A/FPV (MOI 100) and transfected with mEYFP-NP and Rab11-RFP at 2 h p.i. Two-dimensional time-lapse imaging of living cells was performed at 10 h p.i. and 8 h p.t. by epifluorescence microscopy. Image stacks were acquires over 10 min at a frame rate of 2 frames/s. For analysis, cells were selected displaying granular cytoplasmic mEYFP-NP signals. Trajectories of single fluorescent particles were analyzed using ImageJ and the Spot Tracker plugin. The graphic representation was generated with the MTrackJ. For one representative cell (a-d, single optical sections), the movement of 33 particles is indicated, which was separately traced for (b) mEYFP and (c) Rab11-RFP signals. Particle movements which could be detected for only one of the two fluorophores are represented in red. An overlay of the tracks is shown in (d) and demonstrates cotrafficking of mEYFP-NP (yellow lines) with Rab11-RFP (blue lines). Blue lines are concealed by yellow lines in case of overlapping trajectories. Trafficking of mEYFP-NP in the absence of colocalization with Rab11-RFP was rarlely observed (indicated by an arrow). The indicated track describes a movement from the nucleus to the cytoplasm covering a distance of 2.3 µm. Scale bar, 10 µm.

chosen from mEYFP images. Not all of the particles displayed the corresponding signal in mEYFP and RFP fluorescence images, though. In particular, movements of Rab11-RFP were frequently observed in the absence of mEYFP-NP (here: 5 out of 16 tracks, depicted as red lines in Fig. 59c).

Trafficking of mEYFP-NP, on the other hand, did typically not occur independent from Rab11-RFP transport, consistent with a Rab11-dependent transport mechanism. One

exception was observed though: a short trajectory, 5 µm in length and reaching from the nuclear rim into the cytoplasm, displayed mEYFP but not RFP fluorescence (Fig. 59b, arrow). It is possible that this trajectory describes translocation of an mEYFP-tagged vRNP subsequent to nuclear export and before association with the Rab11-dependent recycling endosomal machinery. The movement can be described as a directional movement with an average velocity (± SEM) of 0.23 ± 0.03 µm/s. This is close to reported values for myosin-driven actin-based transport [110,509,510] and further consistent with the existence of a perinuclear actin network. The particle then remained immobile for the rest of the observation time. This movement was not found to be representative though for movements in the perinulear region, which tended to be faster and cover longer distances (see below, Fig. 61).

It is a general limitation that individual mEYFP-NP particles cannot be detected within nuclei since the overall nuclear mEYFP-NP concentrations are too high. Therefore, it cannot be proven with certainty that a particle emerging at the nuclear surface has just been exported from the nucleus. Also particles which move close to the nuclear membrane in the perinuclear space might appear in the two-dimensional image plane close to the nuclear surface as though they exit from the nucleus.

Some considerations can help to interpret the data though. Considering the low probability for sharp turns of movement in one point, a particle movement perpendicular to the nuclear surface is more likely to represent an export event, while a parallel orientation of the track would rather indicate a perinuclear movement. It has to be further distinguished between imaging of the upper part of the nucleus, typically showing also accumulation of NP and Rab11 in the perinuclear region (Fig. 59), and imaging of the middle section of the nuclear compartment (Fig. 61).

In the upper part of the cell, particles moving across the nuclear compartment typically displayed a non-intermittent uniform movement and were distinguishable from the nucleus by distinct fluorescence intensities, suggesting that these particles moved in the perinuclear space above the nuclear compartment. When the middle section of nuclei was monitored instead, it was frequently seen that particles suddenly detached from nuclei and rapidly moved into the cytoplasm in a directed movement (Fig. 60a). These particles were undetectable in the cytoplasm or the nucleoplasm prior to their appearance at the nuclear surface. Yet, some of the particles emerged slightly underneath the nuclear outline, indicating that they were in fact coming from the inside of the nucleus (Fig. 60b). Also cases of retrograde movement towards the nucleus were observed where particles disappeared at the nuclear surface or slightly underneath as though being imported into the nucleus.

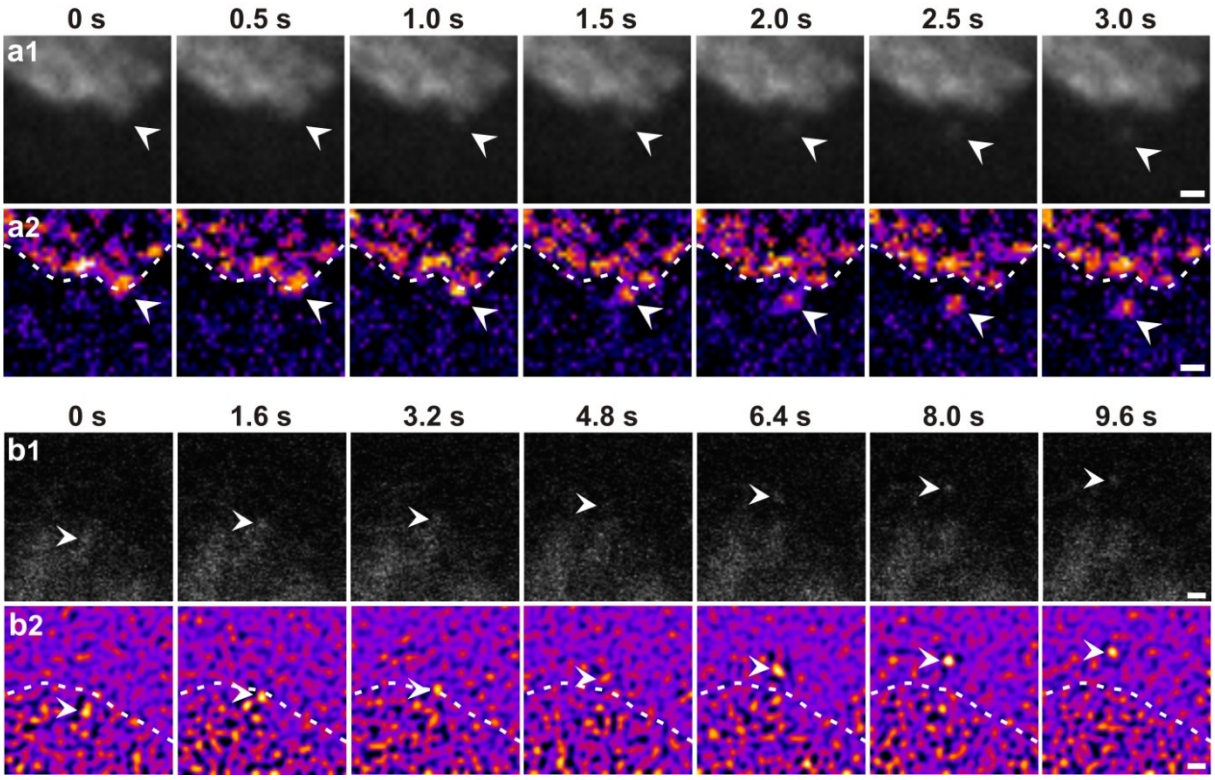

Fig. 60: Live-cell imaging of NP nuclear-cytoplasmic transport in infected cells (8.5 h p.i., 6.5 h p.t.). MDCK II cells were infected with Influenza A/FPV (MOI 100) and transfected with (a) mEYFP-NP or (b) mCherry-NP at 2 h p.i. Time-lapse imaging was performed at 8.5 h p.i. and 6.5 h p.t. (a) by epifluorescence microscopy at intervals of 0.5 s or (b) by confocal laser scanning microscopy at intervals of 1.6 s. Original fluorescence images (single optical sections of different time points) are shown in (a1, b1). Image stacks were then processed by forming of the median projection of the time stack, which was subtracted from each image of the stack, and finally the Spot Enhancement Filter from the ImageJ Spot Tracker plugin was applied. The results of image processing are shown in (a2, b2), represented as pseudo color images using the ImageJ lookup table "fire". Yellow indicates high signal intensity, while blue represents low signal. The nuclear outline was derived from the median projection as the line between the NP-rich nucleoplasm and the NP-depleted cytoplasm and is indicated as a dashed line in (a2, b2). Arrows indicate moving particles emerging at the nuclear boundary and traveling into the cytoplasm. Scale bar, 1 µm.

Particle movements from the nucleus into the cytoplasm were observed in most infected cells coexpressing fluorescent NP constructs. An example is shown in Fig. 61 where coexpression of the red-fluorescent mCherry-NP replaced expression of mEYFP-NP. mCherry-NP is an analogous construct which behaves like mEYFP-NP in experiments, but it has a considerably higher photostability. The trajectories of five particles are shown, which were found to emanate from the same site of the nucleus at short intervals. The time lag between their appearances was 42 s, 22 s, 32 s and 47 s, respectively. The particles performed a directional motion along identical pathways until they disappeared from the image plane. The average instant velocities of the particles ranged between 0.27 and 0.41 µm/s with an average of 0.34 ± 0.04 µm/s. The traveled distances in the cytoplasm varied between 4.7 and 9.3 µm. A highly frequented transport route thus seems to be located at this site of the nuclear surface. This

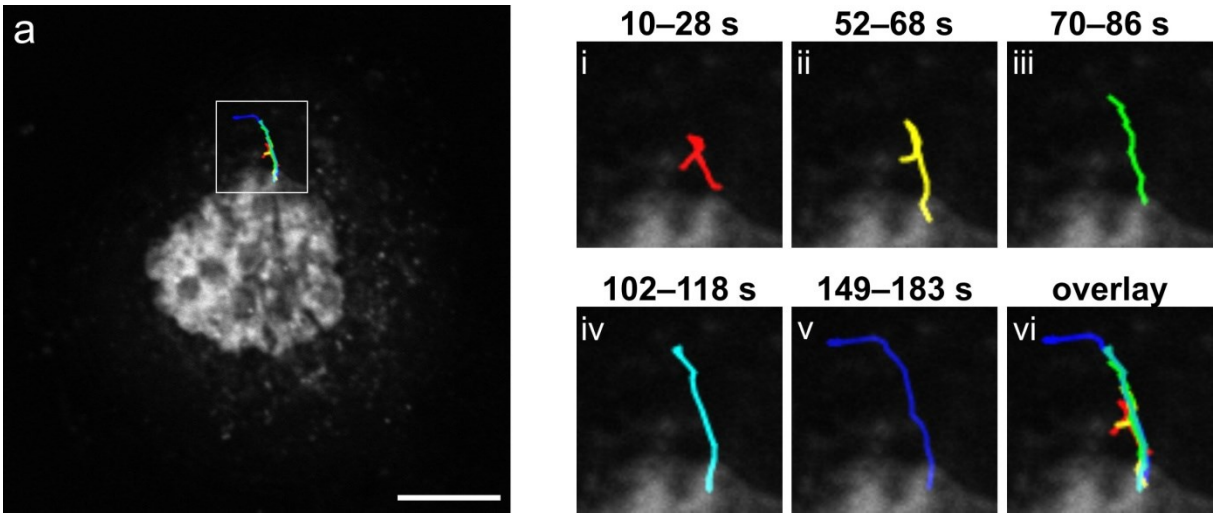

Fig. 61: Single particle tracking of mCherry-NP in living infected MDCK II cells (8.5 h p.i., 6.5 h p.t.). Infection with Influenza A/FPV (MOI 100) was performed 2 h prior to transfection with mCherry-NP. Living cells were monitored by confocal laser scanning fluorescence microscopy at a frame rate of 1 frame/1.1 s. (a) One representative cell is shown, displaying major accumulation of mCherry-NP in the cell nucleus and punctate mCherry-NP signals in the cytoplasm, which are indicative for successful viral infection. Particle movements were analyzed using the Spot Tracker plugin from ImageJ, and selected trajectories were plotted with MTrackJ. The trajectories of five particles are described, which emanate from the same site on the nucleus and traveled along the same route to the cell periphery in quick succession. The corresponding trajectories are plotted into a projection of the analyzed image stack. An enlargement of the indicated section, showing an overlay of the tracks, is given in panel (vi). The individual trajectories and the corresponding time of observation are shown in panels (i) to (v). The average velocity of the particles (± SEM) was calculated to be 0.34 ± 0.04 µm/s. The track lengths varied between 4.7 and 9.3 µm. Scale bar, 10 µm.

could be the exit of a nuclear pore and/or the path of a cytoskeletal structure (e.g. microtubule) passing in very close proximity to the nucleus.

Fluorescent particle movements were detected throughout the cytoplasm. Some of the particles moved in and out of the pericentriolar region where Rab11 concentrates, and part of them traveled in more peripheral regions of the cytoplasm. Both anterograde and retrograde transport were observed. The average instant velocities measured for individual fast saltatory movements as depicted in Fig. 62 ranged from 0.3 to 1.2 µm/s with peaks up to 1.7 µm/s. The values are consistent with the velocities reported for microtubule- and motor protein-dependent transport [511,512,513] and further excellently match the results that were obtained by Amorim *et al.* [280] for microtubule-dependent transport of GFP-tagged reconstituted vRNPs in the absence of infection.

Particularly in regions with high spot densities, the tracking of single particles was difficult to realize. Trajectories were masked by numerous overlapping signals. The continuous path of one single particle was therefore difficult to trace. It is a general issue of SPT that two signals which merge and separate again cannot be unambiguously assigned. Tracks in Fig. 59 are

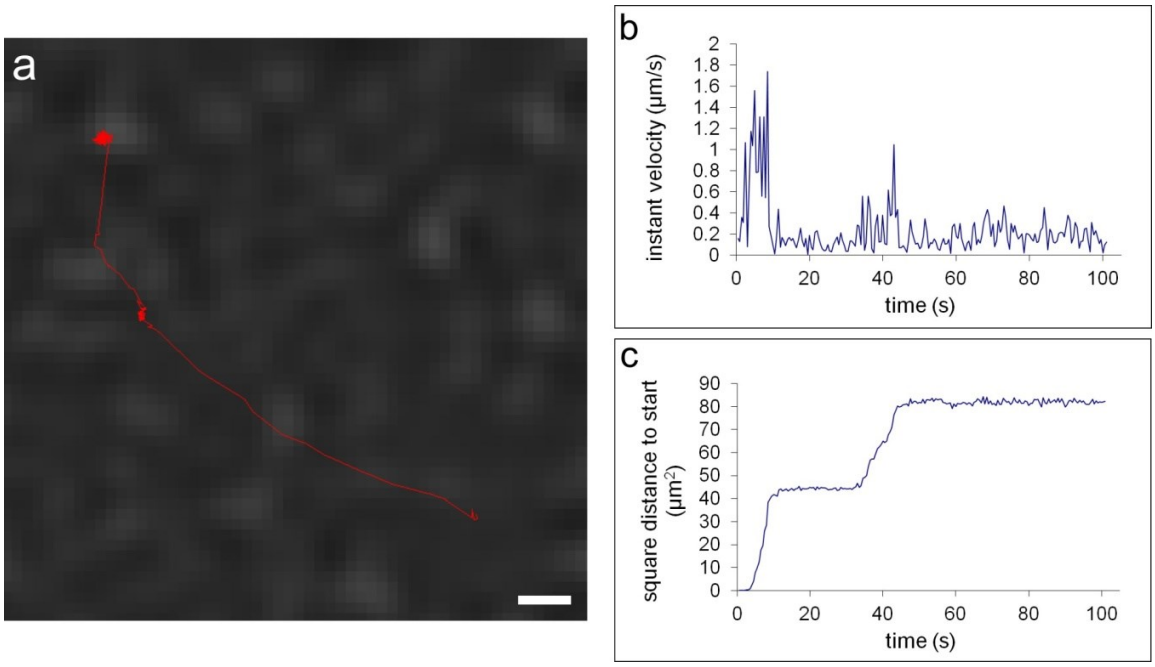

Fig. 62: Long-range movements of mEYFP-NP particles display a saltatory character. (a) A trajectory from SPT of mEYFP-NP particles in infected cells shown in Fig. 59 was selected (Fig. 59b, left trajectory, bright yellow), and it was analyzed for (b) the instant velocity and (c) the square distance to the start point of the trajectory , which were plotted over time. The average instant velocities of the two fast motile events were calculated to be 0.81 ± 0.09 µm/s and 58.8 ± 0.12 µm/s, respectively. Scale bar, 1 µm.

therefore preferentially shown in regions with low particle densities at some distance from the MTOC. Nevertheless, highly mobile particles were also observed in the vicinity of the MTOC.

Most long-range movements can be described as intermittent movements (Fig. 62). They were found to be subdivided into several short movements, covering distances of a few micrometers and being interrupted by a sudden halt. Breakpoints of movements were often located at sites to which also other particles were targeted, indicating nodal points of unknown nature where Rab11-positive transport vesicles (with NP load) transiently accumulate. Numerous events of merging and splitting of signals were accordingly observed. When an encounter between particles comprised not more than two particles, different signal intensities could help to trace the particles.

When mEYFP-NP and Rab11-RFP cotraveled in form of double-labeled particles as shown in Fig. 59, the signals of the two fluorophores were generally not found to separate over time. It has to be considered though that the observation period for each particle was limited since moving particles tended to escape from the image plane. It was therefore not possible under the given conditions to follow one single particle throughout the cell. A fast three dimensional imaging technique would overcome this limitation.

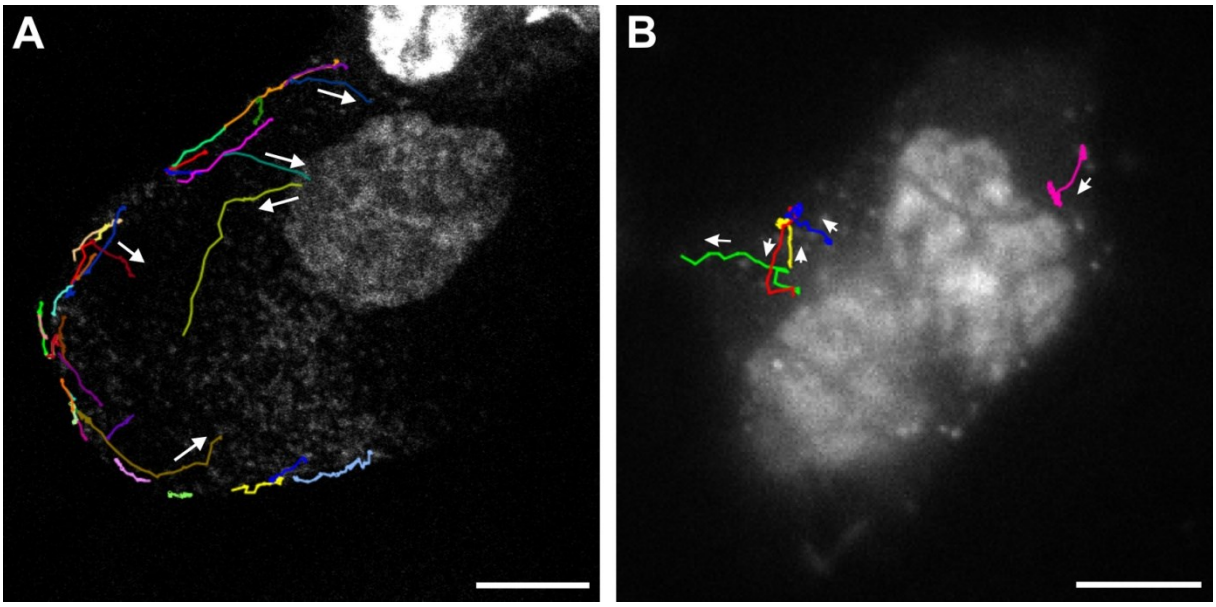

Fig. 63: Single particle tracking of mEYFP-NP at the plasma membrane of infected MDCK II cells (9 h p.i., 7 h p.t.). The cells were infected with Influenza A/FPV (MOI 100) and subsequently transfected with mEYFP-NP at 2 h p.i. Time-lapse imaging was performed at 9 h p.i. and 7 h p.t. (A) by confocal laser scanning microscopy or (B) by epifluorescence microscopy. Images were acquired every 1.6 s or 0.5 s, respectively. SPT was performed using the ImageJ Sport Tracker plugin. Particles were selected which moved close to the plasma membrane, and their trajectories were plotted into a single optical section of the respective image stack. (A) Particles were found to move along the plasma membrane, but also orthogonal movements towards the plasma membrane and back to the cell center were observed. A large fraction of temporarily "immobile" (non-processive) particles is not represented. (B) Particle movements are shown – moving towards and departing from the plasma membrane – which are followed by or precede a period of locally restricted non-processive movement at the plasma membrane. Arrows next to trajectories indicate the direction of the movement. Scale bar, 10 µm.

Long-range movements of mEYFP-NP and Rab11-RFP complexes were unexpectedly more frequently observed to run parallel to the cell boundaries than to target straight to the plasma membrane (Fig. 59). Nevertheless, it occured occasionally that particles moved straight to the cell periphery where they came to stop. Particles which could be traced also after arrival at the plasma membrane tended to remain relatively static for a while and to disappear over time. The simultaneous disappearance of Rab11-RFP signals indicates that these particles had moved out of the image plane rather than having undergone virus budding. This is consistent with observations made in cells where mEYFP-NP particles accumulated along the plasma membrane (Fig. 63A). Single particles that were targeted to the plasma membrane were quickly lost in the crowd of other particles, but the sum of particle movements demonstrated that there was significant movement beneath the plasma membrane. Processive and random movements of different velocities were observed. Particles seemed to move two-dimensionally and in close proximity underneath the plasma membrane. Yet, static particles were frequently found to undergo sudden and rapid transport back towards the cell nucleus (Fig. 63B). Together, the data suggest that mEYFP-NP complexes arrive at the plasma

membrane via microtubule- and recycling endosome-dependent transport where the cargo might be released from microtubules and change to another transportation mode along the plasma membrane before reaching the budding site. Considering the role of the peripheral actin network for transporting endocytic vesicles during viral uptake, an analogous mechanism might be assumed [110]. If this transition fails, the cargo might be redirected into the cell body.

5 Discussion

5.1 The role of vRNP membrane binding for virus assembly

5.1.1 Characterization of purified vRNPs

The first aim of this study was to analyze the intrinsic and M1-mediated interaction capacity of vRNPs with membranes. To this end, vRNPs had to be purified from Influenza A virus particles and to be scrutinized prior to application in experiments. Purification was performed according to an established protocol [117]. Yet, in contrast to that report, M1 was detected in purified vRNP fractions, but could be selectively removed (Fig. 8F). The purity of the proteins was validated by SDS-PAGE (Fig. 8C). The presence of RNA bound to NP in purified samples could be demonstrated indirectly by the novel combinatorial use of two nucleic acid stains with different properties, propidium iodide (PI) and acridine orange (AO), and by spectrofluorometric analysis (4.1.1, Fig. 10). To the best of my knowledge, this approach has not been used before, detecting the presence of single-stranded (ss) nucleic acids by PI and simultaneously verifying protein binding to these nucleic acids via electrostatic phosphate backbone interactions by the use of AO.

PI fluorescence spectra clearly demonstrated the presence of nucleic acids in the samples by characteristic spectral shifts caused by intercalation of the dye molecules, whereas AO fluorescence (a double-strand intercalating and single-strand backbone binding dye [470,471]) lacked any spectral changes and thus indicated the absence of ds nucleic acids and the inaccessibility of the phosphate backbone. Together, the results suggest that the purified samples contained ss nucleic acids with a phosphate backbone fully shielded from interaction with AO. These results are consistent with the model of NP-vRNA complexes that was postulated in 1994 by Baudin *et al.* based on the inaccessibility of the RNA backbone and on the exposure of the ribonucleotide bases as measured by their chemical reactivities [87]. This concept of RNA binding to NP by electrostatic interactions with the phosphate backbone was further supported by the finding that NP binds to RNA with high affinity but without sequence specificity [87,91,514] and by NP crystal structures displaying a highly positively charged arginine-rich groove which could be shown to be crucial for RNA binding by mutational analysis [93,333]. Very early studies in this field further demonstrated that RNA can be efficiently released from NP by competitive addition of the polyanion polyvinylsulfate [82,338]. Based on this set of experimental evidence for a backbone-mediated interaction

between RNA and NP, the data obtained here by PI and AO fluorescence analysis of the purified vRNP samples strongly support that RNA and NP were co-purified and preserved as RNP complexes (Fig. 10). Electron microscopy studies additionally confirmed the presence of intact, elongated flexible structures of appropriate size within these preparations (Fig. 9). vRNPs were previously reported to range from about 30 to 120 nm [8,52,53]. It was thus ensured that the results obtained in flotation experiments reflect properties of intact vRNP complexes.

5.1.2 vRNPs do not directly bind to lipid membranes

Using these purified native vRNPs, the membrane binding capacity of the genomic segments was examined to address the question if vRNPs can potentially use membrane interaction or lipid recognition for specific targeting and association with the budding site (4.1.2, 4.1.3). For Influenza viruses, membrane interactions and targeting motifs (raft targeting and apical targeting) have been well studied in case of the three transmembrane proteins (HA, NA, M2) and in case of the matrix protein M1 (reviewed in [21], [41]). Specific interactions of all four proteins with cellular membranes constitute intrinsic signals that can either independently target these proteins to the apical plasma membrane or contribute to membrane attachment, thereby facilitating their recruitment to the budding site. The role of membrane interactions for the assembly of genomic vRNPs has however not been addressed before. Direct or indirect membrane association might similarly contribute to vesicular trafficking of the vRNPs or to the attachment of vRNPs to the viral budzone. Elucidating this aspect was the goal of the first part of this study.

A first observation indicating the presence of intrinsic targeting signals in vRNPs was made by Carrasco *et al.* [299] and Elton *et al.* [515], who described a lipid raft-dependent apical localization of NP when expressed alone in polarized cells, suggesting that NP as the major vRNP component might contribute to vRNP targeting to the viral budding site. In more recent studies, it has been shown that transport of vRNPs from the nucleus to the apical plasma membrane is mediated by recycling endosomes (RE) [280,297,298]. Even though recruitment of vRNPs to RE seems to be through interaction of PB2 with endosomal Rab11 [280], a contributory effect of other interactions, e.g. membrane interactions, to support the transport of the large vRNP complexes can be imagined.

In the present study, the ability of vRNPs to interact with pure lipid bilayers or with specific lipid species was carefully investigated. Yet, no interaction could be detected (Fig. 11, Fig. 13). A variety of lipid compositions, representing the most abundant phospholipid classes of

cellular membranes, were tested, e.g. the inner leaflet plasma membrane lipids DOPS and DOPE, the classical raft lipid mixture DOPC, SM and Chol and a total lipid extract from native tissue featuring the natural lipid diversity. Since vRNPs are negatively charged complexes, also the combination with divalent Ca^{2+} ions and negatively charged DOPS-containing membranes was tested. The analyzed lipid species represent not only the major lipid classes present in permissive host cell lines like MDCK II cells, but also the major lipid classes that constitute the Influenza virus envelope [16]. Moreover, this study comprised phosphoinositides, an important group of functionally specialized lipids which are involved in signaling and definition of subcellular compartment identity [477]. From these experiments, it cannot entirely be excluded that vRNPs are able to interact with membranes under circumstances that were not covered within this study. However, the examination of a broad variety of lipids and lipid compositions strongly supports the conclusion that vRNPs are not able to associate with pure lipid membrane and that – most likely – direct vRNP membrane interactions do not play a role in viral replication.

5.1.3 Revisiting membrane binding of uncomplexed NP

With regard to the intrinsic, lipid raft-dependent apical targeting of NP that was previously postulated as underlying mechanism for apical targeting of vRNP complexes [299], it could be shown here that neither NP by itself nor vRNP complexes were able to associate with raft lipid mixtures (Fig. 11C, D). This finding suggests that the observed lipid raft-dependent behavior of NP as described by Carrasco *et al.* [299] may have been caused by interaction with a raft-associated cellular component, but not by direct interaction with raft lipids. It should be further considered that the effect of cholesterol depletion, causing perturbation of NP apical distribution (which was interpreted as raft-dependent behavior of NP [299]), might have also been due to a general perturbation of cellular trafficking in cholesterol-depleted cells. In line with this interpretation, NP apical localization in the same study was only slightly affected by cholesterol depletion, whereas apical localization of raft-associated HA was completely impaired by membrane raft disruption. Further, only 12 % of total cytoplasmic NP was shown to be membrane-associated in NP-expressing cells, while apical localization was shown for the vast majority of NP. Taken together, the data provided by Carrasco *et al.* seem to allow another interpretation aside from the one proposed, namely that apical targeting or retention of NP in transfected cells might be determined by factors other than membrane rafts.

The results that were obtained here by flotation of NP with liposomes indicate an alternative contributory factor for the apical localization of NP. NP as a highly positively charged protein could be shown to partially associate with negatively charged liposomes (Fig. 11D). Transferring this finding to a cellular context, this property might be one determinant for NP behavior when NP is expressed in the absence of infection and when its positive charges are not neutralized by vRNA binding. This assumption is based on the work of Yeung *et al.* [286]. They have shown that the subcellular localization of proteins with a polybasic cluster is influenced by electrostatic interaction with cellular membranes. Proteins with a moderately positive charge are directed to endosomal compartments, whereas strongly cationic proteins with charges of about +8 are directed to the plasma membrane. The plasma membrane is considered to feature the most-negative surface charge among the cytoplasmic membrane leaflets due to the presence of PS and phosphoinositides. Low cationic, hydrophobic probes localize preferentially to membranes of the secretory pathway instead [286]. This leads me to the assumption that NP, bearing a positive charge of +14 at pH 6.5 [327] and being able to associate with PS-containing liposomes *in vitro*, might be driven towards the cell periphery when localized in the cytoplasm. Details on the specific surface charges of apical and basolateral membrane domains are not known. Cosegregation of negatively charged PS with sphingolipid- and cholesterol-enriched liquid-ordered domains of cellular membranes was described by Fairn and coworkers [476] and might provide a connection between the formerly suggested, partially raft-dependent behavior of NP in cells and the here observed interaction of NP with negatively charged liposomes *in vitro*.

In conclusion, electrostatic membrane interactions might have contributed to NP targeting to the apical plasma membrane as described by Carrasco and coworkers and might further have partially maintained the NP subcellular distribution even after cholesterol depletion [299]. It should be considered, though, that exposure of the highly positively charged RNA-binding groove of NP and the net positive charge of RNA-free cytoplasmic NP represent artifacts of NP expression in the absence of virus infection, since NP is rapidly imported into the nucleus during infection and re-exported into the cytosol mainly in an RNA-bound form [297], carrying a net negative charge. Thus, NP targeting if driven by electrostatic interactions would be only of limited significance for virus infection and in particular during virus assembly. Since important electrostatic effects can generally not be excluded when studying NP in the absence of virus infection, data obtained for NP in an RNA-free state have to be interpreted carefully, particularly with regard to the transferability of NP behavior to infection.

Carrasco *et al.* studied the NP distribution in transfected cells at 48 h p.t., which is a relatively late time point for standard analysis of exogenously expressed proteins. It may thus be possible that the reported apical distribution of NP established only very slowly, implying a passive process, which is in line with the here proposed electrostatic targeting of NP and with the overall low cytoplasmic mobility of NP that was demonstrated in the present study (Fig. 47A, B). Slow NP diffusion and apical retention due to weak interactions could possibly explain a slow manifestation of NP apical targeting. Due to the timescale, this mechanism would however be hardly relevant for apical targeting of vRNPs during infection. Variation of NP apical targeting in different cell lines was further reported and suggests cell line-specific interactions with the apical compartment.

For a balanced view, it should furthermore be noted that other studies which investigated various cell lines and NP subtypes [44,118,363] did not report intrinsic apical localization of NP, which in accordance with NP expression experiments of the present study (see 4.3.3). Instead, a homogenous cytosolic NP distribution was described for various time points of observation, which could be confirmed here also for 48 h p.t. (Fig. 37). One experimental approach within the present study therefore aimed at verifying the reproducibility of NP apical localization in polarized cells. NP constructs were hence expressed in polarized MDCK II cells (Fig. 52). NP was expressed as wt protein or equipped with a nuclear export signal (NES) for increased amounts of cytosolic protein. The proteins were detected as intrinsically fluorescent fusion proteins or by immunofluorescence. However, none of the constructs displayed apical accumulation after 13 days of polarized growth. Expressed proteins distributed homogenously throughout the cytoplasm, whereas the viral control protein HA, which is known to contain an apical targeting signal [41], was exclusively sorted to the apical plasma membrane (Fig. 52f). The uniform cytoplasmic distribution of NP was the same as in non-polarized cells at 7, 24 and 48 h p.t. Taken together, apical targeting of NP as presented in [299] could not be reproduced, even though analysis was performed under basically comparable conditions, including the same cell line and the same time point. A difference was made by using NP from Influenza A/FPV virus instead of the NP sequence from Influenza A/PR/8 virus. The two proteins share 94 % sequence identity, and a fundamental mechanism like genome targeting should be independent from strain-specific differences. As MDCK II cells are permissive for Influenza virus infection, they are generally suitable to study mechanisms crucial to viral replication. MDCK II cells were one of the cell lines reported to show preferential accumulation of NP at the apical surface. However, the results obtained in the present study imply that NP apical targeting as observed by Carrasco *et*

al. [299] cannot be generalized and thus might play a minor role in Influenza virus replication. Factors that might have driven NP apical accumulation in previously reported cases could not be further investigated due to non-reproducibility. A significant influence of membrane surface charges on NP subcellular localization was furthermore not detectable in the context of these experiments.
Finally, it should be mentioned that immunofluorescence stainings in particular for NP have been found to be prone to artifacts as shown in Fig. 42. Special attention has to be paid when analyzing polarized distributions, as immunofluorescence stainings can give rise to false-positive detections and may have influenced former analyses of NP apical localization.

5.1.4 vRNPs bind to lipid membranes via M1 *in vitro*

A general conclusion can be drawn from *in vitro* membrane binding studies of NP in comparison with vRNPs (Fig. 11C, D). The ability of NP to interact directly with negatively charged liposomes is apparently not relevant for membrane binding of complete vRNP complexes as these failed to associate with the same liposome species.
According to these results, direct interaction of vRNPs with cellular membranes is unlikely to occur and to contribute to processes like vesicular transport or association with the nascent viral envelope. Other factors have to be considered for targeting and anchoring of vRNPs to the viral envelope. M1 is a promising candidate to play a key role in the assembly of virus particles as it is known to be able to interact with all viral components including lipid membranes, the viral membrane proteins and the vRNP complexes (reviewed in [20,41,300]). Topologically, it has been shown to form a layer between the genomic complexes and the viral envelope in intact virus particles. Even though electron microscopy data do not show a tight interaction between M1 and vRNPs in virus particles [8,31], numerous studies have demonstrated efficient vRNP-M1 interaction biochemically by purification of complexes from infected cells [29], from intact virus particles [51,68,113] or by *in vitro* reconstitution [42,275]. However, simultaneous interaction of M1 with the different viral components has not been shown yet, and a temporal and spatial characterization of these interactions during the viral replication cycle is still missing.

In the present study, M1 was analyzed for its ability to mediate association of vRNPs with lipid membranes, and it could be demonstrated that M1 is in fact able to connect vRNPs with lipid bilayers. Despite some technical limitations of the method as outlined in 4.1.2, M1, which is able to interact efficiently with negatively charged membranes by itself (Fig. 12B;

[42,45,445]), was able to attach a fraction of vRNPs to negatively charged liposomes, containing DOPS or total brain lipid extract (Fig. 12A, B). Notably, when M1 was bound to the phosphoinositide PtdIns(4)P in the presence of vRNPs, vRNPs did not associate with the PtdIns(4)P-bound M1 (Fig. 13). Specific binding of M1 to PtdIns(4)P was demonstrated in a binding screen using a lipid-spotted support (PIP strip). This interaction was further confirmed by the work of Nadine Jungnick, using PtdIns(4)P presented in form of a liposomal bilayer and recombinantly generated M1 [445]. Circular dichroism measurements in the same study showed that M1 undergoes differential conformational changes upon binding to DOPS- or PtdIns(4)P-containing liposomes, indicating the formation of different conformational subpopulations of M1 when bound either to DOPS or PtdIns(4)P. These forms of M1 might differ by their ability to interact with vRNPs and thus by their ability to connect vRNPs and membranes. Intriguingly, this assumption is consistent with the previously reported differential subcellular behavior of the two viral components during viral replication [516]. M1 is targeted to the Golgi membrane of transfected and infected cells [38,449] where PtdIns(4)P is known to be localized [477], whereas vRNPs do not localize to the Golgi apparatus during infection [280]. PtdIns(4)P is known to be a functionally defining lipid of the Golgi apparatus [517]. Its interaction with M1 is thus likely to explain the previously reported prominent recruitment of M1 to the Golgi apparatus in transfected and infected cells, although this remains to be demonstrated. Even though M1 is abundantly present and various models postulated that it mediates membrane association of the genomic segments [20,34,41], vRNPs do not colocalize with the Golgi complex (or with HA [298]) during infection [280]. Instead, vRNPs undergo cytoplasmic transport using the endosomal recycling system [280,297,298]. A close proximity of vRNPs to M1 at cellular membranes could so far solely be shown by electron microscopy at the newly forming viral envelope or in intact virus particles [8,35]. This site-specific aspect of (co-)localization of M1 and vRNPs *in situ* might reflect a selective binding mode of M1 to vRNPs depending on the type of lipid interaction that M1 experiences, which is in analogy to observations from *in vitro* experiments (4.1.2 and 4.1.3). This model provides an explanation how M1 can possibly support the attachment of vRNPs to specific sites like the budding site, but not to others like the Golgi apparatus.

In cells, the lipid PS is predominantly present on endosomal membranes and on the inner plasma membrane leaflet [518,519], i.e. on those membranes that are known to recruit vRNPs during viral infection. PS is however hardly found on the cytoplasmic membrane leaflets of the secretory pathway [286,476,519]. Net negative surface charges of subcellular membranes correlate with the presence of PS and phosphoinositides, making the plasma membrane the

most negatively charged and the secretory system the least negatively charged cytosolic membranes [286]. PtdIns(4)P is prevalent on the Golgi membrane. The ability to bind electrostatically to negatively charged membranes [45] and to bind specifically to PtdIns(4)P-containing membranes [445] should enable M1 to interact with most subcellular membranes. Notably, the conformational switch of M1 due to interaction with a compartment-specific lipid most likely allows M1 to distinguish between different subcellular compartments and to exercise coordinated and site-specific functions like interactions with the genomic complexes.

5.1.5 Model for the role of M1 during the infection cycle

Combining these aspects, a model can be formulated describing vRNPs, M1 and their interplay during viral assembly. The first step to assemble the viral core components into progeny virus particles is their export from the cell nucleus. It is a generally accepted model that vRNPs associate with M1 to form vRNP-M1-NEP-CRM1 export complexes to access the cellular nuclear export machinery [269,270,292]. There is convincing evidence for the formation of these 'daisy-chain' complexes: vRNP nuclear export is critically dependent on M1 [116,260], NEP [66,264,270] and CRM1 [266,267], and suitable binary interactions among these components have been demonstrated [42,269,270].

It is not clear, though, if vRNPs remain attached to M1 during the following cytoplasmic transport. Fluorescence microscopy studies convey the impression that M1 and vRNPs might take separate routes [516], vRNPs being targeted to recycling endosomes by specific interaction of PB2 with Rab11 [280], but they do not colocalize with the Golgi apparatus or HA [280,298], whereas M1was shown to accumulate at the Golgi complex together with HA [38]. Yet, M1 is abundantly expressed and can be found diffusely throughout the entire cell, which makes it difficult to assign a specific localization pattern to M1 [520,521,522]. Even though the importance of M1 for vRNP nuclear export and further for the prevention of vRNP reimport [29,124] is well characterized, prominent colocalization of M1 with exported vRNPs or a shift in M1 distribution during infection has not been reported [116,266]. Similarly, M1 was not found to be enriched with peripheral cytoplasmic vRNPs [516], which typically colocalize with the recycling endosomal compartment [297]. Due to the diffuse overall distribution, it cannot be excluded though that a small fraction of M1 remains associated with vRNPs during cytoplasmic transport. Biochemically, M1 could not be coprecipitated with Rab11-vRNP transport complexes [280,298], although M1 is efficiently coprecipitated with vRNPs from infected cells [29]. It is generally believed that the dissociation of M1 from vRNPs is triggered by acidic pH only at the stage of viral entry during endocytosis. The

results obtained here from *in vitro* experiments showing M1-mediated vRNP attachment to DOPS-containing liposomes (Fig. 12) now provide evidence that M1 is potentially able to support vRNP attachment to the negatively charged recycling endosomes by electrostatic interaction during cytoplasmic transport. The electrostatic nature of M1 membrane binding and the fact that high net negative charges on cytoplasmic membranes are limited to endosomes and the plasma membrane might confer a certain degree of specificity to M1-mediated vRNP membrane interaction.

For many years, studies have shown that M1 efficiently associates with membranes *in vitro* and in cells. However, work on virus-like particle (VLP) production with M1 suggests that a membrane anchor is needed to target M1 to the plasma membrane for efficient membrane binding and VLP formation [257,288,289]. Combined with the observation that M1 lacks a clear plasma membrane localization when expressed alone [257], these findings seem to indicate that M1 is not able to target itself or vRNPs to specific cellular membranes like the recycling endosomal or the plasma membrane, despite their negative surface charges. Instead, M1 recruitment to HA, NA or M2 cytoplasmic tails or the recruitment of vRNP-bound M1 by primary targeting of vRNPs to endosomal membranes might be necessary to initiate or stabilize M1 membrane binding, and only then, M1 might be able to efficiently contribute to virus bud formation or to attachment of vRNPs to recycling endosomal transport vesicles.

Most interestingly, apart from its role in virus assembly, electrostatic membrane binding might furthermore enable M1 to exert a regulatory function on recycling endosomal trafficking. This assumption is based on a study by Uchida and coworkers, demonstrating that competitive displacement of the cellular PS-binding protein evectin-2 from recycling endosomes disrupts specifically retrograde transport from recycling endosomes to the *trans*-Golgi network [518]. In infection, inhibition of retrograde transport might contribute to efficient delivery of vRNPs to the plasma membrane by impeding alternative transport routes. It might further reduce retrograde transport of viral membrane proteins from the plasma membrane. Whether M1 binding to negatively charged PS in infection can compete with specific evectin-2 binding to PS on recycling endosomes – and thus interferes with recycling endosomal trafficking – remains to be tested.

Unlike M1 interactions with the plasma membrane and endosomal membranes, targeting of M1 to the Golgi complex is relatively pronounced and independent from other viral proteins. The function of M1 targeting to the Golgi complex is still unclear, though. On the one hand, it would be obvious to assume that M1 may interact with the cytoplasmic tails of the viral

transmembrane proteins during infection and that they might preform an early budzone together with nascent raft domains. On the other hand, by specific targeting of PtdIns(4)P, M1 might interfere with cellular processes to the benefit of viral replication. PtdIns(4)P is known to be involved in the regulation of membrane trafficking from the Golgi complex to the plasma membrane and in sphingolipid metabolism, thereby playing a central role in the control of the plasma membrane composition [517,523]. These functions form a highly interesting connection to Influenza virus replication and make PtdIns(4)P a promising candidate to be targeted by the viral machinery. It can be speculated that, by interaction with PtdIns(4)P, M1 might be able to promote efficient transport of the viral transmembrane proteins to the plasma membrane. Further, it might be able to modulate the lipid composition at the level of the Golgi complex and consequently at the level of the plasma membrane from which the viral envelope is then formed. It was only recently shown that the SM biosynthetic pathway is essential for the transport of viral glycoproteins from the Golgi to the plasma membrane during infection and for the efficient release of virus particles [524]. The activity of the sphingomyelin synthase at the Golgi membrane is furthermore known to require PtdIns(4)-dependent delivery of ceramide [517]. Assuming that M1 interaction with PtdIns(4)P can indeed affect sphingolipid synthesis, this might be a mechanism to supply high levels of SM to match the specific requirements for the formation of the budding site. According to this hypothesis, the Influenza viral envelope may not be specifically enriched in raft lipids in comparison to the lipid composition of the apical plasma membrane as it was previously suggested [16]. Instead, the overall composition of the apical plasma membrane may be changed in infected cells. The study of Gerl and coworkers recently compared the lipidome of the viral envelope with the lipidome of the apical plasma membrane of uninfected cells [16]. Data on the lipid composition of the apical membrane of infected cells was not provided. It could be shown however that whole-cell lipid extracts from Influenza virus-infected cells display a relative reduction in PC and an increase in PI as the most prominent changes in comparison to uninfected control cells. Also an increase of SM was reported with a concomitant decrease of ceramide. A remarkable increase was furthermore reported for dihydro-SM. It might be considered though that effects of altered lipid metabolism and effects of lipid depletion due to virus budding might overlap in infected cells. To verify the above-proposed hyposthesis that M1 interferes with the cellular lipid metabolism, changes in the lipid content of M1-expressing cells may be analyzed.

It was previously reported that mutations within a highly conserved basic amino acid sequence of M1 (residues 76–78) caused aberrant localization of M1 in transfected and

infected cells [520]. The high conservation of this short sequence and the non-viability of mutants with single amino acid changes into acidic residues indicate an essential function of this site, which is obviously furthermore related to intrinsic subcellular targeting of M1. The specific interaction affected by these mutations remains to be determined. As the critical sequence is a cluster of three successive basic amino acids (R/K RR), an interaction with the negatively charged PtdIns(4)P might be considered.

The two above proposed functions for the association of M1 with the Golgi apparatus do not include the presence of vRNPs. A conformational change of M1 presumably allows M1 to interact selectively with vRNPs, which might further allow precluding vRNPs from association with the Golgi complex and with preassembled viral components via M1. It is yet unclear which factor initiates budding and release of virus particles, but the presence of genomic vRNPs should constitute an important checkpoint for efficient formation of infectious progeny virus particles. The premature assembly of vRNPs with other viral components at an early stage at the Golgi complex might bear the risk to initiate processes for bud formation and release before the components reach the plasma membrane. Under this assumption, separate transport of envelope and core components would be an important aspect in viral replication and require regulatory mechanisms that allow independent actions of viral components at an early stage and recognition and assembly at later stages. The decrease of PtdIns(4)P content of membranes in the transition from the Golgi complex to the plasma membrane might restore the ability of M1 to interact with vRNPs and to connect them to the budding site, and it might further enable M1 to polymerize and drive bud formation along with the viral glycoproteins. During this transition, M1 would change from the Golgi-specific PtdIns(4)P-bound conformation to an electrostatic membrane association by interaction with PS, phosphatidic acid and other negatively charged lipids that are present on the plasma membrane inner leaflet. When the two distinct trafficking pathways, transporting vRNPs and viral membrane proteins, join together at the plasma membrane, all components should be able to assemble as a complete set and initiate bud formation. Here, M1 might support vRNP attachment to the viral budzone. Specific incorporation of one set of vRNPs was previously implied by electron microscopy studies, reporting attachment of vRNPs by one terminal end of the segments to one point at the budding tip [31,53,306]. M1 might contribute to stabilize the contact with the envelope and support bud formation along the length of the vRNPs as M1 is a determinant of particle size and shape [31,69].

This model implies that two types of M1 membrane interaction spatially and functionally define different modes of M1 action during replication. They are spatially separated by the

strictly controlled, distinct lipid compositions of subcellular membranes. vRNP complexes appear to be transported and to associate predominantly with negatively charged membranes, possibly supported by interaction with M1. The Golgi membrane, being selectively enriched in PtdIns(4)P, but without a prominent negative surface charge, seems to allow specific recruitment of M1 to PtdIns(4)P, thereby presumably excluding vRNP attachment and enabling M1 functions other than the shuttling of vRNPs. Electrostatic membrane binding at the plasma membrane might furthermore finally allow M1 polymerization and bud formation. This model is an example on how the specific lipid environment at different subcellular locations can influence the functions and the functional interplay of viral components for the spatial coordination of interactions and processes during viral replication.

5.1.6 Summarizing remarks

It could be demonstrated that vRNPs were not able to bind to pure lipid membranes by themselves. Instead, it was shown that M1 was able to mediate association of vRNPs to negatively charged membranes. This is the first time that a simultaneous interaction between M1, vRNPs and membranes was demonstrated and that the requirements for this ternary interaction were characterized with regard to the lipid species. Moreover, it was found that binding of M1 to lipids does not automatically lead to the attachment of vRNPs as in case of M1 binding to PtdIns(4)P. These findings were intensely compared with previous reports on *in vitro* and in-cell studies and set into context with the current knowledge on subcellular organization and virus replication. The generally assumed involvement of M1 in many steps of vRNPs in viral replication – ranging from their nuclear export over the cytoplasmic transport to incorporation into budding virions – was transferred into a more detailed model taking into consideration the coordination of different processes, the local conditions within the cell and the transferability of data from *in vitro* experiments into a cellular context.
Besides the role of M1 in vRNP nuclear export, which is functionally well characterized, the here obtained *in vitro* data on vRNP-M1 membrane binding now provide evidence that M1 can indeed potentially contribute to processes like transport along with negatively charged vesicles and attachment to the plasma membrane. The specificity of targeting might however be additionally conferred by other factors. The mechanism of M1 interaction with lipid membranes via PS – that was characterized as electrostatic by previous studies and that was shown here to be relevant also for vRNP membrane association – indicates to which cellular membranes this interaction may be restricted in infected cells and where M1-mediated attachment of vRNPs to membranes can be accomplished, i.e. at the endosomal and the

plasma membrane. The reported prominent binding of M1 to the Golgi membrane, which does not match the criteria for electrostatic interaction [286], was further suggested to be due to the specific interaction of M1 with the predominatly Golgi-resident lipid PtdIns(4)P. Based on a reported conformational change of M1 upon PtdIns(4)P-binding and on the here observed concurrent inability to bind vRNPs, differing functions of M1 membrane binding were postulated, depending on the specific composition of subcellular membranes. Further, the possibility was deduced that M1-mediated membrane binding of vRNPs can be regulated and coordinated by a conformational switch in M1.

5.2 Generation of recombinant Influenza A virus encoding TC-tagged NP to label progeny vRNP complexes in infection

5.2.1 TC-tag insertions within NP interfere with viral replication

In order to generate a recombinant mutant virus that allows specific labeling of newly formed vRNP complexes during infection for analysis of viral assembly in living cells, various NP variants were engineered containing the TC-tag, a six amino acid sequence (CCPGCC). Based on structure and sequence information of NP as illustrated in 4.2.1, and considering the segment 5 vRNA packaging signal, six different sites in flexible loop regions of NP were selected for insertion of the TC-tag sequence. Two of the constructs failed already preliminary tests of protein expression and subcellular targeting in the absence of infection (Fig. 15): NP-TC100 did not enter the nucleus indicating misfolding or impaired targeting function, even though the nearby inserted TC-tag in NP-TC372 did not disturb nuclear localization. The second construct that clearly differed from NP wt behaviour in transfection by cytoplasmic accumulation was NP-TC247, the only mutant carrying the insertion in the NP head domain, which is more conserved than the NP body domain [331]. This site of insertion between residues 247 and 248 is spatially close to the classical bipartite nuclear localization sequence (aa 198–216), which has been shown to play only a minor role in nuclear import of NP though [123].

The other four constructs NP-TC125, NP-TC288, NP-TC292 and NP-TC372 were efficiently targeted to the nucleus similar to wt NP (Fig. 16). This was considered as a prerequisite for use in reverse genetics. However, none of these virus mutants encoding one of the TC-tagged NP variants could be recovered as replication-competent virus (4.2.2). Supplementation with WSN wt virus nevertheless enabled replication and incorporation of the mutated segment 5 vRNAs into progeny virus particles, and TC-tagged NP was expressed in newly infected cells and successfully labeled with FlAsH (Fig. 20). Thereby, it was demonstrated that TC-tag insertion in vRNA encoding NP-TC125, NP-TC288, NP-TC292 or NP-TC372 did not impair genome packaging, but caused a defect on the level of protein function that could be restored by the presence of wt NP. However, efficient incorporation of TC-tagged NP into functional vRNP complexes in mixed infections was apparently not achieved. Characteristic punctate cytoplasmic NP signals that appear late in infection typically represent newly formed vRNPs which are being transported from the nucleus to the plasma membrane [297]. These structures were detectable in WSN TC125/wt, WSN TC292/wt and WSN TC372/wt virus-

infected cells by immunofluorescence, but not by FlAsH labeling, indicating that TC-tagged NP variants did not efficiently compete with wt NP for incorporation into vRNPs or had major defects in vRNP formation. In conclusion, the here described virus mutants, which encode TC-tagged NP, could be rescued by superinfection with WSN wt virus, but were not suitable to generate TC-tagged vRNP complexes for fluorescence labeling and live-cell studies during infection.

Influenza virus NP is a highly conserved protein [309,328,329,330], and it is involved in numerous interactions with viral RNA, the viral polymerase, M1 and cellular factors. Many regions within the NP structure have been identified as highly conserved and critically important for viral replication [183,317] or have been assigned to specific functions like RNA binding [333,337] or nuclear transport [123]. Even though the sites for TC-tag insertion were carefully selected in this study, it was not possible to insert the short sequence without critically affecting functions essential for viral replication. An alternative approach by choosing a terminal TC-tag for NP was therefore realized (see 4.2.3 and 5.2.3).

5.2.2 NP-TC288 impairs vRNA replication in infection

Despite the failure to generate recombinant virus mutants with TC-tag insertion within NP (4.2.2), valuable information could be extracted from reverse genetics experiments.
Careful analysis of the attempts to generate recombinant virus mutants with TC-tag insertion demonstrated that recombinant WSN TC288 virus differed from the other virus mutants. WSN TC288 virus was the only virus mutant described here that could be successfully recovered from the initial step of plasmid-based virus generation as infectious virus particles (Fig. 18). Its failure to replicate in newly infected cells though provides interesting and relatively detailed information about the type of function that is apparently impaired by TC-tag insertion at position G288/Y289 in NP.
The successful recovery of infectious WSN TC288 virus particles from transfected cells was verified by infection of MDCK II cells and subsequent immunofluorescence analysis of NP expression (Fig. 18, Fig. 19). Evidently, WSN TC288 virus particles were efficiently produced by synthesis of viral mRNA and genomic vRNA from transfected plasmid DNA. The produced set of viral components (with NP-TC288 substituting wt NP) was obviously competent for virus assembly and virus release as well as for subsequent cell entry and viral protein expression in newly infected cells. The mutant protein NP-TC288 therefore can be considered to be a functional protein with regard to many processes of the viral replication

cycle, e.g. encapsidation of viral RNA, nuclear export and transport of vRNP complexes, genome packaging into progeny virus, nuclear import of incoming vRNPs and mRNA synthesis. Accomplishment of various NP functions implies correct folding of NP-TC288. Expression of NP-TC288 in WSN TC288 virus-infected cells moreover demonstrated the efficient incorporation of modified segment 5 vRNA into recombinant virus particles. Yet, infection with WSN TC288 virus turned out to be abortive.

To identify the function that is disabled by TC-tag insertion into NP between residues G288 and Y289, one has to look at those viral processes that are exceptionally carried out by the cellular machinery when producing virus particles by reverse genetics.

The plasmid-based production of viral components in reverse genetics substitutes the viral polymerase functions; viral mRNA and vRNA synthesis are carried out by cellular RNA polymerases and are hence independent of the viral polymerase complex. As WSN TC288 virus assembly, release and uptake were shown to be fully functional once mRNA and vRNA are synthesized from plasmid DNA, the failure of WSN TC288 virus to replicate in infected cells is apparently caused by an impairment of viral polymerase functions in infection and thus most likely by a failure of mRNA or vRNA synthesis. Since expression of NP-TC288 in WSN TC288 virus-infected cells could be verified by NP immunostaining (Fig. 19), viral mRNA synthesis was obviously not inhibited, implying that a failure of WSN TC288 virus replication is most probably caused by a defect specific for full-length cRNA and/or vRNA synthesis. This conclusion is consistent with the finding that nuclear export of progeny vRNP complexes could not be observed at any time during WSN TC288 virus infection, despite detection of abundant amounts of NP in the nucleus (Fig. 19). Since NP-TC288-containing vRNPs are efficiently exported from the nucleus during WSN TC288 virus production from plasmid DNA, a defect of these vRNPs in assembly or nuclear export can be excluded. A failure of vRNP formation due to impaired vRNA synthesis, however, can explain the absence of cytoplasmic vRNPs in WSN TC288 virus-infected cells and the inhibition of viral replication, and this defect can furthermore be overcome by plasmid-based vRNA synthesis.

Remarkably, a significantly reduced nuclear export of vRNPs was also observed in mixed infections with WSN TC288 and WSN wt virus (Fig. 20). In such double-infected cells, not only the mutant protein NP-TC288, but also wt NP was prevented from nuclear export as shown by NP immunodetection. This indicates an impairment of vRNP formation even in the presence of wt NP. Along with a relatively low CPE observed for mixed WSN TC288 and WSN wt virus infections, these findings suggest that the modified protein NP-TC288 is not

only unable to support vRNA replication in infection, but it even appears to dominantly inhibit cRNA and/or vRNA synthesis in the presence of wt NP.

In conclusion, there is evidence that the modification of NP by TC-tag insertion at position G288/Y289 affects the viral polymerase function. The data further suggest that this modification selectively affects full-length genomic RNA replication.

During infection, the viral polymerase complex mediates both the production of 5′ capped and 3′ polyadenylated mRNA (transcription) and the unprimed, full-length RNA synthesis (replication) from vRNP templates. Various models have proposed a regulatory function of NP for switching the viral polymerase activity from transcription to replication (reviewed in [54]). Other studies suggest however an NP-independent, stochastic initiation of mRNA and cRNA synthesis and show a stabilizing effect of NP on viral full-length RNA replication products instead [181,186,343]. Nevertheless, direct interactions between NP and viral polymerase subunits were demonstrated [182,184,343], and various studies have shown the importance of NP and NP-polymerase interactions for the viral polymerase activity [183,188,343,525]. NP-polymerase interactions have further been suggested to be regulated by host-specific factors and to affect polymerase activity and virulence in a host-dependent manner [344,525,526].

An interaction site of NP for the viral polymerase was only very recently identified and located to residues R204, W207, and R208 [188]. This site is situated at the top of the NP head domain, whereas the site of TC-tag insertion in NP-TC288 is located in the body domain. Unlike the mutation in NP-TC288 which seems to selectively impair viral full-length RNA synthesis, residues R204, W207 and R208 were shown to be essential for both mRNA and cRNA synthesis. Accordingly, these two different sites on NP seem to be involved in distinct functional interactions with the viral transcription/replication machinery. In support of the existence of several sites on NP to be involved in the NP-polymerase interplay, other studies reported mutations of NP which affect viral polymerase activity and which localize to the body domain [182,183] or to the RNA-binding groove of NP [525].

Very similar to the here proposed selective inhibitory effect of NP-TC288 on viral full-length RNA synthesis, Mena *et al.* [183] reported four NP mutants which are able to encapsidate viral full-length RNA, but which interfere with cRNA synthesis while being fully functional for mRNA (and vRNA) synthesis. All four mutations (M331K, D340H, F488G, Δ494–498) are situated close to each other inside the NP body domain. Although they are not directly neighbouring the site of TC-tag insertion between residues 288 and 289 at the surface of the NP body domain, they might contribute to conformational changes that impair the same

functional interaction with the viral polymerase as possibly the TC-tag insertion. The work of Mena *et al.* [183] implies that NP is able to selectively affect cRNA synthesis, which is in accordance with the above-derived interpretation of the failure of NP-TC288 to support viral replication due to a defect in viral full-length RNA synthesis. It cannot be distinguished here however between a defect in cRNA or vRNA synthesis. The possibility for a selective regulation of cRNA and vRNA synthesis is supported by another study that demonstrated different initiation mechanisms of viral full-length RNA synthesis on cRNA and vRNA promoters [197]. The role of NP in this context has however not been addressed yet.

The subtype-specific sequence of NP was previously shown to be important for the interaction with the polymerase subunit PB2 and for the host-range adaptation of PB2 [344,527]: Two different NP proteins (from A/swan/Germany/R65/2006(H5N1) [DQ464359.1] and from

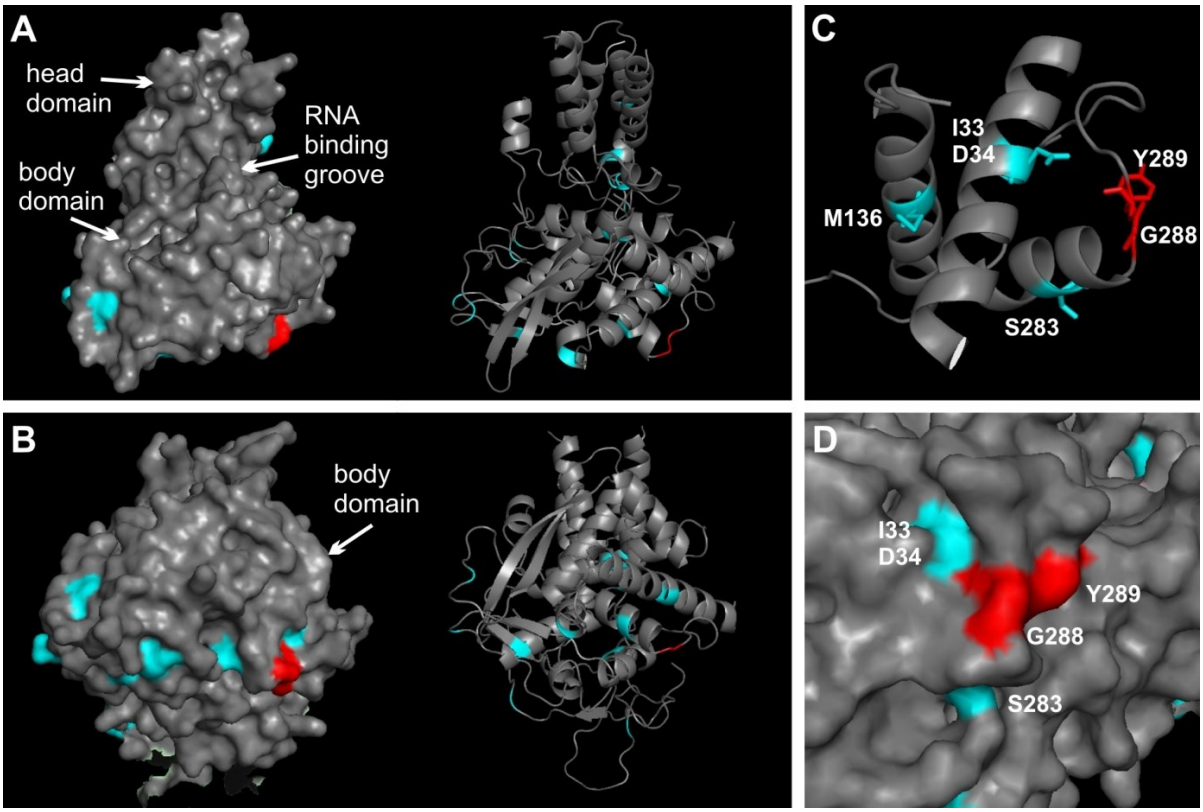

Fig. 64: Comparison of the site of TC-tag insertion in NP-TC288 (red) with residues potentially involved in host-range adaption of polymerase subunit PB2 (blue). The NP sequences of two Influenza virus subtypes (A/swan/Germany/R65/2006 and A/Hong Kong/156/ 97) which were shown to differentially affect adaption of PB2 in mammalian cells differ by 16 amino acids (highlighted in blue). These residues are illustrated within a crystal structure of NP (PDB 2IQH, [93]). Only one subunit of the NP trimer structure is represented. The site of TC-tag insertion in NP-TC288 (residues 288 and 289) is labled in red. The structure was edited with PyMol. (A) Front view of NP. Surface representation (left) and cartoon of the secondary structure elements (right). (B) View of the NP body domain from the bottom site. Surface representation (left) and cartoon of the secondary structure elements (right). (C) Section of the NP secondary structure illustrating residues G288/Y289 and neighbouring residues. (D) Surface representation of a section of NP surrounding residues G288/Y289.

A/Hong Kong/156/ 97(H5N1) [AF036359.1]) which were shown to support replication preferentially with either PB2 K627 or PB2 E627 [527] differ by only 16 amino acids. The sequence alignment was performed using EMBOSS Needle (http://www.ebi.ac.uk/Tools/psa/emboss_needle/). When mapping these residues onto the NP structure to locate residues potentially involved in NP-PB2 interactions (Fig. 64), ten of them are situated in the NP body domain, nine being surface residues (residues 33, 34, 52, 283, 319, 353, 371, 377 and 482). The residues are not clustered, but the majority of them is located at the bottom of the NP body domain (Fig. 64B), as is also the TC-tag in NP-TC288. Especially residues 33, 34 and 283 are structurally close to the site of TC-tag insertion between amino acids 288 and 289 (Fig. 64C, D), supporting a possible role of this site for the NP-polymerase interplay.

In summary, the analysis of the replication defect of WSN TC288 virus in this study supports a model of viral replication in which the polymerase activity is regulated by NP independently of its ability to encapsidate viral RNA and in which NP is critically required to promote viral full-length RNA synthesis [183,332,343]. For future studies, residues G288 and Y289 seem to be a promising site to further investigate the regulatory function of NP that selectively affects viral RNA replication and to elucidate the molecular mechanism of this regulation.
Mutant WSN TC288 virus will represent a useful tool to study the role of NP for viral replication in more detail: Quantitative RT-PCR analysis of RNA species synthesized in WSN TC288 virus infection can provide information on the relative amounts of mRNA, cRNA and vRNA products and help to verify the specific defect. In order to figure out further whether the inhibitory effect of NP-TC288 is specific for either cRNA or vRNA synthesis or whether it affects synthesis of both RNA species, infected cells might be supplemented with cRNA to check if cRNA can compensate the replication defect. Alternatively, a minireplicon assay (analogous to [188]) using NP-TC288 with either cRNA or vRNA as template RNA might be performed. Furthermore, affinity purification of wt NP and NP-TC288 from virus-infected cells should allow the comparative analysis of cellular and viral interaction partners of wt NP and NP-TC288.

5.2.3 Successful recovery of recombinant Influenza A virus encoding NP with an N-terminal tetracysteine motif

As it was not possible to introduce the six amino acid sequence of the TC-tag into the NP sequence without critically affecting the protein functions, the TC-tag was instead fused to the N-terminus of NP. To accomplish this in the genomic background of Influenza A virus, a more

complicated procedure was necessary than simple insertion of the tag into the genomic sequence since modifications of the terminal sequences of the viral ORFs do not only affect the translation products, but also the *cis*-acting functions of the viral RNA. At the protein level, the N-terminus of NP is a flexible sequence which is not resolved in the two known crystal structures of NP [93,331] and which contains an unconventional NLS (residues 3 to 13) responsible for nuclear import of NP [118,121,123]. At the genomic level, the 3′ end of the NP ORF is part of the packaging signal of segment 5, which is important for efficient incorporation of the segment into progeny virus particles (reviewed in [100]). The approximate size of the packaging signals can be inferred from naturally occurrin g, internally deleted defective-interfering (DI) vRNAs that incorporate efficiently into virus particles [528]. Furthermore, the redundancy of the genetic code giving rise to nucleic acid codon variability allows unraveling evolutionary pressure on the RNA sequences independent of amino acid conservation [309]. By studying incorporation of reporter gene constructs of segment 5 into virus particles, Ozawa *et al.* [123] defined a minimal packaging sequence at the 3′ end, spanning nucleotides 1 to 105, which still allows efficient incorporation of the segment into progeny virus particles. Analogous to the work of Ozawa *et al.*, a vRNA construct was engineered in the present study which allowed the conservation of the 3′ packaging signal, while modifications could be introduced into the NP ORF. This was achieved by duplicating the first 60 nucleotides encoding NP as described in 4.2.3. While Ozawa *et al.* used this approach to introduce point mutations, it could be demonstrated here that also insertions of 30 or 39 nt are tolerated by recombinant virus. Two different virus mutants were successfully recovered, WSN nTC and WSN FLN virus, encoding the 10 aa nTC-tag or the 13 aa FLN-tag, respectively. These virus mutants demonstrate that a 3′ terminal insertion into segment 5 vRNA and expression of NP with an N-terminal tag is basically possible in the viral context. This approach might be transferred to other genomic segments.

Since the TC-tag sequence might not be stably maintained in the virus genome in the absence of any selection pressure, passaging of TC-tagged recombinant virus has to be kept to a minimum. The high error rate of the viral RNA-polymerase is expected to foster the loss of the TC-tag [6]. However, when relatively freshly prepared, TC-tagged recombinant mutant viruses will allow studying Influenza virus infection using the TC-tag.

Even though the size of the two TC-tags introduced into WSN nTC and WSN FLN virus, respectively, differed by only nine nucleotides (i.e. by three amino acids at the protein level), differences in viral replication were observed. Replication of WSN FLN virus seemed to be

more attenuated than replication of WSN nTC virus; the titer was typically lower and decreased more rapidly upon serial passaging than the titer of WSN nTC virus (4.2.3, 4.2.5). In infection experiments with FlAsH- and ReAsH-labeled virus particles, the infectivity of WSN FLN virus was clearly lower than that of WSN nTC virus (Fig. 32). Furthermore, the occurrence of cytoplasmic vRNPs late in WSN FLN virus infection was rarely observed (4.2.4.3). For these reasons, WSN FLN virus is evidently less suitable than WSN nTC virus to study vRNPs during infection. It remains unclear if these differences among the two strains are caused at the genomic level or at the level of protein function. The flanking amino acids of the FLN-tag include aromatic, charged and cyclic amino acids, whereas the nTC-tag is encompassed by mainly small and non-polar residues, indicating differing characteristics at the protein level which might affect the functionality of NP during infection.

Both recombinant mutant viruses were found to be attenuated compared to WSN wt virus regarding virus yield and plaque formation, thereby indicating the impairment of one or more processes involving NP or segment 5 vRNA. It is possible that the selected 3′ terminal sequence, which was preserved by duplication, did not cover the complete, optimal packaging signal. Naturally occurring DI RNA of segment 5 which efficiently compete with full-length vRNA for incorporation into virus particles were previously reported to be at least 58 nt larger than the here-applied minimal sequence for efficient incorporation of a reporter gene as defined by Ozawa *et al.*, suggesting a possible contribution of additional nucleotides for optimal genome packaging [528]. Besides the *cis*-acting function of segment 5 vRNA for genome assembly, its translation product NP is the major structural constituent of the genomic vRNP complexes. Modification of NP by TC-tag insertion therefore affects all eight genomic vRNP complexes at the protein level and might thereby generally interfere with genome assembly.

Various observations indeed indicated a packaging defect of the viral genome of WSN nTC and WSN FLN virus: A comparably high degree of CPE was observed relative to the detectable number of infected, NP-expressing cells (Fig. 28D), and in case of WSN nTC virus, a non-linear correlation between the number of plaque-forming units (or the CPE) and the applied virus concentration was noticed (Fig. 28B). Furthermore, there was an unexpected, disproportionate decrease of the number of infected cells upon dilution of WSN nTC or WSN FLN virus (4.2.5, Tab. 8). It remains however unknown if the packaging defect is specific for a subset of vRNAs or if all vRNA segments are equally affected. It is further unclear to what extent each virus particle is affected and how large the fraction of incomplete, packaged genomes may be. To reduce the fraction of abortive infections when working with

WSN nTC and WSN FLN virus, infections with a low MOI are hence to be avoided. Depending on the question to be examined and the experimental set-up, this aspect might have to be specified for a solid interpretation of the experimental data.
As vRNPs constitute the template structure for the viral polymerase complex, replication and transcription processes might also be affected by TC-tagged NP and thus contribute to the attenuated phenotype of the mutant viruses. However, when comparing a time series of infection with wt and mutant virus on the basis of NP detection (Fig. 28), NP expression levels did not notably differ, indicating that at least transcription was not exceptionally reduced by TC-tagged NP. Furthermore, nTC-NP and FLN-NP nuclear import was apparently not prevented (Fig. 22), even though both TC-tags were fused to NP in the immediate vicinity of the N-terminal nuclear localization sequence. However, reduced amounts of cytoplasmic vRNPs late in mutant virus infection compared to the wild-type situation might indicate interference of the TC-tag with vRNP formation or with the formation of the nuclear export complex of vRNPs (Fig. 28, Fig. 25).

In summary, two (attenuated) mutant viruses encoding TC-tagged NP could be generated by reverse genetics which are able to undergo several rounds of replication while maintaining the TC-tag sequence. WSN nTC virus was found to be better suitable to study virus infection than WSN FLN virus. A possible genome packaging defect has to be taken into consideration though, particularly when investigating cells at the single-cell level. At this point, the influence of biarsenical labeling is not yet taken into account.

5.2.4 Biarsenical labeling of TC-tagged NP in WSN nTC and WSN FLN virus infection

After having studied the consequences of TC-tag insertion for virus replication, furthermore, biarsenical labeling was scrutinized qualitatively and quantitatively in the context of infection to assess the potential and the limitations of this experimental system.
Despite numerous advantages of the small genetically encoded TC-tag – including the spectral variability of its ligands enabling pulse-chase experiments in living cells and the option for application in electron microscopy (reviewed in [529]) –, the general and major drawback of the biarsenical-tetracysteine system is the unspecific background labeling in cells and the resulting poor signal-to-noise (S/N) ratio for low-expression TC-tagged proteins [530,531,532]. Multiple approaches to improve this technical deficit have been accomplished, either by improving the properties of the fluorescent ligands or by increasing the affinity of

the peptide tag for its biarsenical ligands in order to allow for more stringent washes with competing dithiols to reduce the unspecific background binding [457,481,484]. Some of these optimized features were considered when designing the TC-tag in the present study. The helix-breaking amino acids proline and glycine were inserted as spacing residues between the two pairs of cysteines, as they were reported to increase the affinity of the tag substantially [457]. Furthermore, the flanking residues FLN and MEP were introduced into one construct (FLN-NP) according to Martin *et al.* [481] for improved affinity and fluorescence quantum yield.

Because unspecific background staining is nonetheless an issue, the labeling specificity was carefully assessed in the context of recombinant mutant virus infection. Since NP is abundantly expressed in infected cells, ReAsH labeling of TC-tagged NP yielded excellent S/N ratios; lower but still acceptable S/N ratios were achieved with FlAsH (Fig. 22, Fig. 24). Being part of the characteristic pattern of cytoplasmic vRNP complexes, nTC-NP furthermore yielded bright, punctate cytoplasmic signals which distinctly stood out from the diffuse cellular background (Fig. 25). The quality of the results was however found to be strongly dependent on labeling conditions, i.e. on dye concentration, incubation time and temperature. Best results were achieved with confocal fluorescence microscopy upon labeling with 1 µM dye for 1 h at RT. When analyzing the cells by epifluorescence microscopy and more sensitive detection, conditions of 0.01 µM dye for 1.5 h at 37 °C were found to be optimal. Concentrations of more than 1 µM, however, caused high background staining, and incubation times longer than 3 h at 37 °C led to considerable accumulation of punctate ReAsH signals which presumably presented endocytosed, vesicular ReAsH and were equally found in control cells infected with WSN wt virus. Optimized labeling conditions for TC-tagged NP in living cells were in agreement with previously reported *in vitro* association and dissociation rate constants of FlAsH with TC model peptides (in the range of $10^5\,M^{-1}s^{-1}$ and $10^{-6}\,s^{-1}$, $K_D \sim 10^{-11}\,M$) [457], when considering additional time for accumulation and distribution of the dye within living cells. FlAsH and ReAsH signals were consistently found to be stable over days.

The specificity of the obtained biarsenical signals under optimized conditions was confirmed by comparison with immunofluorescence detection of NP (Fig. 22, Fig. 25). With the exception of nucleolar staining, the biarsenical dyes did not cause unspecific labeling of cellular structures within the detected range and stained total cellular NP equivalently to immunostaining. The aspect of unspecific labeling of nucleoli in WSN virus-infected cells will be further discussed in section 5.2.6. As nucleoli represent discrete structures which can

be identified even in transmitted light images, they can be easily excluded from analysis. Hence, under optimized labeling conditions, efficient and specific labeling of TC-tagged NP in the cytoplasm and the nucleoplasm of infected cells could be demonstrated, suggesting that recombinant virus strains were generated which allow for the specific detection of NP in living infected cells. However, even though labeling of the constructs was further optimized to establish a well-characterized, versatile experimental system, biarsenical labeling of TC-tagged NP eventually failed to produce fully functional, fluorescently labeled genomic complexes in living cells (see discussion 5.2.5).

The approaches to optimize labeling of TC-tagged NP in infected cells revealed sequence-specific as well as compartment-specific labeling efficiencies. Concentration-independent comparison of the fluorescence signals of each dye when bound to either of the two tag sequences, nTC or FLN, showed that the labeling efficiency was distinctly affected by the amino acid residues adjacent to the core TC sequence. FlAsH labeled nTC-NP more efficiently than FLN-NP, whereas ReAsH yielded higher normalized signal intensities for FLN-NP than for nTC-NP (1224.2.4.2). These differences might be due to sequence-specific binding affinities and/or to a varying fluorescence brightness of the fluorophores depending on the specific molecular environment.
Further, when exploring a labeling strategy specifically for cytoplasmic vRNPs late in infection, also compartment-specific differences of FlAsH and ReAsH labeling were observed based on comparison with NP immunofluorescence signals (Fig. 26). Relative to the immunofluorescence signal, ReAsH labeled cytoplasmic nTC-NP more efficiently than nuclear nTC-NP. FlAsH on the contrary labeled cytoplasmic nTC-NP less efficiently than nuclear nTC-NP. Compartment-specific different states of NP are assumed to be the reason for these distinct labeling efficiencies (4.2.4.3). Yet, differential compartment-specific recognition of the NP epitope by the monoclonal antibody cannot be entirely excluded as a contributing factor to these results; however, opposite behavior of FlAsH and ReAsH labeling relative to the immunofluorescence signals strongly suggests that the observed compartment-specific labeling efficiencies are due to different characteristics of the two dyes.

In infected cells, NP exists as a newly synthesized monomeric or oligomeric protein that is rapidly imported into the cell nucleus and, in the nucleus, it forms the core of actively transcribed and nascent vRNP complexes. Furthermore, vRNPs form nuclear export complexes in which vRNPs associate with M1, NEP and the nuclear export machinery for transport into the cytoplasm [270,292]. M1 most likely remains bound to vRNPs in the

cytoplasm as it prevents the reimport of vRNPs into the nucleus [29,116]. It has been suggested that by association with vRNPs M1 masks the NLS responsible for vRNP nuclear import [117], which resides at the N-terminus of NP [120] and is in close vicinity to the N-terminal TC-tag of nTC-NP and FLN-NP. It is hence not unlikely that the accessibility of the TC-tag may vary in the different conformational states of NP and with varying degree of complexation. In cytoplasmic vRNP complexes, the TC-tag is presumably more constricted than in uncomplexed NP or in actively transcribed vRNPs in the nucleus, and considering the differing molecular size of FlAsH (664.5 Da) and ReAsH (545.4 Da), a sterical constriction of the TC-tag can be expected to affect binding of the larger FlAsH more severely than that of ReAsH. This is consistent with the results of biarsenical labeling (Fig. 26). Besides sterical restrictions and modulation of the binding affinity, also the fluorescence brightness of the complexed biarsenical dye might be influenced by compartment-specific conformational states of NP. For instance, the phosphorylation state of serine 3 [332] or the conformational state of the surrounding residues might affect the electron systems of the nearby fluorophore and thereby alter its spectral characteristics, like quantum yield, extinction coefficient or excitation maximum.

These analyses of biarsenical labeling demonstrate the importance of various factors influencing fluorescence labeling of the TC-tag with biarsenical dyes: the labeling conditions, the dye-specific cellular background staining, the flanking amino acids of the TC-tag, the specific tag-dye combination and furthermore, the changeable *in situ* conformational states of the tagged protein in a biologically relevant context.

In the present study, ReAsH labeling was found to be favourable to study transport and assembly of progeny vRNPs in infection with mutant virus as it provides a considerably better S/N ratio in MDCK II cells than FlAsH and is furthermore better capable of labeling specifically cytoplasmic vRNP complexes in infection. Both FlAsH and ReAsH labeling were found to be suitable for virus entry studies, when the virus particles but not the cells are labeled and cellular background staining is therefore not an issue. In this experimental setup, FlAsH signals were shown to be clearly detectable with an excellent S/N ratio (Fig. 31). Efficient labeling of vRNP complexes in intact virus particles with either dye was demonstrated by SDS-PAGE analysis (Fig. 29). Basically, both dyes are hence suitable to label NP and vRNP complexes. The application of FlAsH is however limited by high cellular background staining.

Yet, in addition to labeling characteristics, virological features needed to be considered for the choice of the mutant virus strain to be used in experiments: The use of WSN FLN virus, even

though yielding better fluorescence signals with ReAsH than nTC-NP, was limited to virus entry experiments since cells infected with WSN FLN virus displayed hardly any cytoplasmic vRNP signals (4.2.4.3). WSN nTC virus was therefore favored for experiments addressing virus assembly.

5.2.5 Interference of biarsenical labeling with nTC-NP and FLN-NP in infection

Two types of experiments were performed in living cells using recombinant TC-tagged mutant viruses for fluorescence detection. However, both experiments indicated that biarsenical labeling interferes with infection in a TC-tag-dependent manner.

First, ReAsH or FlAsH labeling of nTC-NP late in WSN nTC virus infection to study the transport of progeny vRNPs to the site of virus assembly resulted in the detection of mainly immobile cytoplasmic punctate nTC-NP signals (4.2.7). It is unlikely though that such immobility of cytoplasmic NP structures represents standard conditions in infected cells. The TC-tag- and ReAsH-dependent aggregation of cytoplasmic nTC-NP, which was observed upon ReAsH-labeling (Fig. 25), rather suggests that TC-tags were crosslinked through the bifunctional ReAsH molecules. The issue of cross-linking of TC-tags has been reported previously [484], but was interpreted as the formation of intermolecular disulfide linkages. Intermolecular cross-linking under the experimental conditions of the present study might be promoted by the close proximity of polymerized NP molecules in the vRNP structure and by the formation of multisegmental genomic complexes. Immobilization as a result of cross-linking would indicate close proximity or frequent contacts of vRNP segments during transport and/or frequent encounters of their transport vesicles, leading finally to aggregation of large numbers of vRNP complexes and vesicles. In support of this interpretation of the data, results of single particle tracking experiments obtained by another experimental approach within this study (using mEYFP-tagged NP) demonstrated highly dynamic cytoplasmic NP structures in infection (see 4.4.2). At all times, a fraction of mEYFP-tagged cytoplasmic NP complexes was found to perform fast saltatory movements. Data on vRNP transport that was published while the present work was in progress similarly describes dynamic behavior of cytoplasmic NP complexes with fast saltatory movements [280,298]. This transport was further reported to be microtubule-dependent and to be mediated by Rab11-positive recycling endosomes. The results of three different experimental approaches hence provide a consistent picture of the dynamics of cytoplasmic vRNPs and suggest that the accumulation of predominantly immobile nTC-NP in the cytoplasm of WSN nTC virus-infected cells after biarsenical labeling is an artifact induced by the TC-tag and/or biarsenical

labeling. Disruption of the cytoskeleton by biarsenical labeling – possibly an issue for ReASH [482] – was ruled out to be critical when the effect of labeling on WSN wt virus was studied (see 5.2.6). This is consistent with the above-derived hypothesis that cross-linking of nTC-NP might affect the mobility of cytoplasmic nTC-NP structures, but accumulation of non-functional nTC-tagged vRNPs or a transport defect of nTC-tagged vRNPs cannot be excluded. However, aggregation of small punctate cytoplasmic nTC-NP signals into larger structures was observed only after biarsenical labeling. Therefore, it is supposed that biarsenical labeling is the critical factor that induces aggregation and immobilization due to cross-linking of the TC-tags. Extensive formation of disulfide bonds between TC-tags is not expected to occur due to the reducing conditions of the cytoplasm.
Effects of cross-linking are less obvious when studying fixed cells as described in 4.2.4, but become crucial when analyzing dynamic processes. Hence, WSN nTC virus was considered unsuitable to study the dynamic assembly of the viral genome in living cells by means of fluorescence imaging. For WSN FLN, cross-linking between the FLN-tags is expected to occur similarly since the site of the tag on NP is the same.

The second experimental approach using TC-tagged virus for fluorescence imaging of living infected cells was tracking of the viral genome during virus entry (4.2.6). WSN nTC and WSN FLN virus particles were purified and labeled with FlAsH or ReAsH. Successful labeling of TC-tagged NP in intact virus particles was confirmed by SDS-PAGE analysis and fluorescence detection of NP (Fig. 29). When FlAsH-labeled particles were visualized in infected cells by fluorescence microscopy within the first hour after infection, FlAsH signals were clearly detectable and colocalized with the membrane dye DiD, which was used to label the viral envelope (Fig. 31). Separation of the FlAsH-labeled genome from the viral envelope and accumulation of the vRNPs in the cell nucleus was however not observed within the expected time (within 1 h after infection [115]), indicating an impairment at this stage of viral infection. In spite of the apparent uptake of one or more virus particles per cell, abortive infection was confirmed by analyzing the infected cells for NP expression at 17 or 20 h p.i. (Fig. 32). Labeled WSN FLN virus was basically unable to infect the cells, except for some rare cases in which NP expression levels were barely detectable. Labeled WSN nTC virus was able to infect up to > 50 % of the cells depending on the experimental conditions and the virus preparation. A considerable fraction of these cells, however, displayed clearly attenuated NP expression. For comparison, infections with FlAsH- or ReAsH-labeled WSN wt virus were analyzed. The same amount of virus protein was applied for infection with WSN wt and WSN mutant viruses in each experiment and in contrast to WSN nTC and WSN FLN virus, WSN

wt virus infected 100 % of the cells and caused a pronounced CPE due to the high viral load (Fig. 32). It should be noted here that the virus preparations were not filtrated prior to infection. The number of endocytosed virus particles was therefore presumably higher than perceived from single particle studies of virus entry as shown in Fig. 31, where the virus had been filtrated for infection.

The considerably reduced infectivity of labeled TC-tagged mutant viruses compared to wt virus (Fig. 32B) can basically have two reasons: First, the fraction of defective virus particles in WSN nTC and WSN FLN virus preparations might be larger than in case of WSN wt virus. Second, biarsenical labeling of the TC-tagged vRNPs might interfere with infection. Both aspects might contribute synergistically to the obtained results. The observation of impaired release of labeled TC-tagged vRNPs from the endosomes (Fig. 31) is consistent with the detection of a very low number of infected cells at 20 h p.i. relative to the observed number of endocytosed viral particles. From this data, however, it cannot be ultimately distinguished if impairment of infection and genome release is generally caused by the TC-tag itself or by the biarsenical labeling of TC-tagged NP. The almost complete failure of labeled WSN FLN virus to infect cells can however hardly be explained by reduced infectivity only since it was possible to rescue this virus in the first place. Analogous to the above-postulated cross-linking of TC-tags by the biarsenical labeling (causing immobilization and aggregation of cytoplasmic nTC-NP in infection), it is attractive to suppose that biarsenical labeling induces cross-linking of TC-tagged genomic segments in intact virus particles as well and thereby interferes with endosomal release and nuclear transport of vRNPs during virus entry. In SDS-PAGE analysis, the formation of dimeric NP due to cross-linking with biarsenical dyes was not observed. It is possible though that cross-linking of TC-tags by biarsenical dyes represents a rather weak interaction compared to the specific complexation of the dye by a single TC-tag. Therefore, unlike complexation, cross-linking might be not stable under the denaturing conditions of the SDS-PAGE when vRNP complexes completey disintegrate. Under physiological conditions in infected cells, however, cross-linking might become a relevant factor when TC-tags are naturally arranged in close proximity in vRNPs, and a high number of crosslinks can occur synergistically. Formation of intermolecular crosslinks through biarsenical dyes is further consistent with another observation: Cross-linking of TC-tagged NP within or between vRNP complexes would be expected to interfere with transcription and replication in a random way, and indeed, cells infected with labeled WSN nTC virus displayed widely differing NP expression levels at 20 h p.i. (Fig. 32A) with a considerable fraction of cells displaying clearly attenuated NP expression (Fig. 32B). Expression of TC-

tagged NP was shown to be not generally attenuated in infection compared to wt NP (Fig. 28D). Hence, biarsenical labeling of the virus particles has apparently a random inhibitory effect on later transcription in infected cells, basically consistent with a random inactivation of the viral genome. Such inactivation of vRNPs by biarsenical labeling might be verified using a minigenome assay by reconstitution of vRNPs with TC-tagged NP and analysis of transcription and replication in the presence and absence of biarsenical dyes.

In summary, both live-cell imaging approaches assessed here, where recombinant mutant viruses encoding TC-tagged NP were used for fluorescence detection of the viral genome during infection, encountered fundamental drawbacks. The dynamic processes to be investigated were not observable, being apparently non-functional under the experimental conditions. As both mutant virus strains are basically replication-competent, albeit attenuated, the distinct inhibition of fundamental processes like vRNP transport and nuclear entry suggests a critical role of biarsenical labeling, which is believed to induce intermolecular cross-linking of TC-tagged NP.

5.2.6 The biarsenical-tetracysteine system as a general tool to study Influenza virus infection

The general applicability of the biarsenical-tetracysteine system to study Influenza virus infection was assessed using WSN wt virus-infected cells. Transient labeling of infected cells did not lead to a reduction of the virus production (Fig. 27). In another experiment, when plaque assays were performed by infection of cells with WSN wt virus in the presence or absence of FlAsH, plaque formation was not affected by labeling of the cells (data not shown). This observation suggests efficient infection and progression of infection in the presence of the dye also at early stages of infection. In conclusion, biarsenical labeling *per se* does not interfere with Influenza virus replication and can therefore generally be applied to study Influenza virus infection.

When investigating the specificity of biarsenical labeling in Influenza virus-infected cells, unexpected prominent labeling of nucleoli was detected in a fraction of wt virus-infected cells, which was obviously independent of the presence TC-tags (Fig. 23). As these prominent signals were not found in uninfected cells, WSN virus apparently induced association of FlAsH and ReAsH with the nucleolar structure in MDCK II cells. This unspecific labeling was also induced in cells infected with WSN nTC virus independent of the presence of nTC-NP in the nucleoli (Fig. 23B). It is not known whether accumulation of viral proteins in

nucleoli led to unspecific labeling through FlAsH and ReAsH or whether cellular components being able to bind biarsenical molecules were recruited to nucleoli during infection. Even though M1 was found to associate with biarsenical dyes in SDS-PAGE analysis (Fig. 29), M1 is not targeted to nucleoli during infection, but remains homogenously distributed in the nucleoplasm. NS1, a viral protein which is targeted to nucleoli in infected cells, is however abundantly present also in the nucleoplasm of infected cells and is therefore unlikely to cause confined nucleolar labeling. Amongst cellular proteins, zinc finger motifs – which are typically found in DNA and RNA binding proteins – contain two, four or six cysteine residues to coordinate a central zinc ion. These proteins present an example of native cellular motifs which might have an intrinsic ability to bind biarsenical molecules under certain conditions and which are expected to be present in the cell nucleus.

The use of the biarsenical-tetracysteine system to examine aspects of Influenza virus infection was reported by only one other study before [480]. Li *et al.* successfully inserted the TC-tag in the NS1 segment of recombinant Influenza A virus and visualized nuclear import of NS1 in infected cells in real time as well as nucleolar localization of NS1. However, they did not report unspecific biarsenical labeling of the nucleoli using Influenza A/PR8 virus and A549 cells. It is thus possible that unspecific biarsenical labeling of nucleoli is strain-specific or cell type-specific.

Extensive remodeling of the nucleolar structure during Influenza virus infection was described by electron microscopic studies already in the 1960s to 1980s (reviewed in [131]). Only very recently, different patterns of nucleolar remodeling were reported and demonstrate a strain-specific signature of Influenza virus-induced ultrastructural changes [132]. The infection-induced association of the biarsenical dyes with nucleoli, which was observed within the present work, might be related to these infection-induced changes in nucleoli. The strain-specific patterns of nucleolar disruption might further reflect different types of reorganization which are differently prone to unspecific labeling with biarsenical dyes. This can possibly explain the varying results between the present study and the work of Li *et al.* regarding the specificity of biarsenical labeling in infected cells.

Studying nucleolar proteins during Influenza virus infection using the biarsenical-tetracysteine system is therefore presumably conditionally feasible, however, when studying WSN virus-infected MDCK II cells as in the present study, nucleolar processes cannot be investigated by biarsenical labeling.

Another feature of the biarsenical-tetracysteine system was tested for its applicability to study Influenza virus infection: ReAsH being able to mediate photoconversion of diaminobenzidine

(DAB) allows performing correlated fluorescence and electron microscopy. The approach to study ReAsH-labeled TC-tagged vRNPs by high-resolution imaging in infected cells did however not yield the expected results: Even though efficient polymerization of DAB after the photoconversion procedure was visible in form of dark brown precipitates, the specific formation of electron-dense structures in ReAsH-positive cells could not be demonstrated. Electron-dense structures were instead detected in ReAsH-labeled virus-infected cells, irrespective of whether WSN wt or WSN nTC virus was employed, thus independent of a virally encoded TC-tag (Fig. 33). The correlation of electron-dense structures with ReAsH fluorescence signals was possible by comparative analysis of the same selection of cells by fluorescence imaging and electron microscopy. ReAsH-labeled nTC-NP did apparently not induce additional DAB precipitation. Various distinct, infection-induced, electron-dense structures were observed in infected cells: rounded and spindle-shaped cytoplasmic inclusions surrounded by ribosome-like structures, elongated nuclear structures and irregular disruption of the nucleolar structure (Fig. 34). These findings are consistent with previously described ultrastructural changes in Influenza virus-infected cells and WSN virus-specific patterns [132,533]. Consequently, the assignment of electron-dense structures as specific products of ReAsH-mediated photoconversion in infection is complicated by the variety of naturally occurring, infection-induced structures that are observed in Influenza virus-infected cells. The application of ReAsH photoconversion is hence not convenient to specifically detect TC-tagged proteins in Influenza virus-infected cells. Further improvement of ReAsH photoconversion using TC-tagged NP for examination of vRNPs in infected cells was therefore abandoned in the course of this study.

5.2.7 Summarizing remarks

The approach to generate recombinant Influenza A virus in which a TC-tag is inserted into internal regions of the NP sequence did not yield replication-competent virus particles. However, within associated experiments, a region on NP was identified, comprising residues 288 and 289, a disruption of which critically affects the polymerase function by a yet unknown mechanism.

In a second approach, recombinant virus strains were then successfully generated which encode NP with an N-terminal TC-tag. This was achieved by partial duplication of the vRNA packaging signal. Among the two generated viruses, WSN nTC virus was found to be favorable compared to WSN FLN virus for any type of experiment due to (1) a better replication efficiency, (2) better infectivity after labeling of the virus particles and (3) higher

fractions of infected cells with detectable amounts of cytoplasmic vRNPs late in infection. Following the primary goal to study fluorescently labeled vRNPs during assembly and virus entry, the feasibility of biarsenical labeling was analyzed, and even though biarsenical labeling did not generally interfere with Influenza virus infection, interference of biarsenical dyes with infection occurred in a TC-tag-dependent manner. The qualitative results of TC-tag labeling were satisfactory, yielding high signal-to-noise ratios and signal specificity. However, as soon as dynamic processes were under investigation, dynamics seemed to be greatly impaired by biarsenical labeling. Labeling apparently affected the release of the viral genome from endosomes during virus entry and prevented virus replication. It further affected cytoplasmic transport of progeny vRNPs by almost complete inhibition of any particle mobility. Together with the apparent aggregation of cytoplasmic NP following biarsenical labeling, these findings indicate the formation of intermolecular crosslinks by biarsenical dye molecules. Extensive cross-linking within individual vRNPs and between different vRNP segments might not only impair transport mechanisms, but also replication and transcription processes. Thus, even though virus mutants with TC-tagged NP are replication-competent, labeling during infection seems to impose artifacts rendering these mutant viruses inapplicable for dynamic fluorescence imaging in living cells. However, other applications making use of TC-tagged NP in the context of infection may be feasible if they do not require biarsenical labeling, e.g. affinity purification of TC-tagged NP from lysates of infected cells for analysis of associated proteins or the presence of multisegmental complexes.

5.3 Characterization of intrinsic subcellular targeting of NP

5.3.1 NP adopts a non-polarized nuclear-cytoplasmic distribution in the absence of virus infection

The import of Influenza A virus NP into the nucleus is essential for virus replication, namely for the delivery of incoming, newly infecting genomic segments [119] and for the formation of progeny vRNP complexes in ongoing viral replication. NP is known to accumulate in the cell nucleus due to at least one nuclear localization sequence (NLS) [93,118,120,123,361]. Nuclear targeting and a predominantly nuclear localization of NP could be confirmed in this study for the expression of wild-type NP and fluorescent NP fusion proteins (Fig. 35, Fig. 38 & Fig. 41).

A role of NP also in the bidirectional transport of genomic vRNP complexes has repeatedly been proposed. Intrinsic signals that drive nuclear export and apical targeting were suggested [265,299]. The previously reported nuclear export and accumulation of NP in the cytoplasm between 16 and 48 h p.t. [363] could however not be confirmed here. At 48 h p.t., NP-mEYFP was still found predominantly in the cell nucleus of CHO-K1 cells (Fig. 37), and also at 13 d p.t., wild-type NP as well as mEYFP-tagged NP fusion proteins remained primarily in the nucleus of polarized MDCK II cells (Fig. 52 a–c). Nevertheless, a slight increase of the cytoplasmic fraction was observed as compared to 24 h p.t. (Fig. 35, Fig. 41).

Cytoplasmic accumulation of NP was previously reported to be promoted by factors like a high cell density, upregulation of phosphorylation [362] and high NP expression levels [339]. However, even though protein expression was consistently analyzed in densely grown cells (90–100 % confluency) in the present study, a predominantly cytoplasmic localization was not observed.

Discrepancies between the previously reported cytoplasmic localization of NP and the here obtained data, which show nuclear retention of NP, might possibly arise from the use of different experimental systems. Bui *et al.* [362] studied the localization of NP from Influenza A/PR/8/34 strain in cells stably expressing NP together with the three viral polymerase subunits PA, PB1 and PB2. Digard *et al.* [339] also used NP from Influenza A/PR/8/34, but studied transient expression in BHK cells under the control of a T7 RNA polymerase promoter in the presence of recombinant vaccinia virus infection. Neumann *et al.* [363] analyzed expression of NP from Influenza A/WSN/33 in COS-1, MDCK II and HeLa cells under the control of a chicken β-actin promoter, and in the present study, NP from Influenza

A/FPV was expressed in CHO-K1 and MDCK II cells under the control of the CMV promoter. NP expression levels, NP sequences, the cell lines and the absence or presence of other viral proteins are hence not comparable between the different studies.
A general intrinsic property of NP to localize to the cytoplasm cannot be confirmed here. A delayed nuclear export of NP specifically in MDCK II cells compared to other cell lines was furthermore reported by Neumann *et al.* [363]. As MDCK II cells are highly permissive for Influenza virus infection, this does not seem to critically affect virus replication.

A polarized distribution of NP within transfected cells was previously reported in two studies. Elton *et al.* [515] suggested an "hitherto unrecognized polarity of the cell nucleus" and described a polarized peripheral localization of Influenza A/PR/8/34 NP in nuclei of BHK cells at 16 h p.t. However, BHK cells are non-polarizing fibroblasts, and polarity referred to the distribution of NP towards the upper surface of adherent cells in this case. The second work describing apical targeting of NP was realized by the same group and reported the polarized localization of Influenza A/PR/8/34 NP to the apical surface in 293T and BHK cells at 48 h p.t. [299]. The same tendency was also indicated for MDCK II cells. It should be stressed though that a complete polarization of BHK or 293T cells comparable to epithelial cell polarization cannot be expected to occur.
On the contrary, fully polarized MDCK II cells were analyzed in the present work (at 13 d p.t). These cells featured differentiated apical and basolateral membranes as verified by apical sorting of HAmYFP. Yet, they did not show a polarized distribution of NP or mEYFP-tagged NP fusion proteins (Fig. 52).
Strain- and cell type-specific differences cannot be ruled out to be responsible for differing results (compare section 5.1.3), but also differences between the detection methods should be considered, particularly in the light of the results obtained by comparative analysis of mEYFP detection and NP-specific immunodetection of an mEYFP-tagged NP construct (Fig. 42). High expression levels of NP constructs were shown to be prone to the detection of peripheral and polarized immunostaining of NP in nuclei and the cytoplasm, whereas parallel detection of the intrinsically fluorescent protein moiety indicated an even distribution of the construct. Thus, there is a chance that in the immunostaining-based studies of Carrasco *et al.* [299] and Elton *et al.* [515], immunostaining artifacts could have occurred which are very similar to the reported NP distribution, in particular at high expression levels, which were according to those studies the preferred conditions to detect nuclear export and a polarized distribution of NP.

In the present study, in fully polarized MDCK II cells at 13 d p.t, very low expression levels of wild-type NP precluded overexpression-induced immunostaining artifacts of NP. Here, neither immunodetection of wild-type NP nor mEYFP fluorescence detection of fluorescent NP fusion proteins showed any polarity in NP distribution (Fig. 52a–c). In order to increase the amount of cytoplasmic NP, NP with a C-terminal nuclear export signal (NES) was further expressed in polarized cells, but also then a preferential localization of NP to the apical plasma membrane could not be observed (Fig. 52d). mEYFP-tagged NP constructs, which apparently yielded better transfection efficiencies and higher expression levels than non-tagged NP (see also Western blot results, Fig. 40), confirmed the non-polarized distribution.

In summary, an intrinsic property of NP to adopt a polarized distribution in the nucleus or in the cytoplasm of transfected cells could not be confirmed, even though various NP constructs and time points post-transfection were tested, and fully polarized epithelial MDCK II cells were used which are highly permissive for Influenza virus replication.
It is possible that the ability for polarized targeting is specific for NP from Influenza A/PR/8/34. However, NP from the same strain was studied in the work of Bui *et al.* [362], where cytoplasmic accumulation, but no polarized distribution of NP was reported. Polarized distribution of NP in the absence of infection might hence occur under very specific conditions, but cannot be regarded as a general feature of NP. For further discussion, see also section 5.1.3.
In conclusion, the experimental data obtained in this study does not support a role of NP in targeting the genomic segments to the apical plasma membrane. This is consistent with recent reports which picture an alternative model for apical targeting of vRNPs. They showed that coexpression of M1 and NEP is required for nuclear export of reconstituted vRNPs in living cells [280] and that apical transport in infection is mediated by Rab11-positive recycling endosomes [297,298]. It was furthermore suggested that association with this apical compartment is mediated by the polymerase subunit PB2, but not by NP, since only PB2 can directly interact with Rab11 [280,296].

5.3.2 NP specifically targets subnuclear domains

For many years, NP has been regarded primarily as a structural protein of vRNP complexes with related functions as a shuttling protein, mediating the transport of the viral genome, or as a regulatory factor of viral replication and transcription. It is only in recent times that a role of NP in the virus-host interplay has more clearly emerged, and functional (non-transport-

related) interactions of NP with host cell proteins have been described, e.g. with Hsp40 and UAP56 [177,347,534].

5.3.2.1 NP extensively interacts with the nuclear compartment

Characterization of NP expression in the present study revealed that NP is involved in extensive interactions with the nucleus in the absence of virus infection.

For analysis of NP expression, various intrinsically fluorescent NP fusion proteins were generated and allowed the characterization of NP in living cells (4.3.1). Expression of NP fusion proteins was found to be essentially comparable to the expression of wild-type NP, displaying a predominantly nuclear localization and a non-homogeneous subnuclear distribution of NP (Fig. 41). Direct comparison of intrinsic fluorescence and immunofluorescence of NP fusion proteins, however, revealed fundamental qualitative and quantitative differences between the two detection methods and suggested the creation of artifacts by immunofluorescence staining (Fig. 42). It is shown here that in particular subnuclear structures enriched with NP could be visualized more clearly by intrinsic protein fluorescence than by immunofluorescence detection, implying that association of NP with nucleoli as well as its accumulation in punctate and irregular structures in the nucleoplasm are more reliably represented by intrinsic protein fluorescence than by external labeling. The use of intrinsically fluorescent constructs thus provides advantages over immunofluorescence detection of NP in addition to their suitability for live-cell imaging.

The choice of a photoactivatable fluorescent protein tag furthermore opened up the possibility to perform dynamic measurements and to characterize the effect of mutations in NP, not only with regard to the subcellular localization, but also with regard to site-specific affinities (Fig. 47).

As expected for fusion proteins whose localization is unaffected by the protein tag, no differences were observed between the subcellular distributions of C- and N-terminally tagged NP (4.3.1.1). Nevertheless, while the presence of truncated fusion proteins was undetectable in case of N-terminally tagged NP, the formation of free fluorescent protein and minor amounts of truncated protein during expression of C-terminally tagged NP strongly suggested the preferred use of the N-terminal fluorescent protein tag in this study and in future work (Fig. 40).

Together, the results from analysis of intrinsically fluorescent NP fusion proteins corroborate that these are an appropriate and powerful tool for the characterization of NP within cells, in particular for the detailed analysis of NP subnuclear targeting.

Analyzing NP expression in the absence of virus infection, using NP or NP fusion proteins, NP was found to distribute non-homogeneously in the nucleus and to accumulate specifically in the interchromatin space, indicating preferential association of NP with specific sites in the nucleoplasm (Fig. 35–Fig. 38, Fig. 41 & Fig. 44). Consistently, fluorescence photoactivation measurements demonstrated a very slow nuclear mobility of NP (Fig. 46 & Fig. 47) and thereby confirmed the slow nuclear dynamics of NP that were previously reported by Loucaides *et al.* using FRAP experiments [507]. By expression of especially generated monomeric mutant constructs of NP, it was furthermore possible to verify that the formation of prominent local enrichments of NP in the nucleus and the remarkably slow nuclear mobility of NP were independent of NP polymerization (Fig. 39, Fig. 47C). Also sterical restrictions can be excluded to be responsible for localized accumulations and low mobility of (monomeric) NP, since average-sized proteins up to 100 kDa were previously shown to diffuse freely within the nuclear space, unimpeded by the chromatin network [495,498]. Together, these findings demonstrate that NP is involved in extensive interactions with the nuclear compartment and that it targets distinct sites in the interchromatin space by intrinsic affinity.

The observations are further consistent with a large number of potential nuclear interaction partners that have been identified by proteomic and yeast-two-hybrid screens [103,358] and with other previously identified nuclear interaction partners [177,347,349,351,353]. With a few exceptions, the relevance of most of these interactions for viral replication is not yet clear though, and the knowledge on NP-host cell interactions is still fragmentary.

In the present study, the overall strong association of NP with the nuclear compartment evidently underlines the relevance of NP interaction partners in a cellular context and further provides information on the cellular localization and overall strength of these interactions. The kinetic data obtained by photoactivation measurements with NP constructs (monomeric or wild-type) moreover comprise information on the fraction of NP actually being involved in interactions with cellular components. Remarkably, fractions of freely diffusing, fast molecules of NP constructs were not detected (Fig. 47). The vast majority of NP obviously associates with cellular components, displaying a reduced mobility.

As a consequence of the strong association of NP with the nuclear compartment, a particularly high affinity of NP for viral RNA might be required for efficient formation of genomic vRNP complexes in infection. Consistently, a high RNA-binding affinity of NP was previously reported with K_D values in the range of 20 nM [87,187,333,339]. It was furthermore observed by Loucaides *et al.* [507] that the mobility of nuclear NP increased in case of vRNP

reconstitution in the presence of vRNA and viral polymerase, indicating competitive binding of viral and cellular components to NP. Transferring this into the context of virus infection and considering that viral protein synthesis precedes cRNA and vRNA formation [181,535], NP might associate with cellular components early in infection until adequate levels of cRNA, vRNA and the viral polymerase are available and then participate in cRNP and vRNP formation. It was previously suggested that NP might be specifically recruited to viral RNA by the viral polymerase that is bound to the 5' end of nascent cRNA or vRNA, which thereby initiates RNA-encapsidation followed by further recruitment of NP by NP-NP oligomerization [175,177]. Other studies indicate that oligomerization of NP might be a regulated process which is coupled to viral RNA binding and that the cooperativity of RNA-binding and NP oligomerization further enhances viral RNA encapsidation [92,176]. This might enable viral RNA to compete efficiently with cellular interaction partners for NP-binding.
A cytopathic effect of NP in transfection experiments due to nuclear accumulation and extensive interactions with the cells was not observed. Cells transfected with NP constructs remained viable up to 48 h p.t. (Fig. 37).

Summing up, extensive interactions of NP with cellular components together with previous evidence for cellular interaction partners [103,358] support a role of NP in the virus-host interplay and indicate that interactions of NP with viral factors and cellular components might have to be closely coordinated, e.g. by different affinities, by temporal aspects of protein and vRNA synthesis or by involvement and action of other viral proteins.
It could be helpful to be aware of these aspects when studying RNA- or polymerase-binding mutants of NP and their impact on virus replication. Phenotypic effects in cells might not be directly related to the RNA- or polymerase-binding function of NP, but could be indirectly effectuated by an altered availability of NP for cellular interaction partners and for the viral replication machinery, i.e. phenotypic effects might be caused by perturbation of the NP interaction network. This could further give rise to discrepancies between *in vitro* and in-cell measurements.

5.3.2.2 Subnuclear sites display different affinities for NP

Even though it is known that the cell nucleus is a highly organized compartment, which is structured into functionally specialized domains [487,490], it remains unclear what causes the heterogeneous distribution of NP and its localized accumulation.

What, at first glance, may appear as precipitates due to (over)expression of NP in the absence of virus infection, could be shown to be neither due to NP polymerization (Fig. 39) nor to steric hindrance of NP distribution within the nucleus as based on findings from previous studies [495,498]. Fluorescence photoactivation measurements, monitoring protein dynamics, could be effectively applied to distinguish between subnuclear structures that dynamically associate with NP and NP precipitates. Large micrometer-sized subnuclear accumulations highly enriched with NP thus could be shown to consist of immobilized protein that had apparently precipitated within these structures (Fig. 46, 2nd row). Consistently, such structures were absent from nuclei when the local nuclear NP concentration was decreased by expression of NP with an artificial nuclear export sequence (NES) (Fig. 45). This shows that enrichment of NP within this type of structure is unlikely to result from high-affinitiy association with large micrometer-sized nuclear domains, but rather seems to be the result of precipitation due to high local NP concentrations within nuclei. The absence of such compact local accumulations of NP in virus-infected cells (Fig. 43) furthermore indicates that these structures are artifacts of NP (over)expression, as is also the major chromatin rearrangement that is observed upon local accumulation of NP (Fig. 44d).
On the contrary, small punctate accumulations of NP, which measure typically not more than a micrometer in diameter, were shown to dynamically exchange (monomeric) NP with the surrounding nucleoplasm, albeit at very low rate, indicating association of NP with high affinity (Fig. 47C). It was thus possible by application of fluorescence photoactivation measurements to distinguish between different types of subnuclear accumulations and to verify site-specific dynamic associations of NP with subnuclear domains.

Since concurrence of protein precipitation and high-affinity interactions of NP as well as the overall high concentration of NP in nuclei of transfected cells complicated the interpretation of NP subnuclear behavior, two types of NP constructs were generated within this study to facilitate analysis of NP in the nucleus: On the one hand, the obligate monomeric NP mutants E339A and R416A were generated, and on the other hand, the above mentioned NP-NES, a construct that is targeted to nuclear export by a C-terminal NES.

Obligate monomeric NP allowed excluding effects of NP polymerization on the subcellular distribution of NP. It confirmed that local accumulations of NP formed independently from NP self-association and that the overall subcellular distribution was essentially unaffected by the ability of NP to oligomerize (Fig. 39). It furthermore permitted to monitor the dynamics of a uniformly monomeric population of NP, ensuring that the monitored mobilities of NP were

determined primarily by site-specific interactions with cellular components rather than by self-association. Application of obligate monomeric NP in photoactivation studies hence allowed differentiating subnuclear sites according to their affinities for NP and enabled an overall picture of the subcellular interactions of NP.

It could be shown that throughout transfected cells, NP experiences a considerable retardation of diffusion as compared to the diffusion of the free fluorescent protein (Fig. 47). Among the measured mobilities, the mobility of cytoplasmic NP was the highest, very similar to that of the diffuse and homogeneously distributed NP in the nucleoplasm (Fig. 47 (B, C) right). This observation indicates comparably weak interactions with cytoplasmic and nucleoplasmic structures, but also binding of NP to mobile components of the cytoplasm and the nucleoplasm could occur. Substantially lower mobilities were observed for NP which localized in nucleoli or within small punctate subnuclear domains (Fig. 47 (B, C) left).

In case of the small punctate subnuclear domains, the highest local NP concentrations and the lowest mobilities of NP within cells were found to coincide, indicating that a multitude of strong interactions between these domains and NP leads to enrichment and retention of NP. In case of nucleolar NP, however, an equally low mobility of NP was observed, but it was accompanied by the presence of relatively low concentrations of NP. Even though the nucleolar NP mobility was among the lowest measured within the cells, nucleoli frequently appeared depleted of NP relative to the surrounding nucleoplasm. This observation implied strong interactions between NP and nucleolar components, but only a limited number of interaction partners or, alternatively, a limited accessibility of these interaction partners within nucleoli.

Fluorescence photoactivation measurements thus demonstrate that local NP concentrations do not necessarily correlate with local affinities for NP. Nucleoli in general might be particularly prone to the detection of unexpectedly low protein concentration. They seem to have a reduced accessible volume as compared to the surrounding nucleoplasm, which was previously reported for freely diffusing proteins (like EGFP) [494,495] and which was also discussed here before as a possible reason for immunostaining artifacts (Fig. 42, 4.3.1.2). This circumstance might explain the limited accumulation of NP in nucleoli, despite obviously high affinity of NP for this compartment.

The results that were further obtained in nuclear depletion experiments using NP nuclear export constructs excellently match the findings that were obtained by photoactivation measurements with monomeric NP. By expression of NP constructs with an artificial NES sequence, the local nuclear NP concentration could be efficiently decreased in a subset of

cells, thereby preventing protein precipitation and revealing sites of high affinity for NP more clearly (Fig. 45). Two distinct structures were thus found to accumulate NP even at low nuclear concentrations: small punctate interchromatin structures, which were highly enriched with NP, and nucleoli, which displayed comparably low NP concentrations. This was consistent with the results from photoactivation studies as described above, which identified nucleoli and punctate nucleoplasmic structures as subnuclear domains with the highest detectable subcellular affinities for NP and differing NP concentrations. Monitored protein dynamics confirmed very slow NP exchange rates between these domains and the surrounding nucleoplasm (Fig. 47 (B, C) left). Accordingly, in nuclear depletion experiments, NP constructs which were associated with either of the two structures resisted nuclear export more than any other nuclear NP population and remained bound under conditions of ongoing nuclear export in nuclei that were otherwise largely devoid of NP. Apparently, NP-NES constructs had a higher affinity for these specific domains than for the nuclear export machinery. Expression of a reference construct further ascertained that accumulation of NP within these structures was not induced by the NES sequence itself, but in fact by the NP moiety of the construct (Fig. 45c).

While photoactivation studies provided insight into the various local cellular affinities for NP and were able to distinguish NP-binding domains from protein precipitates, nuclear depletion experiments additionally allowed a more detailed description of subnuclear domains with particularly high affinity for NP, thereby facilitating their further characterization. Especially the small interchromatin domains with high affinity for NP, which are – unlike nucleoli – difficult to assign, became more clearly exposed and more easily identifiable at low nuclear NP concentrations and in the absence of NP precipitation (Fig. 45). Up to eight distinct, small interchromatin domains enriched with NP were detected within one cell. They typically measured less than 1.2 µm in diameter. Size and number of the NP-binding domains as well as their localization in the interchromatin space were reminiscent of a class of subnuclear structures known as “nuclear bodies” (NBs), which were thus suspected to form the cellular target structures for NP.

In subsequent experiments, similar patterns of local enrichment of NP were recognized also in cells expressing wild-type NP at low expression levels (Fig. 50). The equivalence of these domains was supported by results of colocalization analysis. They demonstrated that punctate subnuclear accumulations that were formed either by wild-type NP or by residual nuclear NES-tagged NP localized in close proximity to the same specific cellular domains, namely CB and PML NBs (Fig. 49, Fig. 50). These findings thus strongly support that NP-binding

structures which were uncovered by nuclear depletion of NP are representative for structures which accumulate also wild-type NP. The highly speckled nuclear appearance of wild-type NP that is observed at higher expression levels moreover suggests association of NP also with other subnuclear structures (Fig. 38a, b). These might however display lower binding affinities for NP and therefore not be visualized in nuclear depletion experiments.

It should be mentioned that a crystal structure of the obligate monomeric NP-R416A, which was used in this work, was very recently reported and provides a structural basis to understand the connection between the monomeric conformation of NP and a reduced RNA-binding affinity [176]. A model was proposed according to which oligomerization and RNA-binding of NP might be coordinated by phosphorylation of a highly conserved serine residue. Another novel report further showed that NP has a low self-association activity in the absence of RNA, supporting that NP oligomerization might be coupled to RNA-binding [92]. On this basis, it was suggested that wild-type NP may exist primarily as a monomeric protein before incorporation into cRNPs and vRNPs in infection.
Extrapolating these findings to NP expression experiments of the present study, NP might be inherently monomeric in the absence of virus infection. Consistently, neither the subcellular distribution nor the subcellular dynamics of wild-type NP were found to differ significantly from the obligate monomeric NP mutant in transfected cells (Fig. 38, Fig. 39, Fig. 47B). A definitive prediction on the conformational state(s) of wild-type NP within cells is however not made here and would require more detailed analyses.

In summary, the combination of three approaches within this study – the use of monomeric NP mutants, the decrease of the local nuclear NP concentration by fusion of NP to a nuclear export sequence and photoactivation measurements to monitor site-specific protein dynamics – permitted to distinguish protein precipitates from dynamic structures and to differentiate between different NP-binding sites according to their affinities for NP. Identification of subnuclear structures with particularly high affinity for NP furthermore enabled the phenotypic description and subsequent colocalization analyses with known cellular structures (for discussion see 5.3.2.4).

5.3.2.3 The role of site-specific affinities during NP expression and functional implications for virus infection

The following scenario for NP expression is suggested, based on the information obtained on subcellular affinities for NP (4.3.2 and 5.3.2.2):

Newly synthesized NP is rapidly transported into the nucleus and first targets the subnuclear domains with the highest affinities, namely nucleoli and specific, yet unidentified, small interchromatin domains. The latter should become rapidly highly enriched with NP. While the nucleoplasmic level of NP continually increases with increasing nuclear accumulation of NP, the nucleolar concentration, however, will remain constant at some point due to limited accessible space. This will cause nucleoli to appear depleted of NP with increasing NP expression levels. A transient interaction between NP and nucleoli was reported in literature [123], but according to the data obtained here, only a shift of the relative local concentrations can be confirmed. The nucleoplasm features extensive interactions with NP and can accumulate large amounts of NP. With constantly increasing NP levels in the absence of virus infection, at some point, precipitation of NP then occurs in the nucleoplasm. This might partly be due to NP self-association, but since precipitation is also observed for obligate monomeric NP, weak NP-NP interactions, which might occur only at high local concentrations, or a multitude of interactions with cellular components might further contribute to NP precipitation. It is possible that NP becomes entrapped in a growing network of interactions with diverse interaction partners, eventually leading to precipitation, whether or not NP is able to oligomerize.

Since the formation of large nuclear NP precipitates is not observed in virus infection, the timely beginning of vRNP formation might prevent the accumulation of free NP in the nuclei of infected cells, implying that NP expression levels might be somehow coordinated with vRNA synthesis in infection. This conclusion is in accordance with previous studies reporting that NP is involved in regulating the switch from viral mRNA synthesis to the efficient formation of full-length cRNA and vRNA [90,177,181,187,343]. Even though the studies indicate that NP is not solely responsible for directing the switch from viral transcription to replication, NP seems to act as an important auxiliary factor for this transition by stabilizing nascent viral full-length RNA [90,187] and by stimulating elongation and promoter escape of the viral polymerase through direct interactions [177,343]. Initiation of the switch was suggested to be due to other mechanisms, though, involving e.g. the presence of free viral polymerase complexes, small viral RNAs, the viral protein NEP or specific metabolic conditions (reviewed in [54], [177]). Nevertheless, since the presence of NP was shown to significantly promote viral full-length RNA synthesis [177,181,187,343], NP itself contributes to the down-regulation of free NP levels in infection.

The ability of NP to associate with specific subcellular structures even at very low nuclear concentrations most likely ensures targeting of NP to these domains very early during infection. This could indicate a regulatory role of NP, which, just like NS1, is an early protein in infection and might modulate host cell processes according to the viral needs. In addition, the extraordinarily high affinity of nucleoli and small punctate interchromatin domains for NP might ensure that the association with NP persists during infection and can efficiently compete with the recruitment of NP for cRNP and vRNP formation. Consistently, it was only recently reported that bright nuclear foci enriched with NP can be found late in infection and that these are furthermore devoid of vRNA [280]. Nucleoli, on the contrary, were found to disintegrate during infection, which is not due to the presence of NP alone though [132] (Fig. 41). Nucleolar targeting of NP was demonstrated to be critically required for viral transcription [123], but it is unclear if a tight association with the nucleolar compartment persists during infection. The ultimate fate of nucleolar NP might depend on the interplay with other viral components which are involved in nucleolar remodeling during infection [132].

It is further possible that high-affinity association of NP with nucleoli or with small interchromatin domains is a transient event in infection which enables posttranslational modifications or the recruitment of cellular factors to NP before NP is subsequently targeted to the viral replication machinery. In line with this hypothesis, relocalization of the cellular vRNP-binding protein nucleophosmin from nucleoli to sites of viral replication in the nucleoplasm of infected cells was previously reported [103].

The implications for high-affinity targeting of NP most likely differ for subnuclear domains according to their role in infection.

It remains to be investigated if NP is able to target these specific domains also in form of vRNP complexes. Since no vRNA was previously found to colocalize with nucleoli during infection [280], nucleoli apparently do not harbor vRNPs and thus do not represent sites of viral transcription or replication. Nucleolar targeting of NP might therefore rather aim at interference with cellular processes or at the recruitment of cellular factors by NP alone, possibly in concert with other viral proteins as indicated by the work of Terrier *et al.* [132]. As for the small punctate interchromatin domains which are targeted by NP, colocalization with vRNPs during infection has not been addressed so far. It is conceivable though that by targeting these domains, NP might help to direct the incoming viral genome in infection to subnuclear sites that provide an optimal molecular environment for subsequent transcription and replication. Considering that Influenza virus transcription and replication require

numerous cellular factors [127,128,149] and considering further that the nucleus is partitioned into regions of actively transcribed chromatin and transcriptionally inactive regions [488,489], efficient targeting of the Influenza virus genome to subnuclear sites enriched with factors for active transcription might be important for the functioning of the viral transcription and replication machinery. Yet, the sites of active cellular transcription, also known as transcription factories or Pol II sites, do not resemble the distinct punctate subnuclear domains which are preferentially targeted by NP (compare Fig. 3 in [127] with Fig. 45 and Fig. 50). Instead, NBs, which were previously shown to localize in close proximity to sites of active transcription [536,537,538], more closely resemble the punctate NP-binding domains than Pol II sites, and moreover, harbor also numerous enzymes which are involved in cellular transcription and RNA processing. They might therefore represent target structures for NP and RNPs and provide a favorable environment for viral transcription and/or replication.

Since Influenza virus-infected cells are arrested in the G0/G1 phase of the cell cycle [539], targeting of NP or vRNPs to cellular replication sites during infection is rather unlikely. In the present study, NP expression in the absence of virus infection was performed under conditions of serum starvation, which also leads to accumulation of the cells in G1 phase [540]. NP subnuclear targeting was thus investigated under cell cycle conditions comparable to infection. It is therefore excluded that the observed heterogeneous distribution of NP is related to cellular replication sites.

Only a small fraction of total expressed NP localizes within nucleoli or NB-like interchromatin domains. While, above, the targeting of subpopulations of NP to subnuclear sites with high affinity for NP is discussed, colocalization of NP with Pol II sites is not generally ruled out. The vast majority of NP in transfected cells is heterogeneously distributed due to interactions with the nuclear compartment and has a granular or speckled appearance. Whether it partially colocalizes with Pol II sites when expressed alone remains to be demonstrated. There is evidence for a tight interplay between the cellular transcription machinery that is associated with Pol II transcription and the viral machinery [127], but a physical association of NP with Pol II sites has not been shown yet.

Already in 1982, viral RNA synthesis in infection was reported to occur in “nuclear cages” where also cellular RNA is synthesized [140]. By biochemical fractionation experiments, it was shown later on that vRNP complexes in infected cells tightly associate with chromatin and the nuclear matrix fraction [140,260,292,541], and that also the actively transcribing form

of cellular Pol II associates mainly with the nuclear matrix fraction [127]. Consistently, viral RNA synthesis activity was detectable in the nuclear matrix fraction as well [542].
Intriguingly, even when expressed alone, NP was found to associate with the nuclear matrix fraction and with the chromatin fraction. Only little NP was found in the DNAse-sensitive fraction though, which is believed to be obtained from interchromatin components and loosely packed chromatin [541]. In infected cells, however, part of NP just like part of the cRNA and the vRNA could be detected additionally in the DNAse-sensitive fraction [541]. These results from previous studies seem to correspond to the observation reported here that the entire NP is tightly associated with the nuclear compartment when expressed alone (Fig. 47) and to the observation described by Loucaides *et al.* [507] that the nuclear mobility of NP increases when it forms vRNPs in the presence of viral polymerase and vRNA.

It is not clear from these data, though, how association of NP with chromatin and nuclear matrix fractions in biochemical fractionation experiments correlates with the here-observed subnuclear distribution of NP monitored by fluorescence microscopy. According to fluorescence imaging, the majority of NP accumulates in the interchromatin space of transfected cells and only a small fraction of NP seems to colocalize with chromatin (Fig. 44). It has to be considered that the interchromatin space and the chromatin as defined by fluorescence microscopy might differ significantly from the chromatin-derived fraction by high-salt extraction and from the DNAse-sensitive interchromatin fraction as defined by biochemical fractionation.
The nuclear matrix fraction, which is not clearly relatable to the nuclear topology as defined by DNA staining, most likely forms part of both the interchromatin space and the chromatin regions. It comprises cellular transcription machinery like Pol II and cellular splicing factors. The splicing factor UAP56, which is assumed to be a constituent of the nuclear matrix fraction [541], was previously shown to be part of the cellular transcription/export (TREX) complex, which associates with sites of active Pol II transcription and couples cellular transcription, pre-mRNA splicing and mRNA nuclear export [543,544,545]. UAP56 was moreover shown to be an interaction partner of RNA-free viral NP [534] and to play an important role for the efficient replication of Influenza A virus [350]. It was proposed to act as a chaperone facilitating NP incorporation into viral RNPs [177]. UAP56 thus might be a potential candidate to be responsible for association of NP with the nuclear matrix fraction upon biochemical fractionation and for the heterogeneous interchromatin distribution of NP in the absence of virus infection. In fact, the subnuclear distribution of UAP56 has a striking similarity to the distribution of NP. Both concentrate within numerous speckled domains and

extend also diffusely outside of these domains (Fig. 2 in [546] & Fig. 44b, c). It is further known that UAP56 partially colocalizes with splicing speckles [546]. These data indicate that NP, even when expressed alone, might be targeted to sites that are related to cellular transcription. It can be furthermore speculated that the sites enriched with NP and its chaperone might define the sites of viral replication, which appear as granular pattern throughout the nucleus as well. According to current knowledge, colocalization analysis of UAP56 and Influenza virus NP was thus far not performed. Further analysis will be required.
In the context of NP mobility studies, UAP56 might be a contributing factor to the low mobility of NP, linking NP to the nuclear matrix. UAP56 and splicing speckles might be sites with medium affinity for NP, which are responsible for the retardation of NP diffusion within the nucleoplasm, but which do not retain NP upon nuclear export induced by a C-terminal NES (as reported in section 4.3.2.). Since UAP56 was proposed to act as a chaperone [177], less tight association of NP with these sites and a better availability of NP and UAP56 might be favorable for viral RNP formation as compared to NP that is tightly associated with subnuclear structures with high affinity.

In the following last part of this section, chromatin targeting of NP is discussed. Even though, by fluorescence imaging, only a small fraction of NP was found to colocalize with chromatin (Fig. 44), it was previously shown that NP as well as vRNPs are able to bind to histone tails of nucleosomes [352] and that NP specifically recognizes modifications which are characteristic for histone tails in transcriptionally inactive and condensed chromatin [353]. The interaction of NP with histone tails was demonstrated *in vitro* [352,353], and association of NP with chromatin was suggested based on biochemical fractionation and high-salt extraction, which is considered to solubilize the chromatin-binding proteins from tightly packed chromatin [541]. Nonetheless, it is possible that within the native cellular context, interactions of NP with interchromatin structures are prevalent, and only a small fraction of NP might actually associate with heterochromatin.
It is known that structure and function of chromatin can be modulated by modifications of the histone tails why it was suggested that also NP-binding to histone tails might have a regulatory function during infection [352]. The dramatic rearrangement of chromatin that was observed here upon (over)expression of NP could be one consequence of this interaction (Fig. 44d). It is an artifact of NP (over)expression though. Yet, it could be related to a functional molecular mechanism which – during infection – targets progeny vRNPs for nuclear export to heterochromatin in the nuclear periphery, as it was previously suggested [292]. Chromatin rearrangement by NP might furthermore indicate a viral mechanism to change the cellular

transcription pattern or promote host-cell shut-off [352]. In any case, the observed chromatin reorganization clearly demonstrates that NP can affect cellular chromatin, even when the degree of colocalization is relatively low.

Considering the discrepancy between NP subnuclear localization and its chromatin binding capacity, it seems furthermore possible that interactions of NP might be modulated during infection, e.g. by specific protein modifications like phosphorylation [261], ubiquitination [547], sumoylation [548] or caspase-dependent cleavage [549], or simply by incorporation of NP into vRNP complexes, which might increase the affinity of NP for chromatin and thus specifically promote targeting of vRNPs and cRNPs to heterochromatin. Various reasons for the targeting of vRNPs to heterochromatin were previously suggested, e.g. the efficient recruitment of heterochromatin-associated factors for the formation of vRNP nuclear export complexes [292] or, alternatively, the association of vRNPs and cRNPs with heterochromatin as a subnuclear platform for viral transcription and replication processes [541]. The role of NP-chromatin interactions for RNP targeting to chromatin remains to be determined, though. The requirement for a specific regulation of RNP targeting is supported by the finding that cRNA and vRNA associate with chromatin fractions, but only vRNA can be found in the nuclear matrix fraction [541]. This indicates a selective involvement of different subnuclear sites in viral replication and transcription processes. How far NP and regulation of NP interactions might be involved in the selective targeting of viral RNPs is unknown and remains to be investigated.
In general, the modulation of NP affinities might create different populations of NP, enabling NP to associate with chromatin and to be further available for other functional interactions, either as a free protein or as part of viral RNPs. It would not be unexpected for NP to fulfill multiple functions during infection since most of the Influenza virus proteins have various functions due to the limited coding capacity of the viral genome.

Summarizing this paragraph, the distinct affinities of NP for the different subcellular locations are suggested to have functional implications and to reflect the diversity of NP interactions and functions. It is postulated that the sites with the highest affinity for NP accumulate NP early during infection in form of incoming vRNPs or newly synthesized NP. It is suggested that site-specific targeting might support viral replication by interference with cellular processes or by recruitment of cellular factors, but also posttranslational modifications of NP within functionally specialized domains might be an important function of NP subnuclear targeting. The vast majority of NP, however, which associates heterogeneously and with

comparably low affinity with the interchromatin space, is assumed to represent the pool of NP which is available for viral RNP formation. As for the cellular chromatin, its role in the interplay with NP is not obvious, given by colocalization studies and comparison with biochemical data. A regulation of NP affinities by posttranslational modifications or RNP formation during infection is thus suggested.

5.3.2.4 NP specifically targets subnuclear domains in close proximity to PML and Cajal bodies

Nuclear depletion of NP by expression of NP with NES-tag revealed nucleoli and punctate interchromatin domains of yet unknown identity as subnuclear structures with the highest subcellular affinities for NP (Fig. 45). Exposure of these high-affinity domains by nuclear depletion moreover enormously facilitated subsequent colocalization studies to characterize the cellular context of these structures. In case of wild-type NP, these domains might have previously been unnoticed as they might be mostly obscured by excess amounts of nuclear NP and by the typically speckled distribution of NP.

Immunostaining of potential target structures of NP revealed that not only residual nuclear NES-tagged NP, but also wild-type NP accumulated in subnuclear domains (termed NP bodies) which were frequently found in close proximity to PML bodies and Cajal bodies (CBs) (Fig. 48–Fig. 51). The results strongly support that NP bodies do not randomly form within the nucleus. This is further consistent with photoactivation studies which provide evidence that NP dynamically associates with punctate subnuclear domains with high affinity. By expression of a control protein, it could be ruled out that accumulation of NP in subnuclear domains is an artifact of the NES-tag (Fig. 45). It is furthermore unlikely that accumulation of NP in interchromatin domains is due to targeting of NP to nuclear proteasome assemblies, termed clastosomes, which colocalize with a subset of PML bodies. In previous work, an unfolded NP mutant that is targeted for degradation was shown to colocalize together with PML within clastosomes [550]. This differs from the NP constructs in the present study which typically localized adjacent to PML bodies.

As outlined in section 4.3.2, the likelihood of a completely random association of two domains within the nucleoplasm is unknown due to the non-assessable effect of nuclear crowding and limited interchromatin space. Yet, PML and CBs were previously shown to associate non-randomly with each other by direct physical interaction [505]. Here, 68 % of the CBs were found to associate with PML bodies, and only slightly less, 58 %, were involved in triplet arrangements with both PML and NP bodies, indicating a non-random association

with NP bodies as well. Furthermore, close association of NP bodies with PML domains and CBs was observed even at low densities of these structures (Fig. 49c, Fig. 50b), whereas the more numerous splicing speckles displayed only a low degree of colocalization and hardly any overlap with NP bodies (Fig. 48). It was further observed that PML NBs and CBs colocalized more frequently with NP bodies than with each other. It cannot be excluded though that this might be partly due to the larger number of distinct NP bodies compared to PML bodies and a higher probability of colocalization. Nevertheless, the largest fraction of each of the structures was part of a triplet arrangement with the two other structures, and almost the same fraction of NP bodies was found to colocalize pairwise with either PML bodies or CBs (4.3.2.3).

According to these results, PML NBs and CBs seem to localize at subnuclear sites with a high probability of being preferentially targeted by NP. Since one third of NP bodies was further detected as solitary domains, NP apparently targets structures often related to, but not strictly dependent on the presence of PML or CBs. This is not unusual for subnuclear domains since also cellular structures like PML bodies and CBs [504] (or CBs and gemini of CBs (Gems) [551,552]) can be found to correlate with each other, even though they do not depend on each other, indicating a certain heterogeneity among subnuclear domains. In case of PML bodies, it is known that there are different subtypes of PML bodies which differ in ultrastructure and in protein composition, yet, all of them possess the PML protein as a common feature [553,554]. Since NBs are typically defined by marker proteins, also other classes of NBs might comprise a variety subtypes which differ in their specific functions and protein compositions. Similarly, also NP might target to a heterogeneous class of subnuclear domains.

Further analysis will be required to identify the interchromatin domains that are targeted by NP with high affinity. Potential candidates will be subnuclear domains that were previously shown to localize adjacent to PML and CBs, e.g. Gems and cleavage bodies. Both domains are spatially and functionally related to CBs [552,555]. They are involved in snRNP assembly and in cleavage and polyadenlylation steps of pre-mRNA processing, respectively.

5.3.3 Pondering potential biological functions of NP subnuclear targeting in the context of nuclear organization and viral infection

The cell nucleus is known to be highly organized, and even though membraneless, the interchromatin space is compartmentalized into functionally specialized domains [488,489]. Prominent features of the nuclear architecture are the nuclear bodies (NBs). These are proteinaceous structures which assemble and maintain themselves either as constitutive parts

of the nucleus or in response to the metabolic state, to signaling events or to cell cycle progression. NBs are considered to control key cellular processes and represent therefore host cell machinery that can be either targeted or recruited by viruses to promote viral replication [556]. Structural rearrangements, disruption or altered numbers of NBs have been reported in the context of viral infections, although the reasons for these alterations remain often unclear. Specific subnuclear domains are further known to be targeted by Influenza virus protein M1 [277] and by proteins of other nuclear replicating viruses [491,492]. It is shown here that also NP is directed to specific subnuclear domains by intrinsic affinity, namely nucleoli and yet unidentified small punctate interchromatin domains. This work was thus aiming at the identification of these subnuclear structures accessed by NP to enable conclusions on cellular processes that might be targeted by NP and on potential strategies of NP to interfere with or recruit host cell machinery.

The general perception of nuclear bodies in current literature is that of subnuclear organelles [538,557] which carry out specific functions by concentrating substrates for efficient biological reactions in related metabolic processes or reaction chains [558]. They are known as sites for posttranslational modifications of proteins, posttranscriptional modifications and processing of RNA, assembly of RNP complexes and regulation of gene loci. Well studied examples are nuclear speckles, paraspeckles, Polycomb bodies, CBs, Gems, cleavage bodies, PML bodies, clastosomes and nucleoli (for an overview see [502]). They differ in protein composition and are enriched with proteins that can jointly act on biological processes. A non-random spatial correlation among these domains within the nuclear compartment is assumed to have functional implications [486] and to contribute to regulated and efficient gene expression [559,560,561,562].

It is shown in this work that two types of NBs, CBs and PML bodies, frequently localize adjacent to the subnuclear domains that are targeted by NP. Intriguingly, it was previously reported that these domains themselves are affected by Influenza virus infection, and also infections by other viruses reportedly affect CBs and PML bodies.

5.3.3.1 CBs and the related nucleolar compartment

CBs are small punctate interchromatin domains. They are known to be involved in biogenesis of the spliceosomal machinery and posttranscriptional modification of RNAs [563]. They are sites of small nuclear (sn) RNP assembly and of maturation of spliceosomal snRNA. To this end, they harbor scaRNPs, a Cajal body-specific class of small nucleolar (sno) RNPs, which

guide modifications, in particular methylation and pseudouridylation, of snRNAs. They are further involved in nuclear export of precursor U snRNA [564] and in trafficking of proteins in and out of nucleoli [559,565,566]. CBs are related to nucleoli in protein composition and space and can further be found in close proximity to Gems, cleavage bodies, transcriptionally active U snRNA gene loci, PML bodies [563] and histone locus bodies [567]. Although a direct function in cellular stress response has not been assigned, CBs contain further many stress-related components like the tumor suppressor p53, the dsRNA-activated protein kinase R (PKR) and peroxiredoxin V [563].

Implication of CBs in viral infections has so far been described only for a few viruses. CBs reportedly accumulate proteins from picorna-like potato virus [568], groundnut rosette virus [566] and from an avian herpesvirus [569]. Further, they are disrupted by herpesvirus proteins [556] and rearranged in adenovirus infection [570]. Interestingly, the interplay of these viruses with CBs is not reported in the context of cellular antiviral activity, but rather in the context of nucleolar localization of viral proteins [568], trafficking pathways involving CBs [566] and viral protein expression [570].

Also Influenza virus infection was shown to induce changes to the morphology of CBs, increasing the number of CBs while simultaneously decreasing their size [164]. The relevance of viral interference with CBs and the underlying mechanism are still unknown, though. The effect could not be linked to the direct action of the NS1 protein, which is typically considered to be the main actor in the virus-host interplay. Expression of NP constructs in the present study was furthermore not sufficient to induce morphological changes to CBs either. Based on the close functional and compositional relation between CBs and nucleoli [571], a connection between the disintegration of nucleoli [132] and redistribution of CBs during infection might be hypothesized. The reasons for the morphological changes of nucleoli have not been clarified to date either. It is tempting to speculate that the association of NP with nucleoli and in close proximity to CBs might be functionally related to infection-induced processes occurring in these compartments. Even though highly speculative, it is imaginable that dispersal of CBs and targeting of NP to sites in the vicinity of CBs enables the virus to hijack the RNA modifying machinery or components of transport pathways that are located in CBs.

Yet, the mere inhibition of cellular protein synthesis was shown to lead likewise to the redistribution of CBs [572], similarly as in virus infection. Altered morphology of CBs in virus-infected cells thus could be an indirect effect of the Influenza virus-induced host cell shut-off. In case of adenovirus infection, morphological changes of CBs were previously assumed to be side effects of metabolic changes as well, but this point of view was later

replaced by a functional interpretation of adenoviral interference with CBs, and disruption of CBs was then considered as coordinated rearrangement instead [570]. In Influenza virus infection, the infection-induced disassembly of the related nucleolar compartment and the fact that CBs localize in the vicinity of domains that are specifically targeted by Influenza virus proteins (like NP bodies and PML bodies [277]) support a functional implication of CBs in viral replication as well.

With PARP1 (poly(ADP-ribose)-polymerase 1), CBs further contain a protein that was previously shown to be essential for Influenza virus replication and that is furthermore a cellular interaction partner of the trimeric viral polymerase and of reconstituted vRNPs [103]. PARP1 is an obligatory resident of CBs and crucial for the maintenance of CB integrity [565]. Substantial amounts of PARP1 localize also in nucleoli. It has functions in DNA repair, chromatin remodeling, transcription regulation and ribosome biogenesis. By catalyzing posttranslational modification of proteins with poly(ADP-ribose), PARP1 can induce the assembly and activation of multiprotein complexes. It enables the recruitment of DNA repair proteins to sites of DNA damage, thereby initiating DNA repair pathways [573], and it targets proteins essential for rRNA processing to nucleoli [574]. Most interestingly, abolishing PARP1 enzymatic activity leads to disintegration of nucleoli and to aberrant localization of nucleolar proteins, suggesting that the PARP1 reaction product poly(ADP-ribose) might act as a scaffold that is crucial for the recruitment rRNA-processing proteins to sites of rRNA formation, and thus, for the formation of the nucleolar compartment [574,575]. It is possible that this mechanism of nucleolar assembly provides the still missing explanation for the disintegration of nucleoli (and CBs) in Influenza virus-infected cells: The recruitment of PARP1 by the viral polymerase and by vRNP complexes as indicated by Mayer *et al.* [103] might cause depletion of poly(ADP-ribose) in nucleoli and in CBs and thereby lead to the disintegration or dispersal of these domains.

This hypothesis is in accordance with experiments performed by Terrier *et al.* [132], showing that separate expression of NP, M1 or NS1 does not induce disruption of nucleoli. Only reconstitution of viral RNP complexes, including coexpression of the viral polymerase, could be shown to induce nucleolar fragmentation. Intriguingly, the viral polymerase complex is not recruited to nucleoli during infection [139,576,577], supporting its here postulated role to induce nucleolar fragmentation by recruitment of PARP1 from nucleoli to sites of viral polymerase and RNP localization.

Notably, Terrier *et al.* further reported that NS1 was found to contribute to nucleolar remodeling when coexpressed with viral RNP complexes [132]. Even though NS1 is targeted

to nucleoli by an intrinsic signal [578], structural rearrangements by NS1 were only observed in the context of vRNP-induced nucleolar fragmentation, but not in the absence of viral RNP components, implying the possibility that nucleolus-related functions of NS1 may require nucleolar fragmentation. Subtype-specific nucleolar targeting of NS1 was earlier shown to modulate the pathogenicity of Influenza A viruses [579].

Generally, it is not clear if fragmentation of nucleoli is only a side effect of the specific recruitment of nucleolar proteins like PARP1 by the viral machinery. In this case, the fragmentation itself would not fulfill any purpose. Alternatively, nucleolar fragmentation could be also especially induced by depletion of scaffolding proteins like PARP1 to trigger the release of other nucleolar components (compare [574]) in order to interfere with cellular processes or to subsequently recruit nucleolar proteins. In this context, nucleolar fragmentation might enable viral proteins like NP to recruit nucleolar components that are usually tightly associated to the nucleolar matrix. In case of NP, this would be consistent with the strong association that could be demonstrated between nucleoli and NP in the absence of infection (Fig. 47), and it would furthermore couple the recruitment of nucleolar factors by NP to the presence of the viral polymerase. In a third scenario, disassembly of nucleoli might represent the coordinated reorganization of the nucleolar architecture to optimize nucleolar processes in favor of viral replication. This could further facilitate interference by viral proteins like NS1 or NP.

Findings from previous studies support the second hypothesis that disassembly of nucleoli during infection could be related to the release of nucleolar components for subsequent recruitment by the viral machinery: Several nucleolar proteins have been shown to be interaction partners of reconstituted vRNPs [103]. Besides PARP1, also nucleolin, nucleophosmin and some ribosomal proteins could be identified. They are apparently recruited to the viral complexes even in the absence of infection. Intriguingly, nucleolin, nucleophosmin and fibrillarin, which is another pre-rRNA processing protein and NS1-binding protein, share the same mechanism for nucleolar targeting [574]. The three proteins could be shown to be targeted to nucleoli by PARP1 enzymatic reaction, apparently through attachment to a PARP1-generated poly(ADP-ribose) matrix. Therefore, PARP1 represents a central factor that allows regulating the localization of these proteins in concert, suggesting that the virus might induce the release of selected proteins by interaction with PARP1 for subsequent recruitment by the viral machinery.

For nucleophosmin, it was moreover confirmed that it relocalizes indeed from nucleoli to the nucleoplasm late in infection, where it partially colocalizes with NP at sites of viral

replication [103]. Nucleophosmin was furthermore shown to increase the viral polymerase activity, supporting the relevance of nucleophosmin relocalization to viral replication sites. Interestingly, also NS1 nucleolar targeting is mediated by two proteins, whose localization was shown to depend on PARP1 enzymatic activity, namely fibrillarin and nucleolin [578]. The effect of NS1 on the morphology of nucleoli upon fragmentation, as described by Terrier *et al.* [132], thus might be related to the here proposed mechanism of nucleolar fragmentation by depletion of PARP1 and concomittant redistribution of the respective NS1-binding proteins.

Finally, another interesting connection between PARP1 and a virus-related cellular factor should be mentioned. High-mobility-group box protein 1 (HMGB1), a chromatin binding protein, was shown to interact directly with NP and to promote viral polymerase activity [351]. It was further shown to be firmly bound to chromatin in apoptotic cells [580] and to be released from chromatin by PARP1 activity in necrotic cells [581]. Since the DNA-binding function of HMGB1 was shown to be required to enhance viral replication, release of HMGB1 from chromatin by PARP1 enzymatic activity in infection might seem unlikely. However, HMGB1 and PARP1 could work as antagonistic pair. HMGB1 could potentially contribute to the targeting of NP and vRNPs to cellular chromatin, as discussed in section 5.3.2.3, and the polymerase-associated PARP1 in turn could provide a mechanism to regulate the release of progeny vRNPs. This model suggests that PARP1 itself has a specific function during infection, but it does not exclude the possibility that recruitment of PARP1 further induces the release of other nucleolar and CB-specific factors during viral replication, enabling their recruitment by the viral machinery. Lack of PARP1 leading to a considerable decrease of the virus titer underlines the general importance and critical role of PARP1 for viral replication [103].

Even though more data is available (and thus presented here) on nucleolar-related processes and components than on CBs, the close functional and compositional relation between the two subnuclear compartments [571] implies that viral interference with nucleolar functions might also affect or possibly even functionally involve CBs. Specific attention should thus be given also to CBs when studying nucleolar components in the context of virus infection.
In support of the tight connection between nucleoli and CBs, previous work shows that the protein PARP1 is involved in trafficking between the two compartments. It is required for protein delivery into CBs and for interactions between key components of CBs [565]. It has therefore been suggested that the PARP1 machinery plays a role in the biogenesis of CBs by

shuttling proteins from nucleoli to CBs and by regulating protein-protein interactions. Hence, by recruitment of PARP1, the Influenza virus polymerase might not only affect nucleoli, as it was hypothesized above, but it might also affect the size and the number of CBs [164].
For Influenza virus NP, on the other hand, it could be shown in this work that it targets nucleoli with high affinity, but apparently does not accumulate within CBs by intrinsic affinity. It is tempting to speculate though that the targeting of NP to subnuclear domains which partially overlap with CBs might be related to the targeting of NP to nucleoli. Since both NP-binding structures display similar and remarkably high affinities for NP, they might share the same interaction partner for NP (Fig. 47). Interference with the previously identified nucleolar targeting signal of NP (aa 213–216) [123] might help to address this aspect. The nucleolar targeting signal was shown to be essential for viral transcription, even though the precise function of nucleolar targeting is not known.

Apart from recruitment of nucleolar factors to the viral machinery, the reasons for a viral interplay with the nucleolar compartment can be diverse. Nucleoli are multifunctional compartments [582]. They play a significant role not only in ribosome biogenesis, but also in cell cycle control [583], stress response and apoptosis regulation [584,585,586], genome organization [587], RNA processing and RNA trafficking [588,589,590,591]. Due to these central cellular functions, nucleoli apparently represent an attractive target for many different viruses [592].
The nucleolar localization of different viral proteins like HIV-1 Tat [593], HIV-1 Rev [594], herpesvirus ORF56 [595] and Influenza virus NP [123] was shown to be essential for the replication of these viruses. In case of HIV-1 and herpesvirus, nucleoli were further demonstrated to be critically involved in trafficking of viral mRNA [595,596,597]. Since sequestration of cell cycle-related proteins in nucleoli is a common mechanism for cell cycle regulation, also cell cycle control mechanisms have been suggested to be targeted by viruses through interference with the nucleolar compartment [598]. It was shown that various viruses induce changes of the nucleolar proteome during infection [577,599,600]. Each of the studied viruses apparently affects a different subset of nucleolar proteins though. It has been suggested that by regulating the nucleolar composition, viral proteins can adapt nucleolar activities to support virus production. For HIV-1, it was reported that expression of the regulatory nucleolar protein Tat induces significant changes in the composition of the nucleolar proteome even in the absence of virus infection [601]. Affecting particularly biosynthetic activities and metabolic pathways, it was suggested that Tat modulates the

metabolic profile of the host cell to meet the energetic and biosynthetic needs for efficient virus production.

Compositional changes of the nucleolar proteome were found also during Influenza virus infection [577]. However, only a relatively small number of nucleolar proteins showed significant changes in abundance, in particular subunits of the histone H3 methyltransferase complex MLL1, which is a regulator of chromatin structure and transcription, and proteins involved in RNA processing like components of the RNAse P complex and components of paraspeckles. How far nucleolar NP, other viral proteins or virus-induced processes like nucleolar fragmentation are involved in these changes has not been addressed so far. The complex interplay of Influenza viruses with the nucleolar compartment remains elusive.

Besides NP and NS1, also M1, HA, PB2 and NEP were previously reported to associate with nucleolar fractions of infected cells [577]. Nevertheless, an intrinsic nucleolar localization signal has been identified so far only for NP and NS1. While nucleolar targeting of NS1 as well as association of NEP and PB2 with nucleolar fractions was shown to be strain-specific [577,602,603], the nucleolar targeting signal of NP on the other hand is highly conserved among Influenza A strains (residues 213 to 216) [120,328].

NP alone or in concert with other viral proteins or virus-induced processes might be able to interfere with one of the central nucleolar functions like stress response, cell cycle regulation, ribosome biogenesis or RNA trafficking. High affinity-binding of NP to nucleoli (as it was demonstrated in this work) seems to suggest that NP might inhibit dynamic nucleolar processes or cause sequestration of nucleolar proteins (e.g. interfering with the cell cycle). Intriguingly, however, the NP nucleolar targeting signal was previously shown to be critically required for efficient protein expression from vRNPs even in the absence of virus infection, which was demonstrated by functional reconstitution of vRNPs in a mini-replicon assay [123]. Thus, it appears that nucleolar targeting of NP is essential for the transcriptional activity of vRNP complexes. It is difficult to imagine though that NP might be able to promote viral protein expression by interference with nucleolar processes. Instead, it might be assumed that the association of NP with nucleoli becomes more dynamic in the presence of functional vRNPs to allow the recruitment of nucleolar components to the viral machinery. In future experiments, analysis of the nucleolar dynamics of NP in the context of a minireplicon assay might help to understand the role of NP nucleolar targeting for viral transcription in more detail, while NP bodies might be included in these analyses.

5.3.3.2 PML bodies

PML bodies are the second structure apart from CBs that was identified to localize frequently adjacent to or partly overlapping with NP bodies (4.3.2.3). Interestingly, PML bodies are targeted by many viruses [604]. The functions of PML bodies seem rather diverse and less specific than those of other NBs, presumably because they represent a structurally and functionally heterogeneous class of NBs. PML bodies have been reported to be involved in tumor suppression, control of apoptosis, response to DNA damage, antiviral activity, IFN response, proteasomal degradation, maintenance of genome stability, transcription regulation, eIF4E-dependent mRNA export and posttranslational protein modifications [506,553].
Accordingly, the reports on the subnuclear environment of PML bodies are similarly diverse: A subset of PML bodies was found to associate tightly with CBs due to the physical interaction [504,505], and a close correlation was also described with cleavage bodies, splicing speckles and active sites of transcription [504,605,606]. Furthermore, PML bodies were found adjacent to the MHC class I gene cluster, regulating chromatin architecture and transcription [607,608]. The interplay between the PML protein and nucleoli and the formation of a nucleolus-associated PML compartment was moreover suggested to play an important role in tumor suppression and cell cycle regulation [609,610]. PML bodies can be further sites of proteasomal degradation [611,612] and accumulate ubiquitinated proteins and proteasome components [611,613,614]. Also extensive contacts between PML bodies and chromatin were previously described. It could be shown that the stability of PML bodies is affected by changes in chromatin structure due to stress, DNA damage or transcription inhibition, leading to fission of PML bodies and formation of microbodies [491,615,616].

The multiple roles of PML NBs are enabled by the dynamic recruitment of proteins in response to various stimuli like stress or cell cycle progression. Some proteins e.g. PML or SP100 are permanently associated with PML NBs, while other proteins like the tumor suppressor p53 transiently associate with PML NBs under certain conditions [617,618,619]. The PML NB interactome could be described by a network of 166 known PML NB components [620]. Many of these proteins are known to be posttranslationally modified by a small ubiquitin-like modifier (SUMO), or contain SUMO-interaction motifs (SIMs). Assembly of PML bodies has been suggested to be coordinated by SUMOylated PML protein [554,620,621,622]. SUMOylation and SIM of the PML protein were shown to be necessary for PML NB formation and for the recruitment of other proteins to PML NBs. The death

domain-associated protein 6 (DAXX), a major PML NB component, was shown to be targeted to PML NBs through its SIM domain [623].

Most notably, PML NBs are considered to be also hot spots of cellular SUMOylation since they were shown to be one of two main sites of active SUMOylation within cells [624] and since they harbor all components of the SUMOylation machinery which are necessary for a complete SUMOylation cycle. They contain the three SUMO isoforms SUMO1, SUMO2, SUMO3, a SUMO-activating enzyme, a SUMO-conjugating enzyme, several SUMO ligases and SUMO-specific proteases [620]. SUMOylation can alter the activity, the stability, the intracellular localization or the intermolecular interactions of the target proteins, acting as a regulatory factor of many cellular pathways [625]. This might explain the involvement of PML NBs in very different cellular functions. PML NBs harbor also numerous other protein-modifying enzymes, catalyzing e.g. phosphorylation, dephosphorylation, acetylation, deacetylation, ubiquitination and deubiquitination, why it was suggested that PML NBs might provide a general platform for posttranslational protein modifications, leading to activation, sequestration or degradation of proteins [626]. As a consequence, the reasons for viruses to target PML bodies can be diverse.

PML bodies have been extensively studied in the context of virus infections [604,617]. The interplay between PML NBs and viruses is complex. Numerous studies have reported that the PML protein and PML NBs are implicated in antiviral defense and apoptosis regulation. There is accumulating evidence that they help to mediate the cellular IFN response and to establish the cellular antiviral state. It could be shown that IFN upregulates expression of several PML NB-associated proteins including the major PML NB constituents PML and SP100, leading to higher numbers and increased size of these structures [627,628,629]. The genes encoding PML and SP100 were shown to be directly regulated through IFN-stimulated response elements and IFN-gamma activated sequences in their promoter regions [630,631]. Also during Influenza virus infection, expression of SP100 was found to be upregulated, and the number of PML NBs increases [277,628]. Notably, the knockout of PML in mice and in cell culture renders mice and cells more susceptible to viral infections, while overexpression of PML could be shown to restrict replication of human cytomegalovirus (HCMV), adenovirus 5 and several RNA viruses [604,617,632]. The capacity of IFN to protect cells against viral infection was furthermore found to be reduced in PML-knockout cells, consistent with the hypothesis that PML and its partner proteins represent an IFN-induced pathway. Also in case of Influenza viruses, overexpression of different PML isoforms led to inhibition viral replication, while silencing of PML isoforms resulted in enhanced Influenza virus replication

[633,634,635]. The antiviral effect of PML was found to depend on the Influenza virus strain though [635].

The specific function of PML in antiviral defense remains largely unclear. PML was shown to interfere with the replication of viruses through different mechanisms (reviewed in [604,617]). In poliovirus infection, PML recruits p53 to PML NBs, leading to its activation and induction of apoptosis. In case of HCMV and rabies virus, PML inhibits viral mRNA synthesis, while during herpes simplex virus type 1 (HSV-1) infection, the splicing of PML pre-mRNA is altered, leading to inhibition of viral replication. In case of Influenza viruses, the mechanism of PML-mediated antiviral defense is still unknown. Two PML NB-associated proteins, DAXX and SP100, have futher been shown to display antiviral activity. DAXX was shown to suppress replication of adenovirus and HCMV, while SP100 could be shown to be involved in repression of HSV-1.

Viruses have evolved different strategies to counteract the antiviral activity that is mediated by PML and PML NB-associated proteins. Numerous viruses target regulatory proteins to PML NBs and cause the disruption of the NB structure. This is assumed to be part of the viral strategy to antagonize the cellular immune response (reviewed in [604,617]). The best studied example is HSV-1, but also other viruses like HCMV, adenovirus, Epstein Barr virus, human papilloma virus, rabies virus, encephalomyocarditis virus, lymphocytic choriomeningitis virus, hepatitis delta virus and hepatitis C virus adopt this strategy. Regulatory proteins of these viruses were shown to target PML NBs via different mechanisms and components. Some of the proteins cause delocalization of PML or SP100, others induce degradation of PML or DAXX, and still others induce loss of PML SUMOylation. Each of these mechanisms leads to the disorganization of PML NBs.

Influenza viruses encode three proteins that have been shown to localize to PML NBs during infection, namely M1, NS1 and NEP [277]. Major disruption of PML NBs has however not been reported for Influenza viruses, and the role for the targeting of NS1 and NEP to PML NBs is still unknown. For M1, though, an anti-apoptotic function was only recently reported which depends on the interaction of M1 with DAXX [636]. DAXX is one of the major PML NB components and a transcriptional repressor. DAXX together with the NF-κb family member RelB controls epigenetic silencing of RelB-responsive anti-apoptotic genes [637,638]. By binding to DAXX, M1 prevents the repressional function of DAXX. It prevents complex formation between DAXX and RelB, thus impairing promoter binding of DAXX and the recruitment of DNA methyltransferases to RelB-regulated genes. This leads to

activation of anti-apoptotic genes early during Influenza virus infection as demonstrated by Halder *et al.* [636]. Whether targeting of M1 to PML NBs is required for this regulatory transcriptional function of M1 during infection is not known though since DAXX can be found also diffusely in the nucleoplasm. While the association of M1 with PML NBs was shown to depend on infection [277], the binding of M1 to DAXX and efficient inhibition of DAXX-mediated gene repression can be detected also in the absence of virus infection [636]. It thus remains to be clarified if infection-dependent localization of M1 in PML NBs is a side-effect of its ability to interact with DAXX, or if M1 association with PML NBs during infection has an additional functional significance.

Considering the central role of PML NBs in SUMOylation, it is possible that targeting of the various Influenza virus proteins to PML bodies might be related to the targeting of the host cell SUMOylation machinery. Indeed, there is accumulating evidence for an extensive interplay of Influenza viruses with the host cell SUMOylation system [548]. The three viral proteins being targeted to PML NBs (M1, NS1, NEP) and further NP and PB1 have been shown to be authentic SUMOylation targets [548]. Previous reports indicate that SUMOylation motifs found in avian and human strains are evolutionary relatively well conserved [639]. For M1 and NS1, it was confirmed that they become SUMOylated during virus infection, and also for NP and PB1 evidence suggests that they are SUMOylated in infected cells [548,640]. The detection of protein SUMOylation can be difficult (as in case of NP and PB1) due to the rapid turnover of SUMO-conjugation and due to low endogeneous levels of SUMOylated protein fractions.

For NS1, it was first reported that SUMOylation contributes to the stability of NS1 in cells [641], while a more recent study suggests that SUMOylation regulates the abundance of NS1 dimers and trimers in infected cells, thereby affecting the function of NS1 as IFN antagonist [642]. In case of M1, SUMOylation was shown to be required for the interaction between M1 and vRNPs and for vRNP nuclear export during infection, indicating a role of SUMOylation for the formation of M1-vRNP nuclear export complexes [276]. Virus mutants deficient in M1 or NS1 SUMOylation display reduced virus titers, accordingly.

For NP, NEP and PB1, a potential role for SUMOylation has not been addressed so far. Analysis of the NP primary sequence by SUMOplot (http://www.abgent.com/sumoplot) predicts a SUMOylation site at position K198 which appears to be well accessible at the surface of the highly conserved NP head domain (refer to NP crystal structure PDB: 2IQH). The SUMOylation consensus motif ψKXE/G/D [643], where ψ stands for a hydrophobic residue and X for any amino acid, spans amino acids 197 to 200 of NP (IKRG). This is an

interesting site for regulatory posttranslational protein modifications since it is located in close proximity to two important functional sites of NP. NP residues R204, W207, R208 within a neighbouring loop were shown to be involved in the interaction between NP and the viral polymerase and to be essential for viral polymerase activity [188]. The second functional site close to K198 is a nucleolar localization signal that was further shown to be essential for the transcriptional activity of vRNPs (residues 213–216) [123]. Accordingly, the accumulation of NP in NP bodies adjacent to PML NBs might be related to the acquisition of SUMOylation by a small fraction of NP molecules for a regulatory purpose.

Considering further the role of M1 SUMOylation during infection, it is also possible that by targeting to the vicinity of PML NBs, NP might be able to target vRNPs close to sites of M1 SUMOylation for the efficient formation of nuclear export complexes. In this context, it is interesting to note that also NEP as an important component of the nuclear export complex locates to PML NBs and is – just like PB1 – another component that is SUMOylated *in vivo*, supporting the here suggested involvement of these sites in both viral protein SUMOylation and vRNP nuclear export complex formation. Considerable support for a model of vRNP nuclear export complex formation at PML NBs was also provided by the work of Kawaguchi *et al.* [295], showing that vRNA accumulates in PML NBs during infection when the CRM1-dependent nuclear export of vRNPs is inhibited by leptomycin B. Also cellular vRNP-interacting protein YB-1 was shown to be recruited to PML NBs prior to nuclear export together with vRNPs and to be required for subsequent cytoplasmic vRNP transport.

Consistent with the requirement for SUMOylation during Influenza virus infection, PML NBs do not become disrupted in infected cells, but become more numerous instead [277,628]. Remarkably, even a global increase of cellular SUMOylation is observed during Influenza virus infection, while overall cellular protein syntheses are downregulated [548]. In comparison, in HSV-1 infection, disruption of PML NBs is accompanied by a decrease of cellular SUMOylation [625]. And while downregulation of SUMOylation was reported to be a common feature of most studied pathogens [644], an intact SUMOylation system could be shown to be essential for efficient Influenza virus replication: the knockdown of the SUMO-conjugating enzyme Ubc9 dramatically reduces Influenza virus production [276], and large-scale siRNA screenings identified components of the cellular SUMOylation machinery as critical factors for viral replication [645].

In summary, the data suggest that by targeting to sites in the vicinity of PML NBs, NP targets a subnuclear region of general importance during Influenza virus infection. A functional connection between NP bodies and PML NBs remains to be demonstrated though.

How the antiviral effect of PML protein expression can be reconciled with the increasing number of PML NBs during infection and with the requirement for a functional cellular SUMOylation system remains to be further clarified.

Finally, it should be taken into consideration that other data on PML NB-related domains are available which suggest a different view on NP bodies. These data indicate the possibility that the formation of NP bodies adjacent to PML NBs might be induced by cellular antiviral activity. The implied underlying mechanims are discussed in the following:

First, the tripartite motif-containing protein 22 (TRIM22) is an antiviral protein with E3 ubiquitin ligase activity that localizes partially within NBs [646]. TRIM22 was very recently shown to interact directly with Influenza virus NP, causing NP polyubiquitination and proteasomal degradation [647]. It is induced by IFN and p53. The subcellular distribution of TRIM22 seems to vary, depending on the conditions of expression. Very similar to NP bodies, endogenous TRIM22 in HeLa cells was shown to localize in subnuclear domains adjacent to CBs. It interacts with coilin. Its distribution however is cell cycle-dependent and, particularly in G0/G1 phase when exogenously expressed, TRIM22 bodies seem to be more numerous and rather different from the appearance of NP bodies [646] (Fig. 48). In MDCK and A549 cells, which are both permissive for Influenza virus infections, TRIM22 was reported to be barely detectable. It appears to be rather cytoplasmic in MDCK cells when overexpressed [647], while NP bodies, on the other hand, can be clearly observed in the nuclei of MDCK II cells (Fig. 45). A potential connection between NP bodies and TRIM22 NBs therefore will have to be further investigated by direct colocalization analysis.

The second observation, which might help to explain the formation of NP bodies in proximity to PML NBs, is the reported association of PML NBs with the genomes of several DNA viruses, including HSV-1, HCMV and adenovirus 5. While early studies suggested that PML NBs might provide a favorable environment to promote viral transcription and replication and help to establish a viral replication compartment [605] (reviewed in [491,492]), it was demonstrated later on that PML NB-like structures rapidly form *de novo* in association with incoming viral genomes by deposition of PML NB components [648]. According to the current view, this is part of a cellular response leading to repression of viral transcription and replication [604,649]. Hence, in analogy to DNA viruses, NP as a major component of the genomic complexes of Influenza viruses might stimulate the recruitment of PML NB components by an evolutionary conserved mechanism. Yet, the origin of replication of viral DNA was reported to be a requirement (aside from viral proteins) for the association of PML NBs with various viral DNA genomes [491,492], indicating an antiviral mechanism that

might be restricted to DNA viruses. Moreover, recognition of viral DNA as “foreign” DNA, which differs from cellular chromatin, and the involvement of the cellular DNA damage response machinery were suggested to be implicated in the recruitment of PML NB components to viral genomes [649,650]. According to these considerations, the RNA genome from Influenza virus does not match the pattern that seems to be recognized by this type of nuclear antiviral defense. Considering that DNA viruses, but not RNA viruses, typically replicate in the nucleus of infected cells, recruitment of PML NBs might have evolved as an evolutionary conserved mechanism of nuclear antiviral activity that is directed against common characteristic features of DNA viruses. Following this line of argument, it is unlikely that NP bodies are targeted by PML NB components through the same mechanism as the replication compartments of DNA viruses. Furthermore, targeting of PML NB components to NP bodies would not be able to explain the intrinsic affinity of NP for NP bodies, the additional proximity of NP bodies to CBs or the neglectable role of the more abundant nucleoplasmic NP for PML NB recruitment. Unlike the replication compartments of DNA viruses, Influenza virus NP and vRNPs are spread throughout the nucleus during infection [134,280] and thus do not represent a distinct target structure for PML NBs. A small subpopulation of NP might therefore rather be directed to sites in proximity to PML NBs by intrinsic affinity than PML NBs being targeted to NP, which is in accordance with the results of the present study. In conclusion, a relation between NP bodies and PML NBs in analogy to replication compartments of DNA viruses is considered most unlikely.

To summarize this part of the discussion, there are a number of possible implications for NP bodies and how they might be engaged in an interplay with the here identified neighbouring domains during infection. Three major hypotheses could be derived by analysis of the subnuclear context based on data from previous publications:

In case of CBs, there is so far hardly any data supporting a direct involvement of CBs in virus replication. However, considering the functions of CBs, it is speculated here that NP might target vRNPs to NP bodies close-by CBs to connect viral processes like transcription or replication to cellular processes like RNA modification, RNP assembly or nuclear-cytoplasmic transport pathways, which are located in CBs. Yet, there is no evidence to substantiate this hypothesis so far. A second hypothesis suggests that NP body formation could be the result of cellular antiviral activity of TRIM22, which is based on evidence for a direct physical interaction. The most interesting and favored hypothesis, though, evolved from the combination of variety of data, leading to the most complex picture on the potential role of NP bodies. It suggests that PML NBs might be sites of viral protein SUMOylation, which

subsequently enables vRNP nuclear export complex formation depending on SUMOylation of one or more of its components. This hypothesis further includes the assumption that (by targeting to NP bodies) NP might be able to target vRNPs into the vicinity of PML NBs for efficient formation of vRNP export complexes. It suggests moreover that NP undergoes SUMOylation itself to regulate the transcription and replication activity of vRNPs which are destined for nuclear export. It is thus assumed here that NP bodies might be part of a relatively complex infection-induced process, in which adjacent nuclear domains might be jointly involved.
The main focus of the current paragraph was accordingly to figure out connecting factors between NP, CBs, PML NBs and infection-relevant processes. However, the possibility has to be considered that – even though the cellular compartment underlying NP bodies has not been identified yet – NP might interfere with or hijack processes of the subnuclear domain itself independently from the subnuclear context. The identification of this domain is required for further assumptions.

Concerning the nucleolar compartment, it is one important finding of this study that NP displays a remarkably high affinity for nucleoli. This might be crucial information when trying to understand the processes connecting NP nucleolar targeting, the relocalization of nucleolar NP to the nucleoplasm, nucleolar fragmentation and the requirement of NP nucleolar targeting for vRNP transcription. It further underlines the importance to understand the varying dynamics of NP and their regulation within the nucleus for coordinated function. Based on previous studies, coincidences between vRNP interaction partners and nucleolar components, in particular PARP1, seem to indicate a complex interplay between the presence of vRNPs, the recruitment of nucleolar factors, nucleolar fragmentation and the localization of NP. Intriguingly, these data support speculations that recruitment of nucleolar components by NP might be coupled to the presence of the viral polymerase and transcription-competent vRNP complexes.

5.3.4 Summarizing remarks

In this study, analysis of NP subcellular targeting was performed using photoactivation measurements and colocalization analysis. It was demonstrated that NP extensively interacts with cellular structures, in particular with the nuclear compartment. The work focused on the topology of NP interactions taking into account the spatial and functional organization of the nucleus. Distinct populations of NP could be identified differing by subcellular localization

and distinct site-specific affinities. Highest affinities of NP were found within the nucleolus and within small interchromatin domains that were frequently detected in the context of CBs and PML NBs, but which could not be identified. These three subnuclear compartments are known to be affected during Influenza virus infections, suggesting NP targeting to be part of more complex infection-relevant processes. Recruitment of nucleolar proteins upon nucleolar fragmentation or acquisition of posttranslational protein modifications are two of the potential functions of site-specific NP targeting which are proposed here. Based on the small (catalytic) amount of NP which is recruited to these domains, a primarily regulatory function of NP high-affinity targeting to nucleoli and NP bodies is assumed.

The majority of NP was found to be involved in comparably low, but still considerable interactions with the nucleoplasm. It is heterogeneously distributed throughout the nucleoplasm and has a speckled appearance. It is suggested that this fraction of NP might represent the pool of NP that is available for vRNP and cRNP formation during infection. It is further assumed – based on biochemical and microscopy data from literature – that interaction with the splicing factor and NP chaperone UAP56 might be responsible for association of major parts of NP with the nuclear matrix and for the characteristic nuclear distribution of NP in the absence of infection. Further experiments are required for validation.

This study was conducted on NP in the absence of virus infection providing insight into the potential role of NP apart from its function as part of viral RNP complexes. The overall extensive interactions of NP with the nuclear compartment and site-specific affinities strongly imply yet unrecognized functions of NP in the virus-host-interplay. The results further indicate an NP interaction network that might require temporal and spatial regulation during infection, but which might also help to coordinate the replication cycle of vRNPs.

Various models for the potential role of intrinsic site-specific NP subnuclear targeting which were proposed in this work might indicate directions for future investigations.

5.4 Single particle tracking of fluorescent NP constructs in Influenza virus infection

5.4.1 Fluorescent NP constructs can be successfully introduced into virus infection and be traced during Rab11-dependent vesicular transport to the plasma membrane

In this work, an experimental approach was established which allows coexpressing fluorescent NP fusion proteins in Influenza virus infection (4.4.1). Since infection and transfection were found to have a mutually inhibitory effect on each other, the experimental conditions had to be carefully optimized (Fig. 53 & Fig. 54). It was suspected that both the virus-induced host cell shut-off and the premature presence of NP in infection were responsible for these effects. It was further assumed that infection and exogenous NP expression had to be initiated in very close succession so that the infection state of the cell and exogenous NP expression levels could evolve in parallel.
Experimental conditions were accordingly optimized by modulating the delay between infection and transfection. It was found that transfection could be efficiently established in infected cells, but only if not performed later than 3 h p.i., and infection became more robustly established the more time it was allowed to proceed before transfection was performed. The critical time to establish exogenous NP expression in infected cells thus could be localized between 1 h p.i and 3 h p.i. Best results for coexpression of fluorescent NP constructs in the context of virus infection were obtained when transfection was performed at 2 h p.i. (Fig. 55).

According to expectations, successful infection of mEYFP-NP coexpressing cells induced relocalization of the NP construct to the cytoplasm (Fig. 55). The relocalization was specific for infected cells. mEYFP-NP then displayed a characteristic punctate cytoplasmic pattern comparable to the one of vRNPs in infection [280,297], and just like native vRNPs, mEYFP-NP became associated with Rab11-positive recycling endosomes (Fig. 58). Targeting to the asymmetrically organized recycling endosomal compartment apparently determines the characteristic speckled and laterally polarized distribution of both mEYFP-NP and native vRNPs in the cytoplasm of infected cells, reaching from the MTOC in the perinuclear region to the plasma membrane. While association of mEYFP-NP with recycling endosomes was shown to be infection-dependent (Fig. 57 & Fig. 58), it was previously shown that vRNPs colocalize with Rab11 even when reconstituted in the absence of infection, potentially through PB2 [280].

Being aware that no direct evidence is provided for incorporation of mEYFP-NP into vRNPs in infected cells, a variety of findings and reports support though that mEYFP-NP becomes indeed functionally incorporated into newly forming vRNPs during infection and undergoes cytoplasmic transport: (i) N-terminally GFP-tagged NP is reportedly able to form transcription-competent vRNP complexes in cells and in the presence of wt NP [280,507]. (ii) Reconstituted GFP-tagged vRNPs are exported to the cytoplasm upon coexpression of the viral nuclear export factors M1 and NEP, and they associate with Rab11-positive recycling endosomes just like vRNPs in virus infection [280]. (iii) The association of vRNPs with Rab11 is mediated by the viral polymerase, not by NP [280,296,298]. (iv) mEYFP-NP colocalizes with Rab11 only in the context of virus infection, (Fig. 57 & Fig. 58).
Based on these findings, it is postulated that mEYFP-NP and analogous fluorescent NP constructs like mCherry-NP are incorporated into newly forming vRNPs during infection and that the fluorescent protein tag does not critically interfere with processes of viral replication like transcription or nuclear-cytoplasmic transport. It is further postulated that the so formed mEYFP-tagged vRNPs are exported from the nucleus, which leads to their detection as distinct punctate signals in the cytoplasm with a characteristic distribution, as described in section 4.4.2. In analogy to native vRNPs, it is assumed that the viral polymerase is responsible for targeting the fluorescently labeled vRNPs to recycling endosomes (Fig. 58) and that the genomic segments then undergo Rab11-dependent cytoplasmic trafficking to the viral budding site at the plasma membrane, which is in agreement with the monitored cotrafficking of mEYFP-NP and Rab11-RFP (Fig. 59).
It is accordingly claimed that the here established experimental system provides a tool to study the dynamics of vRNP transport in infection and to characterize the different steps of the transport pathway in living cells.

Long-range movements of cytoplasmic mEYFP-NP particles (covering distances between 2 and 20 µm in length) could be described as fast saltatory movements with average velocities between 0.3 and 1.2 µm/s and peaks up to 1.7 µm/s. This is in accordance with values that were determined in other studies using different experimental approaches. Amorim *et al.* [280] reported an overall average velocity of 0.81 µm/s for fast saltatory movements of GFP-tagged Influenza vRNPs in the absence of infection. They further showed that instant velocities ranged between 0.2 and 1.4 µm/s, with single data points reaching up to nearly 3 µm/s. Momose *et al.* [298] on the other hand measured velocities of vRNPs in the context of virus infection. Yet, they applied a different labeling strategy, using transfection to introduce vRNP-specific antibodies into living infected cells, and they determined a mean velocity of

1.45 µm/s. The most recent study addressing the dynamics of vRNPs (conducted by Avilov *et al.* [296]) was based on a recombinant virus strain encoding split-GFP tagged PB2 to label and track vRNPs. The authors reported rapid velocities around 1 µm/s, pointing out though that the motion of the vast majority of vRNP particles was slow (<0.25 µm/s).

The best agreement was obtained with the data from Amorim *et al.* who adopted the same labeling strategy as in the present work, labeling vRNPs by incorporation of a fluorescent NP fusion protein. As a major difference, though, the measurements by Amorim *et al.* were performed in the absence of infection using a plasmid-based minireplicon assay, while measurements in the current work were conducted in infected cells. Apparently, it did not make a difference for the observed velocities of rapid saltatory movements whether they occurred in the presence or absence of virus infection.

The slightly higher velocities reported by Momose *et al.* might be due to differences between the experimental conditions. It is possible that incoporation of unknown numbers of GFP/mEYFP-tags (27 kDa) and binding of fluorescently labeled antibodies (150 kDa) affect the dynamics of vRNPs differently. Alternatively, also transfection of plasmid DNA, as performed in the present study and in the work of Amorim *et al.*, and transfection of antibodies, as performed by Momose *et al.*, might have affected the cells or the vesicular transport differently. In all three cases, lipid-based transfection reagents were used, which are thought to be internalized by endocytosis [651]. In case of vRNP reconstitution experiments, 24 h had elapsed between transfection and measurements, while the transfection of antibodies in infected cells was peformed only 3.5 h prior to measurements. Here in this work, SPT was performed with a time lag of 4–6 h to transfection.

In the study by Avilov *et al.*, the use of a genetically encoded split-GFP-tagged PB2 is likely to overcome artifacts that can be potentially introduced by transfection or by high numbers of large fluorescent labels like the fluorescent NP antibodies or the fluorescent NP protein tags. Yet, the results are basically in agreement with the velocities obtained by other approaches, in particular with the data of Momose *et al.*, tending to velocities higher than 1 µm/s and reaching up to more than 5 µm/s. The authors stress though that fast intermittent movements in comparison to slow movements (<0.25 µm/s) were only rarely observed and that the effect of microtubule depolymerizing drugs on rapid motions was limited, while a more dramatic effect was detected in the work of Amorim *et al.* Since the split-GFP tag of recombinant viruses was attached to the PB2 subunit of the viral polymerase, which also links vRNPs to Rab11 and the transport vesicles, it cannot be entirely excluded that the vesicular transport of vRNPs might be affected and slightly biased towards more actin-dependent movements. Since

only a single fluorophore was further attached to each vRNP complex, it might not always be possible to distinguish a free PB2 molecule from an RNP-bound form. The selection of objects to be traced might further be biased towards a selection of several colocalizing vRNPs.

The bottom line is that all four approaches to study progeny vRNPs in living cells might have potential limitations, but their results are in satisfying agreement supporting each others findings, and they might well serve as complementary approaches to address certain issues of Influenza virus infection.

Using the here established experimental approach, it was not only possible to determine kinetic parameters of vRNP transport, which could be verified with previous studies, but it was also possible to describe site-specific processes like vRNP nuclear-cytoplasmic transport and the targeting to the plasma membrane, two processes which are still very incompletely understood.

Considerable mobility of mEYFP-NP complexes was detected underneath the plasma membrane (Fig. 63A), which indicates that vRNPs might be first transported to the cell periphery and then continue to move along the membrane in search for the viral budding site. Yet, also relatively immobile vRNPs were detected at the plasma membrane, lingering for a while, followed by sudden and fast retrograde transport back into the cytoplasm (Fig. 63B). This could represent a trial and error mechanism. If the transported cargo does not meet the requirements for attachment to the plasma membrane or for further progression to an appropriate target site, it might be recaptured to the microtubular transportation network, move back to the cell center and be again targeted to a different site of the cell periphery. In order to be actually able to trace the trajectories of individual vRNPs or vRNP assemblies during the entire process of targeting to the viral budding site, fast three-dimensional time-lapse imaging would be required. This might further help to investigate the question how far recycling endosomes are involved in delivering vRNPs to the budding site and whether this requires fusion with the plasma membrane or the viral budding site.

The second type of site-specific movements which could be characterized by time-lapse imaging are the nuclear-cytoplasmic transport events and the subsequent movements of vRNPs in the perinuclear space (Fig. 60 & Fig. 61). mEYFP-NP particles were found to undergo unexpectedly fast movements across the nuclear boundaries, immediately followed by relatively rapid long-range directional movements into the cytoplasm with velocities around 0.3–0.4 μm/s. These velocities are not clearly characteristic for one specific mode of transportation. They could represent rapid actin-mediated transport or relatively slow

microtubule-based transport [110,509,510,512,652,653]. Yet, the curvilinear appearance of these movements and the considerable lengths, covering distances of several micrometers, suggest a microtubule-dependent transport.

It is well established that progeny vRNPs are exported through nuclear pore complexes (NPCs) using the CRM1-dependent nuclear export machinery [264,266,267], but aside from extensive biochemical analyses not much is known on the kinetics of vRNP export. Here, the nuclear-cytoplasmic transition was found to be surprisingly rapid, since the observed translocations were not accompanied by an obvious interruption of the movement when images were acquired at intervals as fast as 0.5 s. Yet, this observation is in line with a previously reported average translocation velocity of 0.65 µm/s, measured for model mRNPs of comparable size, and with a NPC translocation time of 0.5 s [654]. Assuming an export rate of one event per 36 s as seen in Fig. 61 and assuming further about 2000 NPCs per nucleus (as reported for CHO cells [655]), one vRNP could theoretically be exported every 18 ms. However, a similarly high frequency of export events of mEYFP-NP complexes was not observed for other nuclear exit sites and it is further not clear if all existent NPCs are functionally equivalent. Considering that not more than five nuclear translocation sites were typically observed per image plane, representing roughly about 1/10 of the nuclear surface, not all potentially available NPCs seem to mediate mEYFP-NP export or to be constantly active. Again, a three-dimensional imaging approach would help to address this issue and give site-specific information on NPCs all over the nucleus.

Similarly unexpected as the fast and apparently uninterrupted movement through NPCs is the directed movement that was observed subsequent to nuclear-cytoplasmic translocations (Fig. 61). It suggests that the translocation through the nuclear pore complexes is directly linked to active cytoskeleton-assisted cytoplasmic transport. For many years, nuclear import and export have been considered to be mediated by soluble import and export receptors through diffusion along molecular concentration gradients [656]. The formation and disintegration of import and export complexes was generally assumed to occur in the vicinity of the nuclear envelope by diffusion limited reactions between freely diffusing substrates and receptors. Also for incoming Influenza vRNPs, it was previously suggested that they are transported to NPCs on the nuclear envelope by diffusion [117]. However, only in 2011, it was shown that nuclear import and microtubule-dependent transport can be closely connected [657]. A microtubule association sequence (MTAS) was identified within proteins, which binds to both microtubules and nuclear import factors so that the protein can be displaced from microtubules by binding to import factors and thus be transferred from the cytoskeleton to the

nuclear import machinery. Even though this was reported specifically for the nuclear import process, an analogous mechanism is conceivable for nuclear export. In the present study, the nuclear-cytoplasmic transport of mEYFP-NP complexes in combination with long-range cytoplasmic movements could be observed in both directions (Fig. 63A). Accordingly, nuclear import and export events seem to be directly linked to cytoskeleton- and motor protein-dependent transport processes, which is an interesting observation also in the light of a recent description that vRNPs themselves can associate with microtubules through interaction with the cellular protein YB-1 [295]. YB-1 was shown to be recruited to vRNPs in the nucleus, most likely involved in nuclear export complex formation, and even though it is not crucial for vRNP export, it was shown to be required to target vRNPs to the perinuclear region around the MTOC.

Very little is so far known on the step of vRNP transport from the nucleus to recycling endosomes. Together though, the observations from SPT in the present study, suggesting cytoskeleton-assisted transport to be directly coupled to vRNP nuclear export, the previously suggested association of a microtubule-binding factor with vRNP nuclear export complexes [295] and further localization of individual vRNPs in close proximity to microtubules after nuclear export [134], indicate two stages of microtubule-based transport. First, the exported progeny vRNPs might be targeted to microtubules independent from vesicular transport and travel towards the MTOC where they then become associated with Rab11-dependent recycling endosomes, which mediate the second stage of transport to the apical plasma membrane [280,297,298]. Recycling endosomes, which procure the information for apical targeting of viral genomes, further mediate transport of the viral protein M2, which was shown to be essential for membrane scission and virus release [30], so that recycling endosomal transport of viral components might be an important determinant of apical virus budding [252]. It remains to be investigated how important the here postulated first stage of microtubule-based transport and initial targeting of vRNPs to recycling endosomes is for efficient apical transport.

It is further poorly understood how and at which stage of the viral replication cycle vRNPs assemble into multisegmental complexes, which finally become packaged into progeny virions. It has been suggested that recycling endosomes might provide a platform for vRNPs to preassemble prior to association with the viral budding site [134,297,298]. Due to the size of multisegmental complexes consisting of eight different segments [306], it seems obvious to assume that assembly takes place only after transport through the NPC. Individual vRNP segments might be targeted to recycling endosomes where they accumulate in close proximity

to each other and become oriented relative to the membrane surface, facilitating coordinated interaction. Dynamics measurements as through the current approach will provide the opportunity to verify this hypothesis and follow individual particles from nuclei to recycling endosomes. Further refinement of the approach, including three-dimensional image information and selective labeling of a subset of particles using photoactivatable fluorophores instead of mEYFP, might enable a coherent picture of vRNP transport from the nucleus to the site of virus assembly and budding.

5.4.2 Summarizing remarks and perspectives

In order to study newly formed vRNPs in Influenza virus infection by fluorescence microscopy, a method was established for fluorescence labeling of vRNPs in living cells. Therefore, an experimental approach was developed which allows coexpression of fluorescent NP fusion proteins in infected cells. Exogeneously expressed NP could be shown to behave similar to native viral NP in infection. It undergoes cytoplasmic transport and targets to the plasma membrane, indicating incorporation of fluorescent NP constructs into vRNP complexes. The experimental system was validated by demonstrating infection-induced cotransport of NP with recycling endosomes, which is specific for vRNP complexes, and by showing that the kinetics of cytoplasmic transport were consistent with previously published data on vRNP transport.

Using SPT, not only transport velocities could be determined, but it was also possible to address site-specific aspects and different stages of vRNP transport. Nucleocytoplasmic transport could be monitored, revealing unexpected details of fast directional transport subsequent to nuclear export, leading to the hypothesis of a two-stage microtubule-based cytoplasmic transport of progeny vRNPs, including vesicular and non-vesicular transport, in line with the recent finding of a vRNP interacting protein that targets vRNPs directly to microtubules and to the MTOC. Furthermore, also plasma membrane targeting of mEYFP-NP-tagged complexes could be studied. Considerable mobility underneath the plasma membrane demonstrated that accumulating vRNPs in the cell periphery, as detected also by FISH and immunostainings in fixed cells (Fig. 43, [280,297]), were not static, but rather indicate a third stage of vRNP transport underneath the plasma membrane. vRNPs might move in close proximity to the membrane until they associate with the viral budding site or become reinternalized into the cell. This hypothesis requires however further investigations, since the particle trajectories are limited by two-dimensional image information.

While the SPT approach has a great potential to study vRNP transport and virus budding and could already provide valuable information, which complements findings from biochemical analyses and fluorescence imaging in fixed cells and adds new aspects to the current model, the approach will have to be further developed to be able to exploit the full potential of this technique. In future experiments, the use of a spinning disc microscope will enable fast three-dimensional time-lapse imaging and permit to follow continuous movements of single particles throughout the cells. This will allow characterizing processes in more detail like the transport from the nucleus to the MTOC, the assembly of vRNPs with recycling endosomes, the targeting to the plasma membrane and the association with the viral budzone, but also virus budding itself possibly can be monitored. Further refinement, like coexpression of fluorescent marker proteins for the plasma membrane, the nuclear envelope, recycling endosomes, microtubules or actin filaments will help to substantiate the results to come to solid conclusions.

In order to reconstruct full-length three-dimensional particle trajectories, another limitation further has to be overcome, which is an inherent problem of single particle tracking. High particle densities like the high local concentrations of vRNPs at the MTOC, at the plasma membrane or in the nucleus do not allow to unambiguously trace individual particles, which complicates data analysis and impairs the reconstruction of tracks. The here established experimental approach provides the important advantage to be relatively flexible with the choice of the fluorescent protein tag, offering the possibility to use photoactivatable fluorescent proteins instead of mEYFP or mCherry. Fluorescent proteins, including photoactivatable fluorescent proteins, are all very similar in size and structure. Fluorescence photoactivation can be applied to selectively label individual particles or a small subset of particles by irradiation, which then can be distinguished and identified throughout the measurement. The versatility of the fluorescent protein tag might be an important advantage of this approach in comparison to the approach using recombinant viruses encoding split-GFP. It is postulated that an experimental approach could be established here which has the potential to provide a coherent picture of vRNP transport from the nucleus to the site of virus assembly and to substantially contribute to characterize the mechanisms and kinetics of virus assembly and virus budding.

Bibliography

[1] Webster, R. G.; Bean, W. J.; Gorman, O. T.; Chambers, T. M. and Kawaoka, Y. (1992): Evolution and ecology of influenza A viruses, Microbiol Rev (vol. 56), No. 1, pp. 152-79.

[2] Wu, Y.; Tefsen, B.; Shi, Y. and Gao, G. F. (2014): Bat-derived influenza-like viruses H17N10 and H18N11, Trends Microbiol (vol. 22), No. 4, pp. 183-191.

[3] Fouchier, R. A.; Munster, V.; Wallensten, A.; Bestebroer, T. M.; Herfst, S.; Smith, D.; Rimmelzwaan, G. F.; Olsen, B. and Osterhaus, A. D. (2005): Characterization of a novel influenza A virus hemagglutinin subtype (H16) obtained from black-headed gulls, J Virol (vol. 79), No. 5, pp. 2814-22.

[4] Kuiken, T.; Holmes, E. C.; McCauley, J.; Rimmelzwaan, G. F.; Williams, C. S. and Grenfell, B. T. (2006): Host species barriers to influenza virus infections, Science (vol. 312), No. 5772, pp. 394-7.

[5] Kasowski, E. J.; Garten, R. J. and Bridges, C. B. (2011): Influenza pandemic epidemiologic and virologic diversity: reminding ourselves of the possibilities, Clin Infect Dis (vol. 52 Suppl 1), pp. S44-9.

[6] Drake, J. W. (1993): Rates of spontaneous mutation among RNA viruses, Proc Natl Acad Sci U S A (vol. 90), No. 9, pp. 4171-5.

[7] Noda, T. (2011): Native morphology of influenza virions, Front Microbiol (vol. 2), p. 269.

[8] Harris, A.; Cardone, G.; Winkler, D. C.; Heymann, J. B.; Brecher, M.; White, J. M. and Steven, A. C. (2006): Influenza virus pleiomorphy characterized by cryoelectron tomography, Proc Natl Acad Sci U S A (vol. 103), No. 50, pp. 19123-7.

[9] Jin, H.; Leser, G. P.; Zhang, J. and Lamb, R. A. (1997): Influenza virus hemagglutinin and neuraminidase cytoplasmic tails control particle shape, EMBO J (vol. 16), No. 6, pp. 1236-47.

[10] Iwatsuki-Horimoto, K.; Horimoto, T.; Noda, T.; Kiso, M.; Maeda, J.; Watanabe, S.; Muramoto, Y.; Fujii, K. and Kawaoka, Y. (2006): The cytoplasmic tail of the influenza A virus M2 protein plays a role in viral assembly, J Virol (vol. 80), No. 11, pp. 5233-40.

[11] Rossman, J. S.; Jing, X.; Leser, G. P.; Balannik, V.; Pinto, L. H. and Lamb, R. A. (2010): Influenza virus m2 ion channel protein is necessary for filamentous virion formation, J Virol (vol. 84), No. 10, pp. 5078-88.

[12] Burleigh, L. M.; Calder, L. J.; Skehel, J. J. and Steinhauer, D. A. (2005): Influenza a viruses with mutations in the m1 helix six domain display a wide variety of morphological phenotypes, J Virol (vol. 79), No. 2, pp. 1262-70.

[13] Elleman, C. J. and Barclay, W. S. (2004): The M1 matrix protein controls the filamentous phenotype of influenza A virus, Virology (vol. 321), No. 1, pp. 144-53.

[14] Bialas, K. M.; Bussey, K. A.; Stone, R. L. and Takimoto, T. (2014): Specific nucleoprotein residues affect influenza virus morphology, J Virol (vol. 88), No. 4, pp. 2227-34.

[15] Roberts, P. C. and Compans, R. W. (1998): Host cell dependence of viral morphology, Proc Natl Acad Sci U S A (vol. 95), No. 10, pp. 5746-51.

[16] Gerl, M. J.; Sampaio, J. L.; Urban, S.; Kalvodova, L.; Verbavatz, J. M.; Binnington, B.; Lindemann, D.; Lingwood, C. A.; Shevchenko, A.; Schroeder, C. and Simons, K. (2012): Quantitative analysis of the lipidomes of the influenza virus envelope and MDCK cell apical membrane, J Cell Biol (vol. 196), No. 2, pp. 213-21.

[17] Skehel, J. J. and Wiley, D. C. (2000): Receptor binding and membrane fusion in virus entry: the influenza hemagglutinin, Annu Rev Biochem (vol. 69), pp. 531-69.

[18] Palese, P.; Tobita, K.; Ueda, M. and Compans, R. W. (1974): Characterization of temperature sensitive influenza virus mutants defective in neuraminidase, Virology (vol. 61), No. 2, pp. 397-410.

[19] Wagner, R.; Matrosovich, M. and Klenk, H. D. (2002): Functional balance between haemagglutinin and neuraminidase in influenza virus infections, Rev Med Virol (vol. 12), No. 3, pp. 159-66.

[20] Nayak, D. P.; Balogun, R. A.; Yamada, H.; Zhou, Z. H. and Barman, S. (2009): Influenza virus morphogenesis and budding, Virus Res (vol. 143), No. 2, pp. 147-61.

[21] Veit, M. and Thaa, B. (2011): Association of influenza virus proteins with membrane rafts, Adv Virol (vol. 2011), p. 370606.

[22] Zebedee, S. L. and Lamb, R. A. (1988): Influenza A virus M2 protein: monoclonal antibody restriction of virus growth and detection of M2 in virions, J Virol (vol. 62), No. 8, pp. 2762-72.

[23] Lamb, R. A.; Zebedee, S. L. and Richardson, C. D. (1985): Influenza virus M2 protein is an integral membrane protein expressed on the infected-cell surface, Cell (vol. 40), No. 3, pp. 627-33.

[24] Zhang, J.; Pekosz, A. and Lamb, R. A. (2000): Influenza virus assembly and lipid raft microdomains: a role for the cytoplasmic tails of the spike glycoproteins, J Virol (vol. 74), No. 10, pp. 4634-44.

[25] Leser, G. P. and Lamb, R. A. (2005): Influenza virus assembly and budding in raft-derived microdomains: a quantitative analysis of the surface distribution of HA, NA and M2 proteins, Virology (vol. 342), No. 2, pp. 215-27.

[26] Schroeder, C.; Heider, H.; Moncke-Buchner, E. and Lin, T. I. (2005): The influenza virus ion channel and maturation cofactor M2 is a cholesterol-binding protein, Eur Biophys J (vol. 34), No. 1, pp. 52-66.

[27] Pinto, L. H.; Holsinger, L. J. and Lamb, R. A. (1992): Influenza virus M2 protein has ion channel activity, Cell (vol. 69), No. 3, pp. 517-28.

[28] Sakaguchi, T.; Tu, Q.; Pinto, L. H. and Lamb, R. A. (1997): The active oligomeric state of the minimalistic influenza virus M2 ion channel is a tetramer, Proc Natl Acad Sci U S A (vol. 94), No. 10, pp. 5000-5.

[29] Bui, M.; Whittaker, G. and Helenius, A. (1996): Effect of M1 protein and low pH on nuclear transport of influenza virus ribonucleoproteins, J Virol (vol. 70), No. 12, pp. 8391-401.

[30] Rossman, J. S.; Jing, X.; Leser, G. P. and Lamb, R. A. (2010): Influenza virus M2 protein mediates ESCRT-independent membrane scission, Cell (vol. 142), No. 6, pp. 902-13.

[31] Calder, L. J.; Wasilewski, S.; Berriman, J. A. and Rosenthal, P. B. (2010): Structural organization of a filamentous influenza A virus, Proc Natl Acad Sci U S A (vol. 107), No. 23, pp. 10685-90.

[32] Fontana, J. and Steven, A. C. (2013): At low pH, influenza virus matrix protein M1 undergoes a conformational change prior to dissociating from the membrane, J Virol (vol. 87), No. 10, pp. 5621-8.

[33] Ito, T.; Gorman, O. T.; Kawaoka, Y.; Bean, W. J. and Webster, R. G. (1991): Evolutionary analysis of the influenza A virus M gene with comparison of the M1 and M2 proteins, J Virol (vol. 65), No. 10, pp. 5491-8.

[34] Rossman, J. S. and Lamb, R. A. (2011): Influenza virus assembly and budding, Virology (vol. 411), No. 2, pp. 229-36.

[35] Noda, T.; Sugita, Y.; Aoyama, K.; Hirase, A.; Kawakami, E.; Miyazawa, A.; Sagara, H. and Kawaoka, Y. (2012): Three-dimensional analysis of ribonucleoprotein complexes in influenza A virus, Nat Commun (vol. 3), p. 639.

[36] Bourmakina, S. V. and Garcia-Sastre, A. (2003): Reverse genetics studies on the filamentous morphology of influenza A virus, J Gen Virol (vol. 84), No. Pt 3, pp. 517-27.

[37] Roberts, P. C.; Lamb, R. A. and Compans, R. W. (1998): The M1 and M2 proteins of influenza A virus are important determinants in filamentous particle formation, Virology (vol. 240), No. 1, pp. 127-37.

[38] Ali, A.; Avalos, R. T.; Ponimaskin, E. and Nayak, D. P. (2000): Influenza virus assembly: effect of influenza virus glycoproteins on the membrane association of M1 protein, J Virol (vol. 74), No. 18, pp. 8709-19.

[39] Barman, S.; Ali, A.; Hui, E. K.; Adhikary, L. and Nayak, D. P. (2001): Transport of viral proteins to the apical membranes and interaction of matrix protein with glycoproteins in the assembly of influenza viruses, Virus Res (vol. 77), No. 1, pp. 61-9.

[40] Chen, B. J.; Leser, G. P.; Jackson, D. and Lamb, R. A. (2008): The influenza virus M2 protein cytoplasmic tail interacts with the M1 protein and influences virus assembly at the site of virus budding, J Virol (vol. 82), No. 20, pp. 10059-70.

[41] Schmitt, A. P. and Lamb, R. A. (2005): Influenza virus assembly and budding at the viral budozone, Adv Virus Res (vol. 64), pp. 383-416.

[42] Baudin, F.; Petit, I.; Weissenhorn, W. and Ruigrok, R. W. (2001): In vitro dissection of the membrane and RNP binding activities of influenza virus M1 protein, Virology (vol. 281), No. 1, pp. 102-8.

[43] Bucher, D. J.; Kharitonenkov, I. G.; Zakomirdin, J. A.; Grigoriev, V. B.; Klimenko, S. M. and Davis, J. F. (1980): Incorporation of influenza virus M-protein into liposomes, J Virol (vol. 36), No. 2, pp. 586-90.

[44] Zhao, H.; Ekstrom, M. and Garoff, H. (1998): The M1 and NP proteins of influenza A virus form homo- but not heterooligomeric complexes when coexpressed in BHK-21 cells, J Gen Virol (vol. 79 (Pt 10)), pp. 2435-46.

[45] Ruigrok, R. W.; Barge, A.; Durrer, P.; Brunner, J.; Ma, K. and Whittaker, G. R. (2000): Membrane interaction of influenza virus M1 protein, Virology (vol. 267), No. 2, pp. 289-98.

[46] Gregoriades, A. (1980): Interaction of influenza M protein with viral lipid and phosphatidylcholine vesicles, J Virol (vol. 36), No. 2, pp. 470-9.

[47] Gregoriades, A. and Frangione, B. (1981): Insertion of influenza M protein into the viral lipid bilayer and localization of site of insertion, J Virol (vol. 40), No. 1, pp. 323-8.

[48] Shishkov, A. V.; Goldanskii, V. I.; Baratova, L. A.; Fedorova, N. V.; Ksenofontov, A. L.; Zhirnov, O. P. and Galkin, A. V. (1999): The in situ spatial arrangement of the influenza A virus matrix protein M1 assessed by tritium bombardment, Proc Natl Acad Sci U S A (vol. 96), No. 14, pp. 7827-30.

[49] El Karadaghi, S.; Zakomirdin, J. A.; Shimane, C.; Bucher, D. J.; Tverdislov, V. A. and Kharitonenkov, I. G. (1984): Interaction of influenza virus proteins with planar bilayer lipid membranes. I. Characterization of their adsorption and incorporation into lipid bilayers, Biochim Biophys Acta (vol. 778), No. 2, pp. 269-75.

[50] Kretzschmar, E.; Bui, M. and Rose, J. K. (1996): Membrane association of influenza virus matrix protein does not require specific hydrophobic domains or the viral glycoproteins, Virology (vol. 220), No. 1, pp. 37-45.

[51] Zhang, J. and Lamb, R. A. (1996): Characterization of the membrane association of the influenza virus matrix protein in living cells, Virology (vol. 225), No. 2, pp. 255-66.

[52] Compans, R. W.; Content, J. and Duesberg, P. H. (1972): Structure of the ribonucleoprotein of influenza virus, J Virol (vol. 10), No. 4, pp. 795-800.

[53] Noda, T.; Sagara, H.; Yen, A.; Takada, A.; Kida, H.; Cheng, R. H. and Kawaoka, Y. (2006): Architecture of ribonucleoprotein complexes in influenza A virus particles, Nature (vol. 439), No. 7075, pp. 490-2.

[54] Resa-Infante, P.; Jorba, N.; Coloma, R. and Ortin, J. (2011): The influenza virus RNA synthesis machine: advances in its structure and function, RNA Biol (vol. 8), No. 2, pp. 207-15.

[55] Sugita, Y.; Sagara, H.; Noda, T. and Kawaoka, Y. (2013): Configuration of viral ribonucleoprotein complexes within the influenza A virion, J Virol (vol. 87), No. 23, pp. 12879-84.

[56] Chou, Y. Y.; Vafabakhsh, R.; Doganay, S.; Gao, Q.; Ha, T. and Palese, P. (2012): One influenza virus particle packages eight unique viral RNAs as shown by FISH analysis, Proc Natl Acad Sci U S A (vol. 109), No. 23, pp. 9101-6.

[57] Yasuda, J.; Nakada, S.; Kato, A.; Toyoda, T. and Ishihama, A. (1993): Molecular assembly of influenza virus: association of the NS2 protein with virion matrix, Virology (vol. 196), No. 1, pp. 249-55.

[58] Richardson, J. C. and Akkina, R. K. (1991): NS2 protein of influenza virus is found in purified virus and phosphorylated in infected cells, Arch Virol (vol. 116), No. 1-4, pp. 69-80.

[59] Lamb, R. A. and Krug, R.M. (2001): Orthomyxoviridae: the viruses and their replication, Knipe, D.M. and Howley, P.M., Fields Virology, 4. ed., pp. 1487–1531, Lippincott Williams & Wilkins, Philadelphia, PA.

[60] Chen, W.; Calvo, P. A.; Malide, D.; Gibbs, J.; Schubert, U.; Bacik, I.; Basta, S.; O'Neill, R.; Schickli, J.; Palese, P.; Henklein, P.; Bennink, J. R. and Yewdell, J. W. (2001): A novel influenza A virus mitochondrial protein that induces cell death, Nat Med (vol. 7), No. 12, pp. 1306-12.

[61] Jagger, B. W.; Wise, H. M.; Kash, J. C.; Walters, K. A.; Wills, N. M.; Xiao, Y. L.; Dunfee, R. L.; Schwartzman, L. M.; Ozinsky, A.; Bell, G. L.; Dalton, R. M.; Lo, A.; Efstathiou, S.; Atkins, J. F.; Firth, A. E.; Taubenberger, J. K. and Digard, P. (2012): An overlapping protein-coding region in influenza A virus segment 3 modulates the host response, Science (vol. 337), No. 6091, pp. 199-204.

[62] Muramoto, Y.; Noda, T.; Kawakami, E.; Akkina, R. and Kawaoka, Y. (2013): Identification of novel influenza A virus proteins translated from PA mRNA, J Virol (vol. 87), No. 5, pp. 2455-62.

[63] Wise, H. M.; Foeglein, A.; Sun, J.; Dalton, R. M.; Patel, S.; Howard, W.; Anderson, E. C.; Barclay, W. S. and Digard, P. (2009): A complicated message: Identification of a novel PB1-related protein translated from influenza A virus segment 2 mRNA, J Virol (vol. 83), No. 16, pp. 8021-31.

[64] Selman, Mohammed; Dankar, Samar K.; Forbes, Nicole E.; Jia, Jian-Jun and Brown, Earl G. (2012): Adaptive mutation in influenza A virus non-structural gene is linked to host switching and induces a novel protein by alternative splicing, Emerg Microbes Infect (vol. 1), p. e42.

[65] Wise, H. M.; Hutchinson, E. C.; Jagger, B. W.; Stuart, A. D.; Kang, Z. H.; Robb, N.; Schwartzman, L. M.; Kash, J. C.; Fodor, E.; Firth, A. E.; Gog, J. R.; Taubenberger, J. K. and Digard, P. (2012): Identification of a novel splice variant form of the influenza A virus M2 ion channel with an antigenically distinct ectodomain, PLoS Pathog (vol. 8), No. 11, p. e1002998.

[66] O'Neill, R. E.; Talon, J. and Palese, P. (1998): The influenza virus NEP (NS2 protein) mediates the nuclear export of viral ribonucleoproteins, EMBO J (vol. 17), No. 1, pp. 288-96.

[67] Huang, S.; Chen, J.; Chen, Q.; Wang, H.; Yao, Y. and Chen, Z. (2013): A second CRM1-dependent nuclear export signal in the influenza A virus NS2 protein contributes to the nuclear export of viral ribonucleoproteins, J Virol (vol. 87), No. 2, pp. 767-78.

[68] Noton, S. L.; Medcalf, E.; Fisher, D.; Mullin, A. E.; Elton, D. and Digard, P. (2007): Identification of the domains of the influenza A virus M1 matrix protein required for NP binding, oligomerization and incorporation into virions, J Gen Virol (vol. 88), No. Pt 8, pp. 2280-90.

[69] Liu, T.; Muller, J. and Ye, Z. (2002): Association of influenza virus matrix protein with ribonucleoproteins may control viral growth and morphology, Virology (vol. 304), No. 1, pp. 89-96.

[70] Desselberger, U.; Racaniello, V. R.; Zazra, J. J. and Palese, P. (1980): The 3' and 5'-terminal sequences of influenza A, B and C virus RNA segments are highly conserved and show partial inverted complementarity, Gene (vol. 8), No. 3, pp. 315-28.

[71] Fodor, E.; Pritlove, D. C. and Brownlee, G. G. (1994): The influenza virus panhandle is involved in the initiation of transcription, J Virol (vol. 68), No. 6, pp. 4092-6.

[72] Tiley, L. S.; Hagen, M.; Matthews, J. T. and Krystal, M. (1994): Sequence-specific binding of the influenza virus RNA polymerase to sequences located at the 5' ends of the viral RNAs, J Virol (vol. 68), No. 8, pp. 5108-16.

[73] Azzeh, M.; Flick, R. and Hobom, G. (2001): Functional analysis of the influenza A virus cRNA promoter and construction of an ambisense transcription system, Virology (vol. 289), No. 2, pp. 400-10.

[74] Brownlee, G. G. and Sharps, J. L. (2002): The RNA polymerase of influenza a virus is stabilized by interaction with its viral RNA promoter, J Virol (vol. 76), No. 14, pp. 7103-13.

[75] Crow, M.; Deng, T.; Addley, M. and Brownlee, G. G. (2004): Mutational analysis of the influenza virus cRNA promoter and identification of nucleotides critical for replication, J Virol (vol. 78), No. 12, pp. 6263-70.

[76] Flick, R.; Neumann, G.; Hoffmann, E.; Neumeier, E. and Hobom, G. (1996): Promoter elements in the influenza vRNA terminal structure, RNA (vol. 2), No. 10, pp. 1046-57.

[77] Park, C. J.; Bae, S. H.; Lee, M. K.; Varani, G. and Choi, B. S. (2003): Solution structure of the influenza A virus cRNA promoter: implications for differential recognition of viral promoter structures by RNA-dependent RNA polymerase, Nucleic Acids Res (vol. 31), No. 11, pp. 2824-32.

[78] Gonzalez, S. and Ortin, J. (1999): Distinct regions of influenza virus PB1 polymerase subunit recognize vRNA and cRNA templates, EMBO J (vol. 18), No. 13, pp. 3767-75.

[79] Gonzalez, S. and Ortin, J. (1999): Characterization of influenza virus PB1 protein binding to viral RNA: two separate regions of the protein contribute to the interaction domain, J Virol (vol. 73), No. 1, pp. 631-7.

[80] Maier, H. J.; Kashiwagi, T.; Hara, K. and Brownlee, G. G. (2008): Differential role of the influenza A virus polymerase PA subunit for vRNA and cRNA promoter binding, Virology (vol. 370), No. 1, pp. 194-204.

[81] York, A.; Hengrung, N.; Vreede, F. T.; Huiskonen, J. T. and Fodor, E. (2013): Isolation and characterization of the positive-sense replicative intermediate of a negative-strand RNA virus, Proc Natl Acad Sci U S A (vol. 110), No. 45, pp. E4238-45.

[82] Pons, M. W.; Schulze, I. T.; Hirst, G. K. and Hauser, R. (1969): Isolation and characterization of the ribonucleoprotein of influenza virus, Virology (vol. 39), No. 2, pp. 250-9.

[83] Hutchinson, E. C. and Fodor, E. (2013): Transport of the influenza virus genome from nucleus to nucleus, Viruses (vol. 5), No. 10, pp. 2424-46.

[84] Fodor, E.; Devenish, L.; Engelhardt, O. G.; Palese, P.; Brownlee, G. G. and Garcia-Sastre, A. (1999): Rescue of influenza A virus from recombinant DNA, J Virol (vol. 73), No. 11, pp. 9679-82.

[85] Kemler, I.; Whittaker, G. and Helenius, A. (1994): Nuclear import of microinjected influenza virus ribonucleoproteins, Virology (vol. 202), No. 2, pp. 1028-33.

[86] Neumann, G.; Watanabe, T.; Ito, H.; Watanabe, S.; Goto, H.; Gao, P.; Hughes, M.; Perez, D. R.; Donis, R.; Hoffmann, E.; Hobom, G. and Kawaoka, Y. (1999): Generation of influenza A viruses entirely from cloned cDNAs, Proc Natl Acad Sci U S A (vol. 96), No. 16, pp. 9345-50.

[87] Baudin, F.; Bach, C.; Cusack, S. and Ruigrok, R. W. (1994): Structure of influenza virus RNP. I. Influenza virus nucleoprotein melts secondary structure in panhandle RNA and exposes the bases to the solvent, EMBO J (vol. 13), No. 13, pp. 3158-65.

[88] Arranz, R.; Coloma, R.; Chichon, F. J.; Conesa, J. J.; Carrascosa, J. L.; Valpuesta, J. M.; Ortin, J. and Martin-Benito, J. (2012): The structure of native influenza virion ribonucleoproteins, Science (vol. 338), No. 6114, pp. 1634-7. U

[89] Moeller, A.; Kirchdoerfer, R. N.; Potter, C. S.; Carragher, B. and Wilson, I. A. (2012): Organization of the influenza virus replication machinery, Science (vol. 338), No. 6114, pp. 1631-4. U

[90] Turrell, L.; Lyall, J. W.; Tiley, L. S.; Fodor, E. and Vreede, F. T. (2013): The role and assembly mechanism of nucleoprotein in influenza A virus ribonucleoprotein complexes, Nat Commun (vol. 4), p. 1591.

[91] Yamanaka, K.; Ishihama, A. and Nagata, K. (1990): Reconstitution of influenza virus RNA-nucleoprotein complexes structurally resembling native viral ribonucleoprotein cores, J Biol Chem (vol. 265), No. 19, pp. 11151-5.

[92] Ye, Q.; Guu, T. S.; Mata, D. A.; Kuo, R. L.; Smith, B.; Krug, R. M. and Tao, Y. J. (2012): Biochemical and structural evidence in support of a coherent model for the formation of the double-helical influenza A virus ribonucleoprotein, MBio (vol. 4), No. 1, pp. e00467-12.

[93] Ye, Q.; Krug, R. M. and Tao, Y. J. (2006): The mechanism by which influenza A virus nucleoprotein forms oligomers and binds RNA, Nature (vol. 444), No. 7122, pp. 1078-82. [94] Klumpp, K.; Ruigrok, R. W. and Baudin, F. (1997): Roles of the influenza virus polymerase and nucleoprotein in forming a functional RNP structure, EMBO J (vol. 16), No. 6, pp. 1248-57.

[95] Coloma, R.; Valpuesta, J. M.; Arranz, R.; Carrascosa, J. L.; Ortin, J. and Martin-Benito, J. (2009): The structure of a biologically active influenza virus ribonucleoprotein complex, PLoS Pathog (vol. 5), No. 6, p. e1000491.

[96] Ortega, J.; Martin-Benito, J.; Zurcher, T.; Valpuesta, J. M.; Carrascosa, J. L. and Ortin, J. (2000): Ultrastructural and functional analyses of recombinant influenza virus ribonucleoproteins suggest dimerization of nucleoprotein during virus amplification, J Virol (vol. 74), No. 1, pp. 156-63.

[97] Murti, K. G.; Webster, R. G. and Jones, I. M. (1988): Localization of RNA polymerases on influenza viral ribonucleoproteins by immunogold labeling, Virology (vol. 164), No. 2, pp. 562-6.

[98] Tchatalbachev, S.; Flick, R. and Hobom, G. (2001): The packaging signal of influenza viral RNA molecules, RNA (vol. 7), No. 7, pp. 979-89.

[99] Goto, H.; Muramoto, Y.; Noda, T. and Kawaoka, Y. (2013): The genome-packaging signal of the influenza A virus genome comprises a genome incorporation signal and a genome-bundling signal, J Virol (vol. 87), No. 21, pp. 11316-22.

[100] Hutchinson, E. C.; von Kirchbach, J. C.; Gog, J. R. and Digard, P. (2010): Genome packaging in influenza A virus, J Gen Virol (vol. 91), No. Pt 2, pp. 313-28.

[101] Brunotte, L.; Flies, J.; Bolte, H.; Reuther, P.; Vreede, F. and Schwemmle, M. (2014): The nuclear export protein of H5N1 influenza A viruses recruits M1 to the viral ribonucleoprotein to mediate nuclear export, J Biol Chem.

[102] Robb, N. C.; Chase, G.; Bier, K.; Vreede, F. T.; Shaw, P. C.; Naffakh, N.; Schwemmle, M. and Fodor, E. (2011): The influenza A virus NS1 protein interacts with the nucleoprotein of viral ribonucleoprotein complexes, J Virol (vol. 85), No. 10, pp. 5228-31.

[103] Mayer, D.; Molawi, K.; Martinez-Sobrido, L.; Ghanem, A.; Thomas, S.; Baginsky, S.; Grossmann, J.; Garcia-Sastre, A. and Schwemmle, M. (2007): Identification of cellular interaction partners of the influenza virus ribonucleoprotein complex and polymerase complex using proteomic-based approaches, J Proteome Res (vol. 6), No. 2, pp. 672-82.

[104] Weinheimer, V. K.; Becher, A.; Tonnies, M.; Holland, G.; Knepper, J.; Bauer, T. T.; Schneider, P.; Neudecker, J.; Ruckert, J. C.; Szymanski, K.; Temmesfeld-Wollbrueck, B.; Gruber, A. D.; Bannert, N.; Suttorp, N.; Hippenstiel, S.; Wolff, T. and Hocke, A. C. (2012): Influenza A viruses target type II pneumocytes in the human lung, J Infect Dis (vol. 206), No. 11, pp. 1685-94.

[105] Matlin, K. S.; Reggio, H.; Helenius, A. and Simons, K. (1981): Infectious entry pathway of influenza virus in a canine kidney cell line, J Cell Biol (vol. 91), No. 3 Pt 1, pp. 601-13.

[106] Chen, C. and Zhuang, X. (2008): Epsin 1 is a cargo-specific adaptor for the clathrin-mediated endocytosis of the influenza virus, Proc Natl Acad Sci U S A (vol. 105), No. 33, pp. 11790-5.

[107] de Vries, E.; Tscherne, D. M.; Wienholts, M. J.; Cobos-Jimenez, V.; Scholte, F.; Garcia-Sastre, A.; Rottier, P. J. and de Haan, C. A. (2011): Dissection of the influenza A virus endocytic routes reveals macropinocytosis as an alternative entry pathway, PLoS Pathog (vol. 7), No. 3, p. e1001329.

[108] Rossman, J. S.; Leser, G. P. and Lamb, R. A. (2012): Filamentous influenza virus enters cells via macropinocytosis, J Virol (vol. 86), No. 20, pp. 10950-60.

[109] Rust, M. J.; Lakadamyali, M.; Zhang, F. and Zhuang, X. (2004): Assembly of endocytic machinery around individual influenza viruses during viral entry, Nat Struct Mol Biol (vol. 11), No. 6, pp. 567-73.

[110] Lakadamyali, M.; Rust, M. J.; Babcock, H. P. and Zhuang, X. (2003): Visualizing infection of individual influenza viruses, Proc Natl Acad Sci U S A (vol. 100), No. 16, pp. 9280-5.

[111] Huotari, J. and Helenius, A. (2011): Endosome maturation, EMBO J (vol. 30), No. 17, pp. 3481-500.

[112] Zhang, K.; Wang, Z.; Liu, X.; Yin, C.; Basit, Z.; Xia, B. and Liu, W. (2012): Dissection of influenza A virus M1 protein: pH-dependent oligomerization of N-terminal domain and dimerization of C-terminal domain, PLoS One (vol. 7), No. 5, p. e37786.

[113] Zhirnov, O. P. (1990): Solubilization of matrix protein M1/M from virions occurs at different pH for orthomyxo- and paramyxoviruses, Virology (vol. 176), No. 1, pp. 274-9.

[114] Helenius, A. (1992): Unpacking the incoming influenza virus, Cell (vol. 69), No. 4, pp. 577-8. U

[115] Martin, K. and Helenius, A. (1991): Transport of incoming influenza virus nucleocapsids into the nucleus, J Virol (vol. 65), No. 1, pp. 232-44.

[116] Martin, K. and Helenius, A. (1991): Nuclear transport of influenza virus ribonucleoproteins: the viral matrix protein (M1) promotes export and inhibits import, Cell (vol. 67), No. 1, pp. 117-30.

[117] Babcock, H. P.; Chen, C. and Zhuang, X. (2004): Using single-particle tracking to study nuclear trafficking of viral genes, Biophys J (vol. 87), No. 4, pp. 2749-58.

[118] Cros, J. F.; Garcia-Sastre, A. and Palese, P. (2005): An unconventional NLS is critical for the nuclear import of the influenza A virus nucleoprotein and ribonucleoprotein, Traffic (vol. 6), No. 3, pp. 205-13.

[119] O'Neill, R. E.; Jaskunas, R.; Blobel, G.; Palese, P. and Moroianu, J. (1995): Nuclear import of influenza virus RNA can be mediated by viral nucleoprotein and transport factors required for protein import, J Biol Chem (vol. 270), No. 39, pp. 22701-4.

[120] Wu, W. W.; Sun, Y. H. and Pante, N. (2007): Nuclear import of influenza A viral ribonucleoprotein complexes is mediated by two nuclear localization sequences on viral nucleoprotein, Virol J (vol. 4), p. 49.

[121] Wang, P.; Palese, P. and O'Neill, R. E. (1997): The NPI-1/NPI-3 (karyopherin alpha) binding site on the influenza a virus nucleoprotein NP is a nonconventional nuclear localization signal, J Virol (vol. 71), No. 3, pp. 1850-6.

[122] Weber, F.; Kochs, G.; Gruber, S. and Haller, O. (1998): A classical bipartite nuclear localization signal on Thogoto and influenza A virus nucleoproteins, Virology (vol. 250), No. 1, pp. 9-18.

[123] Ozawa, M.; Fujii, K.; Muramoto, Y.; Yamada, S.; Yamayoshi, S.; Takada, A.; Goto, H.; Horimoto, T. and Kawaoka, Y. (2007): Contributions of two nuclear localization signals of influenza A virus nucleoprotein to viral replication, J Virol (vol. 81), No. 1, pp. 30-41.

[124] Whittaker, G.; Bui, M. and Helenius, A. (1996): Nuclear trafficking of influenza virus ribonuleoproteins in heterokaryons, J Virol (vol. 70), No. 5, pp. 2743-56.

[125] Stertz, S. and Shaw, M. L. (2011): Uncovering the global host cell requirements for influenza virus replication via RNAi screening, Microbes Infect (vol. 13), No. 5, pp. 516-25.

[126] Su, W. C.; Chen, Y. C.; Tseng, C. H.; Hsu, P. W.; Tung, K. F.; Jeng, K. S. and Lai, M. M. (2013): Pooled RNAi screen identifies ubiquitin ligase Itch as crucial for influenza A virus release from the endosome during virus entry, Proc Natl Acad Sci U S A (vol. 110), No. 43, pp. 17516-21.

[127] Engelhardt, O. G. and Fodor, E. (2006): Functional association between viral and cellular transcription during influenza virus infection, Rev Med Virol (vol. 16), No. 5, pp. 329-45.

[128] Nagata, K.; Kawaguchi, A. and Naito, T. (2008): Host factors for replication and transcription of the influenza virus genome, Rev Med Virol (vol. 18), No. 4, pp. 247-60.

[129] Hale, B. G.; Randall, R. E.; Ortin, J. and Jackson, D. (2008): The multifunctional NS1 protein of influenza A viruses, J Gen Virol (vol. 89), No. Pt 10, pp. 2359-76.

[130] Vreede, F. T. and Fodor, E. (2010): The role of the influenza virus RNA polymerase in host shut-off, Virulence (vol. 1), No. 5, pp. 436-9.

[131] Josset, L.; Frobert, E. and Rosa-Calatrava, M. (2008): Influenza A replication and host nuclear compartments: many changes and many questions, J Clin Virol (vol. 43), No. 4, pp. 381-90.

[132] Terrier, O.; Moules, V.; Carron, C.; Cartet, G.; Frobert, E.; Yver, M.; Traversier, A.; Wolff, T.; Riteau, B.; Naffakh, N.; Lina, B.; Diaz, J. J. and Rosa-Calatrava, M. (2012): The influenza fingerprints: NS1 and M1 proteins contribute to specific host cell ultrastructure signatures upon infection by different influenza A viruses, Virology (vol. 432), No. 1, pp. 204-18.

[133] Huang, T. S.; Palese, P. and Krystal, M. (1990): Determination of influenza virus proteins required for genome replication, J Virol (vol. 64), No. 11, pp. 5669-73.

[134] Chou, Y. Y.; Heaton, N. S.; Gao, Q.; Palese, P.; Singer, R. H. and Lionnet, T. (2013): Colocalization of different influenza viral RNA segments in the cytoplasm before viral budding as shown by single-molecule sensitivity FISH analysis, PLoS Pathog (vol. 9), No. 5, p. e1003358.

[135] Fodor, E. (2013): The RNA polymerase of influenza a virus: mechanisms of viral transcription and replication, Acta Virol (vol. 57), No. 2, pp. 113-22.

[136] Hagen, M.; Chung, T. D.; Butcher, J. A. and Krystal, M. (1994): Recombinant influenza virus polymerase: requirement of both 5' and 3' viral ends for endonuclease activity, J Virol (vol. 68), No. 3, pp. 1509-15.

[137] Chan, A. Y.; Vreede, F. T.; Smith, M.; Engelhardt, O. G. and Fodor, E. (2006): Influenza virus inhibits RNA polymerase II elongation, Virology (vol. 351), No. 1, pp. 210-7.

[138] Amorim, M. J.; Read, E. K.; Dalton, R. M.; Medcalf, L. and Digard, P. (2007): Nuclear export of influenza A virus mRNAs requires ongoing RNA polymerase II activity, Traffic (vol. 8), No. 1, pp. 1-11.

[139] Engelhardt, O. G.; Smith, M. and Fodor, E. (2005): Association of the influenza A virus RNA-dependent RNA polymerase with cellular RNA polymerase II, J Virol (vol. 79), No. 9, pp. 5812-8.

[140] Jackson, D. A.; Caton, A. J.; McCready, S. J. and Cook, P. R. (1982): Influenza virus RNA is synthesized at fixed sites in the nucleus, Nature (vol. 296), No. 5855, pp. 366-8.

[141] Poon, L. L.; Fodor, E. and Brownlee, G. G. (2000): Polyuridylated mRNA synthesized by a recombinant influenza virus is defective in nuclear export, J Virol (vol. 74), No. 1, pp. 418-27.

[142] Robertson, J. S.; Schubert, M. and Lazzarini, R. A. (1981): Polyadenylation sites for influenza virus mRNA, J Virol (vol. 38), No. 1, pp. 157-63.

[143] Luo, G. X.; Luytjes, W.; Enami, M. and Palese, P. (1991): The polyadenylation signal of influenza virus RNA involves a stretch of uridines followed by the RNA duplex of the panhandle structure, J Virol (vol. 65), No. 6, pp. 2861-7.

[144] Plotch, S. J. and Krug, R. M. (1977): Influenza virion transcriptase: synthesis in vitro of large, polyadenylic acid-containing complementary RNA, J Virol (vol. 21), No. 1, pp. 24-34.

[145] Pritlove, D. C.; Poon, L. L.; Devenish, L. J.; Leahy, M. B. and Brownlee, G. G. (1999): A hairpin loop at the 5' end of influenza A virus virion RNA is required for synthesis of poly(A)+ mRNA in vitro, J Virol (vol. 73), No. 3, pp. 2109-14.

[146] York, A. and Fodor, E. (2013): Biogenesis, assembly, and export of viral messenger ribonucleoproteins in the influenza A virus infected cell, RNA Biol (vol. 10), No. 8, pp. 1274-82.

[147] Bier, K.; York, A. and Fodor, E. (2011): Cellular cap-binding proteins associate with influenza virus mRNAs, J Gen Virol (vol. 92), No. Pt 7, pp. 1627-34.

[148] Muller-McNicoll, M. and Neugebauer, K. M. (2014): Good cap/bad cap: how the cap-binding complex determines RNA fate, Nat Struct Mol Biol (vol. 21), No. 1, pp. 9-12.

[149] Read, E. K. and Digard, P. (2010): Individual influenza A virus mRNAs show differential dependence on cellular NXF1/TAP for their nuclear export, J Gen Virol (vol. 91), No. Pt 5, pp. 1290-301.

[150] Buehler, J.; Navi, D.; Lorusso, A.; Vincent, A.; Lager, K. and Miller, C. L. (2013): Influenza A virus PB1-F2 protein expression is regulated in a strain-specific manner by sequences located downstream of the PB1-F2 initiation codon, J Virol (vol. 87), No. 19, pp. 10687-99.

[151] Schmolke, M.; Manicassamy, B.; Pena, L.; Sutton, T.; Hai, R.; Varga, Z. T.; Hale, B. G.; Steel, J.; Perez, D. R. and Garcia-Sastre, A. (2011): Differential contribution of PB1-F2 to the virulence of highly pathogenic H5N1 influenza A virus in mammalian and avian species, PLoS Pathog (vol. 7), No. 8, p. e1002186.

[152] Shapiro, G. I.; Gurney, T., Jr. and Krug, R. M. (1987): Influenza virus gene expression: control mechanisms at early and late times of infection and nuclear-cytoplasmic transport of virus-specific RNAs, J Virol (vol. 61), No. 3, pp. 764-73.

[153] Varich, N. L. and Kaverin, N. V. (1987): Regulation of the replication of influenza virus RNA segments: partial suppression of protein synthesis restores the 'early' replication pattern, J Gen Virol (vol. 68 (Pt 11)), pp. 2879-87.

[154] Hatada, E.; Hasegawa, M.; Mukaigawa, J.; Shimizu, K. and Fukuda, R. (1989): Control of influenza virus gene expression: quantitative analysis of each viral RNA species in infected cells, J Biochem (vol. 105), No. 4, pp. 537-46.

[155] Smith, G. L.; Levin, J. Z.; Palese, P. and Moss, B. (1987): Synthesis and cellular location of the ten influenza polypeptides individually expressed by recombinant vaccinia viruses, Virology (vol. 160), No. 2, pp. 336-45.

[156] Gao, S.; Wang, S.; Cao, S.; Sun, L.; Li, J.; Bi, Y.; Gao, G. F. and Liu, W. (2014): The characteristics of nucleocytoplasmic transport of H1N1 influenza A viruses nuclear export protein (NEP), J Virol.

[157] Schneider, J. and Wolff, T. (2009): Nuclear functions of the influenza A and B viruses NS1 proteins: do they play a role in viral mRNA export?, Vaccine (vol. 27), No. 45, pp. 6312-6.

[158] Wang, W.; Cui, Z. Q.; Han, H.; Zhang, Z. P.; Wei, H. P.; Zhou, Y. F.; Chen, Z. and Zhang, X. E. (2008): Imaging and characterizing influenza A virus mRNA transport in living cells, Nucleic Acids Res (vol. 36), No. 15, pp. 4913-28. U

[159] Robb, N. C. and Fodor, E. (2012): The accumulation of influenza A virus segment 7 spliced mRNAs is regulated by the NS1 protein, J Gen Virol (vol. 93), No. Pt 1, pp. 113-8.

[160] Aragon, T.; de la Luna, S.; Novoa, I.; Carrasco, L.; Ortin, J. and Nieto, A. (2000): Eukaryotic translation initiation factor 4GI is a cellular target for NS1 protein, a translational activator of influenza virus, Mol Cell Biol (vol. 20), No. 17, pp. 6259-68.

[161] Burgui, I.; Aragon, T.; Ortin, J. and Nieto, A. (2003): PABP1 and eIF4GI associate with influenza virus NS1 protein in viral mRNA translation initiation complexes, J Gen Virol (vol. 84), No. Pt 12, pp. 3263-74.

[162] de la Luna, S.; Fortes, P.; Beloso, A. and Ortin, J. (1995): Influenza virus NS1 protein enhances the rate of translation initiation of viral mRNAs, J Virol (vol. 69), No. 4, pp. 2427-33.

[163] Marazzi, I.; Ho, J. S.; Kim, J.; Manicassamy, B.; Dewell, S.; Albrecht, R. A.; Seibert, C. W.; Schaefer, U.; Jeffrey, K. L.; Prinjha, R. K.; Lee, K.; Garcia-Sastre, A.; Roeder, R. G. and Tarakhovsky, A. (2012): Suppression of the antiviral response by an influenza histone mimic, Nature (vol. 483), No. 7390, pp. 428-33.

[164] Fortes, P.; Lamond, A. I. and Ortin, J. (1995): Influenza virus NS1 protein alters the subnuclear localization of cellular splicing components, J Gen Virol (vol. 76 (Pt 4)), pp. 1001-7.

[165] Wang, W. and Krug, R. M. (1998): U6atac snRNA, the highly divergent counterpart of U6 snRNA, is the specific target that mediates inhibition of AT-AC splicing by the influenza virus NS1 protein, RNA (vol. 4), No. 1, pp. 55-64.

[166] Wolff, T.; O'Neill, R. E. and Palese, P. (1998): NS1-Binding protein (NS1-BP): a novel human protein that interacts with the influenza A virus nonstructural NS1 protein is relocalized in the nuclei of infected cells, J Virol (vol. 72), No. 9, pp. 7170-80.

[167] Fortes, P.; Beloso, A. and Ortin, J. (1994): Influenza virus NS1 protein inhibits pre-mRNA splicing and blocks mRNA nucleocytoplasmic transport, EMBO J (vol. 13), No. 3, pp. 704-12.

[168] Lu, Y.; Qian, X. Y. and Krug, R. M. (1994): The influenza virus NS1 protein: a novel inhibitor of pre-mRNA splicing, Genes Dev (vol. 8), No. 15, pp. 1817-28.

[169] Robb, N. C.; Jackson, D.; Vreede, F. T. and Fodor, E. (2010): Splicing of influenza A virus NS1 mRNA is independent of the viral NS1 protein, J Gen Virol (vol. 91), No. Pt 9, pp. 2331-40.

[170] Chen, Z.; Li, Y. and Krug, R. M. (1999): Influenza A virus NS1 protein targets poly(A)-binding protein II of the cellular 3'-end processing machinery, EMBO J (vol. 18), No. 8, pp. 2273-83.

[171] Nemeroff, M. E.; Barabino, S. M.; Li, Y.; Keller, W. and Krug, R. M. (1998): Influenza virus NS1 protein interacts with the cellular 30 kDa subunit of CPSF and inhibits 3'end formation of cellular pre-mRNAs, Mol Cell (vol. 1), No. 7, pp. 991-1000.

[172] Vreede, F. T.; Chan, A. Y.; Sharps, J. and Fodor, E. (2010): Mechanisms and functional implications of the degradation of host RNA polymerase II in influenza virus infected cells, Virology (vol. 396), No. 1, pp. 125-34.

[173] Hay, A. J.; Skehel, J. J. and McCauley, J. (1982): Characterization of influenza virus RNA complete transcripts, Virology (vol. 116), No. 2, pp. 517-22. U

[174] Ortín, J. (2008): Structure and Function of the Influenza A Virus Ribonucleoprotein:Transcription and Replication, Klenk, H.-D. ; Matrosovich, cM.N. and Stech, J., Avian Influenza (vol. 27) p. 294, S.Karger AG, Basel, Switzerland.

[175] Jorba, N.; Coloma, R. and Ortin, J. (2009): Genetic trans-complementation establishes a new model for influenza virus RNA transcription and replication, PLoS Pathog (vol. 5), No. 5, p. e1000462.

[176] Chenavas, S.; Estrozi, L. F.; Slama-Schwok, A.; Delmas, B.; Di Primo, C.; Baudin, F.; Li, X.; Crepin, T. and Ruigrok, R. W. (2013): Monomeric nucleoprotein of influenza A virus, PLoS Pathog (vol. 9), No. 3, p. e1003275.

[177] Kawaguchi, A.; Momose, F. and Nagata, K. (2011): Replication-coupled and host factor-mediated encapsidation of the influenza virus genome by viral nucleoprotein, J Virol (vol. 85), No. 13, pp. 6197-204.

[178] Kawaguchi, A. and Nagata, K. (2007): De novo replication of the influenza virus RNA genome is regulated by DNA replicative helicase, MCM, EMBO J (vol. 26), No. 21, pp. 4566-75.

[179] Naito, T.; Kiyasu, Y.; Sugiyama, K.; Kimura, A.; Nakano, R.; Matsukage, A. and Nagata, K. (2007): An influenza virus replicon system in yeast identified Tat-SF1 as a stimulatory host factor for viral RNA synthesis, Proc Natl Acad Sci U S A (vol. 104), No. 46, pp. 18235-40.

[180] Mark, G. E.; Taylor, J. M.; Broni, B. and Krug, R. M. (1979): Nuclear accumulation of influenza viral RNA transcripts and the effects of cycloheximide, actinomycin D, and alpha-amanitin, J Virol (vol. 29), No. 2, pp. 744-52.

[181] Vreede, F. T.; Jung, T. E. and Brownlee, G. G. (2004): Model suggesting that replication of influenza virus is regulated by stabilization of replicative intermediates, J Virol (vol. 78), No. 17, pp. 9568-72.

[182] Biswas, S. K.; Boutz, P. L. and Nayak, D. P. (1998): Influenza virus nucleoprotein interacts with influenza virus polymerase proteins, J Virol (vol. 72), No. 7, pp. 5493-501.

[183] Mena, I.; Jambrina, E.; Albo, C.; Perales, B.; Ortin, J.; Arrese, M.; Vallejo, D. and Portela, A. (1999): Mutational analysis of influenza A virus nucleoprotein: identification of mutations that affect RNA replication, J Virol (vol. 73), No. 2, pp. 1186-94.

[184] Poole, E.; Elton, D.; Medcalf, L. and Digard, P. (2004): Functional domains of the influenza A virus PB2 protein: identification of NP- and PB1-binding sites, Virology (vol. 321), No. 1, pp. 120-33.

[185] Beaton, A. R. and Krug, R. M. (1986): Transcription antitermination during influenza viral template RNA synthesis requires the nucleocapsid protein and the absence of a 5' capped end, Proc Natl Acad Sci U S A (vol. 83), No. 17, pp. 6282-6.

[186] Vreede, F. T. and Brownlee, G. G. (2007): Influenza virion-derived viral ribonucleoproteins synthesize both mRNA and cRNA in vitro, J Virol (vol. 81), No. 5, pp. 2196-204.

[187] Vreede, F. T.; Ng, A. K.; Shaw, P. C. and Fodor, E. (2011): Stabilization of influenza virus replication intermediates is dependent on the RNA-binding but not the homo-oligomerization activity of the viral nucleoprotein, J Virol (vol. 85), No. 22, pp. 12073-8.

[188] Marklund, J. K.; Ye, Q.; Dong, J.; Tao, Y. J. and Krug, R. M. (2012): Sequence in the influenza A virus nucleoprotein required for viral polymerase binding and RNA synthesis, J Virol (vol. 86), No. 13, pp. 7292-7.

[189] Thierry, F. and Danos, O. (1982): Use of specific single stranded DNA probes cloned in M13 to study the RNA synthesis of four temperature-sensitive mutants of HK/68 influenza virus, Nucleic Acids Res (vol. 10), No. 9, pp. 2925-38.

[190] Falcon, A. M.; Marion, R. M.; Zurcher, T.; Gomez, P.; Portela, A.; Nieto, A. and Ortin, J. (2004): Defective RNA replication and late gene expression in temperature-sensitive influenza viruses expressing deleted forms of the NS1 protein, J Virol (vol. 78), No. 8, pp. 3880-8.

[191] Robb, N. C.; Smith, M.; Vreede, F. T. and Fodor, E. (2009): NS2/NEP protein regulates transcription and replication of the influenza virus RNA genome, J Gen Virol (vol. 90), No. Pt 6, pp. 1398-407.

[192] Manz, B.; Brunotte, L.; Reuther, P. and Schwemmle, M. (2012): Adaptive mutations in NEP compensate for defective H5N1 RNA replication in cultured human cells, Nat Commun (vol. 3), p. 802.

[193] Reuther, P.; Giese, S.; Gotz, V.; Kilb, N.; Manz, B.; Brunotte, L. and Schwemmle, M. (2014): Adaptive mutations in the nuclear export protein of human-derived H5N1 strains facilitate a polymerase activity-enhancing conformation, J Virol (vol. 88), No. 1, pp. 263-71.

[194] Cianci, C.; Tiley, L. and Krystal, M. (1995): Differential activation of the influenza virus polymerase via template RNA binding, J Virol (vol. 69), No. 7, pp. 3995-9.

[195] Li, M. L.; Ramirez, B. C. and Krug, R. M. (1998): RNA-dependent activation of primer RNA production by influenza virus polymerase: different regions of the same protein subunit constitute the two required RNA-binding sites, EMBO J (vol. 17), No. 19, pp. 5844-52.

[196] Honda, A.; Endo, A.; Mizumoto, K. and Ishihama, A. (2001): Differential roles of viral RNA and cRNA in functional modulation of the influenza virus RNA polymerase, J Biol Chem (vol. 276), No. 33, pp. 31179-85.

[197] Deng, T.; Vreede, F. T. and Brownlee, G. G. (2006): Different de novo initiation strategies are used by influenza virus RNA polymerase on its cRNA and viral RNA promoters during viral RNA replication, J Virol (vol. 80), No. 5, pp. 2337-48.

[198] Vreede, F. T.; Gifford, H. and Brownlee, G. G. (2008): Role of initiating nucleoside triphosphate concentrations in the regulation of influenza virus replication and transcription, J Virol (vol. 82), No. 14, pp. 6902-10.

[199] Zhang, S.; Wang, J.; Wang, Q. and Toyoda, T. (2010): Internal initiation of influenza virus replication of viral RNA and complementary RNA in vitro, J Biol Chem (vol. 285), No. 52, pp. 41194-201.

[200] Copeland, C. S.; Zimmer, K. P.; Wagner, K. R.; Healey, G. A.; Mellman, I. and Helenius, A. (1988): Folding, trimerization, and transport are sequential events in the biogenesis of influenza virus hemagglutinin, Cell (vol. 53), No. 2, pp. 197-209.

[201] Saito, T.; Taylor, G. and Webster, R. G. (1995): Steps in maturation of influenza A virus neuraminidase, J Virol (vol. 69), No. 8, pp. 5011-7.

[202] Sugrue, R. J. and Hay, A. J. (1991): Structural characteristics of the M2 protein of influenza A viruses: evidence that it forms a tetrameric channel, Virology (vol. 180), No. 2, pp. 617-24.

[203] Henkel, J. R.; Popovich, J. L.; Gibson, G. A.; Watkins, S. C. and Weisz, O. A. (1999): Selective perturbation of early endosome and/or trans-Golgi network pH but not lysosome pH by dose-dependent expression of influenza M2 protein, J Biol Chem (vol. 274), No. 14, pp. 9854-60.

[204] Schwarz, R. T.; Schmidt, M. F.; Anwer, U. and Klenk, H. D. (1977): Carbohydrates of influenza virus. I. Glycopeptides derived from viral glycoproteins after labeling with radioactive sugars, J Virol (vol. 23), No. 2, pp. 217-26.

[205] Chen, W.; Zhong, Y.; Qin, Y.; Sun, S. and Li, Z. (2012): The evolutionary pattern of glycosylation sites in influenza virus (H5N1) hemagglutinin and neuraminidase, PLoS One (vol. 7), No. 11, p. e49224.

[206] Kordyukova, L. V.; Serebryakova, M. V.; Baratova, L. A. and Veit, M. (2008): S acylation of the hemagglutinin of influenza viruses: mass spectrometry reveals site-specific attachment of stearic acid to a transmembrane cysteine, J Virol (vol. 82), No. 18, pp. 9288-92.

[207] Veit, M.; Klenk, H. D.; Kendal, A. and Rott, R. (1991): The M2 protein of influenza A virus is acylated, J Gen Virol (vol. 72 (Pt 6)), pp. 1461-5.

[208] Roth, M. G.; Compans, R. W.; Giusti, L.; Davis, A. R.; Nayak, D. P.; Gething, M. J. and Sambrook, J. (1983): Influenza virus hemagglutinin expression is polarized in cells infected with recombinant SV40 viruses carrying cloned hemagglutinin DNA, Cell (vol. 33), No. 2, pp. 435-43.

[209] Jones, L. V.; Compans, R. W.; Davis, A. R.; Bos, T. J. and Nayak, D. P. (1985): Surface expression of influenza virus neuraminidase, an amino-terminally anchored viral membrane glycoprotein, in polarized epithelial cells, Mol Cell Biol (vol. 5), No. 9, pp. 2181-9.

[210] Hughey, P. G.; Compans, R. W.; Zebedee, S. L. and Lamb, R. A. (1992): Expression of the influenza A virus M2 protein is restricted to apical surfaces of polarized epithelial cells, J Virol (vol. 66), No. 9, pp. 5542-52.

[211] Barman, S.; Adhikary, L.; Kawaoka, Y. and Nayak, D. P. (2003): Influenza A virus hemagglutinin containing basolateral localization signal does not alter the apical budding of a recombinant influenza A virus in polarized MDCK cells, Virology (vol. 305), No. 1, pp. 138-52.

[212] Mora, R.; Rodriguez-Boulan, E.; Palese, P. and Garcia-Sastre, A. (2002): Apical budding of a recombinant influenza A virus expressing a hemagglutinin protein with a basolateral localization signal, J Virol (vol. 76), No. 7, pp. 3544-53.

[213] Kundu, A.; Avalos, R. T.; Sanderson, C. M. and Nayak, D. P. (1996): Transmembrane domain of influenza virus neuraminidase, a type II protein, possesses an apical sorting signal in polarized MDCK cells, J Virol (vol. 70), No. 9, pp. 6508-15.

[214] Lin, S.; Naim, H. Y.; Rodriguez, A. C. and Roth, M. G. (1998): Mutations in the middle of the transmembrane domain reverse the polarity of transport of the influenza virus hemagglutinin in MDCK epithelial cells, J Cell Biol (vol. 142), No. 1, pp. 51-7.

[215] Barman, S. and Nayak, D. P. (2000): Analysis of the transmembrane domain of influenza virus neuraminidase, a type II transmembrane glycoprotein, for apical sorting and raft association, J Virol (vol. 74), No. 14, pp. 6538-45.

[216] Fiedler, K.; Kobayashi, T.; Kurzchalia, T. V. and Simons, K. (1993): Glycosphingolipid-enriched, detergent-insoluble complexes in protein sorting in epithelial cells, Biochemistry (vol. 32), No. 25, pp. 6365-73.

[217] Scheiffele, P.; Roth, M. G. and Simons, K. (1997): Interaction of influenza virus haemagglutinin with sphingolipid-cholesterol membrane domains via its transmembrane domain, EMBO J (vol. 16), No. 18, pp. 5501-8.

[218] Skibbens, J. E.; Roth, M. G. and Matlin, K. S. (1989): Differential extractability of influenza virus hemagglutinin during intracellular transport in polarized epithelial cells and nonpolar fibroblasts, J Cell Biol (vol. 108), No. 3, pp. 821-32.

[219] Engel, S.; Scolari, S.; Thaa, B.; Krebs, N.; Korte, T.; Herrmann, A. and Veit, M. (2010): FLIM-FRET and FRAP reveal association of influenza virus haemagglutinin with membrane rafts, Biochem J (vol. 425), No. 3, pp. 567-73.

[220] Hess, S. T.; Gould, T. J.; Gudheti, M. V.; Maas, S. A.; Mills, K. D. and Zimmerberg, J. (2007): Dynamic clustered distribution of hemagglutinin resolved at 40 nm in living cell membranes discriminates between raft theories, Proc Natl Acad Sci U S A (vol. 104), No. 44, pp. 17370-5. U

[221] Hess, S. T.; Kumar, M.; Verma, A.; Farrington, J.; Kenworthy, A. and Zimmerberg, J. (2005): Quantitative electron microscopy and fluorescence spectroscopy of the membrane distribution of influenza hemagglutinin, J Cell Biol (vol. 169), No. 6, pp. 965-76.

[222] Scolari, S.; Engel, S.; Krebs, N.; Plazzo, A. P.; De Almeida, R. F.; Prieto, M.; Veit, M. and Herrmann, A. (2009): Lateral distribution of the transmembrane domain of influenza virus hemagglutinin revealed by time-resolved fluorescence imaging, J Biol Chem (vol. 284), No. 23, pp. 15708-16.

[223] Takeda, M.; Leser, G. P.; Russell, C. J. and Lamb, R. A. (2003): Influenza virus hemagglutinin concentrates in lipid raft microdomains for efficient viral fusion, Proc Natl Acad Sci U S A (vol. 100), No. 25, pp. 14610-7.

[224] Simons, K. and van Meer, G. (1988): Lipid sorting in epithelial cells, Biochemistry (vol. 27), No. 17, pp. 6197-202.

[225] van Meer, G. and Simons, K. (1988): Lipid polarity and sorting in epithelial cells, J Cell Biochem (vol. 36), No. 1, pp. 51-8.

[226] Simons, K. and Ikonen, E. (1997): Functional rafts in cell membranes, Nature (vol. 387), No. 6633, pp. 569-72.

[227] Schuck, S. and Simons, K. (2004): Polarized sorting in epithelial cells: raft clustering and the biogenesis of the apical membrane, J Cell Sci (vol. 117), No. Pt 25, pp. 5955-64.

[228] Barman, S.; Adhikary, L.; Chakrabarti, A. K.; Bernas, C.; Kawaoka, Y. and Nayak, D. P. (2004): Role of transmembrane domain and cytoplasmic tail amino acid sequences of influenza a virus neuraminidase in raft association and virus budding, J Virol (vol. 78), No. 10, pp. 5258-69. U

[229] Tall, R. D.; Alonso, M. A. and Roth, M. G. (2003): Features of influenza HA required for apical sorting differ from those required for association with DRMs or MAL, Traffic (vol. 4), No. 12, pp. 838-49. U

[230] Ohkura, T.; Momose, F.; Ichikawa, R.; Takeuchi, K. and Morikawa, Y. (2014): Influenza A Virus Hemagglutinin and Neuraminidase Mutually Accelerate Their Apical Targeting through Clustering of Lipid Rafts, J Virol (vol. 88), No. 17, pp. 10039-55.

[231] Engel, S.; de Vries, M.; Herrmann, A. and Veit, M. (2012): Mutation of a raft-targeting signal in the transmembrane region retards transport of influenza virus hemagglutinin through the Golgi, FEBS Lett (vol. 586), No. 3, pp. 277-82.

[232] Chazal, N. and Gerlier, D. (2003): Virus entry, assembly, budding, and membrane rafts, Microbiol Mol Biol Rev (vol. 67), No. 2, pp. 226-37, table of contents.

[233] Suomalainen, M. (2002): Lipid rafts and assembly of enveloped viruses, Traffic (vol. 3), No. 10, pp. 705-9.

[234] Scheiffele, P.; Rietveld, A.; Wilk, T. and Simons, K. (1999): Influenza viruses select ordered lipid domains during budding from the plasma membrane, J Biol Chem (vol. 274), No. 4, pp. 2038-44.

[235] Goswami, D.; Gowrishankar, K.; Bilgrami, S.; Ghosh, S.; Raghupathy, R.; Chadda, R.; Vishwakarma, R.; Rao, M. and Mayor, S. (2008): Nanoclusters of GPI-anchored proteins are formed by cortical actin-driven activity, Cell (vol. 135), No. 6, pp. 1085-97.

[236] Kusumi, A.; Nakada, C.; Ritchie, K.; Murase, K.; Suzuki, K.; Murakoshi, H.; Kasai, R. S.; Kondo, J. and Fujiwara, T. (2005): Paradigm shift of the plasma membrane concept from the two-dimensional continuum fluid to the partitioned fluid: high-speed single-molecule tracking of membrane molecules, Annu Rev Biophys Biomol Struct (vol. 34), pp. 351-78.

[237] Mueller, V.; Ringemann, C.; Honigmann, A.; Schwarzmann, G.; Medda, R.; Leutenegger, M.; Polyakova, S.; Belov, V. N.; Hell, S. W. and Eggeling, C. (2011): STED nanoscopy reveals molecular details of cholesterol- and cytoskeleton-modulated lipid interactions in living cells, Biophys J (vol. 101), No. 7, pp. 1651-60.

[238] Chichili, G. R. and Rodgers, W. (2009): Cytoskeleton-membrane interactions in membrane raft structure, Cell Mol Life Sci (vol. 66), No. 14, pp. 2319-28.

[239] Viola, A. and Gupta, N. (2007): Tether and trap: regulation of membrane-raft dynamics by actin-binding proteins, Nat Rev Immunol (vol. 7), No. 11, pp. 889-96.

[240] Gudheti, M. V.; Curthoys, N. M.; Gould, T. J.; Kim, D.; Gunewardene, M. S.; Gabor, K. A.; Gosse, J. A.; Kim, C. H.; Zimmerberg, J. and Hess, S. T. (2013): Actin mediates the nanoscale membrane organization of the clustered membrane protein influenza hemagglutinin, Biophys J (vol. 104), No. 10, pp. 2182-92. U

[241] Marjuki, H.; Alam, M. I.; Ehrhardt, C.; Wagner, R.; Planz, O.; Klenk, H. D.; Ludwig, S. and Pleschka, S. (2006): Membrane accumulation of influenza A virus hemagglutinin triggers nuclear export of the viral genome via protein kinase Calpha-mediated activation of ERK signaling, J Biol Chem (vol. 281), No. 24, pp. 16707-15.

[242] Eisenberg, S.; Shvartsman, D. E.; Ehrlich, M. and Henis, Y. I. (2006): Clustering of raft-associated proteins in the external membrane leaflet modulates internal leaflet H-ras diffusion and signaling, Mol Cell Biol (vol. 26), No. 19, pp. 7190-200.

[243] Simpson-Holley, M.; Ellis, D.; Fisher, D.; Elton, D.; McCauley, J. and Digard, P. (2002): A functional link between the actin cytoskeleton and lipid rafts during budding of filamentous influenza virions, Virology (vol. 301), No. 2, pp. 212-25.

[244] Shaw, M. L.; Stone, K. L.; Colangelo, C. M.; Gulcicek, E. E. and Palese, P. (2008): Cellular proteins in influenza virus particles, PLoS Pathog (vol. 4), No. 6, p. e1000085.

[245] Thaa, B.; Herrmann, A. and Veit, M. (2010): Intrinsic cytoskeleton-dependent clustering of influenza virus M2 protein with hemagglutinin assessed by FLIM-FRET, J Virol (vol. 84), No. 23, pp. 12445-9.

[246] McCown, M. F. and Pekosz, A. (2006): Distinct domains of the influenza a virus M2 protein cytoplasmic tail mediate binding to the M1 protein and facilitate infectious virus production, J Virol (vol. 80), No. 16, pp. 8178-89.

[247] Bretscher, M. S. and Munro, S. (1993): Cholesterol and the Golgi apparatus, Science (vol. 261), No. 5126, pp. 1280-1.

[248] Mouritsen, O. G. (2011): Model answers to lipid membrane questions, Cold Spring Harb Perspect Biol (vol. 3), No. 9, p. a004622.

[249] Thaa, B.; Siche, S.; Herrmann, A. and Veit, M. (2014): Acylation and cholesterol binding are not required for targeting of influenza A virus M2 protein to the hemagglutinin-defined budozone, FEBS Lett (vol. 588), No. 6, pp. 1031-6.

[250] Barman, S. and Nayak, D. P. (2007): Lipid raft disruption by cholesterol depletion enhances influenza A virus budding from MDCK cells, J Virol (vol. 81), No. 22, pp. 12169-78.

[251] Henkel, J. R.; Apodaca, G.; Altschuler, Y.; Hardy, S. and Weisz, O. A. (1998): Selective perturbation of apical membrane traffic by expression of influenza M2, an acid-activated ion channel, in polarized madin-darby canine kidney cells, Mol Biol Cell (vol. 9), No. 9, pp. 2477-90.

[252] Bruce, E. A.; Digard, P. and Stuart, A. D. (2010): The Rab11 pathway is required for influenza A virus budding and filament formation, J Virol (vol. 84), No. 12, pp. 5848-59.

[253] Ciampor, F.; Thompson, C. A.; Grambas, S. and Hay, A. J. (1992): Regulation of pH by the M2 protein of influenza A viruses, Virus Res (vol. 22), No. 3, pp. 247-58.

[254] Sakaguchi, T.; Leser, G. P. and Lamb, R. A. (1996): The ion channel activity of the influenza virus M2 protein affects transport through the Golgi apparatus, J Cell Biol (vol. 133), No. 4, pp. 733-47.

[255] Takeuchi, K. and Lamb, R. A. (1994): Influenza virus M2 protein ion channel activity stabilizes the native form of fowl plague virus hemagglutinin during intracellular transport, J Virol (vol. 68), No. 2, pp. 911-9.

[256] Henkel, J. R.; Gibson, G. A.; Poland, P. A.; Ellis, M. A.; Hughey, R. P. and Weisz, O. A. (2000): Influenza M2 proton channel activity selectively inhibits trans-Golgi network release of apical membrane and secreted proteins in polarized Madin-Darby canine kidney cells, J Cell Biol (vol. 148), No. 3, pp. 495-504.

[257] Thaa, B.; Herrmann, A. and Veit, M. (2009): The polybasic region is not essential for membrane binding of the matrix protein M1 of influenza virus, Virology (vol. 383), No. 1, pp. 150-5.

[258] Ye, Z.; Robinson, D. and Wagner, R. R. (1995): Nucleus-targeting domain of the matrix protein (M1) of influenza virus, J Virol (vol. 69), No. 3, pp. 1964-70.

[259] Huang, X.; Liu, T.; Muller, J.; Levandowski, R. A. and Ye, Z. (2001): Effect of influenza virus matrix protein and viral RNA on ribonucleoprotein formation and nuclear export, Virology (vol. 287), No. 2, pp. 405-16.

[260] Bui, M.; Wills, E. G.; Helenius, A. and Whittaker, G. R. (2000): Role of the influenza virus M1 protein in nuclear export of viral ribonucleoproteins, J Virol (vol. 74), No. 4, pp. 1781-6.

[261] Hutchinson, E. C.; Denham, E. M.; Thomas, B.; Trudgian, D. C.; Hester, S. S.; Ridlova, G.; York, A.; Turrell, L. and Fodor, E. (2012): Mapping the phosphoproteome of influenza A and B viruses by mass spectrometry, PLoS Pathog (vol. 8), No. 11, p. e1002993.

[262] Wang, S.; Zhao, Z.; Bi, Y.; Sun, L.; Liu, X. and Liu, W. (2013): Tyrosine 132 phosphorylation of influenza A virus M1 protein is crucial for virus replication by controlling the nuclear import of M1, J Virol (vol. 87), No. 11, pp. 6182-91.

[263] Whittaker, G.; Kemler, I. and Helenius, A. (1995): Hyperphosphorylation of mutant influenza virus matrix protein, M1, causes its retention in the nucleus, J Virol (vol. 69), No. 1, pp. 439-45.

[264] Neumann, G.; Hughes, M. T. and Kawaoka, Y. (2000): Influenza A virus NS2 protein mediates vRNP nuclear export through NES-independent interaction with hCRM1, EMBO J (vol. 19), No. 24, pp. 6751-8.

[265] Elton, D.; Simpson-Holley, M.; Archer, K.; Medcalf, L.; Hallam, R.; McCauley, J. and Digard, P. (2001): Interaction of the influenza virus nucleoprotein with the cellular CRM1-mediated nuclear export pathway, J Virol (vol. 75), No. 1, pp. 408-19.

[266] Ma, K.; Roy, A. M. and Whittaker, G. R. (2001): Nuclear export of influenza virus ribonucleoproteins: identification of an export intermediate at the nuclear periphery, Virology (vol. 282), No. 2, pp. 215-20.

[267] Watanabe, K.; Takizawa, N.; Katoh, M.; Hoshida, K.; Kobayashi, N. and Nagata, K. (2001): Inhibition of nuclear export of ribonucleoprotein complexes of influenza virus by leptomycin B, Virus Res (vol. 77), No. 1, pp. 31-42.

[268] Iwatsuki-Horimoto, K.; Horimoto, T.; Fujii, Y. and Kawaoka, Y. (2004): Generation of influenza A virus NS2 (NEP) mutants with an altered nuclear export signal sequence, J Virol (vol. 78), No. 18, pp. 10149-55.

[269] Akarsu, H.; Burmeister, W. P.; Petosa, C.; Petit, I.; Muller, C. W.; Ruigrok, R. W. and Baudin, F. (2003): Crystal structure of the M1 protein-binding domain of the influenza A virus nuclear export protein (NEP/NS2), EMBO J (vol. 22), No. 18, pp. 4646-55.

[270] Shimizu, T.; Takizawa, N.; Watanabe, K.; Nagata, K. and Kobayashi, N. (2011): Crucial role of the influenza virus NS2 (NEP) C-terminal domain in M1 binding and nuclear export of vRNP, FEBS Lett (vol. 585), No. 1, pp. 41-6.

[271] Ward, A. C.; Castelli, L. A.; Lucantoni, A. C.; White, J. F.; Azad, A. A. and Macreadie, I. G. (1995): Expression and analysis of the NS2 protein of influenza A virus, Arch Virol (vol. 140), No. 11, pp. 2067-73.

[272] Paterson, D. and Fodor, E. (2012): Emerging roles for the influenza A virus nuclear export protein (NEP), PLoS Pathog (vol. 8), No. 12, p. e1003019.

[273] Cao, S.; Liu, X.; Yu, M.; Li, J.; Jia, X.; Bi, Y.; Sun, L.; Gao, G. F. and Liu, W. (2012): A nuclear export signal in the matrix protein of Influenza A virus is required for efficient virus replication, J Virol (vol. 86), No. 9, pp. 4883-91.

[274] Yu, M.; Liu, X.; Cao, S.; Zhao, Z.; Zhang, K.; Xie, Q.; Chen, C.; Gao, S.; Bi, Y.; Sun, L.; Ye, X.; Gao, G. F. and Liu, W. (2012): Identification and characterization of three novel nuclear export signals in the influenza A virus nucleoprotein, J Virol (vol. 86), No. 9, pp. 4970-80.

[275] Ye, Z.; Liu, T.; Offringa, D. P.; McInnis, J. and Levandowski, R. A. (1999): Association of influenza virus matrix protein with ribonucleoproteins, J Virol (vol. 73), No. 9, pp. 7467-73.

[276] Wu, C. Y.; Jeng, K. S. and Lai, M. M. (2011): The SUMOylation of matrix protein M1 modulates the assembly and morphogenesis of influenza A virus, J Virol (vol. 85), No. 13, pp. 6618-28.

[277] Sato, Y.; Yoshioka, K.; Suzuki, C.; Awashima, S.; Hosaka, Y.; Yewdell, J. and Kuroda, K. (2003): Localization of influenza virus proteins to nuclear dot 10 structures in influenza virus-infected cells, Virology (vol. 310), No. 1, pp. 29-40.

[278] Santiago, A.; Li, D.; Zhao, L. Y.; Godsey, A. and Liao, D. (2013): p53 SUMOylation promotes its nuclear export by facilitating its release from the nuclear export receptor CRM1, Mol Biol Cell (vol. 24), No. 17, pp. 2739-52.

[279] Zhirnov, O. P. (1992): Isolation of matrix protein M1 from influenza viruses by acid-dependent extraction with nonionic detergent, Virology (vol. 186), No. 1, pp. 324-30.

[280] Amorim, M. J.; Bruce, E. A.; Read, E. K.; Foeglein, A.; Mahen, R.; Stuart, A. D. and Digard, P. (2011): A Rab11- and microtubule-dependent mechanism for cytoplasmic transport of influenza A virus viral RNA, J Virol (vol. 85), No. 9, pp. 4143-56.

[281] Enami, M. and Enami, K. (1996): Influenza virus hemagglutinin and neuraminidase glycoproteins stimulate the membrane association of the matrix protein, J Virol (vol. 70), No. 10, pp. 6653-7.

[282] Shishkov, A. V.; Bogacheva, E. N.; Dolgov, A. A.; Chulichkov, A. L.; Knyazev, D. G.; Fedorova, N. V.; Ksenofontov, A. L.; Kordyukova, L. V.; Lukashina, E. V.; Mirsky, V. M. and Baratova, L. A. (2009): The in situ structural characterization of the influenza A virus matrix M1 protein within a virion, Protein Pept Lett (vol. 16), No. 11, pp. 1407-13.

[283] Ruigrok, Rob; Baudin, Florence; Petit, Isabelle and Weissenhorn, Winfried (2001): Role of influenza virus M1 protein in the viral budding process, International Congress Series (vol. 1219), No. 0, pp. 397-404.

[284] Fujiyoshi, Y.; Kume, N. P.; Sakata, K. and Sato, S. B. (1994): Fine structure of influenza A virus observed by electron cryo-microscopy, EMBO J (vol. 13), No. 2, pp. 318-26.

[285] Hilsch, M.; Goldenbogen, B.; Sieben, C.; Hofer, C. T.; Rabe, J. P.; Klipp, E.; Herrmann, A. and Chiantia, S. (2014): Influenza A Matrix Protein M1 Multimerizes upon Binding to Lipid Membranes, Biophys J (vol. 107), No. 4, pp. 912-23.

[286] Yeung, T.; Gilbert, G. E.; Shi, J.; Silvius, J.; Kapus, A. and Grinstein, S. (2008): Membrane phosphatidylserine regulates surface charge and protein localization, Science (vol. 319), No. 5860, pp. 210-3.

[287] Gomez-Puertas, P.; Albo, C.; Perez-Pastrana, E.; Vivo, A. and Portela, A. (2000): Influenza virus matrix protein is the major driving force in virus budding, J Virol (vol. 74), No. 24, pp. 11538-47.

[288] Chen, B. J.; Leser, G. P.; Morita, E. and Lamb, R. A. (2007): Influenza virus hemagglutinin and neuraminidase, but not the matrix protein, are required for assembly and budding of plasmid-derived virus-like particles, J Virol (vol. 81), No. 13, pp. 7111-23.

[289] Wang, D.; Harmon, A.; Jin, J.; Francis, D. H.; Christopher-Hennings, J.; Nelson, E.; Montelaro, R. C. and Li, F. (2010): The lack of an inherent membrane targeting signal is responsible for the failure of the matrix (M1) protein of influenza A virus to bud into virus-like particles, J Virol (vol. 84), No. 9, pp. 4673-81. U

[290] Grantham, M. L.; Stewart, S. M.; Lalime, E. N. and Pekosz, A. (2010): Tyrosines in the influenza A virus M2 protein cytoplasmic tail are critical for production of infectious virus particles, J Virol (vol. 84), No. 17, pp. 8765-76.

[291] Zhang, J.; Leser, G. P.; Pekosz, A. and Lamb, R. A. (2000): The cytoplasmic tails of the influenza virus spike glycoproteins are required for normal genome packaging, Virology (vol. 269), No. 2, pp. 325-34.

[292] Chase, G. P.; Rameix-Welti, M. A.; Zvirbliene, A.; Zvirblis, G.; Gotz, V.; Wolff, T.; Naffakh, N. and Schwemmle, M. (2011): Influenza virus ribonucleoprotein complexes gain preferential access to cellular export machinery through chromatin targeting, PLoS Pathog (vol. 7), No. 9, p. e1002187.

[293] Pleschka, S.; Wolff, T.; Ehrhardt, C.; Hobom, G.; Planz, O.; Rapp, U. R. and Ludwig, S. (2001): Influenza virus propagation is impaired by inhibition of the Raf/MEK/ERK signalling cascade, Nat Cell Biol (vol. 3), No. 3, pp. 301-5.

[294] Wurzer, W. J.; Planz, O.; Ehrhardt, C.; Giner, M.; Silberzahn, T.; Pleschka, S. and Ludwig, S. (2003): Caspase 3 activation is essential for efficient influenza virus propagation, EMBO J (vol. 22), No. 11, pp. 2717-28.

[295] Kawaguchi, A.; Matsumoto, K. and Nagata, K. (2012): YB-1 functions as a porter to lead influenza virus ribonucleoprotein complexes to microtubules, J Virol (vol. 86), No. 20, pp. 11086-95.

[296] Avilov, S. V.; Moisy, D.; Naffakh, N. and Cusack, S. (2012): Influenza A virus progeny vRNP trafficking in live infected cells studied with the virus-encoded fluorescently tagged PB2 protein, Vaccine (vol. 30), No. 51, pp. 7411-7.

[297] Eisfeld, A. J.; Kawakami, E.; Watanabe, T.; Neumann, G. and Kawaoka, Y. (2011): RAB11A is essential for transport of the influenza virus genome to the plasma membrane, J Virol (vol. 85), No. 13, pp. 6117-26.

[298] Momose, F.; Sekimoto, T.; Ohkura, T.; Jo, S.; Kawaguchi, A.; Nagata, K. and Morikawa, Y. (2011): Apical transport of influenza A virus ribonucleoprotein requires Rab11-positive recycling endosome, PLoS One (vol. 6), No. 6, p. e21123.

[299] Carrasco, M.; Amorim, M. J. and Digard, P. (2004): Lipid raft-dependent targeting of the influenza A virus nucleoprotein to the apical plasma membrane, Traffic (vol. 5), No. 12, pp. 979-92.

[300] Nayak, D. P.; Hui, E. K. and Barman, S. (2004): Assembly and budding of influenza virus, Virus Res (vol. 106), No. 2, pp. 147-65.

[301] Steinhauer, D. A. and Skehel, J. J. (2002): Genetics of influenza viruses, Annu Rev Genet (vol. 36), pp. 305-32.

[302] Duhaut, S. and Dimmock, N. J. (2000): Approximately 150 nucleotides from the 5' end of an influenza A segment 1 defective virion RNA are needed for genome stability during passage of defective virus in infected cells, Virology (vol. 275), No. 2, pp. 278-85.

[303] Duhaut, S. D. and Dimmock, N. J. (2002): Defective segment 1 RNAs that interfere with production of infectious influenza A virus require at least 150 nucleotides of 5' sequence: evidence from a plasmid-driven system, J Gen Virol (vol. 83), No. Pt 2, pp. 403-11.

[304] Fujii, Y.; Goto, H.; Watanabe, T.; Yoshida, T. and Kawaoka, Y. (2003): Selective incorporation of influenza virus RNA segments into virions, Proc Natl Acad Sci U S A (vol. 100), No. 4, pp. 2002-7.

[305] Fournier, E.; Moules, V.; Essere, B.; Paillart, J. C.; Sirbat, J. D.; Cavalier, A.; Rolland, J. P.; Thomas, D.; Lina, B.; Isel, C. and Marquet, R. (2012): Interaction network linking the human H3N2 influenza A virus genomic RNA segments, Vaccine (vol. 30), No. 51, pp. 7359-67.

[306] Fournier, E.; Moules, V.; Essere, B.; Paillart, J. C.; Sirbat, J. D.; Isel, C.; Cavalier, A.; Rolland, J. P.; Thomas, D.; Lina, B. and Marquet, R. (2012): A supramolecular assembly formed by influenza A virus genomic RNA segments, Nucleic Acids Res (vol. 40), No. 5, pp. 2197-209.

[307] Vijayakrishnan, S.; Loney, C.; Jackson, D.; Suphamungmee, W.; Rixon, F. J. and Bhella, D. (2013): Cryotomography of budding influenza A virus reveals filaments with diverse morphologies that mostly do not bear a genome at their distal end, PLoS Pathog (vol. 9), No. 6, p. e1003413. U

[308] Gerber, M.; Isel, C.; Moules, V. and Marquet, R. (2014): Selective packaging of the influenza A genome and consequences for genetic reassortment, Trends Microbiol (vol. 22), No. 8, pp. 446-55.

[309] Gog, J. R.; Afonso Edos, S.; Dalton, R. M.; Leclercq, I.; Tiley, L.; Elton, D.; von Kirchbach, J. C.; Naffakh, N.; Escriou, N. and Digard, P. (2007): Codon conservation in the influenza A virus genome defines RNA packaging signals, Nucleic Acids Res (vol. 35), No. 6, pp. 1897-907.

[310] Hutchinson, E. C.; Curran, M. D.; Read, E. K.; Gog, J. R. and Digard, P. (2008): Mutational analysis of cis-acting RNA signals in segment 7 of influenza A virus, J Virol (vol. 82), No. 23, pp. 11869-79. U

[311] Hutchinson, E. C.; Wise, H. M.; Kudryavtseva, K.; Curran, M. D. and Digard, P. (2009): Characterisation of influenza A viruses with mutations in segment 5 packaging signals, Vaccine (vol. 27), No. 45, pp. 6270-5.

[312] Marsh, G. A.; Hatami, R. and Palese, P. (2007): Specific residues of the influenza A virus hemagglutinin viral RNA are important for efficient packaging into budding virions, J Virol (vol. 81), No. 18, pp. 9727-36.

[313] Marsh, G. A.; Rabadan, R.; Levine, A. J. and Palese, P. (2008): Highly conserved regions of influenza a virus polymerase gene segments are critical for efficient viral RNA packaging, J Virol (vol. 82), No. 5, pp. 2295-304.

[314] Muramoto, Y.; Takada, A.; Fujii, K.; Noda, T.; Iwatsuki-Horimoto, K.; Watanabe, S.; Horimoto, T.; Kida, H. and Kawaoka, Y. (2006): Hierarchy among viral RNA (vRNA) segments in their role in vRNA incorporation into influenza A virions, J Virol (vol. 80), No. 5, pp. 2318-25.

[315] Gao, Q.; Chou, Y. Y.; Doganay, S.; Vafabakhsh, R.; Ha, T. and Palese, P. (2012): The influenza A virus PB2, PA, NP, and M segments play a pivotal role during genome packaging, J Virol (vol. 86), No. 13, pp. 7043-51. U

[316] Gavazzi, C.; Yver, M.; Isel, C.; Smyth, R. P.; Rosa-Calatrava, M.; Lina, B.; Moules, V. and Marquet, R. (2013): A functional sequence-specific interaction between influenza A virus genomic RNA segments, Proc Natl Acad Sci U S A (vol. 110), No. 41, pp. 16604-9.

[317] Li, Z.; Watanabe, T.; Hatta, M.; Watanabe, S.; Nanbo, A.; Ozawa, M.; Kakugawa, S.; Shimojima, M.; Yamada, S.; Neumann, G. and Kawaoka, Y. (2009): Mutational analysis of conserved amino acids in the influenza A virus nucleoprotein, J Virol (vol. 83), No. 9, pp. 4153-62.

[318] Gavazzi, C.; Isel, C.; Fournier, E.; Moules, V.; Cavalier, A.; Thomas, D.; Lina, B. and Marquet, R. (2013): An in vitro network of intermolecular interactions between viral RNA segments of an avian H5N2 influenza A virus: comparison with a human H3N2 virus, Nucleic Acids Res (vol. 41), No. 2, pp. 1241-54.

[319] Enami, M.; Sharma, G.; Benham, C. and Palese, P. (1991): An influenza virus containing nine different RNA segments, Virology (vol. 185), No. 1, pp. 291-8.

[320] Gao, Q.; Brydon, E. W. and Palese, P. (2008): A seven-segmented influenza A virus expressing the influenza C virus glycoprotein HEF, J Virol (vol. 82), No. 13, pp. 6419-26.

[321] Scholtissek, C.; Rohde, W.; Harms, E.; Rott, R.; Orlich, M. and Boschek, C. B. (1978): A possible partial heterozygote of an influenza A virus, Virology (vol. 89), No. 2, pp. 506-16.

[322] Liang, Y.; Huang, T.; Ly, H. and Parslow, T. G. (2008): Mutational analyses of packaging signals in influenza virus PA, PB1, and PB2 genomic RNA segments, J Virol (vol. 82), No. 1, pp. 229-36. U

[323] Bancroft, C. T. and Parslow, T. G. (2002): Evidence for segment-nonspecific packaging of the influenza a virus genome, J Virol (vol. 76), No. 14, pp. 7133-9.

[324] Fujii, K.; Ozawa, M.; Iwatsuki-Horimoto, K.; Horimoto, T. and Kawaoka, Y. (2009): Incorporation of influenza A virus genome segments does not absolutely require wild-type sequences, J Gen Virol (vol. 90), No. Pt 7, pp. 1734-40.

[325] Ozawa, M.; Maeda, J.; Iwatsuki-Horimoto, K.; Watanabe, S.; Goto, H.; Horimoto, T. and Kawaoka, Y. (2009): Nucleotide sequence requirements at the 5' end of the influenza A virus M RNA segment for efficient virus replication, J Virol (vol. 83), No. 7, pp. 3384-8. U

[326] Lakdawala, S. S.; Wu, Y.; Wawrzusin, P.; Kabat, J.; Broadbent, A. J.; Lamirande, E. W.; Fodor, E.; Altan-Bonnet, N.; Shroff, H. and Subbarao, K. (2014): Influenza a virus assembly intermediates fuse in the cytoplasm, PLoS Pathog (vol. 10), No. 3, p. e1003971.

[327] Winter, G. and Fields, S. (1981): The structure of the gene encoding the nucleoprotein of human influenza virus A/PR/8/34, Virology (vol. 114), No. 2, pp. 423-8. U

[328] Shu, L. L.; Bean, W. J. and Webster, R. G. (1993): Analysis of the evolution and variation of the human influenza A virus nucleoprotein gene from 1933 to 1990, J Virol (vol. 67), No. 5, pp. 2723-9.

[329] ElHefnawi, M.; Alaidi, O.; Mohamed, N.; Kamar, M.; El-Azab, I.; Zada, S. and Siam, R. (2011): Identification of novel conserved functional motifs across most Influenza A viral strains, Virol J (vol. 8), p. 44.

[330] Scholtissek, C.; Ludwig, S. and Fitch, W. M. (1993): Analysis of influenza A virus nucleoproteins for the assessment of molecular genetic mechanisms leading to new phylogenetic virus lineages, Arch Virol (vol. 131), No. 3-4, pp. 237-50.

[331] Ng, A. K.; Wang, J. H. and Shaw, P. C. (2009): Structure and sequence analysis of influenza A virus nucleoprotein, Sci China C Life Sci (vol. 52), No. 5, pp. 439-49.

[332] Portela, A. and Digard, P. (2002): The influenza virus nucleoprotein: a multifunctional RNA-binding protein pivotal to virus replication, J Gen Virol (vol. 83), No. Pt 4, pp. 723-34.

[333] Ng, A. K.; Zhang, H.; Tan, K.; Li, Z.; Liu, J. H.; Chan, P. K.; Li, S. M.; Chan, W. Y.; Au, S. W.; Joachimiak, A.; Walz, T.; Wang, J. H. and Shaw, P. C. (2008): Structure of the influenza virus A H5N1 nucleoprotein: implications for RNA binding, oligomerization, and vaccine design, FASEB J (vol. 22), No. 10, pp. 3638-47.

[334] Ruigrok, R. W. and Baudin, F. (1995): Structure of influenza virus ribonucleoprotein particles. II. Purified RNA-free influenza virus ribonucleoprotein forms structures that are indistinguishable from the intact influenza virus ribonucleoprotein particles, J Gen Virol (vol. 76 (Pt 4)), pp. 1009-14.

[335] Tarus, B.; Bakowiez, O.; Chenavas, S.; Duchemin, L.; Estrozi, L. F.; Bourdieu, C.; Lejal, N.; Bernard, J.; Moudjou, M.; Chevalier, C.; Delmas, B.; Ruigrok, R. W.; Di Primo, C. and Slama-Schwok, A. (2012): Oligomerization paths of the nucleoprotein of influenza A virus, Biochimie (vol. 94), No. 3, pp. 776-85.

[336] Elton, D.; Medcalf, L.; Bishop, K.; Harrison, D. and Digard, P. (1999): Identification of amino acid residues of influenza virus nucleoprotein essential for RNA binding, J Virol (vol. 73), No. 9, pp. 7357-67.

[337] Tarus, B.; Chevalier, C.; Richard, C. A.; Delmas, B.; Di Primo, C. and Slama-Schwok, A. (2012): Molecular dynamics studies of the nucleoprotein of influenza A virus: role of the protein flexibility in RNA binding, PLoS One (vol. 7), No. 1, p. e30038. U

[338] Goldstein, E. A. and Pons, M. W. (1970): The effect of polyvinylsulfate on the ribonucleoprotein of influenza virus, Virology (vol. 41), No. 2, pp. 382-4.

[339] Digard, P.; Elton, D.; Bishop, K.; Medcalf, E.; Weeds, A. and Pope, B. (1999): Modulation of nuclear localization of the influenza virus nucleoprotein through interaction with actin filaments, J Virol (vol. 73), No. 3, pp. 2222-31. U

[340] Boulo, S.; Akarsu, H.; Lotteau, V.; Muller, C. W.; Ruigrok, R. W. and Baudin, F. (2011): Human importin alpha and RNA do not compete for binding to influenza A virus nucleoprotein, Virology (vol. 409), No. 1, pp. 84-90.

[341] Martin-Benito, J.; Area, E.; Ortega, J.; Llorca, O.; Valpuesta, J. M.; Carrascosa, J. L. and Ortin, J. (2001): Three-dimensional reconstruction of a recombinant influenza virus ribonucleoprotein particle, EMBO Rep (vol. 2), No. 4, pp. 313-7.

[342] Medcalf, L.; Poole, E.; Elton, D. and Digard, P. (1999): Temperature-sensitive lesions in two influenza A viruses defective for replicative transcription disrupt RNA binding by the nucleoprotein, J Virol (vol. 73), No. 9, pp. 7349-56.

[343] Newcomb, L. L.; Kuo, R. L.; Ye, Q.; Jiang, Y.; Tao, Y. J. and Krug, R. M. (2009): Interaction of the influenza a virus nucleocapsid protein with the viral RNA polymerase potentiates unprimed viral RNA replication, J Virol (vol. 83), No. 1, pp. 29-36.

[344] Labadie, K.; Dos Santos Afonso, E.; Rameix-Welti, M. A.; van der Werf, S. and Naffakh, N. (2007): Host-range determinants on the PB2 protein of influenza A viruses control the interaction between the viral polymerase and nucleoprotein in human cells, Virology (vol. 362), No. 2, pp. 271-82.

[345] Cauldwell, A. V.; Moncorge, O. and Barclay, W. S. (2013): Unstable polymerase-nucleoprotein interaction is not responsible for avian influenza virus polymerase restriction in human cells, J Virol (vol. 87), No. 2, pp. 1278-84.

[346] Tripathi, S.; Batra, J.; Cao, W.; Sharma, K.; Patel, J. R.; Ranjan, P.; Kumar, A.; Katz, J. M.; Cox, N. J.; Lal, R. B.; Sambhara, S. and Lal, S. K. (2013): Influenza A virus nucleoprotein induces apoptosis in human airway epithelial cells: implications of a novel interaction between nucleoprotein and host protein Clusterin, Cell Death Dis (vol. 4), p. e562.

[347] Sharma, K.; Tripathi, S.; Ranjan, P.; Kumar, P.; Garten, R.; Deyde, V.; Katz, J. M.; Cox, N. J.; Lal, R. B.; Sambhara, S. and Lal, S. K. (2011): Influenza A virus nucleoprotein exploits Hsp40 to inhibit PKR activation, PLoS One (vol. 6), No. 6, p. e20215.

[348] Ludwig, S.; Pleschka, S.; Planz, O. and Wolff, T. (2006): Ringing the alarm bells: signalling and apoptosis in influenza virus infected cells, Cell Microbiol (vol. 8), No. 3, pp. 375-86.

[349] Kakugawa, S.; Shimojima, M.; Neumann, G.; Goto, H. and Kawaoka, Y. (2009): RuvB-like protein 2 is a suppressor of influenza A virus polymerases, J Virol (vol. 83), No. 13, pp. 6429-34. U

[350] Wisskirchen, C.; Ludersdorfer, T. H.; Muller, D. A.; Moritz, E. and Pavlovic, J. (2011): The cellular RNA helicase UAP56 is required for prevention of double-stranded RNA formation during influenza A virus infection, J Virol (vol. 85), No. 17, pp. 8646-55.

[351] Moisy, D.; Avilov, S. V.; Jacob, Y.; Laoide, B. M.; Ge, X.; Baudin, F.; Naffakh, N. and Jestin, J. L. (2012): HMGB1 protein binds to influenza virus nucleoprotein and promotes viral replication, J Virol (vol. 86), No. 17, pp. 9122-33.

[352] Garcia-Robles, I.; Akarsu, H.; Muller, C. W.; Ruigrok, R. W. and Baudin, F. (2005): Interaction of influenza virus proteins with nucleosomes, Virology (vol. 332), No. 1, pp. 329-36.

[353] Alfonso, R.; Lutz, T.; Rodriguez, A.; Chavez, J. P.; Rodriguez, P.; Gutierrez, S. and Nieto, A. (2011): CHD6 chromatin remodeler is a negative modulator of influenza virus replication that relocates to inactive chromatin upon infection, Cell Microbiol (vol. 13), No. 12, pp. 1894-906.

[354] Avalos, R. T.; Yu, Z. and Nayak, D. P. (1997): Association of influenza virus NP and M1 proteins with cellular cytoskeletal elements in influenza virus-infected cells, J Virol (vol. 71), No. 4, pp. 2947-58.

[355] Sharma, S.; Mayank, A. K.; Nailwal, H.; Tripathi, S.; Patel, J. R.; Bowzard, J. B.; Gaur, P.; Donis, R. O.; Katz, J. M.; Cox, N. J.; Lal, R. B.; Farooqi, H.; Sambhara, S. and Lal, S. K. (2014): Influenza A viral nucleoprotein interacts with cytoskeleton scaffolding protein alpha-actinin-4 for viral replication, FEBS J (vol. 281), No. 13, pp. 2899-914.

[356] Gabriel, G.; Klingel, K.; Otte, A.; Thiele, S.; Hudjetz, B.; Arman-Kalcek, G.; Sauter, M.; Shmidt, T.; Rother, F.; Baumgarte, S.; Keiner, B.; Hartmann, E.; Bader, M.; Brownlee, G. G.; Fodor, E. and Klenk, H. D. (2011): Differential use of importin-alpha isoforms governs cell tropism and host adaptation of influenza virus, Nat Commun (vol. 2), p. 156.

[357] Melen, K.; Fagerlund, R.; Franke, J.; Kohler, M.; Kinnunen, L. and Julkunen, I. (2003): Importin alpha nuclear localization signal binding sites for STAT1, STAT2, and influenza A virus nucleoprotein, J Biol Chem (vol. 278), No. 30, pp. 28193-200.

[358] Shapira, S. D.; Gat-Viks, I.; Shum, B. O.; Dricot, A.; de Grace, M. M.; Wu, L.; Gupta, P. B.; Hao, T.; Silver, S. J.; Root, D. E.; Hill, D. E.; Regev, A. and Hacohen, N. (2009): A physical and regulatory map of host-influenza interactions reveals pathways in H1N1 infection, Cell (vol. 139), No. 7, pp. 1255-67.

[359] Gabriel, G.; Herwig, A. and Klenk, H. D. (2008): Interaction of polymerase subunit PB2 and NP with importin alpha1 is a determinant of host range of influenza A virus, PLoS Pathog (vol. 4), No. 2, p. e11.

[360] Ketha, K. M. and Atreya, C. D. (2008): Application of bioinformatics-coupled experimental analysis reveals a new transport-competent nuclear localization signal in the nucleoprotein of influenza A virus strain, BMC Cell Biol (vol. 9), p. 22.

[361] Wu, W. W. and Pante, N. (2009): The directionality of the nuclear transport of the influenza A genome is driven by selective exposure of nuclear localization sequences on nucleoprotein, Virol J (vol. 6), p. 68.

[362] Bui, M.; Myers, J. E. and Whittaker, G. R. (2002): Nucleo-cytoplasmic localization of influenza virus nucleoprotein depends on cell density and phosphorylation, Virus Res (vol. 84), No. 1-2, pp. 37-44.

[363] Neumann, G.; Castrucci, M. R. and Kawaoka, Y. (1997): Nuclear import and export of influenza virus nucleoprotein, J Virol (vol. 71), No. 12, pp. 9690-700.

[364] Almond, J. W. and Felsenreich, V. (1982): Phosphorylation of the nucleoprotein of an avian influenza virus, J Gen Virol (vol. 60), No. Pt 2, pp. 295-305.

[365] Privalsky, M. L. and Penhoet, E. E. (1977): Phosphorylated protein component present in influenza virions, J Virol (vol. 24), No. 1, pp. 401-5.

[366] Privalsky, M. L. and Penhoet, E. E. (1981): The structure and synthesis of influenza virus phosphoproteins, J Biol Chem (vol. 256), No. 11, pp. 5368-76.

[367] Arrese, M. and Portela, A. (1996): Serine 3 is critical for phosphorylation at the N-terminal end of the nucleoprotein of influenza virus A/Victoria/3/75, J Virol (vol. 70), No. 6, pp. 3385-91.

[368] Kistner, O.; Muller, K. and Scholtissek, C. (1989): Differential phosphorylation of the nucleoprotein of influenza A viruses, J Gen Virol (vol. 70 (Pt 9)), pp. 2421-31.

[369] Kistner, O.; Muller, H.; Becht, H. and Scholtissek, C. (1985): Phosphopeptide fingerprints of nucleoproteins of various influenza A virus strains grown in different host cells, J Gen Virol (vol. 66 (Pt 3)), pp. 465-72.

[370] Bullido, R.; Gomez-Puertas, P.; Albo, C. and Portela, A. (2000): Several protein regions contribute to determine the nuclear and cytoplasmic localization of the influenza A virus nucleoprotein, J Gen Virol (vol. 81), No. Pt 1, pp. 135-42.

[371] Chandler, D. (2005): Interfaces and the driving force of hydrophobic assembly, Nature (vol. 437), No. 7059, pp. 640-7.

[372] Krimm, S. (1980): The hydrophobic effect: Formation of micelles and biological membranes, Charles Tanford, Wiley-Interscience, New York, 1980, 233 pp. price: $18.50, Journal of Polymer Science: Polymer Letters Edition (vol. 18), No. 10, pp. 687-687.

[373] Lingwood, D. and Simons, K. (2010): Lipid rafts as a membrane-organizing principle, Science (vol. 327), No. 5961, pp. 46-50.

[374] Simons, K. and Sampaio, J. L. (2011): Membrane organization and lipid rafts, Cold Spring Harb Perspect Biol (vol. 3), No. 10, p. a004697.

[375] Balla, T. (2013): Phosphoinositides: tiny lipids with giant impact on cell regulation, Physiol Rev (vol. 93), No. 3, pp. 1019-137.

[376] Singer, S. J. and Nicolson, G. L. (1972): The fluid mosaic model of the structure of cell membranes, Science (vol. 175), No. 4023, pp. 720-31.

[377] Huang, J. and Feigenson, G. W. (1999): A microscopic interaction model of maximum solubility of cholesterol in lipid bilayers, Biophys J (vol. 76), No. 4, pp. 2142-57.

[378] Terova, B.; Heczko, R. and Slotte, J. P. (2005): On the importance of the phosphocholine methyl groups for sphingomyelin/cholesterol interactions in membranes: a study with ceramide phosphoethanolamine, Biophys J (vol. 88), No. 4, pp. 2661-9.

[379] van Meer, G. (2005): Cellular lipidomics, EMBO J (vol. 24), No. 18, pp. 3159-65.

[380] Shevchenko, A. and Simons, K. (2010): Lipidomics: coming to grips with lipid diversity, Nat Rev Mol Cell Biol (vol. 11), No. 8, pp. 593-8.

[381] Wenk, M. R. (2010): Lipidomics: new tools and applications, Cell (vol. 143), No. 6, pp. 888-95.

[382] Futerman, A. H. and Hannun, Y. A. (2004): The complex life of simple sphingolipids, EMBO Rep (vol. 5), No. 8, pp. 777-82.

[383] Engelman, D. M. (2005): Membranes are more mosaic than fluid, Nature (vol. 438), No. 7068, pp. 578-80.

[384] Takamori, S.; Holt, M.; Stenius, K.; Lemke, E. A.; Gronborg, M.; Riedel, D.; Urlaub, H.; Schenck, S.; Brugger, B.; Ringler, P.; Muller, S. A.; Rammner, B.; Grater, F.; Hub, J. S.; De Groot, B. L.; Mieskes,

G.; Moriyama, Y.; Klingauf, J.; Grubmuller, H.; Heuser, J.; Wieland, F. and Jahn, R. (2006): Molecular anatomy of a trafficking organelle, Cell (vol. 127), No. 4, pp. 831-46.

[385] Kapus, A. and Janmey, P. (2013): Plasma membrane--cortical cytoskeleton interactions: a cell biology approach with biophysical considerations, Compr Physiol (vol. 3), No. 3, pp. 1231-81.

[386] Almen, M. S.; Nordstrom, K. J.; Fredriksson, R. and Schioth, H. B. (2009): Mapping the human membrane proteome: a majority of the human membrane proteins can be classified according to function and evolutionary origin, BMC Biol (vol. 7), p. 50.

[387] Wallin, E. and von Heijne, G. (1998): Genome-wide analysis of integral membrane proteins from eubacterial, archaean, and eukaryotic organisms, Protein Sci (vol. 7), No. 4, pp. 1029-38.

[388] Holthuis, J. C. and Levine, T. P. (2005): Lipid traffic: floppy drives and a superhighway, Nat Rev Mol Cell Biol (vol. 6), No. 3, pp. 209-20.

[389] Zachowski, A. (1993): Phospholipids in animal eukaryotic membranes: transverse asymmetry and movement, Biochem J (vol. 294 (Pt 1)), pp. 1-14.

[390] Lee, S. H.; Meng, X. W.; Flatten, K. S.; Loegering, D. A. and Kaufmann, S. H. (2013): Phosphatidylserine exposure during apoptosis reflects bidirectional trafficking between plasma membrane and cytoplasm, Cell Death Differ (vol. 20), No. 1, pp. 64-76.

[391] Collins, M. D. and Keller, S. L. (2008): Tuning lipid mixtures to induce or suppress domain formation across leaflets of unsupported asymmetric bilayers, Proc Natl Acad Sci U S A (vol. 105), No. 1, pp. 124-8.

[392] Gri, G.; Molon, B.; Manes, S.; Pozzan, T. and Viola, A. (2004): The inner side of T cell lipid rafts, Immunol Lett (vol. 94), No. 3, pp. 247-52.

[393] Kiessling, V.; Crane, J. M. and Tamm, L. K. (2006): Transbilayer effects of raft-like lipid domains in asymmetric planar bilayers measured by single molecule tracking, Biophys J (vol. 91), No. 9, pp. 3313-26.

[394] Wan, C.; Kiessling, V.; Cafiso, D. S. and Tamm, L. K. (2011): Partitioning of synaptotagmin I C2 domains between liquid-ordered and liquid-disordered inner leaflet lipid phases, Biochemistry (vol. 50), No. 13, pp. 2478-85.

[395] Chiantia, S. and London, E. (2012): Acyl chain length and saturation modulate interleaflet coupling in asymmetric bilayers: effects on dynamics and structural order, Biophys J (vol. 103), No. 11, pp. 2311-9.

[396] Devaux, P. F. and Morris, R. (2004): Transmembrane asymmetry and lateral domains in biological membranes, Traffic (vol. 5), No. 4, pp. 241-6.

[397] Simons, K. and Vaz, W. L. (2004): Model systems, lipid rafts, and cell membranes, Annu Rev Biophys Biomol Struct (vol. 33), pp. 269-95.

[398] Brown, D. A. and Rose, J. K. (1992): Sorting of GPI-anchored proteins to glycolipid-enriched membrane subdomains during transport to the apical cell surface, Cell (vol. 68), No. 3, pp. 533-44.

[399] London, E. and Brown, D. A. (2000): Insolubility of lipids in triton X-100: physical origin and relationship to sphingolipid/cholesterol membrane domains (rafts), Biochim Biophys Acta (vol. 1508), No. 1-2, pp. 182-95.

[400] Heerklotz, H. (2002): Triton promotes domain formation in lipid raft mixtures, Biophys J (vol. 83), No. 5, pp. 2693-701.

[401] Munro, S. (2003): Lipid rafts: elusive or illusive?, Cell (vol. 115), No. 4, pp. 377-88. U

[402] Sezgin, E. and Schwille, P. (2011): Fluorescence techniques to study lipid dynamics, Cold Spring Harb Perspect Biol (vol. 3), No. 11, p. a009803.

[403] Owen, D. M.; Magenau, A.; Williamson, D. and Gaus, K. (2012): The lipid raft hypothesis revisited--new insights on raft composition and function from super-resolution fluorescence microscopy, Bioessays (vol. 34), No. 9, pp. 739-47.

[404] Simons, K. and Gerl, M. J. (2010): Revitalizing membrane rafts: new tools and insights, Nat Rev Mol Cell Biol (vol. 11), No. 10, pp. 688-99.

[405] Brameshuber, M.; Weghuber, J.; Ruprecht, V.; Gombos, I.; Horvath, I.; Vigh, L.; Eckerstorfer, P.; Kiss, E.; Stockinger, H. and Schutz, G. J. (2010): Imaging of mobile long-lived nanoplatforms in the live cell plasma membrane, J Biol Chem (vol. 285), No. 53, pp. 41765-71.

[406] Yethiraj, A. and Weisshaar, J. C. (2007): Why are lipid rafts not observed in vivo?, Biophys J (vol. 93), No. 9, pp. 3113-9.

[407] Kaiser, H. J.; Lingwood, D.; Levental, I.; Sampaio, J. L.; Kalvodova, L.; Rajendran, L. and Simons, K. (2009): Order of lipid phases in model and plasma membranes, Proc Natl Acad Sci U S A (vol. 106), No. 39, pp. 16645-50.

[408] Bacia, K.; Scherfeld, D.; Kahya, N. and Schwille, P. (2004): Fluorescence correlation spectroscopy relates rafts in model and native membranes, Biophys J (vol. 87), No. 2, pp. 1034-43.

[409] Gandhavadi, M.; Allende, D.; Vidal, A.; Simon, S. A. and McIntosh, T. J. (2002): Structure, composition, and peptide binding properties of detergent soluble bilayers and detergent resistant rafts, Biophys J (vol. 82), No. 3, pp. 1469-82.

[410] Ipsen, J. H.; Karlstrom, G.; Mouritsen, O. G.; Wennerstrom, H. and Zuckermann, M. J. (1987): Phase equilibria in the phosphatidylcholine-cholesterol system, Biochim Biophys Acta (vol. 905), No. 1, pp. 162-72.

[411] Roduit, C.; van der Goot, F. G.; De Los Rios, P.; Yersin, A.; Steiner, P.; Dietler, G.; Catsicas, S.; Lafont, F. and Kasas, S. (2008): Elastic membrane heterogeneity of living cells revealed by stiff nanoscale membrane domains, Biophys J (vol. 94), No. 4, pp. 1521-32.

[412] Sampaio, J. L.; Gerl, M. J.; Klose, C.; Ejsing, C. S.; Beug, H.; Simons, K. and Shevchenko, A. (2011): Membrane lipidome of an epithelial cell line, Proc Natl Acad Sci U S A (vol. 108), No. 5, pp. 1903-7.

[413] Polozov, I. V.; Bezrukov, L.; Gawrisch, K. and Zimmerberg, J. (2008): Progressive ordering with decreasing temperature of the phospholipids of influenza virus, Nat Chem Biol (vol. 4), No. 4, pp. 248-55.

[414] Sharpe, H. J.; Stevens, T. J. and Munro, S. (2010): A comprehensive comparison of transmembrane domains reveals organelle-specific properties, Cell (vol. 142), No. 1, pp. 158-69.

[415] van Meer, G.; Voelker, D. R. and Feigenson, G. W. (2008): Membrane lipids: where they are and how they behave, Nat Rev Mol Cell Biol (vol. 9), No. 2, pp. 112-24.

[416] Patterson, G. H.; Hirschberg, K.; Polishchuk, R. S.; Gerlich, D.; Phair, R. D. and Lippincott-Schwartz, J. (2008): Transport through the Golgi apparatus by rapid partitioning within a two-phase membrane system, Cell (vol. 133), No. 6, pp. 1055-67.

[417] Mitra, K.; Ubarretxena-Belandia, I.; Taguchi, T.; Warren, G. and Engelman, D. M. (2004): Modulation of the bilayer thickness of exocytic pathway membranes by membrane proteins rather than cholesterol, Proc Natl Acad Sci U S A (vol. 101), No. 12, pp. 4083-8.

[418] Jacobson, K.; Mouritsen, O. G. and Anderson, R. G. (2007): Lipid rafts: at a crossroad between cell biology and physics, Nat Cell Biol (vol. 9), No. 1, pp. 7-14.

[419] Poveda, J. A.; Fernandez, A. M.; Encinar, J. A. and Gonzalez-Ros, J. M. (2008): Protein-promoted membrane domains, Biochim Biophys Acta (vol. 1778), No. 7-8, pp. 1583-90.

[420] Garcia-Saez, A. J.; Chiantia, S. and Schwille, P. (2007): Effect of line tension on the lateral organization of lipid membranes, J Biol Chem (vol. 282), No. 46, pp. 33537-44.

[421] Heberle, F. A.; Petruzielo, R. S.; Pan, J.; Drazba, P.; Kucerka, N.; Standaert, R. F.; Feigenson, G. W. and Katsaras, J. (2013): Bilayer thickness mismatch controls domain size in model membranes, J Am Chem Soc (vol. 135), No. 18, pp. 6853-9.

[422] Baumgart, T.; Hammond, A. T.; Sengupta, P.; Hess, S. T.; Holowka, D. A.; Baird, B. A. and Webb, W. W. (2007): Large-scale fluid/fluid phase separation of proteins and lipids in giant plasma membrane vesicles, Proc Natl Acad Sci U S A (vol. 104), No. 9, pp. 3165-70.

[423] Brewster, R.; Pincus, P. A. and Safran, S. A. (2009): Hybrid lipids as a biological surface-active component, Biophys J (vol. 97), No. 4, pp. 1087-94.

[424] Brewster, R. and Safran, S. A. (2010): Line active hybrid lipids determine domain size in phase separation of saturated and unsaturated lipids, Biophys J (vol. 98), No. 6, pp. L21-3.

[425] Schafer, L. V. and Marrink, S. J. (2010): Partitioning of lipids at domain boundaries in model membranes, Biophys J (vol. 99), No. 12, pp. L91-3.

[426] Ritchie, K.; Iino, R.; Fujiwara, T.; Murase, K. and Kusumi, A. (2003): The fence and picket structure of the plasma membrane of live cells as revealed by single molecule techniques (Review), Mol Membr Biol (vol. 20), No. 1, pp. 13-8.

[427] Suzuki, K. G.; Fujiwara, T. K.; Sanematsu, F.; Iino, R.; Edidin, M. and Kusumi, A. (2007): GPI-anchored receptor clusters transiently recruit Lyn and G alpha for temporary cluster immobilization and Lyn activation: single-molecule tracking study 1, J Cell Biol (vol. 177), No. 4, pp. 717-30.

[428] Raslan, Z. and Naseem, K. M. (2014): Compartmentalisation of cAMP-dependent signalling in blood platelets: The role of lipid rafts and actin polymerisation, Platelets, pp. 1-9.

[429] Gaus, K.; Chklovskaia, E.; Fazekas de St Groth, B.; Jessup, W. and Harder, T. (2005): Condensation of the plasma membrane at the site of T lymphocyte activation, J Cell Biol (vol. 171), No. 1, pp. 121-31.

[430] Zech, T.; Ejsing, C. S.; Gaus, K.; de Wet, B.; Shevchenko, A.; Simons, K. and Harder, T. (2009): Accumulation of raft lipids in T-cell plasma membrane domains engaged in TCR signalling, EMBO J (vol. 28), No. 5, pp. 466-76.

[431] Marsh, D. (2008): Protein modulation of lipids, and vice-versa, in membranes, Biochim Biophys Acta (vol. 1778), No. 7-8, pp. 1545-75.

[432] Yuan, C.; O'Connell, R. J.; Feinberg-Zadek, P. L.; Johnston, L. J. and Treistman, S. N. (2004): Bilayer thickness modulates the conductance of the BK channel in model membranes, Biophys J (vol. 86), No. 6, pp. 3620-33.

[433] Antonny, B. (2011): Mechanisms of membrane curvature sensing, Annu Rev Biochem (vol. 80), pp. 101-23.

[434] Chen, B.J.; Takeda, M. and Lamb, R. A. (2005): Influenza virus hemagglutinin (H3 subtype) requires palmitoylation of its cytoplasmic tail for assembly: M1 proteins of two subtypes differ in their ability to support assembly., J Virol (vol. 79), pp. 13673–13684.

[435] Lipowsky, R. (1993): Domain-induced budding of fluid membranes, Biophys J (vol. 64), No. 4, pp. 1133-8.

[436] Bacia, K.; Schwille, P. and Kuruchalia, T. (2005): Sterol structure determines the separation of phases and the curvature of the liquid-ordered phase in model membranes, Proc Natl Acad Sci U S A (vol. 102), No. 9, pp. 3272-3277.

[437] Sun, X. and Whittaker, G. R. (2003): Role for influenza virus envelope cholesterol in virus entry and infection, J Virol (vol. 77), No. 23, pp. 12543-51.

[438] Pike, L. J. (2006): Rafts defined: a report on the Keystone Symposium on Lipid Rafts and Cell Function, J Lipid Res (vol. 47), No. 7, pp. 1597-8.

[439] Almeida, P. F. (2014): The many faces of lipid rafts, Biophys J (vol. 106), No. 9, pp. 1841-3.

[440] Shlomovitz, R.; Maibaum, L. and Schick, M. (2014): Macroscopic phase separation, modulated phases, and microemulsions: a unified picture of rafts, Biophys J (vol. 106), No. 9, pp. 1979-85.

[441] Veatch, S. L.; Cicuta, P.; Sengupta, P.; Honerkamp-Smith, A.; Holowka, D. and Baird, B. (2008): Critical fluctuations in plasma membrane vesicles, ACS Chem Biol (vol. 3), No. 5, pp. 287-93.

[442] Honerkamp-Smith, A. R.; Veatch, S. L. and Keller, S. L. (2009): An introduction to critical points for biophysicists; observations of compositional heterogeneity in lipid membranes, Biochim Biophys Acta (vol. 1788), No. 1, pp. 53-63.

[443] Lingwood, D.; Ries, J.; Schwille, P. and Simons, K. (2008): Plasma membranes are poised for activation of raft phase coalescence at physiological temperature, Proc Natl Acad Sci U S A (vol. 105), No. 29, pp. 10005-10.

[444] Korte, T.; Ludwig, K.; Krumbiegel, M.; Zirwer, D.; Damaschun, G. and Herrmann, A. (1997): Transient changes of the conformation of hemagglutinin of influenza virus at low pH detected by time-resolved circular dichroism spectroscopy, J Biol Chem (vol. 272), No. 15, pp. 9764-70.

[445] Jungnick, Nadine (2011): Influenza Matrix Protein M1 – An in vitro Membrane Binding Study (Thesis), Department of Biology, Humboldt-Universität zu Berlin, Berlin, Germany.

[446] Zacharias, D. A.; Violin, J. D.; Newton, A. C. and Tsien, R. Y. (2002): Partitioning of lipid-modified monomeric GFPs into membrane microdomains of live cells, Science (vol. 296), No. 5569, pp. 913-6.

[447] Scolari, Silvia (2009): Lateral organization of the transmembrane domain and cytoplasmic tail of influenza virus hemagglutinin revealed by time resolved imaging (Thesis), Department of Biology, Humboldt-Universität zu Berlin, Berlin, Germany.

[448] Wagner, R.; Herwig, A.; Azzouz, N. and Klenk, H. D. (2005): Acylation-mediated membrane anchoring of avian influenza virus hemagglutinin is essential for fusion pore formation and virus infectivity, J Virol (vol. 79), No. 10, pp. 6449-58.

[449] Thaa, Bastian (2011): Assemblierung von Influenzaviren: Wechselwirkung der Proteine M1 und M2 mit Membranen und Membrandomänen (Dissertationsschrift), Mensch und Buch Verlag Berlin, Germany, ISBN: 978-3866649224.

[450] Sherer, N. M.; Lehmann, M. J.; Jimenez-Soto, L. F.; Ingmundson, A.; Horner, S. M.; Cicchetti, G.; Allen, P. G.; Pypaert, M.; Cunningham, J. M. and Mothes, W. (2003): Visualization of retroviral replication in living cells reveals budding into multivesicular bodies, Traffic (vol. 4), No. 11, pp. 785-801.

[451] Hoffmann, E.; Neumann, G.; Kawaoka, Y.; Hobom, G. and Webster, R. G. (2000): A DNA transfection system for generation of influenza A virus from eight plasmids, Proc Natl Acad Sci U S A (vol. 97), No. 11, pp. 6108-13.

[452] Abramoff, M. D.; Magalhaes, P.J.; Ram, S.J. (2004): Image Processing with ImageJ, Biophotonics International (vol. 11), No. 7, pp. 36-42.

[453] Meijering, E.; Dzyubachyk, O. and Smal, I. (2012): Methods for cell and particle tracking, Methods Enzymol (vol. 504), pp. 183-200.

[454] Sage, D.; Neumann, F. R.; Hediger, F.; Gasser, S. M. and Unser, M. (2005): Automatic tracking of individual fluorescence particles: application to the study of chromosome dynamics, IEEE Trans Image Process (vol. 14), No. 9, pp. 1372-83.

[455] Wang, W. and Malcolm, B. A. (1999): Two-stage PCR protocol allowing introduction of multiple mutations, deletions and insertions using QuikChange Site-Directed Mutagenesis, Biotechniques (vol. 26), No. 4, pp. 680-2.

[456] Andreassen, P. R.; Lacroix, F. B.; Villa-Moruzzi, E. and Margolis, R. L. (1998): Differential subcellular localization of protein phosphatase-1 alpha, gamma1, and delta isoforms during both interphase and mitosis in mammalian cells, J Cell Biol (vol. 141), No. 5, pp. 1207-15.

[457] Adams, S. R.; Campbell, R. E.; Gross, L. A.; Martin, B. R.; Walkup, G. K.; Yao, Y.; Llopis, J. and Tsien, R. Y. (2002): New biarsenical ligands and tetracysteine motifs for protein labeling in vitro and in vivo: synthesis and biological applications, J Am Chem Soc (vol. 124), No. 21, pp. 6063-76.

[458] Chudakov, D. M.; Lukyanov, S. and Lukyanov, K. A. (2007): Tracking intracellular protein movements using photoswitchable fluorescent proteins PS-CFP2 and Dendra2, Nat Protoc (vol. 2), No. 8, pp. 2024-32.

[459] Gaietta, G.; Deerinck, T. J.; Adams, S. R.; Bouwer, J.; Tour, O.; Laird, D. W.; Sosinsky, G. E.; Tsien, R. Y. and Ellisman, M. H. (2002): Multicolor and electron microscopic imaging of connexin trafficking, Science (vol. 296), No. 5567, pp. 503-7.

[460] Gaietta, G. M.; Deerinck, T. J. and Ellisman, M. H. (2011): Fluorescence photoconversion of biarsenical-labeled cells for correlated electron microscopy (EM), Cold Spring Harb Protoc (vol. 2011), No. 1, p. pdb prot5548.

[461] Kessler, R. J. and Fanestil, D. D. (1986): Interference by lipids in the determination of protein using bicinchoninic acid, Anal Biochem (vol. 159), No. 1, pp. 138-42.

[462] Mayer, L. D.; Hope, M. J. and Cullis, P. R. (1986): Vesicles of variable sizes produced by a rapid extrusion procedure, Biochim Biophys Acta (vol. 858), No. 1, pp. 161-8.

[463] Bigay, J.; Casella, J. F.; Drin, G.; Mesmin, B. and Antonny, B. (2005): ArfGAP1 responds to membrane curvature through the folding of a lipid packing sensor motif, EMBO J (vol. 24), No. 13, pp. 2244-53.

[464] Laemmli, U. K. (1970): Cleavage of structural proteins during the assembly of the head of bacteriophage T4, Nature (vol. 227), No. 5259, pp. 680-5.

[465] Ornstein, L. (1964): Disc Electrophoresis. I. Background and Theory, Ann N Y Acad Sci (vol. 121), pp. 321-49.

[466] Fontana, J.; Cardone, G.; Heymann, J. B.; Winkler, D. C. and Steven, A. C. (2012): Structural changes in Influenza virus at low pH characterized by cryo-electron tomography, J Virol (vol. 86), No. 6, pp. 2919-29.

[467] Cosa, G.; Focsaneanu, K. S.; McLean, J. R.; McNamee, J. P. and Scaiano, J. C. (2001): Photophysical properties of fluorescent DNA-dyes bound to single- and double-stranded DNA in aqueous buffered solution, Photochem Photobiol (vol. 73), No. 6, pp. 585-99.

[468] Suzuki, T.; Fujikura, K.; Higashiyama, T. and Takata, K. (1997): DNA staining for fluorescence and laser confocal microscopy, J Histochem Cytochem (vol. 45), No. 1, pp. 49-53.

[469] Waring, M. J. (1965): Complex formation between ethidium bromide and nucleic acids, J Mol Biol (vol. 13), No. 1, pp. 269-82.

[470] Kapuscinski, J.; Darzynkiewicz, Z. and Melamed, M. R. (1982): Luminescence of the solid complexes of acridine orange with RNA, Cytometry (vol. 2), No. 4, pp. 201-11.

[471] Kapuscinski, J. (1990): Interactions of nucleic acids with fluorescent dyes: spectral properties of condensed complexes, J Histochem Cytochem (vol. 38), No. 9, pp. 1323-9.

[472] Wah, D. A.; Fernandez-Tornero, C.; Sanz, L.; Romero, A. and Calvete, J. J. (2002): Sperm coating mechanism from the 1.8 A crystal structure of PDC-109-phosphorylcholine complex, Structure (vol. 10), No. 4, pp. 505-14.

[473] Manjunath, P. and Therien, I. (2002): Role of seminal plasma phospholipid-binding proteins in sperm membrane lipid modification that occurs during capacitation, J Reprod Immunol (vol. 53), No. 1-2, pp. 109-19.

[474] Hofer, C. T.; Herrmann, A. and Muller, P. (2010): Use of liposomes for studying interactions of soluble proteins with cellular membranes, Methods Mol Biol (vol. 606), pp. 69-82.

[475] Desnoyers, L. and Manjunath, P. (1992): Major proteins of bovine seminal plasma exhibit novel interactions with phospholipid, J Biol Chem (vol. 267), No. 14, pp. 10149-55.

[476] Fairn, G. D.; Schieber, N. L.; Ariotti, N.; Murphy, S.; Kuerschner, L.; Webb, R. I.; Grinstein, S. and Parton, R. G. (2011): High-resolution mapping reveals topologically distinct cellular pools of phosphatidylserine, J Cell Biol (vol. 194), No. 2, pp. 257-75.

[477] Di Paolo, G. and De Camilli, P. (2006): Phosphoinositides in cell regulation and membrane dynamics, Nature (vol. 443), No. 7112, pp. 651-7.

[478] Griffin, B. A.; Adams, S. R. and Tsien, R. Y. (1998): Specific covalent labeling of recombinant protein molecules inside live cells, Science (vol. 281), No. 5374, pp. 269-72.

[479] Hoffmann, C.; Gaietta, G.; Bunemann, M.; Adams, S. R.; Oberdorff-Maass, S.; Behr, B.; Vilardaga, J. P.; Tsien, R. Y.; Ellisman, M. H. and Lohse, M. J. (2005): A FlAsH-based FRET approach to determine G protein-coupled receptor activation in living cells, Nat Methods (vol. 2), No. 3, pp. 171-6.

[480] Li, Y.; Lu, X.; Li, J.; Berube, N.; Giest, K. L.; Liu, Q.; Anderson, D. H. and Zhou, Y. (2010): Genetically engineered, biarsenically labeled influenza virus allows visualization of viral NS1 protein in living cells, J Virol (vol. 84), No. 14, pp. 7204-13.

[481] Martin, B. R.; Giepmans, B. N.; Adams, S. R. and Tsien, R. Y. (2005): Mammalian cell-based optimization of the biarsenical-binding tetracysteine motif for improved fluorescence and affinity, Nat Biotechnol (vol. 23), No. 10, pp. 1308-14.

[482] Molecular-Probes (2011): TC-FlAsH™ TC-ReAsH™ In-Cell Tetracysteine Tag Detection Kits, MP 35359.

[483] Fuller, J. R.; Kijek, T. M.; Taft-Benz, S. and Kawula, T. H. (2009): Environmental and intracellular regulation of Francisella tularensis ripA, BMC Microbiol (vol. 9), p. 216.

[484] Wang, T.; Yan, P.; Squier, T. C. and Mayer, M. U. (2007): Prospecting the proteome: identification of naturally occurring binding motifs for biarsenical probes, Chembiochem (vol. 8), No. 16, pp. 1937-40.

[485] Sirri, V.; Urcuqui-Inchima, S.; Roussel, P. and Hernandez-Verdun, D. (2008): Nucleolus: the fascinating nuclear body, Histochem Cell Biol (vol. 129), No. 1, pp. 13-31.

[486] Schul, W.; de Jong, L. and van Driel, R. (1998): Nuclear neighbours: the spatial and functional organization of genes and nuclear domains, J Cell Biochem (vol. 70), No. 2, pp. 159-71.

[487] Schneider, R. and Grosschedl, R. (2007): Dynamics and interplay of nuclear architecture, genome organization, and gene expression, Genes Dev (vol. 21), No. 23, pp. 3027-43.

[488] Geyer, P. K.; Vitalini, M. W. and Wallrath, L. L. (2011): Nuclear organization: taking a position on gene expression, Curr Opin Cell Biol (vol. 23), No. 3, pp. 354-9.

[489] Meldi, L. and Brickner, J. H. (2011): Compartmentalization of the nucleus, Trends Cell Biol (vol. 21), No. 12, pp. 701-8.

[490] Mao, Y. S.; Zhang, B. and Spector, D. L. (2011): Biogenesis and function of nuclear bodies, Trends Genet (vol. 27), No. 8, pp. 295-306.

[491] Ching, R. W.; Dellaire, G.; Eskiw, C. H. and Bazett-Jones, D. P. (2005): PML bodies: a meeting place for genomic loci?, J Cell Sci (vol. 118), No. Pt 5, pp. 847-54.

[492] Everett, R. D. (2001): DNA viruses and viral proteins that interact with PML nuclear bodies, Oncogene (vol. 20), No. 49, pp. 7266-73.

[493] Chan, W. H.; Ng, A. K.; Robb, N. C.; Lam, M. K.; Chan, P. K.; Au, S. W.; Wang, J. H.; Fodor, E. and Shaw, P. C. (2010): Functional analysis of the influenza virus H5N1 nucleoprotein tail loop reveals amino acids that are crucial for oligomerization and ribonucleoprotein activities, J Virol (vol. 84), No. 14, pp. 7337-45.

[494] Pack, C.; Saito, K.; Tamura, M. and Kinjo, M. (2006): Microenvironment and effect of energy depletion in the nucleus analyzed by mobility of multiple oligomeric EGFPs, Biophys J (vol. 91), No. 10, pp. 3921-36.

[495] Grunwald, D.; Martin, R. M.; Buschmann, V.; Bazett-Jones, D. P.; Leonhardt, H.; Kubitscheck, U. and Cardoso, M. C. (2008): Probing intranuclear environments at the single-molecule level, Biophys J (vol. 94), No. 7, pp. 2847-58.

[496] Sheval, E. V.; Polzikov, M. A.; Olson, M. O. and Zatsepina, O. V. (2005): A higher concentration of an antigen within the nucleolus may prevent its proper recognition by specific antibodies, Eur J Histochem (vol. 49), No. 2, pp. 117-23.

[497] Johnson, Iain D. (2006): Practical Considerations in the Selection and Application of Fluorescent Probes, Pawley, James, Handbook of Biolocical Confocal Microscopy (vol. 236), 3rd. ed., pp. 355-356, Springer Science + Business Media, New York.

[498] Dross, N.; Spriet, C.; Zwerger, M.; Muller, G.; Waldeck, W. and Langowski, J. (2009): Mapping eGFP oligomer mobility in living cell nuclei, PLoS One (vol. 4), No. 4, p. e5041.

[499] Pollard, V. W. and Malim, M. H. (1998): The HIV-1 Rev protein, Annu Rev Microbiol (vol. 52), pp. 491-532.

[500] Torrano, V.; Navascues, J.; Docquier, F.; Zhang, R.; Burke, L. J.; Chernukhin, I.; Farrar, D.; Leon, J.; Berciano, M. T.; Renkawitz, R.; Klenova, E.; Lafarga, M. and Delgado, M. D. (2006): Targeting of CTCF to the nucleolus inhibits nucleolar transcription through a poly(ADP-ribosyl)ation-dependent mechanism, J Cell Sci (vol. 119), No. Pt 9, pp. 1746-59.

[501] Tseng, Y.; Lee, J. S.; Kole, T. P.; Jiang, I. and Wirtz, D. (2004): Micro-organization and visco-elasticity of the interphase nucleus revealed by particle nanotracking, J Cell Sci (vol. 117), No. Pt 10, pp. 2159-67.

[502] Spector, D. L. (2006): SnapShot: Cellular bodies, Cell (vol. 127), No. 5, p. 1071.

[503] Spector, D. L. and Lamond, A. I. (2011): Nuclear speckles, Cold Spring Harb Perspect Biol (vol. 3), No. 2.

[504] Grande, M. A.; van der Kraan, I.; van Steensel, B.; Schul, W.; de The, H.; van der Voort, H. T.; de Jong, L. and van Driel, R. (1996): PML-containing nuclear bodies: their spatial distribution in relation to other nuclear components, J Cell Biochem (vol. 63), No. 3, pp. 280-91.

[505] Sun, J.; Xu, H.; Subramony, S. H. and Hebert, M. D. (2005): Interactions between coilin and PIASy partially link Cajal bodies to PML bodies, J Cell Sci (vol. 118), No. Pt 21, pp. 4995-5003.

[506] Borden, K. L. and Culjkovic, B. (2009): Perspectives in PML: a unifying framework for PML function, Front Biosci (vol. 14), pp. 497-509.

[507] Loucaides, E. M.; von Kirchbach, J. C.; Foeglein, A.; Sharps, J.; Fodor, E. and Digard, P. (2009): Nuclear dynamics of influenza A virus ribonucleoproteins revealed by live-cell imaging studies, Virology (vol. 394), No. 1, pp. 154-63.

[508] Ullrich, O.; Reinsch, S.; Urbe, S.; Zerial, M. and Parton, R. G. (1996): Rab11 regulates recycling through the pericentriolar recycling endosome, J Cell Biol (vol. 135), No. 4, pp. 913-24.

[509] Pierobon, P.; Achouri, S.; Courty, S.; Dunn, A. R.; Spudich, J. A.; Dahan, M. and Cappello, G. (2009): Velocity, processivity, and individual steps of single myosin V molecules in live cells, Biophys J (vol. 96), No. 10, pp. 4268-75.

[510] Smith, D. A. and Simmons, R. M. (2001): Models of motor-assisted transport of intracellular particles, Biophys J (vol. 80), No. 1, pp. 45-68.

[511] Carter, G. C.; Rodger, G.; Murphy, B. J.; Law, M.; Krauss, O.; Hollinshead, M. and Smith, G. L. (2003): Vaccinia virus cores are transported on microtubules, J Gen Virol (vol. 84), No. Pt 9, pp. 2443-58.

[512] Chambers, R. and Takimoto, T. (2010): Trafficking of Sendai virus nucleocapsids is mediated by intracellular vesicles, PLoS One (vol. 5), No. 6, p. e10994.

[513] Schnitzer, M. J.; Visscher, K. and Block, S. M. (2000): Force production by single kinesin motors, Nat Cell Biol (vol. 2), No. 10, pp. 718-23.

[514] Kingsbury, D. W.; Jones, I. M. and Murti, K. G. (1987): Assembly of influenza ribonucleoprotein in vitro using recombinant nucleoprotein, Virology (vol. 156), No. 2, pp. 396-403.

[515] Elton, D.; Amorim, M. J.; Medcalf, L. and Digard, P. (2005): 'Genome gating'; polarized intranuclear trafficking of influenza virus RNPs, Biol Lett (vol. 1), No. 2, pp. 113-7.

[516] Jo, S.; Kawaguchi, A.; Takizawa, N.; Morikawa, Y.; Momose, F. and Nagata, K. (2010): Involvement of vesicular trafficking system in membrane targeting of the progeny influenza virus genome, Microbes Infect (vol. 12), No. 12-13, pp. 1079-84.

[517] D'Angelo, G.; Vicinanza, M.; Di Campli, A. and De Matteis, M. A. (2008): The multiple roles of PtdIns(4)P -- not just the precursor of PtdIns(4,5)P2, J Cell Sci (vol. 121), No. Pt 12, pp. 1955-63.

[518] Uchida, Y.; Hasegawa, J.; Chinnapen, D.; Inoue, T.; Okazaki, S.; Kato, R.; Wakatsuki, S.; Misaki, R.; Koike, M.; Uchiyama, Y.; Iemura, S.; Natsume, T.; Kuwahara, R.; Nakagawa, T.; Nishikawa, K.; Mukai, K.; Miyoshi, E.; Taniguchi, N.; Sheff, D.; Lencer, W. I.; Taguchi, T. and Arai, H. (2011): Intracellular phosphatidylserine is essential for retrograde membrane traffic through endosomes, Proc Natl Acad Sci U S A (vol. 108), No. 38, pp. 15846-51.

[519] Lee, S.; Uchida, Y.; Emoto, K.; Umeda, M.; Kuge, O.; Taguchi, T. and Arai, H. (2012): Impaired retrograde membrane traffic through endosomes in a mutant CHO cell defective in phosphatidylserine synthesis, Genes Cells (vol. 17), No. 8, pp. 728-36.

[520] Das, S. C.; Watanabe, S.; Hatta, M.; Noda, T.; Neumann, G.; Ozawa, M. and Kawaoka, Y. (2012): The highly conserved arginine residues at positions 76 through 78 of influenza A virus matrix protein M1 play an important role in viral replication by affecting the intracellular localization of M1, J Virol (vol. 86), No. 3, pp. 1522-30.

[521] Watanabe, K.; Fuse, T.; Asano, I.; Tsukahara, F.; Maru, Y.; Nagata, K.; Kitazato, K. and Kobayashi, N. (2006): Identification of Hsc70 as an influenza virus matrix protein (M1) binding factor involved in the virus life cycle, FEBS Lett (vol. 580), No. 24, pp. 5785-90.

[522] Shibata, T.; Tanaka, T.; Shimizu, K.; Hayakawa, S. and Kuroda, K. (2009): Immunofluorescence imaging of the influenza virus M1 protein is dependent on the fixation method, J Virol Methods (vol. 156), No. 1-2, pp. 162-5.

[523] Graham, T. R. and Burd, C. G. (2011): Coordination of Golgi functions by phosphatidylinositol 4-kinases, Trends Cell Biol (vol. 21), No. 2, pp. 113-21.

[524] Tafesse, F. G.; Sanyal, S.; Ashour, J.; Guimaraes, C. P.; Hermansson, M.; Somerharju, P. and Ploegh, H. L. (2013): Intact sphingomyelin biosynthetic pathway is essential for intracellular transport of influenza virus glycoproteins, Proc Natl Acad Sci U S A (vol. 110), No. 16, pp. 6406-11.

[525] Ng, A. K.; Chan, W. H.; Choi, S. T.; Lam, M. K.; Lau, K. F.; Chan, P. K.; Au, S. W.; Fodor, E. and Shaw, P. C. (2012): Influenza polymerase activity correlates with the strength of interaction between nucleoprotein and PB2 through the host-specific residue K/E627, PLoS One (vol. 7), No. 5, p. e36415.

[526] Rameix-Welti, M. A.; Tomoiu, A.; Dos Santos Afonso, E.; van der Werf, S. and Naffakh, N. (2009): Avian Influenza A virus polymerase association with nucleoprotein, but not polymerase assembly, is impaired in human cells during the course of infection, J Virol (vol. 83), No. 3, pp. 1320-31.

[527] Bogs, J.; Kalthoff, D.; Veits, J.; Pavlova, S.; Schwemmle, M.; Manz, B.; Mettenleiter, T. C. and Stech, J. (2011): Reversion of PB2-627E to -627K during replication of an H5N1 Clade 2.2 virus in mammalian hosts depends on the origin of the nucleoprotein, J Virol (vol. 85), No. 20, pp. 10691-8.

[528] Jennings, P. A.; Finch, J. T.; Winter, G. and Robertson, J. S. (1983): Does the higher order structure of the influenza virus ribonucleoprotein guide sequence rearrangements in influenza viral RNA?, Cell (vol. 34), No. 2, pp. 619-27.

[529] Machleidt, T.; Robers, M. and Hanson, G. T. (2007): Protein labeling with FlAsH and ReAsH, Methods Mol Biol (vol. 356), pp. 209-20.

[530] Stroffekova, K.; Proenza, C. and Beam, K. G. (2001): The protein-labeling reagent FLASH-EDT2 binds not only to CCXXCC motifs but also non-specifically to endogenous cysteine-rich proteins, Pflugers Arch (vol. 442), No. 6, pp. 859-66.

[531] Langhorst, M. F.; Genisyuerek, S. and Stuermer, C. A. (2006): Accumulation of FlAsH/Lumio Green in active mitochondria can be reversed by beta-mercaptoethanol for specific staining of tetracysteine-tagged proteins, Histochem Cell Biol (vol. 125), No. 6, pp. 743-7.

[532] Crivat, G.; Tokumasu, F.; Sa, J. M.; Hwang, J. and Wellems, T. E. (2011): Tetracysteine-based fluorescent tags to study protein localization and trafficking in Plasmodium falciparum-infected erythrocytes, PLoS One (vol. 6), No. 8, p. e22975.

[533] Compans, R. W. and Dimmock, N. J. (1969): An electron microscopic study of single-cycle infection of chick embryo fibroblasts by influenza virus, Virology (vol. 39), No. 3, pp. 499-515.

[534] Momose, F.; Basler, C. F.; O'Neill, R. E.; Iwamatsu, A.; Palese, P. and Nagata, K. (2001): Cellular splicing factor RAF-2p48/NPI-5/BAT1/UAP56 interacts with the influenza virus nucleoprotein and enhances viral RNA synthesis, J Virol (vol. 75), No. 4, pp. 1899-908.

[535] Barrett, T.; Wolstenholme, A. J. and Mahy, B. W. (1979): Transcription and replication of influenza virus RNA, Virology (vol. 98), No. 1, pp. 211-25.

[536] Gall, J. G.; Bellini, M.; Wu, Z. and Murphy, C. (1999): Assembly of the nuclear transcription and processing machinery: Cajal bodies (coiled bodies) and transcriptosomes, Mol Biol Cell (vol. 10), No. 12, pp. 4385-402.

[537] Kiesslich, A.; von Mikecz, A. and Hemmerich, P. (2002): Cell cycle-dependent association of PML bodies with sites of active transcription in nuclei of mammalian cells, J Struct Biol (vol. 140), No. 1-3, pp. 167-79.

[538] Lamond, A. I. and Spector, D. L. (2003): Nuclear speckles: a model for nuclear organelles, Nat Rev Mol Cell Biol (vol. 4), No. 8, pp. 605-12.

[539] He, Y.; Xu, K.; Keiner, B.; Zhou, J.; Czudai, V.; Li, T.; Chen, Z.; Liu, J.; Klenk, H. D.; Shu, Y. L. and Sun, B. (2010): Influenza A virus replication induces cell cycle arrest in G0/G1 phase, J Virol (vol. 84), No. 24, pp. 12832-40.

[540] Shin, J. S.; Hong, S. W.; Lee, S. L.; Kim, T. H.; Park, I. C.; An, S. K.; Lee, W. K.; Lim, J. S.; Kim, K. I.; Yang, Y.; Lee, S. S.; Jin, D. H. and Lee, M. S. (2008): Serum starvation induces G1 arrest through suppression of Skp2-CDK2 and CDK4 in SK-OV-3 cells, Int J Oncol (vol. 32), No. 2, pp. 435-9.

[541] Takizawa, N.; Watanabe, K.; Nouno, K.; Kobayashi, N. and Nagata, K. (2006): Association of functional influenza viral proteins and RNAs with nuclear chromatin and sub-chromatin structure, Microbes Infect (vol. 8), No. 3, pp. 823-33.

[542] Lopez-Turiso, J. A.; Martinez, C.; Tanaka, T. and Ortin, J. (1990): The synthesis of influenza virus negative-strand RNA takes place in insoluble complexes present in the nuclear matrix fraction, Virus Res (vol. 16), No. 3, pp. 325-37.

[543] Strasser, K.; Masuda, S.; Mason, P.; Pfannstiel, J.; Oppizzi, M.; Rodriguez-Navarro, S.; Rondon, A. G.; Aguilera, A.; Struhl, K.; Reed, R. and Hurt, E. (2002): TREX is a conserved complex coupling transcription with messenger RNA export, Nature (vol. 417), No. 6886, pp. 304-8.

[544] Masuda, S.; Das, R.; Cheng, H.; Hurt, E.; Dorman, N. and Reed, R. (2005): Recruitment of the human TREX complex to mRNA during splicing, Genes Dev (vol. 19), No. 13, pp. 1512-7.

[545] Shen, H. (2009): UAP56- a key player with surprisingly diverse roles in pre-mRNA splicing and nuclear export, BMB Rep (vol. 42), No. 4, pp. 185-8.

[546] Kota, K. P.; Wagner, S. R.; Huerta, E.; Underwood, J. M. and Nickerson, J. A. (2008): Binding of ATP to UAP56 is necessary for mRNA export, J Cell Sci (vol. 121), No. Pt 9, pp. 1526-37.

[547] Liao, T. L.; Wu, C. Y.; Su, W. C.; Jeng, K. S. and Lai, M. M. (2010): Ubiquitination and deubiquitination of NP protein regulates influenza A virus RNA replication, EMBO J (vol. 29), No. 22, pp. 3879-90.

[548] Pal, S.; Santos, A.; Rosas, J. M.; Ortiz-Guzman, J. and Rosas-Acosta, G. (2011): Influenza A virus interacts extensively with the cellular SUMOylation system during infection, Virus Res (vol. 158), No. 1-2, pp. 12-27.

[549] Zhirnov, O. P. and Klenk, H. D. (2009): Alterations in caspase cleavage motifs of NP and M2 proteins attenuate virulence of a highly pathogenic avian influenza virus, Virology (vol. 394), No. 1, pp. 57-63.

[550] Anton, L. C.; Schubert, U.; Bacik, I.; Princiotta, M. F.; Wearsch, P. A.; Gibbs, J.; Day, P. M.; Realini, C.; Rechsteiner, M. C.; Bennink, J. R. and Yewdell, J. W. (1999): Intracellular localization of proteasomal degradation of a viral antigen, J Cell Biol (vol. 146), No. 1, pp. 113-24.

[551] Liu, Q. and Dreyfuss, G. (1996): A novel nuclear structure containing the survival of motor neurons protein, EMBO J (vol. 15), No. 14, pp. 3555-65.

[552] Gubitz, A. K.; Feng, W. and Dreyfuss, G. (2004): The SMN complex, Exp Cell Res (vol. 296), No. 1, pp. 51-6.

[553] Lallemand-Breitenbach, V. and de The, H. (2010): PML nuclear bodies, Cold Spring Harb Perspect Biol (vol. 2), No. 5, p. a000661.

[554] Bernardi, R. and Pandolfi, P. P. (2007): Structure, dynamics and functions of promyelocytic leukaemia nuclear bodies, Nat Rev Mol Cell Biol (vol. 8), No. 12, pp. 1006-16.

[555] Li, L.; Roy, K.; Katyal, S.; Sun, X.; Bleoo, S. and Godbout, R. (2006): Dynamic nature of cleavage bodies and their spatial relationship to DDX1 bodies, Cajal bodies, and gems, Mol Biol Cell (vol. 17), No. 3, pp. 1126-40.

[556] Salsman, J.; Zimmerman, N.; Chen, T.; Domagala, M. and Frappier, L. (2008): Genome-wide screen of three herpesviruses for protein subcellular localization and alteration of PML nuclear bodies, PLoS Pathog (vol. 4), No. 7, p. e1000100.

[557] Handwerger, K. E. and Gall, J. G. (2006): Subnuclear organelles: new insights into form and function, Trends Cell Biol (vol. 16), No. 1, pp. 19-26.

[558] Morris, G. E. (2008): The Cajal body, Biochim Biophys Acta (vol. 1783), No. 11, pp. 2108-15.

[559] Dundr, M. and Misteli, T. (2001): Functional architecture in the cell nucleus, Biochem J (vol. 356), No. Pt 2, pp. 297-310.

[560] Sexton, T.; Schober, H.; Fraser, P. and Gasser, S. M. (2007): Gene regulation through nuclear organization, Nat Struct Mol Biol (vol. 14), No. 11, pp. 1049-55.

[561] Wang, I. F.; Reddy, N. M. and Shen, C. K. (2002): Higher order arrangement of the eukaryotic nuclear bodies, Proc Natl Acad Sci U S A (vol. 99), No. 21, pp. 13583-8.

[562] Zhao, R.; Bodnar, M. S. and Spector, D. L. (2009): Nuclear neighborhoods and gene expression, Curr Opin Genet Dev (vol. 19), No. 2, pp. 172-9.

[563] Cioce, M. and Lamond, A. I. (2005): Cajal bodies: a long history of discovery, Annu Rev Cell Dev Biol (vol. 21), pp. 105-31.

[564] Suzuki, T.; Izumi, H. and Ohno, M. (2010): Cajal body surveillance of U snRNA export complex assembly, J Cell Biol (vol. 190), No. 4, pp. 603-12.

[565] Kotova, E.; Jarnik, M. and Tulin, A. V. (2009): Poly (ADP-ribose) polymerase 1 is required for protein localization to Cajal body, PLoS Genet (vol. 5), No. 2, p. e1000387.

[566] Kim, S. H.; Ryabov, E. V.; Kalinina, N. O.; Rakitina, D. V.; Gillespie, T.; MacFarlane, S.; Haupt, S.; Brown, J. W. and Taliansky, M. (2007): Cajal bodies and the nucleolus are required for a plant virus systemic infection, EMBO J (vol. 26), No. 8, pp. 2169-79.

[567] Nizami, Z.; Deryusheva, S. and Gall, J. G. (2010): The Cajal body and histone locus body, Cold Spring Harb Perspect Biol (vol. 2), No. 7, p. a000653.

[568] Rajamaki, M. L. and Valkonen, J. P. (2009): Control of nuclear and nucleolar localization of nuclear inclusion protein a of picorna-like Potato virus A in Nicotiana species, Plant Cell (vol. 21), No. 8, pp. 2485-502.

[569] Anobile, J. M.; Arumugaswami, V.; Downs, D.; Czymmek, K.; Parcells, M. and Schmidt, C. J. (2006): Nuclear localization and dynamic properties of the Marek's disease virus oncogene products Meq and Meq/vIL8, J Virol (vol. 80), No. 3, pp. 1160-6.

[570] James, N. J.; Howell, G. J.; Walker, J. H. and Blair, G. E. (2010): The role of Cajal bodies in the expression of late phase adenovirus proteins, Virology (vol. 399), No. 2, pp. 299-311.

[571] Gilder, Andrew and Hebert, Michael (2011): Relationship of the Cajal Body to the Nucleolus, Olson, Mark O. J., The Nucleolus (vol. 15) pp. 361-380, Springer New York.

[572] Rebelo, L.; Almeida, F.; Ramos, C.; Bohmann, K.; Lamond, A. I. and Carmo-Fonseca, M. (1996): The dynamics of coiled bodies in the nucleus of adenovirus-infected cells, Mol Biol Cell (vol. 7), No. 7, pp. 1137-51.

[573] Ahel, D.; Horejsi, Z.; Wiechens, N.; Polo, S. E.; Garcia-Wilson, E.; Ahel, I.; Flynn, H.; Skehel, M.; West, S. C.; Jackson, S. P.; Owen-Hughes, T. and Boulton, S. J. (2009): Poly(ADP-ribose)-dependent regulation of DNA repair by the chromatin remodeling enzyme ALC1, Science (vol. 325), No. 5945, pp. 1240-3.

[574] Boamah, E. K.; Kotova, E.; Garabedian, M.; Jarnik, M. and Tulin, A. V. (2012): Poly(ADP-Ribose) polymerase 1 (PARP-1) regulates ribosomal biogenesis in Drosophila nucleoli, PLoS Genet (vol. 8), No. 1, p. e1002442.

[575] Tulin, A.; Stewart, D. and Spradling, A. C. (2002): The Drosophila heterochromatic gene encoding poly(ADP-ribose) polymerase (PARP) is required to modulate chromatin structure during development, Genes Dev (vol. 16), No. 16, pp. 2108-19.

[576] Avilov, S. V.; Moisy, D.; Munier, S.; Schraidt, O.; Naffakh, N. and Cusack, S. (2012): Replication-competent influenza A virus that encodes a split-green fluorescent protein-tagged PB2 polymerase subunit allows live-cell imaging of the virus life cycle, J Virol (vol. 86), No. 3, pp. 1433-48.

[577] Emmott, E.; Wise, H.; Loucaides, E. M.; Matthews, D. A.; Digard, P. and Hiscox, J. A. (2010): Quantitative proteomics using SILAC coupled to LC-MS/MS reveals changes in the nucleolar proteome in influenza A virus-infected cells, J Proteome Res (vol. 9), No. 10, pp. 5335-45.

[578] Melen, K.; Tynell, J.; Fagerlund, R.; Roussel, P.; Hernandez-Verdun, D. and Julkunen, I. (2012): Influenza A H3N2 subtype virus NS1 protein targets into the nucleus and binds primarily via its C-terminal NLS2/NoLS to nucleolin and fibrillarin, Virol J (vol. 9), p. 167.

[579] Keiner, B.; Maenz, B.; Wagner, R.; Cattoli, G.; Capua, I. and Klenk, H. D. (2010): Intracellular distribution of NS1 correlates with the infectivity and interferon antagonism of an avian influenza virus (H7N1), J Virol (vol. 84), No. 22, pp. 11858-65.

[580] Scaffidi, P.; Misteli, T. and Bianchi, M. E. (2002): Release of chromatin protein HMGB1 by necrotic cells triggers inflammation, Nature (vol. 418), No. 6894, pp. 191-5.

[581] Ditsworth, D.; Zong, W. X. and Thompson, C. B. (2007): Activation of poly(ADP)-ribose polymerase (PARP-1) induces release of the pro-inflammatory mediator HMGB1 from the nucleus, J Biol Chem (vol. 282), No. 24, pp. 17845-54.

[582] Boisvert, F. M.; van Koningsbruggen, S.; Navascues, J. and Lamond, A. I. (2007): The multifunctional nucleolus, Nat Rev Mol Cell Biol (vol. 8), No. 7, pp. 574-85.

[583] Visintin, R. and Amon, A. (2000): The nucleolus: the magician's hat for cell cycle tricks, Curr Opin Cell Biol (vol. 12), No. 3, pp. 372-7.

[584] Holmberg Olausson, Karl; Nistér, Monica and Lindström, Mikael (2012): p53 -Dependent and -Independent Nucleolar Stress Responses, Cells (vol. 1), No. 4, pp. 774-798.

[585] Tollini, LauraA; Frum, RebeccaA and Zhang, Yanping (2011): The Role of the Nucleolus in the Stress Response, Olson, Mark O. J., The Nucleolus (vol. 15) pp. 281-299, Springer New York.

[586] Boyd, M. T.; Vlatkovic, N. and Rubbi, C. P. (2011): The nucleolus directly regulates p53 export and degradation, J Cell Biol (vol. 194), No. 5, pp. 689-703.

[587] Dundr, M. (2012): Nuclear bodies: multifunctional companions of the genome, Curr Opin Cell Biol (vol. 24), No. 3, pp. 415-22.

[588] Bertrand, E.; Houser-Scott, F.; Kendall, A.; Singer, R. H. and Engelke, D. R. (1998): Nucleolar localization of early tRNA processing, Genes Dev (vol. 12), No. 16, pp. 2463-8.

[589] Hopper, Anita K.; Pai, Dave A. and Engelke, David R. (2010): Cellular dynamics of tRNAs and their genes, FEBS Lett (vol. 584), No. 2, pp. 310-317.

[590] Ideue, T.; Azad, A. K.; Yoshida, J.; Matsusaka, T.; Yanagida, M.; Ohshima, Y. and Tani, T. (2004): The nucleolus is involved in mRNA export from the nucleus in fission yeast, J Cell Sci (vol. 117), No. Pt 14, pp. 2887-95.

[591] Bond, V. C. and Wold, B. (1993): Nucleolar localization of myc transcripts, Mol Cell Biol (vol. 13), No. 6, pp. 3221-30.

[592] Matthews, David; Emmott, Edward and Hiscox, Julian (2011): Viruses and the Nucleolus, Olson, Mark O. J., The Nucleolus (vol. 15) pp. 321-345, Springer New York.

[593] Michienzi, A.; Li, S.; Zaia, J. A. and Rossi, J. J. (2002): A nucleolar TAR decoy inhibitor of HIV-1 replication, Proc Natl Acad Sci U S A (vol. 99), No. 22, pp. 14047-52.

[594] Michienzi, A.; De Angelis, F. G.; Bozzoni, I. and Rossi, J. J. (2006): A nucleolar localizing Rev binding element inhibits HIV replication, AIDS Res Ther (vol. 3), p. 13.

[595] Boyne, J. R. and Whitehouse, A. (2006): Nucleolar trafficking is essential for nuclear export of intronless herpesvirus mRNA, Proc Natl Acad Sci U S A (vol. 103), No. 41, pp. 15190-5.

[596] Michienzi, A.; Cagnon, L.; Bahner, I. and Rossi, J. J. (2000): Ribozyme-mediated inhibition of HIV 1 suggests nucleolar trafficking of HIV-1 RNA, Proc Natl Acad Sci U S A (vol. 97), No. 16, pp. 8955-60.

[597] Cochrane, A. W.; Perkins, A. and Rosen, C. A. (1990): Identification of sequences important in the nucleolar localization of human immunodeficiency virus Rev: relevance of nucleolar localization to function, J Virol (vol. 64), No. 2, pp. 881-5.

[598] Emmett, S. R.; Dove, B.; Mahoney, L.; Wurm, T. and Hiscox, J. A. (2005): The cell cycle and virus infection, Methods Mol Biol (vol. 296), pp. 197-218.

[599] Emmott, E.; Rodgers, M. A.; Macdonald, A.; McCrory, S.; Ajuh, P. and Hiscox, J. A. (2010): Quantitative proteomics using stable isotope labeling with amino acids in cell culture reveals changes in the cytoplasmic, nuclear, and nucleolar proteomes in Vero cells infected with the coronavirus infectious bronchitis virus, Mol Cell Proteomics (vol. 9), No. 9, pp. 1920-36.

[600] Lam, Y. W.; Evans, V. C.; Heesom, K. J.; Lamond, A. I. and Matthews, D. A. (2010): Proteomics analysis of the nucleolus in adenovirus-infected cells, Mol Cell Proteomics (vol. 9), No. 1, pp. 117-30.

[601] Jarboui, M. A.; Bidoia, C.; Woods, E.; Roe, B.; Wynne, K.; Elia, G.; Hall, W. W. and Gautier, V. W. (2012): Nucleolar protein trafficking in response to HIV-1 Tat: rewiring the nucleolus, PLoS One (vol. 7), No. 11, p. e48702.

[602] Melen, K.; Kinnunen, L.; Fagerlund, R.; Ikonen, N.; Twu, K. Y.; Krug, R. M. and Julkunen, I. (2007): Nuclear and nucleolar targeting of influenza A virus NS1 protein: striking differences between different virus subtypes, J Virol (vol. 81), No. 11, pp. 5995-6006.

[603] Volmer, R.; Mazel-Sanchez, B.; Volmer, C.; Soubies, S. M. and Guerin, J. L. (2010): Nucleolar localization of influenza A NS1: striking differences between mammalian and avian cells, Virol J (vol. 7), p. 63.

[604] Everett, R. D. and Chelbi-Alix, M. K. (2007): PML and PML nuclear bodies: implications in antiviral defence, Biochimie (vol. 89), No. 6-7, pp. 819-30.

[605] Ishov, A. M.; Stenberg, R. M. and Maul, G. G. (1997): Human cytomegalovirus immediate early interaction with host nuclear structures: definition of an immediate transcript environment, J Cell Biol (vol. 138), No. 1, pp. 5-16.

[606] Wang, J.; Shiels, C.; Sasieni, P.; Wu, P. J.; Islam, S. A.; Freemont, P. S. and Sheer, D. (2004): Promyelocytic leukemia nuclear bodies associate with transcriptionally active genomic regions, J Cell Biol (vol. 164), No. 4, pp. 515-26.

[607] Kumar, P. P.; Bischof, O.; Purbey, P. K.; Notani, D.; Urlaub, H.; Dejean, A. and Galande, S. (2007): Functional interaction between PML and SATB1 regulates chromatin-loop architecture and transcription of the MHC class I locus, Nat Cell Biol (vol. 9), No. 1, pp. 45-56.

[608] Shiels, C.; Islam, S. A.; Vatcheva, R.; Sasieni, P.; Sternberg, M. J.; Freemont, P. S. and Sheer, D. (2001): PML bodies associate specifically with the MHC gene cluster in interphase nuclei, J Cell Sci (vol. 114), No. Pt 20, pp. 3705-16.

[609] Bernardi, R.; Scaglioni, P. P.; Bergmann, S.; Horn, H. F.; Vousden, K. H. and Pandolfi, P. P. (2004): PML regulates p53 stability by sequestering Mdm2 to the nucleolus, Nat Cell Biol (vol. 6), No. 7, pp. 665-72.

[610] Janderova-Rossmeislova, L.; Novakova, Z.; Vlasakova, J.; Philimonenko, V.; Hozak, P. and Hodny, Z. (2007): PML protein association with specific nucleolar structures differs in normal, tumor and senescent human cells, J Struct Biol (vol. 159), No. 1, pp. 56-70.

[611] Fu, L.; Gao, Y. S.; Tousson, A.; Shah, A.; Chen, T. L.; Vertel, B. M. and Sztul, E. (2005): Nuclear aggresomes form by fusion of PML-associated aggregates, Mol Biol Cell (vol. 16), No. 10, pp. 4905-17.

[612] St-Germain, J. R.; Chen, J. and Li, Q. (2008): Involvement of PML nuclear bodies in CBP degradation through the ubiquitin-proteasome pathway, Epigenetics (vol. 3), No. 6, pp. 342-9.

[613] Lafarga, M.; Berciano, M. T.; Pena, E.; Mayo, I.; Castano, J. G.; Bohmann, D.; Rodrigues, J. P.; Tavanez, J. P. and Carmo-Fonseca, M. (2002): Clastosome: a subtype of nuclear body enriched in 19S and 20S proteasomes, ubiquitin, and protein substrates of proteasome, Mol Biol Cell (vol. 13), No. 8, pp. 2771-82.

[614] Lallemand-Breitenbach, V.; Jeanne, M.; Benhenda, S.; Nasr, R.; Lei, M.; Peres, L.; Zhou, J.; Zhu, J.; Raught, B. and de The, H. (2008): Arsenic degrades PML or PML-RARalpha through a SUMO-triggered RNF4/ubiquitin-mediated pathway, Nat Cell Biol (vol. 10), No. 5, pp. 547-55.

[615] Eskiw, C. H.; Dellaire, G. and Bazett-Jones, D. P. (2004): Chromatin contributes to structural integrity of promyelocytic leukemia bodies through a SUMO-1-independent mechanism, J Biol Chem (vol. 279), No. 10, pp. 9577-85.

[616] Kepkay, R.; Attwood, K. M.; Ziv, Y.; Shiloh, Y. and Dellaire, G. (2011): KAP1 depletion increases PML nuclear body number in concert with ultrastructural changes in chromatin, Cell Cycle (vol. 10), No. 2, pp. 308-22.

[617] Geoffroy, M. C. and Chelbi-Alix, M. K. (2011): Role of promyelocytic leukemia protein in host antiviral defense, J Interferon Cytokine Res (vol. 31), No. 1, pp. 145-58.

[618] Ishov, A. M.; Vladimirova, O. V. and Maul, G. G. (2004): Heterochromatin and ND10 are cell-cycle regulated and phosphorylation-dependent alternate nuclear sites of the transcription repressor Daxx and SWI/SNF protein ATRX, J Cell Sci (vol. 117), No. Pt 17, pp. 3807-20.

[619] Kitagawa, D.; Kajiho, H.; Negishi, T.; Ura, S.; Watanabe, T.; Wada, T.; Ichijo, H.; Katada, T. and Nishina, H. (2006): Release of RASSF1C from the nucleus by Daxx degradation links DNA damage and SAPK/JNK activation, EMBO J (vol. 25), No. 14, pp. 3286-97.

[620] Van Damme, E.; Laukens, K.; Dang, T. H. and Van Ostade, X. (2010): A manually curated network of the PML nuclear body interactome reveals an important role for PML-NBs in SUMOylation dynamics, Int J Biol Sci (vol. 6), No. 1, pp. 51-67.

[621] Shen, T. H.; Lin, H. K.; Scaglioni, P. P.; Yung, T. M. and Pandolfi, P. P. (2006): The mechanisms of PML-nuclear body formation, Mol Cell (vol. 24), No. 3, pp. 331-9.

[622] Lang, M.; Jegou, T.; Chung, I.; Richter, K.; Munch, S.; Udvarhelyi, A.; Cremer, C.; Hemmerich, P.; Engelhardt, J.; Hell, S. W. and Rippe, K. (2010): Three-dimensional organization of promyelocytic leukemia nuclear bodies, J Cell Sci (vol. 123), No. Pt 3, pp. 392-400.

[623] Lin, D. Y.; Huang, Y. S.; Jeng, J. C.; Kuo, H. Y.; Chang, C. C.; Chao, T. T.; Ho, C. C.; Chen, Y. C.; Lin, T. P.; Fang, H. I.; Hung, C. C.; Suen, C. S.; Hwang, M. J.; Chang, K. S.; Maul, G. G. and Shih, H. M. (2006): Role of SUMO-interacting motif in Daxx SUMO modification, subnuclear localization, and repression of sumoylated transcription factors, Mol Cell (vol. 24), No. 3, pp. 341-54.

[624] Saitoh, N.; Uchimura, Y.; Tachibana, T.; Sugahara, S.; Saitoh, H. and Nakao, M. (2006): In situ SUMOylation analysis reveals a modulatory role of RanBP2 in the nuclear rim and PML bodies, Exp Cell Res (vol. 312), No. 8, pp. 1418-30.

[625] Everett, R. D.; Boutell, C. and Hale, B. G. (2013): Interplay between viruses and host sumoylation pathways, Nat Rev Microbiol (vol. 11), No. 6, pp. 400-11.

[626] Carracedo, A.; Ito, K. and Pandolfi, P. P. (2011): The nuclear bodies inside out: PML conquers the cytoplasm, Curr Opin Cell Biol (vol. 23), No. 3, pp. 360-6.

[627] Chelbi-Alix, M. K.; Pelicano, L.; Quignon, F.; Koken, M. H.; Venturini, L.; Stadler, M.; Pavlovic, J.; Degos, L. and de The, H. (1995): Induction of the PML protein by interferons in normal and APL cells, Leukemia (vol. 9), No. 12, pp. 2027-33.

[628] Guldner, H. H.; Szostecki, C.; Grotzinger, T. and Will, H. (1992): IFN enhance expression of Sp100, an autoantigen in primary biliary cirrhosis, J Immunol (vol. 149), No. 12, pp. 4067-73.

[629] Regad, T. and Chelbi-Alix, M. K. (2001): Role and fate of PML nuclear bodies in response to interferon and viral infections, Oncogene (vol. 20), No. 49, pp. 7274-86.

[630] Grotzinger, T.; Sternsdorf, T.; Jensen, K. and Will, H. (1996): Interferon-modulated expression of genes encoding the nuclear-dot-associated proteins Sp100 and promyelocytic leukemia protein (PML), Eur J Biochem (vol. 238), No. 2, pp. 554-60.

[631] Stadler, M.; Chelbi-Alix, M. K.; Koken, M. H.; Venturini, L.; Lee, C.; Saib, A.; Quignon, F.; Pelicano, L.; Guillemin, M. C.; Schindler, C. and et al. (1995): Transcriptional induction of the PML growth suppressor gene by interferons is mediated through an ISRE and a GAS element, Oncogene (vol. 11), No. 12, pp. 2565-73.

[632] Everett, R. D. (2006): Interactions between DNA viruses, ND10 and the DNA damage response, Cell Microbiol (vol. 8), No. 3, pp. 365-74.

[633] Chelbi-Alix, M. K.; Quignon, F.; Pelicano, L.; Koken, M. H. and de The, H. (1998): Resistance to virus infection conferred by the interferon-induced promyelocytic leukemia protein, J Virol (vol. 72), No. 2, pp. 1043-51.

[634] Iki, S.; Yokota, S.; Okabayashi, T.; Yokosawa, N.; Nagata, K. and Fujii, N. (2005): Serum-dependent expression of promyelocytic leukemia protein suppresses propagation of influenza virus, Virology (vol. 343), No. 1, pp. 106-15.

[635] Li, W.; Wang, G.; Zhang, H.; Zhang, D.; Zeng, J.; Chen, X.; Xu, Y. and Li, K. (2009): Differential suppressive effect of promyelocytic leukemia protein on the replication of different subtypes/strains of influenza A virus, Biochem Biophys Res Commun (vol. 389), No. 1, pp. 84-9.

[636] Halder, U. C.; Bhowmick, R.; Roy Mukherjee, T.; Nayak, M. K. and Chawla-Sarkar, M. (2013): Phosphorylation drives an apoptotic protein to activate antiapoptotic genes: paradigm of influenza A matrix 1 protein function, J Biol Chem (vol. 288), No. 20, pp. 14554-68.

[637] Puto, L. A. and Reed, J. C. (2008): Daxx represses RelB target promoters via DNA methyltransferase recruitment and DNA hypermethylation, Genes Dev (vol. 22), No. 8, pp. 998-1010.

[638] Croxton, R.; Puto, L. A.; de Belle, I.; Thomas, M.; Torii, S.; Hanaii, F.; Cuddy, M. and Reed, J. C. (2006): Daxx represses expression of a subset of antiapoptotic genes regulated by nuclear factor-kappaB, Cancer Res (vol. 66), No. 18, pp. 9026-35.

[639] Wimmer, P.; Schreiner, S. and Dobner, T. (2012): Human pathogens and the host cell SUMOylation system, J Virol (vol. 86), No. 2, pp. 642-54.

[640] Pal, S.; Rosas, J. M. and Rosas-Acosta, G. (2010): Identification of the non-structural influenza A viral protein NS1A as a bona fide target of the Small Ubiquitin-like MOdifier by the use of dicistronic expression constructs, J Virol Methods (vol. 163), No. 2, pp. 498-504.

[641] Xu, K.; Klenk, C.; Liu, B.; Keiner, B.; Cheng, J.; Zheng, B. J.; Li, L.; Han, Q.; Wang, C.; Li, T.; Chen, Z.; Shu, Y.; Liu, J.; Klenk, H. D. and Sun, B. (2011): Modification of nonstructural protein 1 of influenza A virus by SUMO1, J Virol (vol. 85), No. 2, pp. 1086-98.

[642] Santos, A.; Pal, S.; Chacon, J.; Meraz, K.; Gonzalez, J.; Prieto, K. and Rosas-Acosta, G. (2013): SUMOylation affects the interferon blocking activity of the influenza A nonstructural protein NS1 without affecting its stability or cellular localization, J Virol (vol. 87), No. 10, pp. 5602-20.

[643] Wang, J. and Schwartz, R. J. (2010): Sumoylation and regulation of cardiac gene expression, Circ Res (vol. 107), No. 1, pp. 19-29.

[644] Bekes, M. and Drag, M. (2012): Trojan horse strategies used by pathogens to influence the small ubiquitin-like modifier (SUMO) system of host eukaryotic cells, J Innate Immun (vol. 4), No. 2, pp. 159-67.

[645] Konig, R.; Stertz, S.; Zhou, Y.; Inoue, A.; Hoffmann, H. H.; Bhattacharyya, S.; Alamares, J. G.; Tscherne, D. M.; Ortigoza, M. B.; Liang, Y.; Gao, Q.; Andrews, S. E.; Bandyopadhyay, S.; De Jesus, P.; Tu, B. P.; Pache, L.; Shih, C.; Orth, A.; Bonamy, G.; Miraglia, L.; Ideker, T.; Garcia-Sastre, A.; Young, J. A.; Palese, P.; Shaw, M. L. and Chanda, S. K. (2010): Human host factors required for influenza virus replication, Nature (vol. 463), No. 7282, pp. 813-7.

[646] Sivaramakrishnan, G.; Sun, Y.; Tan, S. K. and Lin, V. C. (2009): Dynamic localization of tripartite motif-containing 22 in nuclear and nucleolar bodies, Exp Cell Res (vol. 315), No. 8, pp. 1521-32.

[647] Di Pietro, A.; Kajaste-Rudnitski, A.; Oteiza, A.; Nicora, L.; Towers, G. J.; Mechti, N. and Vicenzi, E. (2013): TRIM22 inhibits influenza A virus infection by targeting the viral nucleoprotein for degradation, J Virol (vol. 87), No. 8, pp. 4523-33.

[648] Everett, R. D. and Murray, J. (2005): ND10 components relocate to sites associated with herpes simplex virus type 1 nucleoprotein complexes during virus infection, J Virol (vol. 79), No. 8, pp. 5078-89.

[649] Everett, R. D. (2013): The spatial organization of DNA virus genomes in the nucleus, PLoS Pathog (vol. 9), No. 6, p. e1003386.

[650] Rivera-Molina, Y. A.; Rojas, B. R. and Tang, Q. (2012): Nuclear domain 10-associated proteins recognize and segregate intranuclear DNA/protein complexes to negate gene expression, Virol J (vol. 9), p. 222. U

[651] Oba, M. and Tanaka, M. (2012): Intracellular internalization mechanism of protein transfection reagents, Biol Pharm Bull (vol. 35), No. 7, pp. 1064-8.

[652] Rietdorf, J.; Ploubidou, A.; Reckmann, I.; Holmstrom, A.; Frischknecht, F.; Zettl, M.; Zimmermann, T. and Way, M. (2001): Kinesin-dependent movement on microtubules precedes actin-based motility of vaccinia virus, Nat Cell Biol (vol. 3), No. 11, pp. 992-1000.

[653] Arhel, N.; Genovesio, A.; Kim, K. A.; Miko, S.; Perret, E.; Olivo-Marin, J. C.; Shorte, S. and Charneau, P. (2006): Quantitative four-dimensional tracking of cytoplasmic and nuclear HIV-1 complexes, Nat Methods (vol. 3), No. 10, pp. 817-24.

[654] Mor, A.; Suliman, S.; Ben-Yishay, R.; Yunger, S.; Brody, Y. and Shav-Tal, Y. (2010): Dynamics of single mRNP nucleocytoplasmic transport and export through the nuclear pore in living cells, Nat Cell Biol (vol. 12), No. 6, pp. 543-52.

[655] Maul, G. G. and Deaven, L. (1977): Quantitative determination of nuclear pore complexes in cycling cells with differing DNA content, J Cell Biol (vol. 73), No. 3, pp. 748-60.

[656] Kalab, P. and Heald, R. (2008): The RanGTP gradient - a GPS for the mitotic spindle, J Cell Sci (vol. 121), No. Pt 10, pp. 1577-86.

[657] Roth, D. M.; Moseley, G. W.; Pouton, C. W. and Jans, D. A. (2011): Mechanism of microtubule-facilitated "fast track" nuclear import, J Biol Chem (vol. 286), No. 16, pp. 14335-51.

Acknowledgements

The present work was accomplished with the support of various people whom I would like to thank here.

At first, I would like to express my greatest thanks to **Prof. Dr. Andreas Herrmann** for the opportunity to work in his lab and to venture this journey into the fascinating world of Influenza viruses, for his motivation and enduring support throughout the entire time. I am very grateful for his advice, for his confidence, and for providing a supportive environment in the lab, encouraging to explore and to pursue own ideas.

I am also very grateful to **PD Dr. Michael Veit** for giving precious advice and support to this project and for many instructive and enjoyable discussions. I am further thankful for the technical support and for the time he kindly invested to become acquainted with this project and to contribute to its progress.

I would like to thank **PD Dr. Thorsten Wolff** for his help with upcoming questions and for reviewing this work.

I am greatly indebted to **Dr. Bastian Thaa** for his kind support and encouragement during the entire duration of the project, for numerous fruitful discussions and for sharing his experience in the field of virology, including some excellent protocols. I most sincerely thank Bastian also for careful and critical proofreading of this manuscript.

I would especially like to thank **Dr. Thomas Korte** for assisting with all microscopic issues and for taking the time to discuss arising questions.

Special thanks also go to **Matthias Schade** and **Dr. Martin Seeger** for programming software tools that facilitated the analysis of tracking data, and further to Matthias Schade for proofreading parts of this work.

I am indebted to **Dr. Maik Lehmann** for the technical support by electron microscopy and for interesting and helpful discussions.

I am obliged to **Gudrun Habermann, Sabine Schiller and Silvia Kietzmann** for their kind and valuable help and for a great job keeping the daily lab life running.

Further, I would like to thank the present and former members of the Group of Molecular Biophysics. In particular, I would like to thank the following people: **Gabriele Schreiber** for sharing her experience and technical expertise and for her help to analyze occurring problems, **Silvia Scolari** for introducing me into the world of cells and molecular biology, **Christian Sieben** for vivid discussions on the mysteries of Influenza viruses and for support, **Roland Schwarzer** for his kind and valuable help and for sharing his scientific curiosity, **Daniela Serien and Christian Ebbesen** for technical support, and those and all others I would like to thank for the supportive and enjoyable atmosphere, which made every day at work worthwhile and enjoyable. Most sincere thanks also go to **Dr. Peter Müller** for accommodating me in his office where it was easy to keep a clear head and an open mind, for sharing his expertise and providing the essential sense humor for the daily challenges.

And finally, I would like to express my gratitude to **my family** and to **Verena Kiewardt** for always caring and supporting me.

Publications

Manuscripts

Höfer C.T., Herrmann A., Müller P. (2010). Use of liposomes for studying interactions of soluble proteins with cellular membranes. *Methods Mol Biol* **606**, 69-82

Nikolaus J., Czapla S., Möllnitz K., Höfer C. T., Herrmann A., Wessig P., Müller P. (2011). New molecular rods - characterization of their interaction with membranes. *Biochim Biophys Acta* **1808** (12), 2781-2788

Plazzo A.P.*, Höfer C.T.*, Jicsinszky L., Fenyvesi E., Szente L., Schiller J., Herrmann A., Müller P. (2012). Uptake of a fluorescent methyl-β-cyclodextrin via clathrin-dependent endocytosis. *Chem Phys Lip* **165**(5), 505-511 (*contributed equally)

Li S., Sieben C., Ludwig K., Höfer C.T., Chiantia S., Herrmann A., Eghiaian F., Schaap I.A.T. (2014). pH-Controlled Two-Step Uncoating of Influenza Virus. *Biophys J* **106**(7), 1447-1456

Hilsch M., Goldenbogen B., Sieben C., Höfer C.T., Rabe J., Klipp E., Herrmann A. Chiantia S. (2014). Influenza A Matrix Protein M1 Multimerizes upon Binding to Lipid Membranes. *Biophys J* **107**(4), 912-923

Talks

"The role of Influenza A virus ribonucleoprotein complexes in virus assembly", *6th International Virus Assembly Symposium*, Crete (Greece), 3rd – 7th May 2009

"Characterization of the Influenza A nucleoprotein and the viral ribonucleoprotein complexes with regard to virus assembly" *Annual Meeting of the Marie Curie ITN Network "Virus Entry"*, Berlin (Germany), 10th – 11th June 2010

Posters

Höfer C.T.*, Jungnick N.*, Herrmann A. "Interaction of Influenza A virus M1 and RNPs with model membranes", *52nd Annual Meeting of the Biophysical Society*, Long Beach, CA (U.S.A), 2nd – 6th February 2008 (*contributed equally)

Höfer C.T., Herrmann A., "The Role of Influenza A Virus Ribonucleoprotein Complexes in Virus Assembly", *International Symposium - Membranes and Modules*, Berlin (Germany), 10th – 13th December 2009

Höfer C.T., Herrmann A. "Tracking Influenza A Virus Ribonucleoprotein Complex Components by Photoactivatable Fluorophores", *54th Annual Meeting of the Biophysical Society*, San Francisco, CA (U.S.A.), 20th – 24th February 2010

Höfer C.T., Herrmann A. "Approaches to characterize the intracellular trafficking of the Influenza virus nucleoprotein", *21st Annual Meeting of the Society for Virology (GfV-Gesellschaft für Virologie)*, Freiburg (Germany), 23rd - 26th March 2011

Höfer C.T., Veit M., Herrmann A., "Influenza A virus nucleoprotein targets specific subnuclear domains", *3rd International Influenza Meeting*, Münster (Germany), 2nd – 4th September 2012

Eidesstattliche Erklärung

Hiermit erkläre ich, die vorliegende Arbeit selbständig und ohne fremde Hilfe verfasst und nur die angegebene Literatur verwendet zu haben.

Ein Teil der beschriebenen Ergebnisse wurde in Zusammenarbeit mit anderen Mitarbeitern der Arbeitsgruppe Molekulare Biophysik erzielt. Diese sind entsprechend gekennzeichnet.

Ich besitze keinen entsprechenden Doktorgrad und habe mich anderwärts nicht um einen Doktorgrad beworben.

Die dem Promotionsverfahren zugrunde liegende Promotionsordnung ist mir bekannt.

_____ _____

Ort, Datum (Chris Tina Höfer)